Imperial College London

Toughening mechanisms of block copolymer and graphene nanoplatelet modified epoxy polymers

Huang Ming Chong

Department of Mechanical Engineering

Imperial College London

A thesis submitted for the degree of Doctor of Philosophy

of Imperial College London and the Diploma of Imperial College

February 2015

Declaration of Originality

I, Huang Ming Chong, hereby declare that the work presented in this thesis is of my own work and that any material from published or unpublished work of others were fully acknowledged and clearly referenced.

I declare that this thesis has not been submitted for another degree or diploma to any other university or institution.

Copyright Declaration

The copyright of this thesis rests with the author and is made available under a Creative Commons Attribution-Non Commercial-No Derivatives licence. Researchers are free to copy, distribute or transmit the thesis on the condition that they attribute it, that they do not use it for commercial purposes and that they do not alter, transform or build upon it. For any reuse or distribution, researchers must make clear to others the license terms of this work.

Abstract

Epoxies are thermosetting polymers that have uses in a multitude of industrial and consumer applications. The high crosslink density of epoxies gives rise to exceptional mechanical, chemical and heat resistance properties. However, this also results in low toughness, i.e. poor resistance to crack initiation and propagation. The present work discusses the toughening mechanisms of four epoxy polymers modified with several novel modifiers, which create different morphologies.

Nanoscale core-shell rubber (CSR) particles are attractive as epoxy tougheners because they remain well dispersed even at high loadings, do not affect the T_g and most importantly, provide good toughness improvement (900% increase in G_{IC} for a low T_g epoxy system). For a given weight percentage of modifiers, the tensile and compressive properties were better maintained for the much smaller CSR particles as these particles have a lower rubber content. However, the fracture performance of the CSR modified epoxies appear to be limited in low T_g epoxies. Examination of the fracture surfaces using high resolution scanning electron microscopy (SEM) show less plastic void growth due to the higher stresses required to initiate cavitation.

Amphiphilic triblock copolymers (BCP) represent the next generation of phase separating materials for toughening epoxies. The structure/property relationships of epoxies modified with symmetric and asymmetric triblock copolymers were determined. The complex 3D nanostructures that were created offer greatly increased fracture performance over conventional toughening agents for very tough epoxies, while minimising the decrease in mechanical properties. A measured increase in G_{IC} of 1600% was noted. This increased to 2250% when a further addition of silica nanoparticles was considered. This complex nanostructure allows for more gradual and extensive plastic deformation of the epoxy matrix as shear yielding and plastic void growth initiated by debonding at the BCP/epoxy interface. The morphology was further studied numerically using a phase field model which identified parameters that control the evolution of the microstructure.

Graphene nanoplatelets (GNP) vary in size and quality depending on the method of preparation. Thus, a range of GNPs with different platelet sizes, thicknesses and aspect ratios were used to identify the properties that control the mechanical and fracture performance of GNP modified epoxies. The bulk GNP geometry and chemical makeup were first characterised. The optimum dispersion method was determined through systematic experiments using two solvents and an ultrasonic probe, and examined using SEM. Well dispersed GNPs improved the Young's modulus, whereas the fracture energy increased for both well dispersed and poorly dispersed GNPs.

Acknowledgements

Firstly, I would like to thank my supervisor, Dr. Ambrose Taylor, for the support and guidance he has provided me during my time as a PhD student. He has been extremely generous with his time, always being available to help whenever I have a problem or to have a discussion.

I would also like to thank Dr. Stephan Sprenger of Evonik Hanse, Dr. Thomas Fine of Arkema, Mr. Doug Sober of Kaneka and Mr. Ian Walters of Haydale for the supply of materials. Special thanks are also reserved for the Department of Mechanical Engineering at Imperial College London for funding this PhD.

Of course I cannot forget the help I had early on in this project from Seung, Kunal, Jing, James, Giannis and Ruth. Special thanks also go to my friends and colleagues in the division: Declan, Gani, Omer, Idris, Diego, Mark, Paul, Yats, Alex, Tino, Jo and Tasnuva for the many useful discussions and laughs we have had over the years.

Last, but definitely not the least, I am extremely grateful for my family and friends for the encouragement and support they have always provided, and to Tieng, for her love and always being there when I needed her.

Table of Contents

Nomenclature **ix**

1 Introduction **1**
1.1 Background . . . 1
1.2 Aims and objectives . . . 2
1.3 Thesis structure . . . 2

2 Literature Review **4**
2.1 Introduction . . . 4
2.2 Toughening of bulk epoxy polymers . . . 4
2.2.1 Toughening by chemical modification . . . 5
2.2.2 Toughening by addition of second phase . . . 5
2.2.2.1 Rubber particles . . . 5
2.2.2.2 Thermoplastic modifiers . . . 7
2.2.2.3 Block copolymers . . . 9
2.2.2.4 Phase separation . . . 14
2.2.2.5 Phase field model . . . 16
2.2.2.6 Toughening mechanisms for soft modifiers . . . 25
2.2.2.7 Inorganic rigid particles . . . 30
2.2.2.8 Organic rigid particles . . . 31
2.2.2.9 Dispersion methods for carbon nanotubes and graphene nanoplatelets . . . 34
2.2.2.10 Toughening mechanisms for rigid modifiers . . . 37
2.2.2.11 Influence of crosslink density . . . 40
2.2.2.12 Influence of particle size . . . 42
2.2.2.13 Influence of particle/matrix adhesion . . . 44
2.2.2.14 Hybrid toughening . . . 46
2.3 Toughening of fibre-reinforced polymer composites . . . 50
2.4 Analytical modelling of composite stiffness . . . 52
2.4.1 Bounds . . . 53
2.4.2 Spherical particles . . . 54

2.4.3 Platelets . . . 56
2.4.4 Co-continuous structures . . . 56
2.5 Analytical modelling of fracture energy . . . 58
2.5.1 Rubber particle toughening . . . 58
2.5.2 Rigid particle toughening . . . 61
2.6 Finite element modelling studies . . . 62
2.7 Summary . . . 64

3 Materials and Manufacturing 65
3.1 Introduction . . . 65
3.2 Epoxy resins . . . 65
3.2.1 Anhydride cured DGEBA . . . 65
3.2.2 Low viscosity epoxy . . . 66
3.2.3 Polyether-amine cured DGEBA . . . 66
3.2.4 Polyether-amine cured DGEBA/F . . . 66
3.3 Modifiers . . . 68
3.3.1 Block copolymers . . . 68
3.3.2 Reactive liquid rubber particles . . . 69
3.3.3 Core shell rubber particles . . . 69
3.3.4 Silica nanoparticles . . . 70
3.3.5 Graphene nanoplatelets . . . 71
3.4 Manufacturing . . . 75
3.4.1 Bulk epoxy polymer . . . 75
3.4.2 Thin films . . . 76
3.4.3 Fibre composites . . . 77

4 Experimental Methods 79
4.1 Introduction . . . 79
4.2 Characterisation . . . 79
4.2.1 Dynamic mechanical analysis . . . 79
4.2.2 Rheology . . . 80
4.2.3 Atomic force microscopy . . . 80
4.2.4 Scanning electron microscopy . . . 81
4.2.5 Optical microscopy . . . 82
4.2.6 Image analysis . . . 82
4.2.7 Characteristic lengths . . . 85
4.2.8 Particle dispersion . . . 85
4.2.9 Laser light spectroscopy . . . 88
4.2.10 X-ray photoelectron spectroscopy . . . 88

4.2.11 X-ray diffraction . . . 88
4.3 Bulk mechanical tests . . . 89
4.3.1 Tension . . . 89
4.3.2 Single edge notched bending . . . 92
4.3.3 Plane strain compression . . . 93
4.4 Fibre composites mechanical tests . . . 95
4.4.1 Flexure . . . 95
4.4.2 Short beam shear strength . . . 96
4.4.3 Mode I interlaminar fracture energy . . . 96

5 Nanoscale core-shell rubber modified epoxy polymers 99
5.1 Introduction . . . 99
5.2 Morphology . . . 100
5.2.1 Core-shell rubber . . . 101
5.2.2 CTBN rubber . . . 103
5.2.3 Area disorder . . . 106
5.3 Glass transition temperature . . . 107
5.4 Tensile properties . . . 108
5.5 Compressive properties . . . 113
5.6 Fracture properties . . . 116
5.7 Fractography . . . 118
5.7.1 Core-shell rubber . . . 119
5.7.2 CTBN rubber . . . 121
5.8 Modelling fracture energy . . . 123
5.9 Conclusions . . . 127

6 Asymmetric triblock copolymer modified epoxy polymers 130
6.1 Introduction . . . 130
6.2 Morphology . . . 131
6.2.1 E21 SBM . . . 131
6.2.2 E41 SBM . . . 137
6.2.3 Area disorder . . . 141
6.3 Glass transition temperature . . . 142
6.4 Tensile properties . . . 145
6.5 Compressive properties . . . 150
6.6 Fracture properties . . . 153
6.7 Fractography . . . 156
6.7.1 E21 SBM . . . 156
6.7.2 E41 SBM . . . 162

6.8 Characteristic lengths . . . 166
6.9 Modelling fracture energy . . . 167
6.10 Carbon fibre composites . . . 170
6.10.1 Rheology . . . 170
6.10.2 Morphology . . . 171
6.10.3 Mechanical properties . . . 172
6.10.4 Fracture properties . . . 172
6.10.5 Fractography . . . 174
6.11 Conclusions . . . 176

7 Symmetric triblock copolymer modified epoxy polymers 179
7.1 Introduction . . . 179
7.2 Morphology . . . 180
7.2.1 M52N MAM . . . 180
7.2.2 M22N MAM . . . 185
7.2.3 Area disorder . . . 187
7.3 Glass transition temperature . . . 187
7.4 Tensile properties . . . 190
7.5 Compressive properties . . . 193
7.6 Fracture properties . . . 195
7.7 Fractography . . . 197
7.7.1 M52N MAM . . . 198
7.7.2 M22N MAM . . . 203
7.8 Characteristic lengths . . . 204
7.9 Conclusions . . . 205

8 Graphene nanoplatelet modified epoxy polymers 208
8.1 Introduction . . . 208
8.2 GNP Dispersion . . . 209
8.3 Particle size analysis . . . 215
8.4 XPS Spectra . . . 221
8.5 Morphology . . . 222
8.6 Glass transition temperature . . . 230
8.7 Tensile properties . . . 231
8.8 Compressive properties . . . 242
8.9 Fracture properties . . . 245
8.10 Fractography . . . 248
8.11 Modelling fracture energy . . . 254
8.12 Conclusions . . . 260

9 System comparisons and Discussion **263**
9.1 Introduction . . . 263
9.2 Rubber modified epoxies . . . 264
9.2.1 Morphology . . . 264
9.2.2 Tensile properties . . . 267
9.2.3 Fracture properties . . . 270
9.3 Block copolymer modified epoxies . . . 274
9.3.1 Morphology . . . 274
9.3.2 Comparison with phase field model . . . 279
9.3.3 Tensile properties . . . 284
9.3.4 Fracture properties . . . 285
9.4 Discussion . . . 286
9.4.1 Effect of morphology on properties . . . 287
9.4.2 Modifier composition . . . 292
9.4.3 Addition of silica nanoparticles . . . 293
9.5 Graphene nanoplatelets . . . 294
9.6 Conclusions . . . 297

10 Conclusions **298**

11 Future Work **302**
11.1 Rubber particles . . . 302
11.2 Block copolymer . . . 303
11.3 Graphene nanoplatelets . . . 304

References **305**

List of Figures **328**

List of Tables **340**

Appendix A Mechanical and fracture properties of epoxy polymers **347**

Appendix B Compressive properties of epoxy polymers **357**

Appendix C Components for Mori-Tanaka model **366**

Appendix D Crack deflection model by Faber and Evans **368**

List of Publications **370**

Nomenclature

Abbreviations

2D	Two-dimensional
3D	Three-dimensional
at.%	Atomic percentage
AD	Area disorder
AEW	Anhydride equivalent weight
AFM	Atomic force microscope
AHEW	Amine hydrogen equivalent weight
ASTM	American Society for Testing and Materials
BCP	Block copolymer
BI	Poly(butadiene)-polyisoprene
BS	British Standard
CFRP	Carbon fibre reinforced polymer
CNT	Carbon nanotube
CSR	Core shell rubber
CTBN	Carboxyl terminated butadiene acrylonitrile
CVD	Chemical vapor deposition
DCB	Double cantilever beam
DGEBA	Diglycidyl ether of bisphenol-A
DGEBF	Diglycidyl ether of bisphenol-F
DIC	Digital image correlation
DMA	Dynamic mechanical analysis
DMA	N,N-dimethylacrylamide
EEW	Epoxy equivalent weight
FCC	Face-centred cubic
FEA	Finite element analysis
FEGSEM	Field emission gun scanning electron microscope

FIB	Focused ion beam
FRP	Fibre reinforced polymer
FWHM	Full width at half maximum
GIMP	GNU Image Manipulation Program
GNP	Graphene nanoplatelet
IPN	Interpenetrating network
ISO	International Organization for Standardization
LEFM	Linear elastic fracture mechanics
LLS	Laser light spectroscopy
MAM	Poly(methyl methacrylate)-b-poly(butylacrylate)-b-poly(methyl methacrylate)
MDI	Methylene diphenyl diisocyanate
MGI	Poly(methyl acrylate-glycidyl methacrylate)-polyisoprene
MWCNT	Multiwalled carbon nanotubes
NCF	Non-crimp fabric
NMP	N-methyl-pyrrolidone
NS	Silica nanoparticles
PB	Polybutadiene
PBuA	Poly(butylacrylate)
PC	Polycarbonate
PEE	Poly(ethyl ethylene)
PEEK	Poly(ether ether ketone)
PEO	Poly(ethylene oxide)
PEP	Poly(ethylene-alt-propylene)
PES	Polyethersulphone
PET	Poly(ethylene terephthalate)
phr	Parts per hundred resin
PMMA	Poly(methyl methacrylate)
PS	Polystyrene
PSC	Plane strain compression
PTFE	Poly(tetrafluoroethylene)
QI	Quasi-isotropic
RIFT	Resin infusion under flexible tooling
RVE	Representative volume element
SANS	Small-angle neutron scattering
SAXS	Small-angle X-ray scattering
SBM	Polystyrene-b-polybutadiene-b-poly(methyl methacrylate)

SEM	Scanning electron microscope
SENB	Single edge notched bending
SPM	Scanning probe microscope
TEM	Transmission electron microscope
TGAP	Triglycidyl amino phenol
THF	Tetrahydrofuran
vol%	Volume percentage
wt%	Weight percentage
XPS	X-ray photoelectron spectroscopy
XRD	X-ray diffraction

English Alphabet

a	Crack length
a	Surface area of micelle core
A_o	Initial cross-sectional area
A_p	Minimum cross-sectional area
AR	Aspect ratio
b	Width
B	Thickness
B_c	Compressed thickness
c	Concentration
C	Compliance
$C(d)$	Cumulative distribution
d	Particle diameter
E'	Storage modulus
E''	Loss modulus
E_{11}	Composite modulus parallel to loading direction
E_{33}	Composite modulus perpendicular to loading direction
E_c	Compressive modulus
E_c	Composite modulus
E_f	Flexural modulus
E_L	Lower bound of composite modulus
E_m	Matrix modulus
E_p	Particle modulus
E_r	Equilibrium modulus in the rubbery region

E_t	Young's modulus
E_U	Upper bound of composite modulus
f	Friction coefficient
$f(c)$	Free energy density of material with composition, c
F	Load
F	Large displacement correction
G	Shear modulus
G_{CU}	Fracture energy of unmodified epoxy polymer
$G(d)$	Differential distribution
G_{HS}	Hashin-Shtrikman bound shear modulus
G_i	Shear modulus of phase i
G_i	Interfacial fracture energy
G_{IC}	Fracture energy
$G_{IC(composite)}$	Composite mode I fracture energy
G_p	Particle shear modulus
G_Q	Conditional fracture energy
G_u	Epoxy shear modulus
$G(c)$	Free energy of the system
h	Thickness
H	Stress concentration factor
k_E	Einstein coefficient
K	Stress intensity factor
K	Bulk modulus
K	Dimensionless shape factor
K_c	Composite bulk modulus
K_{CU}	Fracture toughness of unmodified epoxy
K_{HS}	Hashin-Shtrikman bound bulk modulus
K_{IC}	Fracture toughness
K_p	Particle bulk modulus
K_Q	Conditional fracture toughness
K_u	Epoxy bulk modulus
K_{vm}	Maximum von Mises stress concentration around particle
l_0	Length of solvent-phobic block
L	Span
L	Lateral size of platelets
L_v	Void length
L_d	Debonded length

L_o	Gauge length
M	Mobility
M_n	Molecular weight
M_{nc}	Molecular weight between crosslinks
N	Load block correction
N	Number of platelets per m^2
N_i	Number of molecules of i
p	Pressure
P	Load
P	Packing parameter
P_Q	Conditional load
r_p	Particle radius
r_{pv}	Void radius
r_{pz}	Irwin plastic zone radius
r_y	Increased plastic zone size due to stress concentration
r/r_{max}	Ratio of random vector length to the side length of the domain
q	Front factor
R	Universal gas constant
S_{ijkl}	Eshelby tensors
T_g	Glass transition temperature
t	Thickness
t_v	Void thickness
U	Corrected energy
U_e	Internal strain energy
U_p	Stationary value of Hashin-Shtrikman functional
v	Volume of micelle core
v_f	Volume fraction
v_{max}	Maximum possible particle volume fraction
W	Width
x_o	Embedded platelet length

Greek Alphabet

α	Coefficient of particle/matrix adhesion
β	Full width at half maximum
γ	Constant related to thickness of interfacial transition

$\dot{\gamma}$	Shear rate
γ_f	Failure strain
Δ	Crack length correction
ΔG_{cd}	Energy contribution from crack deflection
ΔG_{db}	Energy contribution from debonding
ΔG_m	Gibbs free energy of mixing
ΔG_{po}	Energy contribution from pull-out
ΔG_r	Energy contribution from rubber bridging
ΔG_s	Energy contribution from localised shear band yielding
ΔG_v	Energy contribution from void growth
ΔL	Increase in specimen length between the gauge marks
δ	Displacement
δ_{max}	Maximum displacement attained
δ_{offset}	Displacement at zero load
δ_{tc}	Crack opening displacement
ε	True strain
ε_{axial}	Axial strain
ε_B	Tensile strain at break
ε_c	True compressive strain
ε_E	Engineering strain
ε_f	Compressive failure strain
ε_f	Flexural strain
ε_t	Tensile yield strain
ε_{trans}	Transverse strain
ε_{yc}	Compressive yield strain
ζ	Shape factor
η	Viscosity
θ	Scattering angle
λ	Wavelength
μ_A	Standard deviation of areas of Delaunay triangles
μ_m	Pressure-dependent yield stress parameter
ν	Poisson's ratio
ρ	Density
σ	True stress
σ_a	Particle/matrix adhesion strength
σ_A	Mean area
σ_E	Engineering stress

σ_c	True compressive stress
σ_f	Compressive failure stress
σ_f	Flexural stress
σ_f	Fracture stress
σ_0	Applied stress
σ_t	Tensile true strength
σ_y	Tensile yield stress
σ_{yc}	Compressive yield stress
τ	Shear stress
τ	Surface-to-surface interparticle distance
τ_i	Interfacial shear strength
τ_m	Apparent interlaminar shear strength
Φ	Energy calibration factor
ϕ	Order parameter
ϕ^*	Maximum packing fraction
ϕ_p	Particle volume fraction
ψ	Overall toughening contribution from particles
ψ^*	Maximum filled area in plane section

Chapter 1

Introduction

1.1 Background

Epoxy polymers are used extensively in industrial applications such as adhesives, coatings and composite materials. This is because epoxies have properties that make them attractive for high performance applications, including high strength and modulus, creep performance, thermal and chemical resistance. A wide range of commercial epoxy resins and curing agents are currently available, which allows for the optimisation for specific applications using an appropriate combination of both.

The strong hydrogen bonding [1] and highly polar nature [2] of epoxy resin allows it to adhere strongly to dissimilar materials. This is attractive for materials that may not be easily bonded using traditional mechanical fasteners or welding techniques, such as fibre composites. The liquid nature of most epoxy resins during processing means that good wetting of the surfaces is possible such that the stress is more evenly distributed across the whole joint.

One of the major drawbacks of unmodified epoxy polymers is that they are inherently brittle materials due to the highly crosslinked nature of their molecular structure. Early studies have shown that the addition of rubber particles can greatly improve the fracture toughness of epoxy polymers [3, 4], at the expense of processability. More recently, the emergence of nanoscale modifiers has attracted much attention, whether by preformed particles [5] or phase separating structures [6]. The morphology of these new modifiers has been studied extensively, however, the contributions of such complex microstructures to the mechanical and fracture performance is still not well understood. The microstructures that these new modifiers provide are complex, and a

proper understanding of how these are related to the composite performance will these microstructures to be exploited.

1.2 Aims and objectives

The main objective of this study was to investigate the morphology, mechanical properties, fracture toughness and toughening mechanisms of epoxy polymers modified with a range of novel modifiers. These modifiers include nanoscale rubber particles and two types of triblock copolymers (BCP). Four different epoxy polymers were used to compare the effect that these modifiers have in different epoxy systems. Silica nanoparticles were also introduced to the core-shell rubber nanoparticle and block copolymer modified epoxies, which was found to further enhance the mechanical and fracture properties for some of the epoxy systems.

Graphene based materials have shown promising results as functional materials, however the transfer of the extremely high stiffness and strength of graphene to a composite material still proves to be difficult to achieve. The low cost of graphene nanoplatelets relative to other carbon based modifiers, such as carbon nanotubes and single layer graphene, make them attractive for large production of bulk materials. To study the effects of graphene nanoplatelet (GNP) in modified epoxies, GNPs of different lateral size, thickness, aspect ratio and composition were incorporated into an anhydride cured DGEBA epoxy.

The structure/property relationships of these modified epoxies were determined at different weight percentages. Bulk epoxy polymers were manufactured from the constituent components and the morphology of these modified epoxies was characterised. The mechanical and fracture properties were then measured under quasi-static conditions and the toughening mechanisms induced by the modifiers were investigated using high resolution microscopy techniques.

1.3 Thesis structure

The structure of this thesis is organised by the different tougheners examined. The next chapter contains a review of the existing literature on subjects that are closely related to this PhD project. As explained previously, there have been numerous studies on toughening epoxy polymers and these will be reviewed, followed by a summary of the

relevant modelling techniques to predict the tensile and fracture properties of modified epoxies.

The complete list of materials and manufacturing techniques used in this study is detailed in Chapter 3 and the experimental methods are described fully in Chapter 4. This includes the mechanical testing and microscopy techniques used to characterise the materials and obtain micrographs of the fracture surfaces.

The results are presented in Chapters 5, 6, 7 and 8. Chapter 5 contains the experimental results for the nanoscale core-shell rubber and hybrid rubber-silica nanoparticle modified epoxy polymers. Three different epoxy systems were used in this study and the performance of these rubber nanoparticles was compared to conventional micron-sized CTBN rubber particles.

Chapters 6 and 7 describes the use of symmetric and asymmetric triblock copolymers, respectively, as toughening modifiers in different epoxy systems. For each of the triblock copolymers, two grades of BCPs with different block ratios and molecular weights were investigated, giving a total of four BCP modifiers. The morphology of these materials was found to be complex and the structure/property relationships were determined and discussed.

Chapter 8 presents the results of the graphene nanoplatelet modified epoxies. The first part of this chapter outlines the approach taken to optimise the dispersion of GNPs in an epoxy resin. This is followed by a characterisation of the bulk GNPs through a particle size and surface chemical analysis. The morphology, mechanical and fracture properties, and toughening mechanisms of the GNP modified epoxies are presented. The tensile and fracture properties were also modelled analytically by modifying existing models in the literature.

Chapter 9 reviews and discusses the results from Chapters 5 to 7, in addition to relevant results from previous work on different epoxy systems, to provide a full understanding of these modifier types.

The main findings are summarised in Chapter 10, followed by recommendations for future work related to the areas presented in this thesis in Chapter 11.

Chapter 2

Literature Review

2.1 Introduction

The use of epoxy polymers is increasing in areas such as aerospace and automotive, where high performance lightweight structures are essential. As such, there has been an extensive amount of research dedicated to understanding the mechanical properties of epoxy polymers, as bulk materials, adhesives, coatings and fibre composites. This chapter will provide a review of the mechanical and fracture performance of modified epoxy polymers as bulk materials and fibre composites. The finite element studies and analytical models that have been undertaken to further understand the toughening mechanisms taking place will also be discussed.

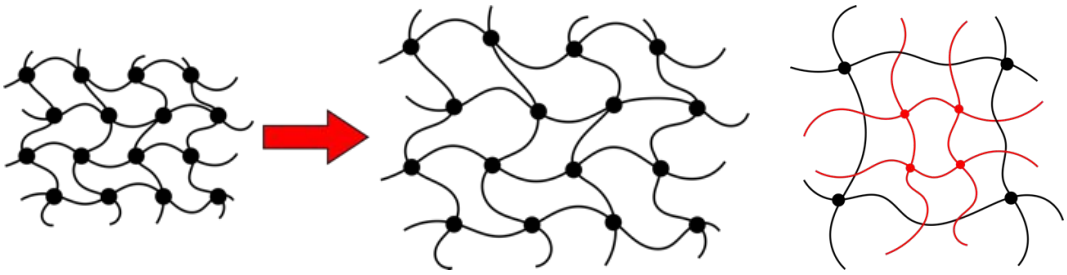
2.2 Toughening of bulk epoxy polymers

Ductile fracture can be promoted by plasticisation of the glassy polymer, giving a more flexible backbone structure. However, this greatly reduces the glass transition temperature and modulus, which can be undesirable. The introduction of a second phase is generally accepted to be a more effective method for the improvement of the fracture performance by initiating other toughening mechanisms to create a larger damage zone ahead of the crack tip [7].

2.2.1 Toughening by chemical modification

Ductile fracture mechanisms such as tearing or shear yielding can be promoted by increasing the chain length by using chain extenders such as aniline [8] or poly(ethylene glycol) [9]. These reduce the crosslink density as shown in Figure 2.2.1(a).

Creating interpenetrating networks (IPN) can also toughen brittle epoxy polymers. The physical interlocking between polymer chains means that although the networks are not covalently bonded to each other, their chemical bonds must be broken to separate the network [10]. In order to create IPNs, the second polymer needs to be initially miscible with the epoxy. Several authors have reported the use of elastomers, such as polyurethane [11], or thermosets, such as cyanate esters [12] and unsaturated polyesters [13, 14] to create IPNs.



(a) Chain extension

(b) Interpenetrating network (IPN) [15]

Figure 2.2.1: Toughening of epoxy polymers by chemical modification.

While there have been some improvements in toughness from chemical modification, there is generally a significant reduction in T_g and modulus, hence these chemical modification methods are not widely used. The next section will discuss the toughening of epoxy polymers by the addition of a second phase.

2.2.2 Toughening by addition of second phase

2.2.2.1 Rubber particles

Rubber particles are the most commonly used modifier for toughening epoxy polymers in research [16, 17] and industry [2]. The first recorded use of rubber modified plastics was by Aylsworth [18] to create a tough, crosslinked material for Thomas Edison's phonograph records. The work by Sultan and McGarry [3] was the first to utilise reactive liquid rubbers to modify brittle epoxy polymers. The butadiene-acrylonitrile

elastomer phase separated into well dispersed micrometre sized particles during the curing process.

The reactive liquid rubbers are typically pre-reacted in epoxy as an adduct [19] with functional end groups to improve compatibility with the epoxy resin, e.g. carboxyl-terminated butadiene-acrylonitrile (CTBN). These liquid rubbers phase separate out of the epoxy resin during the curing process to form rubber particles. Alternatively, rubber modification of epoxy polymers can also be achieved using pre-formed elastomeric particles [20, 21]. These pre-formed particles are usually formed with a rubbery core surrounded by a thin glassy shell which prevents the rubber particles from merging with each other. The core material can be made of butadiene, butyl(acrylate), styrene-butadiene or siloxane, with poly(methyl methacrylate) (PMMA) commonly used as the shell material.

The phase separated rubber can be advantageous over pre-formed core shell rubber (CSR) particles as the CSR particles are prone to agglomeration. However, there is a significant viscosity penalty when using high volume fractions of CTBN rubber. Another disadvantage of reaction-induced phase separated rubber particles is the dependency of the particle size on the curing conditions. Competition between the phase separation and crosslinking rate of reactions makes it difficult to control particle size. The T_g can also be reduced significantly if the reactive liquid rubber does not undergo phase separation, effectively plasticising the epoxy.

Ultimately, rubber particle toughening is used because it is a highly effective method for toughening some commercial epoxies. The fracture energy of epoxy polymers modified using micrometre sized rubber particles can be increased by up to 3500% [22–25] for lightly crosslinked epoxies, which corresponds to a G_{IC} value of approximately 5000 J/m^2. Giannakopoulos *et al.* [20] also showed that CSR particles were as effective as the liquid reactive rubbers in toughening a higher T_g epoxy polymer (an anhydride cured DGEBA with a T_g of 145°C); an increase in G_{IC} of 670% without reducing the T_g was reported. The Young's modulus and yield stress typically exhibit a negative correlation with rubber content, as shown in Figure 2.2.2, due to the low modulus and strength of the rubber.

Kinloch *et al.* [27] studied the effect of temperature and test rate on unmodified and rubber modified epoxy. For their studies, they used a DGEBA epoxy cured using piperidine for 16 hours at 120°C. They found that the value of K_{IC} for the rubber modified epoxy was comparatively more sensitive to the test rate and temperature than that of the unmodified epoxy. The K_{IC} of 15 parts per hundred resin (phr) CTBN

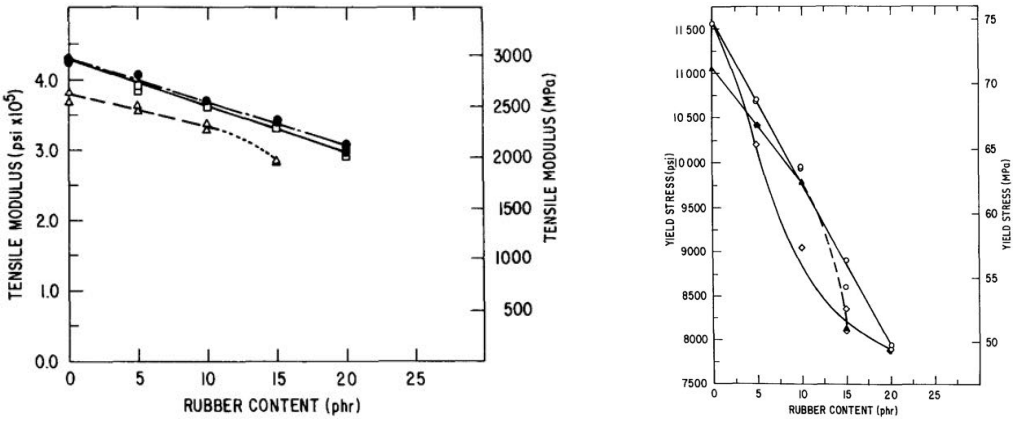


Figure 2.2.2: Variation of Young's modulus and yield strength with CTBN rubber content for: (○) 828-8, (◊) 828-15, (▲) 828-BPA(24)-8. Reproduced from [26].

rubber modified epoxies increased by up to 100% by increasing the temperature from 20 °C to 60 °C. Additionally, below the T_g of the rubber particles (-50 °C), a small increase in K_{IC} was also observed. These results corroborate with more recent results from Chen *et al.* [28] for a rubber modified anhydride cured DGEBA. The epoxy system used in that work was cured at 120 °C for 1 h, followed by a postcure of 160 °C for 2 h, which gives a T_g of 148°C.

2.2.2.2 Thermoplastic modifiers

There are some high T_g epoxies that cannot be toughened with rubber particles, as shown in Figure 2.2.3. Levita *et al.* [29] compared CTBN modified epoxies of varying crosslink density, cured using DDS, and noted no improvement in K_{IC} for highly crosslinked epoxies.

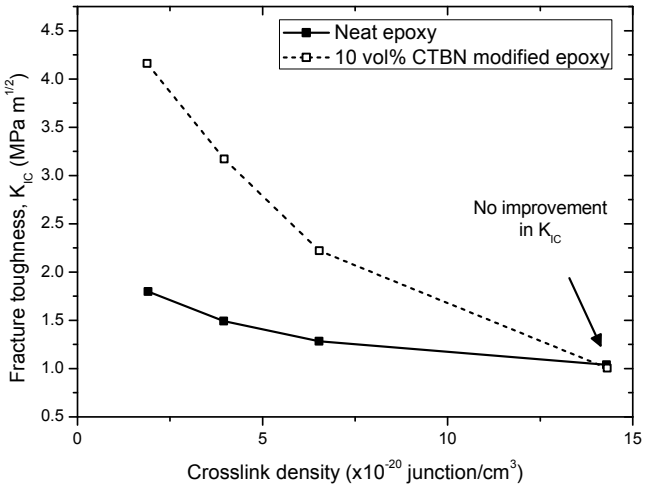


Figure 2.2.3: Fracture toughness of neat and CTBN rubber modified epoxies [29].

As with the rubber particles, thermoplastic particles can be dispersed in epoxy by reaction-induced phase separation [30, 31] or by suspension of pre-formed particles [32]. High performance thermoplastics such as polyethersulphone (PES) and poly(ether ether ketone) (PEEK) incorporated into epoxies were found to moderately increase the fracture toughness without adversely affecting the T_g or modulus [33, 34]. For example, Bucknall and Partridge [30] reported the use of PES in multifunctional epoxies for use in fibre composites. These epoxies have a T_g of 252°C, i.e. have high crosslink density. They measured an increase in K_{IC} of 0.2 MPa $m^{1/2}$ and a corresponding decrease in Young's modulus of only 0.1 GPa. This finding was confirmed by other authors [35–37].

Perhaps of more interest is the phase separation behaviour. The microstructure of a PES modified epoxy showed a change from single phase to particulate, co-continuous and eventually phase inversion as the modifier content increases [35], as shown in Figure 2.2.4. There is reasonable agreement between authors that a co-continuous structure gives a higher toughness than a particulate microstructure. However, this could arguably be the result of a higher concentration of modifier as the increase in K_{IC} and G_{IC} is smooth, rather than a step change.

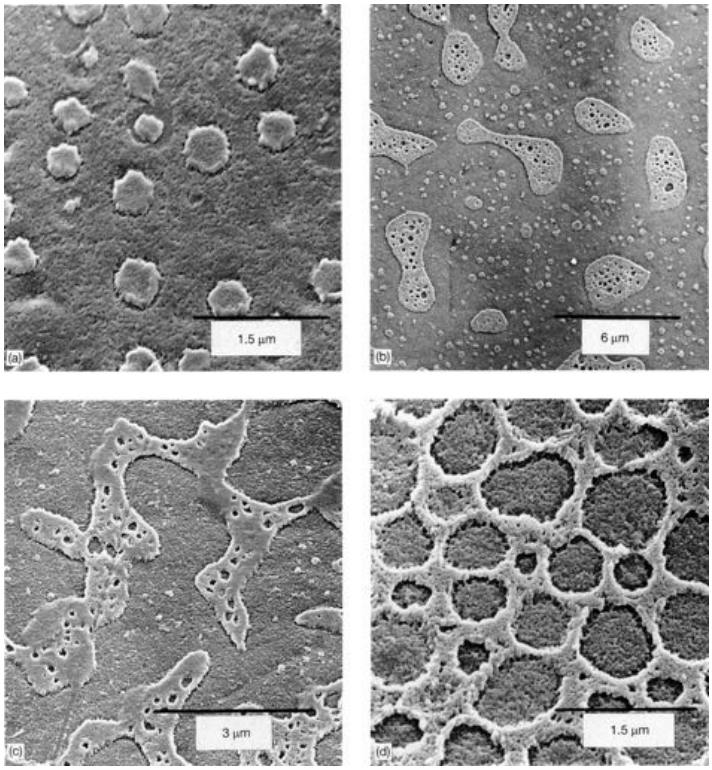


Figure 2.2.4: Change in microstructure for PES modified epoxy polymer. (a) Particulate, (b) Transition between particulate and co-continuous, (c) Co-continuous and (d) Phase-inverted microstructures. Reproduced from [35].

Pearson and Yee [38] tested a range of thermoplastic modified epoxies and found that some thermoplastic modifiers were more effective than others, as shown in Table 2.2.1. This is because both phase separation and a suitable morphology are required for toughening. A review by Hodgkin *et al.* [39] also suggests that thermoplastics can toughen highly crosslinked epoxies more effectively than low crosslink density epoxies, a trend inverse to that for reactive liquid rubbers.

Table 2.2.1: Properties of the thermoplastics used to modify a piperidine cured DGEBA epoxy polymer [38].

Thermoplastic modifier		T_g (°C)	Modulus (MPa)	σ_y (MPa)	Phase separation	Max ΔK_{IC} ($MPa^{1/2}$)
Poly(ether imide)	PEI	220	2.8	105	No	0.0
Poly(phenylene oxide)	PPO	205	2.6	78	Yes	0.9
Poly(carbonate)	PC	145	2.4	62	No	0.0
Poly(butylene terephthalate)	PBT	50	2.3	55	No	0.0
Reactive polystyrene	RPS	105	3.3	35	Yes	-0.1
Poly(butylene terephthalate-butyl ether)	PBT-PBE	-	0.6	-	Yes	0.0
Poly(ether imide-dimethyl siloxane)	PEI-PDMS	-	0.5	<30	Yes	0.9
Poly(carbonate-dimethyl siloxane)	PC-PDMS	120 (PC) -100 (PDMS)	0.3	-	Yes	0.2

2.2.2.3 Block copolymers

Block copolymers (BCP) are the latest type of rubbery modifiers to be investigated in research. Significant advances in polymer synthesis have given researchers and manufacturers the capability to accurately create specific copolymers. Copolymers comprise of at least two monomer species covalently bonded together through copolymerisation. There are several different types of copolymers; BCPs are a class of copolymer that have distinct subunits of monomers [40], as shown in Figure 2.2.5.

— A — A — A — A — A — A — A — A — A — A —

(a) Homopolymer

— A — B — A — B — A — B — A — B — A — B —

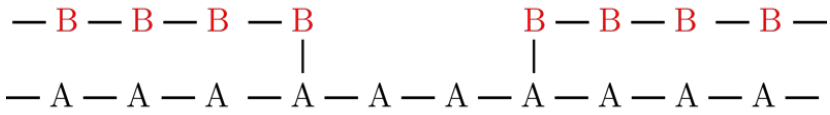
(b) Alternating copolymer

— A — B — B — B — A — A — B — A — A — B —

(c) Random copolymer

— B — B — B — B — B — A — A — A — A — A —

(d) Block copolymer



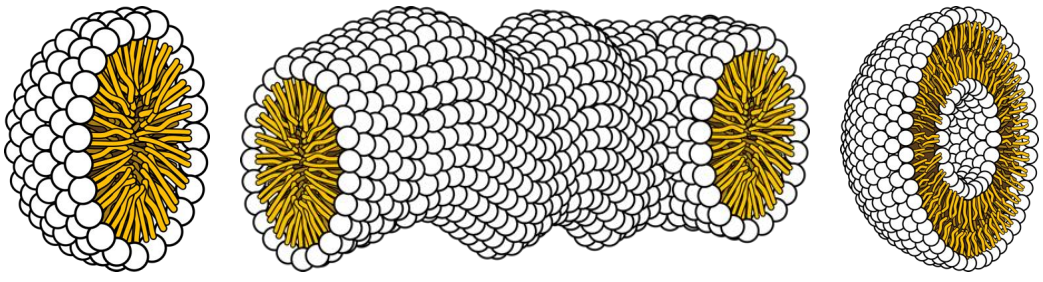
(e) Graft copolymer

Figure 2.2.5: Different types of copolymers [40].

There are many possible combinations of BCPs and amphiphilic block copolymers of particular interest for epoxy toughening. These BCPs have an epoxy-miscible block and an epoxy-immiscible block which allows microphase separation at the length scale of the polymer chains ($\approx$ 10s of nm) due to the thermodynamic immiscibility of the blocks. The amphiphilic nature of the BCPs means they can undergo micellisation to form complex nanostructures such as spherical micelles, worm-like micelles and vesicles, as shown in Figure 2.2.6. The shapes formed depend on the packing parameter [41], defined as [42]:

$$P = \frac{v}{al_0} \tag{2.1}$$

where v is the volume of the core, a is the surface area of the core and l_0 is the length of the solvent-phobic block. For example, spherical micelles form when $P \leq \frac{1}{3}$. The solvent for the BCPs used in this work is the epoxy resin. The critical micelle concentration is defined as the concentration at which micelles will start to form to reduce the system free energy. The epoxy-miscible blocks will aggregate to form the outside of the micelle in contact with the epoxy, almost like a shell, to shield the epoxy-immiscible block in the centre as the core. Of course, the requirement is for these self-assembled nanostructures to form prior to gelation of the epoxy, as they are then "fixed" by the crosslinking process. Note that it is possible for the self-assembled nanostructures to be destroyed at the higher temperatures required to cure some epoxy polymers.



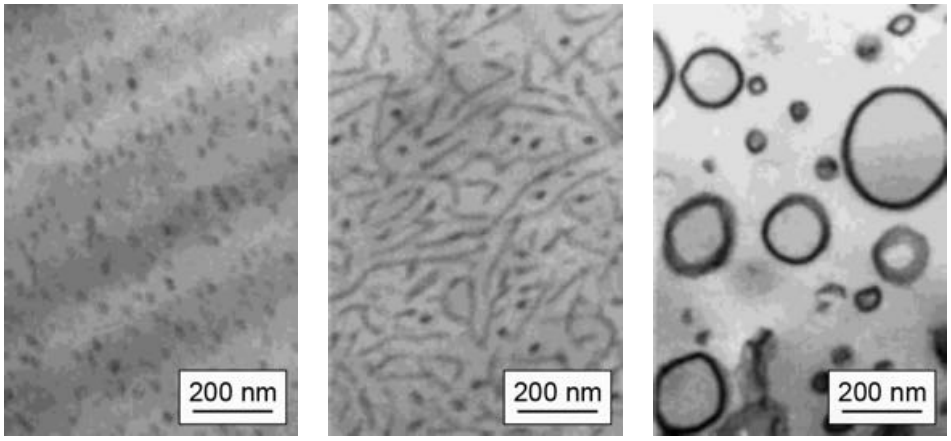
(a) Spherical micelle (b) Worm-like micelle (c) Vesicle

Figure 2.2.6: Possible self-assembly micellar structures. Reproduced from [43].

The alternative mechanism for the formation of ordered BCP nanostructures is by

reaction-induced phase separation, similar to that of reactive liquid rubber modification. This can occur if all of the blocks are miscible with the epoxy precursor.

Hillmyer *et al.* [44] were one of the first to publish work on self-assembled amphiphilic poly(ethylene oxide)-poly(ethyl ethylene) (PEO-PEE) block copolymers in epoxy. Their small-angle X-ray scattering (SAXS) results indicated that the BCPs were self-organised into hexagonally packed cylinders and TEM images revealed a core-shell morphology of those cylinders. Grubbs *et al.* [45] varied the epoxy-miscible block solubility of polybutadiene-polyisoprene (BI) and poly(methyl acrylate-glycidyl methacrylate)-polyisoprene (MGI) block copolymers and found that those with high miscibility with epoxy will microphase separate to form nanoscale structures. Those with low epoxy miscibility will macrophase separate into a phase inverted structure. Their group also noted a transition of the nanostructures from vesicles to wormlike micelles to spherical micelles as the volume fraction of the epoxy-miscible BCP subchain was increased [6], as shown in Figure 2.2.7.

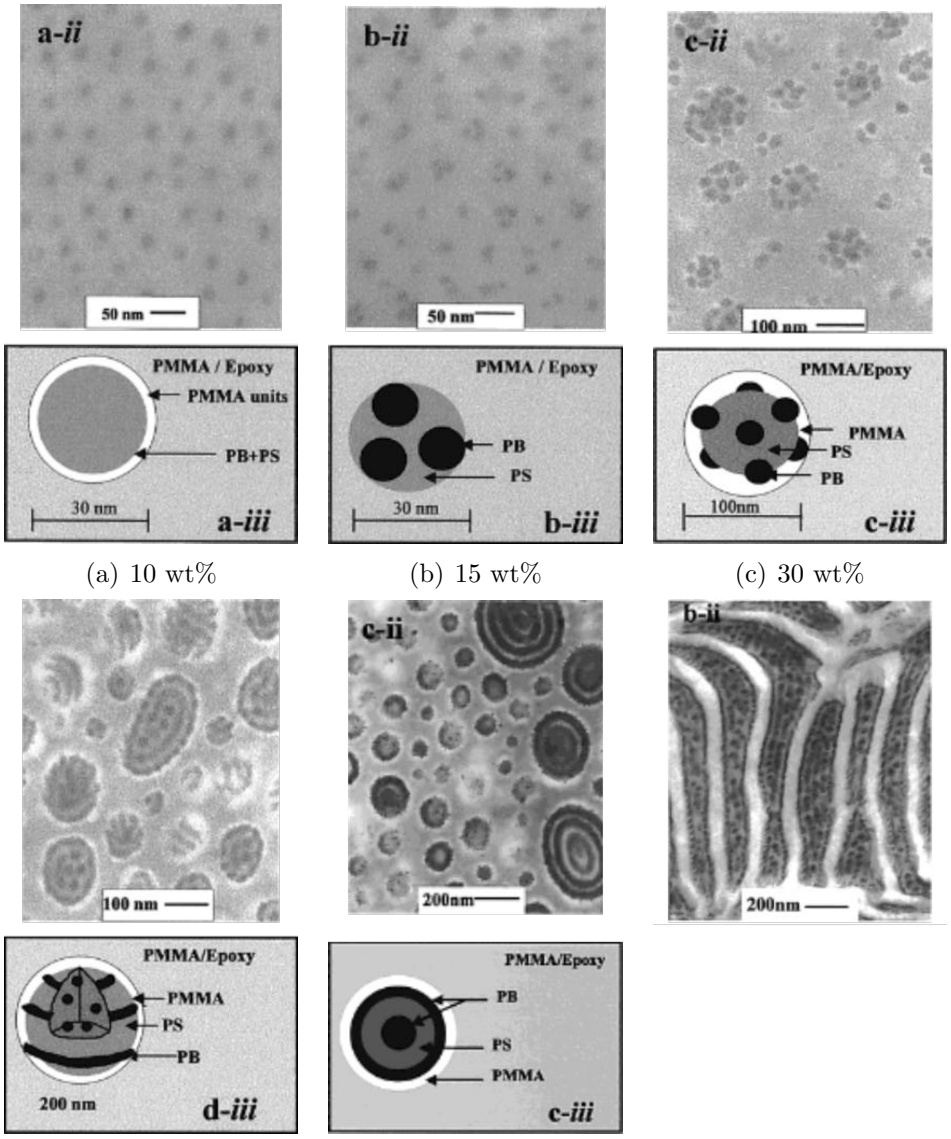


(a) Spherical micelle (b) Wormlike micelle (c) Vesicle

Figure 2.2.7: TEM micrographs showing BCP morphologies in epoxy. Reproduced from [6].

Ritzenthaler *et al.* [46] characterised the change in morphology of the polystyrene-polybutadiene-poly(methyl methacrylate) (SBM) phase with modifier content. The particles change from a core-shell structure (Figure 2.2.8(a)) to a "spheres on spheres" or "raspberry-like" structure (Figures 2.2.8(b) and 2.2.8(c)) to cylindrical PB blocks around a sphere (Figure 2.2.8(d)). There is also an increase in particle size with modifier content. This is in contrast to a SBM BCP with higher PB block ratios, where a core-shell "onion-like" structure was observed (compare Figure 2.2.8(d) with Figure 2.2.8(e)). At very high weight percentages up to 80 wt%, the morphologies tend to be close to that of the neat BCPs, as shown in Figure 2.2.8(f).

From the literature, it can be concluded that a number of parameters control the mor-



(a) 10 wt% (b) 15 wt% (c) 30 wt%

(d) 50 wt% (e) 50 wt%[1] (f) 80 wt%

Figure 2.2.8: Variation of morphology of SBM BCP with content. [1] Higher PB block ratio. Reproduced from [46].

phology of the dispersed phases; the constituents of each block, molecular weight of the BCP, ratio of each block, weight percentage of BCP added and the miscibility of each block with the epoxy. There is a general agreement that the main features of interest are the self-assembled micellar structures and macrophase separated structures [47–58], for all the types of BCP used. Indeed, there are a large number of homopolymers that have been used for these BCPs and they have been extensively reviewed [59]. One of the main factors limiting the use of BCPs is the block miscibility, which controls the phase separation and hence final morphology. However, this can be controlled by the addition of functional groups, such as N,N-dimethylacrylamide (DMA), to produce

different morphologies [60].

While there have been extensive studies of the chemistry and morphology of BCPs in epoxy, the effect of these complex nanostructures on the fracture performance of epoxies is still relatively unknown. Dean *et al.* [61] recorded higher G_{IC} values for a vesicle morphology compared to spherical or worm-like micelle morphologies, presumably because the vesicles encapsulate an epoxy core, giving it a larger effective volume fraction. Hydro and Pearson [62] incorporated three different triblock copolymers in two different epoxies, both of which had low crosslink densities and are very "toughenable". They found a maximum increase in fracture toughness at 10 phr from 0.6 to 2.5 MPa $m^{1/2}$ and 0.4 to 2.7 MPa $m^{1/2}$ for aminoethyl-piperazine and piperidine cured DGEBA epoxies, respectively. This is higher compared to the same epoxy systems modified with CTBN rubber at the same content, tested by the same research group, where a maximum of 2.1 MPa $m^{1/2}$ [21] and 2.4 MPa $m^{1/2}$ [26] was measured. However, they also found the value of K_{IC} to be lower for the other BCPs that have a lower soft-block content or a phase inverted morphology. Gerard *et al.* [56] also compared SBM and PMMA-poly(butylacrylate)-PMMA (MAM) against CTBN modified epoxies and found the co-continuous and worm-like micellar structure of the BCPs to be more effective than CTBN. For a low T_g and lightly crosslinked epoxy system, they measured K_{IC} values of 3.0 MPa $m^{1/2}$ for the SBM and MAM compared to 1.4 MPa $m^{1/2}$ for the CTBN at a concentration of 10 wt%. However, they also noted that the BCP modified epoxies did not comply with LEFM conditions, which can affect the validity of the results. The effects of the core material were investigated by Declet-Perez *et al.* [63], comparing a glassy, rigid polystyrene (PS) core to a rubbery poly(ethylene-alt-propylene) (PEP) core. PS has a modulus of approximately 3 GPa, whereas PEP has a modulus of approximately 5 MPa. Their results show the fracture energy of the modified epoxies containing the BCP with the softer PEP block was about 2 times that of the BCP with the rigid PS core.

In summary, the literature suggests that the block copolymer morphology and chemistry strongly affects the fracture performance of epoxy polymers. There are results which prove the higher performance of BCP modified epoxies compared to CTBN modification, however there are still disagreements on the exact mechanisms which contribute to that extra performance.

2.2.2.4 Phase separation

The previous section has shown that a wide variety of morphologies can be obtained from rubber and block copolymer modified epoxies. This section will summarise briefly the factors that govern phase separation.

One of the main factors that controls the morphology is the miscibility of the second phase. For example, the acrylonitrile content in CTBN controls the miscibility of the liquid reactive rubber in epoxy [64]. This, in effect, determines the phase separated rubber particle size [26]. Reactive liquid rubbers, thermoplastics and BCPs are initially mixed with the epoxy polymer to give a homogeneous mixture. During the curing process, the molecular weight of the epoxy increases as crosslinking occurs. The increase in molecular weight decreases the configurational entropy, and thus changes the free energy of mixing [65, 66]. This leads to a reduction in solubility of the modifiers and subsequently, phase separation. There are two main categories in phase separation; nucleation and growth and spinodal decomposition [67], as shown in Figure 2.2.9.

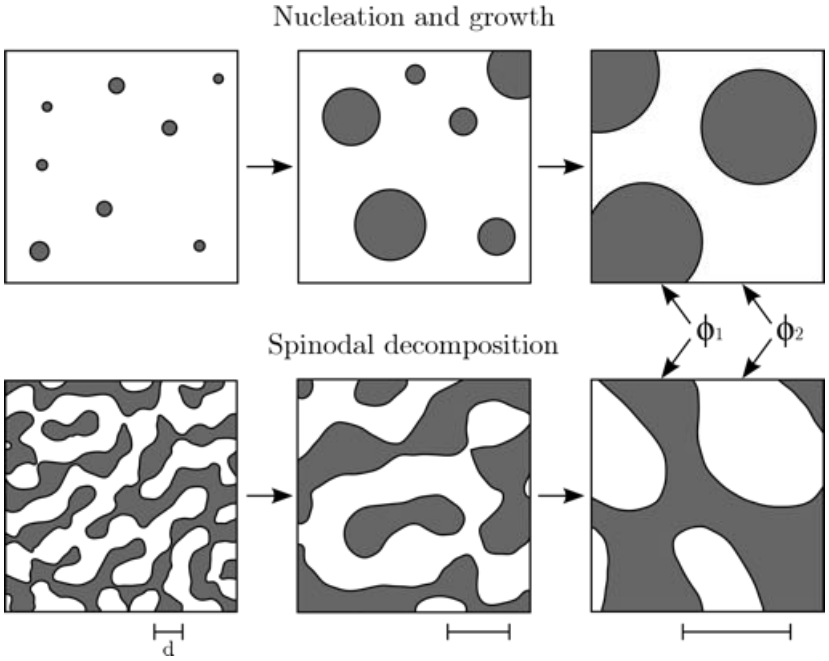
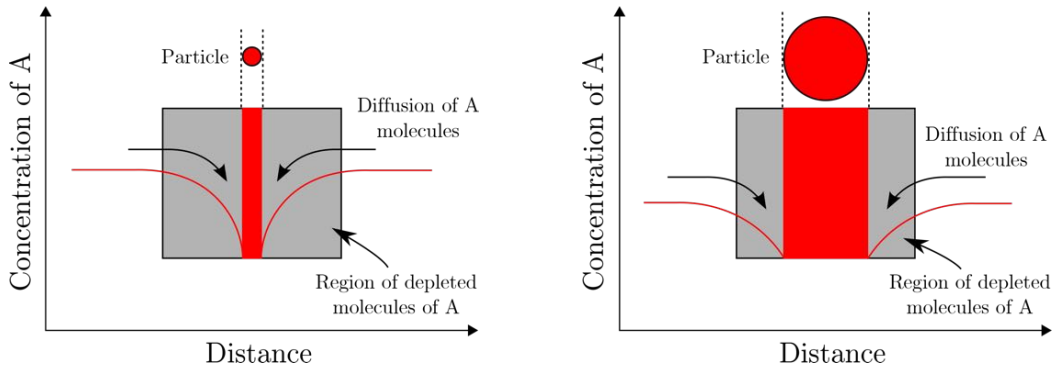


Figure 2.2.9: Time evolution of structure by two phase separation methods. Reproduced from [67].

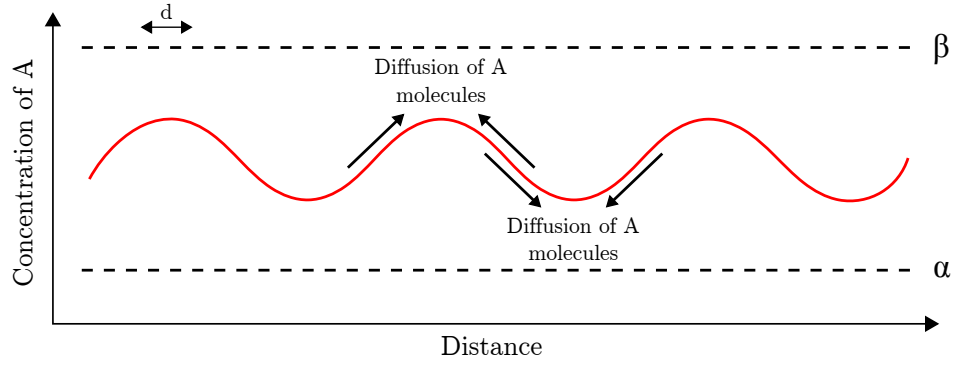
The nucleation and growth process requires an activation energy, which is overcome when a nucleus of critical size is formed. The particle then grows in size at a rate determined by the diffusion rate and time until vitrification. In comparison, there is no activation energy to overcome for spinodal decomposition. The nucleation and growth process is driven by a change in local concentration, as shown in Figure 2.2.10.



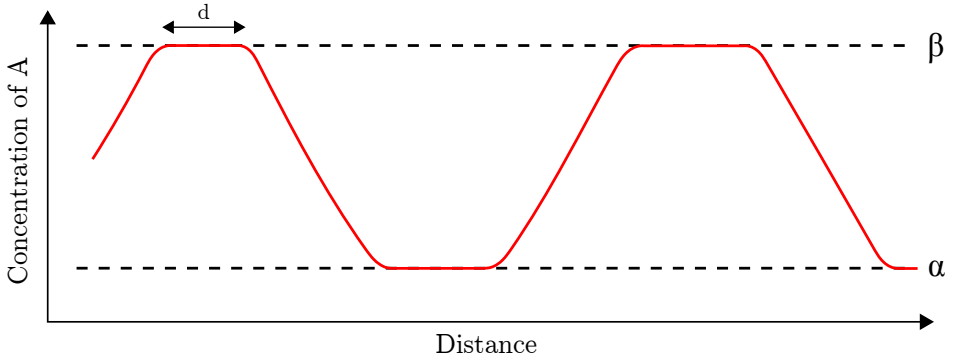
(a) At time = 1 (b) At time = 2

Figure 2.2.10: Nucleation and growth process.

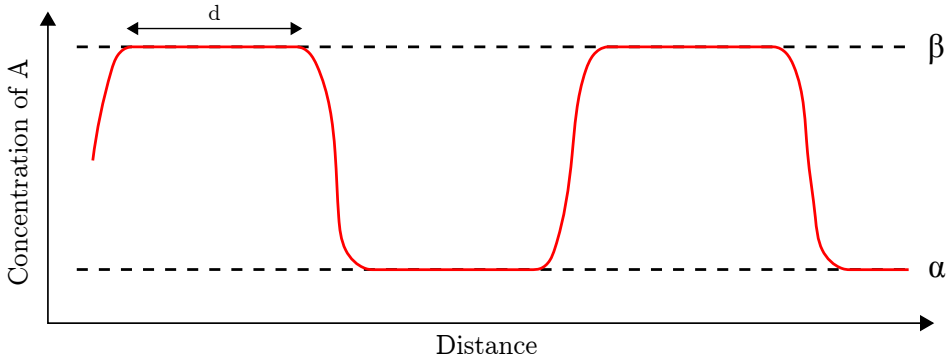
In spinodal decomposition, diffusion is driven by the difference in chemical potential in order to lower the Gibbs free energy of mixing. Figure 2.2.11 illustrates the evolution of a phase by spinodal decomposition. At an early stage (Figure 2.2.11(a)), the domain size, d, and concentration increases with time. At an intermediate stage, when the local concentration reaches the limits, α and β, the maximum concentration remains constant while the domain size continues to increase and the interface width decreases (Figure 2.2.11(b) to 2.2.11(c)).



(a) Early stage. Growth of domain size, d, and concentration.



(b) Intermediate stage. Concentration limits, α and β, reached.



(c) Late stage. Domain size grows and interface width decreases.

Figure 2.2.11: Three main stages of spinodal decomposition process.

2.2.2.5 Phase field model

To assist in further understanding the parameters that control the morphology of the phase separating process, a phase field model was constructed based on the Cahn-Hilliard equation [68]:

$$\frac{\partial \phi}{\partial t} = M\Delta\left[\phi^3 - \phi - \gamma\Delta\phi\right] \tag{2.2}$$

where M is the mobility. The Cahn-Hilliard equation [68] was originally proposed in 1958 by Cahn and Hilliard to model phase separation in binary alloys such as iron-nickel alloys. In addition to its use in phase field modelling [69], it has been used in a wide range of applications, including tumour growth [70] and image inpainting [71, 72].

The equation was used to predict the evolution of microstructure with time from an initially homogeneous mixture. The microstructure is defined entirely by one variable, the order parameter ϕ, as a composition field and can only take a value between -1 and 1. The values $\phi = -1$ and $\phi = 1$ correspond to the matrix and modifier phases, and the choice of which is arbitrary. For the current study, the matrix is -1 (blue) and the modifier is 1 (red), as shown by the scale bar in Figure 2.2.12.

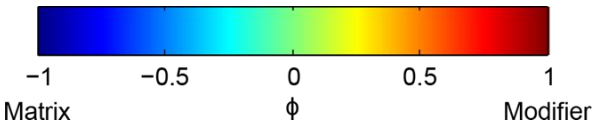


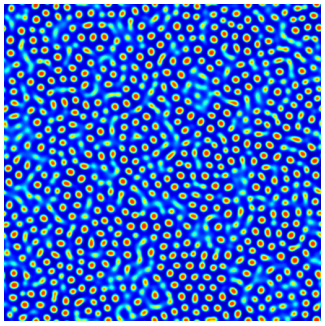
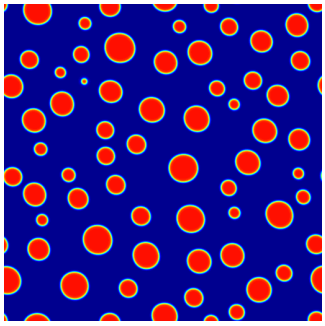
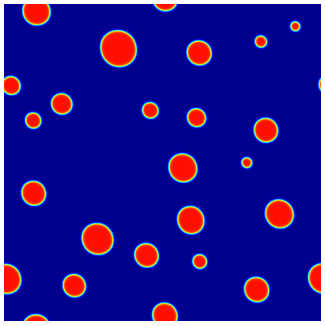
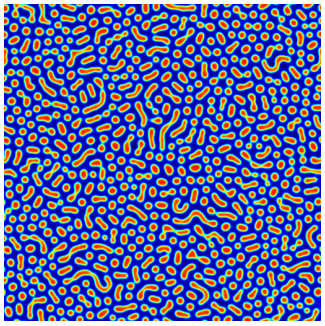
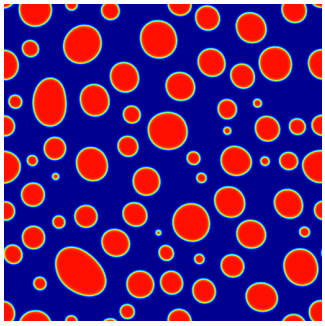
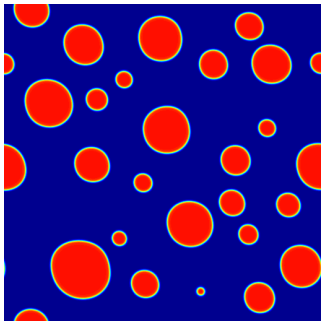
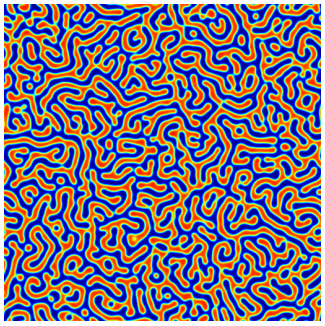
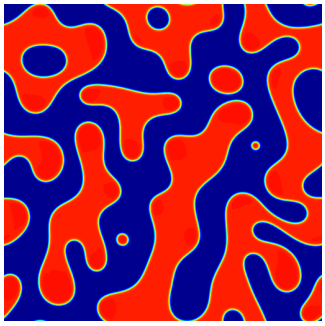
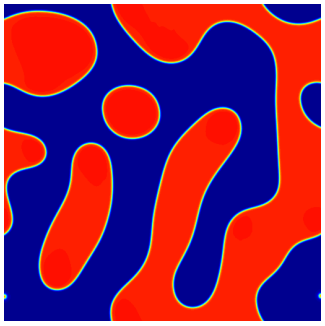
Figure 2.2.12: Colour scale bar for the order parameter, ϕ, for the phase fields diagrams.

The initial concentration of the homogeneous mixture represents the volume fraction of modifier added to the matrix. To initiate the phase separation, a uniform random distribution with an interval of 0.5% of the total range about the mean of the initial concentration was applied, which corresponds to an initially well mixed mixture.

The initial concentration was varied and the resulting microstructures generated from each initial condition were evaluated. By varying the mobility, M, and free energy density, $f(c)$, the effect of varying the viscosity and miscibility can also be explored.

Table 2.2.2 shows the temporal evolution of the morphology for different values of initial concentration. At an initial concentration of the minority phase of 0.32, the morphology observed was a dispersion of droplets (red) in the matrix (blue). Once nucleation of the initial particles starts (see left column), the droplets begin to grow by diffusion of material from the surrounding mixture until it has become saturated. With more simulation time (see centre to right columns), further increases in size occurs by droplet coalescence and Ostwald ripening [67]. This reduces the number of particles in favour of the more thermodynamically stable larger particles. Also, as the initial volume fraction of the minority phase is increased, the size and number of the droplets were increased.

Table 2.2.2: Evolution of morphology with time at different volume fractions, v_f.

v_f	t = 200	t = 10,000	t = 30,000
0.32			
0.4			
0.5			

With an initial concentration of 0.5, a dispersion of droplets is formed first at very early stages. This quickly evolves into a co-continuous morphology via merging with adjacent particles, as shown in the bottom left of Table 2.2.2. With increasing simulation time, the characteristic lengths of the co-continuous features grow larger and the interfacial area reduces. The phase separation occurs spontaneously throughout the mixture, as shown by the rapid transition to a saturated continuum, i.e. there are fewer regions of $-1 < \phi < 1$ and the mixture phase separates quickly to $\phi = -1$ and $\phi = 1$. The minority phase also grew in size with time for the co-continuous structure.

Note that the location of the binodal and spinodal curve, i.e. the initial mixture concentration at which a co-continuous morphology occurs, is dependent on the free energy function, $f(c)$. In the current phase field models, a symmetric double-well function was used, hence a co-continuous morphology is observed around $v_f = 0.5$. The peak of the free energy function, $f(c)$, can be changed to shift the spinodal curve to represent specific polymer mixtures which are observed experimentally.

The growth, or coarsening, process of the minority phase can be quantified by measuring the characteristic lengths of each respective phase over time. Lifshitz and Slyozov [73] and Wagner [74] independently formulated analytical proofs for the growth in domain size due to Ostwalt ripening, commonly known as the Lifshitz-Slyozov-Wagner (LSW) theory. Both solutions concluded that the average radius cubed grows as a linear function of time, i.e. $\frac{\partial R^3}{\partial t} = \text{constant}$. The change in characteristic lengths as a function of the cube root of time is shown in Figure 2.2.13.

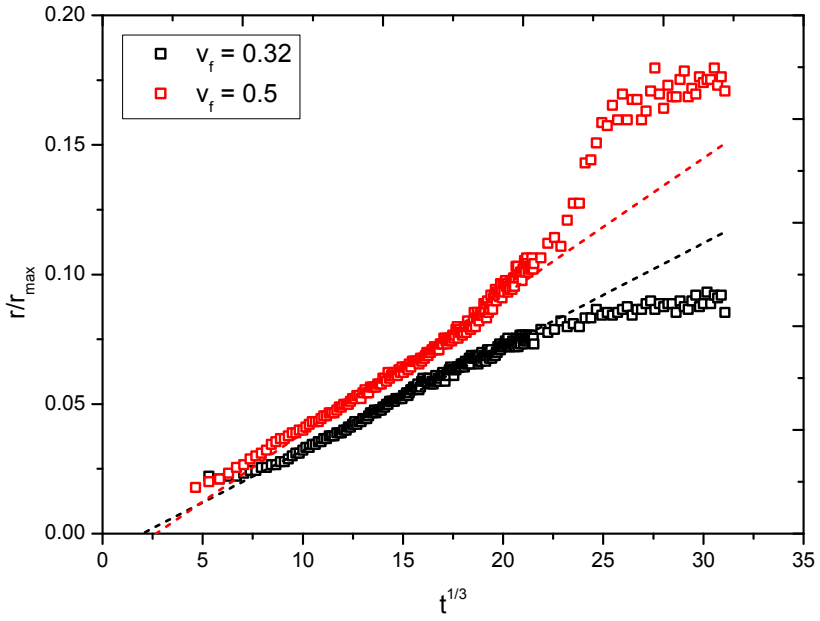
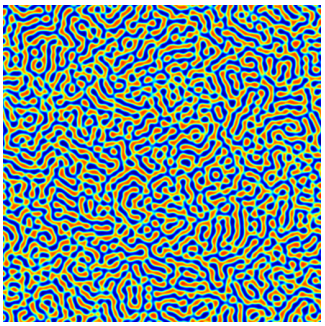
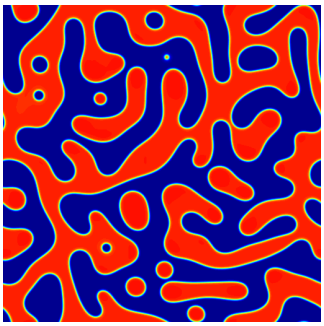
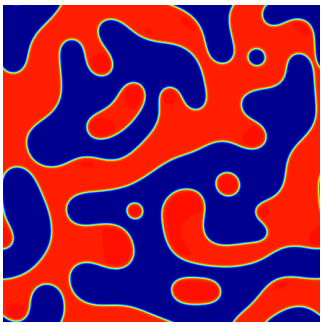
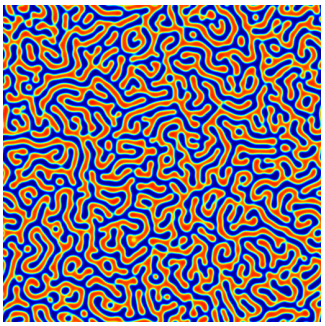
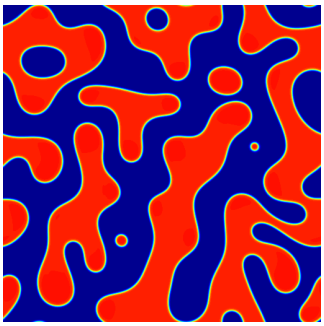
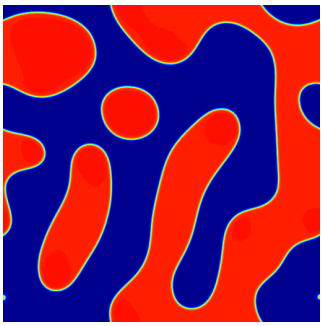
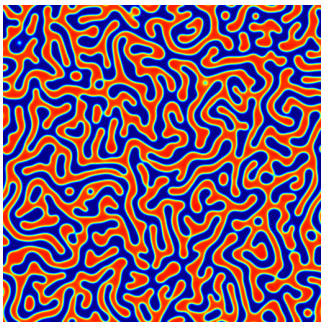
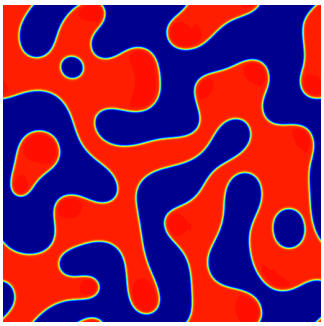
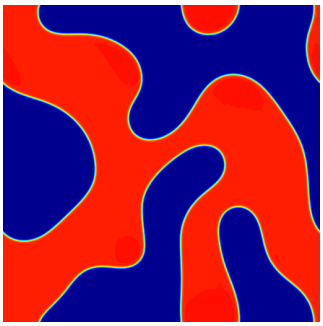
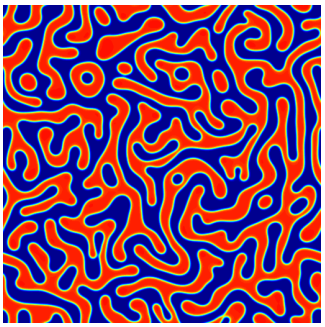
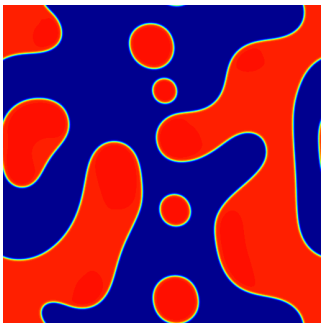
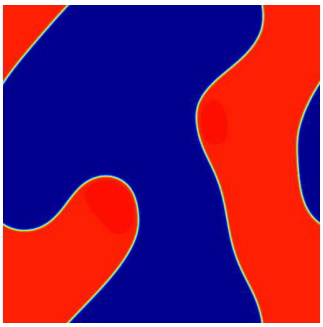


Figure 2.2.13: Evolution of characteristic length with time for $v_f = 0.32$ and $v_f = 0.5$.

The coarsening process appears to follow the LSW theory trend well. At a value of $t^{1/3} \approx 25$, a large increase in characteristic length was observed for the co-continuous structure ($v_f = 0.5$). In contrast, this was not observed for the droplet-type morphology ($v_f = 0.32$). This corresponds to the transition into a fully co-continuous structure, resulting in the large increase in characteristic length. The small inclusions of each phase disappear during this transition. This is followed by a more gradual increase in characteristic length. The numerical results show that the characteristic length of the minority phase increases at a higher rate for an initial v_f of 0.5 than for an initial v_f of 0.32. It is not possible to determine whether this is because of the co-continuous nature of the morphology at $v_f = 0.5$, as it could also be an effect of higher concentration gradients from the higher initial v_f.

The effects of initial mixture viscosity were investigated by changing the value of the mobility, M, as shown in Table 2.2.3. For a higher value of mobility (see bottom row), hence a lower viscosity, the growth rate of the minority phase is higher, achieving steady state in a shorter time. Comparing the phase fields for M = 0.5 (first row) and M = 5 (last row) in Table 2.2.3, less time is required for the mixture to reach a more ordered state. The minority phases at specific times were clearly larger at higher values of mobility. It should also be noted that the time steps had to be reduced significantly to run the model accurately at M = 5.

Table 2.2.3: Evolution of morphology with time at different values of mobility, M, for an initial concentration of $v_f = 0.5$.

Mobility	t = 200	t = 10,000	t = 30,000
0.5			
1.0			
2.0			
5.0			

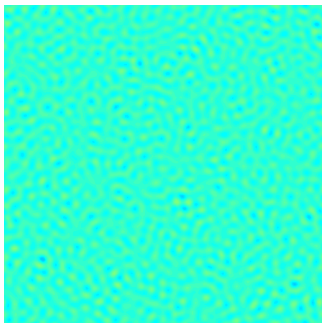
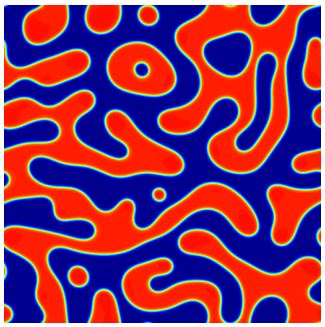
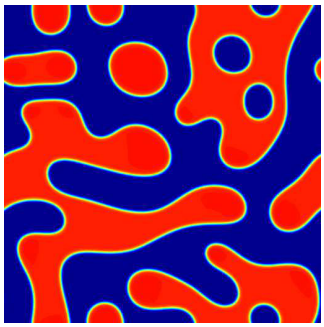
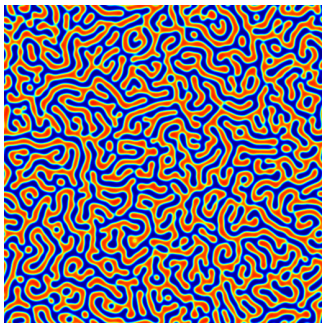
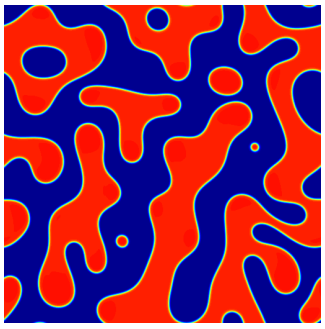
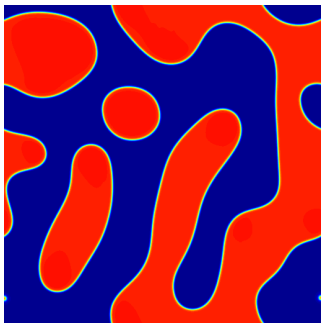
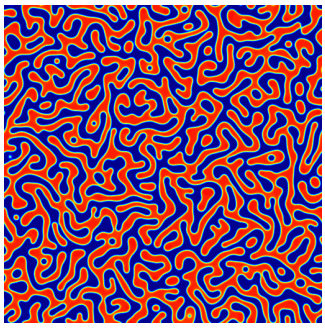
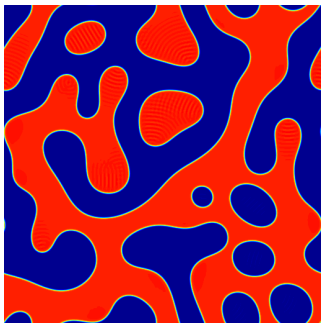
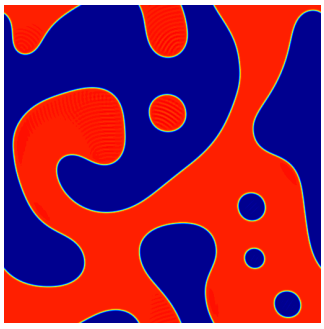
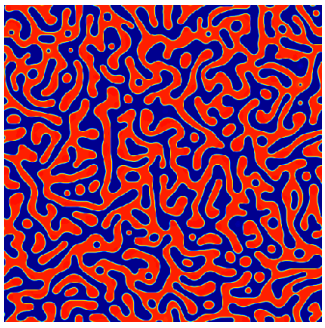
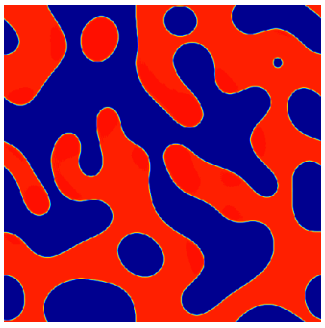
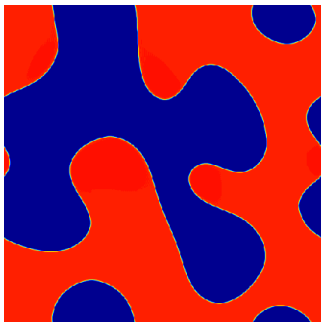
The miscibility of the minority phase can also be examined in a similar manner by changing the thermodynamic barrier. The free energy barrier can be varied by changing the height of the double-well potential used to define the local free energy function, i.e. changing the value of A:

$$f(c) = A\left(a - (b\phi)^2\right)^2 \tag{2.3}$$

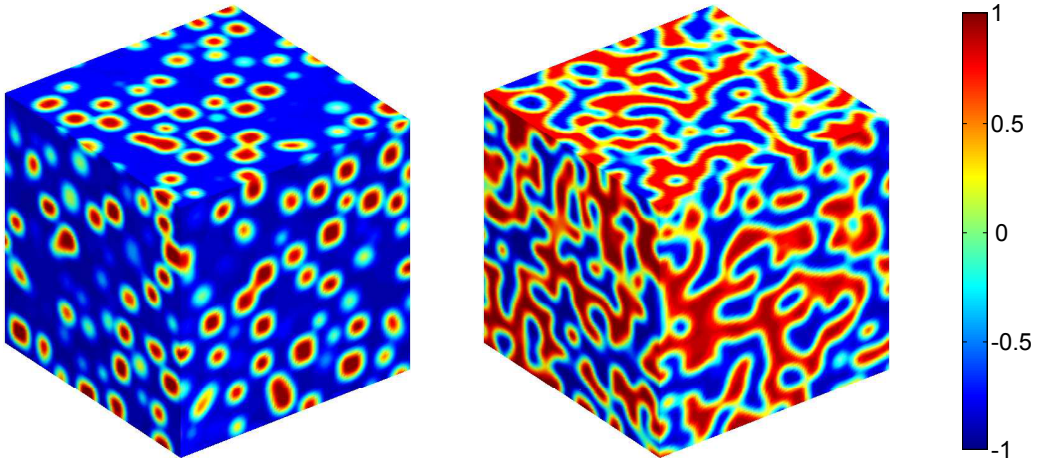
where a and b are constants. Raising the value of A increases the gradient of $f(c)$, allowing the result to converge more quickly towards $\phi = 1$ or $\phi = 0$. Thus, high values of A represent lower thermodynamic barriers. The phase fields for different values of A are shown in Table 2.2.4. At low values of A (first row), a longer time is required for phase separation to initiate. This is analogous to phase separation of rubber in epoxy which requires a higher value of conversion to initiate or nucleate. These results also show that the growth rate of the second phase is reduced at lower values of A.

At higher values of A (see bottom row of Table 2.2.4 for A = 5), the results were similar to high values of mobility. Phase separation initiates at an earlier stage and coarsening proceeds at higher growth rates at higher values of A. Smaller time steps were also used to achieve accurate results at high values of A.

Table 2.2.4: Evolution of morphology with time at different values of energy barrier, A, for an initial concentration of $v_f = 0.5$.

A	t = 200	t = 10,000	t = 30,000
0.5			
1.0			
2.0			
5.0			

The Cahn-Hilliard equation can also be extended to 3D to obtain a more realistic representation of the microstructure. Figure 2.2.14 shows the phase fields in 3D at a time of 10,000 for two different initial concentrations. Qualitatively, a similar trend to the 2D cases was observed, where a low initial concentration results in droplet-like morphology, see Figure 2.2.14(a), and increasing the initial concentration creates a co-continuous microstructure, see Figure 2.2.14(b).

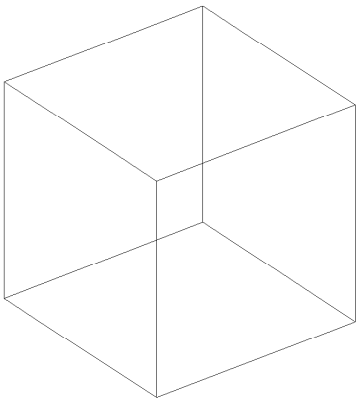
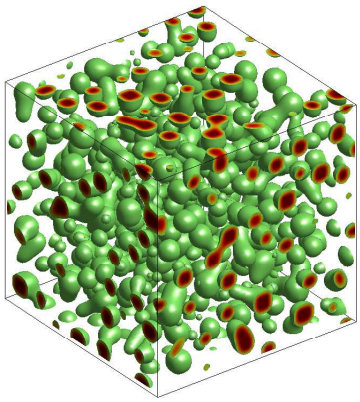
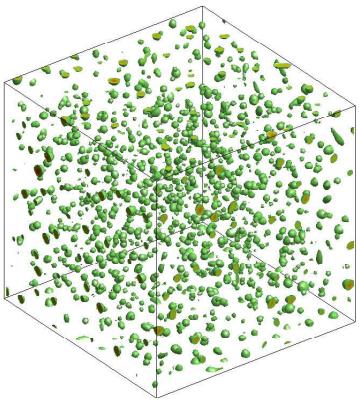
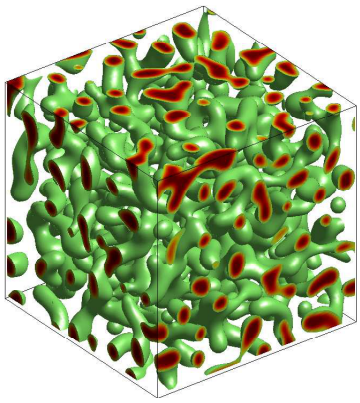
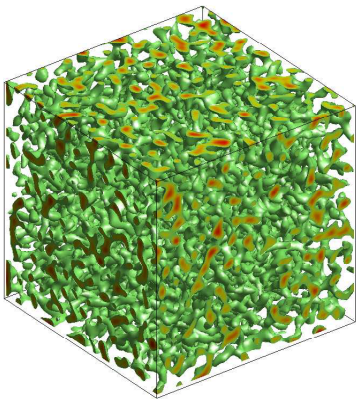
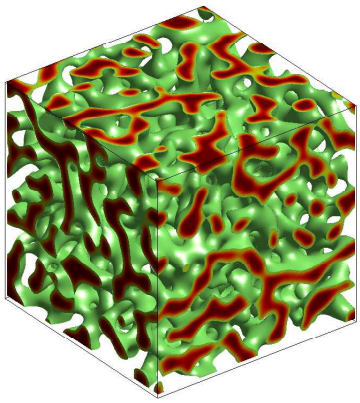
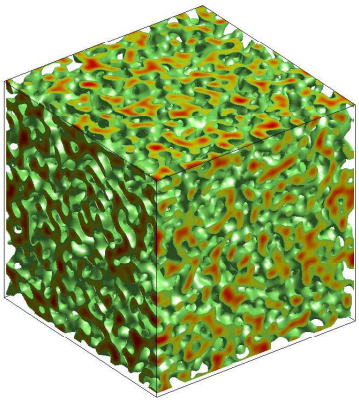
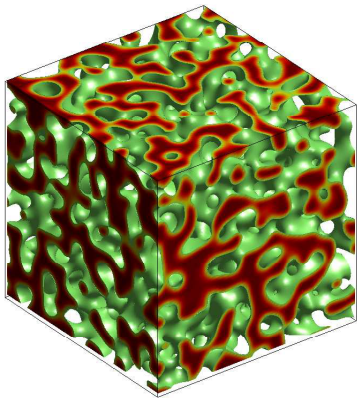


(a) $v_f = 0.24$ (b) $v_f = 0.5$

Figure 2.2.14: 3D phase fields as predicted using the Cahn-Hilliard equation at t = 10,000.

Table 2.2.5 shows the change in morphology with time at different initial concentrations. The matrix phase has been removed for clarity in this Table. At an initial concentration of 0.24, a longer time is required to initiate nucleation. Increasing the initial concentration reduces the time required for nucleation and increases the growth rate. At a time of 10,000 (see right column), the system is close to equilibrium and the temporal evolution of the microstructure changes much slower with time.

Table 2.2.5: Evolution of morphology with time at different values of initial concentration, v_f.

v_f	t = 1,000	t = 10,000
0.24		
0.3		
0.4		
0.5		

The change in normalised free energy of the mixture with time is shown in Figure 2.2.15. The free energy decreases with time, which signifies that the system is converging towards a lower energy state. An S-shape curve is typically observed, where the initial drop in free energy corresponds to the nucleation of the modifiers. The time at which the free energy drops initially decreases with increasing initial concentration, which makes sense given that it is related to the resultant morphology. This is followed by a sharp, linear decrease in free energy as more particles are formed. The free energy gradient then starts to decrease during the coarsening phase and the free energy tends towards a steady state value. The steady state value of free energy was found to be lower for higher initial concentrations. This could be related to the total interfacial surface area or just be a consequence of the difference in total concentration. The total mass was also calculated and found to be conserved. This is sufficient to confirm the validity of the model.

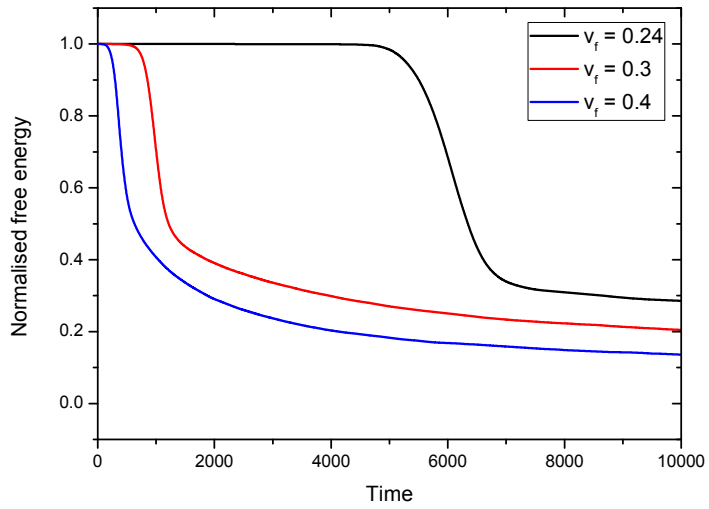


Figure 2.2.15: Normalised free energy of Cahn-Hilliard phase field models with time.

2.2.2.6 Toughening mechanisms for soft modifiers

In order to understand the significant increases in G_{IC}, the toughening mechanisms need to be studied. The major toughening mechanisms associated with soft modifiers are generally accepted [2, 16, 75, 76] to be (i) shear yielding of the epoxy polymer, (ii) plastic void growth initiated by cavitation of the rubbery particles and (iii) rubber particle bridging. These mechanisms are illustrated in Figure 2.2.16.

Kunz-Douglass *et al.* [77] initially suggested that rubber particle bridging was a major toughening mechanism for rubber modified epoxies. They found ligaments of rubber attached to both sides of the crack which stretched as the crack opened. This ligament

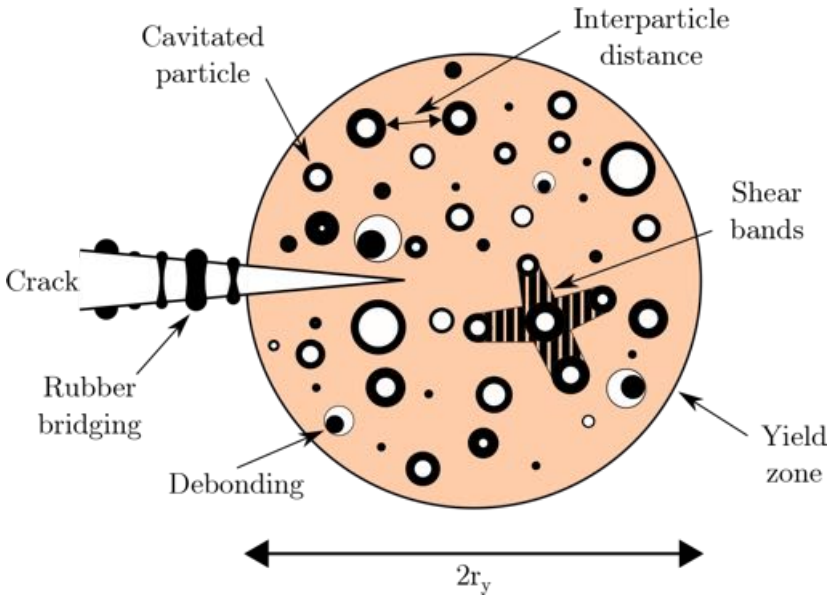
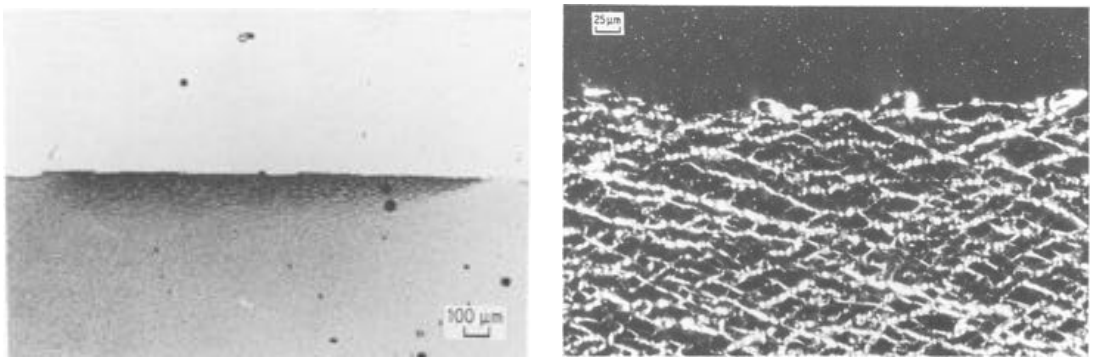


Figure 2.2.16: Schematic representation of toughening mechanisms for soft modifiers. Reproduced from [75, 77].

would then tear and result in an increase in toughness. Kinloch *et al.* [23] has since reported this to be only a minor contribution to toughness based on the inconsistencies with experimental observations of the fracture surface when tested at different temperatures and strain rates. When compared with the energy contributions from shear yielding and plastic void growth from the Huang and Kinloch model [75], rubber bridging accounts for only 8% of the total increase in toughness of a rubber modified epoxy. This is because the rubber particles that have cavitated cannot bridge across a crack as they can no longer sustain a load. The rubber particles must have a radius in the order of the crack tip radius in order to bridge a crack, thus nanometre sized rubber particles do not exhibit crack bridging.

Shear yielding is a constant volume process [78] that absorbs energy and can be induced to occur at multiple sites. Shear bands are narrow regions of material which have been subjected to intense shear strains during deformation. In rubber modified epoxies, the rubber particles act as stress concentrations, which can initiate localised shear bands between the particles. Finite element model studies [79, 80] on the growth of these localised shear bands indeed show that there is a region of increased stress between two particles and this contributes to the plastic energy dissipation. Localised shear band yielding can also be observed experimentally, as first shown by Pearson and Yee [81] for rubber modified epoxies (see Figure 2.2.17).

Shear band yielding can also be observed from cross-sections of plane strain compression samples loaded to the strain softening region [82]. This region is typically at compres-

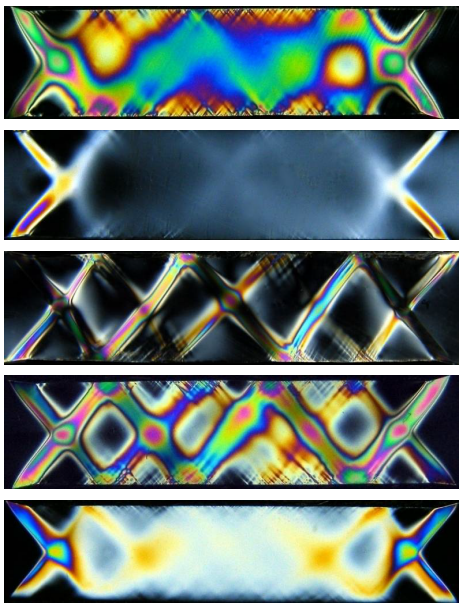


(a) Bright field optical micrograph of rubber modified epoxy showing plastic zone

(b) Cross polarised optical micrograph showing localised shear bands

Figure 2.2.17: Observation of plastic zone with optical microscopy. Reproduced from [81].

sive true strain values of 0.15 to 0.20. Birefringent shear bands are formed in the strain softening region due to inhomogeneous plastic deformation [83], as shown by Masania [84] for five different epoxy polymers (see Figure 2.2.18). The amine cured triglycidyl amino phenol (TGAP) epoxy shows no birefringence in the compressed region, which indicates a lack of shear yielding.



(a) Amine cured TGMDA

(b) Amine cured TGAP

(c) Polyether-amine cured DGEBA/F

(d) Polyether-amine cured DGEBA

(e) Anhydride cured DGEBA

Figure 2.2.18: Polished cross-sections of unmodified epoxy polymers tested under plane strain compression, loaded to the strain softening region (typically at true compressive strain values of 0.15 to 0.20) observed by cross-polarised light [84].

When the material exhibits strain softening, deformation occurs at decreasing levels of stress with strain. Any variations in stress will lead to a large difference in local strain rate and this induces localised plastic deformation [85]. Thus, the post-yield behaviour of polymers under compression can provide an indication of the deformation

mechanisms present, i.e. the competition between strain softening and hardening [86]. Meijer *et al.* [87] compared the uniaxial compression curves of polystyrene (PS), which is brittle, and polycarbonate (PC), which is tough, as shown in Figure 2.2.19. Clearly, PS exhibits more strain softening and a lower hardening modulus than PC. The strain softening leads to strain localisation, and for PC the strain hardening stabilises the deformation such that it develops across the whole section of the material and this gives it toughness. For PS, there is insufficient strain hardening and the deformation zone is extremely limited, which results in brittle failure [88].

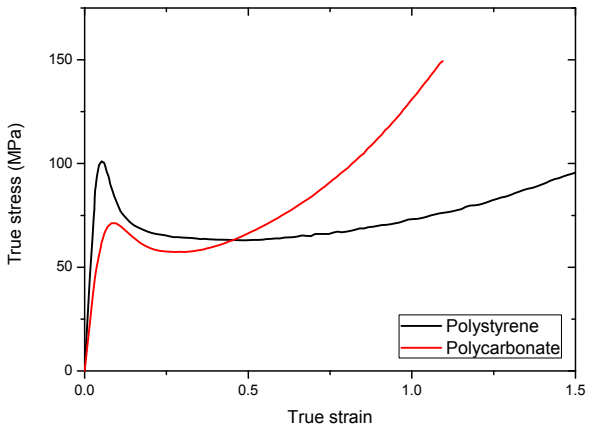
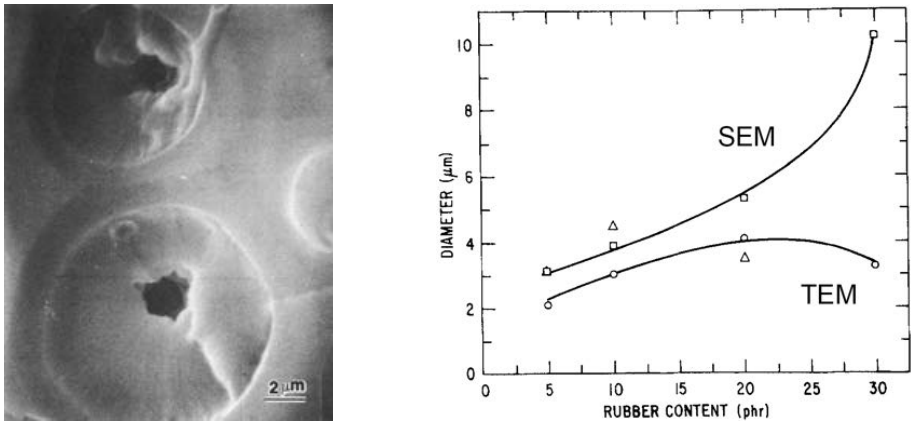


Figure 2.2.19: Uniaxial compression stress-strain curve for polystyrene and polycarbonate. Reproduced from [87].

The cavitation of rubber particles is known to absorb little energy [89], but is essential in relieving the triaxial stress state ahead of the crack tip by the formation of a void to allow plastic void growth of the epoxy polymer to occur. It is this plastic void growth that absorbs a significant amount of energy. Plastic void growth has been observed experimentally by the increased void size after fracture compared with the initial particle size, as shown in Figure 2.2.20(b).



(a) (b)

Figure 2.2.20: Rubber particle cavitation observed by electron microscopy. (a) Rubber particle cavitation observed on fracture surface, (b) Size of rubber particles and voids before and after loading. TEM images obtained before loading represent undeformed particles and SEM images are of the cavities. Reproduced from [81].

The change in stress state after particle cavitation can also further enhance shear yielding because it is preferential to shear yield at lower triaxial states due to the von Mises type yield stress [90]. Whether the onset of cavitation or shear yielding occurs first is dependent on the properties of the soft modifier [91]. A rubber particle with a high Poisson's ratio and modulus would cavitate before shear yielding of the epoxy because the high bulk modulus limits plastic deformation.

Ultimately, the influence of cavitation resistance, i.e. when cavitation occurs, is unimportant, according to a study by Bagheri and Pearson [21]. They measured the fracture toughness of particles with a range of cavitation resistance, including microvoids which have no cavitation resistance, and found no difference in the toughness or toughening mechanisms, as shown in Figure 2.2.21.

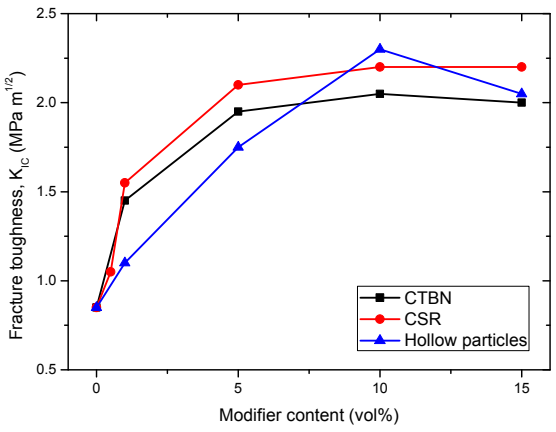


Figure 2.2.21: Fracture toughness for particles with a range of cavitation resistance. Reproduced from [21].

2.2.2.7 Inorganic rigid particles

Incorporating rigid particles can improve the fracture performance of epoxy polymers while also increasing the strength and modulus, as shown in Figure 2.2.22. Unlike liquid reactive rubbers, the T_g is unaffected when using rigid particles. Several authors have studied the use of rigid inorganic particles such as glass [92–95], titania (TiO_2) [96], alumina (Al_2O_3) [97, 98], silicates [99] and silica (SiO_2) [100–102].

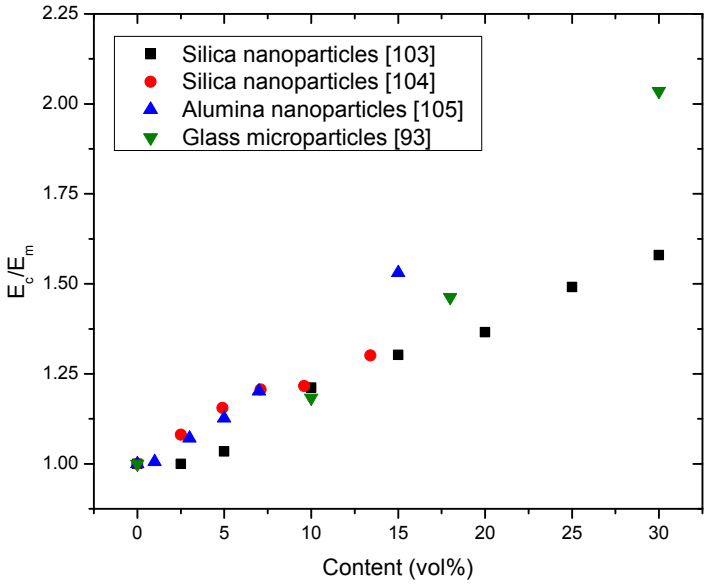


Figure 2.2.22: Relative modulus (E_c/E_m) of some rigid particle modified epoxy polymers [93, 103–105].

More recently, the availability of nanoparticles has meant that their use has become more widespread [106]. One of the major advantages of particles of the nanometre scale is the ability to use these materials in resin infusion processes. This is because conventional micron sized particles are typically larger than the inter-fibre spacing and as a result, can be filtered out during the infusion process. In addition, the viscosity penalty for nanoparticles is also significantly lower than that of micron sized particles [84].

There has been extensive research on silica nanoparticle modified epoxies from many researchers [5, 76, 103, 104, 107–110] and the toughening mechanisms are well understood. Hsieh *et al.* [5] reported the fracture performance of various epoxies modified with silica nanoparticles and modelled the fracture energy based on the toughening mechanisms observed, see Figure 2.2.23. The analytical modelling of fracture energy is discussed in §2.5.

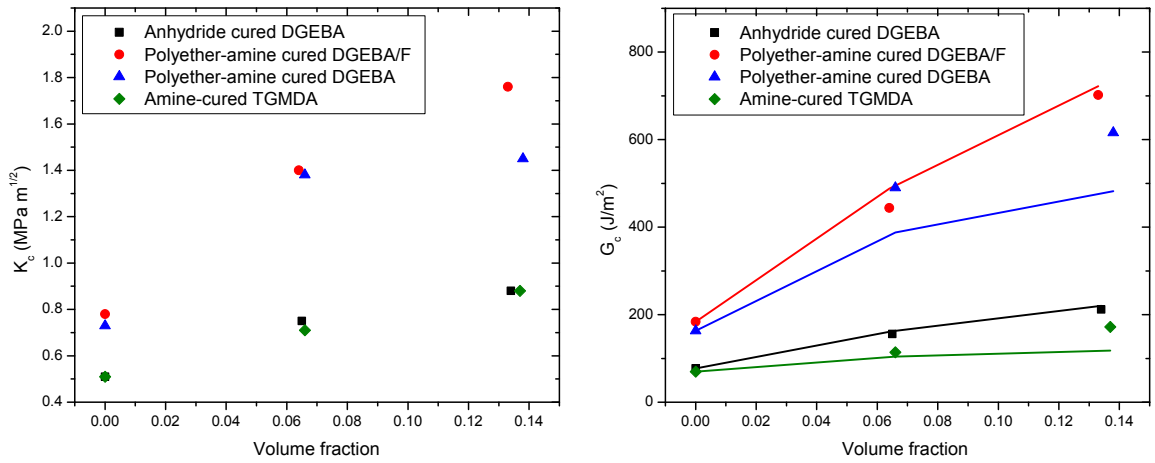


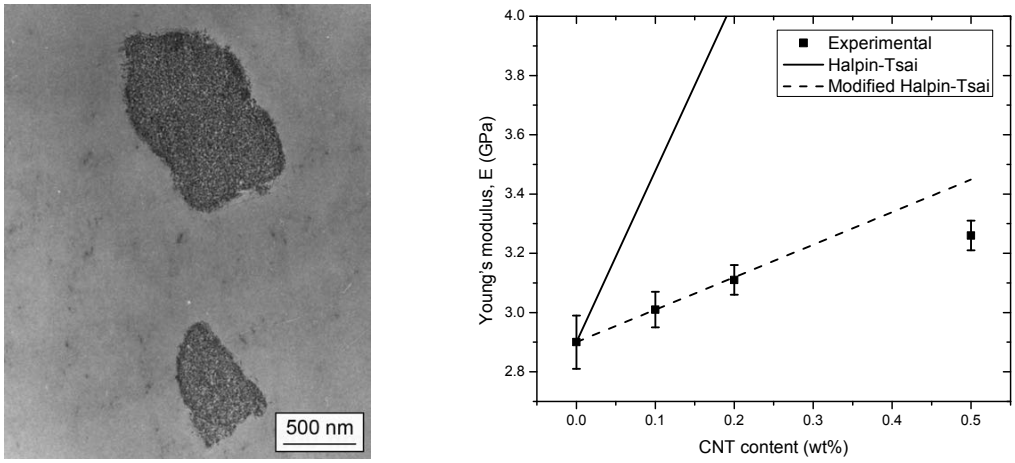
Figure 2.2.23: Fracture properties of silica nanoparticle modified epoxies; Experimental (■), Model (−). Reproduced from [5].

2.2.2.8 Organic rigid particles

Organic rigid particles such as carbon nanotubes (CNTs) [111], graphene [112], and carbon 60 fullerenes [113, 114] have attracted more attention recently, given the extraordinary mechanical performance of these modifiers. An elastic modulus of 1.0 TPa and tensile strength of 130 GPa were measured by nanoindentation for single layer graphene [115], making it one of the stiffest and strongest materials known.

The research conducted on epoxy polymers modified with carbon nanotubes covers a wide range of parameters such as the number of layers, aspect ratio, length and functionality [116–118]. The general consensus from the literature is that, while there is some improvement in modulus and fracture performance, the difficulties in dispersing the carbon nanotubes limit the effectiveness of these materials. Figure 2.2.24 shows the extent of CNT agglomeration and how this has resulted in the relatively low values of modulus determined experimentally, compared with the Halpin-Tsai model. The anisotropic nature of CNTs means that the CNTs need to be highly oriented to fully exploit the mechanical properties.

Carbon nanotubes are typically manufactured by a catalytic chemical vapour deposition (CVD) method. The output of this method is relatively low, even at large scale implementations, and this drives the price of CNTs up. Graphene nanoplatelets (GNPs) can be manufactured on a large scale at a higher rate, resulting in a cheaper product with similar properties. Structurally, GNPs share many similarities with layered silicates, which have been studied very extensively in the past 30 years [120]. Both are platelet type modifiers with a high aspect ratio that can increase the fracture toughness and modulus of epoxy polymers. Several authors have also reported other



(a) Agglomeration of carbon nanotubes. Reproduced from [119].

(b) Modulus of CNT modified epoxy. Reproduced from [117].

Figure 2.2.24: Incorporation of carbon nanotubes in epoxy polymer.

beneficial properties such as reduced gas permeability and increased thermal stability [121, 122]. There are four types of morphologies for epoxy-silicate composites, as shown in Figure 2.2.25. When the polymer matrix is inserted into the regions between the platelets, it is known as an intercalated microstructure. An exfoliated microstructure, both ordered and disordered, has a higher spacing between each platelet, which can be up to hundreds of times along the c-axis (out of plane) [123].

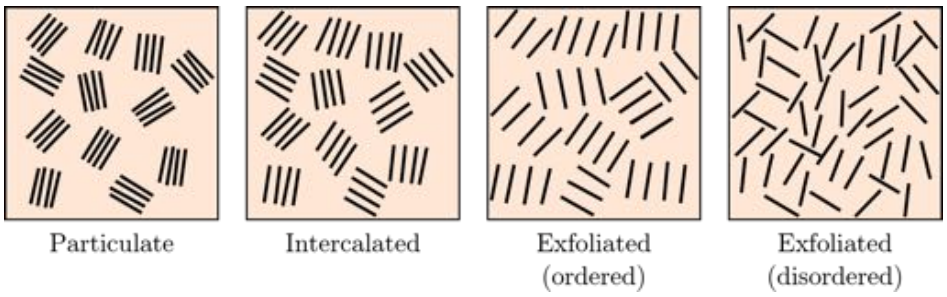
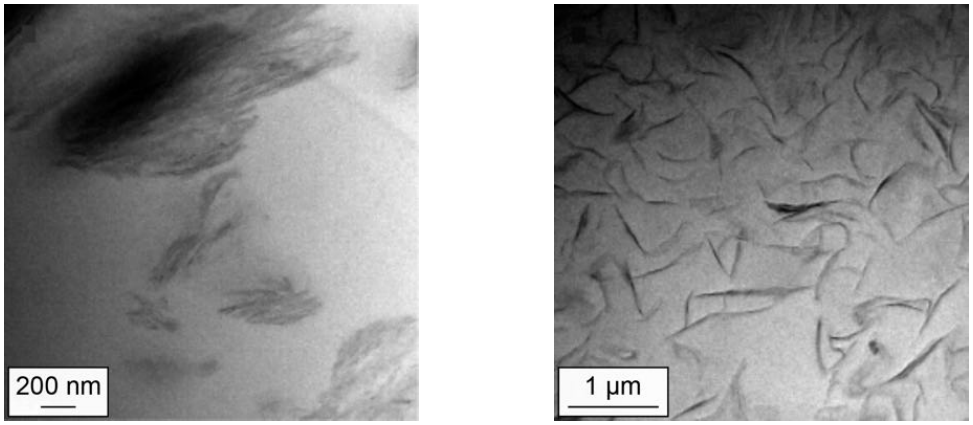


Figure 2.2.25: Microstructures of silicate modified epoxy polymers. Reproduced from [99].

Wang *et al.* [124] developed a method to disperse nanoclay by a "slurry-compounding" process. By fully exfoliating the nanoclays, as shown in Figure 2.2.26, they were able to improve the modulus and fracture toughness of epoxy polymers. Kinloch and Taylor [99] examined the use of five silicates with a range of sizes, aspect ratios and surface treatments. They found a maximum increase of 210% in modulus and 150% in fracture toughness for the untreated mica modified epoxy polymers. Similar results were also reported by other authors [125, 126]. This suggests that an intercalated structure may not be preferable, as this increases the thickness of the silicates, thus reducing the

aspect ratio.



(a) Mechanical mixing (b) "Slurry compounding process"

Figure 2.2.26: TEM micrographs of nanoclay modified epoxy polymers. Reproduced from [124].

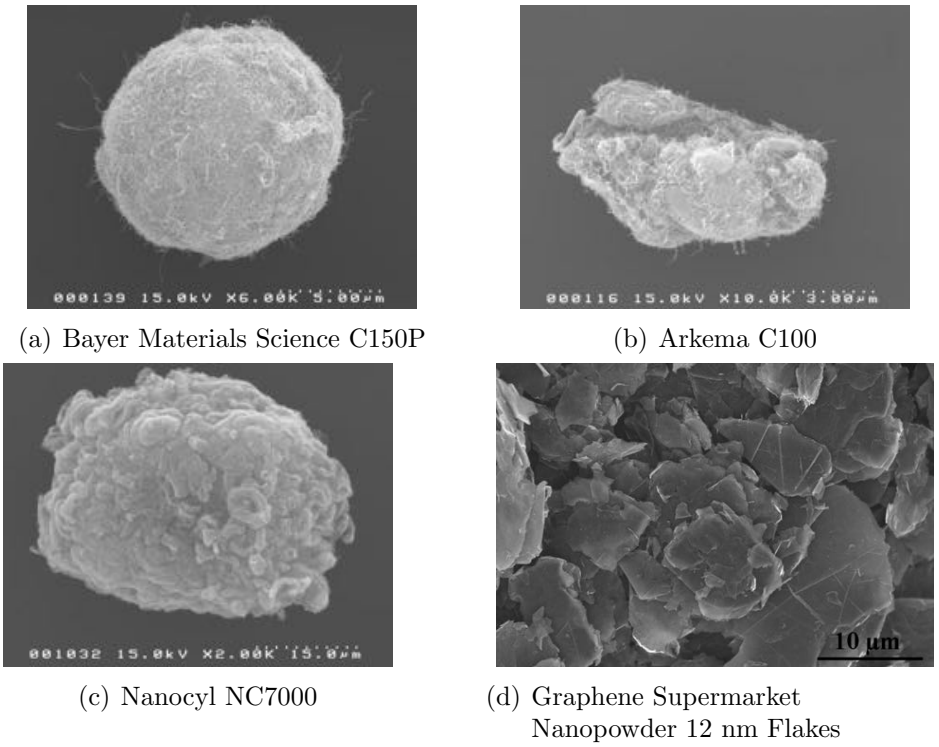
Detailed reviews on graphene research have been published [127, 128], specifically regarding their use as polymer reinforcement. The majority of the early research is based on graphene oxide [129–132] which can be easily exfoliated and dispersed in epoxy due to the attached functional groups. However, these functional groups reduce the mechanical properties and the presence of these heavy groups causes wrinkling of the graphene sheets [133]. Recent studies on the use of graphene in the form of graphene nanoplatelets [134–136] has shown some positive results although the mechanisms involved are not fully understood.

One of the first publications regarding the mechanical properties of GNP modified epoxy by Rafiee *et al.* compared epoxies modified with GNPs to CNTs. At the low weight percentages used, they showed that GNPs were more effective at increasing the modulus and toughness. However, they did not report on the quality of dispersion [135]. Chatterjee *et al.* [134] concluded that GNPs with a larger lateral dimension toughen epoxies more effectively but did not report on the aspect ratios and dispersion quality. Additionally, only two micrometre scale GNPs were tested. Zaman *et al.* incorporated GNPs into two epoxy polymers, one with a high T_g and one with a low T_g, and found higher values of K_{IC} for the high T_g epoxy system [137]. The authors claimed this was due to better compatibility between the epoxy and GNP, as well as dispersion quality in the high T_g system. However, this was not clearly presented and compared in their SEM images. In a separate study, they modified the GNPs with methylene diphenyl diisocyanate (MDI) to increase the interfacial adhesion between the GNPs and the epoxy [136]. Although they measured a higher fracture toughness for the surface modified GNPs, the Young's modulus decreased. This indicates a weaker

interfacial strength and also resulted in more agglomerated GNPs, as evident in their TEM micrographs.

2.2.2.9 Dispersion methods for carbon nanotubes and graphene nanoplatelets

The dispersion of carbon nanotubes and graphene nanoplatelets can significantly affect the mechanical and fracture performance of epoxy nanocomposites. The as-manufactured CNTs and GNPs from conventional suppliers are typically highly agglomerated, as shown in Figure 2.2.27, and need to be dispersed sufficiently in order to influence positively the nanocomposite properties.



(a) Bayer Materials Science C150P

(b) Arkema C100

(c) Nanocyl NC7000

(d) Graphene Supermarket Nanopowder 12 nm Flakes

Figure 2.2.27: Typical CNTs and GNPs as-received from suppliers. Reproduced from [138, 139].

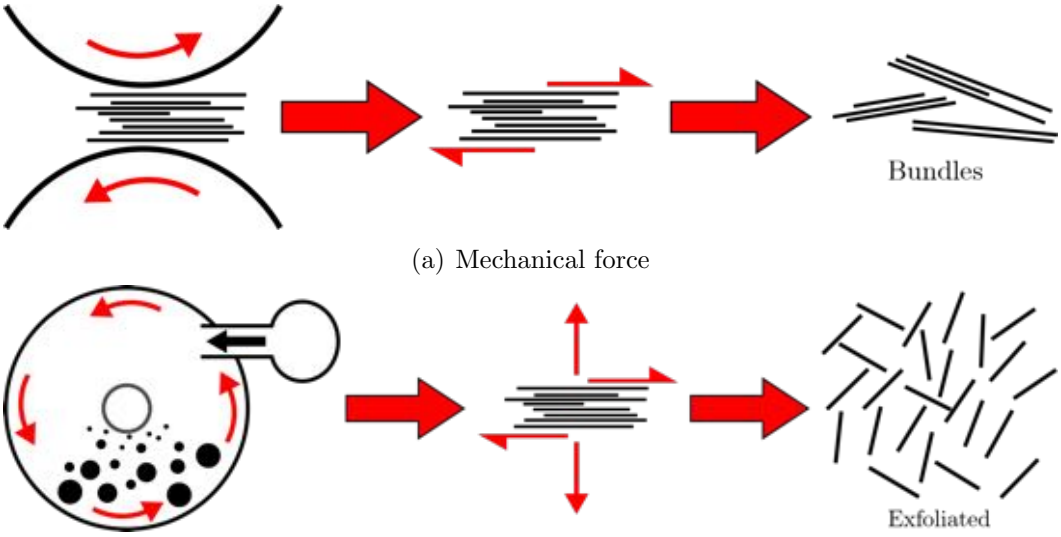
Graphene has a strong tendency to agglomerate due to its microstructure. The large surface areas contribute to strong van der Waals forces and the sp^2 bonded carbon structure means that there is significant $\pi - \pi$ stacking between each graphene sheet.

The main dispersion techniques that have been employed involve turbulent flow, cavitation and mechanical force [140]. Cavitation can be achieved by ultrasonication, which refers to a method of agitating particles by using ultrasonic waves (>20 kHz). Alternating waves of low pressure, which create bubbles or voids, and high pressure,

which then violently cavitate these bubbles, generate a large amount of energy locally. These shock waves effectively "peel off" each particle from the agglomerate to separate them [141]. Ultrasonication can be applied by either an ultrasonic bath or probe. Previous work [142] showed that the use of an ultrasonic probe was more effective than a bath, requiring less time and providing a higher level of nanotube dispersion. Several authors have also reported a good level of GNP dispersion in epoxy by ultrasonicating [136, 143].

Ultrasonication is only effective for low viscosity liquids because it is more difficult to achieve the cavitation for high viscosity or high surface tension liquids [144]. So for high viscosity liquids, such as epoxy, the use of a solvent is required. This is undesirable because solvent entrapment can be detrimental to the properties of the final product. Dispersing by a mechanical force mechanism typically involves a three roll mill [118, 119, 134, 145], screw extruder [146–149], ball-mill [150, 151] or high shear dispersers [140]. These techniques achieve dispersion by generating high shear forces in a viscous liquid between the rollers. Using a three roll mill, higher shear stresses can be generated by progressively reducing the gap between the rollers and/or increasing the speed of the rollers. A higher shear stress generally results in better dispersion. The process of shearing the sheets also has the effect of aligning them, which can be desirable. A ball-mill differs slightly in that it uses a grinding media which pulverises by impacting the ball with the particles, in addition to shearing.

Turbulent flow methods are similar to mechanical force in that they use shear forces to separate the bundles of material. An example of a turbulent flow method is a jet mill, which causes size reduction through collisions between particles at high velocities. It is different from mechanical methods in that it does not involve the use of a grinding media and that it applies a biaxial shear rather than a uniaxial shear force, as illustrated in Figure 2.2.28.



(a) Mechanical force

(b) Turbulent flow

Figure 2.2.28: Illustration showing difference in shear loading between mechanical force and turbulent flow methods. Reproduced from [140].

The use of a three roll mill for dispersing GNPs reported in the literature has been positive with regards to the quality of dispersion [119, 134, 145]. However, as with ultrasonication, it can cause damage to the CNTs or GNPs. Herceg *et al.* [146] showed that it was possible to incorporate up to 20 wt% of CNTs in epoxy using a twin screw extruder to exert very high shear forces. The nanocomposite was then collected from extruder and ground into a powder with a cryogenic ball mill. This powder was then consolidated into moulds to be cured in a vacuum bag under pressure. Subsequent investigations of the nanocomposites show well dispersed individual CNTs within the matrix, as shown in Figure 2.2.29.

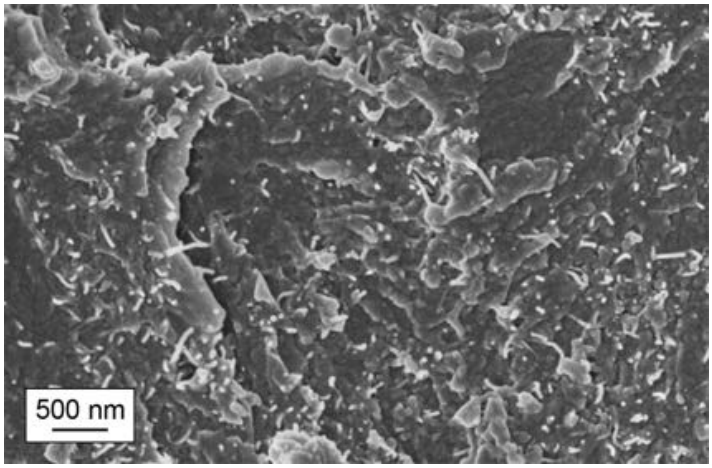


Figure 2.2.29: SEM micrograph showing dispersion of CNTs obtained using a twin screw extruder. Reproduced from [146].

For very high aspect ratio materials such as graphene and GNPs, the edges can be considered one-dimensional. These interfaces disrupt the symmetry of the graphene structure, which can cause an imbalance of local strain. Figure 2.2.30 illustrates some of the possible ways graphene sheets can be distorted due to the edge effects. In a folded structure, the edge is pulled up and back around the platelet. This is possible due to the flexibility of the graphene layers in the out-of-plane direction. Tubing is similar to folding with an additional process of rebonding into the top sheet to create a "pseudo-nanotube" at its edge. The rebonding process occurs by forming sp^3 bonds between the edge and surface carbon atoms. Scrolling refers to a process of rolling of the graphene layers to form a spiral structure at the edge [152]. Rippling and twisting are out-of-plane distortions caused by large functional groups terminated at the edges of the graphene sheet, which cause local strains, electrostatic repulsion or inter-group bonding along the edge [153]. Wrinkles are different from ripples in that they can be directional and form from the interior of the graphene sheets rather than the edges [154].

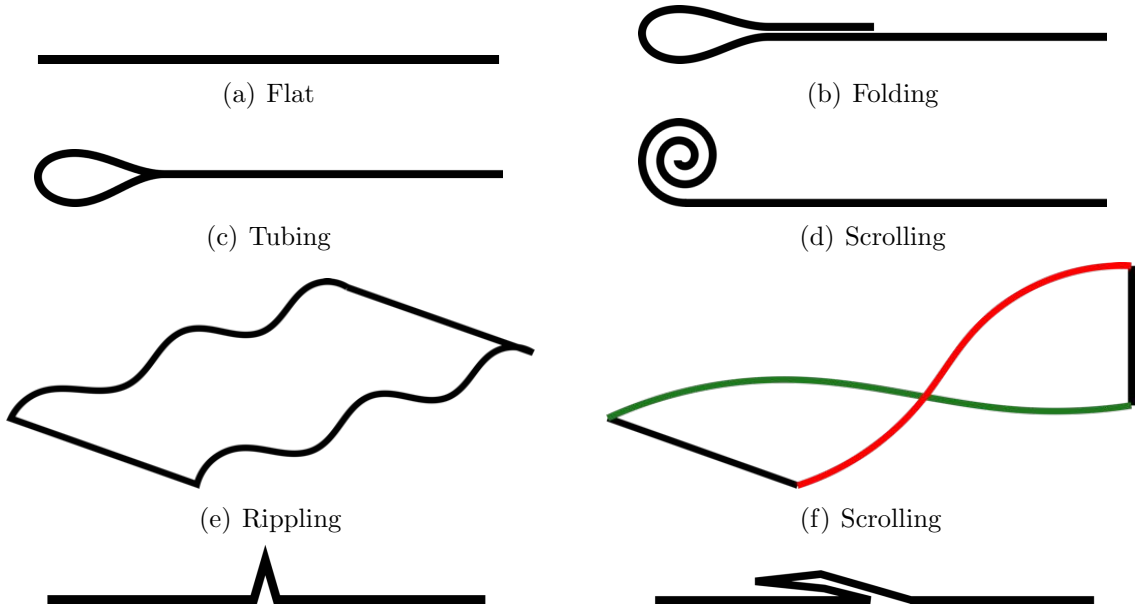


Figure 2.2.30: Illustrations showing possible distortion shapes of graphene sheets. Reproduced from [152].

2.2.2.10 Toughening mechanisms for rigid modifiers

The toughening mechanisms for rigid modifiers can be similar for both micro- and nano-sized modifiers. These mechanisms are crack pinning, crack deflection, crack bridging,

debonding, plastic void growth, pull-out and shear band yielding.

Crack pinning [155] increases the length of the crack front as it bows out between the particles while remaining pinned at the particles. Energy is also dissipated to create the fracture surface when the cracks from different planes meet. This can be observed experimentally as tails or steps behind a particle as shown in Figure 2.2.31.

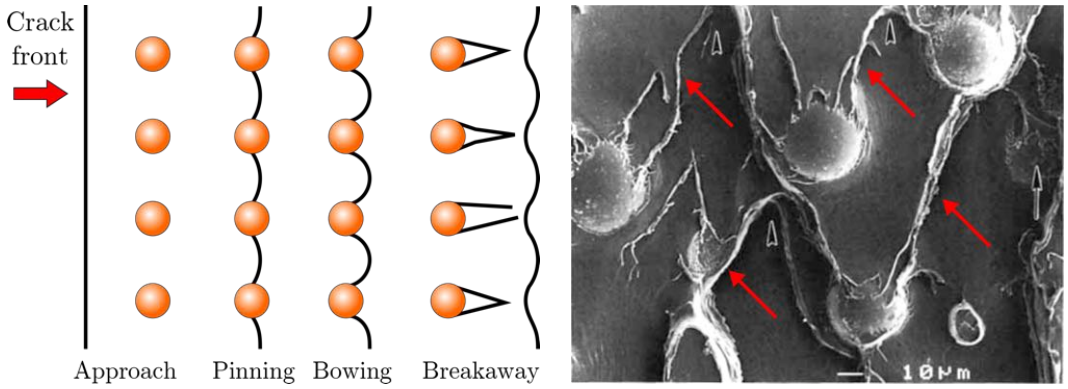
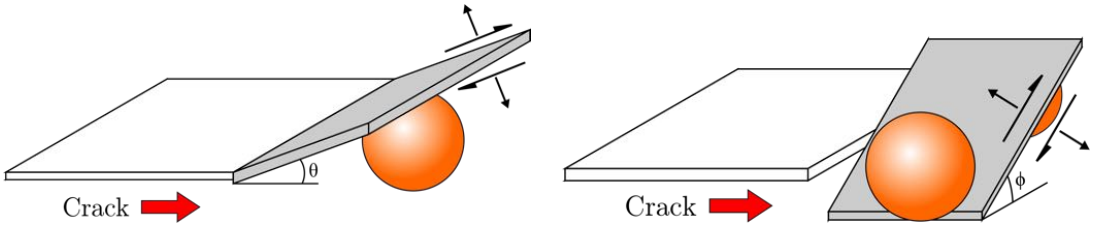


Figure 2.2.31: Crack pinning mechanism. Some of the tails are identified with arrows. Reproduced from [92].

Crack deflection is the tilting and twisting of the crack front as it encounters a rigid obstacle. This is promoted by the stress concentrations at the poles of rigid particles [156]. This is illustrated in Figure 2.2.32. A tilted crack induces local Mode I and Mode II loading and a twisted crack induces Mode I and Mode III loading [157].



(a) Crack tilt (b) Crack twist

Figure 2.2.32: Crack deflection mechanism. Reproduced from [157].

The two aforementioned mechanisms involve disrupting the crack front. While these mechanisms have been observed for micrometre scale rigid particles, they may not operate for nanometre scale particles such as the 20 nm silica nanoparticles used in this work, as described by Johnsen *et al.* [104]. They argued that the particle diameters should be of the same order of magnitude as the crack opening displacement in order to cause in-plane mechanisms, as illustrated in Figure 2.2.33.

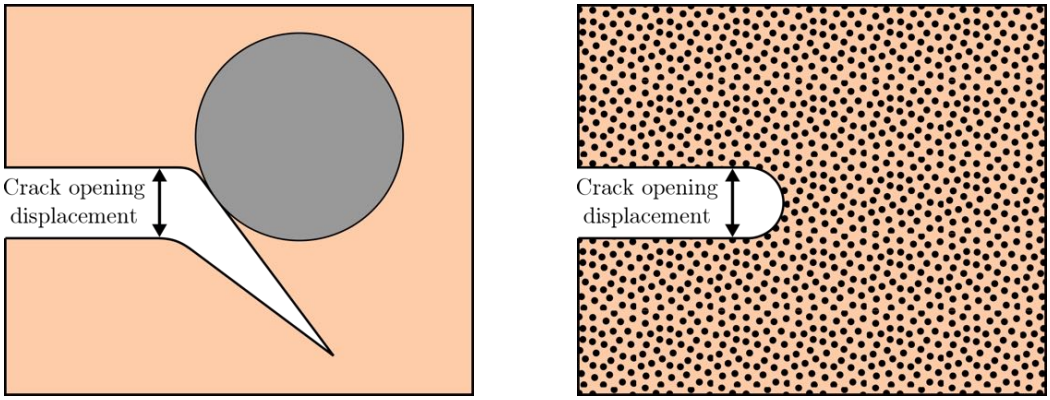


Figure 2.2.33: Crack deflection for micro and nanocomposites. Reproduced from [104].

The debonding process is similar to cavitation in that it does not absorb much energy, but relieves the triaxiality locally at the crack tip to allow plastic void growth to occur [89]. This has been observed for relatively large micron sized particles and for nanoparticles, as shown in Figure 2.2.34. Rubber particles can also debond if the particle/matrix adhesion is weak [158].

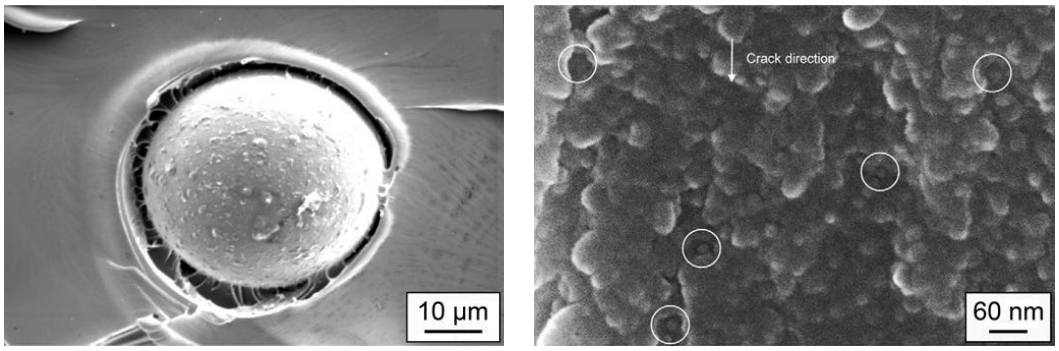


Figure 2.2.34: Debonding of glass microparticles and silica nanoparticles from the epoxy matrix. Reproduced from [5, 159].

Debonding is also required for the pull-out of CNTs or GNPs to occur, where frictional sliding can absorb significant quantities of energy [160]. The fracture of CNTs or GNPs is also a mechanism of energy dissipation [161], and those mechanisms are illustrated in Figure 2.2.35.

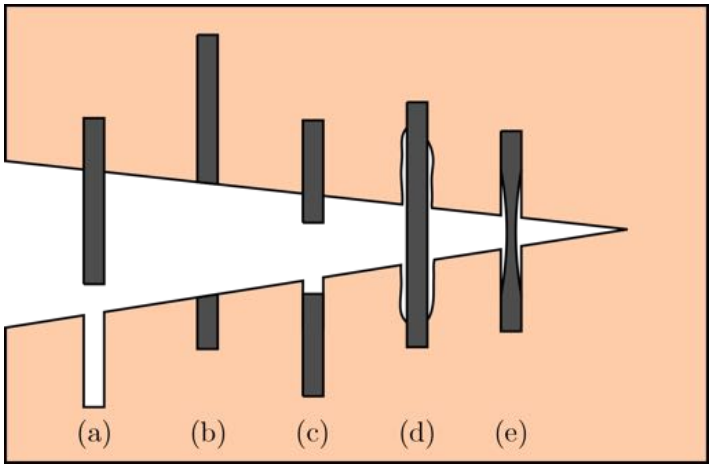


Figure 2.2.35: Toughening mechanisms for CNT and GNP modified epoxy polymers: (a) Pull-out, (b) Fracture, (c) Fracture and pull-out, (d) Debonding, (e) Bridging.

2.2.2.11 Influence of crosslink density

Following on from the discussion on toughening by chain extension (see Section 2.2.1), several authors [22, 23, 29, 162] have reported the effects of crosslink density on the toughenability of epoxies. The crosslink density can be quantified as the molecular weight between crosslinks, M_{nc}, determined using the theory of rubber elasticity:

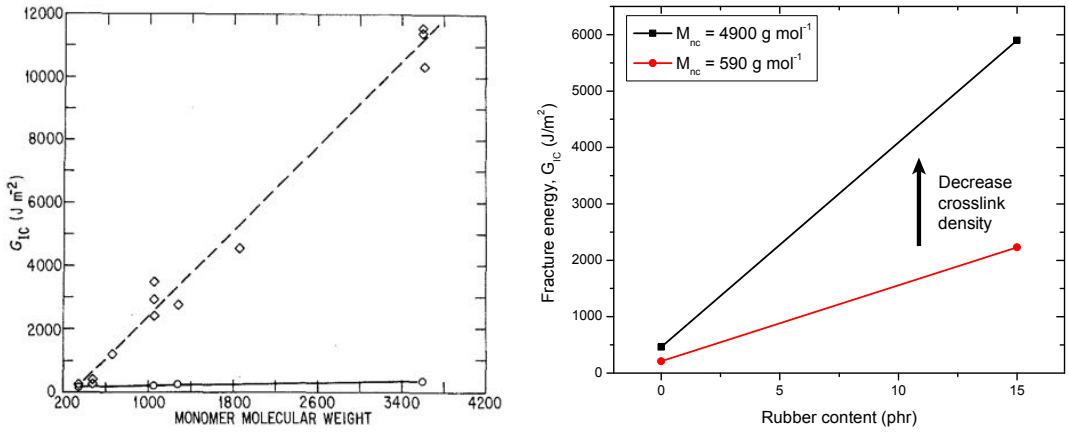
$$M_{nc} = \frac{q\rho \mathrm{R}T}{E_r} \tag{2.4}$$

where q is the front factor, ρ is the density at temperature T, R is the universal gas constant and E_r is the equilibrium modulus in the rubbery region. The M_{nc} can be altered by changing the molecular weight of the base epoxy resin [22], the curing agent [82], or the cure cycle [162].

Figure 2.2.36 shows how the crosslink density has a much stronger effect on the CTBN rubber modified epoxies than the unmodified epoxies. Pearson and Yee [22] used six different DGEBA epoxy resins of varying molecular weight, cured using DDS, to investigate the effect of crosslink density on the micromechanical deformation mechanisms of unmodified and rubber modified epoxies. They found that the G_{IC} of the unmodified epoxy was largely independent of the epoxy resin molecular weight. However, the G_{IC} of the rubber modified epoxies were highly dependent on the epoxy monomer molecular weight, i.e. crosslink density, as shown in Figure 2.2.36(a). They also noted that the toughening mechanisms were the same for the epoxies with different crosslink densities.

Kinloch *et al.* [162] changed the crosslink density by altering the cure cycle of a piperi-

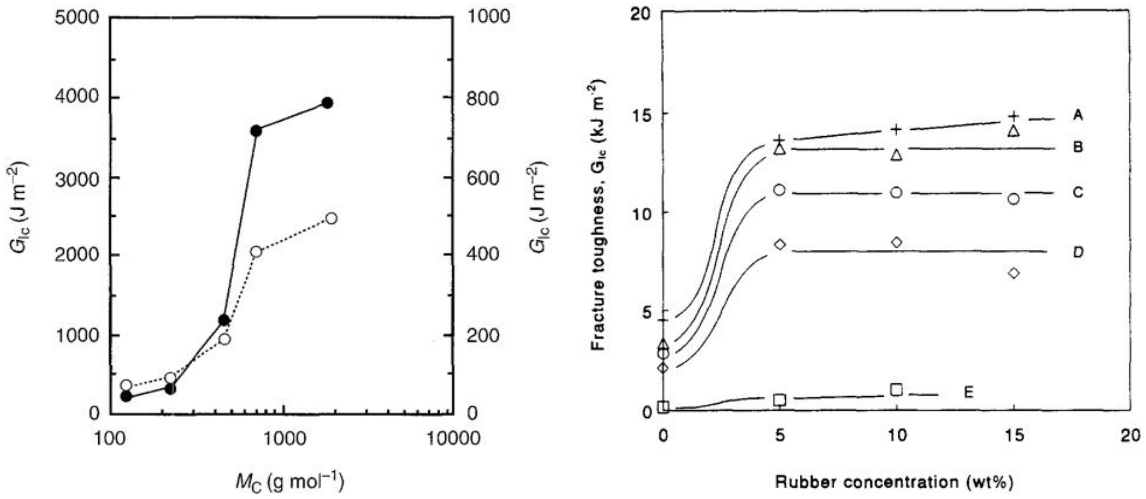
dine cured DGEBA epoxy. This allowed them to maintain a similar microstructure for different cure cycles. They measured a much higher increase in G_{IC} for a lower crosslink density epoxy, shown as the black line in Figure 2.2.36(b).



(a) From [22] (b) From [162]

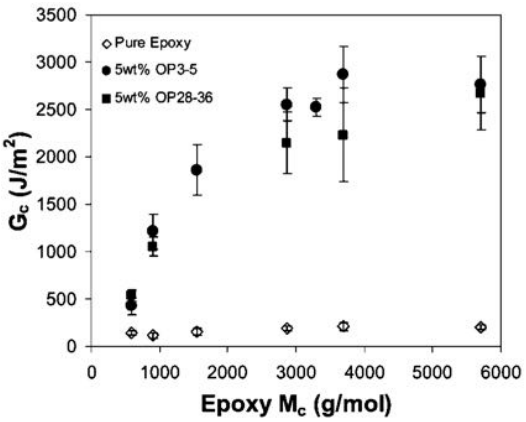
Figure 2.2.36: Effect of crosslink density on the toughness of CTBN rubber modified epoxy polymers.

The effect of crosslink density on the toughenability of epoxy polymers is not limited to CTBN rubber modifiers. Other studies involving CSR, BCP and silica nanoparticles have shown similar trends in toughenability, as shown in Figure 2.2.37. The premise is that reducing the crosslink density can increase the flexibility of the molecular chains, which in turn enhances the toughening mechanisms. The change in chain mobility did not affect the toughening mechanisms observed in these studies [5, 52, 163, 164].

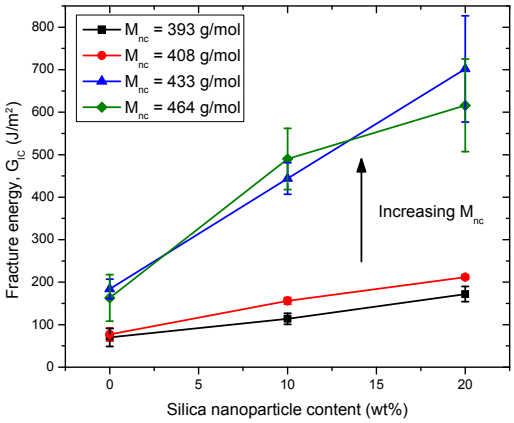


(a) (○) Unmodified and (●) CSR modified epoxies. Left hand scale for modified epoxy and right hand scale for unmodified epoxy. Reproduced from [163].

(b) CSR modified epoxies. M_c=(A) 6.79; (B) 4.38; (C) 1.64; (D) 0.88; (E) 0.26 kg mol^{-1}. Reproduced from [164].



(c) BCP. Reproduced from [52].



(d) Silica nanoparticle. Reproduced from [5].

Figure 2.2.37: Effect of crosslink density on the fracture energy of various modified epoxy polymers.

It should be noted that the crosslink density is not directly related to the ductility of the epoxy. Epoxy polymers with the same crosslink density can have different ductility due to the flexibility of the different molecular chains.

2.2.2.12 Influence of particle size

The role of particle size plays an important role in both fracture toughness and material processing. Early work suggested that the fracture toughness of rubber modified epoxy polymers is independent of particle size [3, 81]. Since then, many authors have studied the effect of particle size on rubber modified epoxies [21, 165–168]. The general agreement between the studies was that it is the cavitation of these particles that increases the fracture toughness, as it allows shear yielding and plastic void growth to occur. For a given plastic zone size, the number of particles present is related to the size, and more particles allow more cavitation and localised shear yielding to occur. But there is no agreement on a definite size below which the particles do not cavitate.

Girard-Reydet *et al.* [169] reported cavitation of 15 nm SBM particles. However, several investigations on small CTBN rubber particles found that particles smaller than ∼0.1 μm do not cavitate [170]. The particle size effect arises from the difference in energy contributions. The energy applied is dependent on the volume of material ($\propto r^3$), whereas the surface energy is dependent on the area of the void created ($\propto r^2$).

The size effect of rubber particles were investigated by Guild *et al.* [80] using an energy approach to predict the onset of particle cavitation under uniaxial and triaxial loading conditions. The model was developed with a combination of experimental observations

and finite element simulations. The surface energy of a void created by cavitation was calculated by simulations based on experimental deductions of the onset of cavitation under applied uniaxial strain. This value of surface energy was then used in further simulations to deduce the onset of cavitation for different particle sizes and loading conditions. Unsurprisingly, larger particles cavitate at a lower applied strain and a triaxial stress state is preferred for cavitation, as shown in Figure 2.2.38. At rubber particle radii above 1 μm, the level of applied strain does not change much. However, below particle radii of 1 μm, the applied strain required to cause cavitation increases rapidly. This also implies that particles ahead of a crack cavitates at a lower applied strain than those under uniaxial loading without a crack.

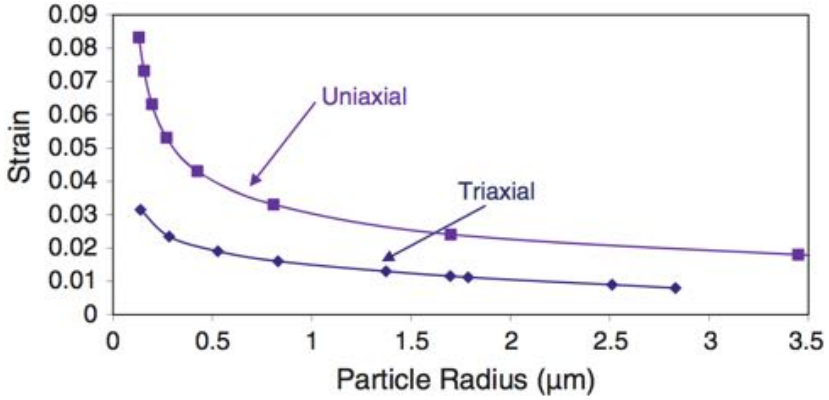


Figure 2.2.38: Particle size effect from cavitation criterion under uniaxial and triaxial loading. Reproduced from [80].

The stress required to debond a particle was modelled analytically by Chen *et al.* [110] and Lauke [171], as shown in Figure 2.2.39. There is a sharp increase in the critical stress required to debond a particle as the particle size decreases. To optimise the nanocomposite, the stress to debond should be roughly equivalent to the yield strength of the polymer [84]. The difference between the two models stems from the fact that Chen *et al.* considers a viscoelastic matrix material, whereas the model from Lauke considers only an elastic material. The Chen model is more conservative, predicting values that are approximately double that using the Lauke model. At 10 nm, the critical stress required to debond a particle was calculated to be 67 MPa using the Lauke model and 131 MPa using the Chen model.

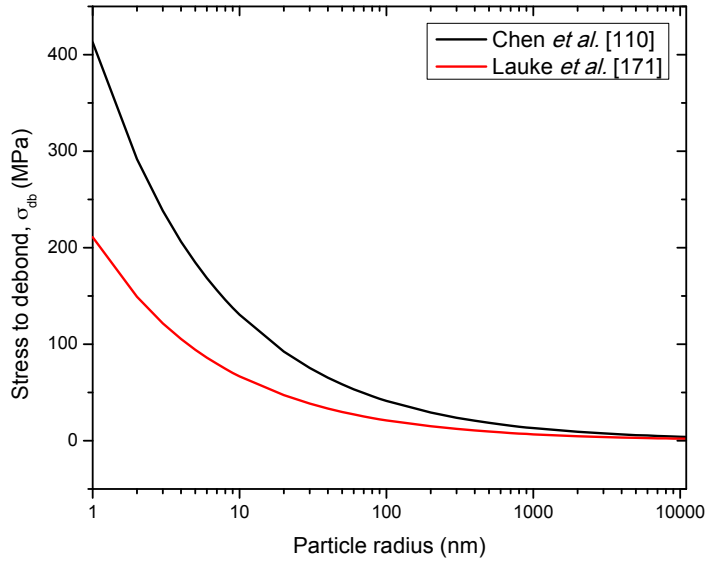
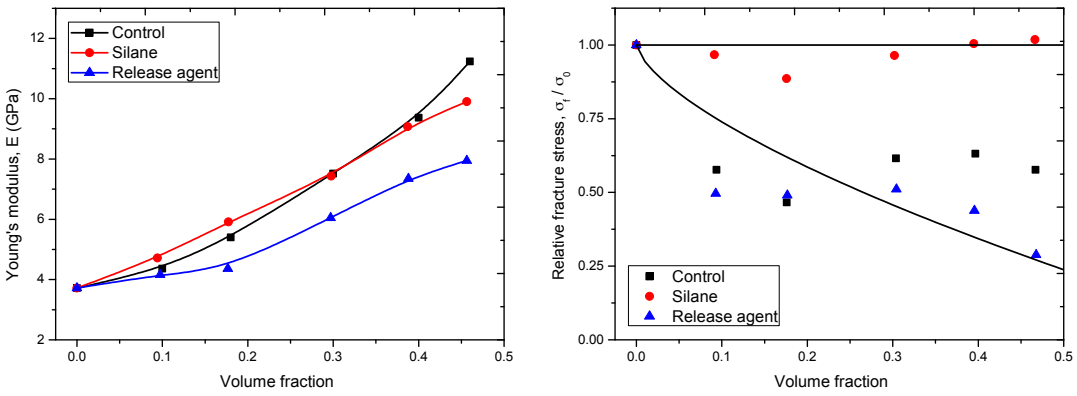


Figure 2.2.39: Critical stress to debond for different particle sizes [110, 171].

2.2.2.13 Influence of particle/matrix adhesion

The role of particle/matrix adhesion on the mechanical and fracture performance was first investigated by Spanoudakis and Young [94] using glass spheres. The particles were mixed with a silane adhesion promoter and a release agent to increase and decrease the level of adhesion, respectively. The release agent significantly reduced the Young's modulus due to poorer stress transfer into the much stiffer glass spheres, as shown in Figure 2.2.40(a), whereas the silane treated glass spheres did not further improve the Young's modulus. At a volume fraction of 40%, the Young's modulus was measured to be approximately 8.5 GPa for the untreated and silane treated glass sphere modified epoxy and 7 GPa for the release agent treated glass sphere modified epoxy. Furthermore, the silane surface treatment maintained the fracture stress as the unmodified epoxy, whereas the untreated and release agent treated glass spheres caused a reduction in fracture stress, as shown in Figure 2.2.40(b). The improved adhesion effectively minimises the stress concentrations due to the particles.

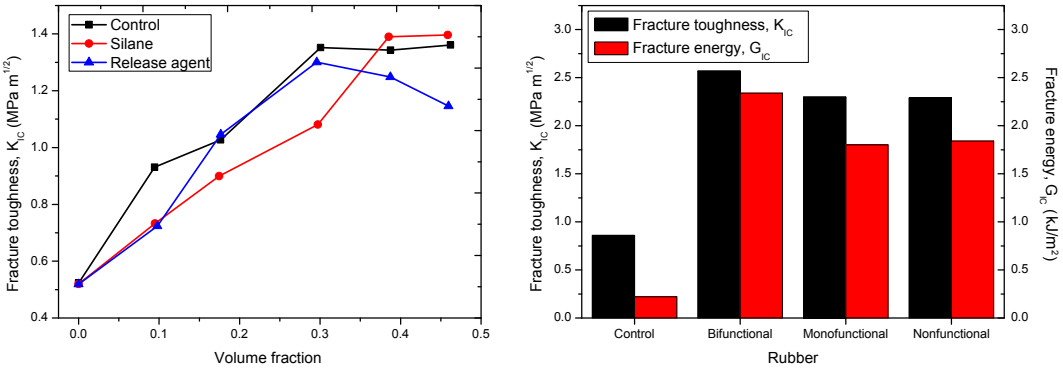
The reported values of K_{IC} were largely independent of the surface treatment as shown in Figure 2.2.41. For glass spheres, Spanoudakis and Young [94] suggested that well bonded particles toughen by crack pinning and poorly bonded particles toughen by crack blunting. Studies by other authors on different modifiers have confirmed these trends [101, 159, 172]. Huang *et al.* [170] investigated rubber modified epoxies with different levels of particle/matrix adhesion by changing the reactivities of the rubbers. The nonfunctional rubbers have the weakest particle/matrix adhesion and the bifunctional rubbers have the strongest levels of particle/matrix adhesion due to the ability



(a) Young's modulus (b) Relative fracture stress

Figure 2.2.40: Young's modulus and fracture strength of glass filled epoxies with varying interfacial adhesion. Reproduced from [94].

to form primary bonds at the interface. The bifunctional rubbers phase separated into much smaller particles than the nonfunctional rubbers (particle diameters of 1.8 μm compared to 30 μm). Despite this large discrepancy in particle size, the particle/matrix adhesion has little effect on the measured value of fracture toughness and fracture energy, as shown in Figure 2.2.41(b). The authors attribute this to competition between the particle cavitation and debonding processes. Both mechanisms dissipate little energy, but are crucial in relieving the stress state ahead of the crack tip to initiate plastic void growth and shear yielding.

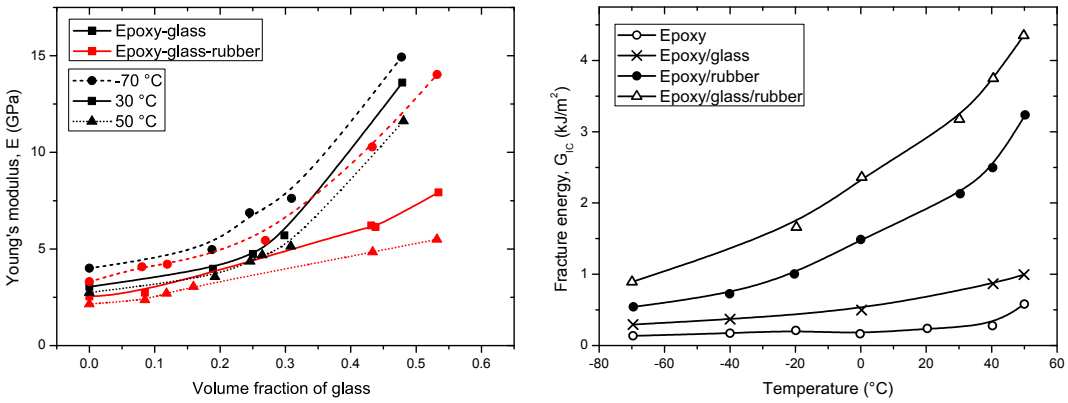


(a) Reproduced from [94] (b) Reproduced from [170]

Figure 2.2.41: Fracture properties as a function of particle/matrix adhesion. Reproduced from [94, 170].

2.2.2.14 Hybrid toughening

Hybrid toughening in this context refers to the use of two or more types of tougheners. Typically, this involves the use of both rigid and soft modifiers in an attempt to minimise the deficit in modulus of rubber modified epoxies. Kinloch *et al.* were one of the first research groups to take this approach [173–175] and investigated epoxy polymers modified with CTBN rubber and 50 μm glass spheres. The modulus and fracture energies of the hybrid modified epoxies are shown in Figure 2.2.42. The trend at each temperature was similar, with the Young's modulus greatly reduced by the addition of 15 phr rubber. They also found that the rubber toughened epoxy can be toughened further by the addition of 10 vol% of the glass spheres. They attributed this toughness to crack pinning around the glass spheres and localised shear yielding enhanced by the rubber particles.

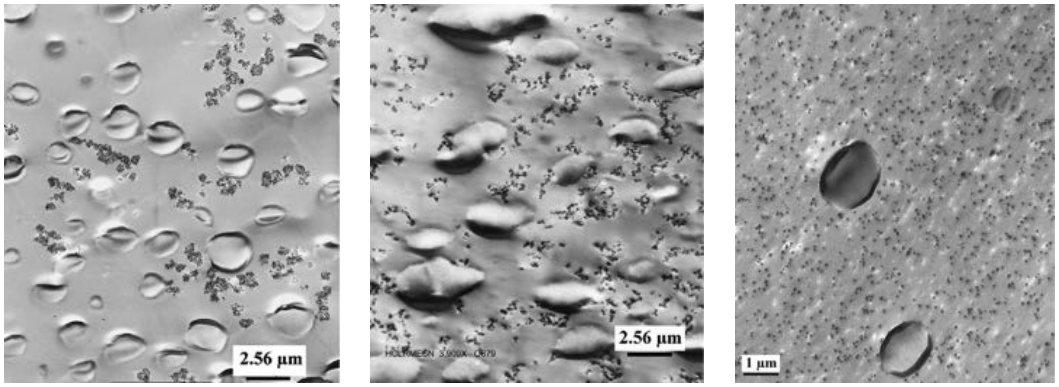


(a) Young's modulus. Reproduced from [175]. (b) Fracture energy. Reproduced from [174].

Figure 2.2.42: Hybrid modified epoxy polymers.

Several other authors [76, 92, 142, 176–183] have since reported on soft/rigid particle hybrid systems. The soft and rigid phases typically used are of those discussed in the previous sections, as these materials are already well understood and readily available. The materials that have received the most attention recently are those that use CTBN or CSR particles with silica nanoparticles. The addition of CTBN in epoxy already imposes a significant viscosity penalty. Therefore the use of silica nanoparticles rather than glass microparticles is preferred. The morphology of these materials appears to be dependent on the content of each modifier, as shown in Figure 2.2.43. Liang and Pearson [179] found that above 12 vol% of CTBN, 20 nm and 80 nm silica nanoparticles agglomerate into clusters. Mohammed [184] found larger agglomerates of silica nanoparticles form when more silica was added and the presence of silica nanoparticles can indeed affect the cure kinetics, causing more of the rubber to remain dissolved in

the epoxy.



(a) 3.1 vol% 80 nm NS and 20.9 vol% CTBN (b) 3.1 vol% 20 nm NS and 20.9 vol% CTBN (c) 3.1 vol% 80 nm NS and 12 vol% CTBN

(d) 3.1 vol% 80 nm NS and 16.6 vol% CTBN (e) 2.3 wt% 20 nm NS and 9 wt% CTBN (f) 15.4 wt% 20 nm NS and 9 wt% CTBN

Figure 2.2.43: TEM micrographs of hybrid CTBN-silica nanoparticle (NS) modified epoxy polymers. Reproduced from [179, 184].

Synergy has been reported for some hybrid modified polymers, which has created some very tough materials that would otherwise not be possible by simply increasing the modifier content [76, 179, 182, 185, 186]. The synergy comes from additional toughening mechanisms or interactions between the two different modifiers that results in higher fracture energy. The term synergy in this case is defined as additional fracture energy when considering the individual contributions from each modifier as additive, i.e.:

$$\Delta G_{Hybrid} = \Delta G_{CTBN} + \Delta G_{silica} + \boldsymbol{\Delta G_{synergy}} \tag{2.5}$$

Figure 2.2.44 shows the fracture toughness for hybrid CTBN-silica nanoparticle modified DGEBA epoxy cured with piperidine [109, 179]. Liang and Pearson [179] showed that the further addition of silica nanoparticles at low quantities (3.3 vol%) to a CTBN modified epoxy can further improve the G_{IC} above that achievable by CTBN modification alone. However, they also noted that synergy was not observed when the silica

nanoparticles were heavily clustered, which occurs at high CTBN contents.

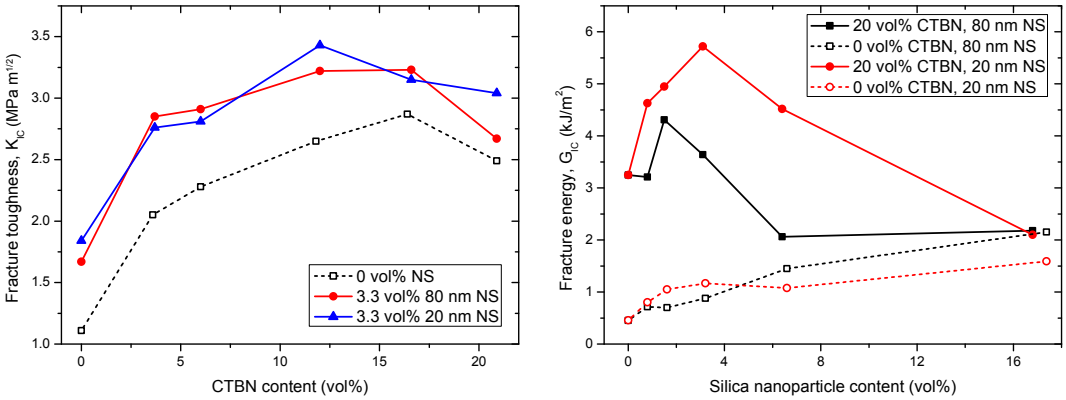


Figure 2.2.44: Fracture energy for hybrid CTBN-silica nanoparticle modified epoxy polymers. Reproduced from [109, 179].

Similarly for a higher T_g epoxy system, Hsieh *et al.* [76] measured values of $G_{synergy}$ that contributed to up to 18% of the total G_{IC} value by further adding silica nanoparticles to a CTBN modified epoxy. Carbon nanotubes have also been used in conjunction with CTBN rubber to modify DDS cured DGEBA epoxy [182]. The authors measured an increase in the K_{IC} value of the 5 wt% CTBN modified epoxy by 10% when a further 0.3 wt% of CNTs were added.

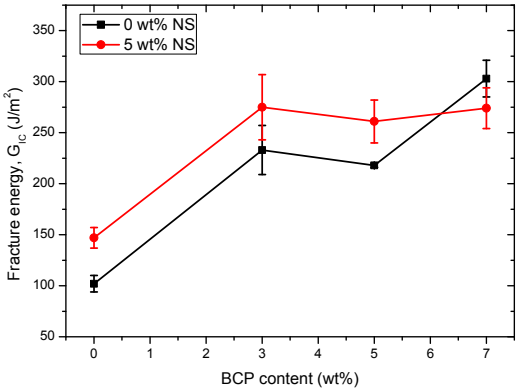
Thus, a significant improvement in fracture performance can be found when a small amount of secondary modifier is added to create these hybrid, ternary systems. There are several hypotheses towards explaining where the extra $G_{synergy}$ may arise from. Liang and Pearson [179] considered the role of interparticle distance to explain the synergy observed between micron sized rubber particles and silica nanoparticles. The surface-to-surface interparticle distance, τ is given by:

$$\tau = d\left[\left(\frac{\pi}{6\phi_p}\right)^{\frac{1}{3}} - 1\right] \tag{2.6}$$

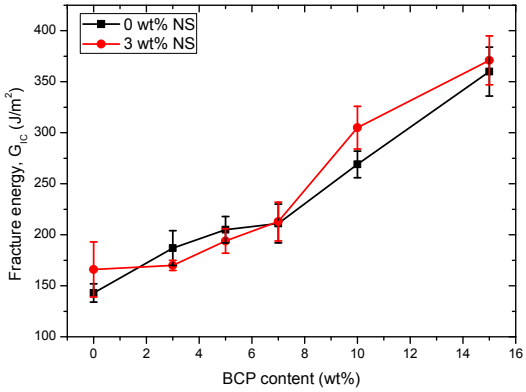
where d is the particle diameter and ϕ_p is the particle volume fraction. The authors suggest that large interparticle distances allow the nanoparticles to initiate additional toughening mechanisms in those regions. However, it is well known that the regions between particles exhibit significant plastic deformation through shear yielding and stress field overlaps.

Synergistic behaviour is not always observed for ternary systems where the modifiers have similar particle sizes [84, 180, 187], as shown in Figure 2.2.45. Chen [180] added silica nanoparticles to high T_g epoxies which were modified with block copolymers, and

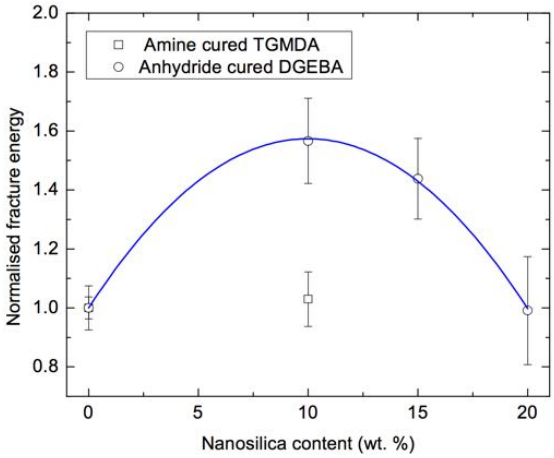
found no further increases in G_{IC} as shown in Figures 2.2.45(a) and 2.2.45(b). Masania [84] noted that synergy was observed in a CTBN-NS hybrid modified DGEBA epoxy cured with an acid anhydride, but not in an amine cured TGMDA, as shown in Figure 2.2.45(c). This behaviour appears to change with the epoxy system and the modifiers used, and indicates the need to look into the mechanisms at play. Hsieh *et al.* [76] considered two possible mechanisms: (i) stress field interactions between particles of very different moduli, Poisson's ratio and size or (ii) cavitation of rubber particles that enhance the shear band yielding inititating from all the particles. Sprenger [188] suggested that the silica nanoparticles increased the amount of CTBN that remains dissolved in the epoxy. This in turn plasticised the polymer, increased the ductility and thus enhanced the rubber toughening effect.



(a) MAM modified anhydride cured DGEBA.



(b) MAM modified aromatic amine cured DGEBA.



(c) 9 wt% CTBN modified epoxy polymers.

Figure 2.2.45: Fracture energy for hybrid modified epoxy polymers. Reproduced from [84, 180].

2.3 Toughening of fibre-reinforced polymer composites

Fibre reinforced polymer (FRP) composites are comprised of strong and stiff fibres, typically of carbon, glass or aramid, held together by matrix material which serves to transfer the load to these fibres and protect them from damage. Thermosetting polymers, such as epoxies, are the most commonly used because of the low shrinkage, good chemical and thermal resistance and superior mechanical performance to other matrix materials [189].

The toughening mechanisms of FRPs are typically fibre dominated: fibre fracture, fibre bridging, interfacial debonding and fibre pull-out. However, premature failure can occur due to defects such as microcracks in the matrix and surface flaws on the fibres. Delamination of the laminates is also a common failure mechanism for FRP composites. For example, microcracking caused the failure of the Lockheed Martin X-33 spaceplane CFRP liquid hydrogen tank [190]. The resistance to these failure modes can be increased by changing the fibre/matrix adhesion and matrix toughness. This section of the literature review will focus on the contribution from the matrix toughness, as that is the main investigation of this thesis.

Hunston *et al.* [191] reviewed the effect of matrix toughness on the interlaminar fracture toughness of FRPs for various types of matrix material mentioned in the literature. They found that for low G_{IC} epoxies, the composite G_{IC} values were almost three times higher due to the fibre dominated mechanisms. However the high G_{IC} epoxies did not transfer the bulk toughness into a high composite toughness. The transition between the two regions occured at an epoxy G_{IC} of approximately 300 J/m^2, as shown in Figure 2.3.1. They found that the size of the deformation zone was roughly equal to the interfibre spacing, suggesting that the much stiffer fibres restricted the plastic zone. Similar findings were also reported by other authors [192–195].

More recently, Hsieh *et al.* [76] reported an increase in the bulk G_{IC} from 77 J/m^2 to 212 J/m^2 when 20 wt% of silica nanoparticle was added to an anhydride cured DGEBA epoxy, which translated to an increase in interlaminar fracture energy of fibre reinforced composites, as shown in Figure 2.3.2. When used with rubber particles to form a 'hybrid' material matrix, they found improved fibre/matrix adhesion which lead to higher composite G_{IC} values.

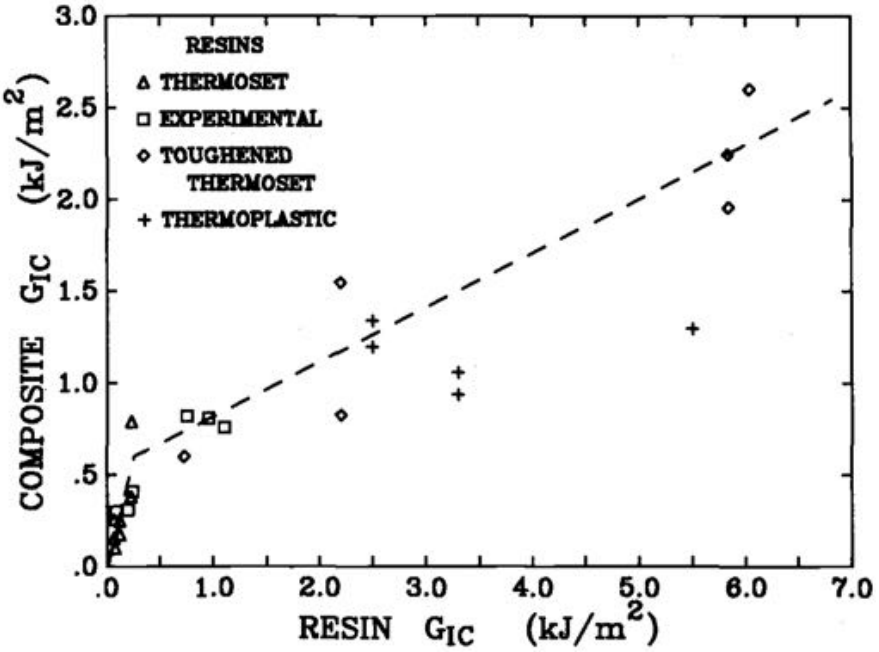


Figure 2.3.1: Composite interlaminar fracture energy as a function of resin fracture energy. Reproduced from [191].

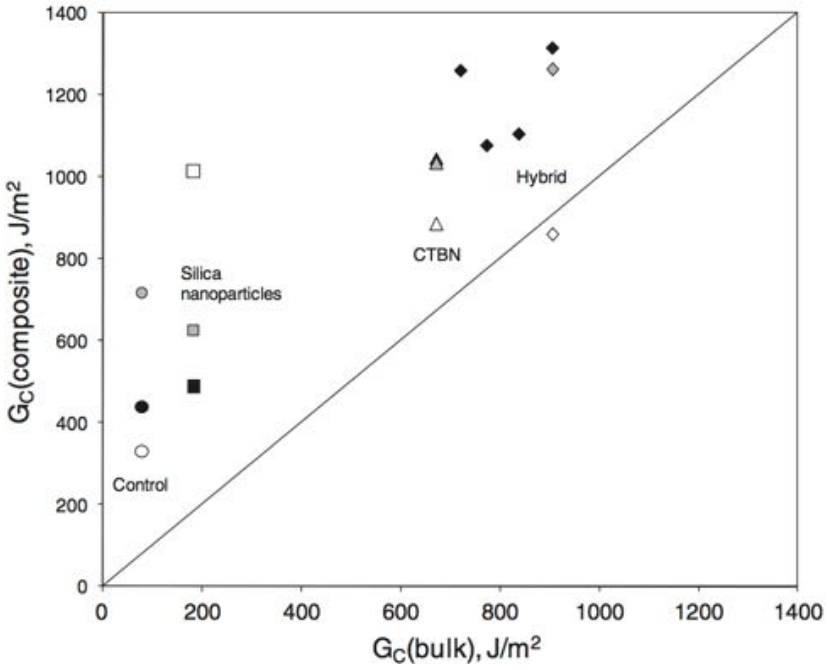
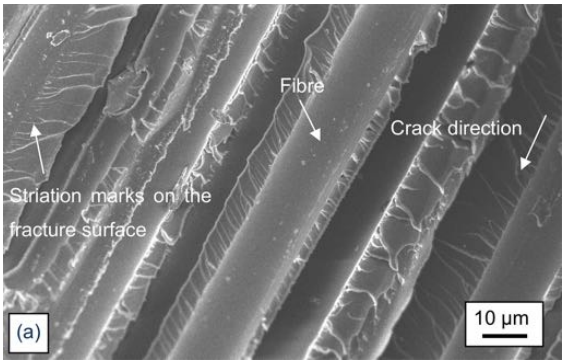


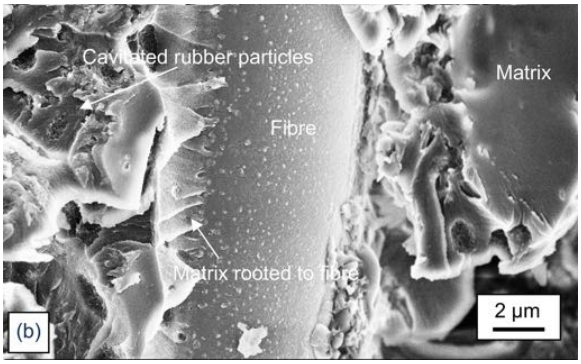
Figure 2.3.2: Transfer of G_{IC} from bulk to interlaminar fracture energy $G_{IC}(composite)$. Reproduced from [76].

The improved fibre/matrix adhesion and matrix deformation can be observed on the fracture surfaces of a DCB sample tested in mode I, as shown in Figure 2.3.3. The fibres in the unmodified epoxy matrix were relatively clean with little evidence of epoxy on the surfaces, as shown in Figure 2.3.3(a). This indicates failure at the fibre/matrix

interface. When a hybrid modified epoxy matrix was used, residual matrix was observed to have remained on the fibres, as shown in Figure 2.3.3(b), which suggests stronger fibre/matrix adhesion than the unmodified epoxy. The bulk toughening mechanisms are present in the inter-fibre regions which dissipate energy and increase the fracture toughness of these hybrid modified FRPs.



(a) Unmodified epoxy matrix



(b) Hybrid modified epoxy matrix

Figure 2.3.3: Fracture surfaces of DCB test samples of glass fibre reinforced composites tested in mode I. Reproduced from [84].

Bacigalupo and Pearson [167] observed a smaller damage zone for block copolymer modified epoxy, compared to rubber modified epoxy. These block copolymers could be useful for improving FRP interlaminar fracture toughness, as the composite G_{IC} appears to be limited by the size of the deformation zone.

2.4 Analytical modelling of composite stiffness

The prediction of the mechanical properties, such as the modulus and Poisson's ratio, of heterogeneous composites is key to understanding the mechanical response of such composite materials. As such, the determination of the elastic properties of two phase composite materials has received considerable attention [196–198]. The following

section reviews the most widely used analytical solutions from the literature for the prediction of elastic properties of two phase composites. The composite properties can be derived as a function of filler shape, size, distribution, filler/matrix adhesion, modulus and Poisson's ratio of each phase. These analytical models have been developed from constitutive relationships or by a semi-empirical method.

2.4.1 Bounds

The simplest models are the upper and lower bounds of the composite modulus. These constitute values of moduli which the composite material cannot exceed. The upper bound of the composite modulus, E_U, is given by the Voigt model [199]. This is also known as the "rule of mixtures" or parallel model:

$$E_U = v_f E_p + (1 - v_f) E_m \tag{2.7}$$

The lower bound, E_L, is given by the Reuss model [200], also known as the series model:

$$\frac{1}{E_L} = \frac{v_f}{E_p} + \frac{(1 - v_f)}{E_m} \tag{2.8}$$

where v_f is the volume fraction of modifier, E_p is the modifier modulus and E_m is the matrix modulus. The Voigt model assumes constant strain and the Reuss model assumes constant stress across both phases.

The tightest upper and lower limits of moduli that can be specified without considering phase geometries are known as the Hashin-Shtrikman bounds [201]. Hashin and Shtrikman derived the effective elastic moduli bounds using the variational theorems of the theory of elasticity. The upper and lower bounds can be derived by finding the maxima and minima of the stationary value of the functional, U_p, where U_p is equal to the strain energy U stored in the changed body [201]. These limits are more meaningful and are given as:

$$K_{HS} = K_1 + \frac{v_{f2}}{\frac{1}{K_2 - K_1} + \frac{v_{f1}}{\left(K_1 + \frac{4}{3}G_1\right)}} \tag{2.9}$$

$$G_{HS} = G_1 + \frac{v_{f2}}{\frac{1}{G_2 - G_1} + \frac{2v_{f1}(K_1 + 2G_1)}{5G_1\left(K_1 + \frac{4}{3}G_1\right)}} \tag{2.10}$$

where K is the bulk modulus, G is the shear modulus and v_f is the volume fraction. The subscripts 1 and 2 represent the soft and rigid phases. The upper bound is obtained when phase 1 is the stiffer material and the lower bound for the inverse. Figure 2.4.1

shows an example of the upper and lower bounds predicted by the Voigt, Reuss and Hashin-Shtrikman bounds.

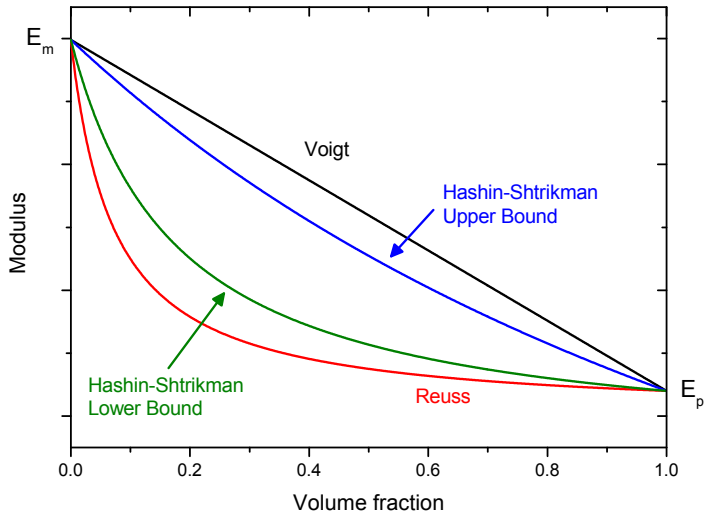


Figure 2.4.1: Example of upper and lower bounds of predicted modulus.

2.4.2 Spherical particles

The Halpin-Tsai model [197, 202] is a semi-empirical model that calculates the composite modulus, E_c, as a function of matrix, E_m, and particle, E_p, modulus, taking into account the aspect ratio through the use of a shape factor, ζ. The composite modulus, E_c, is calculated by:

$$E_c = \frac{1 + \zeta \eta v_f}{1 - \eta v_f} E_m \tag{2.11}$$

where ζ is the shape factor, v_f is the volume fraction of particles and η is given by:

$$\eta = \frac{\frac{E_p}{E_m} - 1}{\frac{E_p}{E_m} + \zeta} \tag{2.12}$$

By comparing the predictions with the results from a finite element analysis, Halpin and Kardos [197] suggested a shape factor of $\zeta = 2w/t$, where w is the width and t is the thickness, when the particles are aligned with the loading direction. The aspect ratio of spherical particles is 1, so the shape factor, $\zeta = 2$.

Lewis and Nielsen [203] proposed a modification to the Halpin-Tsai model to account for a limit in maximum packing and particle-matrix adhesion. The Lewis-Nielsen model, using the work of McGee and McCullough [204], gives the composite modulus, E_c, as:

$$E_c = \frac{1 + (k_E - 1)\,\beta v_f}{1 - \beta\mu v_f} E_m \tag{2.13}$$

where k_E is the generalised Einstein coefficient, v_f is the particle volume fraction, and β and μ are constants given by:

$$\beta = \frac{\frac{E_p}{E_u} - 1}{\frac{E_p}{E_u} + (k_E - 1)} \tag{2.14}$$

$$\mu = 1 + \left(\frac{1 - v_f}{v_{max}}\right)\left[v_{max} v_f + (1 - v_{max})\,(1 - v_f)\right] \tag{2.15}$$

The constant β takes into account the relative moduli of the particle and matrix, and μ is dependent on the particle volume fraction and the maximum particle volume fraction possible, v_{max}. The theoretical values of v_{max} have been calculated by Nielsen and Landel [198] for various types of packing and arrangement. Randomly distributed, close packing particles which are not agglomerated take a value of $v_{max} = 0.632$, and agglomerated particles take a value of $v_{max} = 0.37$.

The value of k_E varies with the level of particle/matrix adhesion, where $k_E = 2.5$ for a 'no-slip' condition and $k_E = 1$ for a 'slip' condition, provided the Poisson's ratio of the matrix is 0.5 [198]. If the Poisson's ratio is less than 0.5, the value of k_E is reduced. For a material with a Poisson's ratio of 0.35, the value of k_E should be multiplied by 0.867 [205].

The Mori-Tanaka model [206] estimates the elastic behaviour of a two-phase composite while taking into account particle interactions, assuming a homogeneous dispersion and perfectly bonded interface. This method estimates the average strain in the interacting particles, or inclusions, from the solution of a single particle in an infinite matrix subjected to a uniform average matrix strain. While the original work was for ellipsoidal inclusions, the case for spherical inclusions was shown by Benveniste [207]. The composite bulk, K_c, and shear, G_c, moduli can be calculated by:

$$K_c = K_u + \frac{v_f\,(K_p - K_u)}{1 + v_f\left[\frac{K_p - K_u}{K_u + \frac{4}{3}G_u}\right]} \tag{2.16}$$

$$G_c = G_u + \frac{v_f\,(G_p - G_u)}{1 + \frac{(1 - v_f)(G_p - G_u)}{G_u + \frac{G_u(9K_u + 8G_u)}{6(K_u + 2G_u)}}} \tag{2.17}$$

where v_f is the volume fraction of particles and the subscripts c, u and p are for the composite, unmodified epoxy and particle, respectively. The composite modulus, E_c,

can then be calculated by:

$$E_c = \frac{9G_cK_c}{G_c + 3K_c} \tag{2.18}$$

2.4.3 Platelets

The Halpin-Tsai model can be used to model the composite modulus of polymers modified with platelet or disc-shaped particles by changing the shape factor, ζ. Van Es [208] suggested that for the calculation of axial (11) and transverse (33) moduli, the following shape factors should be used:

$$\zeta_{11} = \frac{2w}{3t} \qquad \zeta_{33} = 2 \tag{2.19}$$

Equations for the Mori-Tanaka model for platelets with an aspect ratio not equal to one have also been derived [209]. The composite modulus is dependent on the orientation of the particles relative to the loading direction. The composite modulus when the platelets are aligned with the long axis parallel to the loading direction can be calculated by [209]:

$$E_{11} = \frac{E_m}{1 + v_f \left(A_1 + 2v_m A_2\right)/A} \tag{2.20}$$

The transverse composite modulus can be calculated by [209]:

$$E_{33} = \frac{E_m}{1 + v_f \left(-2v_m A_3 + \left(1 - v_f\right) A_4 + \left(1 - v_f\right) A_5 A\right)/2A} \tag{2.21}$$

where the variables A, A_2, A_3, A_4 and A_5 are functions of volume fraction, aspect ratio and Poisson's ratio of the matrix and fillers, and are given in Appendix C. Van Es [208] used laminate theory to derive approximations for the modulus of a composite with oriented disc-shaped particles. The modulus of a composite with randomly oriented particles can be estimated using:

$$E_c = 0.49E_{11} + 0.51E_{33} \tag{2.22}$$

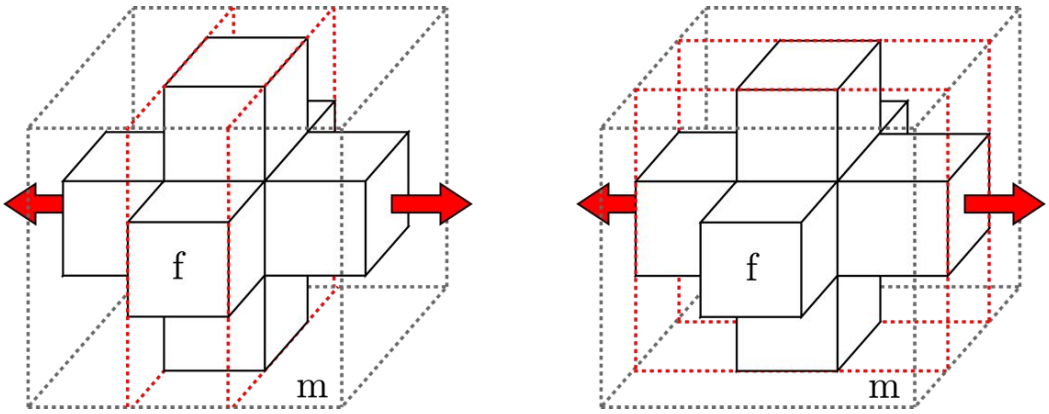
2.4.4 Co-continuous structures

Several authors [210–214] have developed models to predict the tensile moduli of co-continuous microstructures. Davies [215] proposed that the modulus of a co-continuous

polymer composite, with two interpenetrating continuous phases, can be predicted by:

$$E_c^{1/5} = E_u^{1/5}\,(1 - v_f) + E_p^{1/5} v_f \tag{2.23}$$

The assumption was based on the fact that E_c becomes ∞ if either E_1 or E_2 approaches ∞. The other methods involve a derivation from an approximated unit cell. The approach described by Veenstra *et al.* [210] was thought to be most relevant as it accounted for the different influences of a dispersion of soft modifier in a stiff matrix and vice versa. There were also no fitting parameters used in the model. Figure 2.4.2 illustrates the framework Veenstra *et al.* adopted to model the co-continuous structure. The model was derived by considering the structure as a series model of parallel parts (see Figure 2.4.2(a)) or a parallel model of serial-linked parts (see Figure 2.4.2(b)).



(a) Series model of parallel parts (E_m<E_f)

(b) Parallel model of serial-linked parts (E_f<E_m)

Figure 2.4.2: Framework of co-continuous model. m and f represent the matrix and filler, respectively. Reproduced from [210].

For a co-continuous blend where the matrix is stiffer than the filler, the matrix modulus dominates the composite modulus, i.e. a series model of parallel parts is more appropriate. If the filler is stiffer than the matrix, the matrix at the interface between the two phases undergoes greater elongation and hence the parallel model of serial-linked parts is more suited. The composite moduli, E_c and E_d, for the series model of parallel parts and parallel model of serial-linked parts respectively can be derived as

[210]:

$$E_c = \frac{(a^4 + 2a^3b)E_1^2 + 2(a^3b + 3a^2b^2 + ab^3)E_1E_2 + (2ab^3 + b^4)E_2^2}{(a^3 + a^2b + 2ab^2)E_1 + (2a^2b + ab^2 + b^3)E_2} \tag{2.24}$$

$$E_d = \frac{a^2bE_1^2 + (a^3 + 2ab + b^3)\,E_1E_2 + ab^2E_2^2}{bE_1 + aE_2} \tag{2.25}$$

where $3a^2 - 2a^3 = v_f$ and $b = 1 - a$.

Veenstra *et al.* [210] found excellent agreement across the complete composition range using the model that they derived for co-continuous polymer structures, as shown in Figure 2.4.3.

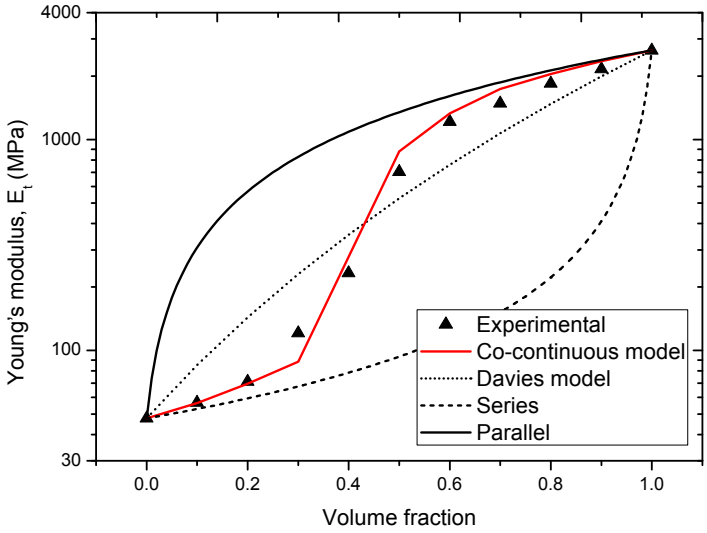


Figure 2.4.3: Experimental and predicted values of Young's modulus for PS/poly(ether-ester) polymer blend. Reproduced from [210]

2.5 Analytical modelling of fracture energy

2.5.1 Rubber particle toughening

Through an understanding of the structure/property relationships of rubber modified epoxies, Huang and Kinloch [75] proposed a generalised solution for the toughening increment of fracture energy as:

$$G_{IC} = G_{CU} + \psi \tag{2.26}$$

where G_{CU} is the fracture energy of the unmodified epoxy polymer and ψ represents the overall toughening contribution provided by the presence of the particulate phase. The model directly addresses the toughening mechanisms observed from the experimental observations and assumes that the mechanisms are mutually exclusive to each other. The overall toughening contribution, ψ is split into the relative toughening contributions; (i) localised shear band yielding, ΔG_s, (ii) plastic void growth of the epoxy polymer, ΔG_v, and (iii) rubber bridging, ΔG_r, as:

$$\psi = \Delta G_s + \Delta G_v + \Delta G_r \tag{2.27}$$

The energy contribution from plastic shear band yielding, ΔG_s, initiated by the particles is related to the size of the plastic zone from [76] as:

$$\Delta G_s = 0.5 v_f \sigma_{yc} \gamma_f F'(r_y) \tag{2.28}$$

where v_f is the volume fraction of particles, σ_{yc} is the plane strain compressive true yield stress, γ_f is the true fracture strain for the unmodified epoxy, and $F'(r_y)$ is given by [76]:

$$F'(r_y) = r_y \Bigg[\left(\frac{4\pi}{3v_f} \right)^{\frac{1}{3}} \left(1 - \frac{r_p}{r_y} \right)^3 - \frac{40}{35} \left(\frac{r_p}{r_y} - 1 \right)^{\frac{3}{2}} \left(\frac{r_p}{r_y} \right) \left(\frac{7}{5} - \frac{r_p}{r_y} \right) - 2 \left(1 - \frac{r_p}{r_y} \right)^2 + \frac{16}{35} \Bigg] \tag{2.29}$$

where r_p is the particle radius. r_y is an increased plastic zone size due to the stress concentrations in the epoxy and is defined as:

$$r_y = K_{vm}^2 \left(1 + \frac{\mu_m}{3^{\frac{1}{2}}} \right)^2 r_{pz} \tag{2.30}$$

where K_{vm} is the maximum stress concentration for the von Mises stresses around the particle and μ_m is a material constant which allows for the pressure-dependency of the yield stress. The value of μ_m is a material constant relating to the hydrostatic dependence of yielding, and was measured to be between 0.175 and 0.225 for rubber modified epoxy polymers [3]. The value of K_{vm} is dependent on the volume fraction of particles, and was calculated numerically by Huang and Kinloch [79]. The value of K_{vm} varies with volume fraction and a simple linear relationship can be used for soft modifiers:

$$K_{vm} = 3.9337 v_f + 2.1126 \tag{2.31}$$

The value of r_{pz}, the Irwin prediction of plane strain plastic zone radius for the unmodified epoxy at fracture, was calculated using [30]:

$$r_{pz} = \frac{1}{6\pi}\frac{K_{CU}^2}{\sigma_{yt}^2} \tag{2.32}$$

where K_{CU} is the fracture toughness and σ_{yt} is the tensile true yield strength for the unmodified epoxy polymer.

The contribution of ΔG_v via the plastic void growth mechanism can be calculated using [75]:

$$\Delta G_v = \left(1 - \frac{\mu_m^2}{3}\right)(v_{fv} - v_f)\,\sigma_{yc} r_{pz} K_{vm}^2 \tag{2.33}$$

where μ_m is a material constant (as above), v_{fv} is the volume fraction of voids and v_f is the particle volume fraction. The term $v_{fv} - v_f$ can either be determined experimentally from electron micrographs, or predicted from the following relationship:

$$r_v = (1 + \gamma_f)\, r_p \tag{2.34}$$

$$v_{fv} - v_f = v_f \frac{r_v^3 - r_p^3}{r_p^3} \tag{2.35}$$

where r_v is the void radius and γ_f is the failure strain. The calculated value of v_{fv} was found to agree well with the values measured from the fracture surfaces within experimental error by several authors [5, 28]. Liang and Pearson [109] proposed a different method to derive the term:

$$v_{fv} - v_f = \frac{v_v}{v_v + v_m} - \frac{v_p}{v_p + v_m} \tag{2.36}$$

where v_v and v_p are the average volume of voids and particles, respectively, and v_m is the volume of matrix. There were no significant differences between the two methods to calculate $v_{fv} - v_f$.

The contribution of rubber bridging, ΔG_r, was proposed by Kunz-Douglass *et al.* [77] to be:

$$\Delta G_r = 4\Gamma_t v_f \tag{2.37}$$

where Γ_t is the tearing energy of the rubber particles, which was estimated to be approximately 460 J/m^2 [24].

The energy contributions calculated for a typical rubber modified epoxy is shown in

Figure 2.5.1. Clearly, the contributions from shear band yielding and void growth dominates the total energy contribution at various volume fractions, as well as at different test temperatures [75]. The contribution from shear band yielding and void growth is of similar orders of magnitude up to a volume fraction of 10%. Above 10 vol%, plastic void growth becomes the dominant toughening mechanism. Rubber bridging does not appear to be a significant toughening mechanism based on the model, contributing only 12% of the total toughening contribution at 10 vol%.

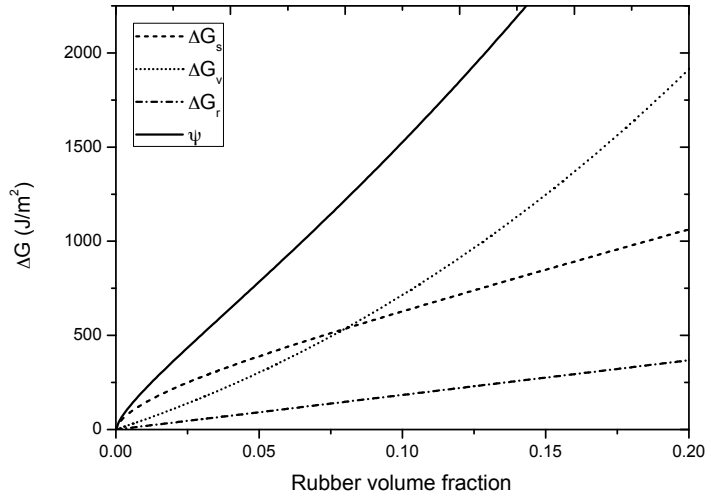


Figure 2.5.1: Comparison of the energy contributions from shear banding, void growth and rubber bridging from the Huang-Kinloch model.

2.5.2 Rigid particle toughening

The Huang-Kinloch model [75] can also be used to predict the fracture energy of epoxies modified with rigid particles. By taking the same assumption of additive energy contributions from each toughening mechanism, the variables in the model can be adapted for rigid particles. For the case of shear band yielding, the maximum von Mises stress concentration factor, K_{vm}, is different for rigid particles. The variable in this case is changed to K_p to avoid confusion. K_p was calculated numerically by Guild and Young [156] to be of the form:

$$K_p = 0.59v_f + 1.65 \tag{2.38}$$

The value of K_{vm} for the void growth mechanism remains the same because the particles have already debonded and the von Mises stress concentration factors around a void is similar to a rubber particle [79]. While shear bands can be expected to initiate from all

the particles [216], not all rigid particles will debond and initiate void growth. Hsieh *et al.* [76] accounted for this by multiplying the contribution from void growth by the fraction of particles which were observed experimentally to debond from electron micrographs of the fracture surfaces.

Other toughening mechanisms such as crack deflection, debonding and pull-out are discussed in more detail in §8.11.

2.6 Finite element modelling studies

Finite element analysis (FEA) is useful in the design and analysis of adhesive joints or composite structures where conventional testing regimes would be very costly and impractical. FEA has also been used to study the micromechanical aspects of particulate toughening in epoxies, e.g. [156, 217, 218]. These models involve an idealised unit cell or representative volume element (RVE) to isolate the particle/matrix interactions.

The simplest model is an axisymmetric model, as shown by Guild and Young [156, 217], which simplifies randomly dispersed spherical particles in an infinite matrix to a sphere at the centre of a cylinder. The model, as shown in Figure 2.6.1, shows good agreement with the experimental results for both rigid and soft particles.

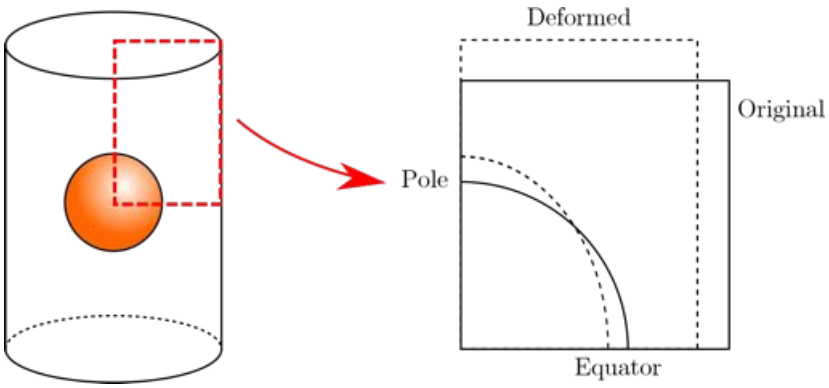


Figure 2.6.1: Axisymmetric finite element model. Reproduced from Guild and Young [217].

This allowed the authors to study the stress distributions in and around the particle and at the particle/matrix interface. The results from these models helped to explain the toughening mechanisms observed experimentally by other authors, namely shear yielding and particle cavitation. Huang and Kinloch [79] developed a different arrangement in order to model the localised shear yielding in rubber modified epoxies. They found that their model predicted higher stress concentrations for the two-dimensional (2D)

plane strain model than the axisymmetric model due to the interparticle interactions, as shown in Figure 2.6.2.

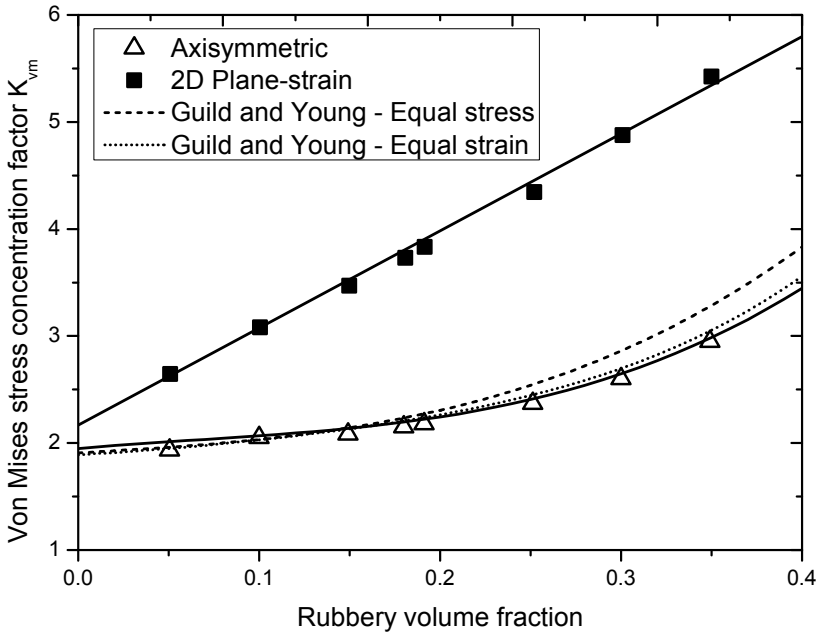


Figure 2.6.2: Von Mises stress concentration factors as a function of volume fraction. Reproduced from [79, 156, 217].

The 2D plane strain model used by Huang and Kinloch could not accurately model cavitation or debonding and the subsequent void growth. To address this, Guild and Kinloch [219] modelled a single spherical particle enclosed by an annulus of matrix, as shown in Figure 2.6.3. They noted the importance of the rubber properties and the effect that they have on the sequence of toughening mechanisms. They predicted that the bulk modulus of the rubber toughened epoxy can increase by up to two times by increasing the Poisson's ratio of the rubber particle from 0.499 to 0.4999.

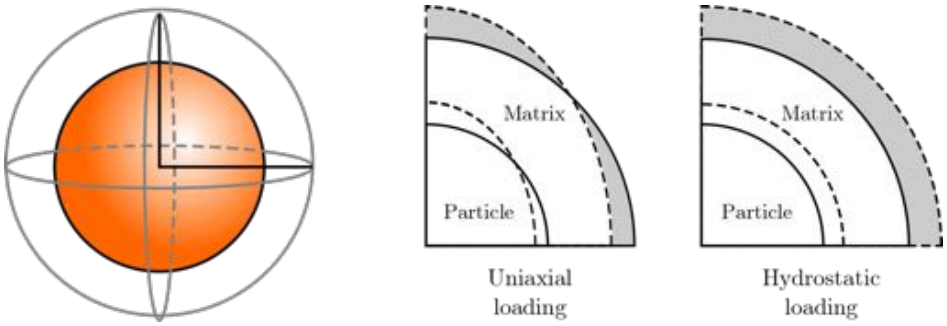


Figure 2.6.3: Single spherical cell model. Reproduced from Guild and Kinloch [219].

Poon *et al.* [220] combined the single spherical cell model with the statistical approach as described by Davy and Guild [221] to accurately model the elastic properties of a

glass particulate modified epoxy. The modification takes into account the influence of particle distribution on the stress state around each particle.

Chen and Mai [222] proposed the use of a three-dimensional (3D) one-eighth face-centred cubic (FCC) layout, using an elastic-plastic material model for the matrix and a linear elastic model for the rubber. They found that this layout was better able to predict the elastic properties than using a 2D plane strain model. They suggested that the axisymmetric model underestimates the inter-particle interactions and the 2D plane strain model overestimates them. More recently, Guild *et al.* used the one-eighth FCC model to predict the onset of rubber particle cavitation [80]. This was the first step towards the prediction of the fracture toughness of a rubber modified epoxy [218] and is important in the development of materials with particles of various sizes.

2.7 Summary

This chapter has reviewed the relevant literature regarding the toughening of epoxy polymers by introducing a second phase material. The toughening mechanisms of these modifiers have been studied in detail and will provide the framework to examine the mechanisms in the new materials in this study. Other factors that govern the fracture performance of these composite materials such as particle size,crosslink density and particle/matrix interactions were also reviewed.

The effect of the matrix toughness on the fracture performance of FRP composites were also briefly evaluated. Finally, previous studies regarding the analytical and numerical modelling of composite materials were reviewed. These are primarily related to modelling the modulus and fracture energy of modified epoxy polymers, and describing the stress fields and interactions around the second phase particles.

The following Chapters will detail the materials and the techniques employed to produce and test the samples used in this work.

Chapter 3

Materials and Manufacturing

3.1 Introduction

This chapter describes the formulations of the epoxy polymers and modifiers that were used. The manufacturing of the unmodified and modified bulk epoxy polymers, and fibre composites are also outlined. Four different epoxy systems were used; an anhydride cured diglycidyl ether of bisphenol-A (DGEBA), an anhydride cured cycloaliphatic epoxy, a polyether-amine cured DGEBA and a polyether-amine cured DGEBA/F. This covers a wide range of glass transition temperatures and mechanical properties.

3.2 Epoxy resins

3.2.1 Anhydride cured DGEBA

The base epoxy resin for this system was a standard DGEBA with an epoxide equivalent weight (EEW) of 185 g/eq, 'Araldite LY556' from Huntsman, UK. The curing agent used was an accelerated methylhexahydrophtalic acid anhydride with an anhydride equivalent weight (AEW) of 170 g/eq, 'Albidur HE600' from Evonik Hanse, Germany, used at stoichiometric quantities. Both the epoxy resin and anhydride curing agent were liquids at room temperature. The cure cycle consists of a cure at 90°C for 1 hour, followed by a ramp of 1°C/min to the post-cure temperature of 160°C for 2 hours. It is then cooled to room temperature inside the oven at a rate of 2°C/min.

3.2.2 Low viscosity epoxy

A low viscosity epoxy, formulated without the use of solvents, was previously developed for easy impregnation of carbon nanotube mats [223]. The low viscosity epoxy comprises of a cycloaliphatic epoxy, 'Araldite CY179', as its base epoxy resin and trimethylolpropane triglycidylether, 'Araldite DY-T/CH', as a diluent epoxy resin, both from Huntsman, UK. The curing agent used was a 4-methyl hexahydrophthalic anhydride, 'Lindride 52D' from Lindau Chemicals, UK, and dimethyl benzylamine, 'DY 062' from Sigma-Aldrich, UK, was used as a tertiary amine catalyst to provide more crosslinking. The formulation of the low viscosity epoxy is shown in Table 3.2.1. The cure cycle for this epoxy polymer was 120°C for 1 hour, followed by a post-cure at 175°C for 1 hour to further develop the crosslinks and T_g.

Table 3.2.1: Formulation of low viscosity epoxy polymer.

Chemical	**Name**	**wt%**
3, 4-Epoxycyclohexylmethyl 3, 4-Epoxycyclohexane Carboxylate	Araldite CY 179	35.65
Trimethylolpropane Triglycidylether	Araldite DY-T/CH	10.69
4-Methyl Hexahydrophthalic Anhydride	Lindride 52D	53.09
Dimethyl Benzylamine	DY 062	0.57

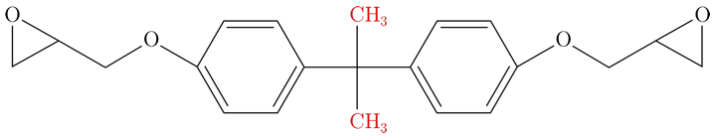
3.2.3 Polyether-amine cured DGEBA

A standard DGEBA, 'Araldite LY556' from Huntsman, UK, was used in this epoxy system. This was cured with a difunctional primary polyether-amine, 'Jeffamine D-230' from Huntsman, UK, at stoichiometric quantities. This is a polyoxypropylenediamine with an amine hydrogen equivalent weight (AHEW) of 60 g/eq. Both the epoxy resin and polyether-amine were liquids at room temperature. The epoxy is cured at 75°C for 3 hours, followed by a ramp of 1°C/min to the post-cure temperature of 110°C for 12 hours and cooled to room temperature inside the oven at a rate of 2°C/min.

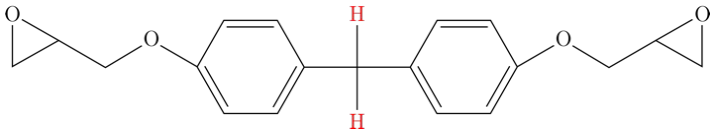
3.2.4 Polyether-amine cured DGEBA/F

This epoxy system formulation consists of a DGEBA/F resin, a pre-blended mixture of DGEBA and diglycidyl ether of bisphenol-F (DGEBF), 'Araldite AY105-1' from Huntsman, UK, cured with 'Jeffamine D-230' polyether-amine curing agent. The DGEBA/F

resin blend contains up to 40% of DGEBA resin. The curing agent was added at a ratio of 1:0.3 to the epoxy resin to obtain a sub-stoichiometric composition [224]. The preparation and cure cycle of this epoxy system follows that of the polyether-amine cured DGEBA discussed in the previous section. The main difference between the DGEBA and DGEBF epoxy resins is the presence of hydrogen groups, rather than methyl groups (CH_3), between the ring structures (see Figure 3.2.1). The additional chain flexibility for the DGEBF molecule results in a lower viscosity and higher functionality. DGEBF resins typically have higher heat and chemical resistance than DGEBA resins and is commonly blended with DGEBA to inhibit crystallisation of the liquid resin and improve overall performance.



(a) DGEBA



(b) DGEBF

Figure 3.2.1: Molecular structures of epoxy resins.

A summary of the epoxy systems used in this study is presented in Table 3.2.2.

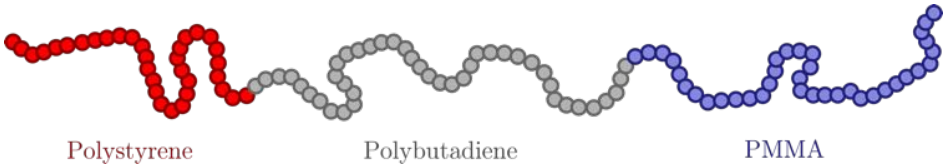
Table 3.2.2: Summary of epoxy systems used in this study.

Epoxy system		**Chemical name**	**Commercial name**	**Supplier**	**Cure cycle**
Anhydride cured DGEBA	LH	Diglycidyl ether of bisphenol-A (DGEBA)	Araldite LY556	Huntsman, UK	90°C for 1 h, then 160°C for 2 h
		Accelerated methyl-hexahydrophtalic acid anhydride	Albidur HE600	Evonik Hanse, Germany	
Anhydride cured cycloaliphatic epoxy with diluent (Low Viscosity)	LV	3, 4-Epoxycyclohexylmethyl 3, 4-Epoxycyclohexane Carboxylate	Araldite CY179	Huntsman, UK	120°C for 1 h, then 175°C for 1 h
		Trimethylolpropane Triglycidylether	Araldite DY-T/CH	Huntsman, UK	
		4-Methyl Hexahydrophthalic Anhydride	Lindride 52D	Lindau Chemicals, UK	
		Dimethyl Benzylamine	DY 062	Sigma-Aldrich, UK	
Polyether-amine cured DGEBA	LD	DGEBA	Araldite LY556	Huntsman, UK	75°C for 3 h, then 110°C for 12 h
		Polyether-amine	Jeffamine D-230	Huntsman, UK	
Polyether-amine cured DGEBA/F	AD	Pre-blended DGEBA and DGEBF	Araldite AY105-1	Huntsman, UK	75°C for 3 h, then 110°C for 12 h
		Polyether-amine	Jeffamine D-230	Huntsman, UK	

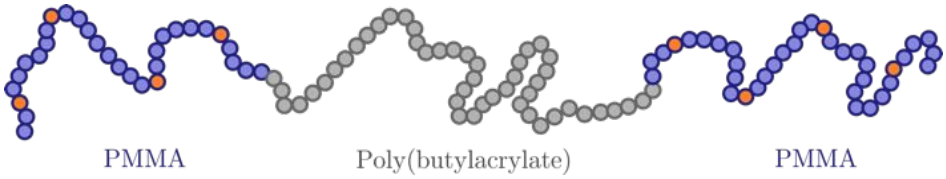
3.3 Modifiers

3.3.1 Block copolymers

Two types of block copolymers (BCP) from Arkema, France, were used in this study. The first is an asymmetric triblock copolymer of polystyrene-b-1,4-polybutadiene-b-syndiotactic poly(methyl methacrylate), i.e. SBM, as shown in Figure 3.3.1(a). Two different grades of SBM were used and these were Nanostrength 'E21' and 'E41'. The two grades differ in that E21 has a much higher concentration of butadiene and molecular weight compared to E41. The second BCP is a pure acrylic symmetric triblock copolymer of poly(methyl methacrylate)-b-poly(butylacrylate)-b-poly(methyl methacrylate), i.e. MAM, as shown in Figure 3.3.1(b). The poly(methyl methacrylate) (PMMA) blocks in MAM are atactic. The two different grades of MAM were Nanostrength 'M52N' and 'M22N'. The MAM BCPs are polar and have dimethylacrylamide (DMA) incorporated into the PMMA blocks as functional groups to improve compatibility and introduce reactive sites [60]. The percentages of the soft blocks are 50% and 40% for M52N and M22N respectively [225]. The SBM BCPs were synthesised using an anionic polymerisation method at a pilot scale [226] and MAM BCPs were synthesised using a nitroxide mediated polymerisation method based on alkoxyamine [56].



(a) ABC triblock copolymer of polystyrene-b-1,4-polybutadiene-b-poly(methyl methacrylate)



(b) ABA triblock copolymer of poly(methyl methacrylate-co-dimethylacrylamide)-b-poly(butylacrylate)-b-poly(methyl methacrylate-co-dimethylacrylamide)

Figure 3.3.1: Molecular structure of block copolymer modifiers used [227].

In the SBM block copolymer, the PMMA block is miscible in epoxy, while the polybutadiene (PB) and polystyrene (PS) blocks are immiscible. In the MAM block copolymer, the PMMA block is miscible and the poly(butylacrylate) (PBuA) block is immiscible. Amphiphilic block copolymers like the SBM and MAM can self-assemble into various

morphologies during the formation of the network. During the curing phase, an increase in molar mass causes phase separation of the block copolymers, which then in turn decreases the conformational entropy of mixing [228].

The block copolymers were incorporated by dissolving the BCP powder into the epoxy resin. This was done by mechanical mixing at 120°C for approximately 4 hours at 90 rpm until all of the powder has fully dissolved in the resin. The mixture was degassed overnight in a vacuum oven at 60°C and -1 atm to remove air bubbles trapped during stirring. The curing agent was then added, followed by a degassing step, and cured as described previously.

3.3.2 Reactive liquid rubber particles

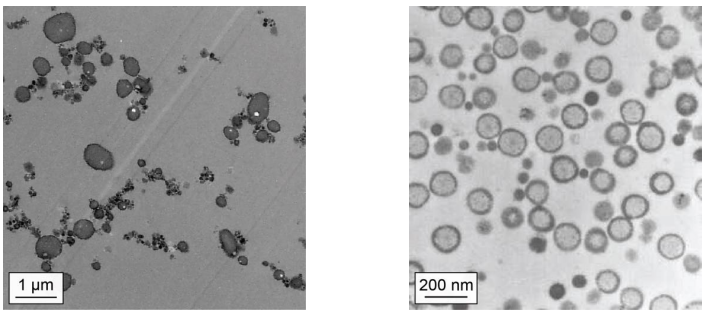
A conventional reactive liquid rubber, a random copolymer of butadiene and acrylonitrile with carboxyl-terminated end groups (CTBN), was used in this study. This was received pre-reacted as an adduct of 40 wt% 'Hycar 1300x8' CTBN from Emerald Performance Materials, USA, in a DGEBA epoxy resin ('Albipox 1000' from Evonik Hanse, Germany), and in a cycloaliphatic epoxy resin ('Albipox XP 23/0175-2' from Evonik Hanse, Germany). This grade of CTBN rubber contains 18% acrylonitrile and has a molecular weight, M_n, of 3,550 g/mol [229]. The adducted CTBN was diluted by adding more resin to provide the required concentrations. This was achieved by mechanically mixing at 60°C for 30 mins at 200 rpm. The resin was then degassed in a vacuum oven at 60°C and -1 atm. Next, the curing agent was added, followed by a second degassing step and cured as described previously.

3.3.3 Core shell rubber particles

The pre-formed core shell rubber (CSR) particles used in this study were the 'Kane Ace MX 156' and 'Kane Ace MX 551' from Kaneka, USA. These particles have polybutadiene and styrene-butadiene cores, respectively, with a diameter of approximately 100 nm and a functionalised PMMA shell [230, 231]. CSR particles are typically supplied as a dry powder (such as the 'Dow Paraloid'), however this can result in agglomerated particles. This is due to the large difference in viscosity as it is difficult to generate the high shear stresses required to separate them. Core shell rubber particles are typically produced by a two stage process. First, a latex of rubber particles dispersed in water is produced by emulsion polymerisation. An initiator is then used to form free radicals which react with the monomer molecules to form oligomers of increasing molecular

weight. The shell is then formed by the addition of monomers using a dropwise or swelling method [232].

The CSR particles used were received pre-dispersed at a concentration of 25 wt% of CSR in DGEBA and cycloaliphatic epoxy resin, respectively. The pre-dispersed medium allows the CSR particles to remain uniformly dispersed. The difference between using pre-dispersed CSR particles and loose dry powder is shown in Figure 3.3.2, where the pre-dispersed CSR particles remain well dispersed after curing. The required concentration was obtained by diluting with more epoxy resin. A mechanical stirrer was used to mix the two components at 60°C for 15 mins at 200 rpm. The resin was then degassed in a vacuum oven at 60°C and -1 atm. Next, the curing agent was added, followed by a degassing step and cured as described previously.



(a) Conventional powder based core shell rubber particles dispersed in epoxy

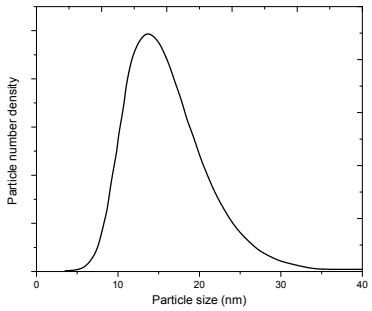
(b) Kaneka core shell rubber particles dispersed in epoxy

Figure 3.3.2: Comparison of conventional and core shell rubber used in this study [233].

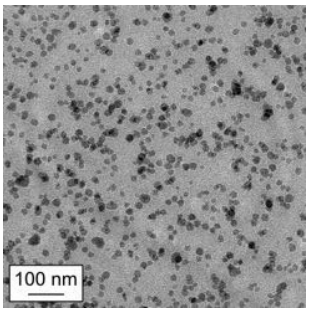
3.3.4 Silica nanoparticles

Synthetic SiO_2 nanospheres with an average diameter of 20 nm were used as a rigid particle modifier. These silica nanoparticles were produced from an aqeuous sodium silicate solution through a condensation reaction. The resulting silica sol is then treated with a silane to modify the surfaces. The silane surface treatment ensures a good epoxy-particle bond and reduces agglomeration of the nanoparticles in the resin by compatibilising the particles with the epoxy resin. A processing matrix is then mixed in and the water is separated. Finally, the processing matrix is replaced with the epoxy resin [234]. This modified sol-gel process allows for a better control of the particle size distribution than other conventional methods such as grinding natural SiO_2 or flame hydrolysis of silicon halogen compounds. Small angle neutron scattering (SANS) results from the manufacturer, as shown in Figure 3.3.3(a), show the narrow

particle size distribution with a maximum diameter of approximately 40 nm. The TEM image shown in Figure 3.3.3(b) demonstrates the well dispersed nature of the silica nanoparticles in epoxy.



(a) Particle size distribution of silica nanoparticles used in this study



(b) Transmission electron micrograph of 5 wt% silica nanoparticle modified epoxy showing good dispersion

Figure 3.3.3: Properties of the silica nanoparticles used in this study [184].

The masterbatches of 40 wt% of silica nanoparticles pre-dispersed in DGEBA ('Nanopox F400') and cycloaliphatic epoxy resin ('Nanopox A 610', both from Evonik Hanse, Germany) were diluted to obtain the required concentration. The mixture was mixed with a mechanical stirrer at 50°C for 15 mins at 200 rpm. The resin was then degassed in a vacuum oven at 50°C and -1 atm. Next, the curing agent was added, followed by a degassing step and cured as described before.

3.3.5 Graphene nanoplatelets

Graphene nanoplatelets (GNP) with a wide range of platelet geometries, manufacturing technique and functionalisation were examined as toughening modifiers for epoxy. Table 3.3.1 summarises the properties of the various carbon-based modifiers used in this study. In total, six graphene nanoplatelets, a multiwalled carbon nanotube (MWCNT) and a graphite flake modifier were used. The graphene nanoplatelets from XG Sciences, USA, and Graphene Supermarket, USA, had a carbon content of greater than 99.2% [139, 235, 236]. The modifiers from HDPlas, UK, had a carbon purity of 93.8%, 94.1% and 98.9% for the GNP-COOH, GNP-O_2 and CNT-COOH, respectively [237–239]. The graphite flakes have a median lateral dimension of 7 to 10 μm.

The graphene nanoplatelets from XG Sciences and Graphene Supermarket were manufactured from nitric acid and sulphuric acid intercalated natural crystalline graphite flakes. The graphite intercalate compounds were exfoliated by microwave heating

Table 3.3.1: Various carbon-based modifiers used in this study. Values quoted are from manufacturer data sheets [139, 235–240].

Supplier	Product name	Abbreviation	Thickness (nm)	Average lateral size (nm)
XG Sciences, USA	xGnP-C-750	XG-C	2	2,000
	xGnP-H-5	XG-H	11 - 15	5,000
	xGnP-M-25	XG-M	6	25,000
Graphene Supermarket, USA	Graphene nanopowder flakes	GS	12	1,500 - 10,000
Haydale HDPlas, UK	GNP-COOH	GNP-COOH	< 50	300 - 5,000
	GNP-O_2	GNP-O_2	< 50	300 - 5,000
	MWCNT-COOH	CNT-COOH	ø1 - 5	1,000
Alfa Aesar, UK	Graphite flake	GF	> 100	70,000 - 100,000

rapidly to 900°C. When heated, the acids vaporises and forces the layers apart. The exfoliated graphite were then pulverised into nanoplatelets by ultrasonic agitation in acetone [241]. This process is illustrated in Figure 3.3.4.

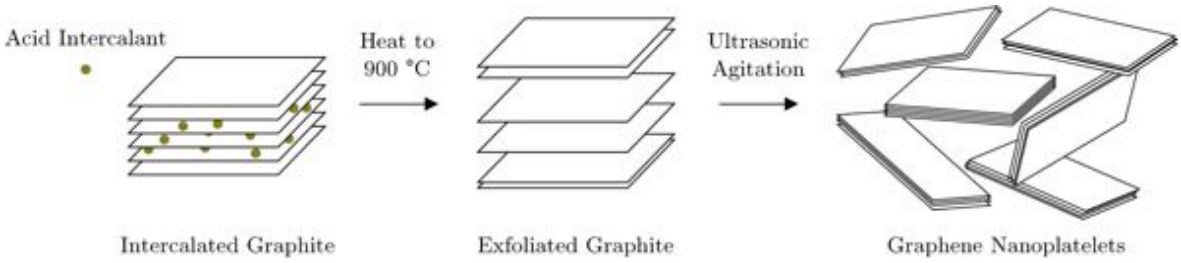
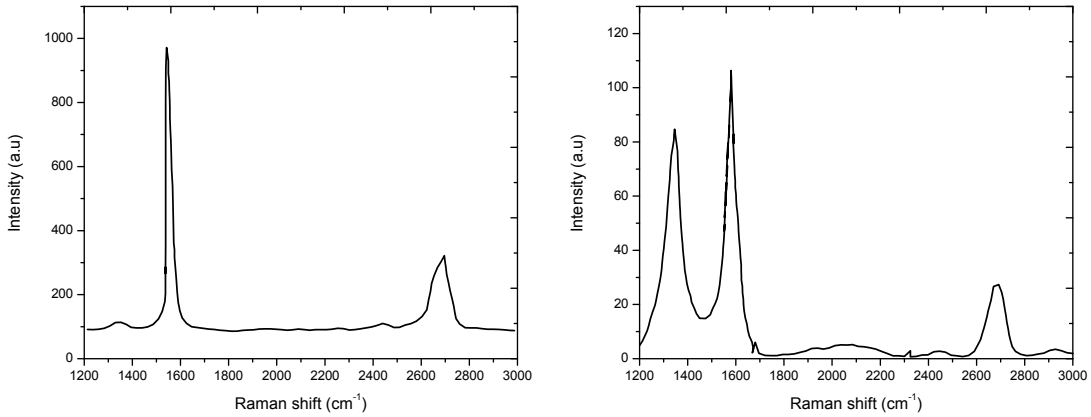


Figure 3.3.4: Illustration of graphene nanoplatelet manufacturing process by microwave exfoliation of intercalated graphite.

The acid exfoliation process can cause functional groups to form on the edges of the nanoplatelets. Indeed, X-ray photoelectron spectroscopy (XPS) analysis data for the XG-C GNP shows atomic concentrations of 8.3 at.% and 1.5 at.% for O_2 and N_2, respectively [236]. By comparison, manufacturer data sheets for the larger XG-H and XG-M GNPs have oxygen and acid contents less than 1 at.%. The smaller XG-C GNPs have more edges per gram, thus more functional groups are expected to be present. The results from Raman spectroscopy (as shown in Figure 3.3.5) show peaks at 1560 cm^{-1} (G peak), corresponding to the C-C bonds of the crystalline graphite structure, and 1360 cm^{-1} (D peak), which reflects disordered structures, i.e. defects or edges [242]. The ratio between the D and G intensity peaks for the XG-H GNPs is approximately 0.12, which suggests that there are few defects. It is not appropriate in this case to use the Raman spectra to compare the XG-C and XG-H GNPs because the average XG-C platelets are smaller than the laser diameter, thus the edge of the GNPs affects

the results.



(a) xGnP-H GNP (b) xGnP-C-750 GNP

Figure 3.3.5: Raman spectra for xGnP GNPs [235, 242].

The graphene nanoplatelets from Haydale, UK, were produced using a "Split Plasma" process. The GNPs produced from graphite intercalate compounds use strong acids that can damage the material structure and require a drying process downstream. The "Split Plasma" process is a low temperature, less aggressive process which does not damage the material surface and structure. It is a process with a lower risk of contamination and produces a dry product. Zaldivar *et al.* [243] measured the Raman spectra of the GNP-O_2 modifier as received and found little disturbance to the crystalline structure of the sp^2 hybridised structure. Plasma processing also provides the ability to functionalise the surface with the desired chemical groups by processing in oxygen, acid vapour, etc. The main functionalities to be expected in the GNP-O_2 and GNP-COOH GNPs are shown in Table 3.3.2.

Table 3.3.2: Functionalities of HDPlas modifiers.

Modifier	**Functionalities**		**Plasma**
GNP-COOH	Carboxyl Carbonyl	COOH C=O	Acid vapour
GNP-O_2	Carbonyl Hydroxyl	C=O OH	Oxygen
CNT-COOH	Carboxyl Carbonyl	COOH C=O	Acid vapour

XPS analysis from the manufacturer's data sheets [244] shows an atomic weight percentage of 6.1 at.% and 6.5 at.% of oxygen in the GNP-COOH and GNP-O_2 GNPs, respectively. The particle size distribution obtained by dynamic light scattering is

shown in Figure 3.3.6.

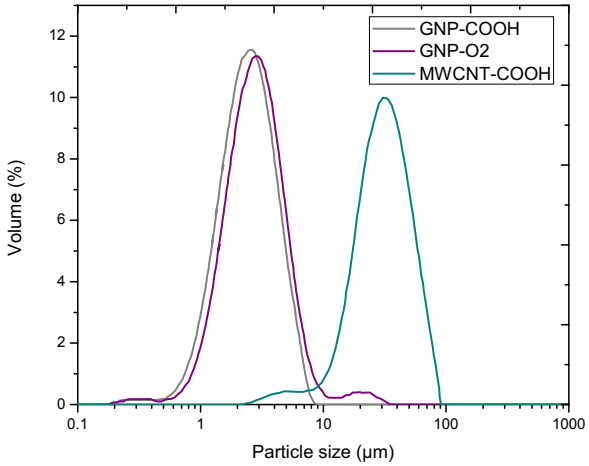


Figure 3.3.6: Particle size distribution of the HDPlas graphene nanoplatelets measured using dynamic light scattering [237–239].

The GNP modifiers were supplied as dry powders, which had to be dispersed into the epoxy resin. The modifiers were first dispersed by ultrasonication with a Cole-Parmer CPX 750 ultrasonic probe in tetrahydrofuran (THF) or n-methyl-pyrrolidone (NMP) for 10 min, followed by a further 10 min with the addition of epoxy resin, or directly into the epoxy resin for 30 min. The solvents were from Sigma-Aldrich, UK, and used as received. The ultrasonic probe was used at a power of 225 W and a frequency of 20 kHz. The epoxy resin was then added into the modifier/solvent mixture and sonicated again for a further 10 min. The solvent was subsequently removed by stirring and heating above the solvents' boiling point (90°C for THF and 220°C for NMP). Next, the mixture was degassed in a vacuum oven at 60°C to ensure all of the solvent was removed. This was monitoring by weighing the mass of the mixture at 30 minute intervals.

The solvents were also added at a concentration of 10 wt% to test the effects of the solvents on the unmodified epoxy polymers. For one set of results, the solvents were evaporated as per the method described and another set was made without removing the solvent.

A summary of the modifiers used in this study is presented in Table 3.3.3.

Table 3.3.3: Summary of modifiers used in this study.

Modifier		Commercial name	Supplier	Epoxy systems used	With silica nanoparticle (Hybrid)	Chapter
Carboxyl-terminated butadiene-acrylonitrile rubber	CTBN	Albipox XP 23/0175-2 Albipox 1000	Evonik Hanse, Germany	LV LD AD	LV LD AD	5
Core-shell rubber	CSR	Kane Ace MX551 Kane Ace MX156	Kaneka, USA	LV LD AD	– LD AD	5
Polystyrene-b-1,4-polybutadiene-b-poly(methyl methacrylate)	SBM	Nanostrength E21 & Nanostrength E41	Arkema, France	LH LV LD AD	LH – LD AD	6
Poly(methyl methacrylate)-b-poly(butylacrylate)-b-poly(methyl methacrylate)	MAM	Nanostrength M52N & Nanostrength M22N	Arkema, France	LD AD	LD AD	7
Graphene nanoplatelets Carbon nanotubes	GNP CNT	see Table 3.3.1		LH LH	– –	8

3.4 Manufacturing

3.4.1 Bulk epoxy polymer

The bulk epoxy polymers were cast into steel vertical moulds. This allows the air bubbles to escape through the top of the mould as the temperature is raised and viscosity decreases. The moulds used were of 3 mm and 6 mm thickness. The moulds were first cleaned and degreased with acetone. A release agent, 'Frekote 770NC' from Loctite, UK, was then applied on the surfaces and left for 30 min to dry in a fume cupboard. The moulds were then assembled with G-clamps and preheated in an oven.

The epoxy resin, modifier and/or diluent were first mixed together with a 'RZR 2012' mechanical stirrer from Heidolph, Germany, as described previously. After this mixture has been degassed, the curing agent and/or anhydride accelerator were blended in with a mechanical overhead stirrer for 15 min followed by a second degassing step. The anhydride cured systems were mixed and degassed at 60°C, and the polyetheramine cured systems at 40°C. The moulds were then filled from the top, maintaining a constant flow rate when pouring in the resin to minimise the aeration of the resin.

As the moulds are cooled down while they are out of the oven, the cure cycle cannot be started immediately when the moulds are placed in the ovens. A thermocouple attached to the mould, in contact with the resin, indicated that a temperature hold

of 10 min at the desired temperature was required to ensure the resin was at the oven temperature. A ramp rate of 1°C/min was used to minimise the temperature overshoot as the curing process is an exothermic process. The cured polymer plates were cooled slowly to room temperature in the oven before they were removed from the moulds.

The rubber and hybrid modified epoxies from hereafter will be termed as such:

- CTBN : yR
- CTBN-NS hybrid : xNyR
- CSR : yC
- CSR-NS hybrid : xNyC
- E21 SBM or E41 SBM : yE21 or yE41
- E21 SBM-NS hybrid : xNyE21
- M52N MAM or M22N MAM : yM52N or yM22N
- M52N MAM-NS hybrid : xNyM52N

where x refers to the weight percentage (wt%) of silica nanoparticles and y refer to the wt% of each rubber modifier. The weight percentage is defined as:

$$\text{wt\%} = \frac{\text{wt}_{\text{modifier}}}{\text{wt}_{\text{modifier}} + \text{wt}_{\text{epoxy}} + \text{wt}_{\text{curing agent}}} \times 100 \tag{3.1}$$

3.4.2 Thin films

Thin films of the pure block copolymers were prepared by first dissolving the BCP powders in toluene by mechanical mixing with a 'RZR 2012' mechanical stirrer from Heidolph, Germany. The solution was then poured onto a poly(tetrafluoroethylene) (PTFE)-coated steel plate. The plate was then placed in a fume cupboard, then in a vacuum oven to allow the solvent to evaporate to form a thin film of BCP approximately 0.5 mm in thickeness. The samples were then cut using a razor blade or dumb-bell shaped die cutter.

3.4.3 Fibre composites

Carbon-fibre reinforced-polymer (CFRP) plates were manufactured using the SBM modified epoxy matrices. A quasi-isotropic (QI) layup consisting of 16 plies of biaxial stitched, non-crimp fabric (NCF), 'XC 305/1270 carbon' fabric from Gurit, UK, was manufactured by resin infusion under flexible tooling (RIFT). This lay-up produced composite panels roughly 6 mm thick.

The carbon fabric was first cut into 330 × 330 mm^2 squares with a cutting knife. The QI layup is balanced and symmetric, $[+/\text{-}45,0/90,\text{-}/+45,90/0]_s$, about the mid-plane to give a '0/0' interface of fibres in the fracture plane. A strip of PTFE film less than 13 μm in thickness was inserted in the mid-plane to initiate the pre-crack for fracture specimens.

A temperature-controlled anodised aluminium hot plate, 'HP1836URS' from Wenesco, USA, was utilised to produce the composite plates. A 50 μm thick layer of polyethylene terephthalate (PET) film, 'Melinex 401' from DuPont, UK, was first laid on the hot plate to protect the surface, held down with polyester flash tape. The infusion stack is then laid up on top of the PET film as shown in Figure 3.4.1.

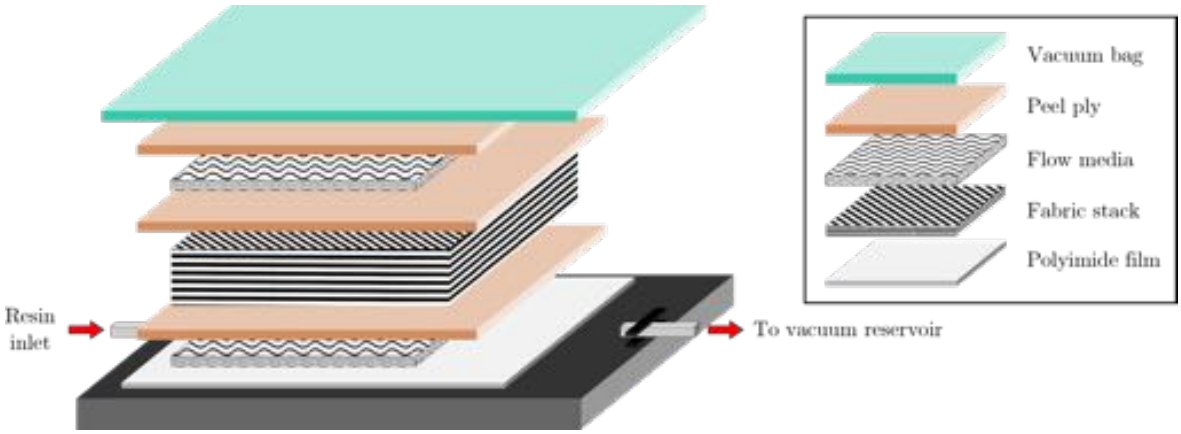


Figure 3.4.1: Cross-section showing RIFT set-up.

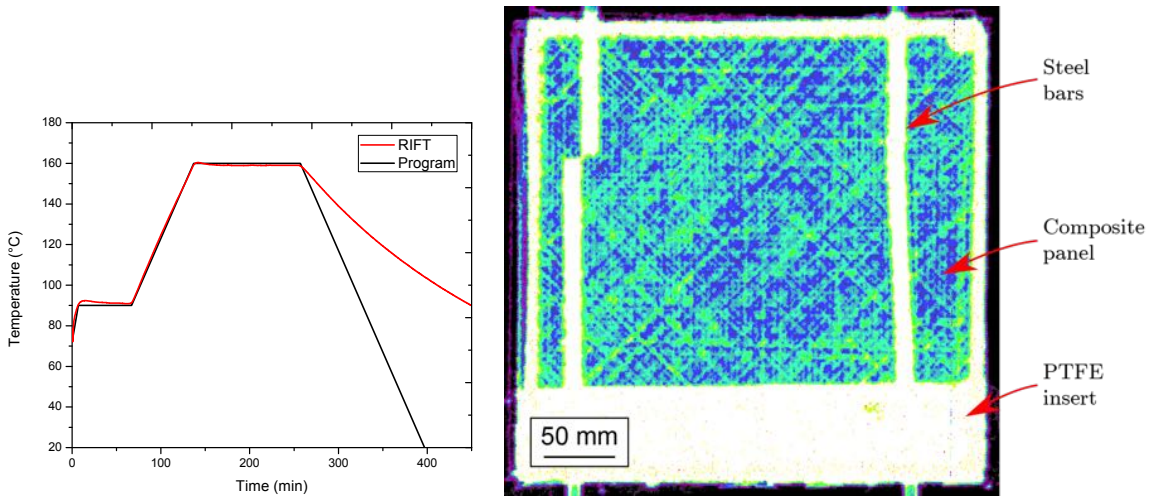
Arranging the flow media, 'N1031' from Newbury Engineered Textiles, UK, as shown in Figure 3.4.1 ensured that the resin would have time to infuse through the thickness of the infusion stack after the inlet port is closed. If this was not the case, the resin would simply flow rapidly through the flow media and out of the outlet tube without wetting the fibres properly, hence resulting in defects in the composite plate.

The vacuum bag was held down with vacuum bag sealant tape, 'Tacky Tape SM5127' from Aerovac, UK, to complete the lay-up. The pressure in the mould was reduced

using a vacuum pump, connected to the mould through a resin catch pot, 'ASK2128' from Aerovac, UK, for at least 1 hour to ensure there were no leaks. The desired matrix resin was then prepared as per the bulk material and heated to the desired temperature in a vacuum oven before being infused into the mould. The resin was left to infuse until it reached a distance of 10 mm beyond the fabric stack.

The inlet was then closed by tying a knot in the tube, secured with a clamp or tape. Steel plates were then placed on top to apply pressure and minimise warping. A thermal insulating material (wool) was also used to prevent heat loss to the surroundings. The same cure cycle as the bulk material was then used via the program mode on the controller for the hot plate. The temperature controller with a programmable PID control loop feedback algorithm allowed for a very precise control of the temperature during the cure cycle, resulting in very little overshoot as shown in Figure 3.4.2(a).

Some of the cured fibre composite panels were inspected with a non-destructive ultrasonic C-scan to ensure the resin has fully penetrated in the through-thickness direction. The composite panels were immersed in a tank of water where it was suspended on two metal bars above a glass panel. A pulse-echo transmission method was utilised, where the intensity and time of the reflected wave is analysed using 'Midas-V2' software. A typical C-scan image is shown in Figure 3.4.2(b). The intensity of the reflected signal is represented by a colour scale, where the bright sections are regions of high intensity, i.e. voids.



(a) (b)

Figure 3.4.2: (a) Cure cycle used for RIFT panels and (b) Typical C-scan image.

Chapter 4

Experimental Methods

4.1 Introduction

This chapter outlines the various test methods and procedures that were utilised to characterise the material properties and microstructure.

4.2 Characterisation

4.2.1 Dynamic mechanical analysis

Dynamic mechanical analysis (DMA) was performed to obtain the glass transition temperatures (T_g) of the bulk epoxy polymers using a Q800 DMA from TA Instruments, UK, on 60 × 10 × 3 mm^3 samples in double cantilever beam mode at 1 Hz. A temperature sweep from -100°C to 250°C at a heating rate of 2°C/min was used, according to ASTM D5418 [245]. This temperature range was selected such that the α and β transitions of the epoxy polymers were within this region. A strain sweep at 23°C was performed to determine the applied strain within the linear elastic region of the materials. This was determined to be 0.005%.

For the BCP thin films, 30 × 5 × 0.5 mm^3 samples were used in tension mode at 1 Hz. For the powder material, a powder clamp [246] was used in double cantilever beam mode at 1 Hz. Approximately 10 mg of powder was compacted into the powder clamp. A small quantity of calcinated alumina powder was added to the lower tray and on top of the powder to prevent the upper plate and lower tray from sticking to the sample

as it melts within the temperature range used. A temperature sweep from -138°C to 200°C at a heating rate of 2°C/min was used. A strain of 0.001% was used for the tensile clamp and an amplitude of 20 μm was used for the powder pocket clamp. The storage modulus (E'), loss modulus (E'') and tan δ were calculated as a function of temperature, where:

$$\tan \delta = \frac{E''}{E'} \tag{4.1}$$

The T_g was determined at the peak tan δ value. The Fox equation [247] can be used to estimate the amount of toughener that remains dissolved in the epoxy resin:

$$\frac{1}{T_{g,modified}} = \frac{wt_{epoxy}}{T_{g,epoxy}} + \frac{wt_{modifier}}{T_{g,modifier}} \tag{4.2}$$

where wt is the weight fraction and T_g is the glass transition temperature.

4.2.2 Rheology

The viscosity was determined using an AR2000EX Rheometer from TA Instruments, UK. Each formulation was first mixed and degassed under the same conditions as the bulk material, then placed on 25 mm diameter disposable aluminium parallel plates on the machine. The tests were conducted under a constant shear rate of 0.25 s^{-1} and constant gap height of 1000 μm. A temperature ramp from 25°C to 120°C over 30 minutes was used to allow enough time for the polymer to respond to the change in temperature.

The shear stress was measured by the machine, and the viscosity, η, can be calculated using:

$$\eta = \frac{\tau}{\dot{\gamma}} \tag{4.3}$$

where τ is the shear stress (Pa) and $\dot{\gamma}$ is the shear rate (1/s).

4.2.3 Atomic force microscopy

An atomic force microscope (AFM) was employed to determine the morphology of the bulk material. A MultiMode scanning probe microscope (SPM) controlled with a NanoScope IV controller and an 'E' scanner from Veeco, USA, was used. The samples were prepared by cutting thin layers of material off the surface of a cured sample. This was done using a PowerTome XL cryo-microtome from RMC Products, USA, at

room temperature and -50°C. This process created a very smooth surface for scanning. Figure 4.2.1 illustrates the process of preparing an AFM sample.

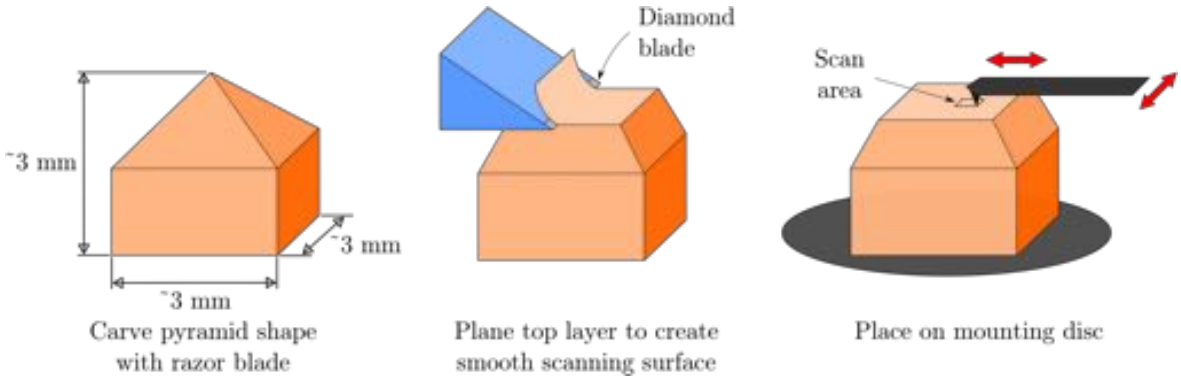


Figure 4.2.1: Illustration of AFM sample preparation.

The scans of height and phase images were obtained using a silicon probe, a microfabricated cantilever with an 8 nm tip radius, operating in tapping mode at a scan rate of 1 Hz. The cantilever is oscillated by a piezoelectric element near its resonance frequency as it contacts the surface intermittently. A laser reflected off the cantilever onto a photodiode measures the deflection and a feedback loop ensures the cantilever is kept at a constant deflection. The phase image originates from the phase lag between the input signal that drives the cantilever oscillation and the output signal. A typical image resolution of 512 × 512 pixels at scan sizes of 10 × 10 μm^2, 5 × 5 μm^2 and 2 × 2 μm^2 was obtained using these settings.

4.2.4 Scanning electron microscopy

A LEO Gemini 1525 field emission gun scanning electron microscope (FEGSEM) from Carl Zeiss, Germany, was used to obtain high resolution images of the fracture surfaces using the in-lens detector. The samples were first cut shorter with a Struers Accutom-5 precision cutter, equipped with a saw blade. The samples were then mounted on aluminium pin stubs using conductive tape. To prevent charging, the samples were then sputter coated with an approximately 5 nm thick layer of chromium using a K575X sputter coater from Emitech, France. Conductive silver paint, from RS Components, UK, was then painted to electrically connect the surface of the sample to the pin stub. An accelerating voltage of 5 kV and a typical working distance of 6 to 8 mm was used.

For some of the higher resolution images, an Ultra Plus FEGSEM from Carl Zeiss, Germany, was used. These samples were sputter coated with an approximately 1 nm

thick layer of gold/palladium (Au/Pd) alloy using a 208HR High Resolution sputter coater, controlled with a MTM-20 High Resolution film thickness controller, both from Cressington, UK. The thickness monitor/controller monitors the film thickness by the change in oscillating frequency of the quartz crystal caused by the increase in mass due to the deposited film on the face. An accelerating voltage of 2 kV and working distance of 3 mm was used.

Figure 4.2.2 illustrates the process of preparing an SEM sample.

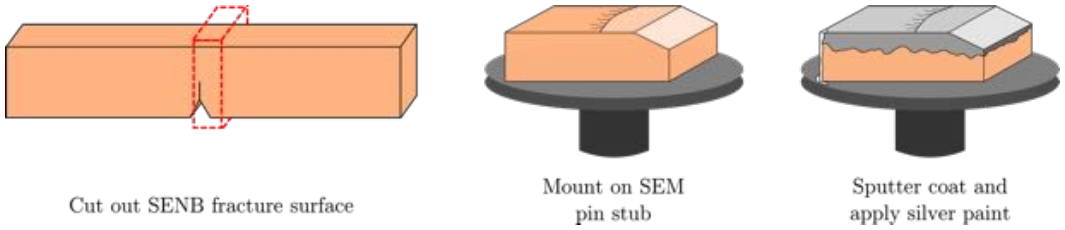


Figure 4.2.2: Illustration of SEM sample preparation.

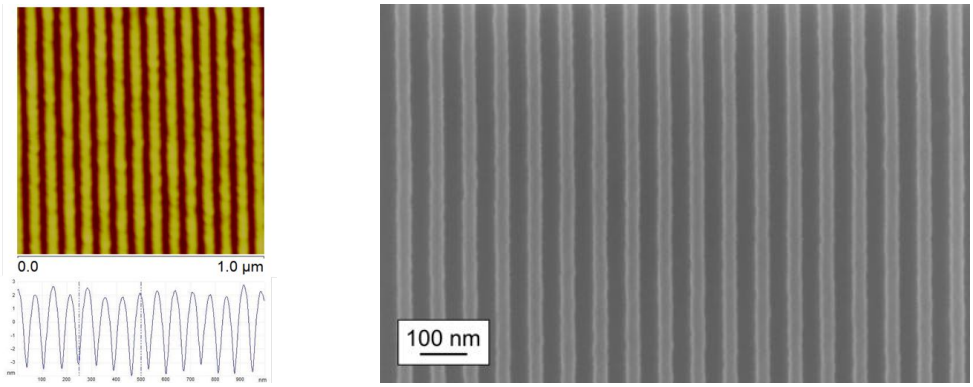
4.2.5 Optical microscopy

An Axio Scope.A1 optical microscope from Carl Zeiss, Germany, was used to obtain optical images of the epoxy samples. A THMS 600 hot stage from Linkam, UK, was used to heat epoxy resins under the optical microscope to observe the change in morphology of the modified epoxies during cure.

4.2.6 Image analysis

The volume fraction, size and distribution of the particles and voids can be determined from the AFM and SEM images, respectively. It should be noted that the AFM and FEGSEM were initially calibrated using micron sized calibration samples. Therefore, a calibration sample with a certified pitch of 70.078 ±0.038 nm was first used to ensure the accuracy of using these techniques for nanoscale measurements. The calibration sample consists of silicon dioxide ridges on silicon from Agar Scientific, UK. Figure 4.2.3 shows the calibration sample imaged on the AFM and FEGSEM.

At least three random locations were sampled and the measured pitches were 67.259 ±0.072 nm and 68.996 ±0.033 nm for the AFM and FEGSEM. Although not calibrated, the height image from the AFM also shows a consistent height profile, as shown in Figure 4.2.3(a).



(a) AFM height image of calibration grid

(b) FEGSEM image of calibration grid

Figure 4.2.3: Calibration of AFM and FEGSEM.

The AFM phase images were typically sharper than the height images, so the phase images were used for image analysis. However, the AFM phase images can be affected by silica nanoparticles under the planed surface (subsurface particles) due to the relative stiffness of the silica particles and the epoxy. This can be evident as particles that appear to be overlapping. In this case, the height images were compared to eliminate false identification.

The images were first processed with GNU Image Manipulation Program (GIMP) v2.6.11 to identify the particles with either the colour picker tool or were manually selected. An image processing program, ImageJ v1.45s, was then used to calculate the area fractions from the processed images. The images processed using GIMP were first thresholded before running them through the 'Particle Analyzer' function. Figure 4.2.4 illustrates the sequence of processing an AFM micrograph. The volume fraction can then be obtained from the well-known equivalency to the area fraction, based on quantitative stereological relationships first developed by Delesse [248].

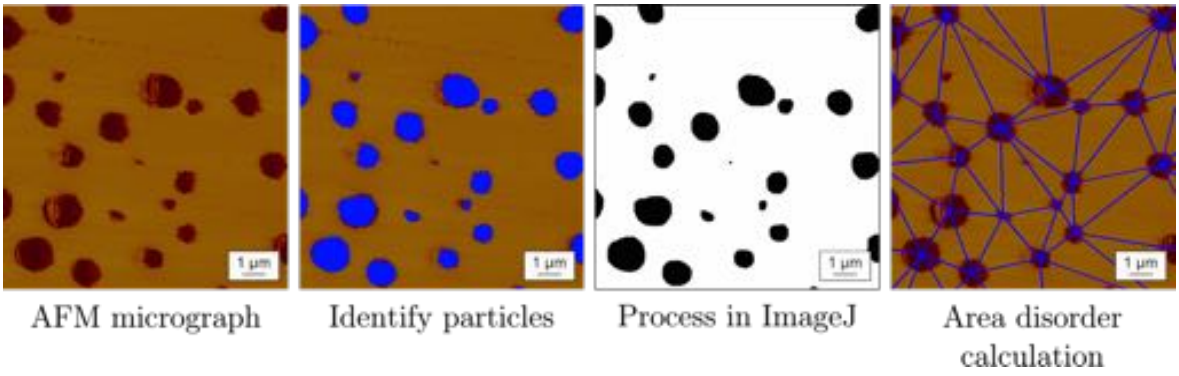


Figure 4.2.4: AFM micrograph image processing sequence.

Although the volume fraction can be obtained accurately, the measured mean diameter

of the particles will always be lower than the actual diameter. This discrepancy arises from the microtome process of preparing the AFM samples. If a spherical particle is not cut at its equator, the perceived diameter will be less than the actual diameter. Figure 4.2.5 illustrates the cutting process and difference in observed diameters at various cutting depths.

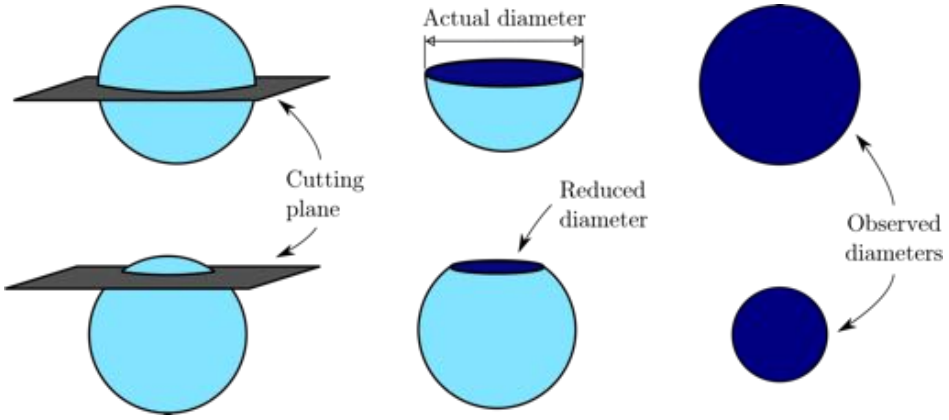


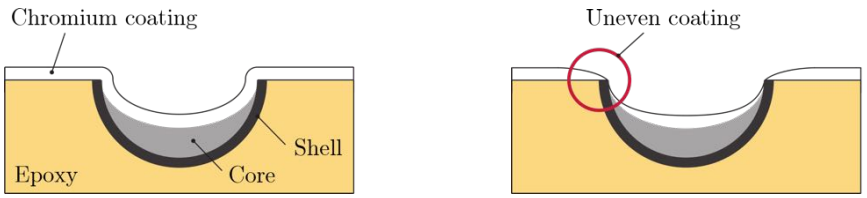
Figure 4.2.5: Illustration showing difference in observed diameters from sectioning.

Given that it is unlikely for all the particles to be cut at the equator, the mean diameter measured from the AFM images would not be expected to be the true diameter. The maximum diameter measured can be used as a guide for the actual particle diameter. The actual diameter of the spheres, D_{sphere}, can be shown analytically to be related to the mean diameter measured, d_{mean}, using [249]:

$$D_{sphere} = \frac{4d_{mean}}{\pi} \tag{4.4}$$

However this assumes that all the particles are of the same size, i.e. monodisperse, which isn't the case (see Figure 3.3.3(a)).

The FEGSEM images of the fracture surfaces were also analysed in a similar manner to calculate the percentage of void growth. A previous study [250] determined that the sputter coating indeed did not affect the particle size, even at the nanoscale, i.e. the sputter coating process is not uniform as illustrated in Figure 4.2.6(b).



(a) Uniform thickness of coating (b) Prediction of actual coating

Figure 4.2.6: Illustration of sputter coated specimens. Reproduced from [250].

4.2.7 Characteristic lengths

The characteristic lengths of the morphological structures can be measured using a two point correlation function [251, 252]. The thresholded AFM and FEGSEM images were used in this analysis. A set of functions, P_{ij}, is defined which denote the probability that a randomly located vector of length r, begins in phase i and ends in phase j. i and j can be either 0 or 1, where phase 0 is the matrix and phase 1 is the modifier. At the limits when r $\rightarrow 0$ and r $\rightarrow \infty$, the correlation functions are defined by the volume fraction, v_f [253, 254]:

$$\lim_{r\to 0} P_{00}(r) = 1 - v_f \tag{4.5}$$

$$\lim_{r\to 0} P_{11}(r) = v_f \tag{4.6}$$

$$\lim_{r\to 0} P_{01}(r) = P_{10}(r) = 0 \tag{4.7}$$

$$\lim_{r\to \infty} P_{00}(r) = (1 - v_f)^2 \tag{4.8}$$

$$\lim_{r\to \infty} P_{11}(r) = v_f^2 \tag{4.9}$$

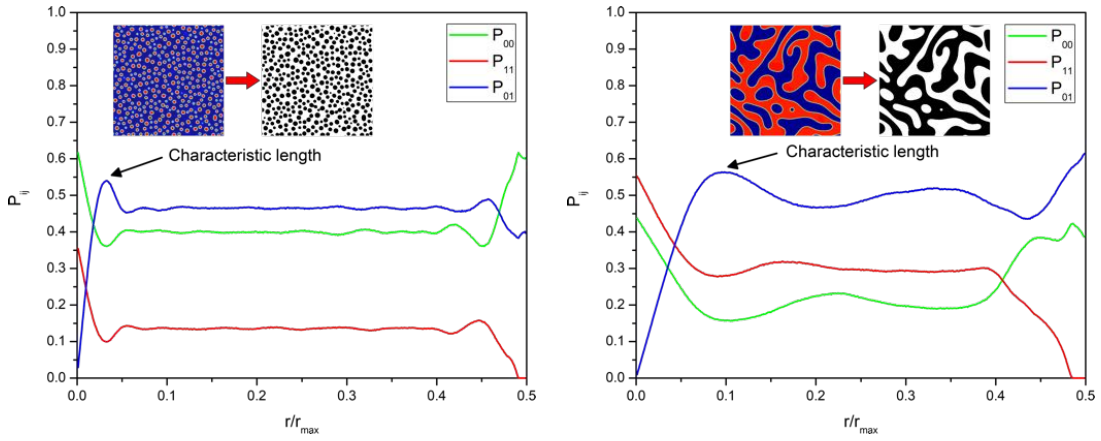
$$\lim_{r\to \infty} P_{01}(r) = P_{10}(r) = v_f\,(1 - v_f) \tag{4.10}$$

The minimum value of P_{ii} or maximum value of P_{ij} can be used as an estimate of the characteristic lengths of the microstructures. For a system where spherical particles are dispersed in a matrix, this value corresponds to the particle diameter or the distance between the particles. For a co-continuous morphology, this value represents the average thickness of each phase. Figure 4.2.7 shows an example of the typical results from the two point correlation for a droplet and co-continuous microstructure. r/r_{max} is the ratio of the random vector length to the side length of the domain.

Figure 4.2.8 shows an example of an image with randomly located vectors used to determine the characteristic lengths. For each image, 500,000 vectors of each vector length from 2 pixels up to half the image size, were randomly located within the image. The probability function, P_{ij}, can then be determined from these vectors.

4.2.8 Particle dispersion

The particle dispersion was quantified by the area disorder approach as described by Bray *et al.* [255]. This technique exploits the properties of the Delaunay network, which itself is the counterpart to a Voronoi tessellation. A Voronoi tessellation defines regions



(a) Droplet microstructure (b) Co-continuous microstructure

Figure 4.2.7: Two point characteristic functions.

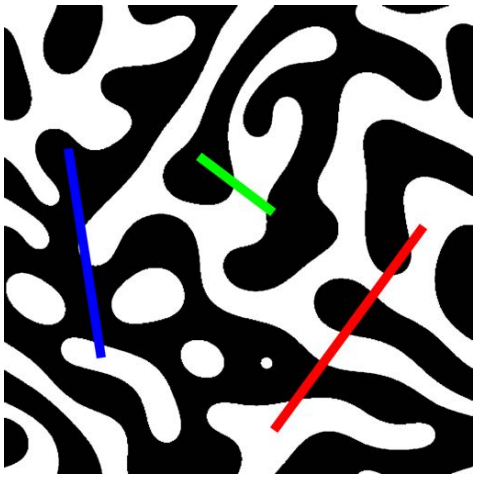


Figure 4.2.8: Randomly located vectors on a thresholded image.

of points which are closest to a particle. The area disorder, AD, is a dimensionless value between 0 and 1, defined as:

$$AD = 1 - \frac{1}{(1 + \sigma_A/\mu_A)} \tag{4.11}$$

where σ_A is the mean area and μ_A is the standard deviation of the area of the Delaunay triangles. Figure 4.2.9 illustrates the process to obtain the values of area disorder. In order to obtain an accurate value of AD, a very large number of micrographs would be required [256]. However, a lower magnification micrograph would include more particles and require fewer micrographs to obtain a meaningful result. At least 3 micrographs were used for each area disorder calculation.

The value of AD represents the quality of the particle dispersion. A value of AD = 0 denotes perfectly dispersed particles in a lattice arrangement. The value of AD

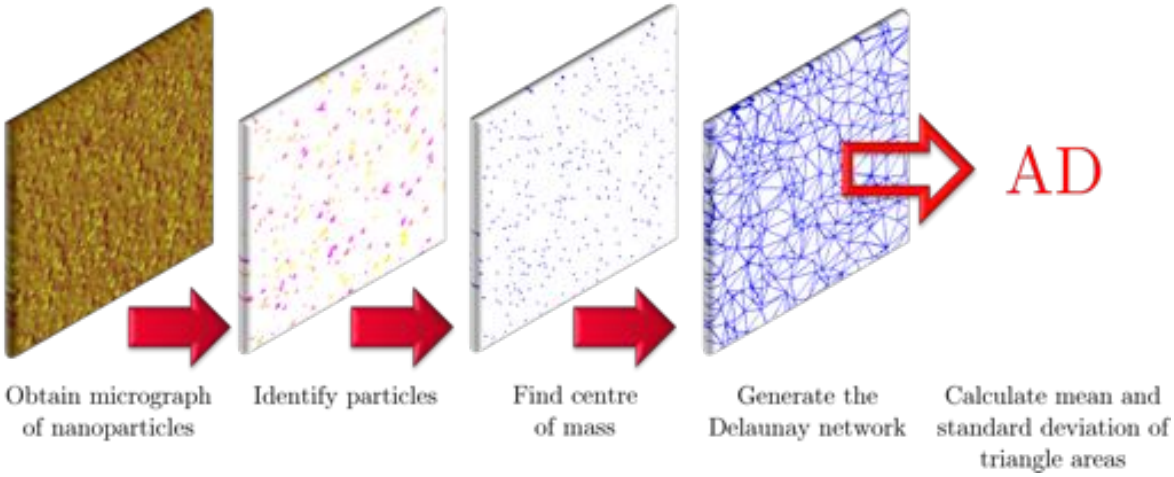


Figure 4.2.9: Process of obtaining the area disorder [255].

that represents "random-like" distribution varies with the area fraction, and AD values higher than this signify a clustered dispersion of particles. There is also a region of high AD values that cannot be attained. These involve the overlapping of the particles and hence is unphysical. The results were then plotted on a correspondence diagram, as shown in Figure 4.2.10, which allows the dispersion to be compared quantitatively.

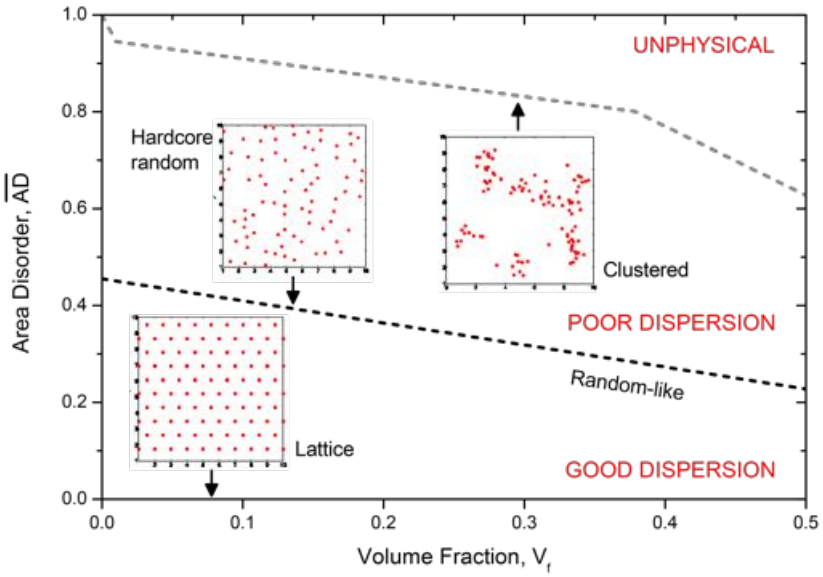


Figure 4.2.10: Correspondence diagram of dispersion for combinations of area disorder and area fraction. Insets shown are for samples of a lattice-like, random or clustered system [255].

4.2.9 Laser light spectroscopy

The particle sizes of the GNPs were measured with laser light spectroscopy (LLS) using a ZetaPALS Zeta Potential Analyser, from Brookhaven, USA. A 35 mW red diode laser with a wavelength of 660 nm was used and the results were averaged over 10 runs. The platelets were dispersed in distilled water by sonicating for 30 min. The results are given as the differential distribution, $G(d)$, and cumulative distribution, $C(d)$, of the intensity of scattered light at each value of diameter. The effective diameters were taken as the modal average of the differential distribution of the intensity of the scattered light.

4.2.10 X-ray photoelectron spectroscopy

The surface chemical compositions of the GNPs were analysed with angle-resolved X-ray photoelectron spectroscopy (XPS) using a Theta Probe spectrometer, from ThermoFisher Scientific, UK. A MXR1 monochromatic Al Kα X-ray source operating at a photon energy of 1486.6 eV, a spot size of 400 μm diameter and operating base pressure of 10^{-9} mbar were used. For the survey spectra, a pass energy of 300 eV and step size of 0.4 eV were used over 3 sweeps. Quantitative surface chemical compositions were measured from high resolution spectra with a pass energy of 20 eV, 50 eV and 100 eV for the core level C1s, O1s and all other spectra, respectively, using a step size of 0.2 eV over 20 sweeps. The atomic concentrations were obtained from the peak areas after removing the non-linear (Shirley) background baseline (see Figure 4.2.11) and correcting for the sensitivity factors and electron energy analyser transmission functions using Thermo Fisher Scientific's Avantage software. The transmission function corrects for the detection efficiency of the spectrometer, which is a function of the electron kinetic energy and can vary with the pass energy [257]. The GNP powder samples were fixed to the sample bar using double sided tape.

4.2.11 X-ray diffraction

The GNPs were characterised with X-ray diffraction (XRD) using a X'Pert Pro multi purpose diffractometer, from PANalytical, Netherlands, fitted with a PW3064/60 diffractometer and X'Celerator detector. The samples were placed on a powder sample tray and exposed to Cu Kα X-ray radiation, which have a characteristic wavelength of 1.540598 Å. The X-rays were generated from the Cu anode at a generator voltage of 40

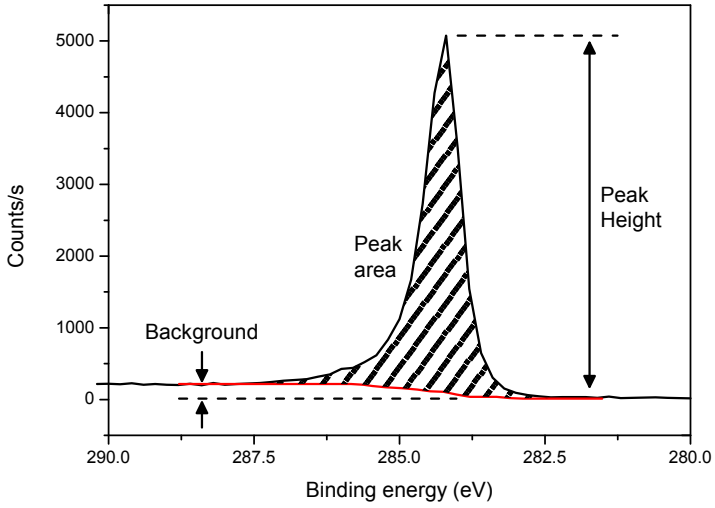


Figure 4.2.11: High resolution XPS spectra with Shirley baseline background subtraction.

kV and tube current of 40 mA. Continuous scans were collected over a range of 2θ from 5 to 60° with a step size of 0.02° and dwell time of 20 s per step. Quantitative analysis was conducted using the accompanying software, PANalytical High Score Plus.

The distance between individual platelets, known as the d-spacing, can be calculated using Bragg's Law:

$$2d \sin\theta = n\lambda \tag{4.12}$$

where θ is the scattering angle, n is an integer related to the order of the reflection and λ is the wavelength. The crystal size, L, can be calculated using the Scherrer equation [258]:

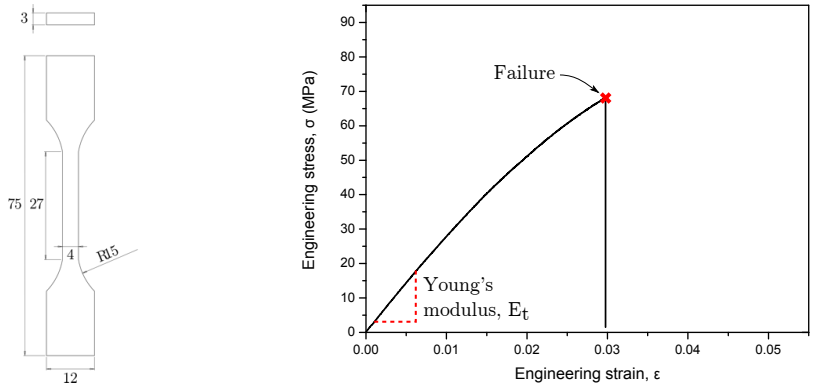
$$L = \frac{K\lambda}{\beta \cos\theta} \tag{4.13}$$

where K is a dimensionless shape factor and β is the width at half the maximum intensity (FWHM) in radians. The crystal size calculated using the Scherrer equation can be used as an estimation of the GNP stack thickness.

4.3 Bulk mechanical tests

4.3.1 Tension

Tensile tests were performed to obtain the Young's modulus and tensile yield stress according to the ISO 527 [259] test standard. The tests were performed with dumb-bell shaped test specimens of type 1BA (see Figure 4.3.1(a)), machined from 3 mm thick bulk plates with a router.



(a) Type 1BA dumb-bell test specimen geometry (in mm)

(b) Typical tensile test stress-strain curve

Figure 4.3.1: Tensile test.

A gauge length of 25 mm and displacement rate of 1 mm/min were used. The tests were performed with an Instron 3392 universal testing machine and the displacement was measured with an Instron 2620-601 dynamic extensometer attached to the sample during testing. At least 5 samples were tested for each formulation.

Digital image correlation (DIC) was also used to measure the axial and transverse strains for some of the tensile test samples. A stochastic speckle pattern was applied to the front surface of the sample as shown in Figure 4.3.2(a). This was achieved by using matt acrylic spray paint, which has good flexibility and adhesion to the sample. A high contrast pattern was obtained by first applying a white base coat, then spraying the black paint intermittently once it has dried. A series of photographs taken every three seconds at a resolution of 3888 x 2592 pixels were obtained during the test using a Canon 400D digital SLR camera. The strains on the surface of the sample was calculated using 'ARAMIS' image correlation software, from GOM, Germany.

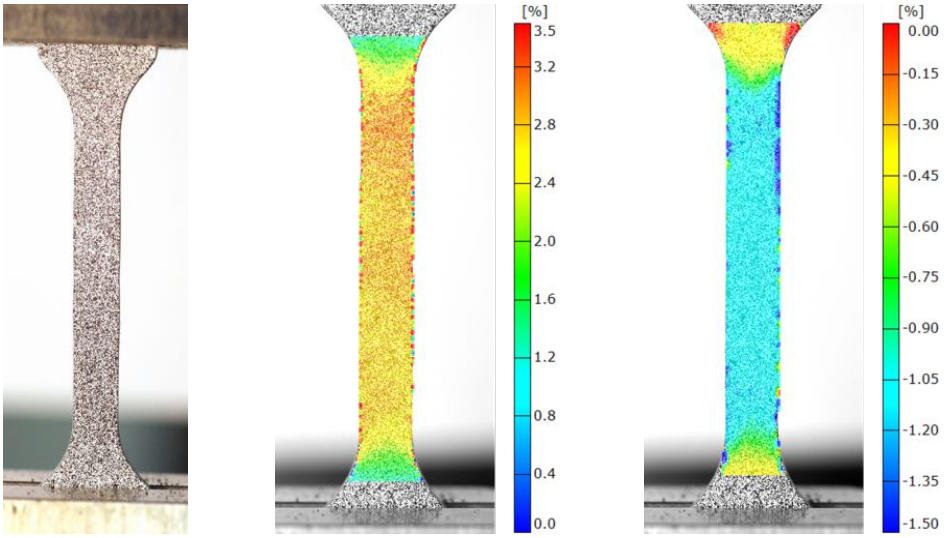
The Poisson's ratio, ν, can then be calculated as:

$$\nu = -\frac{d\varepsilon_{trans}}{d\varepsilon_{axial}} \tag{4.14}$$

where ε_{trans} is the transverse strain and ε_{axial} is the axial strain.

For the pure BCP thin films, the dumb-bell shaped test specimens of type 5A [259] were cut out using a die and tested at a displacement rate of 1 mm/min. The strain was measured by tracking the displacement of markers drawn on the sample. A series of photographs taken every three seconds at a resolution of 3888 x 2592 pixels were obtained during the test with a Canon 400D digital SLR camera.

The engineering stress, σ_E and strain, ε_E, were then calculated from the load and



(a) Speckle pattern (b) Strain (ε_{axial}) map (c) Strain (ε_{trans}) map

Figure 4.3.2: Tensile test sample.

displacement data collected respectively:

$$\sigma_E = \frac{P}{A_o} \qquad \varepsilon_E = \frac{\Delta L}{L_o} \tag{4.15}$$

where P is the load, A_o is the initial cross-sectional area, ΔL is the increase in specimen length between the gauge marks and L_o is the gauge length. The true stress, σ, and true strain, ε, can be calculated from σ_E and ε_E using:

$$\sigma = \sigma_E \left(1 + \varepsilon_E\right) \qquad \varepsilon = ln\left(1 + \varepsilon_E\right) \tag{4.16}$$

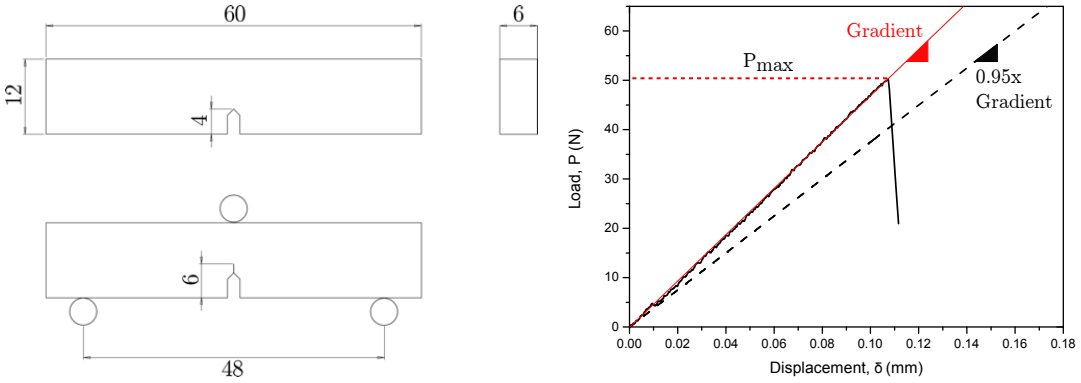
The stress was then plotted against the strain, and the tensile yield stress is defined as the 'first stress at which an increase in strain occurs without an increase in stress' [260], or the maximum tensile stress if this does not occur. The Young's modulus, E_t, can be calculated by:

$$E_t = \frac{\sigma_2 - \sigma_1}{\varepsilon_2 - \varepsilon_1} \tag{4.17}$$

where σ_2 is the stress measured at $\varepsilon_2 = 0.0025$, and σ_1 is the stress measured at $\varepsilon_1 = 0.0005$.

4.3.2 Single edge notched bending

Single edge notched bending (SENB) tests were conducted to determine the fracture toughness (K_{IC}) and fracture energy (G_{IC}) of the materials according to ISO 13586 [261]. Test specimens with a size of 60 × 12 × 6 mm^3 were cut from the bulk plates, and then notched 4 mm deep using a horizontal mill (see Figure 4.3.3(a)). A sharp crack of length a/W ≈ 0.5 was then initiated by tapping a liquid nitrogen chilled razor blade into the notch, where a is the crack length and W is the width. Salazar *et al.* [262] showed that the typical crack tip radius of a crack obtained in this manner is approximately 0.2 μm. The tests were performed on an Instron 3392 universal testing machine at a constant displacement rate of 1 mm/min under three-point bending (see Figure 4.3.3(b)). The displacement was measured with an Instron 2620-601 dynamic extensometer and at least 6 samples were tested for each formulation. The crack lengths were measured post-test using a Nikon SMZ800 optical microscope.



(a) SENB test sample geometry (in mm) (b) Typical SENB load-displacement curve

Figure 4.3.3: Single edge notched bending (SENB) test.

The conditional fracture toughness, K_Q, was then calculated using:

$$K_Q = \left(\frac{P_Q}{\mathrm{B}\sqrt{\mathrm{W}}}\right) f(x) \tag{4.18}$$

where P_Q is the load at a point as specified in the test standard, B is the thickness, W is the width, and:

$$f(x) = 6\sqrt{x}\frac{1.99 - x(1-x)(2.15 - 3.93x + 2.7x^2)}{(1+2x)(1-x)^{\frac{3}{2}}} \tag{4.19}$$

$$x = \frac{\mathrm{a}}{\mathrm{W}} \tag{4.20}$$

The validity of the K_Q values were then checked to determine if they satisfy the size criteria for LEFM using:

$$\mathrm{B, a, W - a} > 2.5 \left(\frac{K_Q}{\sigma_y} \right)^2 \tag{4.21}$$

where σ_y is the tensile yield stress. The load is also checked against the intersection of the 0.95x gradient line with the load-displacement curve measured, as described in ISO 13586 [261]. If they are valid, then the plane strain fracture toughness can be quoted, i.e. $K_{IC} = K_Q$.

G_{IC} was calculated from the area under the load versus displacement curve using Equation 4.22. The linear elastic fracture mechanics (LEFM) method, see Equation 4.23 below, was not preferred due to the viscoelastic nature of polymers, which means that the Young's modulus should be calculated at the same time and conditions. To check the results, both methods were used and compared.

The integration method states:

$$G_Q = \frac{U}{BW\Phi} \tag{4.22}$$

where U is the corrected energy and Φ is the energy calibration factor [261]. $G_Q = G_{IC}$ if the size criteria is met (Equation 4.21).

For the LEFM method:

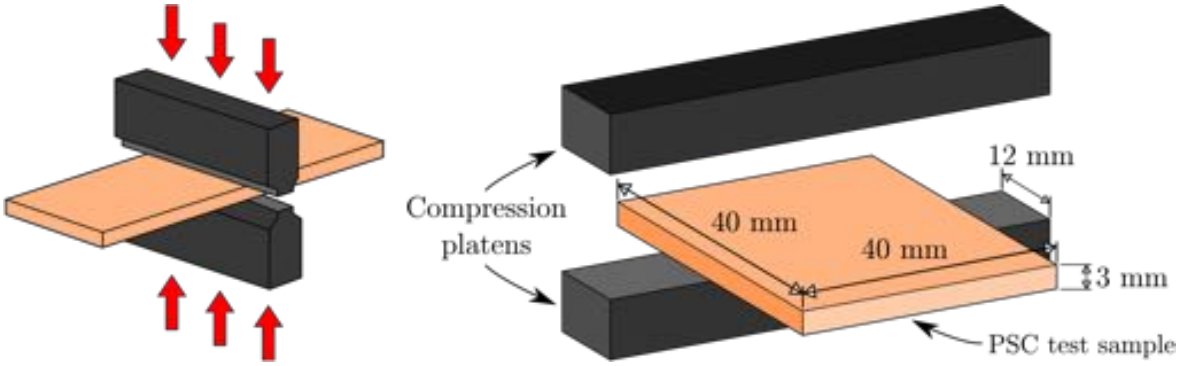
$$G_{IC} = \frac{K_{IC}^2}{E_t}(1 - \nu^2) \tag{4.23}$$

where ν is the Poisson's ratio, taken as 0.35 [2].

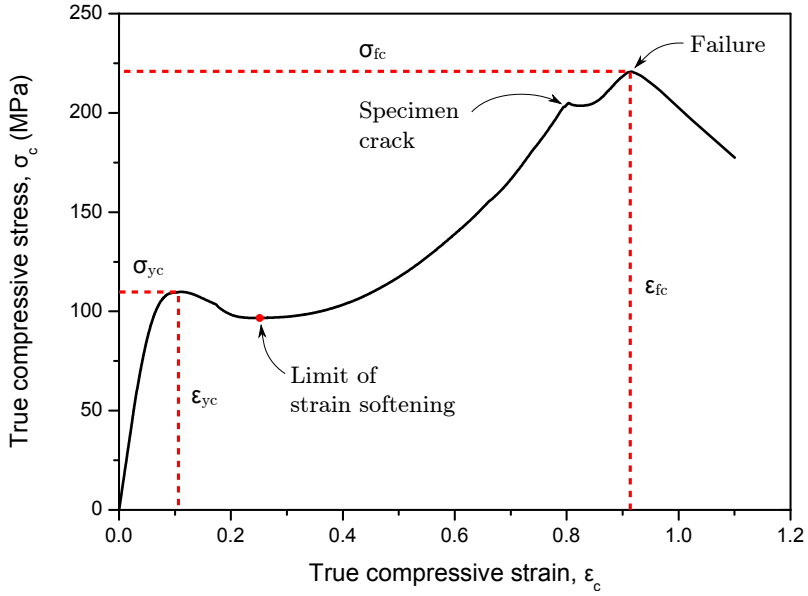
4.3.3 Plane strain compression

Plane strain compression (PSC) tests were conducted to determine the compressive yield stress and failure strain, as described by Williams and Ford [263]. Test specimens of size 40 × 40 × 3 mm^3 were loaded in compression between two parallel dies of 12 mm width at a displacement rate of 0.1 mm/min on an Instron 5585H universal testing machine. The results were then corrected for machine and test rig compliance by compressing the two dies together and subtracting the resulting extensions from the results. At least 2 samples were tested for each formulation. The test set-up and typical true stress-strain curves are illustrated in Figure 4.3.4.

The test is highly sensitive to the surface finish [263] so the platens and specimen



(a) Plane strain compression test set up



(b) Typical true stress-true strain curve from PSC test

Figure 4.3.4: Plane strain compression (PSC) test.

surfaces were polished with 4000 grit sandpaper using a LaboPol-21 polishing machine from Struers, Denmark. The contact surfaces were lubricated to further reduce friction effects using 'BRZ plus multi-grease EP' grease from Dow Corning, UK. The true compressive stress, σ_c, and true compressive strain, ε_c, can be calculated as [263]:

$$\sigma_c = \left(\frac{\sqrt{3}}{2}\right)\sigma_E \qquad \varepsilon_c = \left(\frac{2}{\sqrt{3}}\right)\ln\left(\frac{\mathrm{B}_C}{\mathrm{B}}\right) \tag{4.24}$$

where σ_E is the engineering stress, B_C is the compressed thickness and B is the initial thickness. The yield behaviour of glassy polymers is highly dependent on the hydrostatic pressure [83]. However, the tensile yield stress, σ_{yt} can be related to the compressive yield stress, σ_{yc}, by the relationship [75]:

$$\sigma_{yt} = \sigma_{yc}\frac{3^{1/2} - \mu_m}{3^{1/2} + \mu_m} \tag{4.25}$$

where μ_m is a material constant, usually taken as 0.2 [3].

A cross-section from each formulation which had been loaded to the strain softening region was examined by cross-polarised light microscopy. The samples were first cut with a Struers Accutom-5 precision cutter, equipped with a 10S15 silicon carbide cut-off wheel, polished, and mounted on glass microscopy slides with an optically transparent adhesive, Araldite 2020 from Huntsman, UK. The samples were then ground to a thickness of 100 μm and polished before being examined. This process is illustrated in Figure 4.3.5.

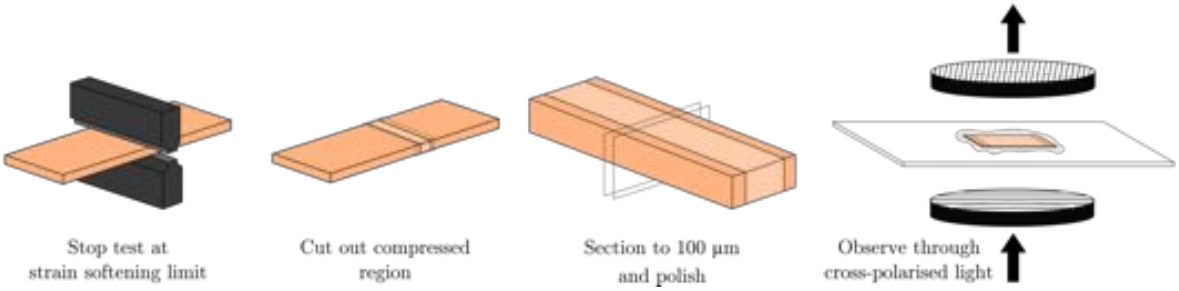


Figure 4.3.5: Illustration of steps to observe shear bands from PSC test samples.

4.4 Fibre composites mechanical tests

4.4.1 Flexure

The flexural modulus of the CFRP composites was measured using a three point bend method in accordance with ISO 14125 [264]. Composite beams of 300 × 15 × 5 mm^3 were machined from the composite plates using a diamond wet saw. The tests were performed on an Instron 5584 universal testing machine at a constant displacement rate of 1 mm/min and a span of 240 mm. The test samples were visually inspected to ensure interlaminar shear did not occur. The flexural stress, σ_f, and flexural strain, ϵ_f are calculated using:

$$\sigma_f = \frac{3PL}{2bh^2} \qquad s' = \frac{\varepsilon'_f L^2}{6h} \qquad s'' = \frac{\varepsilon''_f L^2}{6h} \tag{4.26}$$

where P is the load, L is the span, b is the width and h is the thickness. s' and s'' are the midpoint deflections at $\varepsilon'_f = 0.0005$ and $\varepsilon''_f = 0.0025$, respectively. The flexural

modulus, E_f, is then calculated using:

$$E_f = \frac{P^3}{4bh^3}\left(\frac{\Delta F}{\Delta s}\right) \tag{4.27}$$

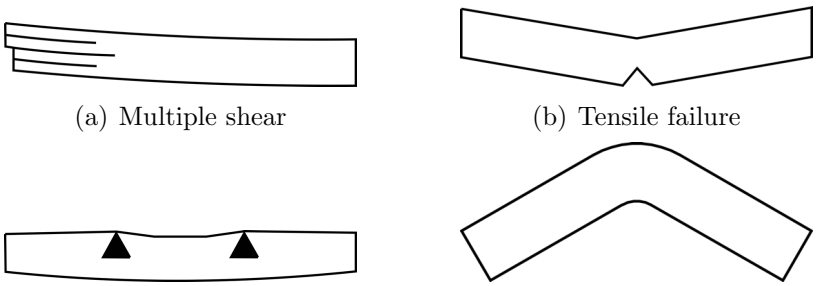
where ΔF is the difference in load at s' and s'', and Δs is the difference between s'' and s'.

4.4.2 Short beam shear strength

Short beam shear tests were conducted to determine the interlaminar shear strength of the CFRP composites in accordance with ISO 14130 [265]. The test specimens were machined to a size of 50 × 25 × 5 mm^3 using a diamond wet saw. These dimensions ensured that the failure mode was by interlaminar shear. The tests were performed on an Instron 5584 universal testing machine at a constant displacement rate of 1 mm/min and a span of 25 mm. The apparent interlaminar shear strength, τ_M, can be calculated using:

$$\tau_M = \frac{3P}{4bh} \tag{4.28}$$

where P is the maximum load, b is the width and h is the thickness. The test samples were visually inspected to ensure there were no tensile or compressive failure, or plastic shearing (see Figure 4.4.1).



(a) Multiple shear (b) Tensile failure

(c) Compressive failure (d) Plastic shear

Figure 4.4.1: Short beam shear failure modes [265].

4.4.3 Mode I interlaminar fracture energy

Double cantilever beam (DCB) tests were used to measure the composite mode I fracture energy, $G_{IC(composite)}$, in accordance with ISO 15024 [266]. Figure 4.4.2 illustrates a typical DCB test sample. Test specimens of 150 × 20 × 5 mm^3 were machined from the composite panels using a diamond wet saw such that the 12 μm thick starter crack

was at a length of 60 mm. Aluminium alloy (6082 T6) load blocks were bonded onto the CFRP specimens, both of which were grit blasted and degreased, using 'Araldite 2014-1' epoxy adhesive from Huntsman, UK. The adhesive was cured at 40°C for 120 min [267]. The tests were performed using an Instron 5584 universal testing machine at a displacement rate of 1 mm/min. The loads and displacements were recorded and the crack lengths monitored with a travelling microscope. Once the crack reached a total length of 110 mm, the test samples were unloaded at a displacement rate of approximately 1 mm/min. The occurence of plastic deformation can be checked by examining the displacement at zero load, δ_{offset}. Values of $\delta_{offset}/\delta_{max} > 0.05$ (where δ_{max} is the maximum displacement attained during the test) signify excessive plastic deformation, and these results were discarded [268]. At least 6 valid specimens were tested for each formulation.

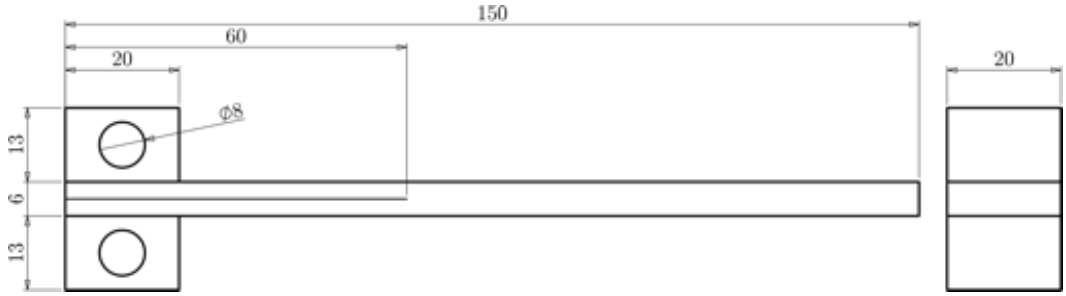


Figure 4.4.2: Dimensions for DCB test sample.

A typical load-displacement curve is shown in Figure 4.4.3.

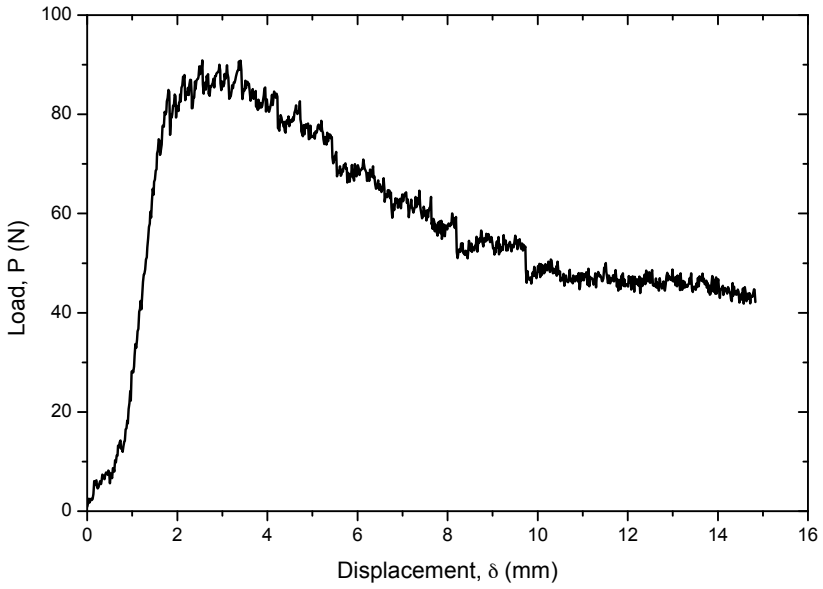


Figure 4.4.3: Typical DCB load-displacement curve.

The composite fracture energy, $G_{IC(composite)}$, was calculated using the corrected beam

theory (CBT) method [268] given by:

$$G_{IC} = \frac{3P\delta}{2B\left(a + |\Delta|\right)} . \frac{F}{N} \tag{4.29}$$

where P is the load, δ is the displacement, B is the width, a is the crack length and Δ is the crack length correction. F is the large displacement correction and N is the load block correction given by:

$$F = 1 - \frac{3}{10}\left(\frac{\delta}{a}\right)^2 - \frac{3}{2}\left(\frac{l_1\delta}{a^2}\right) \tag{4.30}$$

$$N = 1 - \left(\frac{l_2}{a}\right)^3 - \frac{9}{8}\left[1 - \left(\frac{l_2}{a}\right)^2\right]\frac{l_1\delta}{a^2} - \frac{9}{35}\left(\frac{\delta}{a}\right)^2 \tag{4.31}$$

where l_1 and l_2 are dimensions related to the load block [268]. The crack length correction, $|\Delta|$, accounts for deflections and rotations at the crack tip due to the low shear modulus of the matrix. $|\Delta|$ can be obtained as the x-intercept of a plot of $C^{1/3}$ against crack length, where C is the compliance of the beam given by:

$$C = \frac{8a^3}{Ebh^3} \tag{4.32}$$

Chapter 5

Nanoscale core-shell rubber modified epoxy polymers

5.1 Introduction

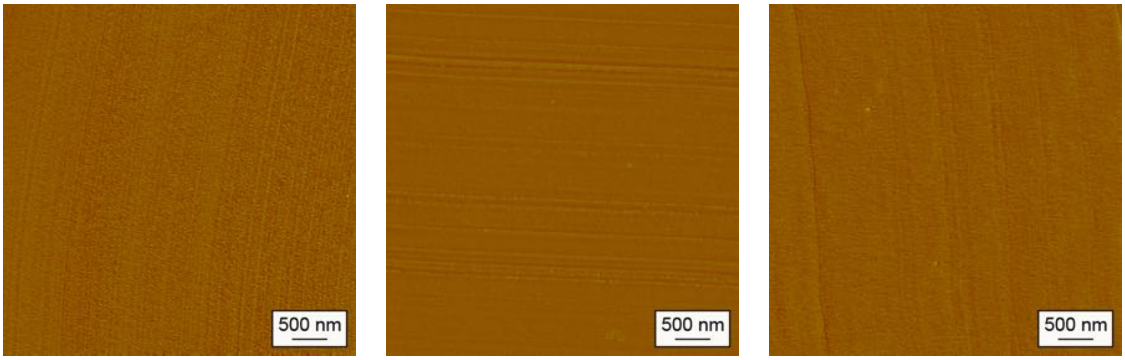
This chapter investigates the use of nanometre sized core-shell polybutadiene rubber particles (CSR), 'Kane Ace MX156' and 'Kane Ace MX551' from Kaneka, USA, to increase the fracture toughness of three epoxy polymers. The epoxy systems used are the DGEBA and DGEBA/F epoxy resins cured with a polyether-amine curing agent, denoted as LD (LY556/D230) and AD (AY105/D230) respectively, and the low viscosity epoxy, denoted as LV. The fracture performance of these core-shell rubber nanoparticles were compared with standard CTBN micron-sized rubber particles. Silica nanoparticles (NS) were also added to create hybrid toughened epoxies, consisting of soft and rigid phases. These are denoted as 10NyR or 10NyC, where the 10N refers to 10 wt% of silica nanoparticles and y refers to the wt% of CTBN rubber (R) or core-shell rubber (C). The formulations of the CSR and CTBN modified epoxies studied in this Chapter are summarised in Table 5.1.1. The synergy of hybrid toughening is still not fully understood and this chapter will aim to examine the role of particle size of the toughening mechanisms.

Table 5.1.1: Summary of CSR and CTBN formulations used in this chapter.

Epoxy system	Modifier CSR wt%	NS wt%	Abbreviation	Modifier CTBN wt%	NS wt%	Abbreviation
Low viscosity epoxy (LV)	2.5	–	2.5CLV	2.5	–	2.5RLV
	5	–	5CLV	5	–	5RLV
	7.5	–	7.5CLV	7.5	–	7.5RLV
	10	–	10CLV	10	–	10RLV
	–	–	–	9	10	10N9RLV
Polyether-amine cured DGEBA (LD)	1	–	1CLD	1	–	1RLD
	3	–	3CLD	3	–	3RLD
	5	–	5CLD	5	–	5RLD
	7	–	7CLD	7	–	7RLD
	9	–	9CLD	9	–	9RLD
	1	10	10N1CLD	1	10	10N1RLD
	3	10	10N3CLD	3	10	10N3RLD
	5	10	10N5CLD	5	10	10N5RLD
	7	10	10N7CLD	7	10	10N7RLD
	9	10	10N9CLD	9	10	10N9RLD
Polyether-amine cured DGEBA/F (AD)	1	–	1CAD	1	–	1RAD
	3	–	3CAD	3	–	3RAD
	5	–	5CAD	5	–	5RAD
	7	–	7CAD	7	–	7RAD
	9	–	9CAD	9	–	9RAD
	1	10	10N1CAD	1	10	10N1RAD
	3	10	10N3CAD	3	10	10N3RAD
	5	10	10N5CAD	5	10	10N5RAD
	7	10	10N7CAD	7	10	10N7RAD
	9	10	10N9CAD	9	10	10N9RAD

5.2 Morphology

The morphologies of the rubber modified epoxy polymers were investigated with atomic force microscopy (AFM). The unmodified epoxies were featureless and homogeneous, as shown in Figure 5.2.1.



(a) (b) (c)

Figure 5.2.1: AFM phase micrographs of unmodified (a) LV, (b) LD and (c) AD epoxy polymer.

5.2.1 Core-shell rubber

The CSR particles are softer than the epoxy and hence, show up as dark circles. For the three epoxy systems examined, the CSR particles were well dispersed up to 10 wt%, as shown in Figures 5.2.2, 5.2.3(a) and 5.2.4(a). Some of the CSR particles show a light coloured ring around the soft cores, indicating the PMMA shell [20]. There were no significant differences in morphology between the different epoxy systems, indicating a good compatibility between the rubber and epoxy. The average core radii of the CSR particles were about 23 ± 1 nm. This agrees well with the literature [20] for these materials.

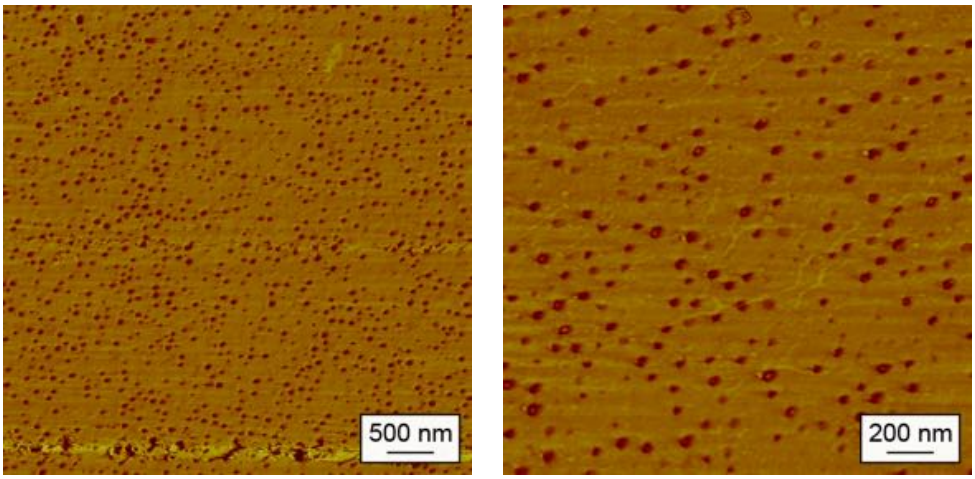
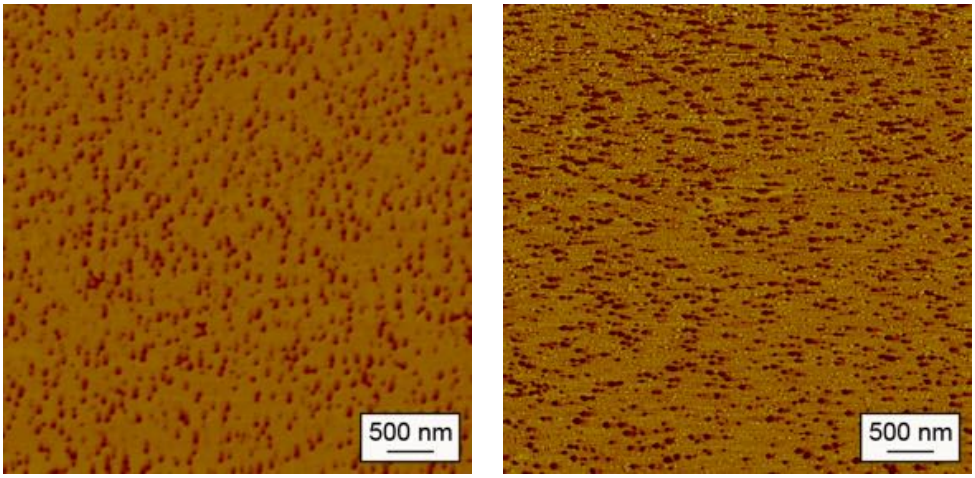


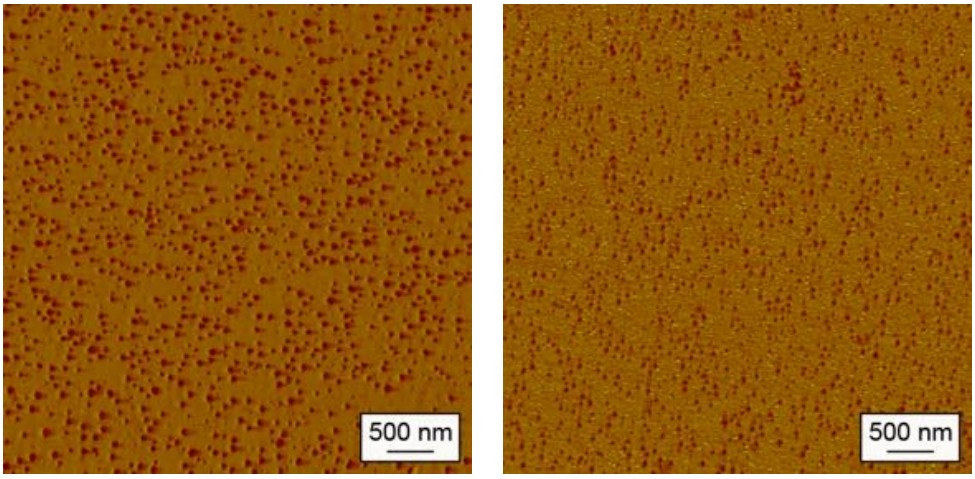
Figure 5.2.2: AFM phase micrographs of MX551 CSR modified LV epoxy polymer.

When silica nanoparticles were added to the CSR modified LD and AD epoxies, both the CSR rubber particles and silica nanoparticles were found to be well dispersed within the epoxy matrix, as shown in Figures 5.2.3(b) and 5.2.4(b).



(a) 9C (b) 10N9C

Figure 5.2.3: AFM phase micrographs of CSR and CSR-NS hybrid modified LD epoxy polymer.



(a) 9C (b) 10N9C

Figure 5.2.4: AFM phase micrographs of MX156 and MX156-NS hybrid modified AD epoxy polymer.

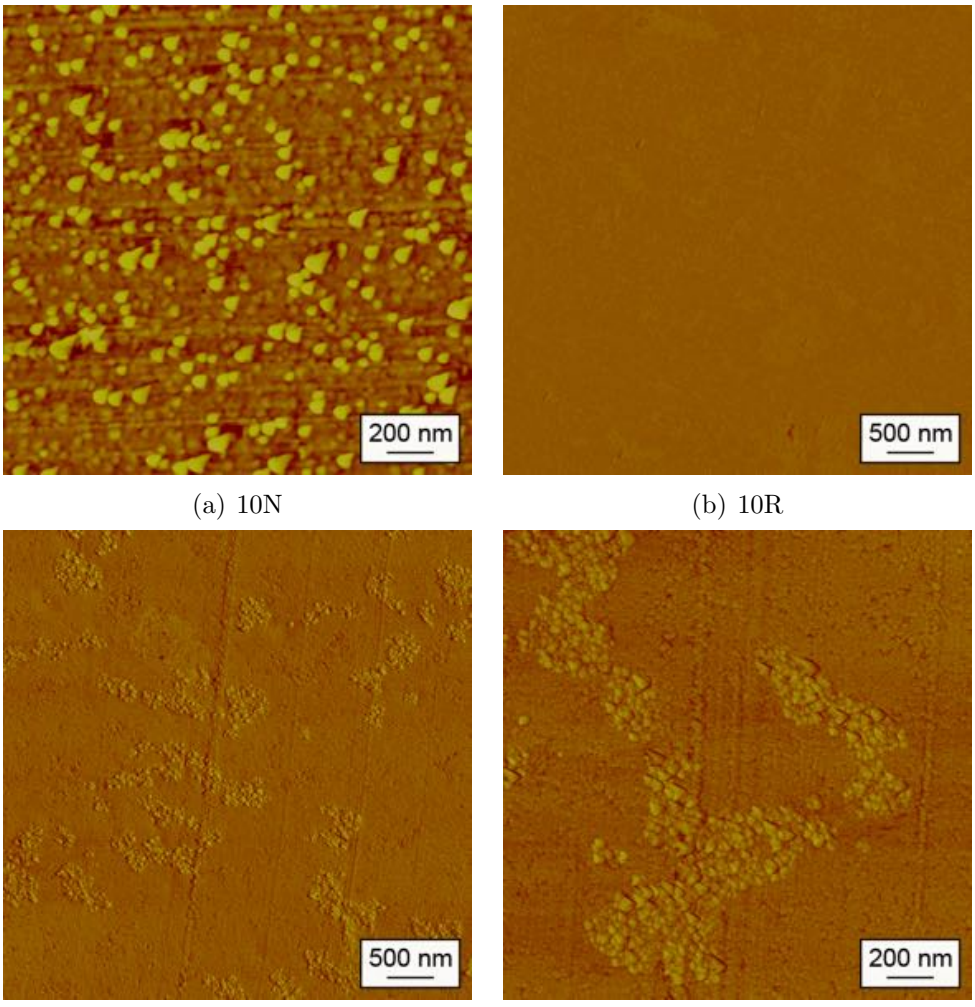
Table 5.2.1 shows the volume fractions of rubber and silica as measured from the AFM phase images. The measured values of CSR volume fraction were typically lower than the theoretical values because the PMMA shells could not be distinguished from the phase images. However, if only the CSR core volume fractions were taken, assuming a shell diameter of 115 nm [20], the volume fractions show better agreement. From the formulations observed, only the measured CSR and silica nanoparticle volume fractions from the AD epoxy system was lower than expected. This indicates loss of information from the removal of particles during the microtome process, or experimental errors due to the small particle size.

Table 5.2.1: Comparison of theoretical and measured values of volume fraction for CSR and NS modified epoxies.

Epoxy system	Content (wt%)		CSR Volume fraction (vol%)			NS Volume fraction (vol%)	
	CSR	NS	Theoretical (incl. shell)	Theoretical (excl. shell)	Measured	Theoretical	Measured
LV	5	0	6.1	4.0	6.1 ± 0.3	–	–
	10	0	12.1	8.0	9.2 ± 0.6	–	–
LD	9	0	10.3	6.8	8.4 ± 0.7	–	–
	9	10	10.8	7.1	8.4 ± 1.2	6.3	5.3 ± 1.9
AD	9	0	10.4	6.8	8.3 ± 1.3	–	–
	9	10	10.8	7.1	4.8 ± 1.1	6.4	2.3 ± 0.3

5.2.2 CTBN rubber

The morphology of the silica nanoparticle, CTBN rubber and hybrid CTBN-NS modified low viscosity epoxy are shown in Figure 5.2.5. The CTBN rubber did not phase separate in the low viscosity epoxy during cure. The 20 nm silica nanoparticles were well dispersed at a loading of 10 wt% in the low viscosity epoxy; however, the particles were found to be clustered with the addition of CTBN rubber, which also did not phase separate, in the hybrid modified epoxy.



(a) 10N (b) 10R

(c) 10N9R (d) 10N9R

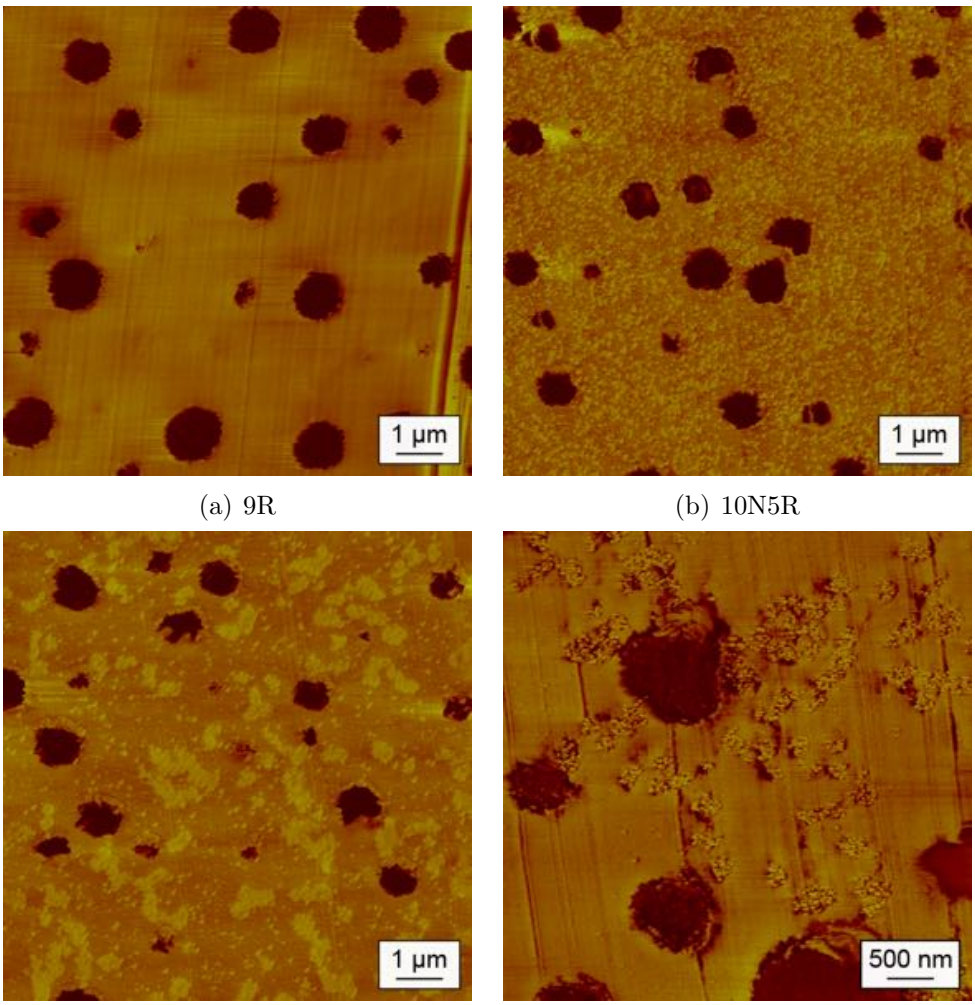
Figure 5.2.5: AFM phase micrographs of NS, CTBN and CTBN-NS hybrid modified LV epoxy polymer.

For the LD and AD epoxy systems, the AFM phase images of the CTBN modified epoxies show well dispersed rubber particles. The average rubber particle radius at 5 wt% is slightly larger than at 9 wt% loading, as summarised in Table 5.2.2, although the differences were within the standard error.

Table 5.2.2: Mean particle radius of CTBN rubber particles for LD and AD epoxy systems.

Modifier	Particle radius (μm)	
	LD	AD
5R	0.53 ± 0.11	n.d.
9R	0.42 ± 0.01	0.51 ± 0.03
10N5R	0.24 ± 0.04	n.d.
10N7R	0.26 ± 0.01	n.d.
10N9R	0.46 ± 0.05	0.53 ± 0.05

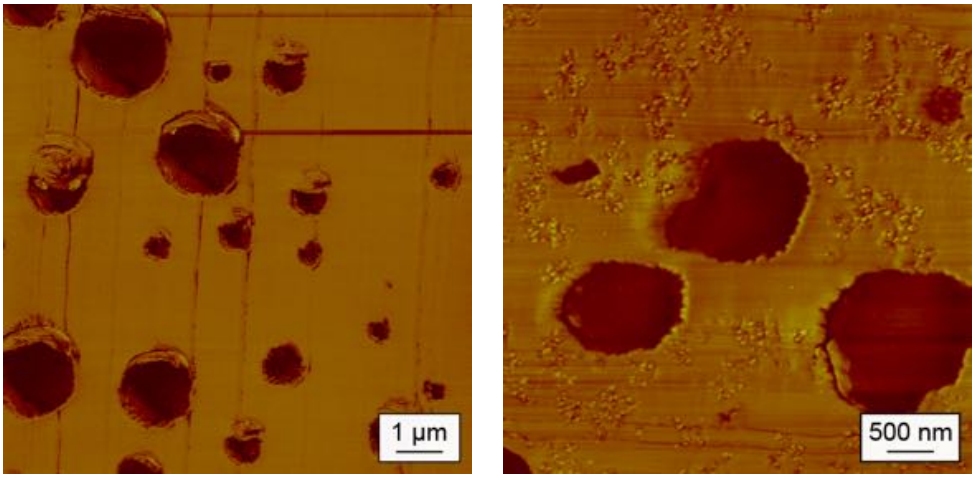
For both of these epoxy systems, the 10 wt% silica nanoparticle modified epoxies are known to have well dispersed particles [5]. However, these 20 nm silica nanoparticles were found to be agglomerated when used in conjunction with a CTBN content above 5 wt% to form a hybrid modified epoxy, as shown in Figure 5.2.6 and Figure 5.2.7.



(a) 9R (b) 10N5R

(c) 10N7R (d) 10N9R

Figure 5.2.6: AFM phase micrographs of CTBN and CTBN-NS hybrid modified LD epoxy polymer.



(a) 9R (b) 10N9R

Figure 5.2.7: AFM phase micrographs of CTBN and CTBN-NS hybrid modified AD epoxy polymer.

Two trends in the rubber particle size were observed for the CTBN-NS hybrid modified epoxies. Firstly, the addition of the silica nanoparticles causes a reduction in rubber particle size. Secondly, increasing the rubber content in the hybrid modified epoxies increases the rubber particle radius.

Compared to the CTBN modified LD epoxy, the rubber particles in the AD epoxy system are slightly larger in diameter, due to the lower viscosity of the DGEBA/F epoxy resin, as shown in Figure 5.2.8, which affects the diffusion rate. As with the rubber modified LD epoxy, there were no changes in particle size when adding silica nanoparticles to the 9 wt% CTBN modified epoxy.

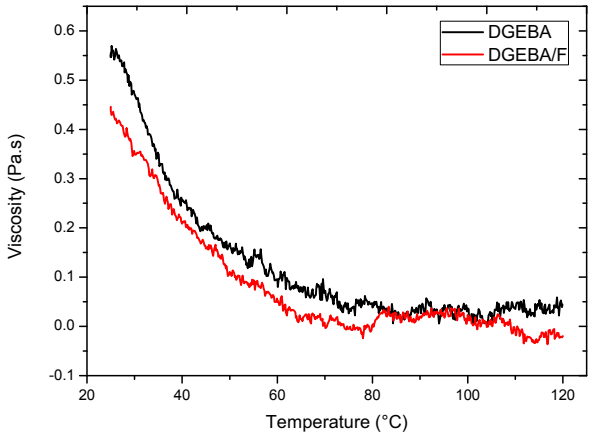


Figure 5.2.8: Viscosity as a function of temperature for the unmodified LD and AD epoxy polymers.

5.2.3 Area disorder

The dispersion of the rubber and hybrid modified epoxies were quantified using the area disorder method as described by Bray *et al.* [255]. The results are shown in Figures 5.2.9 to 5.2.11. The dispersion quality for all three epoxy systems share the same trend. For the CSR and CSR-NS hybrid modified epoxies, the rubber particles and silica nanoparticles were both within the "random-like" dispersion region. For CTBN and CTBN-NS hybrid modified epoxies, the rubber particles were also "randomly" dispersed. However, the area disorder of the silica nanoparticles increase with rubber content, tending towards the "clustered" region of the correspondence diagram as the rubber content increases. The area disorder of the rubber particles in the CTBN-NS hybrid modifeid epoxies did not change significantly with rubber content, and were in the "randomly" dispersed region.

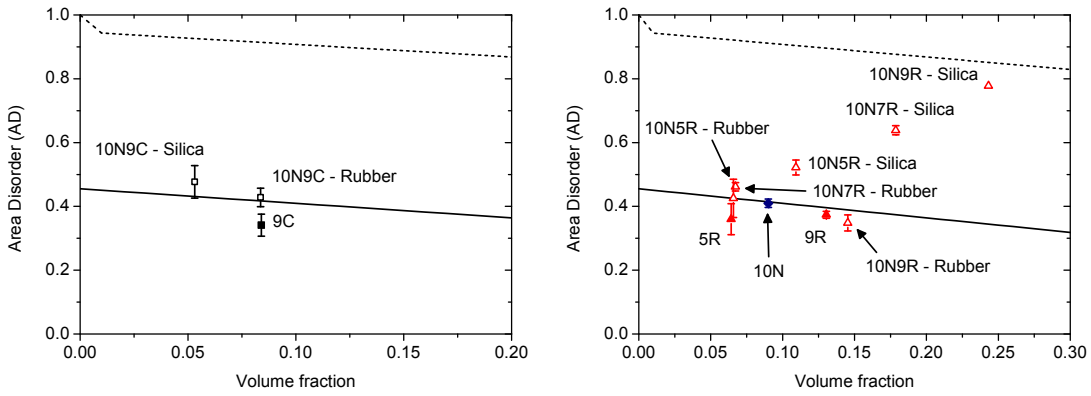


Figure 5.2.9: Area disorder of rubber modified LD epoxy.

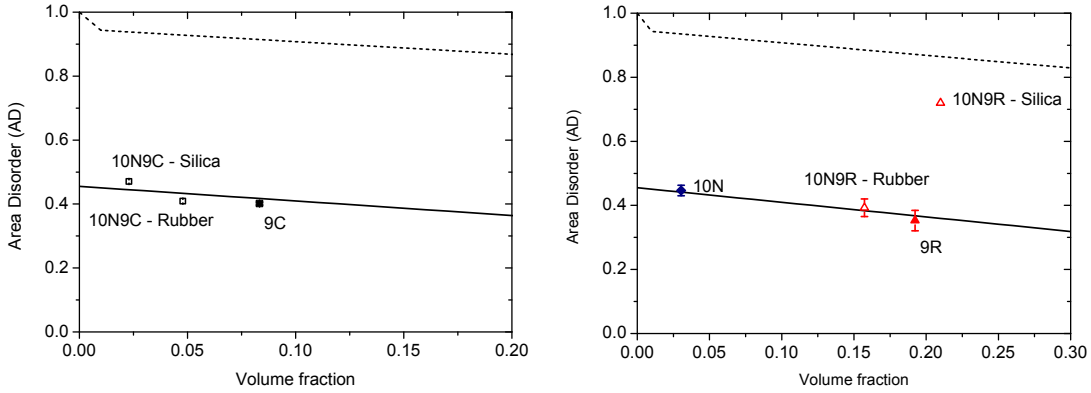


Figure 5.2.10: Area disorder of rubber modified AD epoxy.

In summary, the quantitative analysis shows good agreement with the qualitative discussion in the previous section. None of the micrographs showed any indication that the dispersion was "lattice-like". There were also no points in the "unphysical" region,

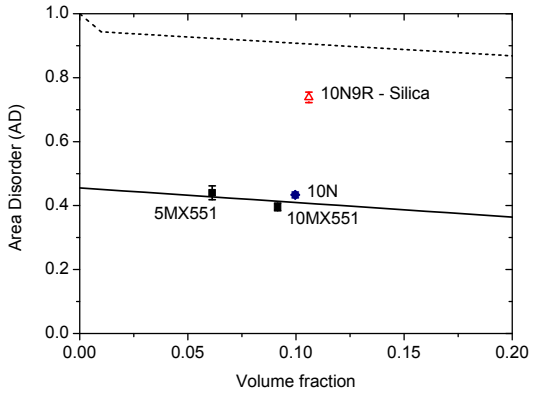


Figure 5.2.11: Area disorder of rubber modified LV epoxy.

indicating no particle overlapping.

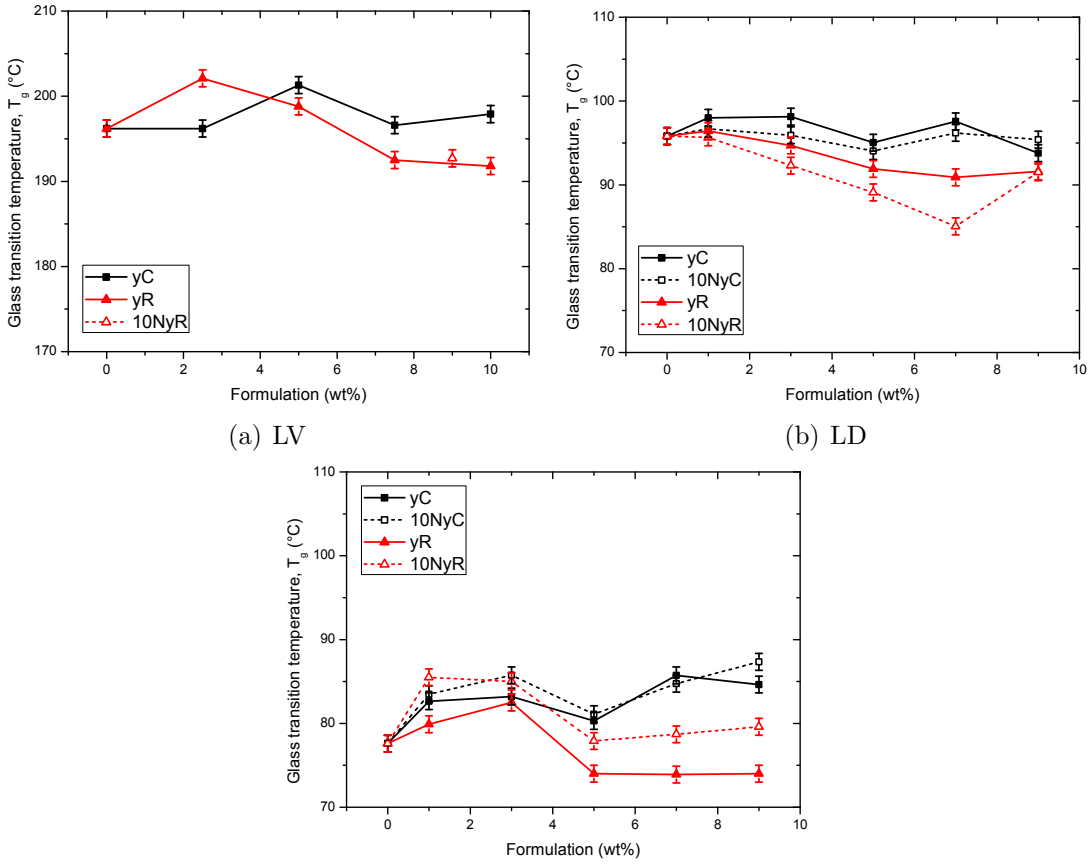
5.3 Glass transition temperature

The glass transition temperatures, T_g, were compared for the different modifiers and epoxy systems using DMA, and the results are summarised in Figure 5.3.1. The T_gs of the unmodified epoxies were 196 °C, 96 °C and 78 °C for the LV, LD and AD epoxies respectively.

The addition of CSR particles did not affect the T_g of the LV epoxy, as expected. The CTBN rubber modified LV epoxy shows a reduction in the T_g to a minimum of 192 °C at a content of 10 wt%. The Fox equation (see Equation 4.2 [247]) predicts that the T_g should be 150 °C if all the CTBN remains dissolved in the LV epoxy. Clearly, the Fox equation does not work in this case due to the CTBN rubber being overcooked and breaking down during the high curing temperatures.

The T_g of the LD epoxy also remained unchanged when CSR particles were added to the epoxy. The T_g of the CTBN modified LD epoxy shows a decrease of 2 °C at 9 wt%, which corresponds to an estimated 1.8 wt% of CTBN rubber remaining dissolved in the epoxy, based on the Fox equation. The addition of silica nanoparticles to the CTBN modified epoxy reduced the T_g further, indicating that there was more rubber dissolved in the epoxy, up to 4.6 wt% for the 10N7R hybrid modified epoxy. There is a clear correlation between the amount of CTBN remaining dissolved, hence T_g, and particle size.

The CSR rubber and CSR-NS hybrid modified AD epoxy increased the T_g up to a maximum of 87 °C. This is due to the increasing fraction of DGEBA in the DGEBA/F



(a) LV (b) LD

(c) AD

Figure 5.3.1: Glass transition temperatures of rubber modified epoxy polymers. Error bars represent standard error of ±1°C.

epoxy blend as the CSR rubber used was pre-dispersed in DGEBA only. A decrease in T_g to 74°C for the CTBN modified AD epoxy was measured. Using the Fox equation, the amount of CTBN rubber remaining dissolved in the epoxy was estimated to be up to 1.9 wt%. With the further addition of 10 wt% silica nanoparticles, the fraction of DGEBA in the DGEBA/F epoxy resin blend consists of even more DGEBA, and this increases the T_g.

5.4 Tensile properties

The Young's modulus, E_t, of the unmodified epoxies were measured to be 2.9, 3.0 and 3.6 GPa for the LV, LD and AD epoxies respectively. This agrees well with the previously reported values for these materials [5]. Typical true stress-strain curves for the unmodified and rubber modified LD epoxies are shown in Figure 5.4.1.

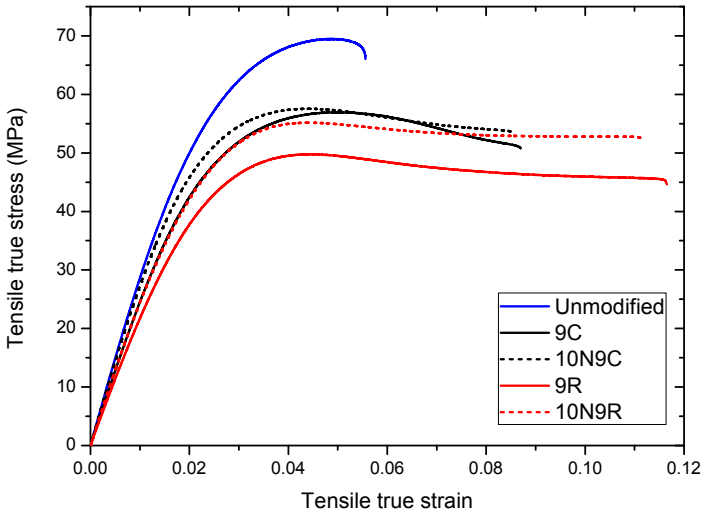


Figure 5.4.1: Typical tensile true stress-strain curves for unmodified and rubber modified LD epoxies tested at room temperature.

The Young's moduli of the rubber modified epoxies are summarised in Figures 5.4.2 to 5.4.4.

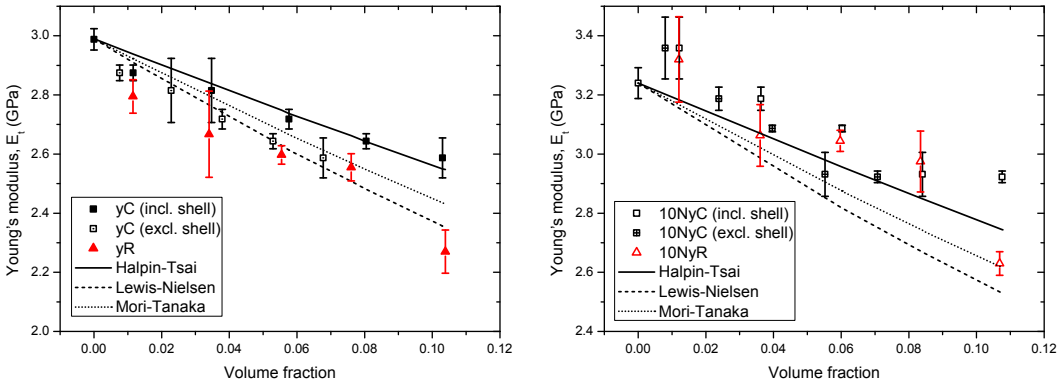


Figure 5.4.2: Young's moduli of rubber modified LD epoxy.

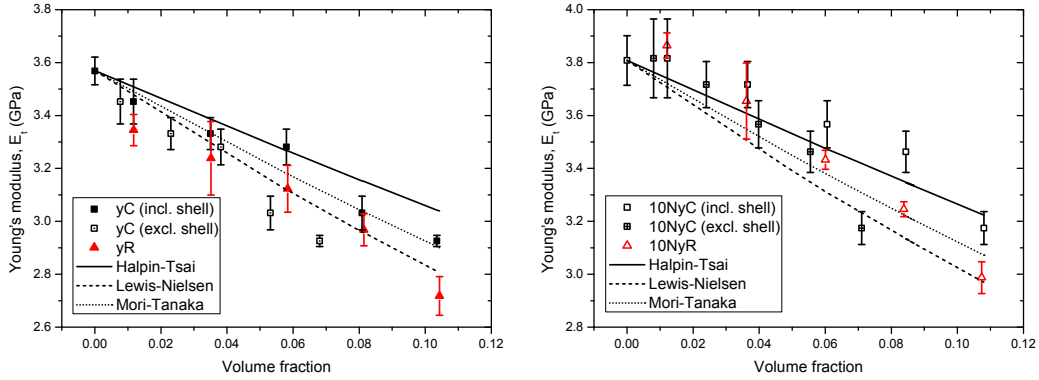


Figure 5.4.3: Young's moduli of rubber modified AD epoxy.

The addition of the CSR or CTBN rubber reduces the E_t of the epoxies linearly with

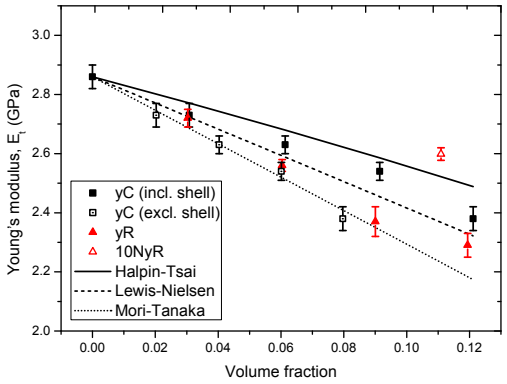


Figure 5.4.4: Young's moduli of rubber modified LV epoxy.

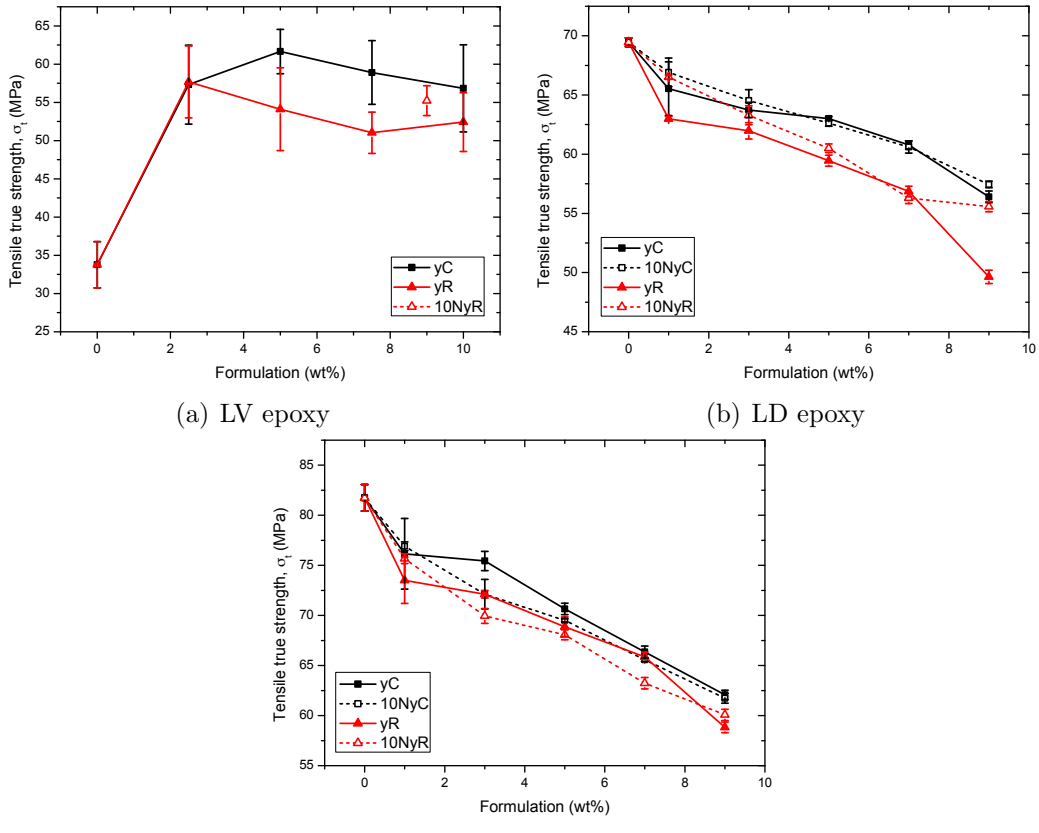
an increasing rubber content. This was expected because the rubber particles are much softer than the epoxy matrix (E_{rubber} = 2 MPa versus E_{epoxy} = 3 GPa). For a given weight percentage of modifier, the smaller CSR rubber particles might appear to retain the tensile modulus better than the larger CTBN rubber particles, as seen for the LD and AD epoxy systems. This can be accounted for by considering only the rubber content of the CSR modified epoxies, subtracting the volume fractions corresponding to the PMMA shell. This is shown as the CSR (excl. shell) modified epoxies in Figures 5.4.2 to 5.4.4, which now show similar results to the CTBN modified epoxies.

The modulus of bulk silica is approximately 70 GPa [269], which is much higher than that of the bulk epoxy polymers. Thus, as expected, the modulus for both CSR and CTBN rubber modified epoxies were able to be recovered by the addition of the much stiffer silica nanoparticles. It is also interesting to note that the agglomeration of the silica nanoparticles did not affect the increase in stiffness, as both CSR-NS and CTBN-NS hybrid modified epoxies show similar increases in stiffness.

The measured values of Young's modulus for the rubber modified epoxies were compared to analytical models. For both the CSR and CTBN rubber particles, a particle modulus, E_p, of 2 MPa and a Poisson's ratio, ν_p, of 0.49 was used [24]. The matrix modulus, E_m, and Poisson's ratio, ν_m, were measured experimentally. For the Lewis-Nielsen model, the 'no slip' condition was applied to assume a strong particle/matrix adhesion, as no debonding was observed from the fracture surfaces §5.7. For the hybrid modified epoxies, the matrix modulus, E_m, was taken as the 10 wt% silica nanoparticle modified epoxy. In general, the predictions of moduli appear to match the experimental data for the rubber modified epoxies quite well, as shown in Figures 5.4.2 to 5.4.4. The Lewis-Nielsen model showed the best agreement with the experimental results. The predictions of moduli for the hybrid modified were underestimated compared to the measured values, which could be due to the errors introduced

by assuming a homogeneous matrix of epoxy and silica nanoparticles as that does not account for inter-particle interactions.

In general, the tensile true strength, σ_t, of the epoxies was reduced by the addition of the rubber particles, as shown in Figure 5.4.5. This is consistent with previous findings for rubber modified epoxies [84]. This was due to internal cavitation of the rubber particles, which leads to the formation of voids. These voids act as defects, which in turn reduces σ_t. The σ_t of the CTBN modified epoxies tend to be slightly lower than the CSR modified epoxies. The CTBN rubber particles are larger than the CSR particles, hence more particles will cavitate at a given stress level and the voids will be larger, further reducing the σ_t. The addition of 10 wt % of silica nanoparticles did not have an effect on the σ_t of the rubber modified epoxies. It should be noted that the unmodified low viscosity epoxy show a very low tensile strength of 32 MPa due to the brittle nature of the material. Hence the addition of rubber increases σ_t initially.



(a) LV epoxy

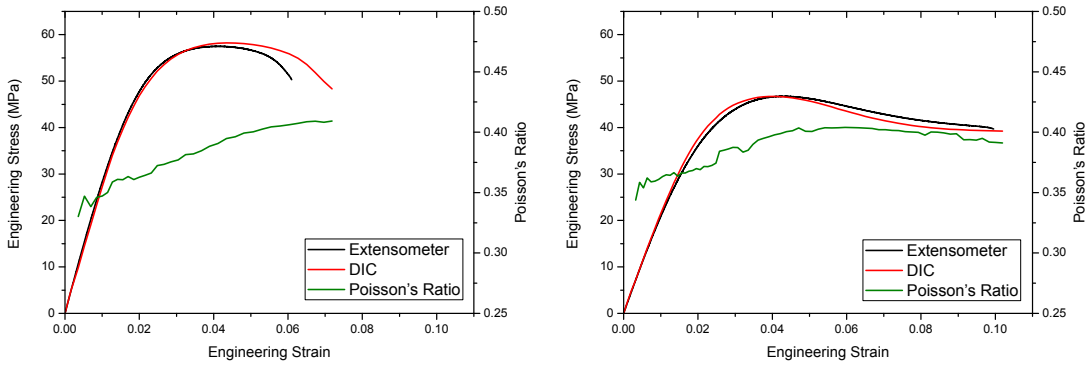
(b) LD epoxy

(c) AD epoxy

Figure 5.4.5: Tensile true strength, σ_t, of rubber modified epoxy polymers.

A digital image correlation (DIC) technique was used to obtain the strains in the axial and transverse directions. The stress-strain curves from the tensile tests, comparing

the different methods to measure strain, are shown in Figure 5.4.6. There were no significant differences between the strains measured using the extensometer and DIC.



(a) Unmodified (b) 9R

Figure 5.4.6: Tensile engineering stress versus engineering strain for unmodified and 9R modified LD epoxy.

The measured values of Poisson's ratio, ν, for the unmodified and 9R modified LD epoxy are shown in Figure 5.4.7. The value of ν for the unmodified epoxy was found to increase from 0.35 to 0.40 as the sample was loaded, as expected [270]. Other authors [23, 80, 270] have noted that the Poisson's ratio would decrease before yield, at strains of approximately 0.024, due to cavitation of the rubber particles. The value of ν did not change when 9 wt% of CTBN rubber was added to the LD epoxy. However, this does not imply that cavitation did not occur in the rubber modified epoxies. This discrepancy could be due to the loading condition, i.e. uniaxial tension, or accuracy of the DIC method to measure the Poisson's ratio.

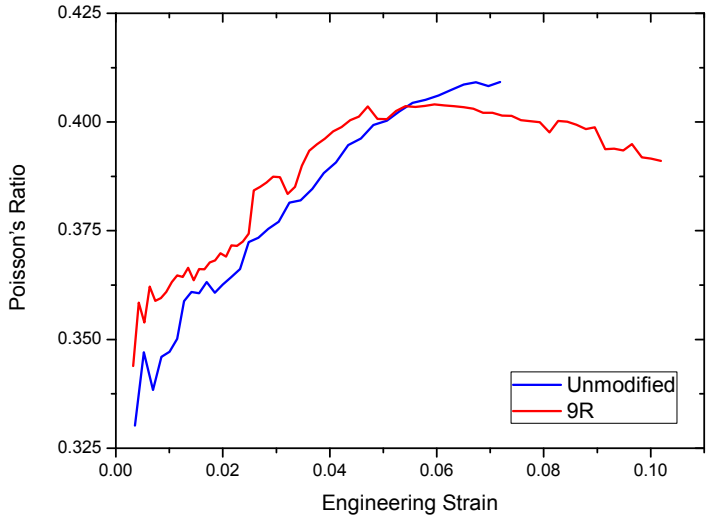
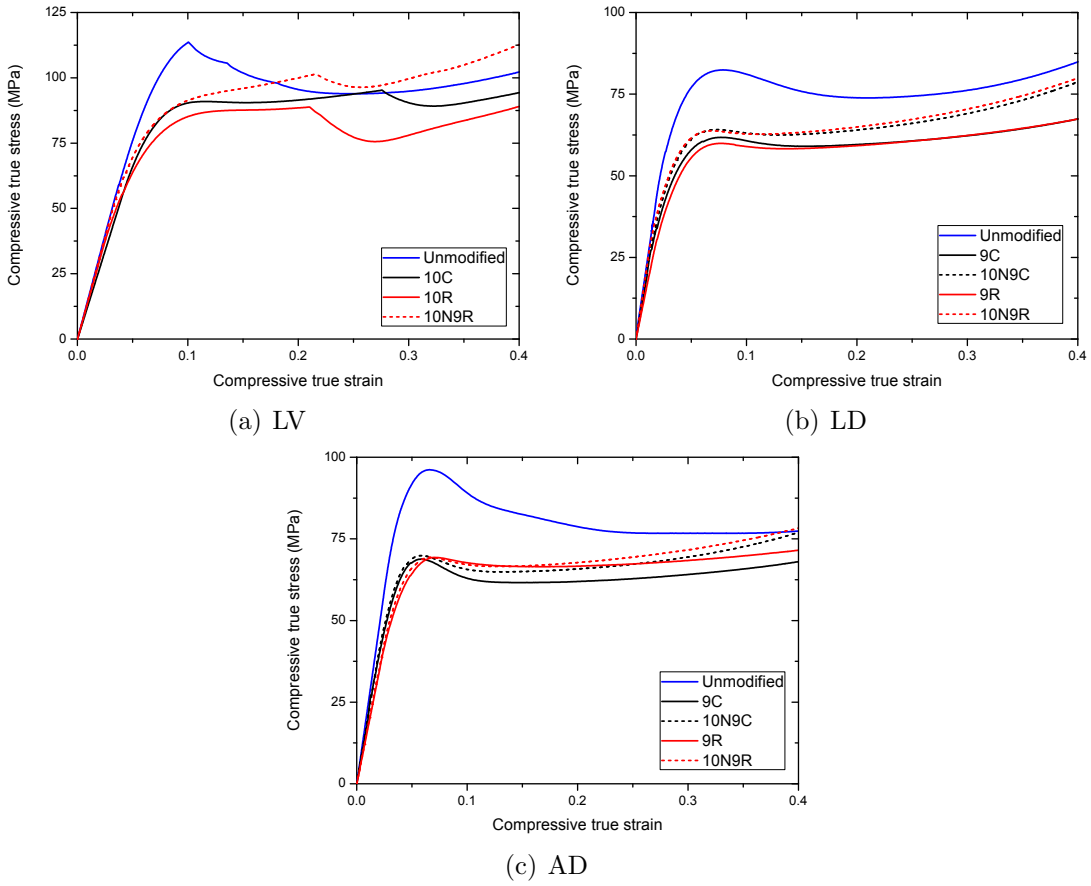


Figure 5.4.7: Poisson's ratio of unmodified and 9R modified LD epoxy under uniaxial tensile loading.

5.5 Compressive properties

The compressive modulus, E_c, and compressive true yield stress, σ_{yc}, decrease with the rubber content as shown in Figure 5.5.1, a trend which agrees well with the tensile properties. The measured values of E_c tend to be lower than E_t due to the compliance correction and frictional effects; for example for the unmodified LD epoxy, $E_c = 2.3$ GPa and $E_t = 3.0$ GPa.



(a) LV (b) LD

(c) AD

Figure 5.5.1: Compressive true stress-true strain curves for unmodified and rubber modified epoxy polymers.

For the LD and AD epoxies, the yield stresses, σ_y, measured from the tensile and compression tests show very good agreement when using Equation 4.25 to convert between the two, as shown in Table 5.5.1. The LV epoxies fractured before yielding in the tensile tests, so the tensile yield stresses can be obtained from the compression tests.

Table 5.5.1: Compressive true yield stress, σ_{yc}, Tensile true yield stress, σ_{yt}, and σ_{yt} calculated using Equation 4.25 for the unmodified epoxy polymers.

Epoxy	σ_{yc} (MPa)	σ_{yt} (MPa)	σ_{yt} from Equation 4.25
LD	83	69	65
AD	97	82	77
LV	115	34	91

The addition of the stiffer silica nanoparticles recovers some of the loss in E_c, e.g. the value of E_c measured for the unmodified, 9C and 10N9C modified LD epoxies were 2.2, 1.9 and 2.2 GPa respectively. An increase in σ_{yc} of 2 MPa when 10 wt% of silica nanoparticles were added was only observed for the LV and LD epoxies. Although this value may seem low, it is noticable and repeatable. In contrast, there was no effect on the σ_{yc} for the CTBN-NS and CSR-NS hybrid modified epoxies compared to the rubber modified AD epoxies. There is a marked decrease in yield strain, ε_{yc}, when silica nanoparticles were added to the rubber modified LD epoxy.

Strain softening, where the stress decreases with increasing strain, was observed with continued loading beyond the yield point for the unmodified LD and AD epoxies. The unmodified LV epoxy fractures in compression before reaching the yield point so the yield properties could not be measured. The degree of strain softening (drop in stress after ε_{yc}) was reduced by the addition of the CTBN and CSR rubber particles and for the hybrid modified epoxies compared to the unmodified epoxies. This is caused by the suppression of the macroscopic inhomogeneous deformations such as shear banding [271], and can be caused by microscopic yield processes such as localised shear yielding induced by the modifiers occuring homogeneously across the material. Work hardening was observed for all of the formulations as the sample was continually loaded until failure. A greater degree of work hardening was evident for the hybrid CSR-NS and CTBN-NS modified epoxies, which can induce a higher toughness by more stable ductile plastic deformation throughout the bulk of the material [88]. The compressive true failure strains, γ_f, of the unmodified epoxies were measured to be 0.98, 0.84 and 1.16 for the LV, LD and AD epoxies. There does not appear to be a trend for the failure strain, γ_f, and failure stress, σ_f, for the rubber modified epoxies. This suggests that other factors such as defects or surface roughness may play a more important role in the ultimate failure point in the PSC tests than the presence of these rubber and silica particles.

Shear band yielding was observed as birefringence in the unmodified epoxy polymers, as shown in Figures 5.5.2 and 5.5.3.

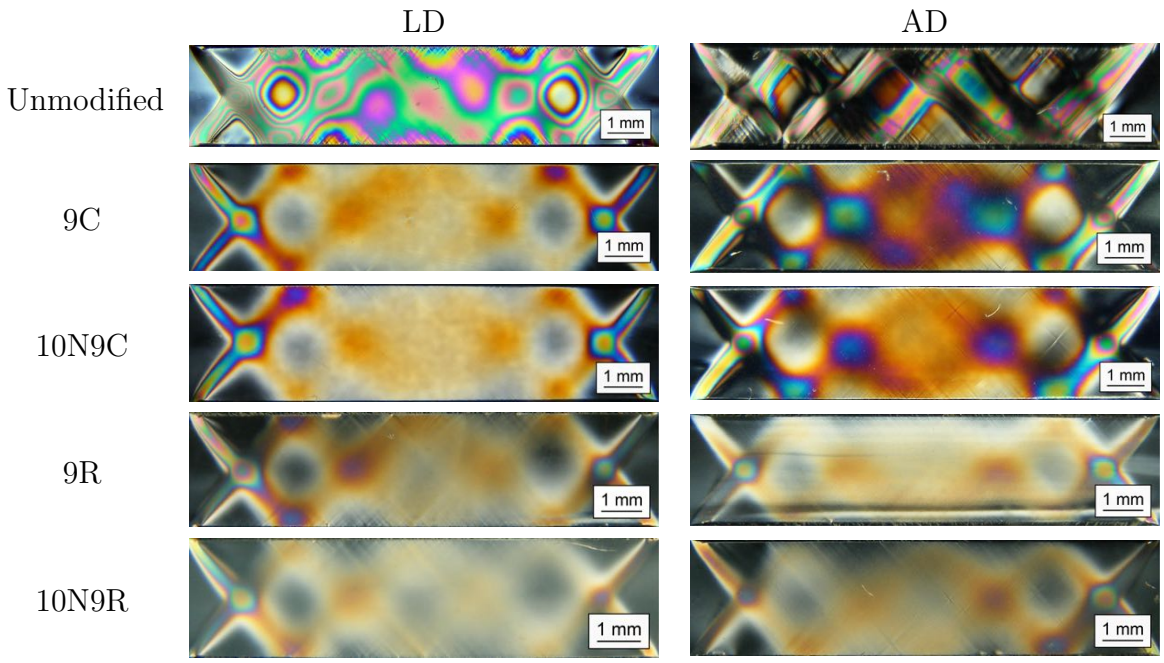


Figure 5.5.2: Transmission optical micrographs, using cross polarised light, of polished specimens loaded to the strain softening region for the LD and AD epoxy polymers.

The AD epoxy polymer shows less birefringence than the LD epoxy, with more highly focused shear bands, suggesting limited shear band yielding. This is consistent with the observations of the ratio of softening/hardening observed for the AD epoxy. For the rubber modified epoxies, the shear bands appear to be more diffuse. This suggests that localised shear band yielding is an active toughening mechanism, which was promoted by the presence of these particles acting as stress concentrations. Furthermore, the addition of silica nanoparticles did not change the appearance of these diffuse shear bands. Thus, it concludes that these images give evidence that shear yielding is occuring in the modified LD and AD epoxies.

For the rubber modified LV epoxies, the intensity of the diffuse shear bands appear to be more suppressed when either CSR or CTBN rubber was added. For the 10N9R modified LV epoxy, the compressed region shows no shear band yielding, indicated by the lack of birefringence. This correlates with the lack of strain softening and low strain hardening modulus from the PSC stress-strain curves.

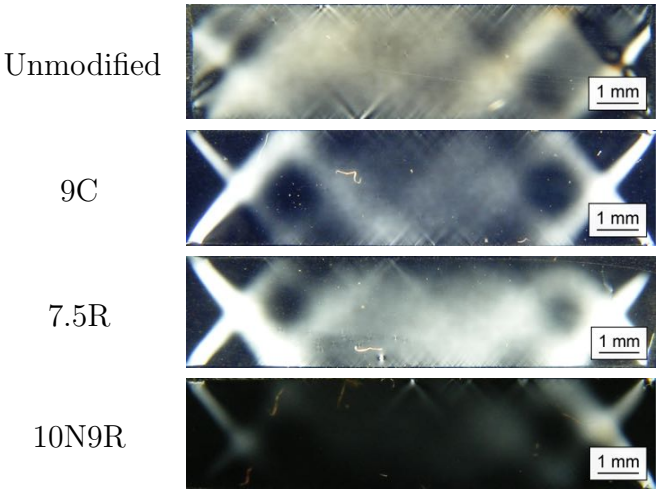


Figure 5.5.3: Transmission optical micrographs, using cross polarised light, of polished specimens loaded to the strain softening region for the LV epoxy polymers.

5.6 Fracture properties

The fracture toughness, K_{IC}, and fracture energy, G_{IC}, of the epoxies were measured using SENB tests. The values for the unmodified and 10 wt% silica nanoparticle modified epoxies are summarised in Table 5.6.1. The toughening contributions of the silica nanoparticles, ΔG_{IC}, are also shown. The LD and AD epoxy systems, with a lower T_g than the LV epoxy, show a much higher ΔG_{IC}, as low crosslink density epoxies are more toughenable [5]. The toughening mechanisms will be discussed in §5.7.

Table 5.6.1: Fracture toughness, K_{IC}, and fracture energy, G_{IC} of unmodified and 10 wt% silica nanoparticle modified epoxy polymers [84].

Epoxy system	NS wt%	K_{IC} (MPa m$^{1/2}$)	G_{IC} (kJ/m^2)	ΔG_{IC} (kJ/m^2)
LV	0	0.5 ± 0.0	0.1 ± 0.0	–
	10	0.8 ± 0.0	0.1 ± 0.0	0.0
LD	0	0.9 ± 0.1	0.2 ± 0.0	–
	10	1.4 ± 0.1	0.5 ± 0.1	0.3
AD	0	0.9 ± 0.0	0.2 ± 0.0	–
	10	1.4 ± 0.1	0.4 ± 0.0	0.2

The change in K_{IC} and G_{IC} with rubber content for the LV epoxy is shown in Figure 5.6.1. An increase in G_{IC} of about 400% was observed with the addition of 10 wt% of CSR particles and CTBN. A linear increase with CSR rubber content was observed to a maximum of 0.2 kJ/m^2, compared to 0.2 kJ/m^2 for the CTBN modified LV epoxy. The 10N9R modified LV epoxy had the highest G_{IC} of 0.3 kJ/m^2.

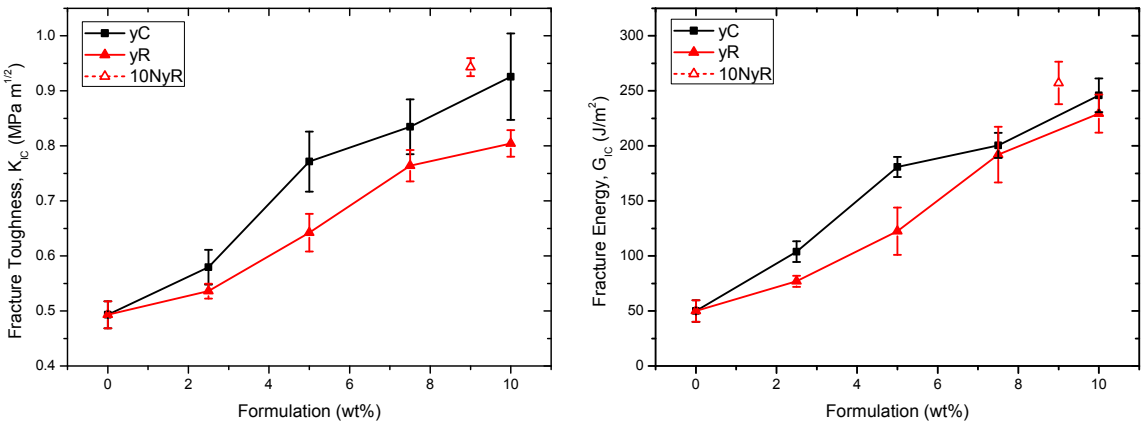


Figure 5.6.1: Fracture toughness and fracture energy of rubber modified LV epoxy.

The polyether-amine cured epoxies show much more substantial increases in K_{IC} and G_{IC} from the addition of the CTBN and CSR rubber particles compared to the LV epoxy, as shown in Figures 5.6.2 and 5.6.3. For the LD epoxy, a plateau in the value of G_{IC} was observed from a concentration of 3 wt% for both CTBN and CSR rubber modified epoxies. The smaller CSR particles have a lower maximum G_{IC} of 1.9 kJ/m^2 at 5 wt%, compared to 2.1 kJ/m^2 for the 7 wt% CTBN modified epoxy. There was little or no increase in fracture performance when silica nanoparticles were introduced into the rubber modified epoxies. The maximum G_{IC} values measured were 2.0 kJ/m^2 and 2.5 kJ/m^2 for the CSR and CTBN epoxies modified with 10 wt% silica nanoparticles, respectively. For the LD epoxy system, no synergy was found between the rubber particles and silica nanoparticles.

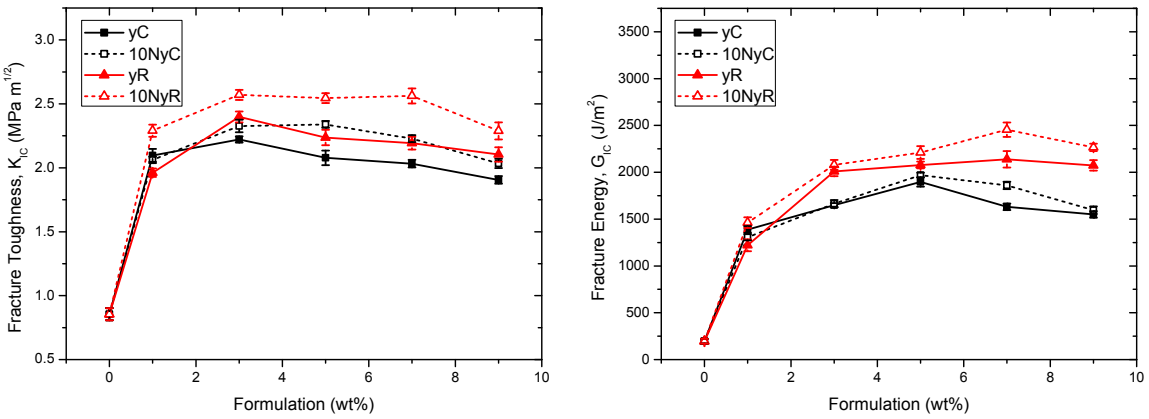


Figure 5.6.2: Fracture toughness and fracture energy of rubber modified LD epoxy.

For the AD epoxy, the increase in G_{IC} showed a linear trend with the rubber content. There were no significant differences in G_{IC} when comparing the CTBN and CSR modified AD epoxies, up to a rubber concentration of 7 wt%. The maximum fracture energies were measured at 9 wt% rubber content; G_{IC} = 2.0 kJ/m^2 and G_{IC}

= 2.9 kJ/m^2 for the CSR and CTBN modified epoxies. With the addition of silica nanoparticles, significant increases in G_{IC} were measured at lower rubber contents, below 9 wt% CTBN and 7 wt% CSR. At higher rubber contents, the addition of silica nanoparticles did not affect the fracture performance of these hybrid epoxies, i.e. a plateau in fracture energy was observed. The maximum G_{IC} measured was 2.0 kJ/m^2 and 3.1 kJ/m^2 for the hybrid CSR-NS and CTBN-NS modified epoxies.

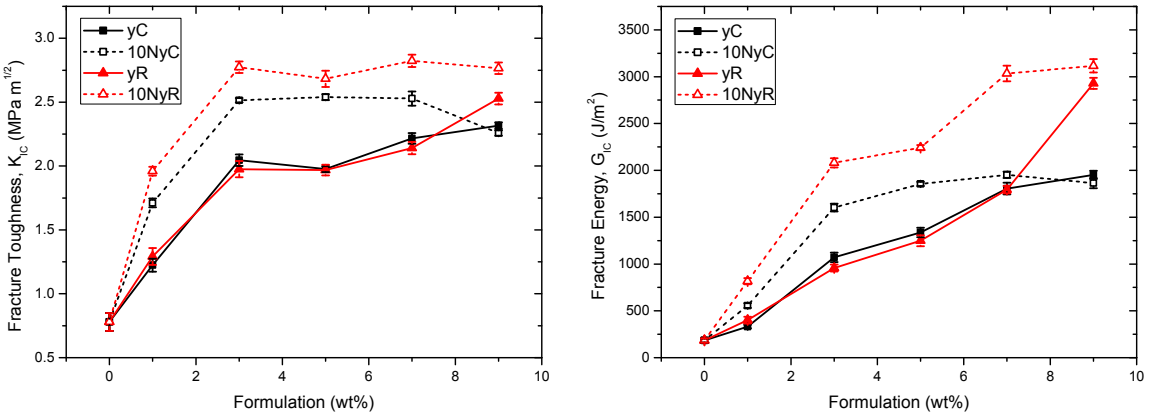


Figure 5.6.3: Fracture toughness and fracture energy of rubber modified AD epoxy.

5.7 Fractography

Field emission gun scanning electron microscopy (FEGSEM) of the fracture surfaces was conducted to determine the toughening mechanisms. The crack propagation direction of the selected images shown is from right to left. The fracture surfaces for the unmodified epoxies, as shown in Figure 5.7.1 for the AD epoxy, show a smooth appearance. This indicates a lack of plastic deformation during the fracture process. The steps and changes in level of the crack were caused by crack forking, associated with fast crack growth. This is consistent with other findings from the literature [104, 272] for brittle thermoset polymers.

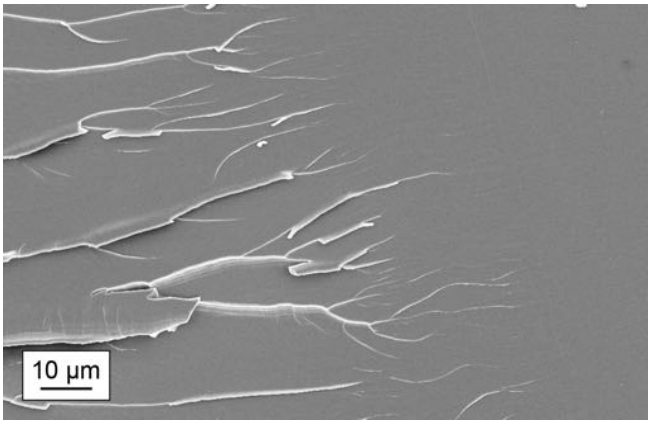
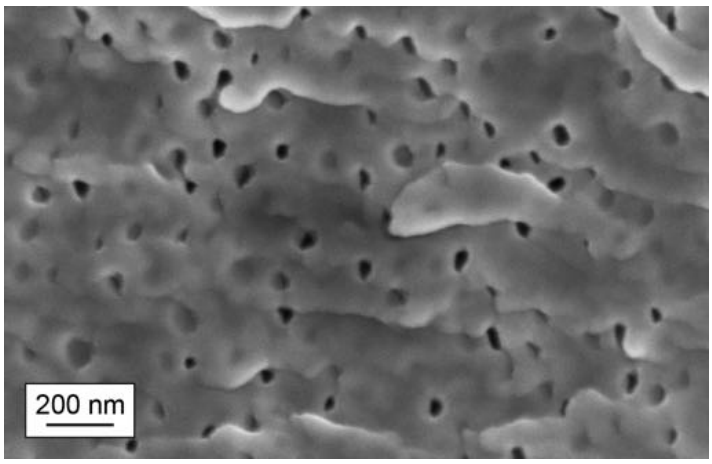


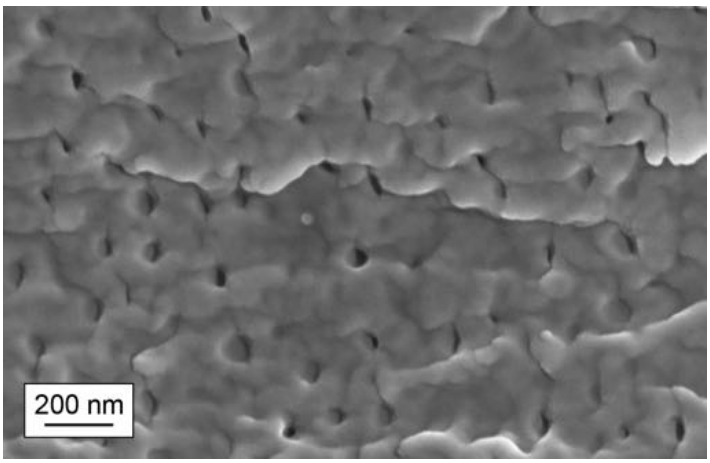
Figure 5.7.1: FEGSEM micrograph of unmodified AD epoxy.

5.7.1 Core-shell rubber

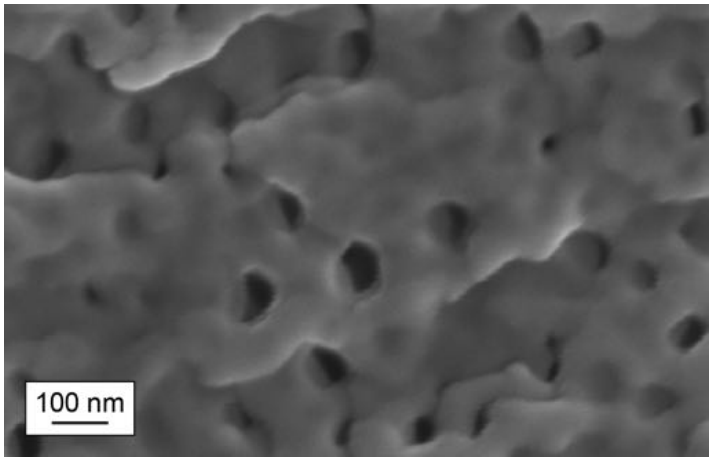
For the CSR particle modified epoxies, a much rougher fracture surface was observed compared with the unmodified epoxies. Using high resolution FEGSEM, cavitated rubber particles are visible as voids as shown in Figure 5.7.2. The mean void radii were measured from the fracture surfaces to be 23 ±1 nm for the LV epoxy, 27 ±1 nm for the LD epoxy and 27 ±1 nm for the AD epoxy. The size of these voids can be compared to the particle radii measured using the AFM. These voids are slightly larger than the particles, signifying plastic void growth of the matrix after cavitation of the CSR particles. There were no signs of the CSR particles debonding from the matrix.



(a) 10C modified LV epoxy



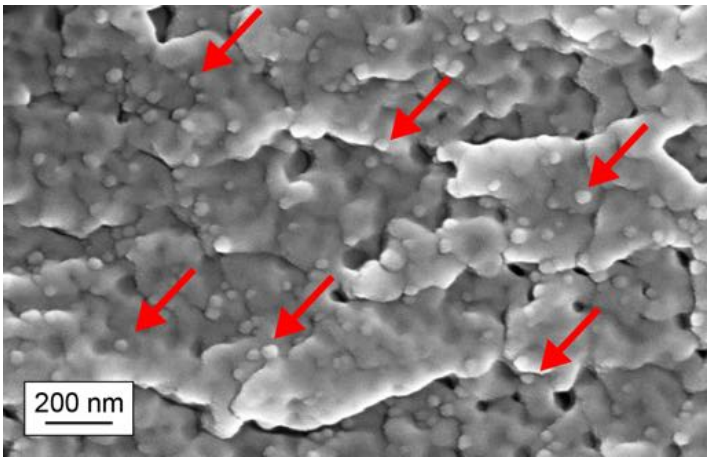
(b) 9C modified LD epoxy



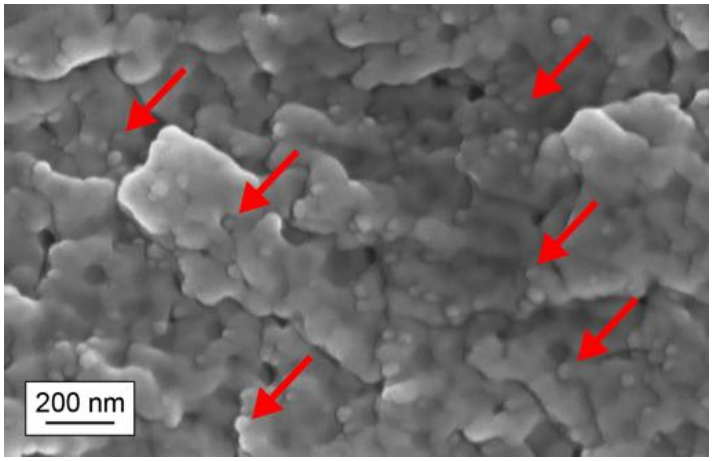
(c) 9C modified AD epoxy

Figure 5.7.2: FEGSEM micrograph of CSR modified epoxy fracture surfaces.

The measured mean void radii decreased to 26 ±1 nm and 24 ±1 nm, respectively, when silica nanoparticles were added to the CSR modified LD and AD epoxies. This indicates that the void growth process was inhibited by the presence of the silica nanoparticles. Some of the silica nanoparticles are identified with arrows on Figure 5.7.3. There was no evidence of debonding observed, and hence no plastic void growth, around the silica nanoparticles for both LD and AD epoxies. The nanoparticles were well bonded to both epoxy polymers.



(a) 10N9C modified polyether-amine cured DGEBA

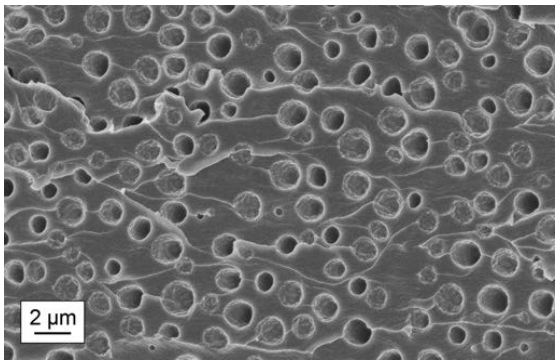


(b) 10N9C modified polyether-amine cured DGEBA/F

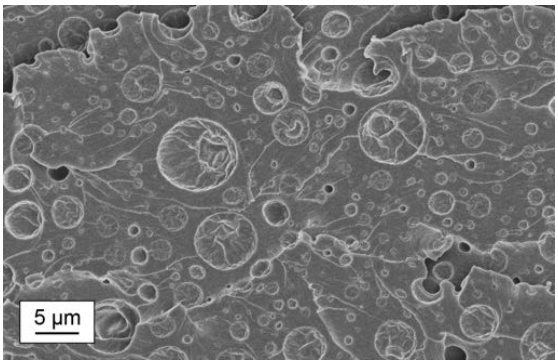
Figure 5.7.3: FEGSEM micrograph of CSR-NS hybrid modified epoxy fracture surfaces. Some silica nanoparticles are identified with arrows.

5.7.2 CTBN rubber

For the CTBN rubber modified LD and AD epoxy polymers, cavitation and subsequent plastic void growth of the rubber particles were also observed, as shown in Figures 5.7.4. The mean void radii of 0.56 μm and 1.02 μm were measured from the fracture surfaces for the LD and AD epoxies, respectively. The void radius, r_v, can be estimated by taking $(1+\gamma_f)\, r_p$, where γ_f is the fracture strain and r_p is the particle radius. This calculated value of r_v agrees well with the values measured from the fracture surfaces within experimental error; $r_v = 0.78$ μm and 1.10 μm for the 9R modified LD and AD epoxies, respectively.



(a) 9R modified LD epoxy

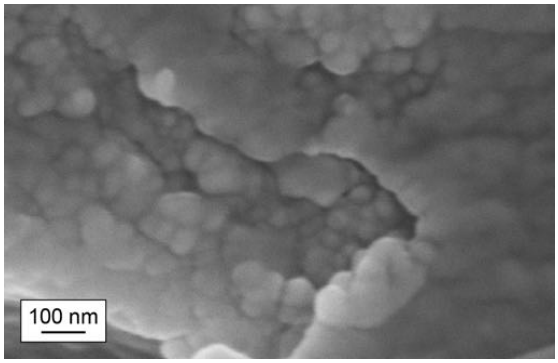


(b) 9R modified AD epoxy

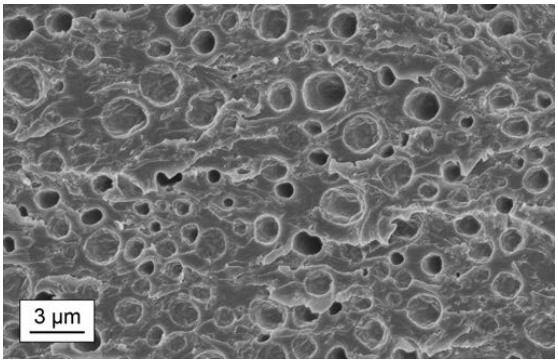
Figure 5.7.4: FEGSEM micrograph of CTBN modified epoxy fracture surfaces.

When silica nanoparticles were added to the CTBN rubber modified LD epoxy polymers (see Figure 5.7.5), there was no significant change in the average cavitated rubber particle radius. The average void radius calculated was 0.60 μm. However, the CTBN-

NS hybrid modified AD epoxy shows a decrease in the void radius to 0.74 μm (see Figure 5.7.6). This could be caused by the presence of the much stiffer silica nanoparticles. The silica nanoparticles in both hybrid modified epoxy polymers were also observed to have not debonded and there was no evidence of plastic void growth around the nanoparticles.

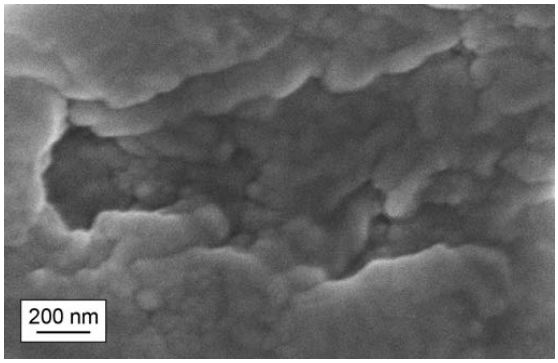


(a) x250k magnification

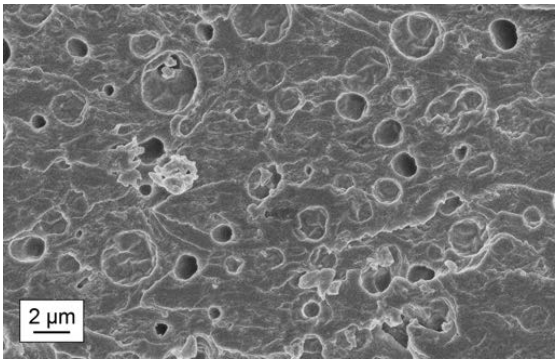


(b) x10k magnification

Figure 5.7.5: FEGSEM micrograph of CTBN-NS hybrid 10N9R modified LD epoxy fracture surfaces.



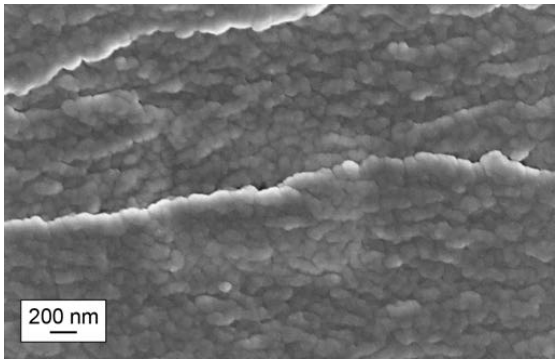
(a) x150k magnification



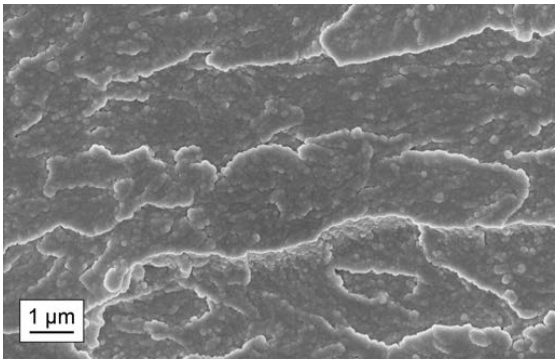
(b) x10k magnification

Figure 5.7.6: FEGSEM micrograph of CTBN-NS hybrid 10N9R modified AD epoxy fracture surfaces.

The CTBN rubber did not phase separate out of the low viscosity epoxy, hence there were no rubber particles observed on the fracture surfaces, as shown in Figure 5.7.7(a). The surfaces appeared rougher which would indicate more plastic deformation than the unmodified epoxy, caused by the plasticising effect of the overcooked CTBN liquid rubber. The surface roughness is not an artifact of the chrome coating as these were not observed for the unmodified epoxies at the same magnification. The silica nanoparticles were well bonded to the epoxy as no debonding or plastic void growth was observed for the 10N9R modified low viscosity epoxy, as shown in Figure 5.7.7(b).



(a) 10R



(b) 10N9R

Figure 5.7.7: FEGSEM micrograph of CTBN modified LV epoxy fracture surfaces.

5.8 Modelling fracture energy

The major toughening mechanisms for the CSR and CTBN rubber modified epoxy polymers were identified as localised shear yielding and plastic void growth, initiated by the cavitation of the rubber particles. As described in §2.5, the individual contributions from each toughening mechanism can be predicted, and the predictions were compared to the experimental results. The parameters in the modelling of the rubber modified epoxies are tabulated in Table 5.8.1.

Table 5.8.1: Parameters used in modelling fracture energy.

Name	Variable	Units	Value		
			LV	LD	AD
Core-shell rubber particle radius	$r_{p,CSR}$	nm	24	22	22
CTBN rubber particle radius	$r_{p,CTBN}$	μm	–	0.42	0.51
Void radius	r_{pv}	nm	$(1+\gamma_f)\,r_p$		
Plane strain compressive yield true stress	σ_{yc}	MPa	115	83	97
Uniaxial tensile yield true stress	σ_{yt}	MPa	91	66	77
Plane strain compressive fracture true strain	γ_f	–	0.98	0.84	1.16
Pressure-dependent yield stress parameter [3]	μ_m	–		0.2	
Unmodified epoxy fracture energy	G_{CU}	kJ/m^2	0.1	0.2	0.2
Unmodified epoxy fracture toughness	K_{CU}	MPa m$^{1/2}$	0.5	0.9	0.9

The predicted and measured values of fracture energy are summarised in Tables 5.8.2 and 5.8.3 for the CSR and CTBN modified epoxies, respectively. It is difficult to accurately determine the volume fraction of particles that undergo cavitation experimentally. Finite element studies by Guild *et al.* [273] suggest that all rubbery particles should cavitate, and analysis of the fracture surfaces confirms this. Additionally, it is not expected that all the cavities would undergo the maximum extent of plastic void growth, i.e. until $r_{pv} = (1 + \gamma_f)r_p$, due to a local reduction in stress near a void. An

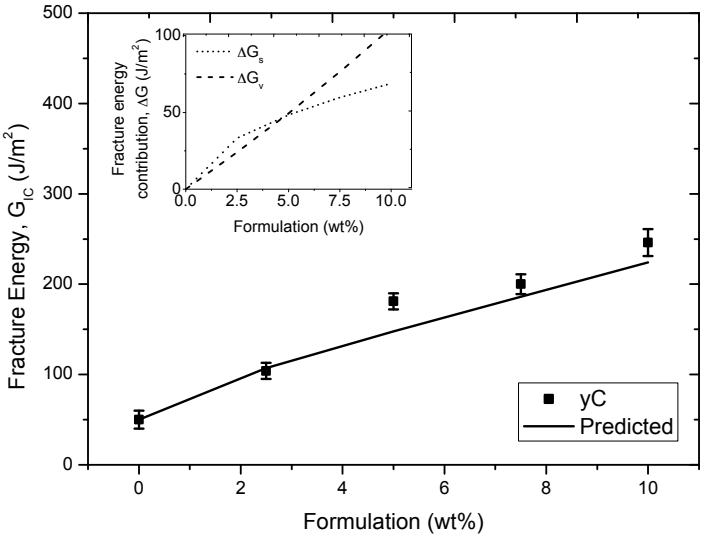
upper bound of 100% and lower bound of 14.3% [76, 273] of particles which cavitate and undergo full plastic void growth would be expected. For the epoxy systems used, a value of 100% for the LD epoxy and 14.3% for the AD and LV epoxies was found to give the best result. This proposes that the LD epoxy undergoes plasticity much more readily than the AD and LV epoxy. This is not surprising given that the LD epoxy has a low crosslink density and σ_{yc}.

Table 5.8.2: Predicted and measured values of fracture energy for CSR modified epoxy polymers.

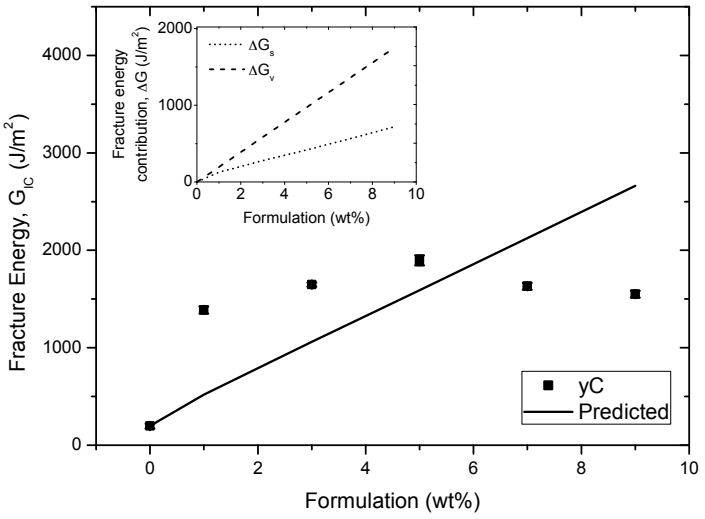
LV epoxy wt%	v_f	ΔG_s J/m^2	ΔG_v J/m^2	G_{IC} predicted kJ/m^2	G_{IC} experimental kJ/m^2
0	0.00	0	0	0.1	0.1 ± 0.0
2.5	0.03	33	24	0.1	0.1 ± 0.0
5	0.07	48	49	0.1	0.2 ± 0.0
7.5	0.10	60	76	0.2	0.2 ± 0.0
10	0.14	69	105	0.2	0.2 ± 0.0
LD epoxy wt%	v_f	ΔG_s J/m^2	ΔG_v J/m^2	G_{IC} predicted kJ/m^2	G_{IC} experimental kJ/m^2
0	0.00	0	0	0.2	0.2 ± 0.0
1	0.01	128	195	0.5	1.4 ± 0.0
3	0.04	278	586	1.1	1.6 ± 0.0
5	0.06	419	975	1.6	1.9 ± 0.1
7	0.08	565	1363	2.1	1.6 ± 0.0
9	0.10	718	1748	2.7	1.6 ± 0.0
AD epoxy wt%	v_f	ΔG_s J/m^2	ΔG_v J/m^2	G_{IC} predicted kJ/m^2	G_{IC} experimental kJ/m^2
0	0.00	0	0	0.2	0.2 ± 0.0
1	0.01	159	51	0.4	0.3 ± 0.0
3	0.04	346	182	0.7	1.1 ± 0.1
5	0.06	523	354	1.0	1.3 ± 0.1
7	0.08	705	573	1.4	1.8 ± 0.1
9	0.10	895	841	1.9	2.0 ± 0.0

The predicted values of G_{IC} for the CSR modified LV and AD epoxies show excellent agreement with the experimental results. However, the calculated values of G_{IC} for the CSR modified LD epoxies does not agree with the experimental results at all weight percentages.

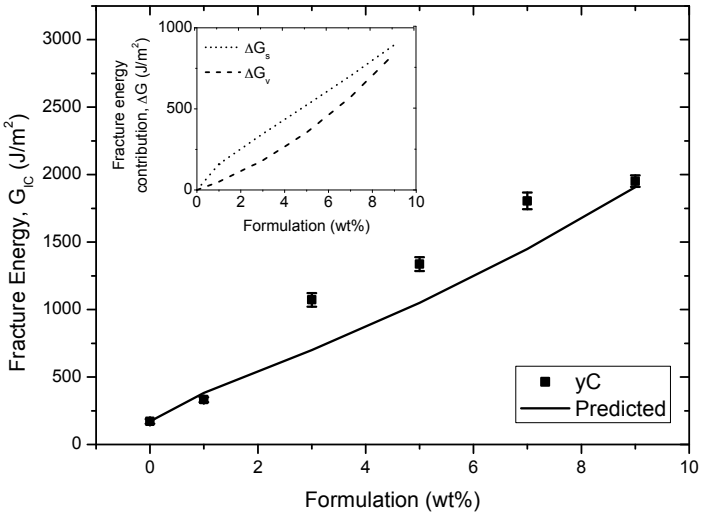
The contributions from both ΔG_s and ΔG_v are directly proportional to σ_{yc} and the value of γ_f has little effect on the relative differences between the two values. For the CSR modified LV and AD epoxies, the contribution from shear band yielding and



(a) LV



(b) LD



(c) AD

Figure 5.8.1: Predicted and measured values of fracture energy for CSR modified epoxy polymers. Insets show contributions from shear yielding, ΔG_s, and void growth ΔG_v.

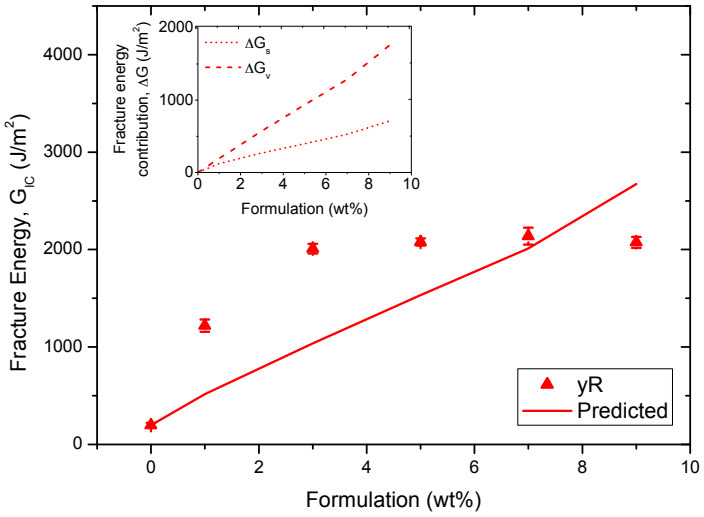
plastic void growth are of similar magnitude. For the CSR modified LD epoxy, the G_{IC} contribution from plastic void growth was about two to three times the contribution from shear band yielding. The difference lies in the assumption that 100% of rubber particles in the LD epoxy will undergo the full extent of void growth.

Table 5.8.3: Predicted and measured values of fracture energy for CTBN modified epoxy polymers.

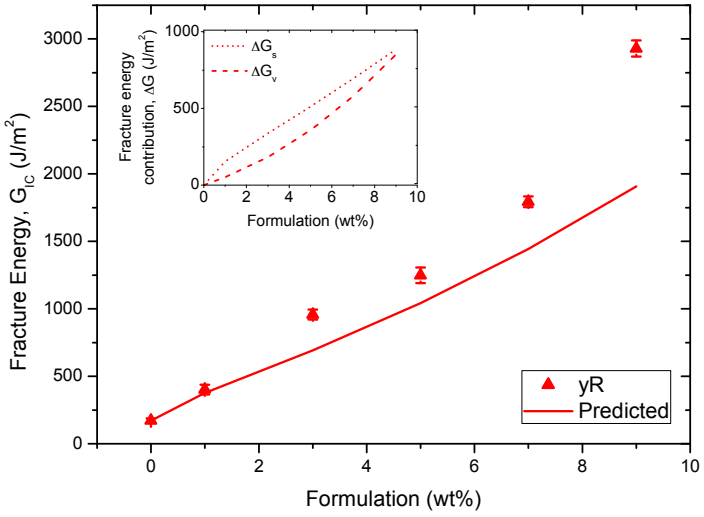
LD epoxy wt%	v_f	ΔG_s J/m^2	ΔG_v J/m^2	G_{IC} predicted kJ/m^2	G_{IC} experimental kJ/m^2
0	0.00	0	0	0.2	0.2 ± 0.0
1	0.01	124	195	0.5	1.2 ± 0.1
3	0.03	268	574	1.0	2.0 ± 0.1
5	0.06	398	937	1.5	2.1 ± 0.0
7	0.08	528	1287	2.0	2.1 ± 0.1
9	0.10	714	1763	2.7	2.1 ± 0.1
AD epoxy wt%	v_f	ΔG_s J/m^2	ΔG_v J/m^2	G_{IC} predicted kJ/m^2	G_{IC} experimental kJ/m^2
0	0.00	0	0	0.2	0.2 ± 0.0
1	0.01	154	51	0.4	0.4 ± 0.0
3	0.04	338	183	0.7	1.0 ± 0.0
5	0.06	512	358	1.0	1.2 ± 0.1
7	0.08	694	579	1.4	1.8 ± 0.0
9	0.10	884	852	1.9	2.9 ± 0.1

The predicted values of G_{IC} for the CTBN rubber modified LD epoxy polymers also show poor agreement with the experimental results, both in trend and absolute value. The predictions for the AD epoxies show better agreement, but were generally under-predicted compared to the measured values of G_{IC}. The values of G_{IC} calculated were not too dissimilar to those for the CSR modified epoxies, as the only change is in the particle size. This illustrates how insensitive the Huang-Kinloch model is to particle size. As with the CSR modified epoxy, the main contribution to the G_{IC} of the CTBN modified LD epoxy was plastic void growth. Shear band yielding was more prominent for the CTBN modified AD epoxy, at roughly equal fracture energy contributions to plastic void growth.

The poor agreement of the Huang-Kinloch model for the rubber modified LD epoxies at low wt% comes from the assumption in size of the shear bands. The cross-sectional area, and hence total size of the shear bands, were determined from an empirical "scaling factor" [75]. Thus, it would not be expected to work for all epoxy systems. Indeed, the contribution from shear yielding, ΔG_s, for the LD epoxy is typically much lower than the contribution from void growth, ΔG_v. At higher wt%, the model is incapable



(a) LD



(b) AD

Figure 5.8.2: Predicted and measured values of fracture energy for CTBN modified epoxy polymers. Insets show contributions from shear yielding, ΔG_s, and void growth ΔG_v.

of modelling the plateau in G_{IC} as it does not consider particle-particle interactions and stress field overlaps.

5.9 Conclusions

Butadiene based core-shell rubber particles with an average outer radius of approximately 50 nm and core radius of 20 nm were used to modify three different epoxy systems, a polyether-amine cured DGEBA (LD), a polyether-amine cured DGEBA/F (AD) and an anhydride cured cycloaliphatic epoxy (LV). The mechanical and fracture properties of these nanometre scale rubber particles were compared to those of conven-

tional CTBN rubber modified epoxies. Silica nanoparticles were also added to create hybrid modified epoxies. Both the CSR and CTBN rubbers were randomly dispersed in the LD and AD epoxy matrix, however, the CTBN did not phase separate in the LV epoxy. Instead, the high post-cure temperatures overcooked the CTBN, breaking it down. When silica nanoparticles were added to the CSR modified LD and AD epoxies, both rubber and silica particles were well dispersed in the CSR modified epoxy. When used with CTBN contents below than 7 wt%, the silica nanoparticles were well dispersed but would agglomerate into increasingly larger clusters when used with at higher concentrations of CTBN.

The glass transition temperatures were unaffected by the addition of the CSR particles but were reduced by the CTBN rubber, indicating some dissolved rubber in the epoxy. The Young's modulus was reduced by the addition of the much softer rubber particles; for a given volume fraction of butadiene, the Young's modulus of the CSR and CTBN modified epoxies were comparable. The addition of silica nanoparticles restored some of the lost modulus and strength of the rubber modified epoxies, and the presence of agglomerates did not affect this increase. Similar trends were observed for the compressive modulus and yield strength from the plane strain compression tests.

For the LV epoxy, the fracture toughness and fracture energy increased linearly with rubber content from 0.1 kJ/m^2 to a maximum of 0.2 kJ/m^2 for the CSR and CTBN modified epoxies. A maximum G_{IC} of 0.3 kJ/m^2 was measured for the 10N9R modified LV epoxy. For the LD and AD epoxies, the CTBN modified epoxies tend to have higher G_{IC} values than the CSR modified epoxies across the range of weight percentages tested. Maximum G_{IC} values of 1.8 kJ/m^2 and 2.1 kJ/m^2 were measured for the CSR and CTBN modified LD epoxy, respectively, and 1.9 kJ/m^2 and 2.9 kJ/m^2 for the CSR and CTBN modified AD epoxy, respectively. This is due to the higher cavitation resistance of the smaller CSR particles. The smaller rubber particles cavitate at a later stage, and hence less plastic void growth occurs.

With the addition of silica nanoparticles, the G_{IC} of the rubber modified LD epoxy was unchanged or showed little effect and no synergy was observed. For the AD epoxy, synergy between the silica nanoparticles and rubber particles was observed at the lower rubber contents. At higher rubber contents, the maximum G_{IC} does not increase beyond the plateau observed, at approximately 2.0 kJ/m^2 and 3.5 kJ/m^2 for the CSR and CTBN rubber, respectively.

The main toughening mechanisms observed from the fracture surfaces were cavitation of the rubbery particles, followed by plastic void growth of the adjacent epoxy matrix.

The silica nanoparticles in the hybrid modified epoxies did not debond from the epoxy for all the the epoxy systems observed. Polished sections of the compression samples showed extensive shear band yielding for the rubber modified LD and AD epoxies. The shear bands for the rubber modified epoxies appeared more diffuse in nature, representative of more localised shear band yielding.

Chapter 6

Asymmetric triblock copolymer modified epoxy polymers

6.1 Introduction

This chapter investigates the use of two commercially available asymmetric triblock copolymers, 'Nanostrength E21' and 'Nanostrength E41' from Arkema, France, to increase the fracture toughness of four epoxy polymers. The BCP used is polystyrene-b-polybutadiene-b-poly(methyl methacrylate), or SBM for short. The E21 SBM has a higher polybutadiene (PB) block ratio and molecular weight than the E41 SBM. The epoxy systems used are the DGEBA and DGEBA/F epoxy resins cured with a polyether-amine curing agent, denoted as LD (LY556/D230) and AD (AY105/D230) respectively, an anhydride cured DGEBA epoxy, denoted as LH (LY556/HE600), and the low viscosity epoxy, denoted as LV. Silica nanoparticles (NS) were also added to the E21 SBM modified epoxies to create hybrid toughened epoxies, consisting of soft and rigid phases. These are denoted as 10NyE21, where the 10N refers to 10 wt% of silica nanoparticles and y refers to the wt% of E21. The formulations of the SBM and SBM-NS hybrid modified epoxies studied in this Chapter are summarised in Table 6.1.1.

Table 6.1.1: Summary of SBM formulations used in this chapter.

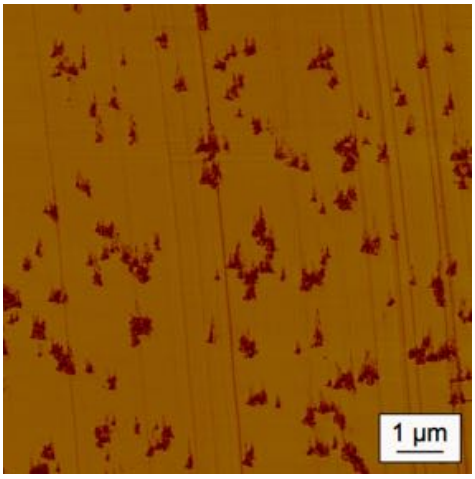
Epoxy system	Modifier E21 SBM wt%	NS wt%	Abbreviation	Modifier E41 SBM wt%	Abbreviation
Anhydride cured DGEBA (LH)	2.5	–	2.5E21LH	2.5	2.5E41LH
	5	–	5E21LH	5	5E41LH
	7.5	–	7.5E21LH	7.5	7.5E41LH
	10	–	10E21LH	10	10E41LH
	15	–	15E21LH	15	15E41LH
	10	10	10N10E21LH	–	–
Low viscosity epoxy (LV)	2.5	–	2.5E21LV	2.5	2.5E41LV
	5	–	5E21LV	5	5E41LV
	7.5	–	7.5E21LV	7.5	7.5E41LV
	10	–	10E21LV	10	10E41LV
Polyether-amine cured DGEBA (LD)	0.5	–	0.5E21LD	–	–
	1	–	1E21LD	–	–
	2.5	–	2.5E21LD	2.5	2.5E41LD
	5	–	5E21LD	5	5E41LD
	7.5	–	7.5E21LD	7.5	7.5E41LD
	10	–	10E21LD	10	10E41LD
	2.5	10	10N2.5E21LD	–	–
	10	10	10N10E21LD	–	–
Polyether-amine cured DGEBA/F (AD)	2.5	–	2.5E21AD	2.5	2.5E41AD
	5	–	5E21AD	5	5E41AD
	7.5	–	7.5E21AD	7.5	7.5E41AD
	10	–	10E21AD	10	10E41AD
	2.5	10	10N2.5E21AD	–	–
	10	10	10N10E21AD	–	–

6.2 Morphology

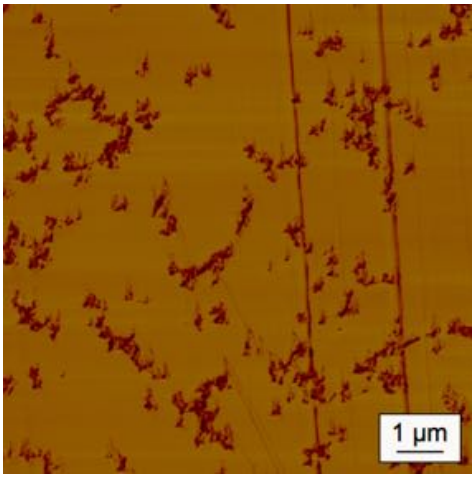
The AFM phase images of the unmodified epoxies have been shown in Figure 5.2.1 in §5.2. The unmodified epoxy is a single phase thermoset material, and thus was found to be homogeneous and featureless in all cases.

6.2.1 E21 SBM

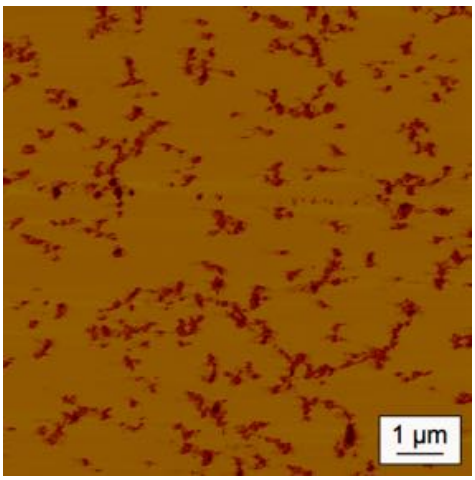
The E21 SBM BCPs were initially dissolved in the epoxy resin. This mixture then phase separates during the curing process to form a network of small agglomerates at E21 SBM concentrations up to 5 wt%, as shown in Figures 6.2.1 to 6.2.3.



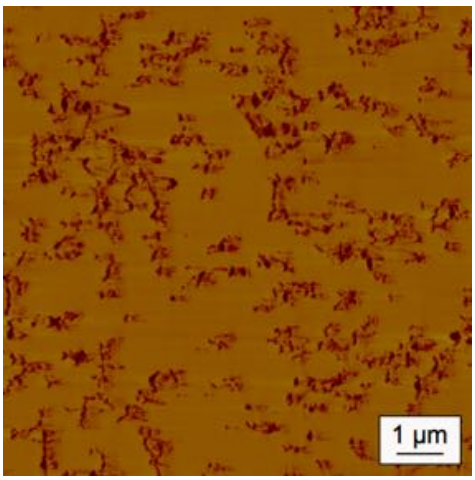
(a) 2.5 wt% E21



(b) 5 wt% E21

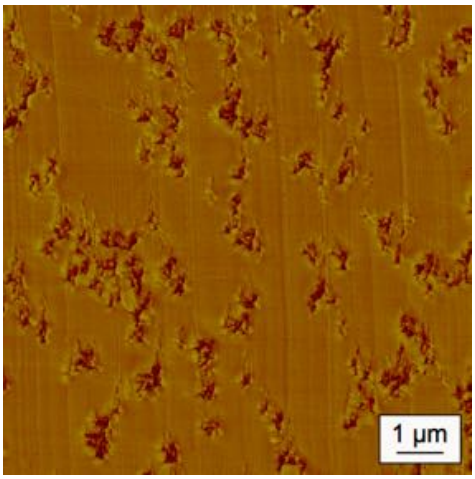


(c) 7.5 wt% E21

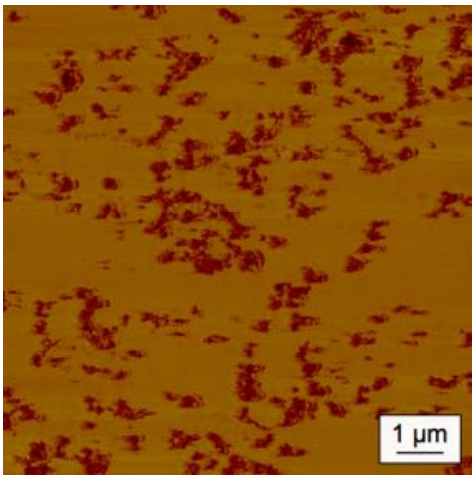


(d) 10 wt% E21

Figure 6.2.1: AFM phase micrographs of E21 SBM modified LD epoxy polymer.

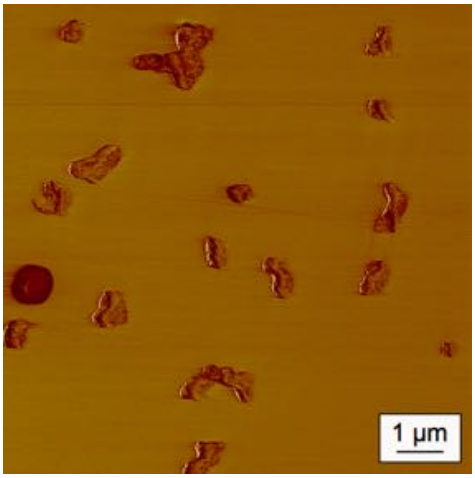


(a) 5 wt% E21

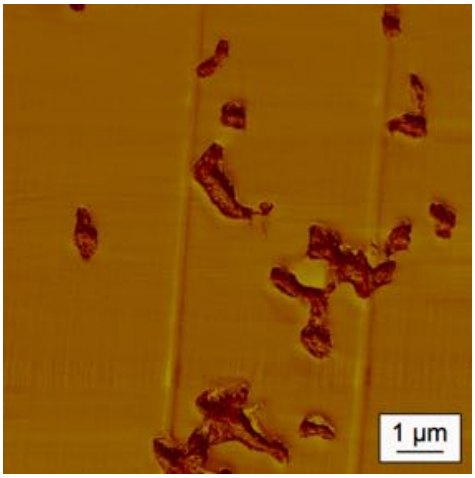


(b) 10 wt% E21

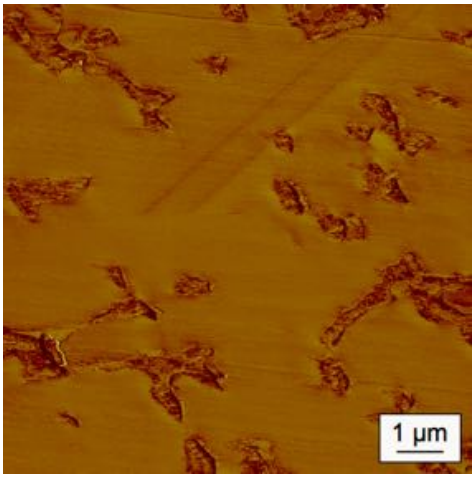
Figure 6.2.2: AFM phase micrographs of E21 SBM modified AD epoxy polymer.



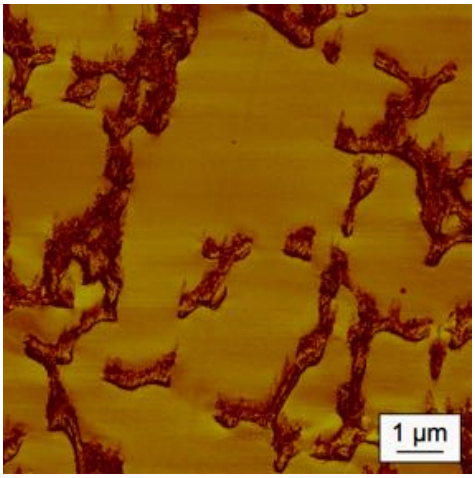
(a) 2.5 wt% E21



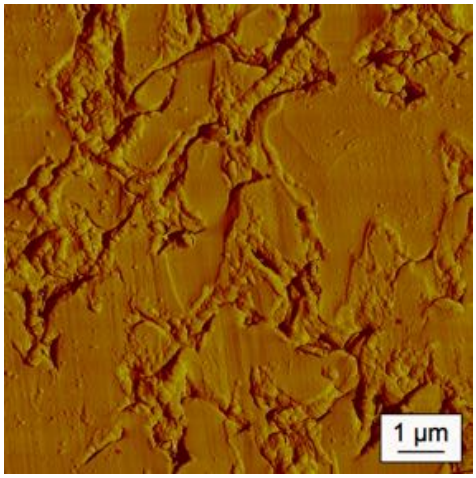
(b) 5 wt% E21



(c) 7.5 wt% E21



(d) 10 wt% E21



(e) 15 wt% E21

Figure 6.2.3: AFM phase micrographs of E21 SBM modified LH epoxy polymer.

The mean particle radius and characteristic lengths of the E21 SBM phase is shown in Table 6.2.1. There are some differences between the calculated values of mean particle radius and characteristic lengths due to the approximation of the SBM phases as spheres.

Table 6.2.1: Mean particle radius and characteristic lengths of E21 SBM phases in epoxy.

Content (wt%)		Particle radius (μm)			
SBM	NS	LD[a]	AD[a]	LH[a]	LV
2.5	0	0.10 ± 0.01	–	0.39 ± 0.05	0.37 ± 0.02
5	0	0.13 ± 0.03	0.20 ± 0.01	0.30 ± 0.02	–
2.5	10	0.12 ± 0.01	0.16 ± 0.00	–	–
Content (wt%)		Characteristic length (μm)			
SBM	NS	LD	AD	LH	LV
2.5	0	0.65 ± 0.05	–	1.24 ± 0.01	1.07 ± 0.17
5	0	0.72 ± 0.12	0.68 ± 0.01	1.60 ± 0.50	–
7.5	0	0.79 ± 0.13	–	1.59 ± 0.15	1.68[b]
10	0	0.83 ± 0.05	1.05 ± 0.02	1.88	1.55 ± 0.20[b]
15	0	–	–	1.89 ± 0.07	–
2.5	10	0.60 ± 0.13	0.50 ± 0.05	–	–
10	10	0.77 ± 0.05	1.20 ± 0.23	2.12 ± 0.30[b]	–

[a] Approximated as spheres

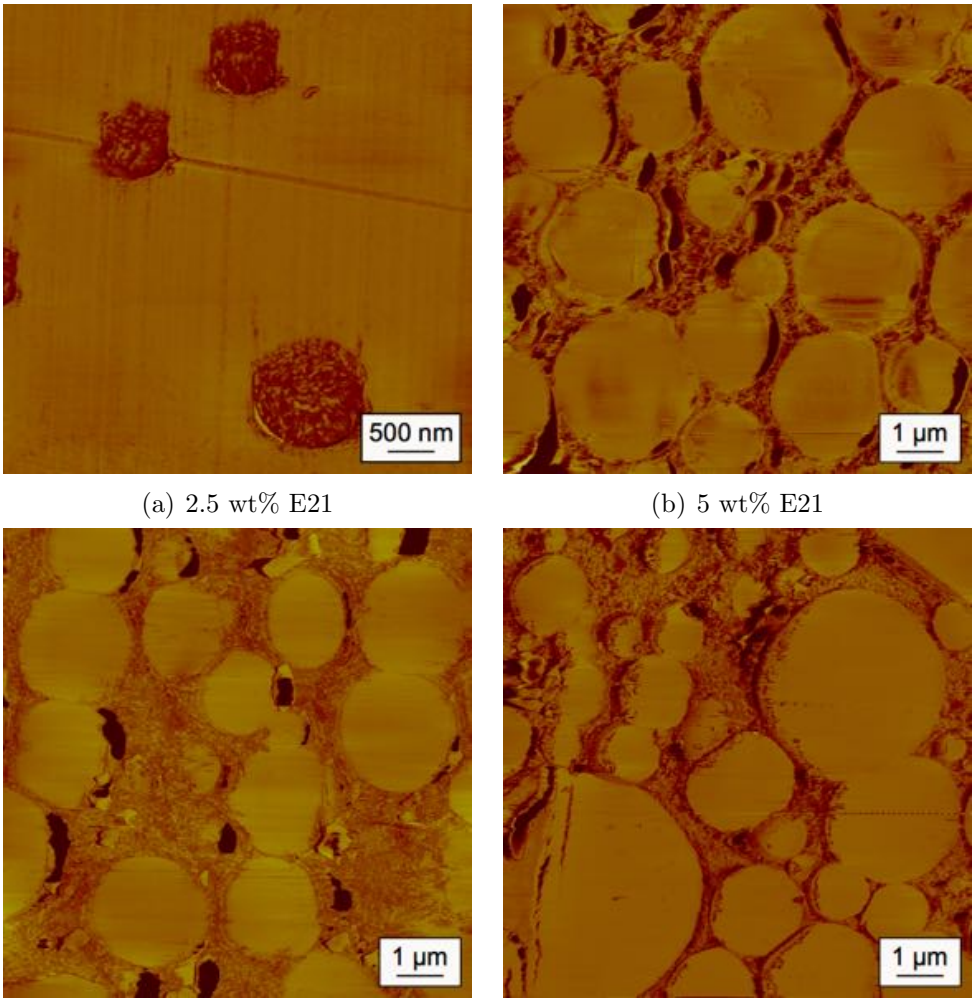
[b] Epoxy inclusions

The characteristic lengths of the E21 SBM modified epoxies increase as the amount of E21 is increased. For the E21 modified LD epoxies, the average characteristic length increases from 0.65 μm at 2.5 wt% to 0.83 μm at 10 wt%. The E21 modified AD epoxy has a slightly larger SBM phase, with a characteristic length of approximately 1.05 μm. For the LH epoxy, the E21 features have an average characteristic length of approximately 1.07 to 1.55 μm.

At concentrations of 7.5 wt% and above for the E21 SBM modified LD, AD and LH epoxies, the small agglomerates become increasingly interconnected to form a co-continuous structure, see Figure 6.2.3(c) for example. This is where both the SBM and epoxy phases are continuous in structure. The presence of light and dark areas within the second phase suggests that the PS and PB have phase separated, as shown in Figure 6.2.1. It should also be noted that the interconnecting regions of SBM for the LH epoxies are coarser than the LD and AD epoxies. That is, the width of the interconnecting sections for the LH epoxy system, measured to be as narrow as 130 nm up to 1 μm, is thicker than the LD and AD epoxy sytems, which range from 50 nm to 400 nm.

In contrast, the E21 SBM modified LV epoxy phase separates into well dispersed spherical particles with a radius of 0.36 μm for the 2.5 wt% E21 modified LV epoxy, as shown

in Figure 6.2.4. At 5 wt% and above, partial phase inversion of the cured E21 SBM modified epoxies was observed, presumably due to stability issues between the BCP and epoxy resin. The radius of the epoxy inclusions in the SBM rich phase for these phase inverted structures were between 750 and 800 nm, and did not change with SBM content.



(a) 2.5 wt% E21 (b) 5 wt% E21

(c) 7.5 wt% E21 (d) 10 wt% E21

Figure 6.2.4: AFM phase micrographs of E21 SBM modified LV epoxy polymer.

10 wt% of silica nanoparticles were added to the SBM modified epoxies, denoted E21 SBM-NS hybrid modified epoxies. For the E21 SBM-NS hybrid modified LD and AD epoxies, the appearance of the SBM phase remains unchanged with the addition of the silica nanoparticles. The characteristic lengths of the SBM phase are unaffected by the presence of the rigid nanoparticles. However, this does not mean that the miscibility of the E21 SBM with the LD and AD epoxies is unaffected by the silica nanoparticles, as the volume fraction was found to decrease, as shown in Table 6.2.3. Table 6.2.3 compares the volume fractions as measured from the AFM phase images to the known

amounts added as summarised in Table 6.2.2.

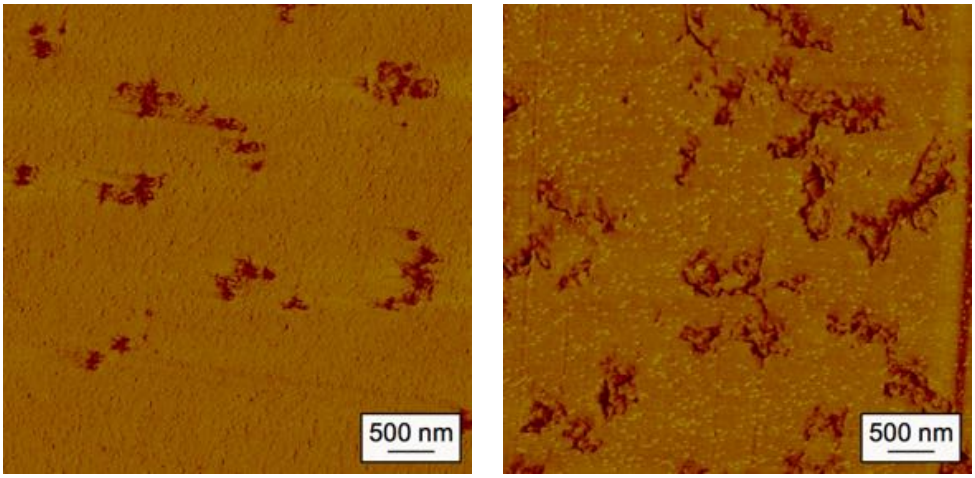
Table 6.2.2: Formulations of SBM block copolymer modified epoxies.

Formulation	SBM content wt%	SBM content vol%				Silica nanoparticle content wt%	Silica nanoparticle content vol%			
		LD	AD	LH	LV		LD	AD	LH	LV
SBM only	2.5	3.9	3.9	4.0	4.1	-	-	-	-	-
	5	7.7	7.7	7.8	8.0	-	-	-	-	-
	7.5	11.4	11.4	11.6	11.8	-	-	-	-	-
	10	15.0	15.0	15.2	15.5	-	-	-	-	-
	15	-	-	22.1	-	-	-	-	-	-
Hybrid	2.5	4.1	4.1	-	-	10	5.8	5.8	-	-
	10	15.6	15.7	15.8	-	10	5.6	5.6	5.7	-

Table 6.2.3: Measured values of volume fraction from AFM phase images.

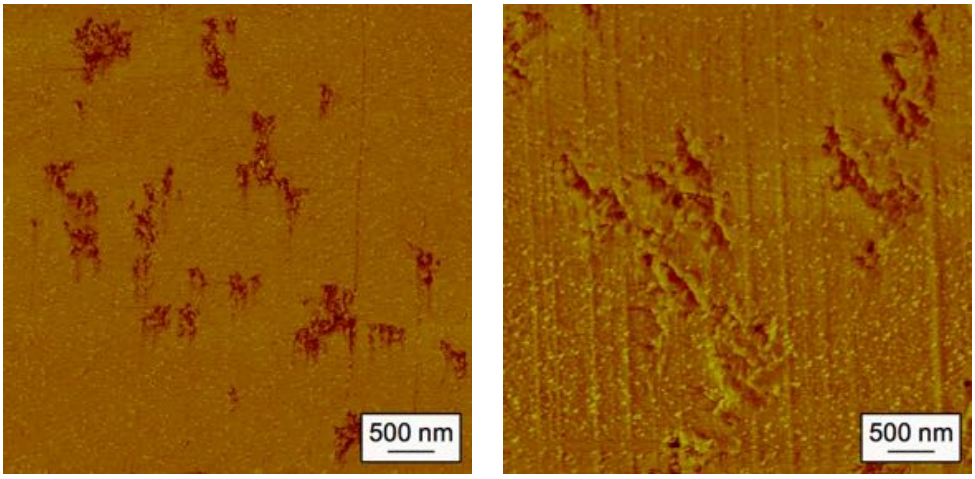
SBM Type	Content (wt%) SBM	NS	SBM Volume fraction (vol%) LD	AD	LH	LV
E21	2.5	0	5.6 ± 0.2	–	7.5 ± 0.2	3.7 ± 0.9
	5	0	8.4 ± 1.7	6.4 ± 0.7	7.1 ± 1.4	–
	7.5	0	9.7 ± 1.3	–	14.9 ± 1.0	–
	10	0	15.2 ± 5.5	15.0 ± 0.8	26.5	–
	2.5	10	3.0 ± 0.2	5.7 ± 1.3	–	–
	10	10	13.6 ± 1.4	14.0 ± 2.6	13.4 ± 0.3	–
E41	5	0	5.8 ± 2.4	4.7 ± 1.1	6.0 ± 1.3	6.3 ± 0.7
	10	0	18.2 ± 5.4	11.2 ± 0.1	50.6 ± 1.9	5.5 ± 0.7

The silica nanoparticles were well dispersed within the epoxy matrix, as shown in Figures 6.2.5 and 6.2.6. Furthermore, no silica nanoparticles were present within the SBM phase.



(a) 10N2.5E21 (b) 10N10E21

Figure 6.2.5: AFM phase micrographs of E21 SBM-NS hybrid modified LD epoxy polymer.



(a) 10N2.5E21 (b) 10N10E21

Figure 6.2.6: AFM phase micrographs of E21 SBM-NS hybrid modified AD epoxy polymer.

When the silica nanoparticles were added to the 10 wt% E21 SBM modified LH epoxy, the morphology changed from a co-continuous, see Figure 6.2.3(d), to a phase inverted structure, see Figure 6.2.7. The morphology consists of well dispersed silica nanoparticles in the epoxy rich phase with an interconnected network of SBM struts. This suggests that the silica nanoparticles are affecting the stability between the SBM and LH epoxy.

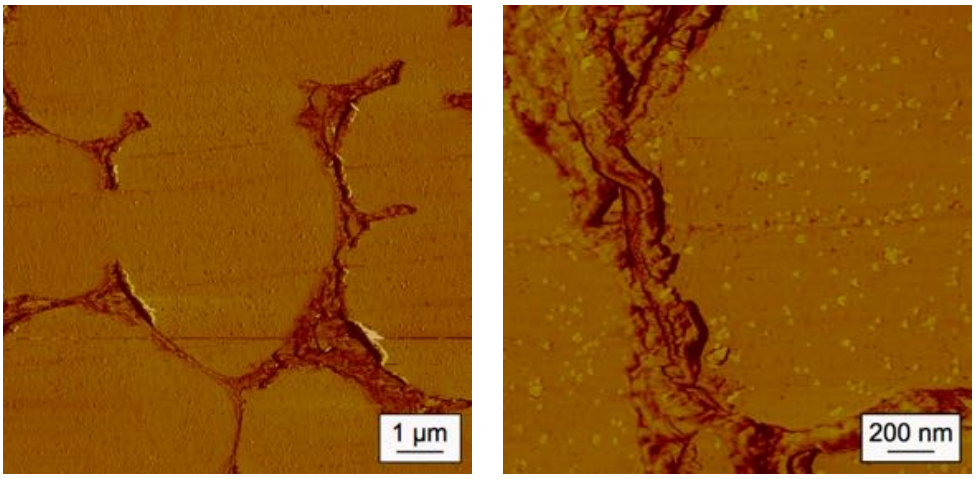
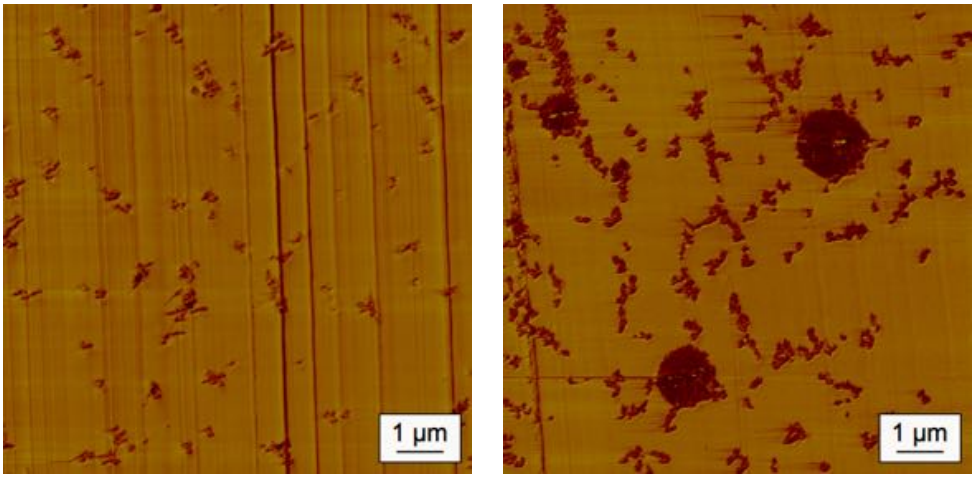


Figure 6.2.7: AFM phase micrographs of 10N10E21 hybrid modified LH epoxy polymer.

6.2.2 E41 SBM

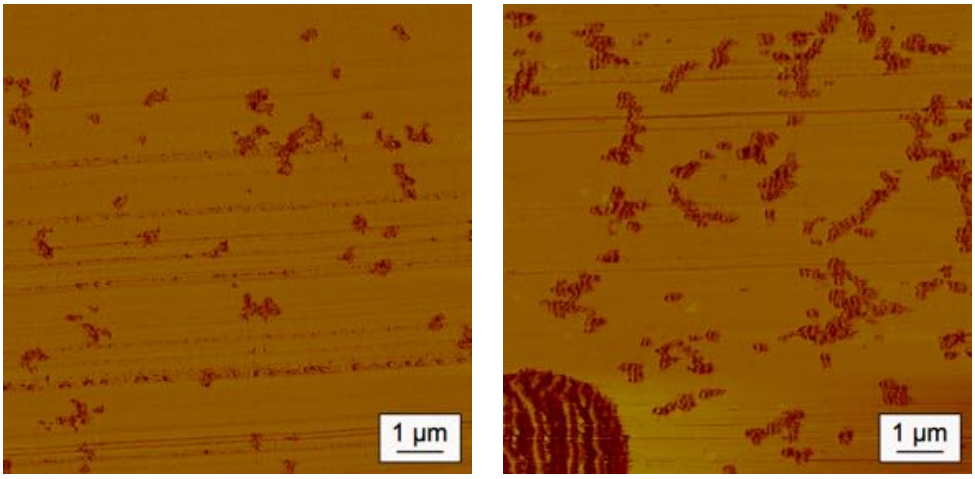
The morphology of the E41 SBM modified LD and AD epoxies at a loading of 5 wt% is similar to that for the E21 SBM. The E41 SBM phase separated as small agglomerates,

as shown in Figures 6.2.8 and 6.2.9. At a higher E41 content of 10 wt%, a multi-scale material consisting of micron sized soft spherical particles and a co-continuous structure of small aggregates was observed instead. The spherical particles were 1 – 5 μm in diameter, whereas the agglomerates of E41 SBM were up to 2 μm in length and 0.2 μm wide.



(a) 5 wt% E41 (b) 10 wt% E41

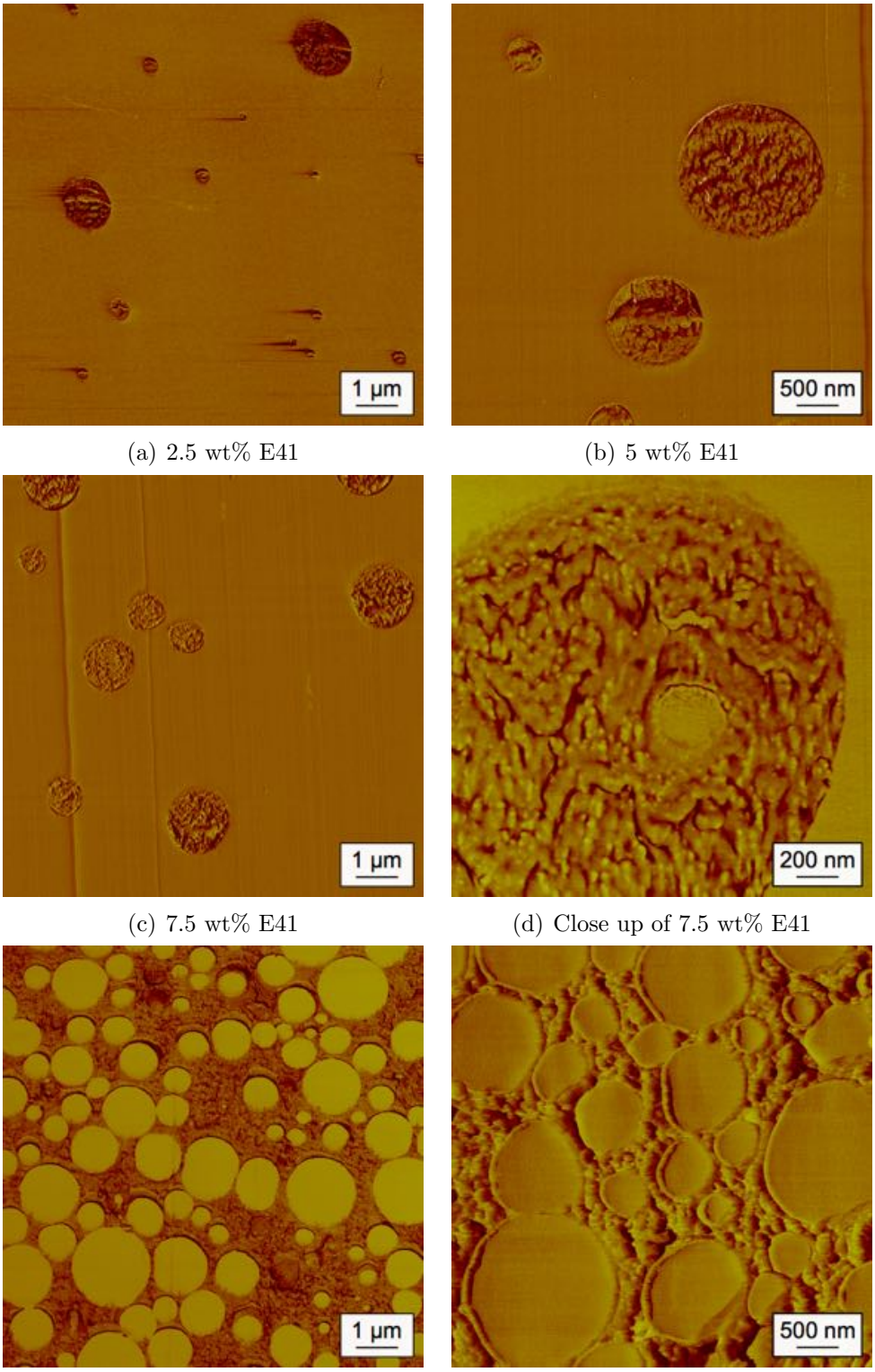
Figure 6.2.8: AFM phase micrographs of E41 SBM modified LD epoxy polymer.



(a) 5 wt% E41 (b) 10 wt% E41

Figure 6.2.9: AFM phase micrographs of E41 SBM modified AD epoxy polymer.

The morphology for the E41 modified LH epoxy show well dispersed SBM particles phase separated with a "raspberry"-like microstructure, as shown in Figure 6.2.10. This "sphere-on-sphere" morphology has a polystyrene (PS) core with polybutadiene (PB) particles on the surface which appear as the dark spots (as they are the softer phase, they appear dark in the AFM phase images) [46]. This is illustrated more clearly from the FEGSEM micrographs, such as those in Figure 6.7.16(a).



(a) 2.5 wt% E41 (b) 5 wt% E41

(c) 7.5 wt% E41 (d) Close up of 7.5 wt% E41

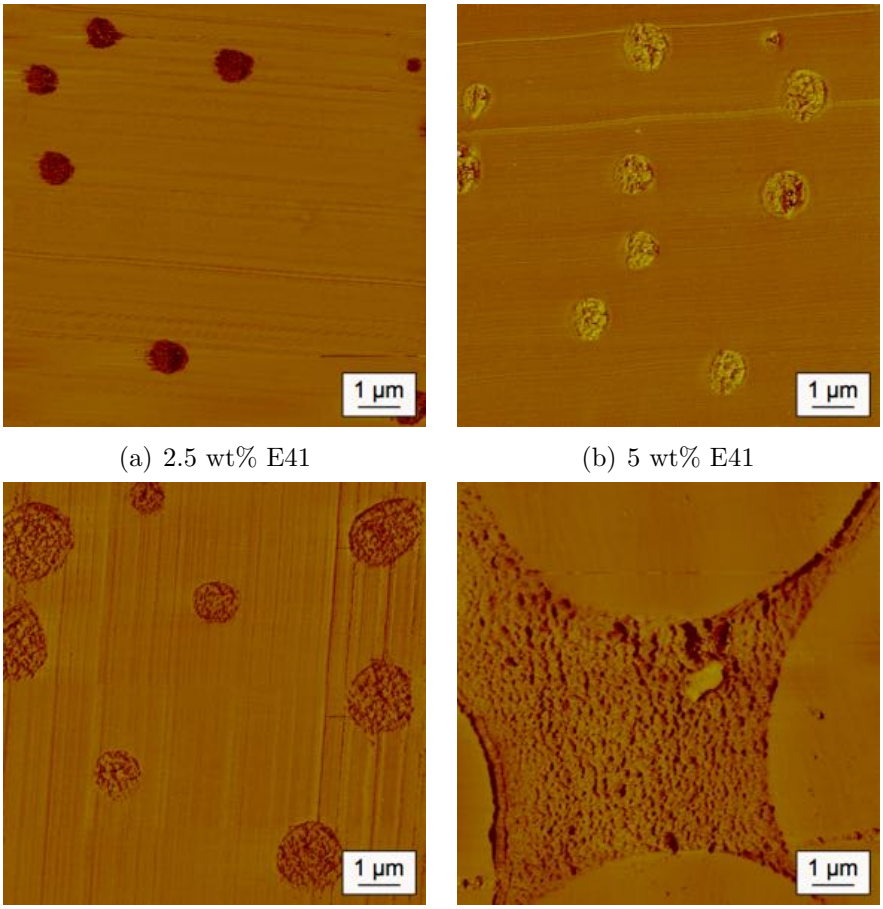
(e) 10 wt% E41 (f) 15 wt% E41

Figure 6.2.10: AFM phase micrographs of E41 SBM modified LH epoxy polymer.

A particle from the 7.5 wt% E41 modified LH epoxy is examined at higher resolution, as shown in Figure 6.2.10(d). This image shows the internal morphology of a single

particle, as the microtome cuts through the particles. The phase image shows bright particles of approximately 20 nm in diameter, i.e. rigid particles. This could be epoxy, PS or PMMA particles as they both have similar stiffnesses and are stiffer than the core material. The mean particle radii increased linearly from 0.22 μm for 2.5 wt% E41, to 0.52 μm for the formulation containing 7.5 wt% E41, as summarised in Table 6.2.4. At concentrations of 10 wt% and higher of E41 SBM, a partially phase inverted microstructure was observed, consisting of epoxy-rich regions with "raspberry"-like SBM particles, and SBM-rich regions with epoxy particles. Figure 6.2.10(e) shows a phase-inverted area with the epoxy particles (lighter areas) within the SBM matrix (darker areas).

The morphology of the E41 modified LV epoxy at contents of 7.5 wt% and below also show well dispersed "raspberry"-like particles, as shown in Figure 6.2.11. The mean particle radius increased with E41 SBM content from 0.31 μm for 2.5 wt% E41, to 0.65 μm for 7.5 wt% E41. Increasing the loading to 10 wt% E41 SBM, resulted in a phase inverted structure, as shown in Figure 6.2.11(d).



(a) 2.5 wt% E41 (b) 5 wt% E41

(c) 7.5 wt% E41 (d) 10 wt% E41

Figure 6.2.11: AFM phase micrographs of E41 SBM modified LV epoxy polymer.

The mean particle radius and characteristic lengths of the E41 SBM phase is shown in Table 6.2.4. Similar to the E21 modified epoxies, an increase in particle radius and characteristic lengths was observed with increasing E41 concentration. The measured values of characteristic lengths were typically higher than the particle radius, as the two point correlation method takes into account the length of the small agglomerates, whereas assuming the particles as spheres would give an inaccurate dimension.

Table 6.2.4: Mean particle radius and characteristic lengths of E41 SBM phases in epoxy.

Content (wt%)	Particle radius (μm)			
	LD[a]	AD[a]	LH	LV
2.5	–	–	0.22 ± 0.02	0.31 ± 0.03
5	0.12 ± 0.02	0.13 ± 0.04	0.35 ± 0.07	0.44 ± 0.02
7.5	–	–	0.52 ± 0.02	0.65 ± 0.05
Content (wt%)	Characteristic length (μm)			
	LD	AD	LH	LV
2.5	–	–	1.16 ± 0.03	0.81 ± 0.16
5	0.83 ± 0.06	0.66 ± 0.02	1.36 ± 0.08	1.14 ± 0.01
7.5	–	–	1.49 ± 0.03	1.48 ± 0.27
10	1.48 ± 0.23	1.09 ± 0.01	1.09[b]	2.28 ± 0.02
15	–	–	1.06[b]	–

[a] Approximated as spheres

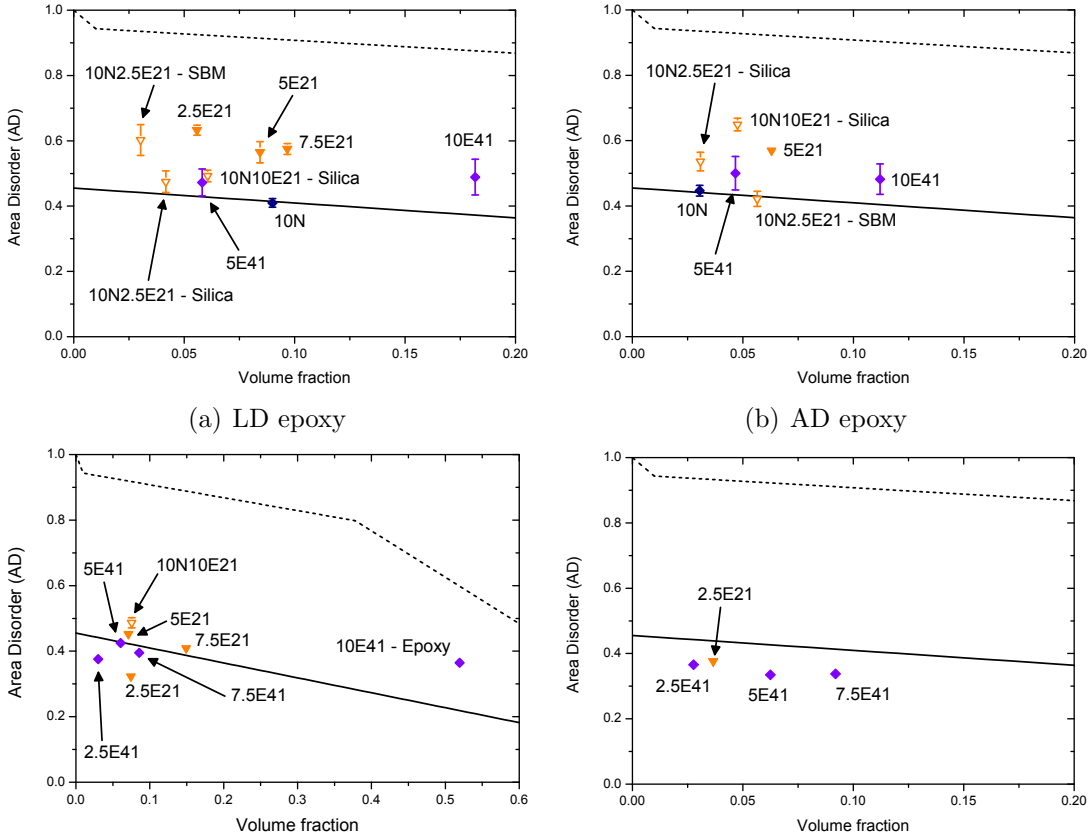
[b] Epoxy inclusions

The mean values of measured volume fraction generally show good agreement with the calculated values for both E21 and E41 SBM modified epoxies. This indicates complete phase separation of the SBM block copolymers from the epoxy during cure. The measured values of volume fraction tended to be higher than the calculated values, indicating that the SBM phase may contain epoxy. When silica nanoparticles were added, the measured volume fraction of E21 SBM was reduced. This suggests that some SBM did not phase separate and remains dissolved in the epoxy. This was also observed as a decrease in glass transition temperature, T_g, as discussed in the following section.

6.2.3 Area disorder

The dispersion of the SBM and hybrid SBM-NS modified epoxies were quantified by the area disorder method as described by Bray *et al.* [255]. The results for the SBM modified epoxies are shown in Figure 6.2.12.

The E21 SBM modified LD and AD epoxies show a clustered dispersion, which agrees well with the qualitative analysis of the AFM micrographs. Interestingly, the value of area disorder, or degree of agglomeration, does not change with an increase in SBM



(a) LD epoxy (b) AD epoxy

(c) LH epoxy (d) LV epoxy

Figure 6.2.12: Area disorder of SBM block copolymer modified epoxy polymers.

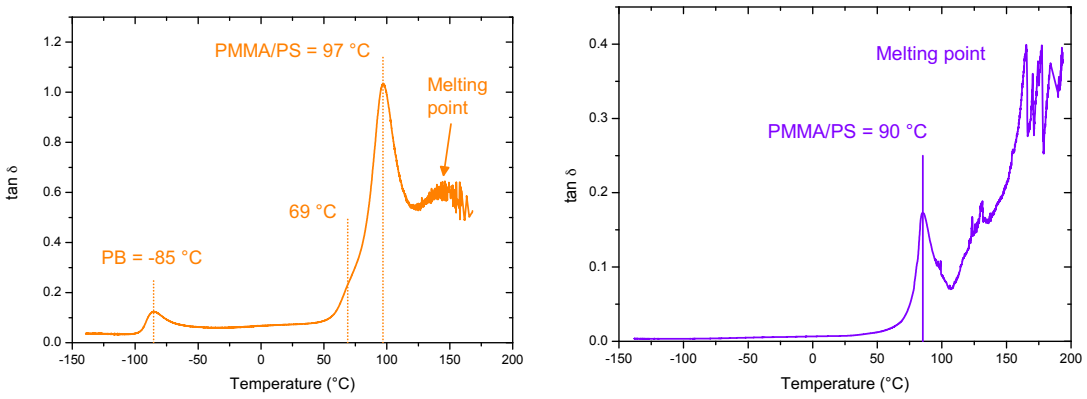
content. For the E21 modified LH and LV epoxies, the analysis describes the dispersion of the E21 SBM particles as "random-like". For the E21 SBM-NS hybrid modified epoxies, the SBM particles maintain the same area disorder, i.e. the silica nanoparticles do not affect the dispersion of the SBM particles, and the silica nanoparticles have AD values corresponding to "random-like" dispersion.

The particles in the E41 SBM modified LD and AD epoxies show slightly higher values of area disorder than the "random-like" condition. This is due to the multi-scale size distribution of these particles. For the E41 SBM modified LH and LV epoxies, the particles were described as randomly dispersed.

6.3 Glass transition temperature

The glass transition temperatures, T_g, of the block copolymers were measured for the E21 and E41 SBM block copolymers. The E41 SBM was found to be too brittle to be clamped using the tension grips on the DMA, and thus was tested using the powder

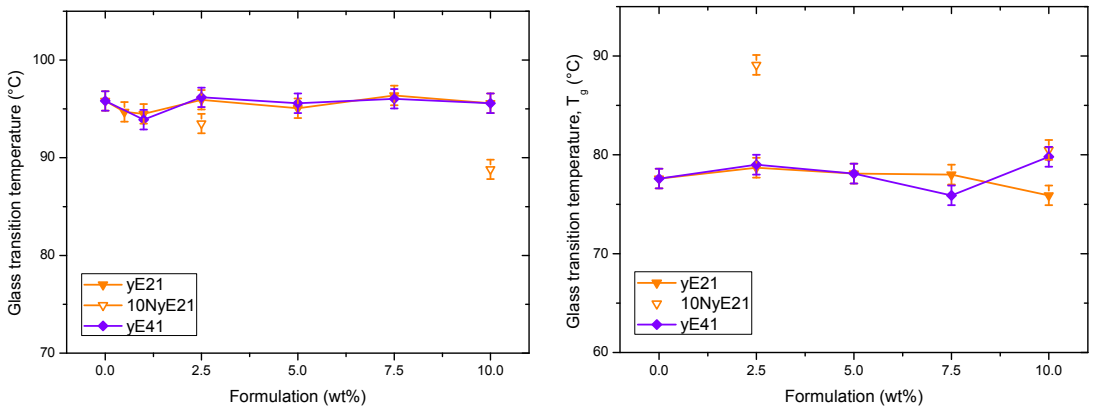
clamp on the DMA. The results from the DMA are shown in Figure 6.3.1(a). Two main peaks at -85°C and 97°C were observed for the E21 SBM, which correspond to the PB and PMMA or PS blocks in the E21 SBM. There is also an additional peak at 69°C, caused by a combination of PB and PMMA blocks and indicates the presence of some random copolymers [274]. The E41 SBM only shows one peak at 90 °C corresponding to the PMMA or PS block, as shown in Figure 6.3.1(b). The E41 SBM, however, did not show a peak for the PB block.



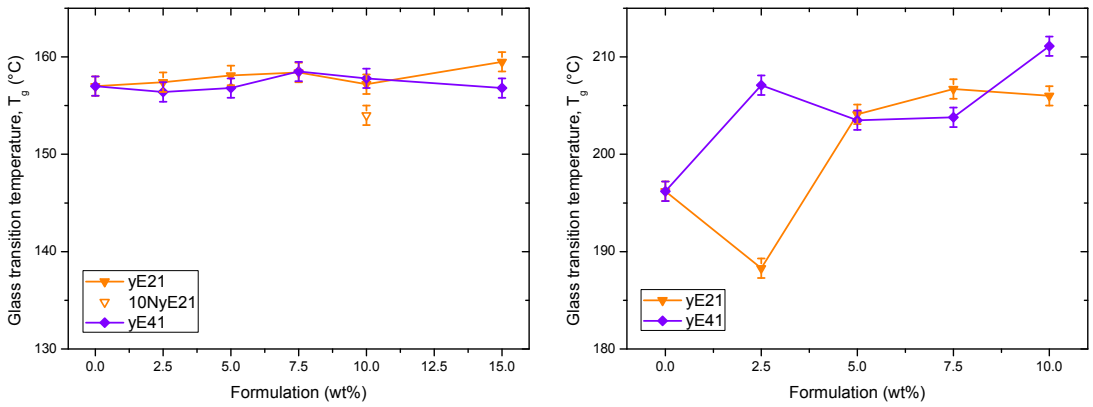
(a) E21 SBM (b) E41 SBM

Figure 6.3.1: Variation of tan δ with temperature of E21 and E41 SBM block copolymer.

The values of T_g were also measured for the unmodified and SBM modified epoxies using DMA and are summarised in Figure 6.3.2. The T_g values of the unmodified epoxies were 96 °C, 74 °C, 157 °C and 196 °C for the LD, AD, LH and LV epoxies respectively. The addition of E21 or E41 does not have a significant effect on the T_g of the LD, AD and LH epoxy systems. However, the T_g values of the SBM modified LV epoxies fluctuate significantly with the addition of SBM. The 2.5 wt% E21 SBM modified LV epoxy shows a 8°C decrease in T_g, indicating approximately 1.1 wt% remain dissolved in the epoxy according to the Fox equation. The AFM micrographs show that up to 0.8 wt% of SBM remained dissolved in the epoxy.



(a) LD epoxy (b) AD epoxy



(c) LH epoxy (d) LV epoxy

Figure 6.3.2: Glass transition temperatures of SBM modified epoxy polymers. Error bars represent standard error of ±1°C.

The addition of silica nanoparticles increases the amount of SBM that remains dissolved in the epoxy, as shown in Table 6.2.3, and hence causes a change in the T_g. Indeed, the AFM images show a decrease in volume fraction of 1.6 vol% when 10 wt% of silica nanoparticles were added to the E21 modified LD epoxies. The Fox equation [247] predicts that the 10N10E21 modified LD epoxy has approximately 1.9 wt% of SBM remaining dissolved in the epoxy. The 10N10E21 LH modified epoxy also show a decrease in T_g, to 154 °C, which the Fox equation predicts as 0.5 wt% of SBM remaining dissolved. For the AD epoxy system, there was no decrease in volume fraction and the T_g remains the same after adding the silica nanoparticles.

The change in tan δ with temperature for the SBM modified LV epoxy polymer is shown in Figure 6.3.3, and is typical for all four epoxy systems. A beta transition peak, T_β, is observed at -47°C. The PB peak at -86 °C is visible for the E21 modified but not for the E41 modified epoxy, indicating the relative content of PB in E21 is higher than in the E41 SBM. Further peaks at 75 to 130 °C correspond to the other blocks in the SBM block copolymer.

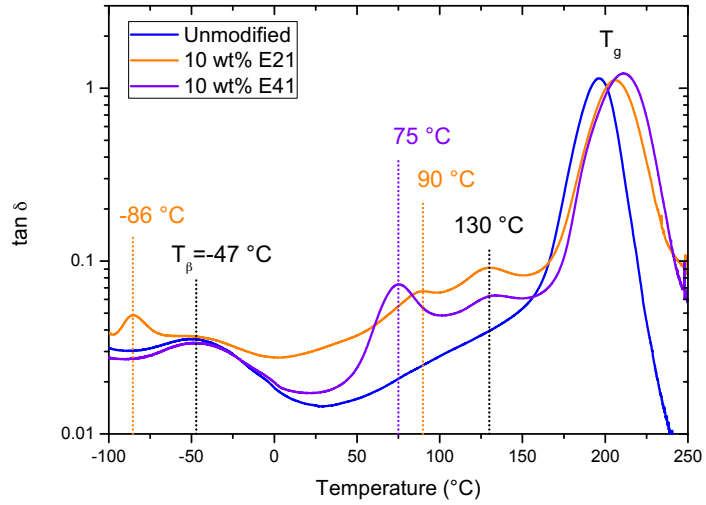


Figure 6.3.3: Variation of tan δ with temperature of E21 and E41 SBM modified LV epoxy polymer.

6.4 Tensile properties

The tensile properties of the E21 and E41 SBM block copolymers were measured and are summarised in Figure 6.4.1 and Table 6.4.1. The tensile Young's modulus was measured as 0.3 GPa and 0.1 GPa for the E21 and E41 SBM block copolymers, respectively. However, the result for the E41 SBM should not be considered to be reliable as the BCP was too brittle to be clamped with sufficient force to be tested.

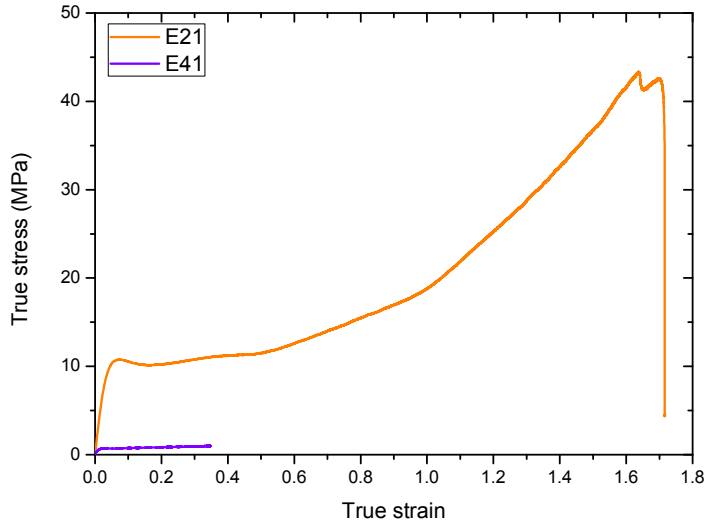


Figure 6.4.1: Tensile true stress-true strain curves for E21 and E41 SBM block copolymers.

The Young's modulus, E_t, of the unmodified epoxies were measured to be 3.0, 3.6, 2.9 and 2.9 GPa for the LD, AD, LH and LV epoxies respectively. Typical true stress-strain curves for the unmodified and SBM modified LD epoxies are shown in Figure 6.4.2.

Table 6.4.1: Young's modulus, E_t, yield stress, σ_y, yield strain, ε_y, fracture strength, σ_f, and fracture strain, ε_f for E21 and E41 SBM block copolymers.

SBM	E_t (GPa)	σ_y (MPa)	ε_y	σ_f (MPa)	ε_f
E21	0.3 ± 0.0	10 ± 0	0.11 ± 0.00	43	1.6
E41	0.1 ± 0.0	1 ± 0	0.12 ± 0.00	1	0.4

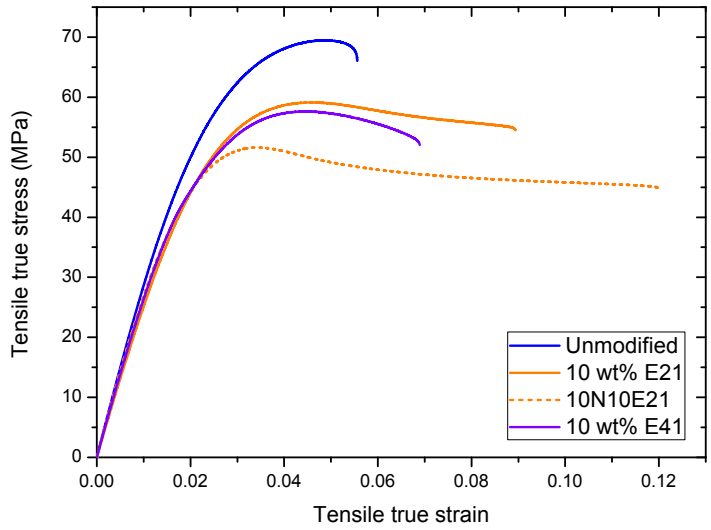


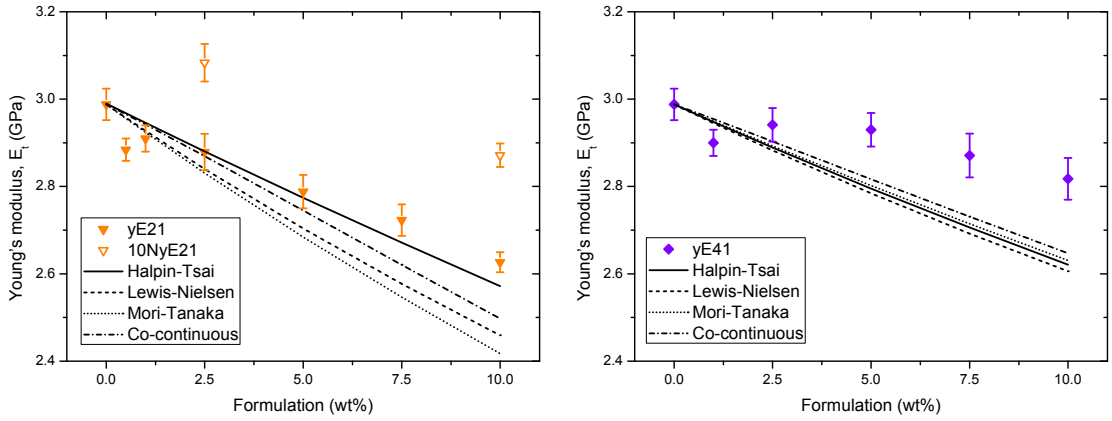
Figure 6.4.2: Typical tensile true stress-strain curves for unmodified and SBM modified LD epoxies.

The addition of the relatively soft SBM BCPs reduced the E_t of the epoxy as expected, as shown in Figures 6.4.3 to 6.4.6. The E21 SBM modified epoxies show a lower modulus than the E41 SBM modified epoxies due to the higher PB content (the soft block of the SBM BCP) in the E21 SBM. The modulus for the E21 SBM modified epoxies decreased linearly with increasing SBM content. At loadings of 10 wt%, the values of E_t were measured as 2.6, 3.0, 2.4, 2.1 GPa for the LD, AD, LH and LV epoxies respectively. This corresponds to a decrease of about 15% for the co-continuous microstructures, the LD, AD and LH epoxy systems, and a decrease of 26% for the LV epoxy system, which has a phase inverted structure.

A further addition of 10 wt% of silica nanoparticles to the E21 modified epoxies recovered a portion of the modulus lost from the addition of the BCPs. The percentage of modulus recovered is similar to the increase observed in the unmodified epoxies [5], up to 10%.

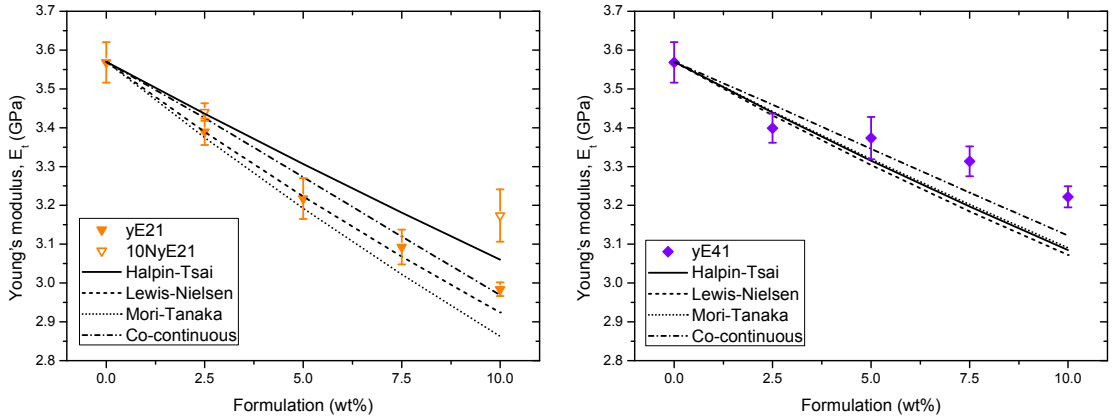
For the E41 SBM modified epoxies, a similar trend in Young's modulus with morphology was observed. The modulus decreases linearly with SBM content for the co-continuous microstructures (for the LD and AD epoxies) and there is a sharp decrease when a phase inversion occurs (for the LH and LV epoxies). At loadings of 10

wt% E41, the values of E_t were measured as 2.8, 3.2, 2.6, 2.2 GPa for the LD, AD, LH and LV epoxies respectively.



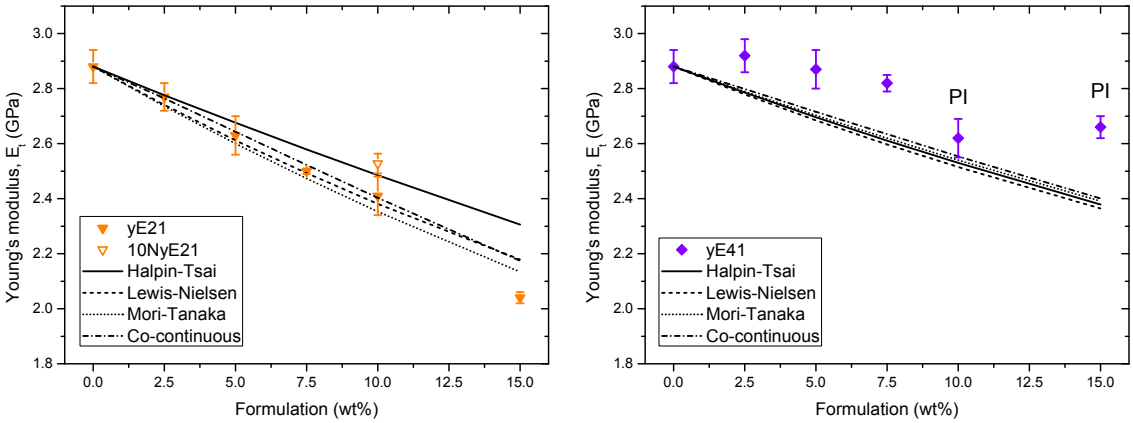
(a) E21 SBM (b) E41 SBM

Figure 6.4.3: Young's moduli of SBM modified LD epoxy.



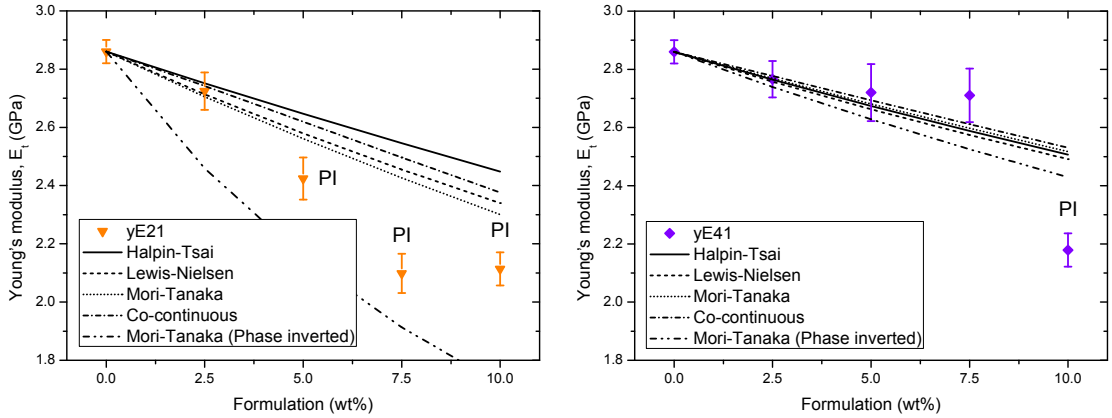
(a) E21 SBM (b) E41 SBM

Figure 6.4.4: Young's moduli of SBM modified AD epoxy.



(a) E21 SBM (b) E41 SBM

Figure 6.4.5: Young's moduli of SBM modified LH epoxy. Epoxies with phase inverted structures are labelled PI.



(a) E21 SBM (b) E41 SBM

Figure 6.4.6: Young's moduli of SBM modified LV epoxy. Epoxies with phase inverted structures are labelled PI.

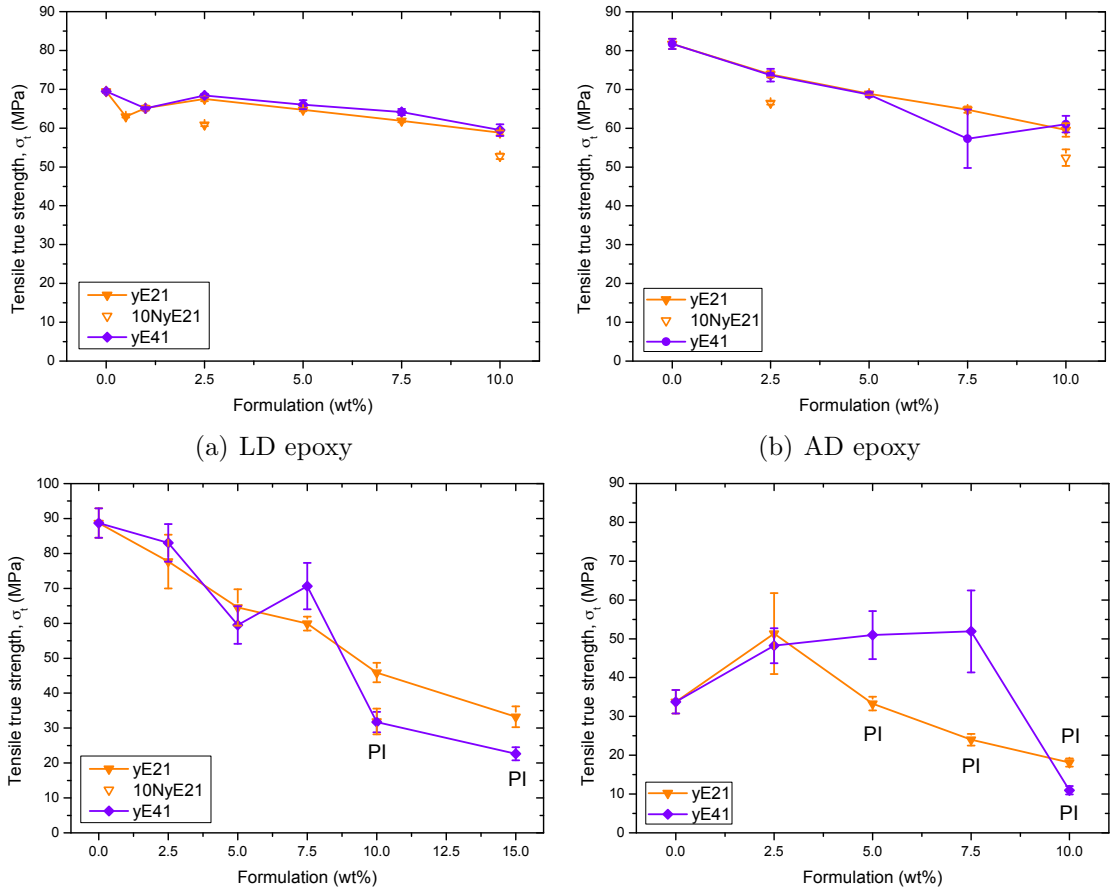
The Young's modulus for the SBM modified epoxies measured from the tensile tests were compared to the Halpin-Tsai, Lewis-Nielsen, Mori-Tanaka and Veenstra *et al.* [210] co-continuous analytical models. A particle modulus, E_p, of 0.3 GPa and 1 GPa was used for the E21 and E41 SBM, respectively, and a Poisson's ratio, ν_p, of 0.49 was used. The value of E_p for the E41 SBM was chosen as it gave the best prediction to the experimental results. The matrix modulus, E_m, and Poisson's ratio, ν_m, were measured experimentally. For the Lewis-Nielsen model, the 'random agglomerate' condition was applied, as observed from the AFM.

It was found that the different analytical solutions to the predictions of moduli resulted in similar values, as shown in Figures 6.4.3 to 6.4.6. This is due to the relatively low volume fractions used and difference in stiffness between the epoxy and modifier. The Lewis-Nielsen model shows the best agreement with most of the experimental results, except for the systems that have phase inverted structures, namely the E21 SBM modified LV epoxies. The predictions for the E41 modified epoxies also did not agree well and tended to be underpredicted. However, this could also be a result of the chosen value of E_p.

The Mori-Tanaka model was also applied for the phase inverted structure found in the SBM modified LV epoxy, as shown in Figure 6.4.6. The predictions in this case were very low and represents the lower bound case where the microstructure is fully phase inverted. The Mori-Tanaka model is also known to not work well at high volume fractions due to complex inter-particle interactions.

The tensile true strength, σ_t, of the SBM modified LD, AD and LH epoxies decreased with the SBM content, as shown in Figure 6.4.7. The E41 modified LH epoxy shows the

highest decrease in σ_t, decreasing from 86 MPa for the unmodified epoxy to 31 MPa at 10 wt%. For the LV epoxy, the σ_t was initially increased at low weight percentages as the unmodified epoxy is very brittle and fails at a low stress before the onset of yielding. A sharp drop in σ_t was typically measured when phase inversion was observed, as seen for the 10 wt% E41 modified LH epoxy, 5 wt% E21 modified LV epoxy and 10 wt% E41 modified LV epoxy.



(a) LD epoxy

(b) AD epoxy

(c) LH epoxy

(d) LV epoxy

Figure 6.4.7: Tensile true strength, σ_t, of SBM modified epoxy polymers.

For the LH epoxy system, samples containing E21 at concentrations of 7.5 wt% and above exhibited extensive stress whitening across their gauge length in the tensile tests, as shown in Figure 6.4.8. The sample stiffness decreased during this stress whitening phase, and then increased again after the entire region had stress whitened. During this stress whitening phase, the SBM particles debond (see 6.7) and form voids, which scatter light and cause the white appearance. This debonding occurs before yielding. The stress versus strain trace is non-linear, but the yield point has not been reached when fracture occurs. The stiffness before whitening is greater than that after whitening, due to the voids which reduce the stiffness of the sample. For the

formulation containing 10 wt% E21, a tensile yield stress of 67 MPa was calculated from the plane strain compression tests, so Figure 6.4.8 shows that fracture during the tensile test occurs well before yield.

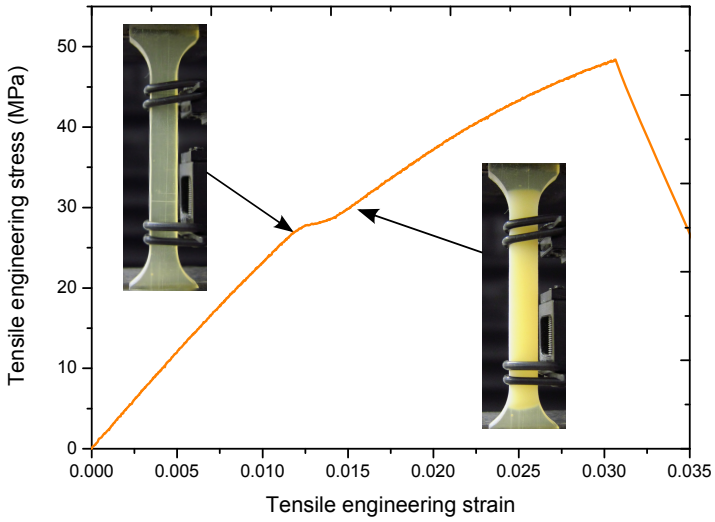
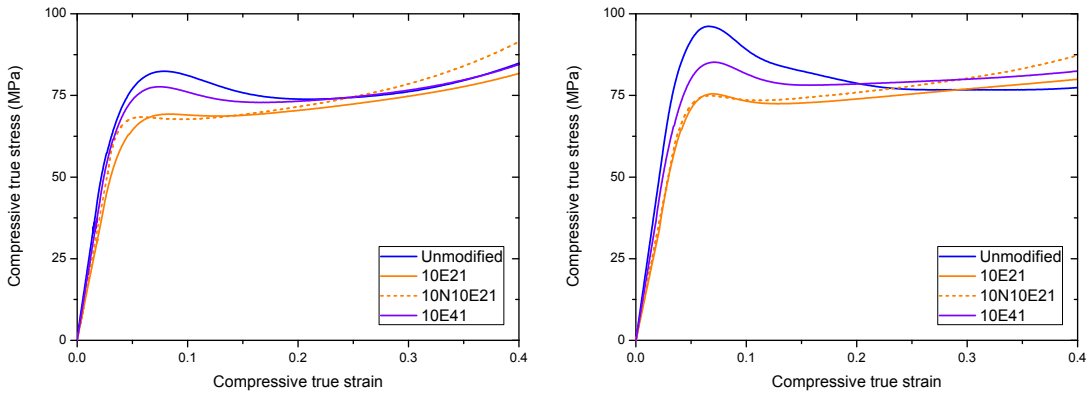


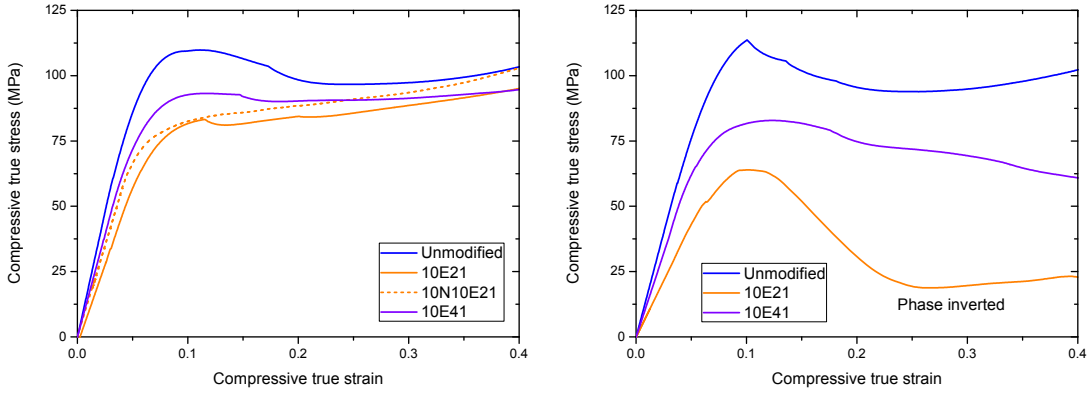
Figure 6.4.8: Extensive stress whitening along gauge length of 10 wt% E21 modified LH epoxy polymer.

6.5 Compressive properties

The compressive true stress-true strain curves for the unmodified and the 10 wt% SBM block copolymer modified epoxies are shown in Figure 6.5.1. When comparing the unmodified epoxies, the values of compressive true yield stresses, σ_{yc}, increases with the T_g. For example, the value of σ_{yc} was measured to be 83 and 115 MPa for the LD and LV epoxies, respectively, which have T_g values of 96°C and 196°C. This is because the higher T_g epoxies have higher crosslink density, hence more energy is required to break the bonds. The addition of SBM BCPs causes a decrease in the compressive modulus, E_c, and σ_{yc}, similar to the trend observed from the tensile tests.



(a) LD epoxy (b) AD epoxy



(c) LH epoxy (d) LV epoxy

Figure 6.5.1: Compressive true stress-true strain curves for unmodified and 10 wt% SBM modified epoxy polymers.

The compressive true yield strain, ε_{yc}, was not affected by the addition of the SBM block copolymers, i.e. the addition of SBM only does not affect the onset of yield from intrinsic yield processes such as shear banding. The values of ε_{yc} were measured to be 0.08, 0.07, 0.10 and 0.10 for the unmodified LD, AD, LH and LV epoxies, respectively. For the 10N10E21 modified LD epoxy, however, a significant decrease in ε_{yc} was measured. This was not observed for the other SBM-NS hybrid modified epoxies.

The further addition of 10 wt% of silica nanoparticles recovers some of the loss in E_c. Interestingly, the σ_{yc} of the SBM modified epoxies remains constant with the addition of the silica nanoparticles. The silica nanoparticles also increased the degree of work hardening, i.e. hardening modulus, compared to the SBM modified epoxies without silica nanoparticles.

The degree of strain softening was found to be reduced with the addition of the SBM BCPs, identified as the decrease in stress after yield. This could be a result of suppressed macroscopic inhomogeneous yielding and strain localisation [271], which can be caused by microscopic, highly localised shear yielding. For the SBM modified LV epoxies, work hardening was not observed after significant strain softening. With a phase inverted microstructure, the low strength of SBM results in a significant loss in strength and stiffness of the composite material, as shown in Figure 6.5.1(d).

Figures 6.5.2 and 6.5.3 show cross-polarised images of the sectioned compressed regions of the SBM modified epoxies taken at the strain softening limit. Extensive shear band yielding can be observed as birefringence in the unmodified epoxy polymers. It should be noted that the AD epoxy shows more highly focused shear bands than the other epoxy systems. As the SBM content was increased, the shear bands in the compressed region appear more diffuse, indicating the occurence of localised shear band yielding.

All the epoxy systems tested show this trend, and thus localised shear yielding would be expected to be a major toughening mechanism for the SBM modified epoxies.

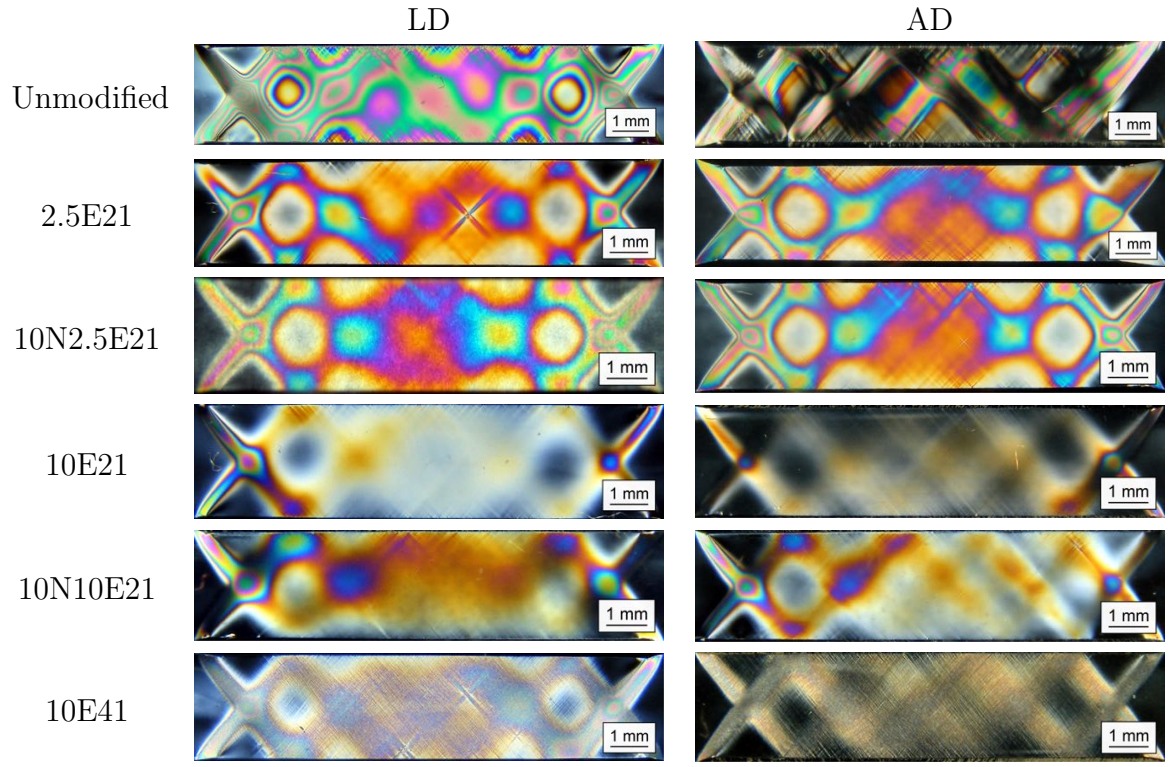


Figure 6.5.2: Transmission optical micrographs, using cross polarised light, of polished PSC specimens loaded to the strain softening region for the LD and AD epoxies.

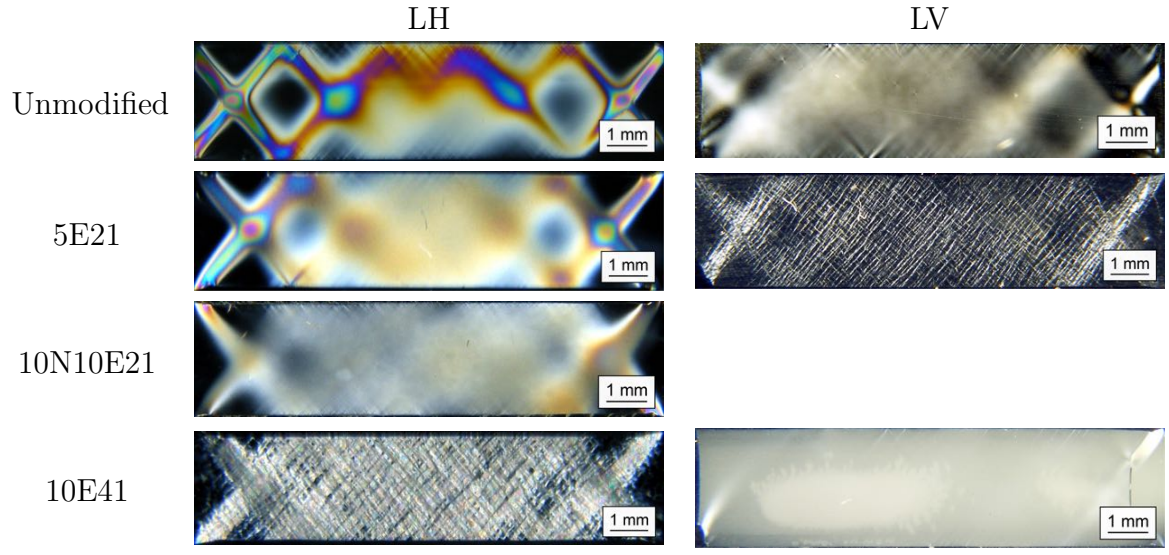


Figure 6.5.3: Transmission optical micrographs, using cross polarised light, of polished PSC specimens loaded to the strain softening region for the LH and LV epoxies.

The compressed regions of the 10 wt% E41 modified LH and 5 wt% E21 modified LV epoxies show well defined shear bands, which increase in number and length but not

width, as with a diffuse shear zone. These are the materials which show partially phase inverted structures.

6.6 Fracture properties

The fracture toughness, K_{IC}, and fracture energy, G_{IC}, of the epoxies were measured using SENB tests. The results are shown in Figures 6.6.1 to 6.6.4. The values of G_{IC} for the unmodified epoxies were measured to be 0.2 kJ/m^2 for the LD and AD epoxies, and 0.1 kJ/m^2 for the LH and LV epoxies, respectively. These values are consistent with those from the literature [5] for the same epoxy systems. The toughening mechanisms will be discussed in §6.7.

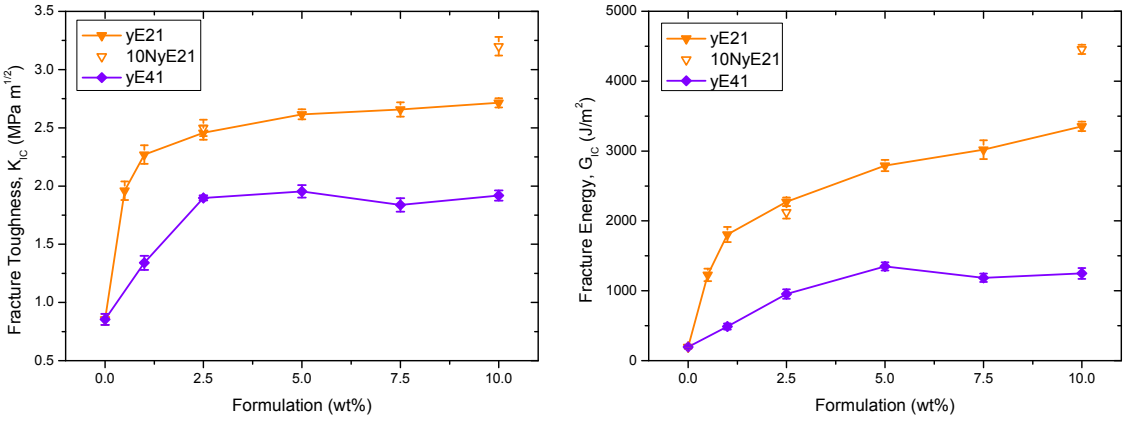


Figure 6.6.1: Fracture toughness and fracture energy of SBM modified LD epoxy.

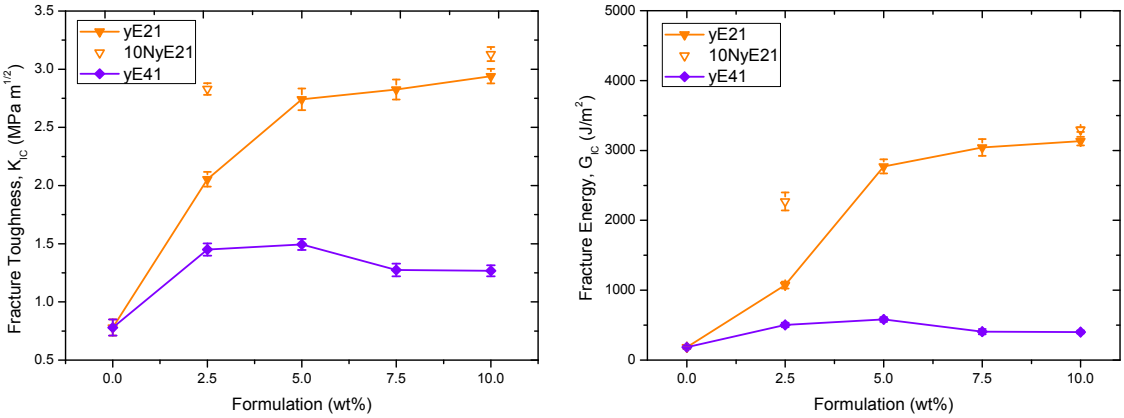


Figure 6.6.2: Fracture toughness and fracture energy of SBM modified AD epoxy.

The E21 SBM modified LD epoxy shows a large increase in fracture performance up to a loading of 2.5 wt%, followed by a gradual increase in G_{IC}, as the microstructure transitions from a particulate to a co-continuous structure, to a maximum value of 3.4

kJ/m^2 at 10 wt%. This corresponds to an increase of 1600%, as shown in Figure 6.6.1. For the E21 SBM modified AD epoxy, the G_{IC} value at 2.5 wt% is significantly lower at 1.1 kJ/m^2 (compared to 2.3 kJ/m^2 for the LD epoxy). However, the maximum values of G_{IC} measured for the AD epoxy were of similar order to the LD epoxy sytem, 3.1 kJ/m^2 at 10 wt% as shown in Figure 6.6.2.

When an additional 10 wt% of silica nanoparticles was added to the 2.5 wt% E21 modified AD epoxy (10N2.5E21 hybrid modified AD epoxies), a significant increase in G_{IC} was measured, shown as open triangles ($\bigtriangledown$) in Figure 6.6.2. However, the LD epoxy system shows no increase in fracture performance. The trend for the 10N10E21 hybrid modified epoxies is reversed, in that the 10N10E21 modified LD epoxy shows an increase in G_{IC} compared to the 10 wt% E21 modified LD epoxy, but the AD epoxy system does not. A maximum G_{IC} of 4.5 kJ/m^2 was measured for the 10N10E21 modified LD epoxy.

To elucidate the effect of silica nanoparticles, the difference between the G_{IC} values with and without silica nanoparticles, ΔG_{IC}, were calculated. $G_{synergy}$ can then be determined by subtracting ΔG_{IC} with the fracture energy contributions of silica nanoparticles, ΔG_{silica}. The value of ΔG_{silica} is 0.3 kJ/m^2 for the LD and AD epoxies [5]. The extent of synergy observed for the E21 SBM-NS hybrid modified LD and AD epoxies is summarised in Table 6.6.1.

Table 6.6.1: Fracture energy, G_{IC}, change in fracture energy, ΔG_{IC}, and synergy, $G_{synergy}$, for hybrid E21 SBM-NS modified epoxies.

Modifier	LD (kJ/m^2)			AD (kJ/m^2)		
	G_{IC}	ΔG_{IC}	G$_{synergy}$	G_{IC}	ΔG_{IC}	G$_{synergy}$
2.5E21	2.3	-0.2	No synergy	1.1	+1.2	0.9
10N2.5E21	2.1			2.3		
10E21	3.4	+1.1	0.8	3.1	+0.1	No synergy
10N10E21	4.5			3.3		

The degree of synergistic effects for the E21 SBM-NS hybrid modified epoxies can be significant; for example, the $G_{synergy}$ of the 10N2.5E21 modified AD epoxy accounts for 40% of the total G_{IC}. However, such benefits were not observed for the same modifiers in the LD epoxy system. Similarly for the 10N10E21 modified LD epoxy, where synergistic effects increase the G_{IC} by a further 21% but not for the AD epoxy system. Clearly, the silica nanoparticles are affecting the toughening mechanisms in these materials. These will be explored further in §6.7.

The E41 SBM was less effective in toughening both the LD and AD epoxy polymers compared to the E21 SBM. A plateau in G_{IC} at 1.4 kJ/m^2 for the LD and 0.6 kJ/m^2 for the AD epoxy was measured from 5 wt%. This corresponds to an increase of 600% and 240% for the LD and AD epoxies, respectively.

The E21 SBM modified LH epoxy shows a linear increase in G_{IC} to a maximum of 0.5 kJ/m^2 at a loading of 15 wt%, as shown in Figure 6.6.3. The G_{IC} increases as the SBM content is increased from 10 wt% to 15 wt%, whereas K_{IC} does not. This is because the Young's modulus decreases at a higher rate at the higher concentration. The 10N10E21 modified LH epoxy shows a sharp drop in G_{IC}, which coincided with the formation of a phase inverted structure.

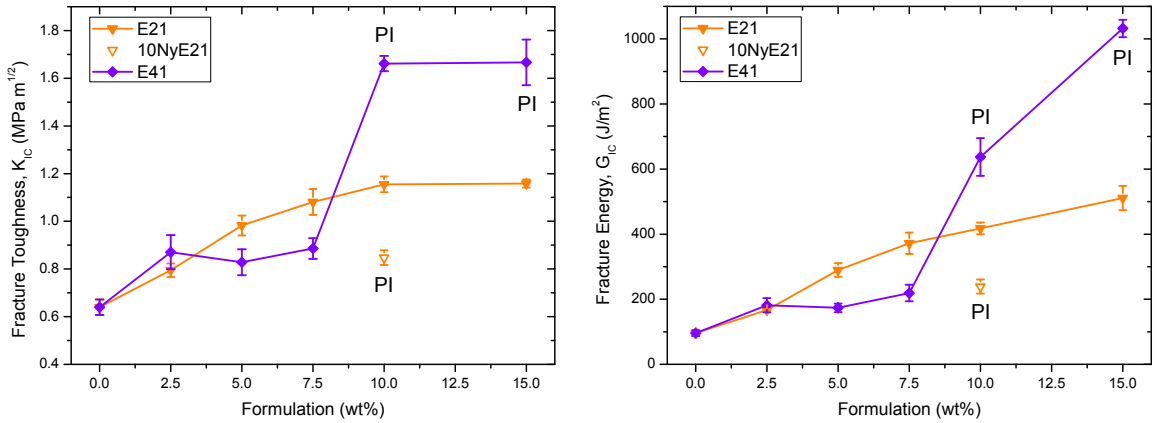


Figure 6.6.3: Fracture toughness and fracture energy of SBM modified LH epoxy. Epoxies with phase inverted structures are labelled PI.

The E41 modified LH epoxy shows a small increase in G_{IC} to 0.2 kJ/m^2 at 7.5 wt% of SBM. However, there is a significant increase in G_{IC} to 0.6 kJ/m^2 at 10 wt% as the morphology changes to a partially phase-inverted structure. The fracture energy increases further at 15 wt% to 1.0 kJ/m^2, as shown in Figure 6.6.3(b).

The results of the SENB tests for the SBM modified LV epoxies are shown in Figure 6.6.4. The fracture energies for the E21 modified LV epoxy increased linearly up to 5 wt%, followed by a significant increase in G_{IC} corresponding to a change in morphology to a partially phase inverted microstructure. A maximum fracture energy of 0.5 kJ/m^2 was measured for the 10 wt% E21 modified LV epoxy, which is an increase of 860%. In contrast to the E21 SBM, the E41 SBM modified LV epoxies show no improvement in fracture toughness. The G_{IC} value at a loading of 7.5 wt% was measured to be 0.1 kJ/m^2. The 10 wt% E41 sample could not be tested due to the difficulty in introducing a sharp crack in the porous material. The cracks would either be deflected by the large particles or split the sample completely when tapped.

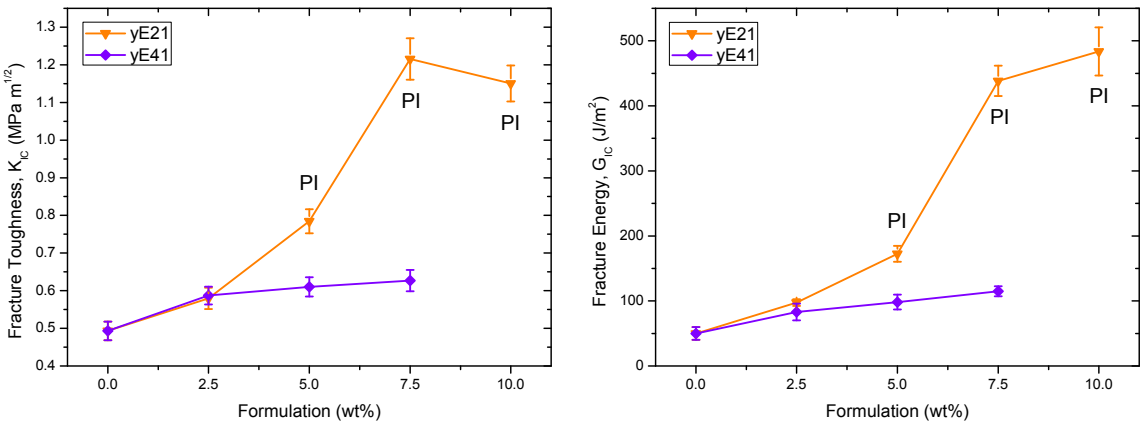


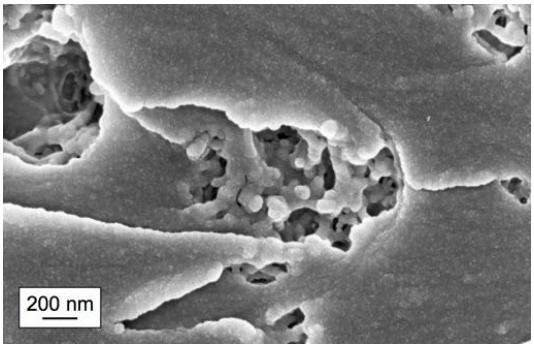
Figure 6.6.4: Fracture toughness and fracture energy of SBM modified LV epoxy. Epoxies with phase inverted structures are labelled PI.

6.7 Fractography

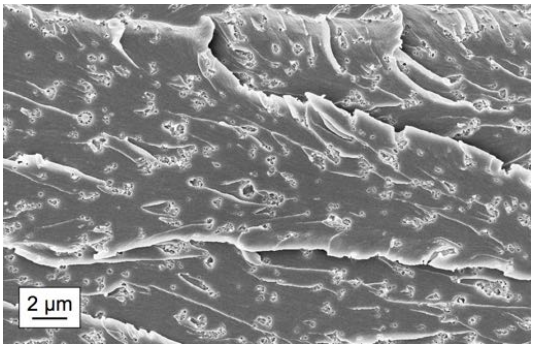
Field emission gun scanning electron microscopy (FEGSEM) of the fracture surfaces was conducted to observe the toughening mechanisms. The crack propagation direction of the selected images shown is from right to left. Note that the fracture surfaces of the unmodified epoxies were smooth and glassy, as discussed in §5.7.

6.7.1 E21 SBM

The addition of E21 SBM to the epoxy polymers caused the fracture surfaces to appear rougher, with more step changes in the crack plane, indicating more plastic deformation. At low concentration, the toughening mechanisms were the same for all four epoxies. The fracture surfaces of the materials with particulate SBM structures, as shown in Figures 6.7.1, 6.7.2 and 6.7.3, show partial debonding of the SBM particles, which initiated void growth around these particles. As the voids around the E21 particles grew, fibrils of polybutadiene were formed, which connected the stiffer polystyrene core to the epoxy matrix. It was observed using the FEGSEM that almost all of the visible particles exhibited this behaviour. Dean et al. [6] have shown that the formation of drawn fibrils only results from a strong interfacial adhesion by the use of reactive functionalities. The use of nonreactive block copolymers resulted in a weaker interfacial adhesion and thus would not produce a fibrillar structure. In the current work, as the BCPs are covalently bonded between the blocks, and PB is the central block, fibrils would be expected. The mean width of the fibrils were measured to be 59 $\pm$25 nm, hence these fibrils are not single linear polymer chains which are of the order of several angstroms.

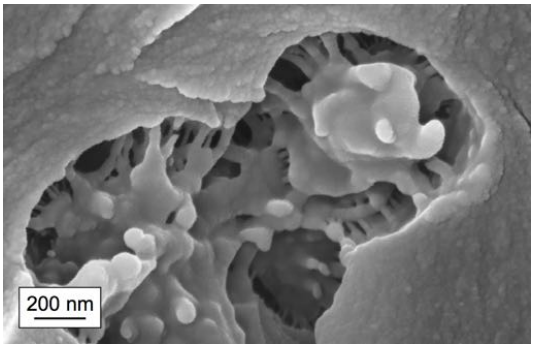


(a) x100k magnification

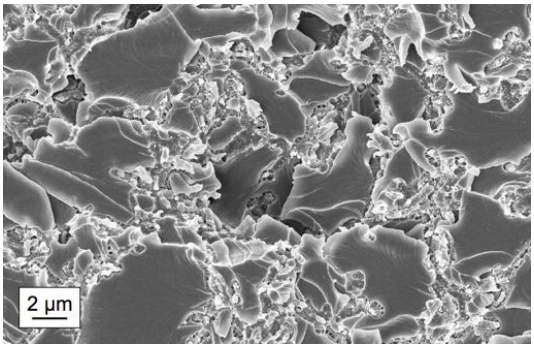


(b) x10k magnification

Figure 6.7.1: FEGSEM micrograph of 2.5 wt% E21 SBM modified LD epoxy fracture surface.

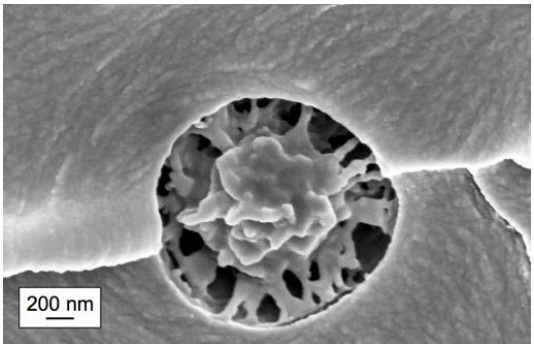


(a) x150k magnification

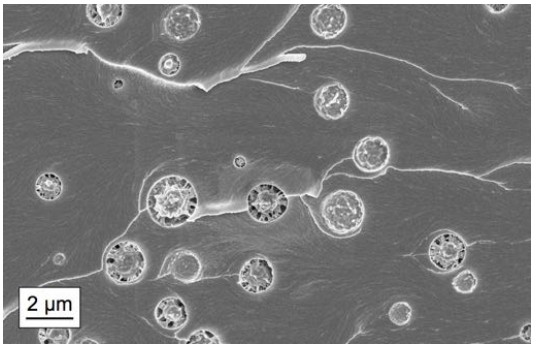


(b) x10k magnification

Figure 6.7.2: FEGSEM micrograph of 5 wt% E21 SBM modified LH epoxy fracture surface.



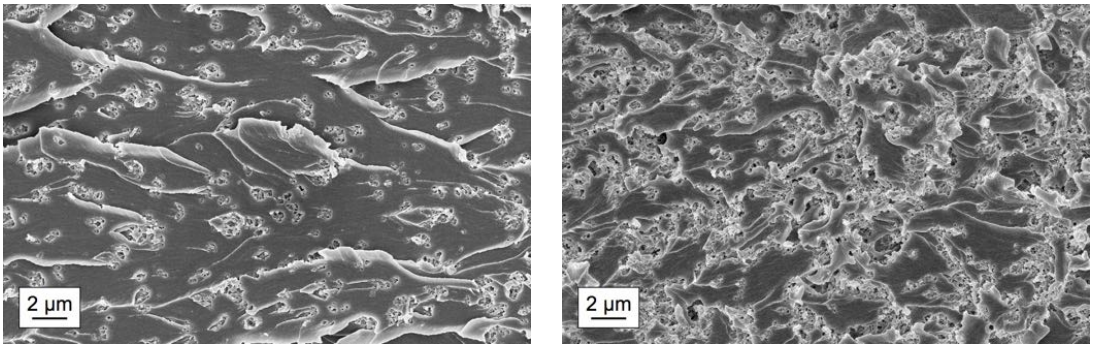
(a) x30k magnification



(b) x5k magnification

Figure 6.7.3: FEGSEM micrograph of 2.5 wt% E21 SBM modified LV epoxy fracture surface.

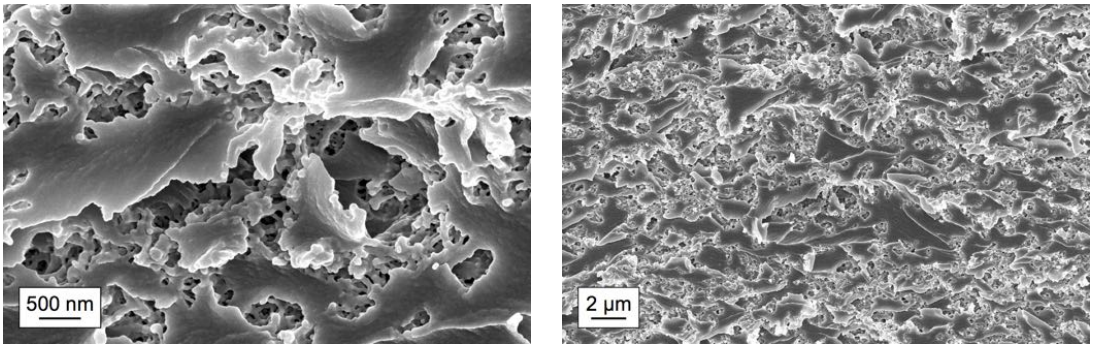
At higher concentrations of E21 SBM, the particles become increasingly more interconnected to form a co-continuous network structure. Figure 6.7.4 shows the change in morphology from a loading of 2.5 wt% to 5 wt% for the E21 SBM modified AD epoxy.



(a) 2.5 wt% E21 (b) 5 wt% E21

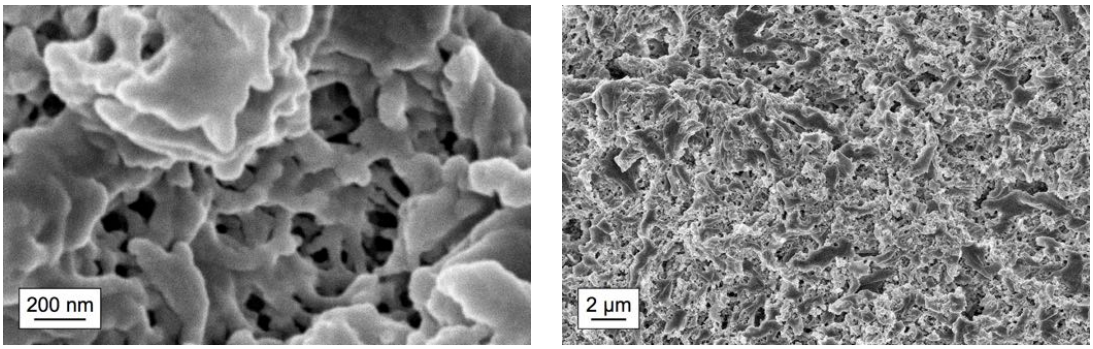
Figure 6.7.4: FEGSEM micrograph of E21 SBM modified AD epoxy fracture surface.

At 10 wt% of E21, as shown in Figures 6.7.5 to 6.7.7, long thin ligaments of the SBM network can be seen around the epoxy matrix, which appears flat and smooth. The fracture surfaces of the E21 SBM modified LD and AD epoxies reveal similar toughening mechanisms between the two. The SBM ligaments show partial debonding from the epoxy matrix, which subsequently allows plastic void growth to occur. This is observed as the large voids in the SBM ligaments. The 10 wt% E21 SBM modified LH and LV epoxies show slightly different mechanisms.



(a) x50k magnification (b) x10k magnification

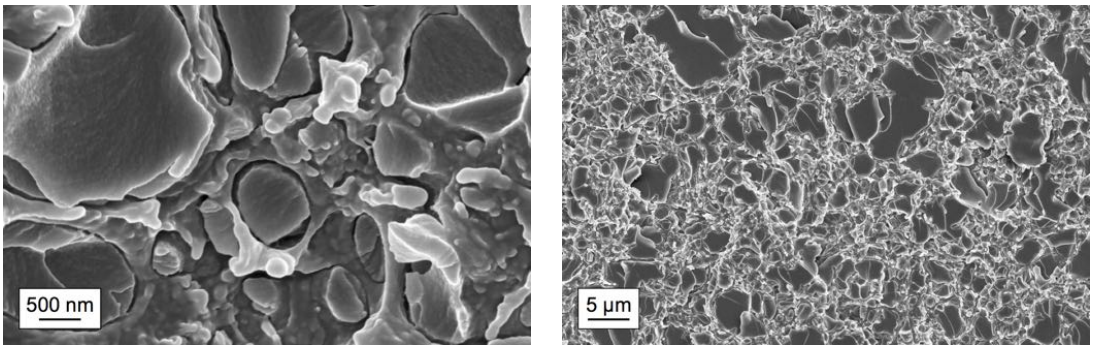
Figure 6.7.5: FEGSEM micrograph of 10 wt% E21 SBM modified LD epoxy fracture surface.



(a) x150k magnification (b) x10k magnification

Figure 6.7.6: FEGSEM micrograph of 10 wt% E21 SBM modified AD epoxy fracture surface.

For the 10 wt% E21 modified LH epoxies, the SBM ligaments debonded fully from the epoxy. Unlike the 5 wt% E21 modified epoxy, there were no fibrils connecting the debonded particles to the epoxy, as shown in Figure 6.7.7. For the 10 wt% E21 modified LD and AD epoxies, there is significantly more void growth around the SBM phase. The degree of void growth is much lower for the LH epoxy system, which limits the fracture toughness.



(a) x150k magnification (b) x10k magnification

Figure 6.7.7: FEGSEM micrograph of 10 wt% E21 SBM modified LH epoxy fracture surface.

The morphology of the 10 wt% E21 SBM modified LV epoxy has been shown to be a partially phase inverted structure which increases the G_{IC} significantly, but at the expense of the tensile properties. The insets in Figure 6.7.8 show the SBM particles in the epoxy rich regions, and epoxy particles in the SBM rich domains. The SBM particles in the epoxy rich domains were measured to be approximately 170 nm in radius, and did not exhibit any debonding or cavitation. The epoxy inclusions in the SBM rich regions were measured to be approximately 1.1 μm in radius, an increase compared to the radius of 0.8 μm measured from the AFM, which might indicate plastic deformation. However, the crack propagates around the epoxy inclusions through the SBM matrix, rather than through the inclusions. Thus it was not possible to take into account the thickness of the layer of SBM that covers these epoxy inclusions (see right inset in Figure 6.7.8).

The main toughening mechanism was the plastic deformation of the large regions of SBM-rich phase, as indicated by the change in height observed on the fracture surface. These may have been initiated from the debonding between the SBM-rich and epoxy-rich regions, as shown in Figure 6.7.8.

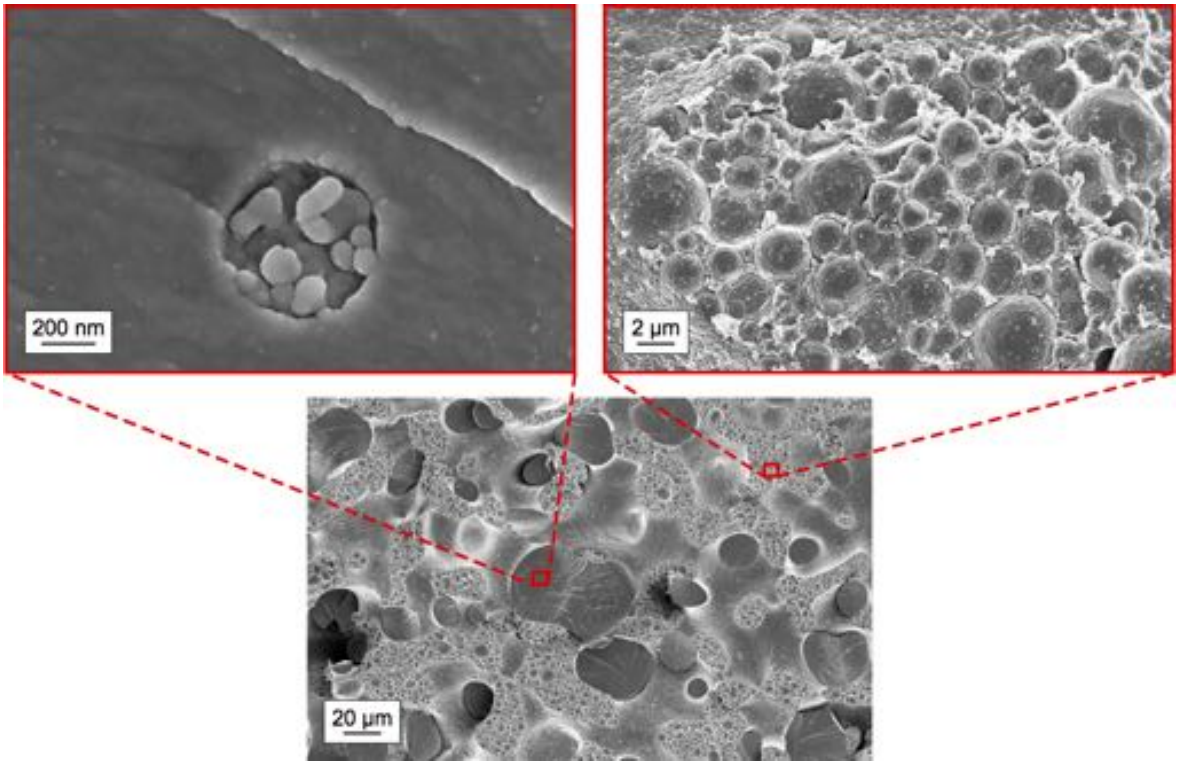
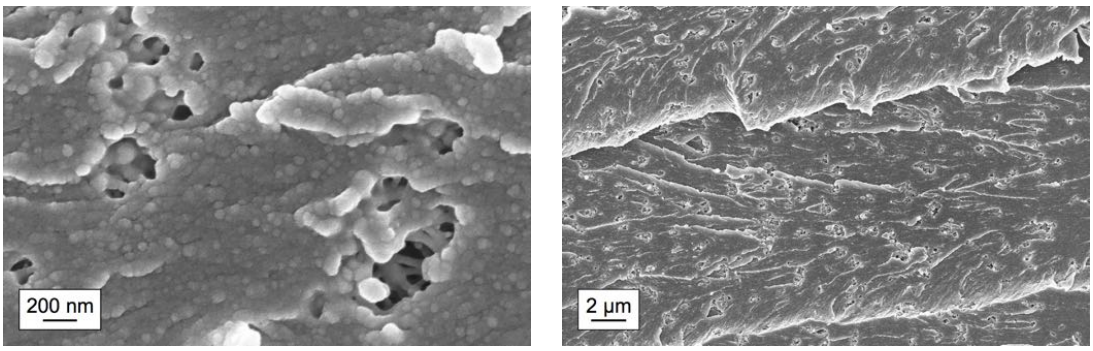


Figure 6.7.8: FEGSEM micrograph of 10 wt% E21 SBM modified LV epoxy fracture surface.

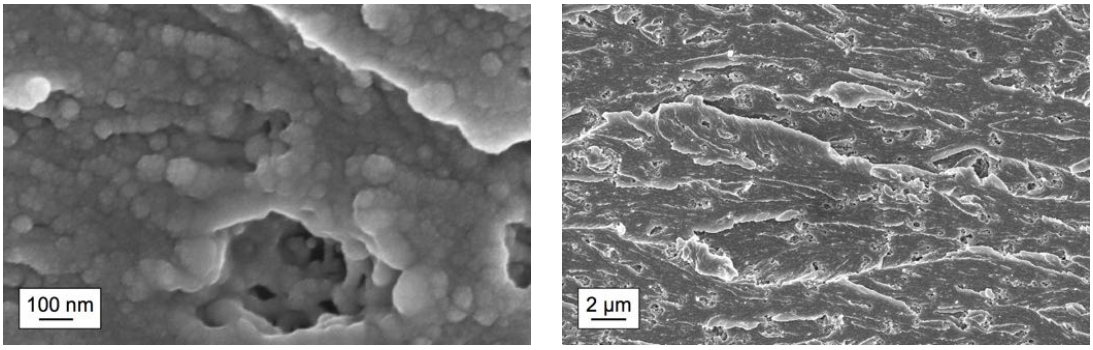
FEGSEM micrographs of the fracture surfaces for the hybrid E21 SBM-NS modified epoxies are shown in Figures 6.7.9 to 6.7.13. As with the 2.5 wt% E21 modified epoxies, the SBM particles in the 10N2.5E21 hybrid modified LD and AD epoxies show partial debonding and subsequently initiated plastic void growth of the epoxy, as shown in Figures 6.7.9 and 6.7.10. The average size of the voids around the SBM particles for both LD and AD epoxies were found to be smaller in the hybrid materials compared to the epoxies without silica nanoparticles. Approximating the agglomerates as spheres, the mean particle radius for the 2.5E21LD epoxy was measured to be 0.20 μm, which decreased to 0.16 μm for the 10N2.5E21LD epoxy.



(a) x100k magnification (b) x10k magnification

Figure 6.7.9: FEGSEM micrograph of hybrid 10N2.5E21 modified LD epoxy fracture surface.

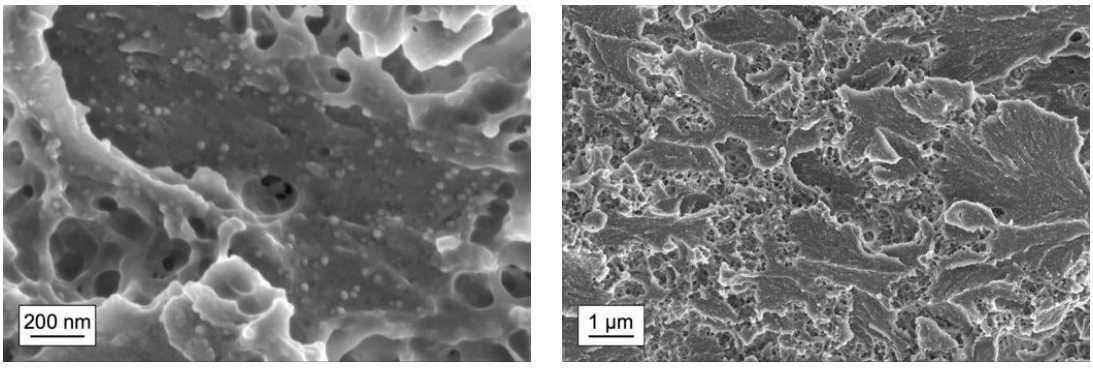
For the AD epoxy, the mean particle radius was measured to be 0.26 μm for the 2.5E21AD epoxy and 0.20 μm for the 10N2.5E21AD epoxy. Furthermore, the well dispersed silica nanoparticles did not show any debonding.



(a) x200k magnification (b) x10k magnification

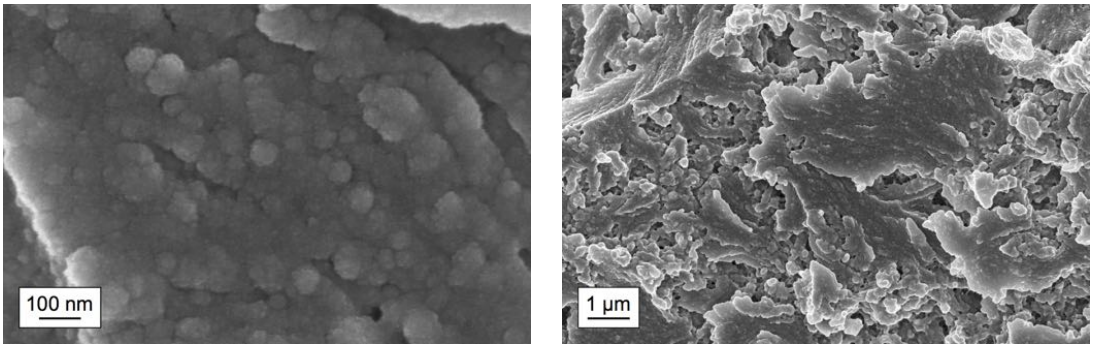
Figure 6.7.10: FEGSEM micrograph of hybrid 10N2.5E21 modified AD epoxy fracture surface.

The 10 wt% of silica nanoparticles in the hybrid 10N10E21 modified LD and AD epoxies were also well dispersed, as clearly seen in Figures 6.7.11 and 6.7.12. The SBM phase in the LD epoxy system shows significantly more void growth when the silica nanoparticles were present, compared to the 10 wt% E21 modified epoxy. For the AD epoxy system however, the degree of void growth appears to be lower. Note how there are less voids present in Figure 6.7.12(b) compared to Figure 6.7.11(b). This is reflected in the characteristic lengths as shown in Table 6.8.1, where the 10N10E21 modified LD epoxy shows an increase in characteristic length but not the AD epoxy.



(a) x150k magnification (b) x25k magnification

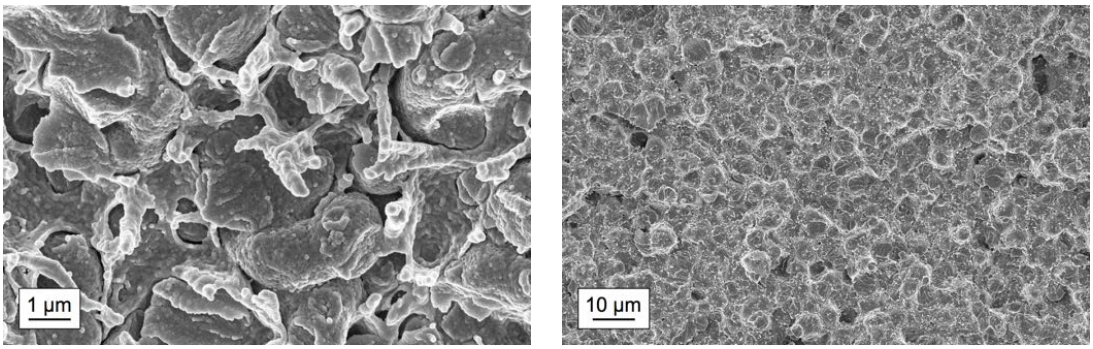
Figure 6.7.11: FEGSEM micrograph of hybrid 10N10E21 modified LD epoxy fracture surface.



(a) x250k magnification (b) x25k magnification

Figure 6.7.12: FEGSEM micrograph of hybrid 10N10E21 modified AD epoxy fracture surface.

The fracture surface of the 10N10E21 modified LH epoxy is shown in Figure 6.7.13. The particles of epoxy appear to be covered in the SBM, as observed in Figure 6.7.13(b). The epoxy inclusions did not show any debonding or void growth, as the mean particle radius of 1.56 μm, measured from the fracture surface, shows no change to that from the AFM, which was measured to be 1.63 μm. At higher resolution some SBM ligaments were observed to have debonded from the SBM matrix, as shown in Figure 6.7.13(a). Although there is some debonding observed, there is very little void growth, hence a low value of G_{IC} was measured.



(a) x25k magnification (b) x2.5k magnification

Figure 6.7.13: FEGSEM micrograph of hybrid 10N10E21 modified LH epoxy fracture surface.

6.7.2 E41 SBM

The E41 SBM was found to be less effective in toughening the LD and AD epoxy polymers compared to the E21 SBM, CTBN and CSR modifiers. The fracture surfaces (see Figures 6.7.14 and 6.7.15) show less debonding of the smaller SBM particles, and consequently these particles are unable to initiate plastic void growth. It is thought that the larger spherical particles would be expected to debond first, as the stress required to debond is lower for larger particles [110], hence relieving the constraint at

the crack tip. The larger micron-sized spherical particles failed in a brittle manner and the charging (observed as the horizontal black streaks) from the FEGSEM indicates that these particles are no longer attached to the epoxy matrix. These large particles are a mixture of SBM and epoxy, rather than pure epoxy, as the AFM micrographs identify them as soft. The failure of the particles in this manner is not thought to absorb significant energy as the E41 SBM has a low strength.

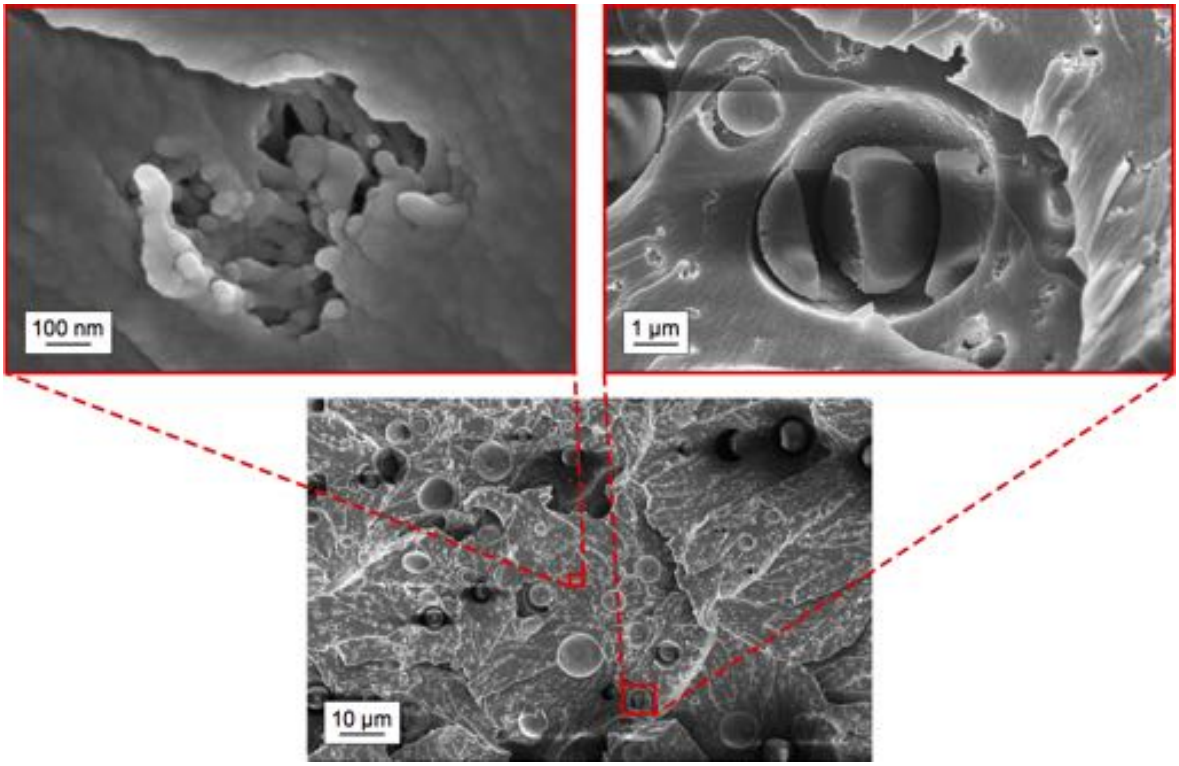
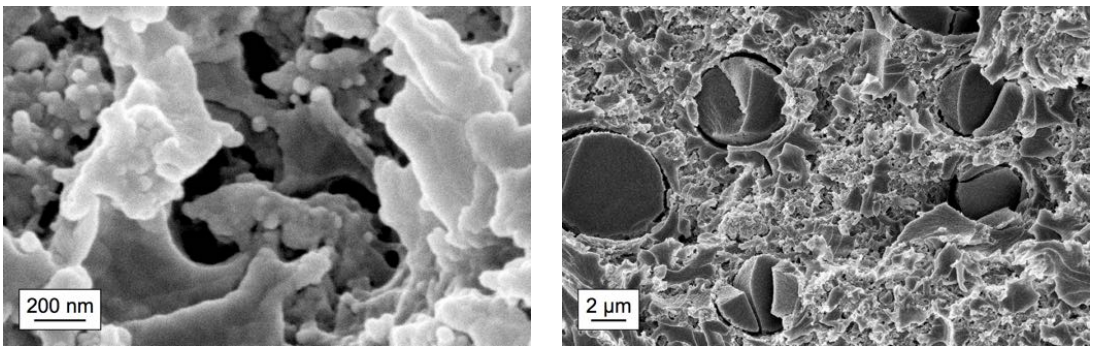


Figure 6.7.14: FEGSEM micrograph of 5 wt% E41 SBM modified LD epoxy fracture surface.

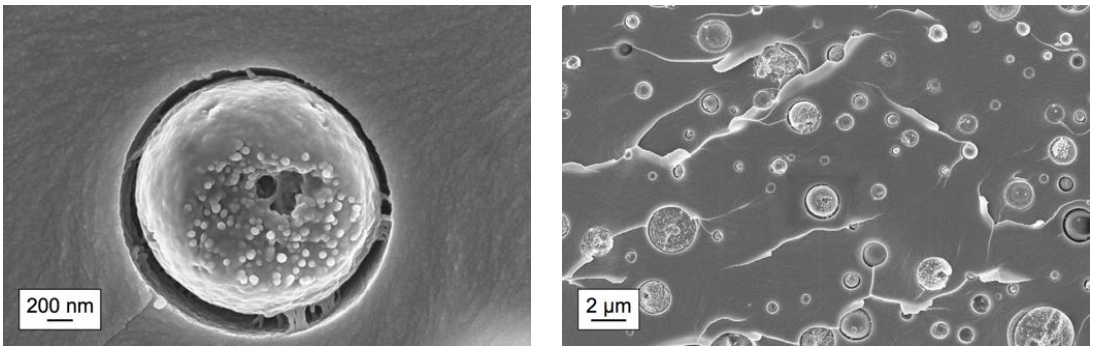


(a) x150k magnification (b) x10k magnification

Figure 6.7.15: FEGSEM micrograph of 10 wt% E41 SBM modified AD epoxy fracture surface.

The fracture surfaces of the E41 modified LH epoxy with a loading of up to, and including, 7.5 wt% show that the particles were well dispersed in the epoxy, as shown in Figure 6.7.16. The "raspberry"-like structures are much clearer from the FEGSEM

images than those observed using the AFM in Figure 6.2.10. The average particle diameter increased with E41 loading, from 0.76 μm to 1.22 μm as measured from FEGSEM images. These were slightly larger than the diameters calculated from the AFM phase images. This is expected as the microtome process cuts through the particles randomly, whereas the fracture surfaces have step changes which deviate toward higher stress concentrations at the equator [217]. The fracture surfaces show debonding of the SBM particles followed by plastic void growth. Particle debonding together with internal damage of the SBM particles relieves the constraint at the crack tip, hence allowing plastic void growth of the matrix to occur. Although particle cavitation does not occur, some internal damage of the particles can be seen in Figure 6.7.16(a). The difference in roughness of the fracture surfaces between the E21 and E41 is indicative of their relative fracture toughness values. The fracture surfaces of the E41 modified LH epoxies appeared much smoother, demonstrating less plastic deformation, and smaller voids were formed. There were also fewer fibrils connecting the particles to the epoxy matrix than for the E21 modified epoxies as the PB content (fibril is PB) is lower.



(a) x75k magnification (b) x10k magnification

Figure 6.7.16: FEGSEM micrograph of 5 wt% E41 SBM modified LH epoxy fracture surface.

Partially phase inverted structures were clearly visible on the fracture surfaces for LH epoxies modified with 10 wt% and above of E41, as shown in Figure 6.7.17. A close up of a particle within the epoxy-rich region shows the same "raspberry"-like structure as with the lower E41 SBM loadings. The particles in this region were much smaller than at lower concentrations (0.36 μm diameter for 10 wt%, compared to 0.82 μm diameter for 5 wt%). This is because the epoxy-rich regions can be viewed as areas with lower concentrations of E41, hence the smaller particles. The size of the epoxy inclusions within the SBM-rich regions measured from the fracture surface (0.74 μm diameter) correlates well with the sizes calculated from the AFM images (0.71 μm diameter) which suggest that there was no significant plastic deformation of the epoxy in the SBM rich region as expected. Both the epoxy and SBM particles were well dispersed within their respective matrices. Furthermore, the interface between the SBM-rich and

epoxy-rich regions show complete debonding, which suggests weak adhesion between the two phases.

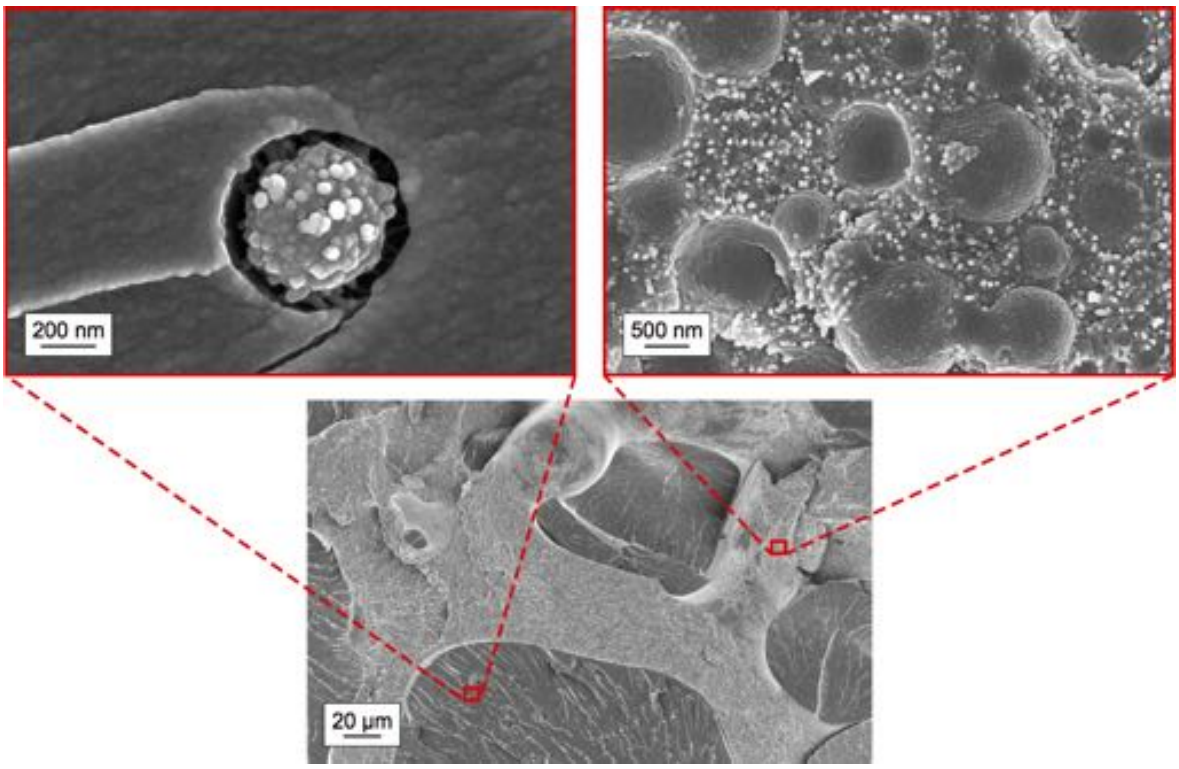
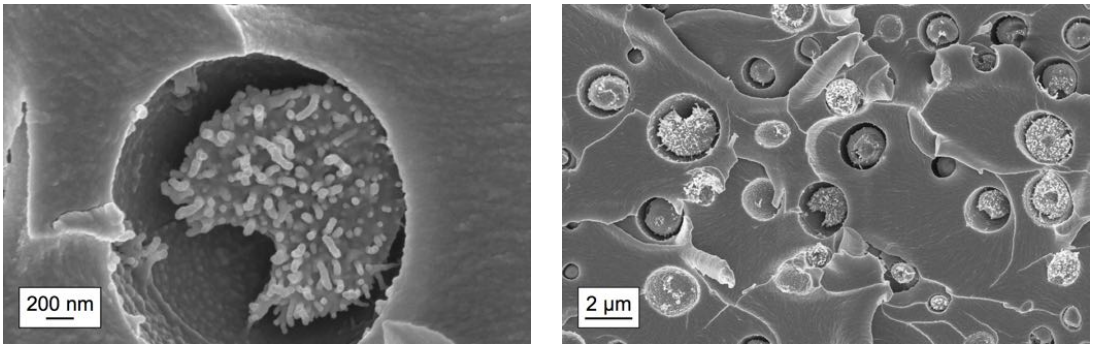


Figure 6.7.17: FEGSEM micrograph of 10 wt% E41 SBM modified LH epoxy fracture surface.

The 5 wt% E41 SBM modified LV epoxy fracture surface shows well dispersed particles of SBM, where approximately half have debonded from the epoxy. The particles appear to be damaged and the fibrils are no longer attached to the epoxy. The mean particle radii, measured from the fracture surface, show an increase, compared to that measured from the AFM images, of up 60% and the mean void radii show an increase of up to 90%. However, the toughening performance of the E41 SBM modified LV epoxies was limited.



(a) x30k magnification (b) x5k magnification

Figure 6.7.18: FEGSEM micrograph of 5 wt% E41 SBM modified LV epoxy fracture surface.

6.8 Characteristic lengths

The characteristic lengths of the SBM features, observed from the AFM and FEGSEM, were measured using a two point correlation function, as described in §4.2.7. The vector lengths corresponding to the characteristic lengths are summarised in Tables 6.8.1 to 6.8.4. The values from the AFM refer to the microstructure that has not been tested, and the values from the FEGSEM refer to the images from the SENB test sample fracture surfaces.

The calculated values of characteristic lengths of the E21 SBM modified epoxies were able to accurately reflect the qualitative observations observed from the AFM and FEGSEM images. The characteristic lengths increase with SBM content as the microstructure becomes more interconnected. The addition of silica nanoparticles also do not affect the lengths significantly. The characteristic lengths measured from the FEGSEM images were consistently higher than the values from the AFM, which is indicative of the plastic void growth mechanism occuring.

Table 6.8.1: Characteristic lengths of E21 SBM phase in modified LD and AD epoxies.

E21 (wt%)	LD (μm)		AD (μm)	
	AFM	FEGSEM	AFM	FEGSEM
2.5	0.65 ± 0.05	0.71 ± 0.04	–	0.81 ± 0.15
5	0.72 ± 0.12	0.79 ± 0.04	0.68 ± 0.07	1.08 ± 0.21
7.5	0.79 ± 0.13	–	–	–
10	0.83 ± 0.07	1.00 ± 0.09	1.05 ± 0.02	1.27 ± 0.09
10N2.5E21	0.60 ± 0.13	0.63 ± 0.08	0.50 ± 0.05	0.77 ± 0.17
10N10E21	0.77 ± 0.05	0.94 ± 0.02	1.20 ± 0.23	1.26 ± 0.19

Table 6.8.2: Characteristic lengths of E21 SBM phase in modified LH and LV epoxies.

E21 (wt%)	LH (μm)		LV (μm)	
	AFM	FEGSEM	AFM	FEGSEM
2.5	1.24 ± 0.01	1.65 ± 0.11	1.07 ± 0.17	2.00 ± 0.27
5	1.60 ± 0.50	2.02 ± 0.15	–	1.07 ± 0.09
5[1]	–	–	1.86 ± 0.08	1.87 ± 0.06
7.5	1.59 ± 0.15	2.32 ± 0.05	1.68[1]	–
10	1.88	2.44 ± 0.10	1.55 ± 0.20[1]	1.59 ± 0.01[1]
15	1.89 ± 0.07	2.42	–	–
10N10E21[1]	2.12 ± 0.30	3.55 ± 0.13	–	–

[1] Characteristic lengths of epoxy inclusions.

For microstructures with spherical features, such as the E21 modified LV epoxy and E41 modified epoxies, the characteristic lengths correspond to the average diameters of the

particles. As for the E21 modified epoxies, the size of the E41 SBM phase increases with SBM content. The characteristic lengths measured from the FEGSEM images were much larger than the voids measured from the AFM, indicating that significant plastic void growth had occurred. However, this did not translate to a high fracture energy.

Table 6.8.3: Characteristic lengths of E41 SBM phase in modified LD and AD epoxies.

E41 (wt%)	LD (μm)		AD (μm)	
	AFM	FEGSEM	AFM	FEGSEM
5	0.83 ± 0.06	3.71 ± 1.11	0.67 ± 0.02	1.41 ± 0.27
10	1.48 ± 0.23	4.71 ± 0.67	1.09 ± 0.01	1.82 ± 0.30

Table 6.8.4: Characteristic lengths of E41 SBM phase in modified LH and LV epoxies.

E41 (wt%)	LH (μm)		LV (μm)	
	AFM	FEGSEM	AFM	FEGSEM
2.5	1.16 ± 0.03	1.20 ± 0.09	0.81 ± 0.16	1.21 ± 0.21
5	1.36 ± 0.08	2.15 ± 0.04	1.14 ± 0.01	1.43 ± 0.19
7.5	1.49 ± 0.03	2.35 ± 0.22	1.48 ± 0.27	2.83 ± 0.28
10	–	0.75 ± 0.11	2.28 ± 0.02	–
10[1]	1.09	1.10	–	–
15[1]	1.06	0.81 ± 0.12	–	–

[1] Characteristic lengths of epoxy inclusions.

6.9 Modelling fracture energy

The major toughening mechanisms for the E21 and E41 SBM modified epoxy polymers were localised shear yielding and plastic void growth, initiated by the debonding of the SBM particles. As described in §2.5, the individual contributions from each toughening mechanism can be predicted and was compared to the experimental results. The parameters in the modelling of the SBM modified epoxies are tabulated in Table 6.9.1.

Table 6.9.1: Parameters used in modelling fracture energy.

Name	Variable	Units	Value			
			LH	LV	LD	AD
Particle radius	r_{pv}	nm	Table 6.2.1			
Void radius	r_{pv}	nm	$(1+\gamma_f)\, r_p$			
$v_{fv} - v_{fp}$	–	–	§6.2 and §6.7			
Plane strain compressive yield true stress	σ_{yc}	MPa	107	115	83	97
Uniaxial tensile yield true stress	σ_{yt}	MPa	89	91	66	77
Plane strain compressive fracture true strain	γ_f	–	0.91	0.98	0.84	1.16
Pressure-dependent yield stress parameter	μ_m	–	0.2			
Unmodified epoxy fracture energy	G_{CU}	kJ/m^2	0.1	0.1	0.2	0.2
Unmodified epoxy fracture toughness	K_{CU}	MPa m$^{1/2}$	0.6	0.5	0.9	0.9

The calculated and measured values of fracture energy are summarised in Tables 6.9.2 and 6.9.3 for the E21 and E41 SBM modified epoxies, respectively. The model was only applied to the nanocomposites with spherical particles, i.e. at low loadings. The term $v_{fv} - v_{fp}$ was determined experimentally from the AFM and FEGSEM micrographs.

The predicted values of G_{IC} for the E21 SBM modified LH, LV and AD epoxies were overpredicted compared to the experimentally measured values of G_{IC}, whereas they were underpredicted for the LD epoxies. This is because of the inherent error in modelling partially co-continuous structures as spherical particles. The shear band yielding contribution was observed to be higher for the LH and LV epoxies, while the void growth components for the LD and AD epoxies were significantly higher than the shear yielding component.

Table 6.9.2: Predicted and measured values of fracture energy for E21 modified epoxy polymers.

LH epoxy		ΔG_s	ΔG_v	G_{IC} predicted	G_{IC} experimental
wt%	v_f	J/m^2	J/m^2	kJ/m^2	kJ/m^2
0	0.00	0	0	0.1	0.1 ± 0.0
2.5	0.04	109	64	0.3	0.2 ± 0.0
5	0.08	173	113	0.4	0.3 ± 0.0
LV epoxy		ΔG_s	ΔG_v	G_{IC} predicted	G_{IC} experimental
wt%	v_f	J/m^2	J/m^2	kJ/m^2	kJ/m^2
0	0.00	0	0	0.1	0.1 ± 0.0
2.5	0.04	63	20	0.1	0.1 ± 0.0
LD epoxy		ΔG_s	ΔG_v	G_{IC} predicted	G_{IC} experimental
wt%	v_f	J/m^2	J/m^2	kJ/m^2	kJ/m^2
0	0.00	0	0	0.2	0.2 ± 0.0
0.5	0.01	88	134	0.4	1.2 ± 0.1
1	0.02	132	267	0.6	1.8 ± 0.1
2.5	0.04	215	663	1.1	2.3 ± 0.1
5	0.08	297	1312	1.8	2.8 ± 0.1
AD epoxy		ΔG_s	ΔG_v	G_{IC} predicted	G_{IC} experimental
wt%	v_f	J/m^2	J/m^2	kJ/m^2	kJ/m^2
0	0.00	0	0	0.2	0.2 ± 0.0
2.5	0.04	264	1033	1.5	1.1 ± 0.1
5	0.08	365	2042	2.6	2.8 ± 0.1

For the E41 SBM modified epoxies, a good agreement was found between the predicted and experimentally measured values of G_{IC}. In particular, the trends with SBM content were well predicted. The energy contributions for shear band yielding was the main toughening mechanism for the E41 SBM modified LH, LV and AD epoxies, whereas for the LD epoxy, plastic void growth was predicted to be the main toughening mechanism.

Table 6.9.3: Predicted and measured values of fracture energy for E41 modified epoxy polymers.

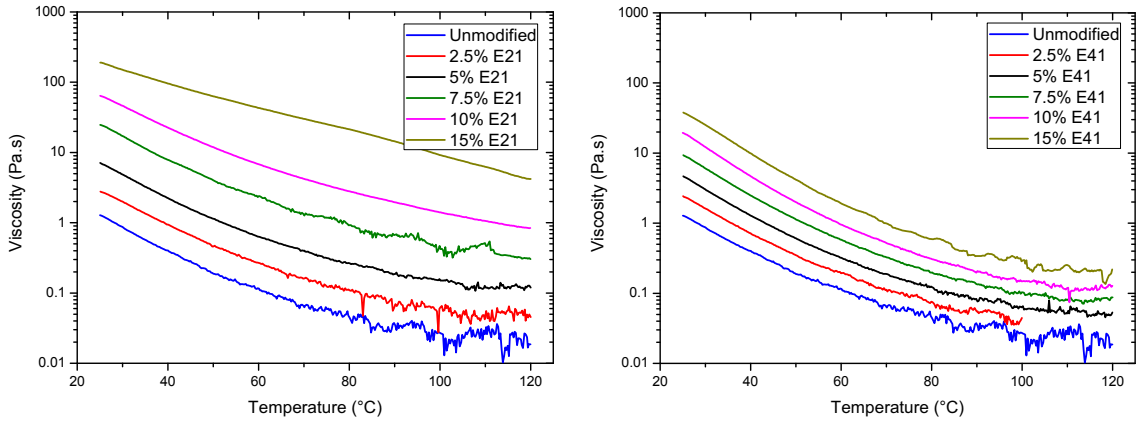
LH epoxy wt%	v_f	ΔG_s J/m^2	ΔG_v J/m^2	G_{IC} predicted kJ/m^2	G_{IC} experimental kJ/m^2
0	0.00	0	0	0.1	0.1 ± 0.0
2.5	0.04	115	19	0.2	0.2 ± 0.0
5	0.08	177	19	0.3	0.2 ± 0.0
7.5	0.12	229	66	0.4	0.2 ± 0.0
LV epoxy wt%	v_f	ΔG_s J/m^2	ΔG_v J/m^2	G_{IC} predicted kJ/m^2	G_{IC} experimental kJ/m^2
0	0.00	0	0	0.1	0.1 ± 0.0
2.5	0.04	64	45	0.2	0.1 ± 0.0
5	0.08	98	56	0.2	0.1 ± 0.0
7.5	0.12	123	90	0.3	0.1 ± 0.0
LD epoxy wt%	v_f	ΔG_s J/m^2	ΔG_v J/m^2	G_{IC} predicted kJ/m^2	G_{IC} experimental kJ/m^2
0	0.00	0	0	0.2	0.2 ± 0.0
2.5	0.04	133	663	1.0	1.0 ± 0.1
5	0.08	188	640	1.0	1.4 ± 0.1
10	0.15	255	515	1.0	1.2 ± 0.1
AD epoxy wt%	v_f	ΔG_s J/m^2	ΔG_v J/m^2	G_{IC} predicted kJ/m^2	G_{IC} experimental kJ/m^2
0	0.00	0	0	0.2	0.2 ± 0.0
2.5	0.04	163	152	0.5	0.5 ± 0.0
5	0.08	231	53	0.5	0.6 ± 0.0
10	0.15	314	112	0.6	0.4 ± 0.0

6.10 Carbon fibre composites

This section discusses the mechanical and fracture properties of carbon fibre reinforced polymer (CFRP) infused with E21 SBM modified epoxy matrix. The anhydride cured DGEBA (LH) epoxy was used for this study.

6.10.1 Rheology

The change in viscosity with temperature of the unmodified and E21 SBM modified LH epoxy resins are shown in Figure 6.10.1. A general trend of decreasing viscosity with temperature was observed with a logarithmic trend for all of the formulations tested. The viscosity also increases with increasing BCP content. The viscosities of the E41 modified epoxy resins were found to be lower than the E21 modified resins, as expected given the higher molecular weight of the E21 SBM BCP. For example, the addition of 10 wt% of E41 increases the viscosity by almost an order of magnitude, but 10 wt% of E21 increases the viscosity by a factor of 50. Although the viscosity is increased by the addition of the BCPs, it is still low enough that composite panels can be readily manufactured using RIFT. The results of the rheological tests were used to identify the optimum infusion temperatures which give a sufficiently low viscosity for the manufacture of the CFRP panels.



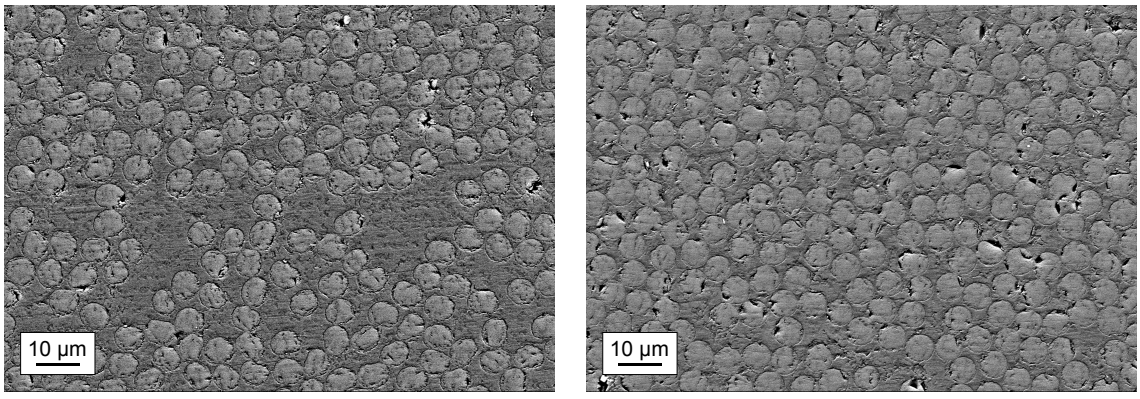
(a) E21 SBM (b) E41 SBM

Figure 6.10.1: Change in viscosity as a function of temperature for SBM modified LH epoxy resins.

6.10.2 Morphology

The morphology of the composites were examined using SEM on polished cross-sections of the samples. Backscattered electron micrographs of the unmodified and 10 wt% E21 modified CFRP are shown in Figure 6.10.2. Each fibre appears to be well wetted by the matrix, and the fibres were well dispersed. Apart from some defects at the interface between the fibre and matrix due to fibre damage from polishing, there were no visible voids on the polished cross-sections, even with 10 wt% of E21 added to the epoxy matrix. This shows that there is excellent consolidation of the fibre preforms by the resin. Unlike particulate modification with micron-sized particles, there was no filtering of the modifiers by the fibres as the SBM was initially dissolved, which then phase separate during curing (i.e. after infusion). The size of these phase separated particles (characteristic lengths of less than 2 μm) are smaller than the interfibre distances, hence would not be expected to be affected by the presence of the carbon fibres. This is an advantage as even the smallest gaps between very closely packed fibres can contain toughening particles and hence these regions will not be compromised by lacking a toughened matrix. This is essential for preventing microcracking.

The average fibre volume fraction of the CFRP laminates was measured from the polished cross-sections, and was calculated to be 56.9 $\pm$2.7%, typical of composite panels made using RIFT [76]. There was no significant variation between the different formulations used.



(a) Unmodified (b) 10 wt% E21

Figure 6.10.2: Backscattered electron micrograph showing cross-section for unmodified and E21 SBM modified LH CFRP.

6.10.3 Mechanical properties

The measured values of interlaminar shear strength, τ_{SBS}, flexural modulus, E_f, and mode I interlaminar fracture energy, $G_{IC(composite)}$ for the E21 modified LH CFRP are summarised in Table 6.10.1. The flexural modulus remains unchanged with increasing concentration of E21, as expected given that the flexural modulus is strongly dependent on the fibre volume fraction [184] and the fibre volume fraction is constant. The low variation in flexural modulus confirms that the laminates were manufactured to a consistent quality with regards to fibre volume fraction, as shown in Figure 6.10.2. A decrease in the interlaminar shear strength was observed which results from a reduction of matrix modulus with the addition of SBM. The increasing mismatch in stiffness between fibre and matrix with added SBM reduces the compression strength of a composite [275].

Table 6.10.1: Interlaminar shear strength, τ_{SBS}, flexural modulus, E_f, and propagation fracture energy, $G_{IC(composite)}$, for E21 SBM modified LH CFRP.

E21 (wt%)	τ_{SBS} (MPa)	E_f (GPa)	$G_{IC(composite)}$ (kJ/m^2)
Unmodified	40 ± 1	27 ± 1	0.30 ± 0.01
2.5	42 ± 1	29 ± 1	0.43 ± 0.01
5	38 ± 0	28 ± 1	0.39 ± 0.02
7.5	30 ± 1	27 ± 2	0.38 ± 0.02
10	27 ± 1	28 ± 1	0.31 ± 0.01

6.10.4 Fracture properties

The 'R-curves' for the unmodified and E21 SBM modified LH CFRP are shown in Figure 6.10.3. It can be seen from the R-curves that a steady state value has been reached, which correspond to the propagation fracture energy. The increase in fibre bridging as the crack propagates is balanced by the breaking of the carbon fibres, hence a steady state value is achieved.

The mean propagation fracture energy for the unmodified LH CFRP was measured to be 0.30 kJ/m^2. This is an increase of 200% compared to the bulk material, which can be attributed to the additional fibre pullout and bridging toughening mechanisms in the composite. The maximum $G_{IC(composite)}$ for propagation was measured for the 2.5 wt% E21 SBM modified matrix, and resulted in an increase to 0.43 kJ/m^2. Further addition of E21 resulted in a decrease in the fracture energy. This decrease is partly due to a reduction in the amount of fibre bridging, as the modified matrix can have stronger

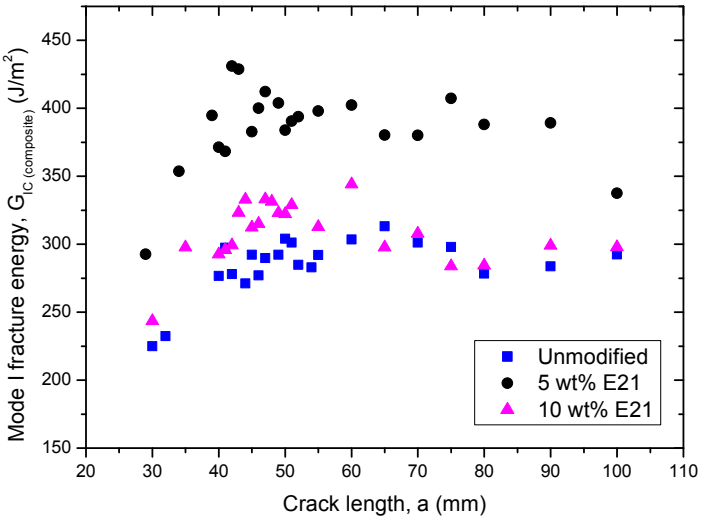


Figure 6.10.3: R-curve showing mode I fracture energy, $G_{IC(composite)}$, versus crack length, a, for unmodified and E21 SBM modified LH CFRP.

fibre/matrix adhesion [84]. Figure 6.10.4 can be used to compare the amount of fibre bridging by comparing the relative difference between the initiation and propagation fracture energy values, i.e. the increase in height from the R-curves.

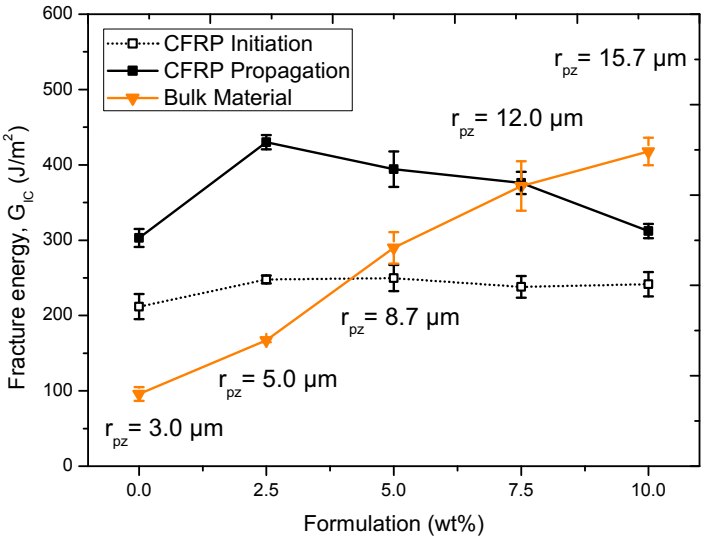


Figure 6.10.4: Propagation G_{IC} and initiation G_{IC} for E21 SBM modified LH CFRP, showing plastic zone radius (r_{pz}) calculated using the Irwin model for the bulk materials.

The increase in toughness of the bulk epoxy polymer from the addition of E21 SBM was not transferred to give a significant increase in interlaminar fracture energy for the CFRP. Figure 6.10.4 compares the composite fracture energy, $G_{IC(composite)}$ to the bulk material fracture energy, G_{IC}. The initiation values of $G_{IC(composite)}$ show no significant change even though the fracture energy of the bulk material, and hence of the composite matrix, is linearly increasing.

This can be explained by considering the plane strain plastic zone radius (r_{pz}) for the bulk materials, which can be calculated using the Irwin model [276]. From Figure 6.10.4, it is clear that the plastic zone sizes at higher concentrations are large in comparison with the inter-fibre distances, which are in the order of 10 μm. This means that the plastic zone will be inhibited from growing by the presence of the stiff fibres and explains the discrepancy between the CFRP initiation and bulk fracture energies [191, 192]. Hunston *et al.* [191] showed that brittle polymers with G_{IC} values less than 200 J/m^2 benefit the most from fibre reinforcement. In their tests, the tough matrices had incomplete transfer of toughness attributed to the crack tip deformation zone restricted by the closely packed fibres. Bradley *et al.* [192] established that matrices with G_{IC} below 500 J/m^2 showed linear correlation with the $G_{IC(composite)}$. Above a matrix G_{IC} = 500 J/m^2, the transfer in toughness is less. The transition between the two behaviours occurs approximately at the point where the deformation zone is equal to the inter-fibre spacing, as shown in Figure 6.10.4. Similar behaviour was observed in the present work, where the interlaminar fracture energy was lower than the bulk G_{IC} when the plastic zone size was above the inter-fibre spacing. Plastic deformation will also be limited by the fact that the fibres are significantly stiffer than the matrix, hence constraining the crack tip deformation zone [189].

Quaresimin et al. [277] attributed poor fracture performance for their E20 SBM modified CFRP composites to the quality of the laminate (E20 SBM has a lower molecular weight compared to E21 SBM). They observed a significant number of voids, presumably caused by the entrapment of solvent that they used for processing to counteract the increase in viscosity. They also noticed that the SBM phase-separated into micron-sized particles instead of nanostructures. However, such effects were not observed in the present work as a co-continuous microstructure was formed instead.

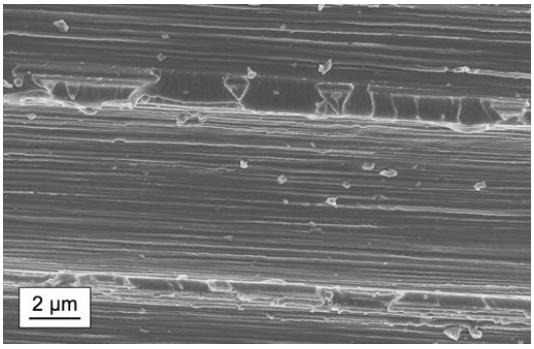
6.10.5 Fractography

The fracture surface of the unmodified CFRP, as shown in Figure 6.10.5(a), shows a relatively clean fibre surface, indicating an interfacial failure resulting from poor fibre-matrix adhesion. The appearance of the epoxy matrix between the individual fibres was similar to the bulk unmodified epoxy. River lines and step changes in the crack level were visible throughout the entire specimen. The weak interfacial adhesion also explains the fibre bridging and pullout observed during the test and on the fracture surfaces, although this is somewhat limited due to the woven nature of the fabrics.

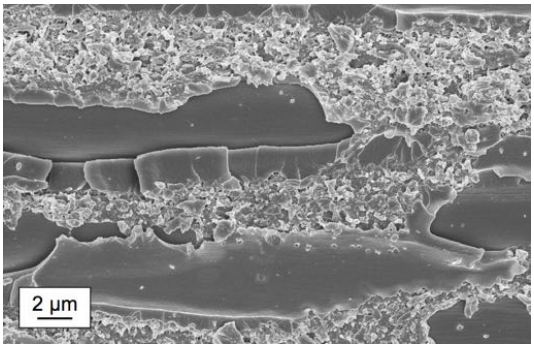
When the LH epoxy matrix was modified with E21 SBM, a much rougher fracture sur-

face was observed with very few fibres visible, suggesting that a cohesive failure through the matrix had occurred, as shown in Figures 6.10.5(b) to 6.10.5(d). The microstructure was also slightly different from the bulk material in that the co-continuous structure was more evident. This can be explained by the space constraint of the tightly packed fibres which impedes the mobility of the SBM, and hence the SBM phase separates as a co-continuous structure.

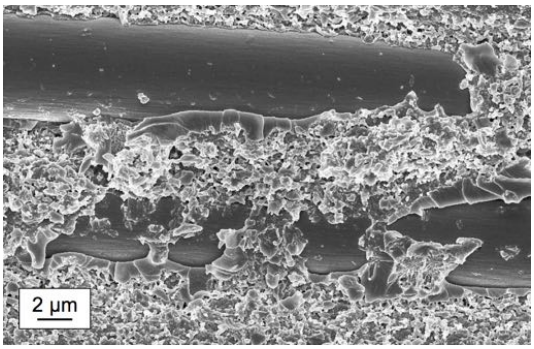
There was also a lack of fibre bridging observed on the fracture surfaces, which is reflected in the relatively small R-curves as shown in Figure 6.10.3. This reduction in fibre bridging was also visibly noticeable during testing. The main toughening mechanisms can be identified from the fracture surfaces, as shown in Figure 6.10.5, as debonding and plastic void growth around the SBM structure of the modified matrices. This is similar to the findings for the bulk material. However, any improvements in the matrix fracture energy could not be translated fully to the composite fracture energy because the plastic zone size is restricted by the relatively small inter-fibre distances as described in the previous section.



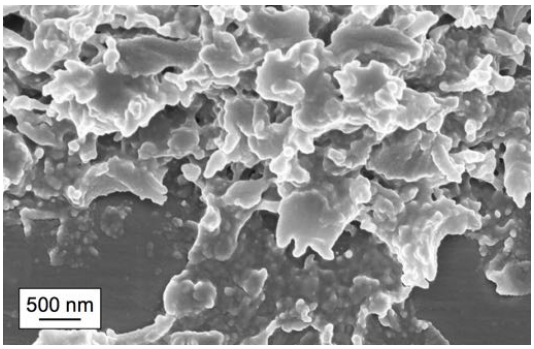
(a) Unmodified



(b) 5 wt% E21



(c) 10 wt% E21 (x10k magnification)



(d) 10 wt% E21 (x50k magnification)

Figure 6.10.5: FEGSEM micrograph of unmodified and E21 SBM modified CFRP fracture surface.

6.11 Conclusions

Two asymmetric triblock copolymers of polystyrene-b-polybutadiene-b-poly(methyl methacrylate) (SBM) were used to modify four epoxy systems; a polyether-amine cured DGEBA (LD), a polyether-amine cured DGEBA/F (AD), an anhydride cured DGEBA (LH) and an anhydride cured cycloaliphatic epoxy (LV). The two SBM modifiers have different ratios of polybutadiene and molecular weight; E21 SBM has a higher PB content and molecular weight than E41 SBM. The tensile, compression and fracture properties of the SBM modified epoxy polymers were measured and compared. Silica nanoparticles were then added to the E21 modified epoxies to create hybrid modified epoxies, and the effect of this on the mechanical properties were evaluated.

For the LD, AD and LH epoxies, the E21 SBM phase separated as a network of small agglomerates. The characteristic lengths of these microstructures increased with the SBM content, until eventually co-continuous structures were formed from a loading of 7.5 wt% and above. This resulted in a significant increase in G_{IC} from 0.2 kJ/m^2 to 3.4 kJ/m^2, and 0.2 kJ/m^2 to 3.1 kJ/m^2 for the 10 wt% modified LD and AD epoxies, respectively. The G_{IC} of the E21 modified LH epoxy increased linearly from 0.1 kJ/m^2 to 0.5 kJ/m^2 at a loading of 15 wt%.

The addition of 10 wt% of silica nanoparticles to the 2.5 wt% and 10 wt% E21 modified LD and AD epoxies did not significantly change the morphology of the SBM phase. The silica nanoparticles were well dispersed in the epoxy. A further increase in G_{IC} was observed with the 10N10E21 modified LD epoxy, up to 4.5 kJ/m^2, but not for the AD epoxy system, where no synergy was observed. This is due to more extensive plastic void growth and shear yielding in the hybrid modified LD epoxy. The hybrid 10N10E21 modified LH epoxy showed a change in morphology from a co-continuous to a partially phase inverted structure, where the silica nanoparticles were well dispersed in the epoxy-rich domains. This resulted in a decrease in fracture energy, due to premature failure of the weaker SBM phase being unable to bridge the crack opening. The E21 SBM modified LV epoxy showed well dispersed spherical particles at 2.5 wt%, which transitions into a partially phase inverted structure from 5 wt% and above as stability problems between the SBM and epoxy begin to arise.

For the LD and AD epoxies, the E41 SBM phase separated into a multi-scale material consisting of micron sized soft spherical particles and small agglomerates. The E41 SBM was less effective in toughening the LD and AD epoxies; maximum G_{IC} values were measured to be 1.4 kJ/m^2 and 0.6 kJ/m^2, for the 5 wt% modified LD and AD

epoxies respectively. In the E41 modified LH epoxies, a "raspberry"-like microstructure was observed, i.e. spheres of PB on the surface of a core of PS. At 10 wt% and above of E41 SBM, a partially phase inverted structure was observed instead. The fracture toughness of the E41 SBM modified LH epoxies remained constant with loading up to the point where partial phase inversion occurs. A sharp increase in G_{IC} to a maximum of 1.0 kJ/m^2 was then measured, corresponding to an increase of 1000%. A similar trend was found for the LV epoxy system, where well dispersed spherical particles of E41 SBM were observed up to 7.5 wt%. At a loading of 10 wt%, the structure becomes fully phase inverted and porous.

The characteristic lengths and particle diameters were measured for the various SBM modified epoxies, and was found to increase with SBM content. The main toughening mechanism observed from the fracture surfaces was debonding of the SBM phase from the matrix, which initiated plastic void growth of the epoxy. This was also observed as an increase in characteristic length, compared to the AFM images. As the voids around the E21 SBM phase grew, drawn fibrils of PB were formed, indicating a strong adhesion of the E21 SBM to the epoxy matrix. For the E41 SBM particles, these fibrils appear to be broken, representative of poor adhesion to the matrix. This was also evident in the phase inverted E41 modified structures, where the boundaries between the SBM-rich and epoxy-rich domains show complete debonding. The silica nanoparticles in the hybrid E21 SBM-NS modified epoxies did not show any debonding or plastic void growth.

The T_g of the E21 and E41 SBM modified epoxies was found to be consistent up to a loading of 15 wt%. However, the further addition of 10 wt% of silica nanoparticles reduced the T_g of the hybrid LD and LH epoxies, which was due to SBM remaining dissolved in the epoxy. This was also observed as a decrease in volume fraction from the AFM micrographs and showed good agreement with the values calculated with the Fox equation. The Young's modulus and tensile strength decreased with SBM content. The further addition of silica nanoparticles was able to restore some of the stiffness lost by the addition of SBM to the epoxies, but further reduced the tensile strength due to enhanced cavitation or debonding of the SBM phase. The compressive properties showed similar trends as the tensile tests. Polished sections of the compressed samples tested to the strain softening region show shear banding which became more diffuse with SBM content. This indicates more localised shear yielding around the SBM phases.

Continuous carbon-fibre reinforced-polymer (CFRP) composites with a quasi-isotropic lay-up were manufactured using resin infusion under flexible tooling (RIFT). The com-

posite panels were free of voids and had a typical fibre volume fraction of $56.9 \pm 2.7\%$, as measured from polished cross-sections. The toughness improvements shown in the E21 SBM modified LH bulk epoxies were not transferred into a CFRP composite system. The main toughening mechanisms for a fibre composite; i.e. fibre bridging, fibre debonding and fibre pullout, were suppressed when the matrix was modified with E21 due to increased fibre-matrix adhesion. The crack tip deformation zone was also restricted by the tightly packed fibres at higher SBM contents such that the measured composite fracture energy reached a plateau at approximately 0.4 kJ/m^2.

Chapter 7

Symmetric triblock copolymer modified epoxy polymers

7.1 Introduction

This chapter investigates the modification of two epoxy polymers using two commercially available symmetric acrylic triblock copolymers, 'Nanostrength M52N' and 'Nanostrength M22N' from Arkema, France. The BCP used is a poly(methyl methacrylate)-b-poly(butylacrylate)-b-poly(methyl methacrylate), or MAM for short. The M52N MAM has a higher PBuA block ratio and lower molecular weight than the M22N MAM. The epoxy systems used are the DGEBA and DGEBA/F epoxy resins cured with a polyether-amine curing agent, denoted as LD (LY556/D230) and AD (AY105/D230) respectively. Silica nanoparticles (NS) were also added to the M52N MAM modified epoxies to create hybrid toughened epoxies, consisting of soft and rigid phases. These are denoted as 10NyM52N, where the 10N refers to 10 wt% of silica nanoparticles and y refers to the wt% of M52N. The formulations of the MAM and MAM-NS hybrid modified epoxies studied in this Chapter are summarised in Table 7.1.1. The hybrid M22N-NS MAM bulk epoxy material could not be manufactured due to a chemical reaction resulting from the addition of the nanosilica masterbatch to the MAM-epoxy mixture which caused the mixture to start curing before the curing agent was added.

Table 7.1.1: Summary of MAM formulations used in this chapter.

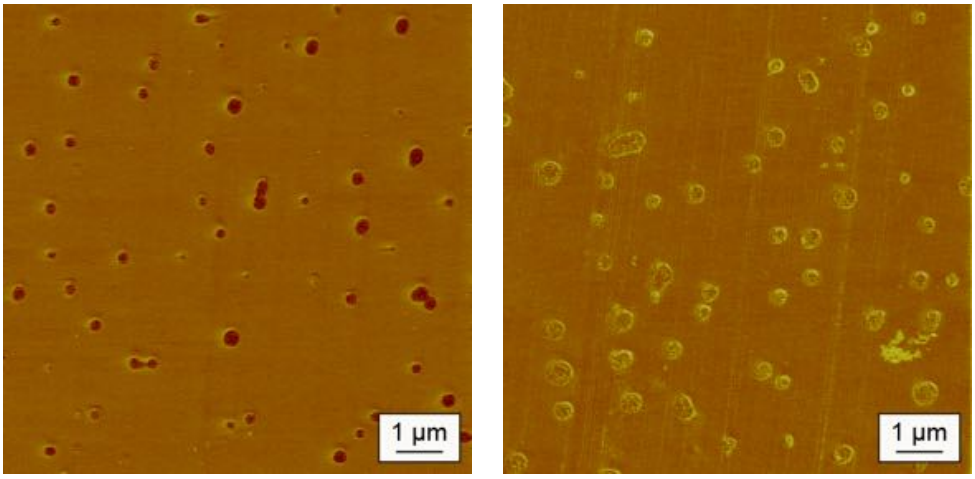
Epoxy system	Modifier M52N MAM wt%	NS wt%	Abbreviation	Modifier M22N MAM wt%	Abbreviation
Polyether-amine cured DGEBA (LD)	1	–	1M52NLD	–	–
	2.5	–	2.5M52NLD	2.5	2.5M22NLD
	5	–	5M52NLD	5	5M22NLD
	7.5	–	7.5M52NLD	7.5	7.5M22NLD
	10	–	10M52NLD	10	10M22NLD
	20	–	20M52NLD	–	–
	2.5	10	10N2.5M52NLD	–	–
	7.5	10	10N7.5M52NLD	–	–
	10	10	10N10M52NLD	–	–
Polyether-amine cured DGEBA/F (AD)	2.5	–	2.5M52NAD	2.5	2.5M22NAD
	5	–	5M52NAD	5	5M22NAD
	7.5	–	7.5M52NAD	7.5	7.5M22NAD
	10	–	10M52NAD	10	10M22NAD
	2.5	10	10N2.5M52NAD	–	–
	10	10	10N10M52NAD	–	–

7.2 Morphology

The AFM phase images of the unmodified epoxies were shown in Figure 5.2.1 in §5.2. The unmodified epoxy is a single phase thermoset material, and thus was found to be homogeneous and featureless.

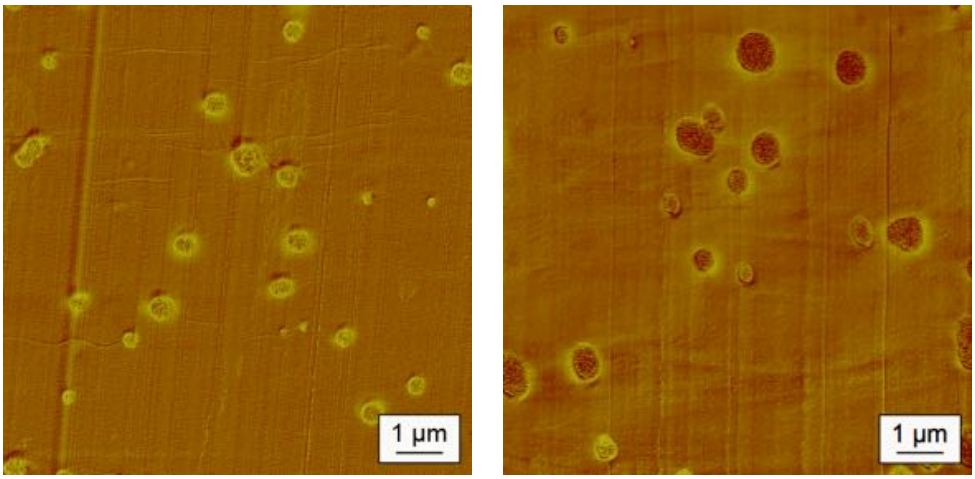
7.2.1 M52N MAM

The M52N MAM BCP was initially dissolved in the epoxy resin and phase separates during the cure process into well dispersed spherical particles at concentrations of 5 wt% and below (see Figures 7.2.1 and 7.2.2). The spherical particles can be characterised by the light rings around the particles, indicating different materials as the shell and the core. The mean particle radius increased with the weight percentage, as summarised in Table 7.2.1. For the LD epoxy, the particle radius increased from 0.12 μm at 2.5 wt% to 0.16 μm at 5 wt%. For the AD epoxy, the particle radius increased from 0.16 μm to 0.25 μm. The shells have a mean thickness of 27$\pm$7 nm and did not change with weight percentage or epoxy system.



(a) 2.5 wt% M52N (b) 5 wt% M52N

Figure 7.2.1: AFM phase micrographs of M52N MAM modified LD epoxy polymer.



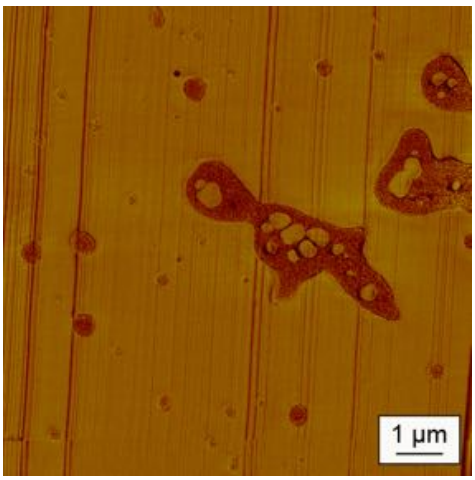
(a) 2.5 wt% M52N (b) 5 wt% M52N

Figure 7.2.2: AFM phase micrographs of M52N MAM modified AD epoxy polymer.

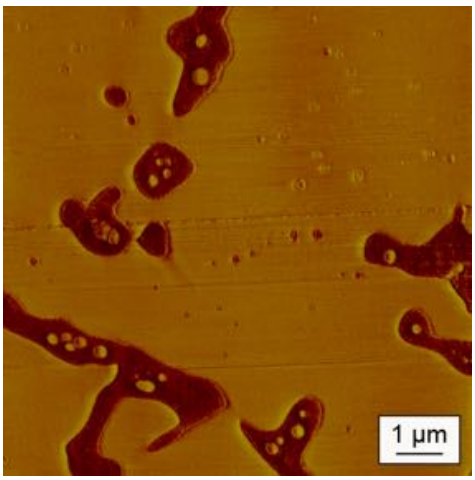
Above a loading of 5 wt% M52N MAM, a combination of co-continuous and spherical particles was observed, as shown in Figures 7.2.3 and 7.2.4. The co-continuous microstructure refers to a morphology where the MAM-rich and epoxy-rich phases are both continuous in nature. The width of the MAM-rich phases range from 200 nm to 2 μm. The mean radius of the spherical particles was approximately 95 nm at 7.5 wt% and decreased to 80 nm at 10 wt%. Increasing the concentration of M52N in the epoxy increases the characteristic length of these M52N regions, as shown in Table 7.2.1, and decreases the number of smaller particles.

Table 7.2.1: Mean particle radius and characteristic lengths of M52N MAM phases in epoxy.

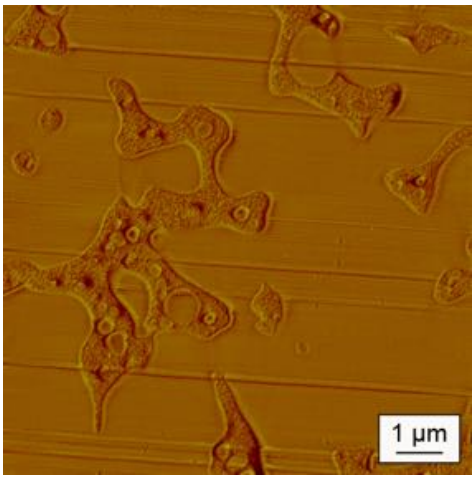
Content (wt%)		Particle radius (μm)	
MAM	NS	LD	AD
2.5	0	0.12 ± 0.01	0.16 ± 0.00
5	0	0.16 ± 0.00	0.25 ± 0.00
2.5	10	0.12 ± 0.01	0.13 ± 0.02
Content (wt%)		Characteristic length (μm)	
MAM	NS	LD	AD
2.5	0	0.40 ± 0.03	0.52 ± 0.05
5	0	0.51 ± 0.05	0.76 ± 0.09
7.5	0	1.58 ± 0.05	1.25 ± 0.46
10	0	2.47 ± 0.22	2.51 ± 0.10
20	0	2.05 ± 0.32	–
2.5	10	0.35 ± 0.02	0.42 ± 0.15
7.5	10	1.78 ± 0.04	–
10	10	1.95 ± 0.30	1.50 ± 0.30



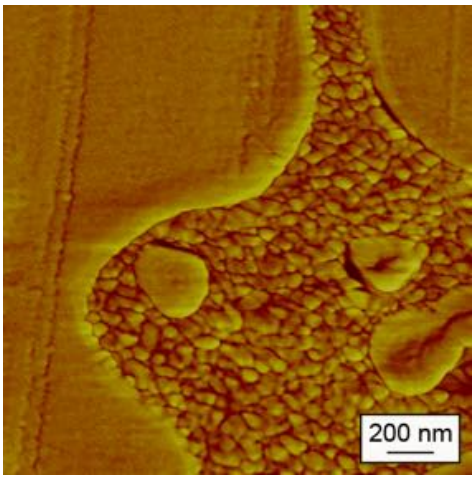
(a) 7.5 wt% M52N



(b) 10 wt% M52N

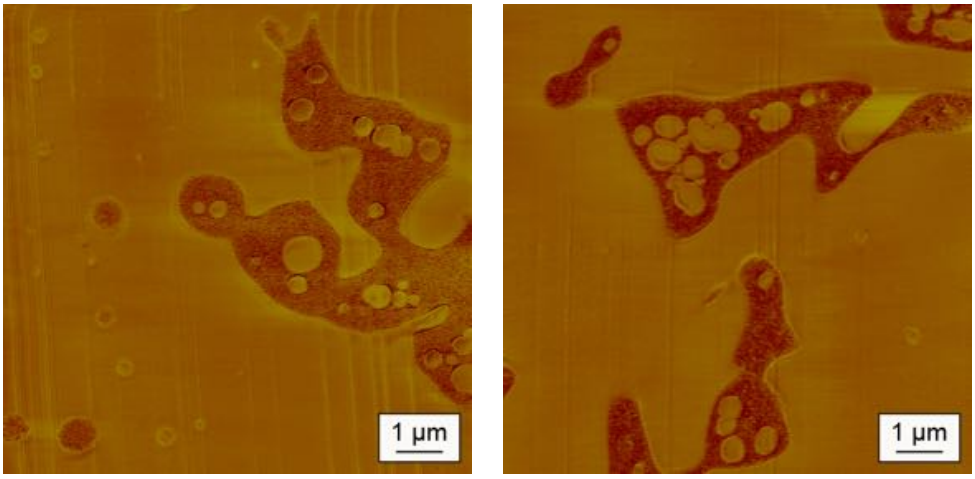


(c) 20 wt% M52N



(d) 20 wt% M52N

Figure 7.2.3: AFM phase micrographs of M52N MAM modified LD epoxy polymer.



(a) 7.5 wt% M52N (b) 10 wt% M52N

Figure 7.2.4: AFM phase micrographs of M52N MAM modified AD epoxy polymer.

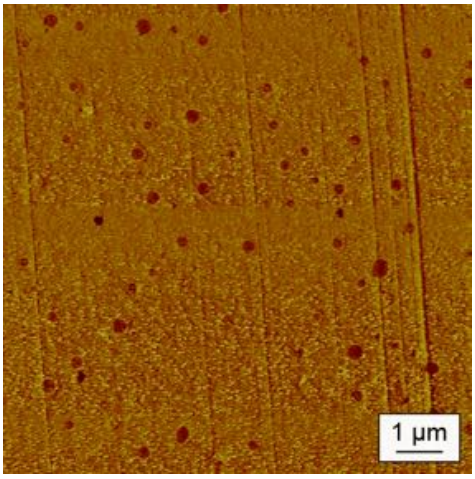
Further addition of M52N MAM results in a partially phase inverted structure where there are large MAM-rich regions containing epoxy particles. The mean radius of these epoxy inclusions in the MAM-rich regions did not change with MAM content, as shown in Table 7.2.2. For example, the epoxy inclusions have a mean radius of 0.11±0.01 μm and 0.18±0.02 μm for the 10 wt% M52N MAM modified LD and AD epoxies, respectively.

Table 7.2.2: Mean radius of epoxy inclusions in M52N MAM modified LD and AD epoxy polymers.

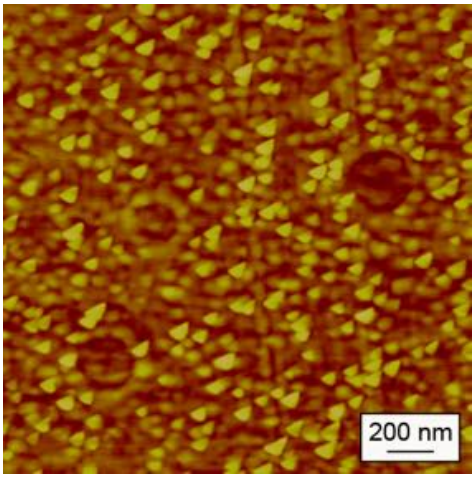
Content (wt%)		Epoxy inclusion radius (μm)	
MAM	NS	LD	AD
7.5	0	0.14 ± 0.01	0.19 ± 0.00
10	0	0.11 ± 0.01	0.18 ± 0.02
20	0	0.16 ± 0.01	–
7.5	10	0.11 ± 0.02	–
10	10	0.13 ± 0.02	0.16 ± 0.01

10 wt% of 20 nm silica nanoparticles were added to the M52N MAM modified epoxies to create hybrid modified epoxies, as shown in Figures 7.2.5 and 7.2.6. The addition of these nanoparticles did not significantly affect the size of the MAM particles, as summarised in Table 7.2.1. The silica nanoparticles were well dispersed when added to the 2.5 wt% M52N MAM modified epoxies, however, became increasingly more agglomerated as the wt% of MAM was increased; e.g. compare Figure 7.2.5(a) with Figure 7.2.5(d). The 10N7.5M52N modified LD epoxy shows agglomerates of silica of approximately 1 μm by 2 μm and some dispersed individual particles. For the 10N10M52N modified LD epoxy, the silica agglomerated into even larger clusters of up to 5 μm by 1 μm. It should also be noted that sub-surface silica nanoparticles can be seen in the higher magnification image of the 10N2.5M52N modified LD epoxy, as

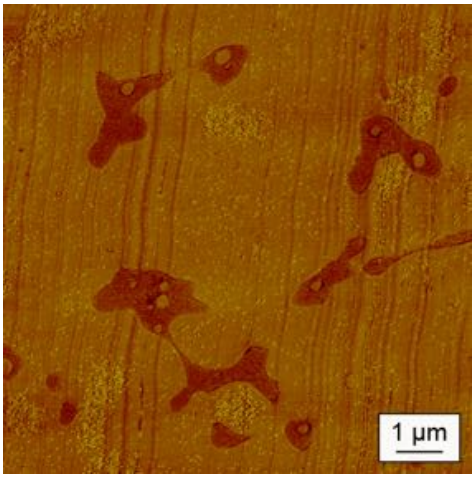
shown in Figure 7.2.5(b). The dispersion will be quantified and discussed in Section §7.2.3.



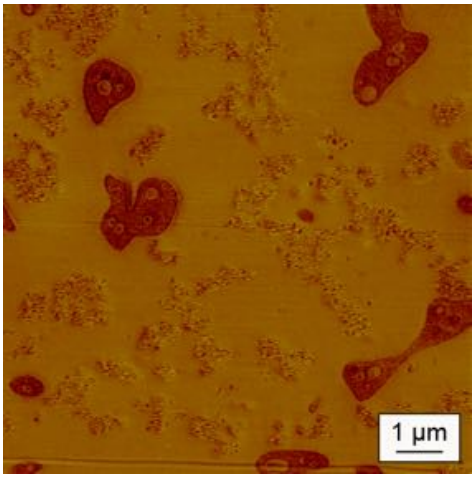
(a) 10N2.5M52N



(b) 10N2.5M52N

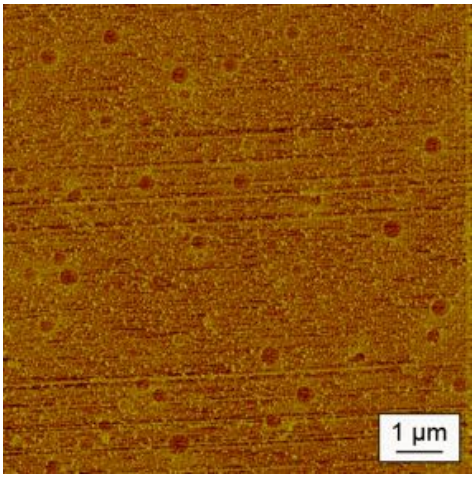


(c) 10N7.5M52N

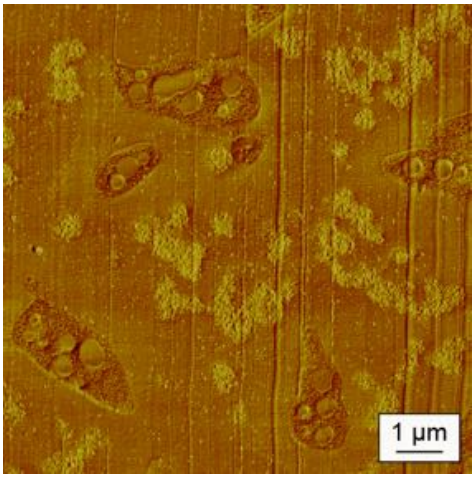


(d) 10N10M52N

Figure 7.2.5: AFM phase micrographs of M52N MAM-NS hybrid modified LD epoxy polymer.



(a) 10N2.5M52N



(b) 10N10M52N

Figure 7.2.6: AFM phase micrographs of M52N MAM-NS hybrid modified AD epoxy polymer.

Table 7.2.3 compares the volume fractions as measured from the AFM phase images to the known amounts added. The mean values of measured volume fraction show good agreement with the theoretical values for the M52N modified LD epoxy system up to 10 wt%. This indicates an almost complete phase separation of the M52N MAM from the epoxy during cure, which is confirmed by the T_g values which show no change with MAM content. Only the 20 wt% M52N modified LD epoxy shows a lower volume fraction than expected, a measured value of 17 vol% from the AFM phase image compared to the 28 vol% added. Furthermore, the MAM modified AD epoxies tended to have lower than the expected values of volume fraction, except for a content of 10 wt%. This causes the T_g of the modified AD epoxy to increase, as discussed in the following section.

Table 7.2.3: Comparison of theoretical and measured values of volume fraction.

MAM Type	Content (wt%)		MAM Volume fraction (vol%)		
	MAM	NS	Calculated	Measured LD	Measured AD
M52N	2.5	0	3.9	2.5 ± 0.3	2.4 ± 0.1
	5	0	7.7	5.9 ± 0.8	4.4 ± 0.4
	7.5	0	11.4	11.1 ± 1.4	8.3 ± 3.2
	10	0	15.0	12.6 ± 4.0	14.5 ± 0.6
	20	0	28.4	17.0 ± 1.7	–
	2.5	10	4.1	2.4 ± 0.2	3.3 ± 0.3
	7.5	10	11.8	7.9 ± 1.4	–
	10	10	15.5	8.6 ± 3.2	8.8 ± 4.2
M22N	10	0	15.0	13.5 ± 1.4	10.5 ± 1.0

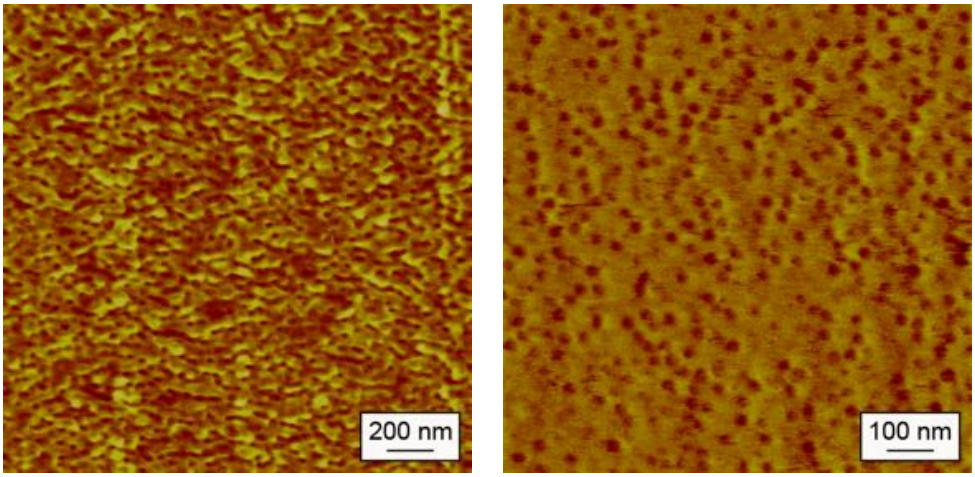
The addition of silica nanoparticles decreased the volume fraction measured, indicating phase separation was suppressed. The somewhat high standard deviations and errors for the higher wt% MAM is a result of the small maximum scan size of the AFM used. The necessary magnification level was not achievable to include the required number of MAM rich regions obtain a reliable estimate of the volume fraction.

7.2.2 M22N MAM

The cured M22N MAM modified epoxies were optically translucent up to the 10 wt% used in this study. The AFM phase images show two different morphologies for the 10 wt% M22N modified LD and AD epoxies. For the LD epoxy, worm-like micelles with a size of up to 250 nm in length and approximately 20 nm in diameter were observed, as shown in Figure 7.2.7(a). Chen [54] postulated that the worm-like micelles might have a 3D bicontinuous gyroid structure, or be co-continuous. However, this would be

difficult to show with a 2D microscopy technique such as AFM or TEM. Laboratory grade X-ray microtomography techniques do not have sufficient resolution to resolve the relatively small dimensions of the worm-like micelles.

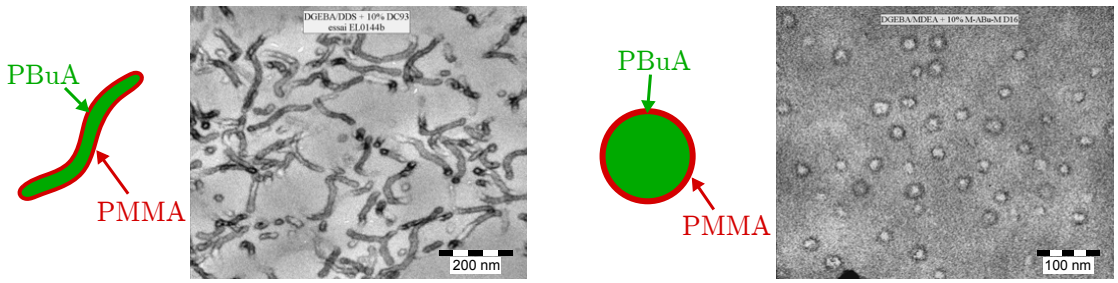
For the AD epoxy, well dispersed soft particles with an average radius of 9 nm were observed, as shown in Figure 7.2.7(b). The particles were too small to determine if these particles were spherical micelles, had a core-shell structure or phase separated as homogeneous MAM. Indeed, the translucency of the M22N MAM modified epoxies was due to the nanoscale structures.



(a) LD epoxy (b) AD epoxy

Figure 7.2.7: AFM phase micrographs of 10 wt% M22N MAM modified epoxy polymers.

Several other authors have also reported such morphologies for MAM modified epoxies [54, 278]. The microstructure of the worm-like micelles and core-shell particles can be determined by considering the amphiphilic nature of the block copolymers. The PMMA block is miscible in the epoxy and "epoxy-philic", whereas the PBuA block is immiscible and "epoxy-phobic". Hence the PBuA block would naturally self-assemble as the core, with the PMMA block as the shell, as shown in Figure 7.2.8.



(a) (b)

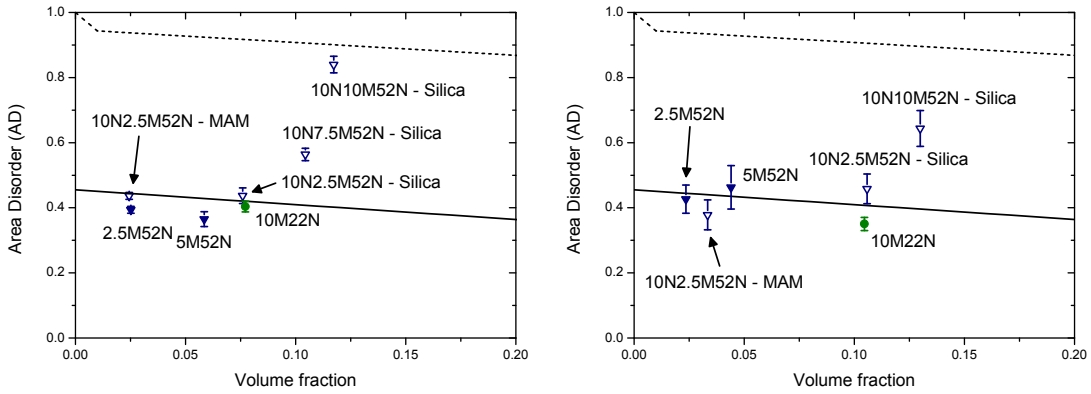
Figure 7.2.8: TEM images of self-assembled nanostructures in epoxy: (a) Worm-like micelles (b) Core-shell particle. Reproduced from [278].

The mean values of measured volume fraction show good agreement with the calculated values for the 10 wt% M22N modified LD epoxy only, as shown in Table 7.2.3. The M22N modified AD epoxy had more MAM remaining dissolved in the epoxy, which has also resulted in a small increase in T_g, as will be discussed in the following section.

7.2.3 Area disorder

The quality of the dispersion for the MAM and MAM-NS hybrid modified epoxies was quantified by the area disorder method as described by Bray *et al.* [255]. The results for the MAM modified LD and AD epoxies are shown in Figures 7.2.9(a) and 7.2.9(b), respectively. The dispersion quality for both LD and AD epoxies show a similar trend.

The 2.5 wt%, 5 wt% M52N MAM and 10N2.5M52N modified epoxy show "random-like" dispersion, which agrees well with the qualitative analysis of the AFM micrographs. The dispersion of the silica nanoparticles were also accurately represented by this approach, as the area disorder increases with M52N MAM content.



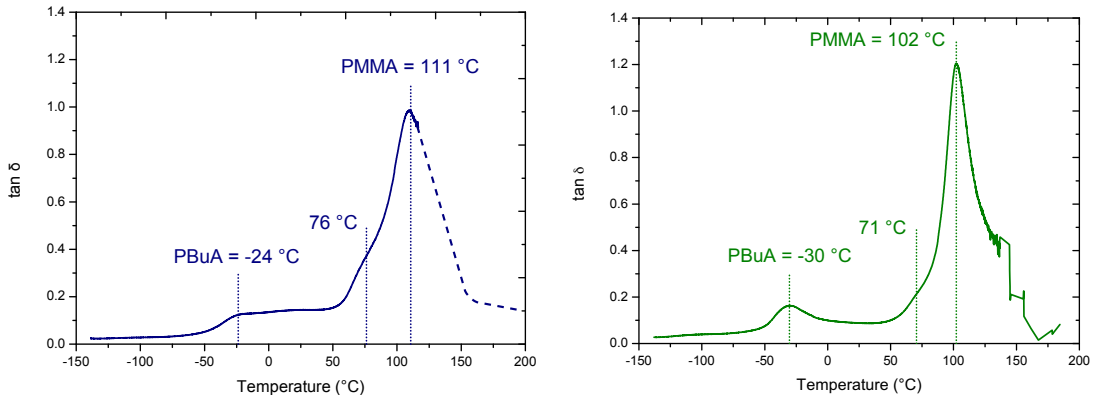
(a) LD epoxy (b) AD epoxy

Figure 7.2.9: Area disorder of MAM block copolymer modified epoxy polymers.

7.3 Glass transition temperature

The glass transition temperatures, T_g, of the block copolymers were measured for both M52N and M22N MAM block copolymers in tension the DMA. The results from the DMA are shown in Figure 7.3.1. The T_g peaks were similar for both M52N and M22N BCPs, and the small differences are due to the different block ratios. This indicates the similarity in block ratios between the two MAM BCPs [225]. Two main peaks

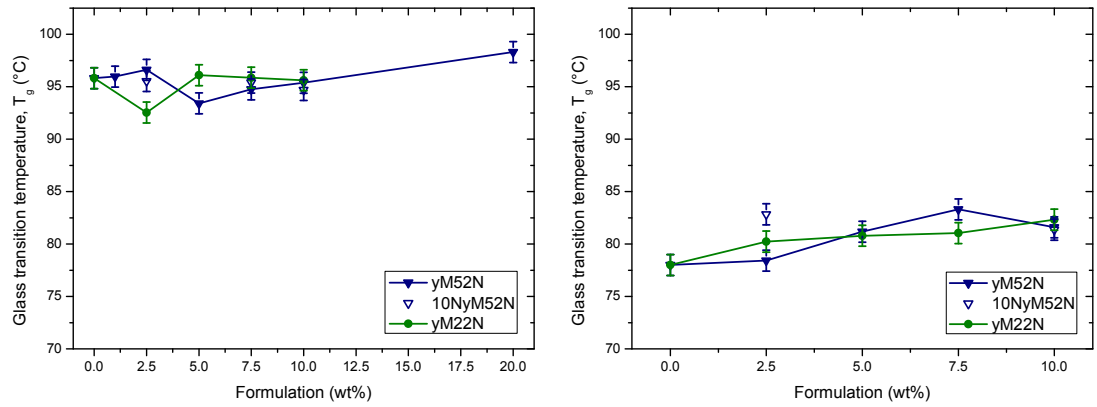
were observed for both M52N and M22N BCPs, as expected for a symmetric triblock copolymer, corresponding to the two different polymers. There is also a third peak, caused by a mixture of PBuA and PMMA and indicates the presence of some random copolymers [274].



(a) M52N MAM (b) M22N MAM

Figure 7.3.1: Variation of tan δ with temperature of M52N and M22N MAM block copolymers.

The values of T_g were measured for the unmodified and MAM modified epoxies using DMA and are summarised in Figure 7.3.2. The T_g of the unmodified epoxies were 96 °C and 74 °C for the LD and AD epoxies, respectively.

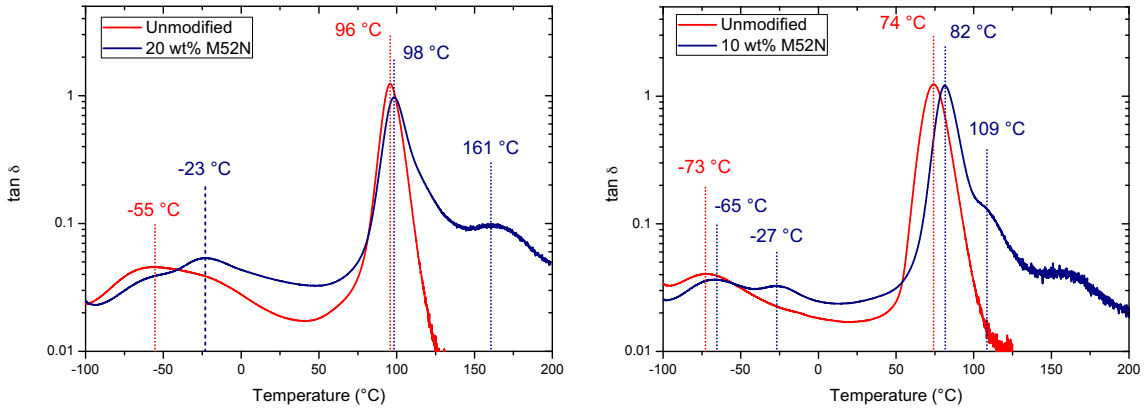


(a) LD epoxy (b) AD epoxy

Figure 7.3.2: Glass transition temperatures of MAM modified epoxy polymers. Error bars represent standard error of ±1°C.

The addition of M52N MAM block copolymers to the LD epoxy did not significantly affect the T_g of the bulk epoxy polymers. Although Table 7.2.3 shows that the MAM did not fully phase separate, the T_g of the PMMA block is quite similar to that of the LD epoxy (111 °C versus 96 °C). The T_g for the 20 wt% M52N MAM modified LD epoxy was measured to be 98 °C. A second minor tan δ peak was observed at 161 °C corresponding to the melting point of the M52N MAM, as shown in Figure 7.3.3. The

β transition temperature at -55 °C remains present with the addition of the MAM and a tan δ peak at -23 °C was observed corresponding to the PBuA block.



(a) LD epoxy (b) AD epoxy

Figure 7.3.3: Variation of tan δ with temperature of M52N MAM modified epoxy polymers.

The M52N MAM block copoloymer did not completely phase separate in the AD epoxies which resulted in a small increase in T_g of the bulk epoxy polymers. This was expected as the PMMA block has a much higher T_g than the AD epoxy (111 °C versus 74 °C). The trend is consistent with that from the volume fractions measured from the AFM phase images, which show more MAM remaining in the AD epoxy. A minor peak at 109 °C was observed, corresponding to the PMMA block. The same peak was not as clearly distinguishable in the MAM modified LD epoxy, as shown in Figure 7.3.3(a), because the main T_g peak of the epoxy is superimposed on top of it. This is visible as a wider band on the right, compared to the left, of the peak.

The addition of silica nanoparticles did not significantly affect the T_g of the M52N LD epoxy, despite a higher vol% of MAM remaining dissolved in the epoxy. The T_g of the M52N-NS MAM hybrid modified AD epoxies increased slightly due to the greater fraction of DGEBA in the DGEBA/F resin precursor. This is due to the fact that the silica nanoparticles used were pre-dispersed in DGEBA only.

The M22N MAM modified LD epoxy also showed no change in T_g, except at a concentration of 2.5 wt% which may have been due to experimental errors. The M22N MAM modified AD epoxy shows an increase in T_g with weight percentage, to the same degree as the M52N MAM modification, indicating some MAM remains in solution, as shown in Table 7.2.3.

7.4 Tensile properties

The tensile properties of the M52N and M22N MAM block copolymers were measured and are summarised in Figure 7.4.1 and Table 7.4.1. The Young's modulus was measured as 0.5 GPa for both the M52N and M22N MAM BCPs. It was expected that the M22N MAM would have a higher modulus than the M52N MAM due to the higher PMMA block ratio, however there does not appear to be any difference. The M22N MAM also has a higher yield strength but a lower failure strain than the M52N MAM. Additionally, the yield strain and fracture stress was found to be similar for both MAM BCPs.

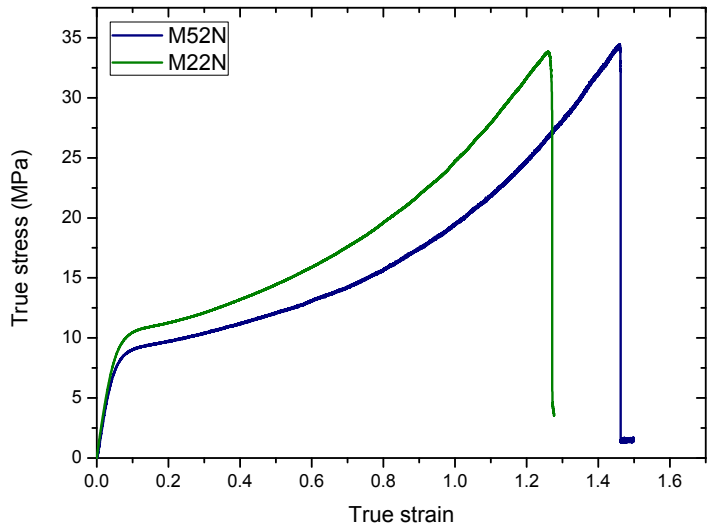


Figure 7.4.1: Tensile true stress-true strain curves for M52N and M22N MAM block copolymers.

Table 7.4.1: Young's modulus, E_t, yield stress, σ_y, yield strain, ε_y, fracture strength, σ_f, and fracture strain, ε_f for M52N and M22N MAM block copolymers.

MAM	E_t (GPa)	σ_y (MPa)	ε_y	σ_f (MPa)	ε_f
M52N	0.5 ± 0.1	8 ± 1	0.11 ± 0.00	35	1.5
M22N	0.5 ± 0.0	10 ± 1	0.12 ± 0.00	34	1.3

The Young's modulus, E_t, of the unmodified epoxies were measured to be 3.0 and 3.6 GPa for the LD and AD epoxies respectively. Typical true stress-strain curves for the unmodified and MAM modified LD epoxies are shown in Figure 7.4.2.

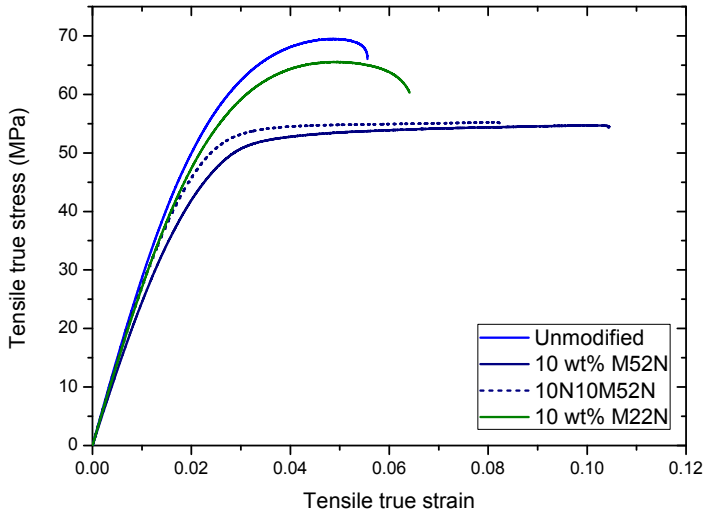
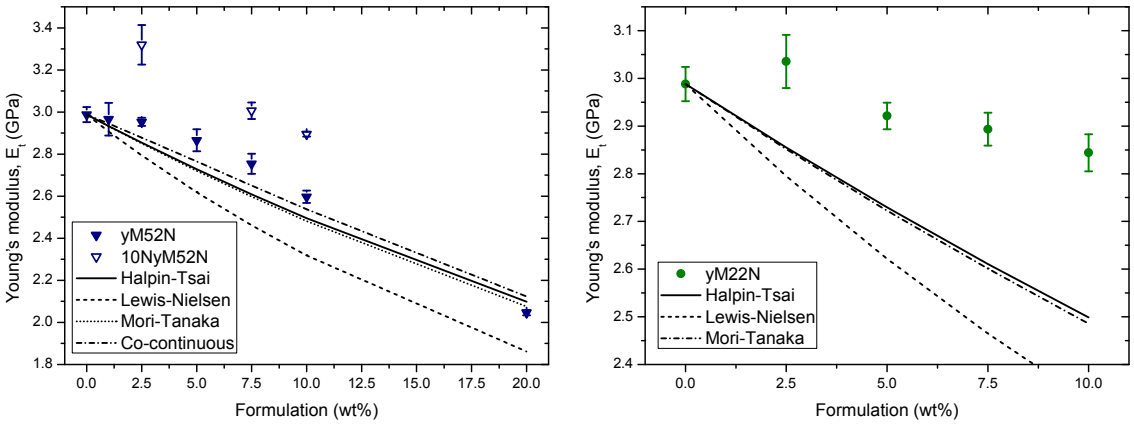


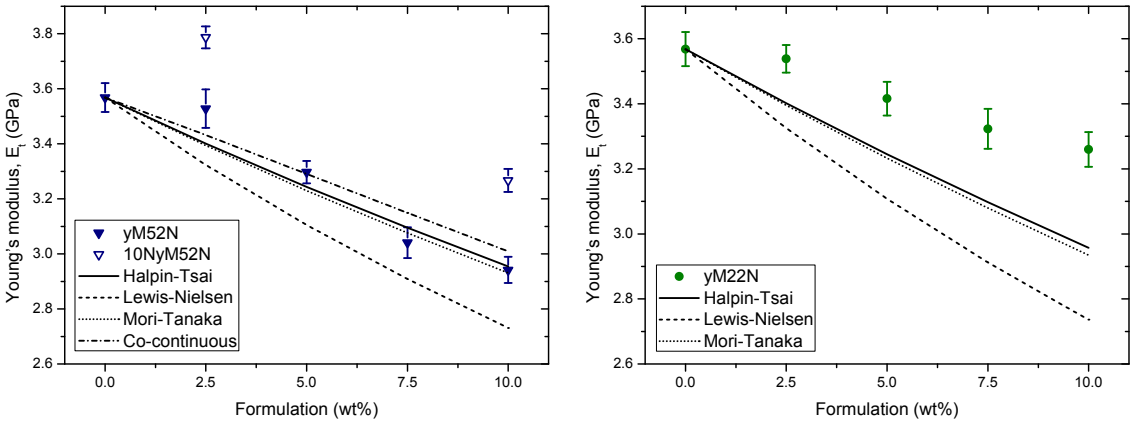
Figure 7.4.2: Typical tensile true stress-strain curves for unmodified and MAM modified LD epoxies.

The addition of the MAM block copolymers reduced the Young's modulus, E_t, of the epoxies with BCP content, as shown in Figures 7.4.3 and 7.4.4. This was expected given that the moduli of the MAM BCPs were much lower than the unmodified epoxies, as shown in Table 7.4.1. The addition of 10 wt% M52N and M22N MAM decreased the value of E_t to 2.6 GPa and 2.8 GPa, respectively. Clearly, the M22N MAM modified epoxies retain the tensile modulus better than the M52N MAM despite both BCPs having similar values of E_t. The same trend was also observed for the AD epoxy system; values of E_t for the 10 wt% M52N and M22N MAM modified epoxies were measured as 2.9 GPa and 3.3 GPa, respectively.



(a) M52N MAM (b) M22N MAM

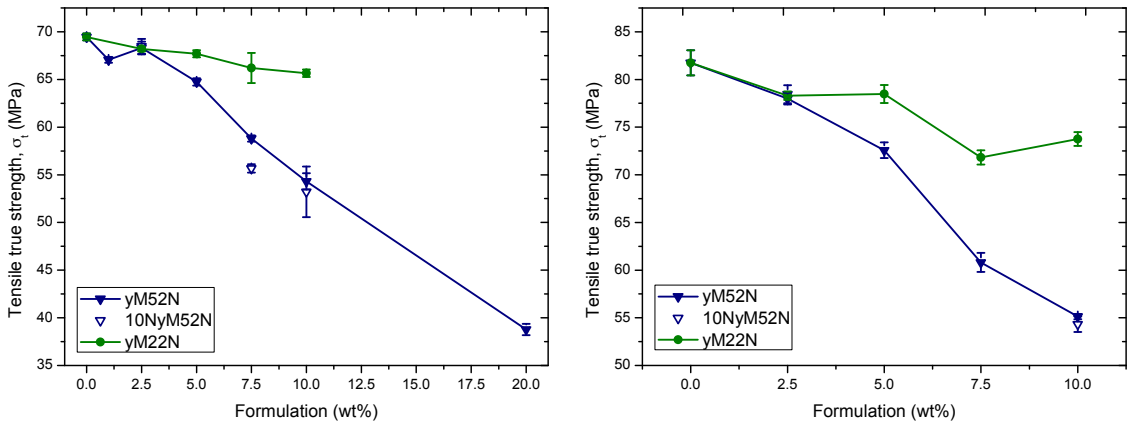
Figure 7.4.3: Young's moduli of MAM modified LD epoxy.



(a) M52N MAM (b) M22N MAM

Figure 7.4.4: Young's moduli of MAM modified AD epoxy.

A further addition of 10 wt% of silica nanoparticles increased the E_t of the M52N MAM modified epoxies by up to 13%. It should be noted that the increase in E_t was independent of the degree of NS agglomeration observed. Additionally, the value of σ_t remains unchanged for the M52N-NS hybrid modified epoxies. The tensile true strength, σ_t, decreases with MAM content due to cavitation processes and subsequent plastic void growth, as shown in Figure 7.4.5.



(a) LD epoxy (b) AD epoxy

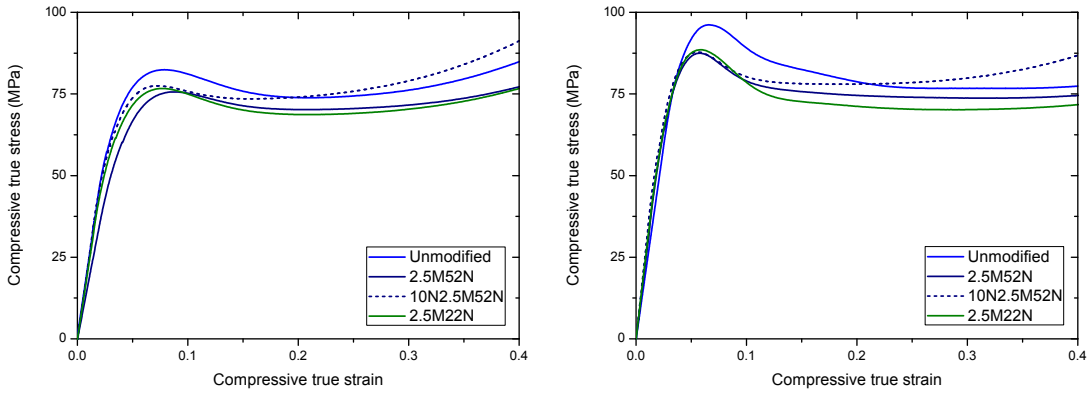
Figure 7.4.5: Tensile true strength, σ_t, of MAM modified epoxy polymers.

The measured values of Young's modulus for the MAM modified epoxies were compared to analytical models, as shown in Figures 7.4.3 and 7.4.4. The modifier modulus, E_p, was determined from tensile tests and a Poisson's ratio, ν_p, of 0.49 was used, assuming a rubber-like material. The matrix modulus, E_m, and Poisson's ratio, ν_m, were measured experimentally for the unmodified epoxies. For the Lewis-Nielsen model, a well dispersed random close packed dispersion was assumed and the 'no slip' condition was applied to assume a strong particle/matrix adhesion. In general, the Halpin-Tsai,

Mori-Tanaka and co-continuous models gave similar predictions and agreed well with the experimental data for the M52N MAM modified epoxies. The Lewis-Nielsen models did not show good agreements with the experimental data due to overcompensations for the influence on packing geometry. The models did not agree at all with the M22N modified epoxies and were typically underpredicted. In order for the models to fit the experimental data, the value of E_p would have to be approximately 2 GPa. This is much higher compared with the experimentally determined value of 0.49 GPa.

7.5 Compressive properties

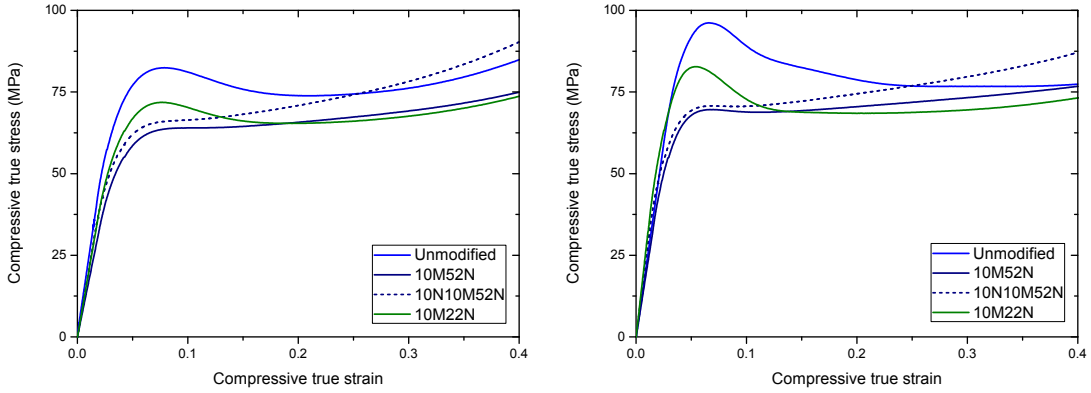
The compressive true stress-true strain curves are shown for the 10 wt% MAM block copolymer modified epoxies in Figures 7.5.1 and 7.5.2. There is a linear decrease in the compressive modulus, E_c, and compressive true yield stress, σ_{yc}, with MAM content. This was expected when modifying the epoxies with a modifier that has a lower strength and stiffness, and is comparable to the observations from the tensile tests. For the 10 wt% M52N modified LD epoxy, the E_c decreased from 2.2 GPa to 1.7 GPa and the σ_{yc} decreased from 83 MPa to 64 MPa, both reductions of 23%. For the 10 wt% M22N modified LD epoxy, the E_c and σ_{yc} decreased to 2.0 GPa and 72 MPa, respectively, corresponding to reductions of 11% and 13%, respectively. The compressive true yield strain, ε_{yc}, did not change with increasing MAM content, a trend that was also noted for the SBM modified epoxies. At a M52N content of 10 wt% and above, there was no clear maximum in stress to define as the yield point i.e. no strain softening, thus the point of minimum gradient was taken as the yield point.



(a) LD epoxy (b) AD epoxy

Figure 7.5.1: Compressive true stress-true strain curves for unmodified and 2.5 wt% MAM modified epoxy polymers.

The addition of 10 wt% silica nanoparticles recovers some of the loss of E_c from the



(a) LD epoxy (b) AD epoxy

Figure 7.5.2: Compressive true stress-true strain curves for unmodified and 10 wt% MAM modified epoxy polymers.

modification with MAM. An increase in σ_{yc} was observed for the M52N-NS hybrid modified LD epoxies compared to the M52N modified LD epoxies. The ε_{yc}, on the other hand, decreased when silica nanoparticles were added to the M52N modified LD epoxy, which indicates localised shear yielding processes induced at an earlier stage by the presence of the nanoparticles. This behaviour was not seen for the AD epoxy system; note how the curves for the M52N-NS hybrid modified epoxies (dotted lines) are almost identical to the M52N modified epoxies (solid lines) in Figures 7.5.1 and 7.5.2 up to the yield point.

Figure 7.5.1 shows strain softening behaviour for the unmodified LD and AD epoxies. The extent of strain softening was reduced by the addition of the M52N MAM modifier, which would imply that there is less global inhomogeneous deformation in the form of shear band yielding [271, 279] and can be the result of more localised shear yielding caused by the presence of the modifiers occuring homogeneously across the material. However, the strain hardening is more pronounced for the M52N modified epoxy compared to the unmodified epoxy, resulting in a larger deformation zone by stabilising the plastic deformation [88]. The addition of silica nanoparticles to the M52N modified epoxies further enhances the strain hardening, which in turn increases the size of the deformation zone. The M22N modified epoxies, however, show little change in strain softening and hardening behaviour, and this is reflected in the sectioned compressed regions when viewed using cross polarised light.

Extensive shear band yielding evident as birefringence was observed in the unmodified epoxy polymers, as shown in Figure 7.5.3. The shear bands in the M52N MAM modified epoxies appear more diffuse in nature compared to the unmodified epoxies, indicating the presence of localised shear band yielding. The much softer MAM BCPs are

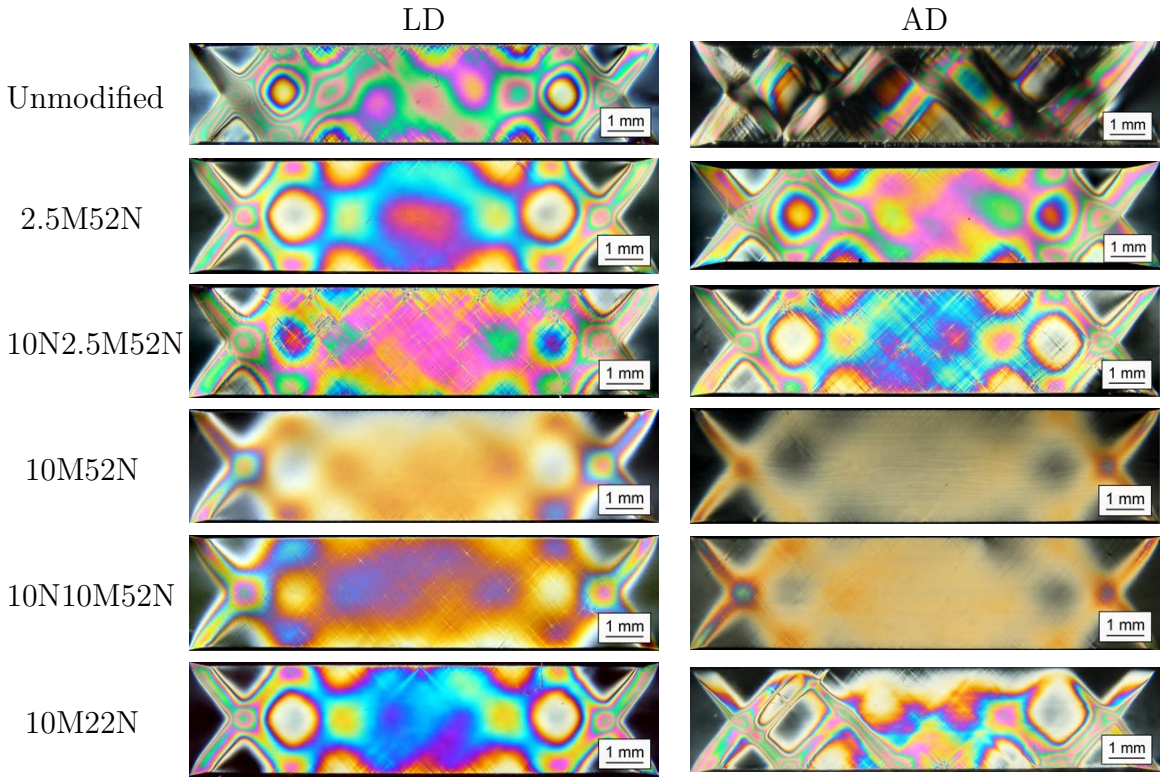


Figure 7.5.3: Transmission optical micrographs, using cross polarised light, of polished specimens loaded to the strain softening region.

effectively stress concentrations in the epoxy, which induce the formation of localised shear bands between the modifier phases. The addition of 10 wt% of silica nanoparticles to the M52N MAM modified epoxies also shows diffuse shear bands within the compressed region. The 10 wt% M22N MAM modified epoxies did not show significant differences compared to the unmodified epoxies, and thus has limited localised shear yielding. This was expected as the softening and hardening behaviour show little difference compared to the unmodified epoxy.

7.6 Fracture properties

The fracture toughness, K_{IC}, and fracture energy, G_{IC}, of the MAM modified epoxies were measured using SENB tests. The results are shown in Figures 7.6.1 and 7.6.2. The values of G_{IC} for the unmodified epoxies were measured to be 0.2 kJ/m^2 for the LD and AD epoxies.

For the M52N MAM modified epoxy polymers, the two epoxy polymers showed different trends in fracture performance with MAM content. When used with the LD epoxy polymer, an increase in G_{IC} to 2.2 kJ/m^2 at 5 wt% loading was followed by a decrease

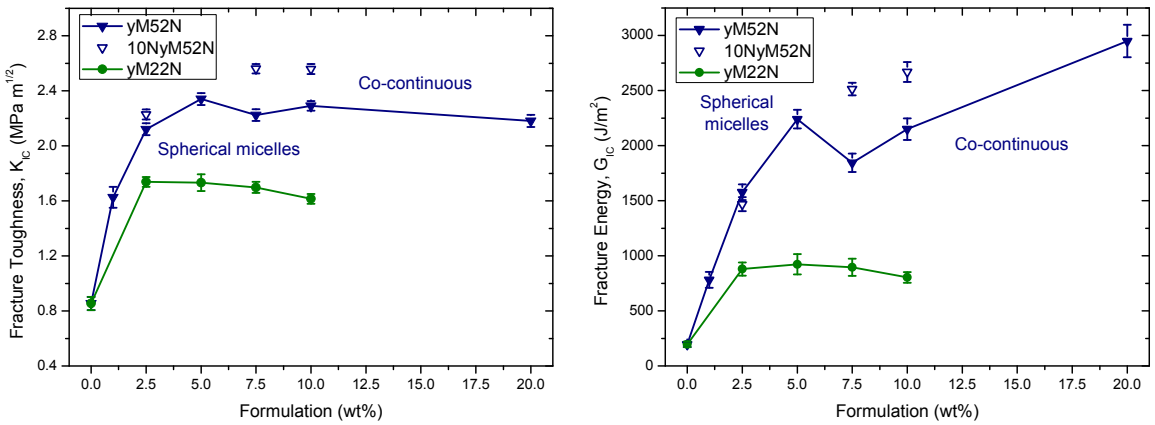


Figure 7.6.1: Fracture toughness and fracture energy of MAM modified LD epoxy.

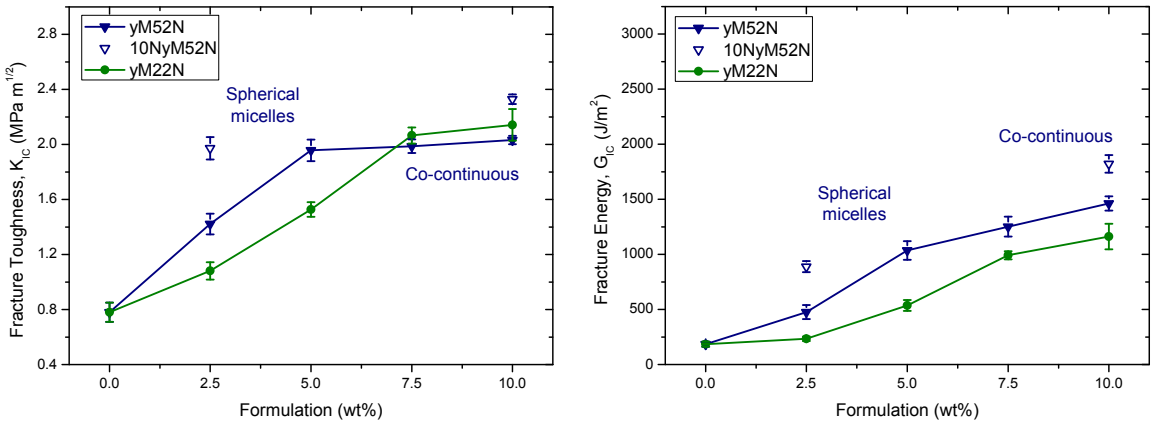


Figure 7.6.2: Fracture toughness and fracture energy of MAM modified AD epoxy.

as the microstructure changed to a co-continuous structure. The G_{IC} then increases up to a maximum of 3.0 kJ/m^2 at 20 wt% loading. For the AD epoxy polymer, a linear increase in fracture energy, to a lower maximum of 1.5 kJ/m^2 at 10 wt% loading was observed instead, despite possessing the similar morphologies as the LD epoxy (see §7.2.1). This will be explored in more detail in §7.7.

The influence of an additional 10 wt% of silica nanoparticles on the fracture performance of the M52N MAM modified epoxies is complex. To simplify the effect that these silica nanoparticles have on the MAM modified epoxies, the additional fracture energy due to synergistic effects, $G_{synergy}$, should be investigated. $G_{synergy}$ is calculated by subtracting ΔG_{IC} with the fracture energy contributions of silica nanoparticles only, where $\Delta G_{silica} = 0.3$ kJ/m^2 for the LD and AD epoxies [5]. The results are shown in Table 7.6.1.

Table 7.6.1: Fracture energy, G_{IC}, change in fracture energy, ΔG_{IC}, and synergy, $G_{synergy}$, for hybrid M52N-NS modified epoxies.

Modifier	LD (kJ/m^2)			AD (kJ/m^2)		
	G_{IC}	ΔG_{IC}	$G_{synergy}$	G_{IC}	ΔG_{IC}	G$_{synergy}$
2.5M52N	1.6	-0.1	No synergy	0.5	+0.4	0.1
10N2.5M52N	1.5			0.9		
7.5M52N	1.8	+0.7	0.4		—	
10N7.5M52N	2.5					
10M52N	2.2	+0.5	0.2	1.5	+0.4	0.1
10N10M52N	2.7			1.8		

For the 2.5 wt% M52N modified epoxies, where the morphology was a dispersion of spherical particles, synergy was observed for the AD epoxy but not for the LD epoxy. Note however, that the absolute values of G_{IC} for the modified AD epoxy is much lower than the LD epoxy. The 2.5M52N modified LD epoxy has reached a plateau in G_{IC}, thus the addition of silica nanoparticles does not provide additional toughening effects.

At higher concentrations, where a co-continuous structure was observed, synergy was observed when silica nanoparticles were added for all of the formulations tested. The value of $G_{synergy}$ can be significant, contributing up to 15% of the total G_{IC} for the 10N7.5M52N modified LD epoxy. It appears then that the agglomeration of the silica nanoparticles did not play a role in the overall fracture performance.

The M22N MAM contains less poly(butylacrylate), the soft phase, and as such was less effective in toughening the epoxies than the M52N MAM, as shown in Figures 7.6.1 and 7.6.2. Maximum G_{IC} values were measured to be 0.9 kJ/m^2 and 1.2 kJ/m^2 for the M22N MAM modified LD (at 5 wt%) and AD (at 10 wt%) epoxies. The M22N modified LD epoxy reaches a plateau in fracture performance at 2.5 wt%, whereas the G_{IC} and K_{IC} for the AD epoxy increases linearly with M22N content.

7.7 Fractography

Field emission gun scanning electron microscopy (FEGSEM) of the fracture surfaces was conducted to observe the toughening mechanisms. The crack propagation direction of the selected images shown are from right to left. The fracture surface of the unmodified LD epoxy, as shown in Figure 7.7.1, appears smooth and featureless. Brittle materials such as the unmodified epoxies absorb energy by the crack forking mechanism

[272].

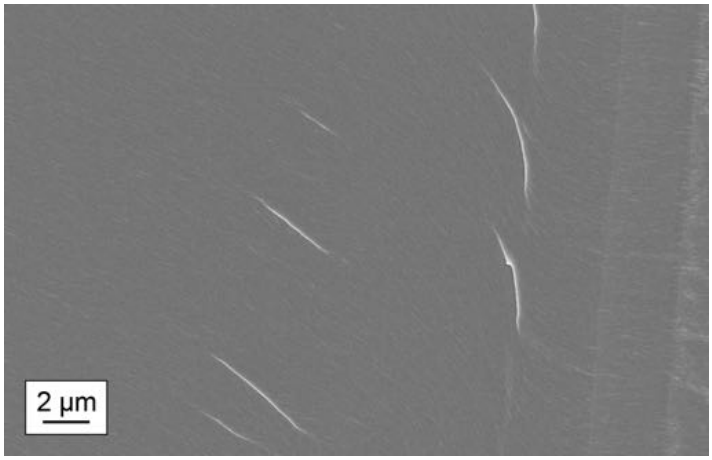
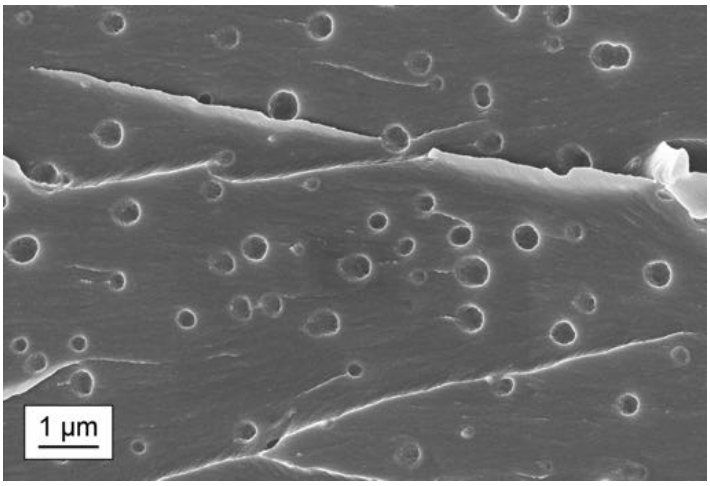


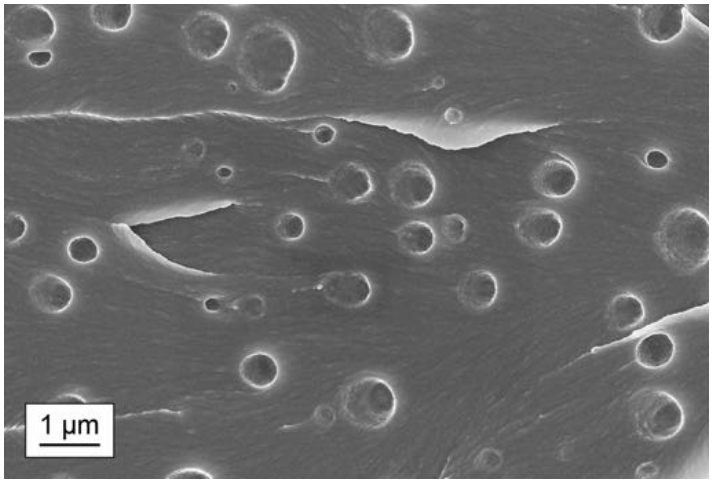
Figure 7.7.1: FEGSEM micrograph of unmodified LD epoxy.

7.7.1 M52N MAM

At low concentrations, i.e. 5 wt% and below, of M52N MAM modified epoxy polymers, well dispersed voids were observed, as shown in Figures 7.7.2. Mean void radii of 0.16 and 0.24 μm, for the 2.5 wt% M52N MAM modified LD and AD epoxy polymers respectively, were measured from the fracture surfaces. Compared to the mean radius of the particles measured using the AFM, 0.12 μm and 0.16 μm for the LD and AD epoxies respectively, this corresponds to an increase of approximately 40% for both epoxy systems. The increase in particle/void radii indicates that cavitation and subsequent plastic void growth of the MAM particles has occured. The volume fraction of the cavities, measured from the FEGSEM micrographs, was also found to increase to 5.6±1.0 vol% and 7.7±1.5 vol% for the LD and AD epoxies. This suggests that all the particles have cavitated [273].



(a) LD epoxy



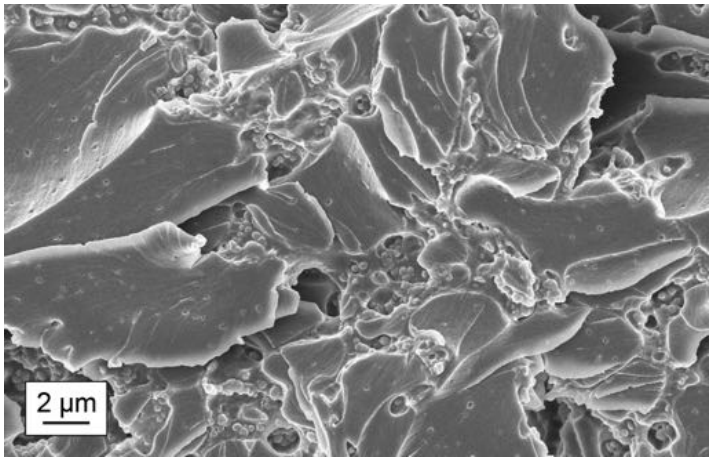
(b) AD epoxy

Figure 7.7.2: FEGSEM micrograph of 2.5 wt% M52N MAM modified epoxy fracture surfaces.

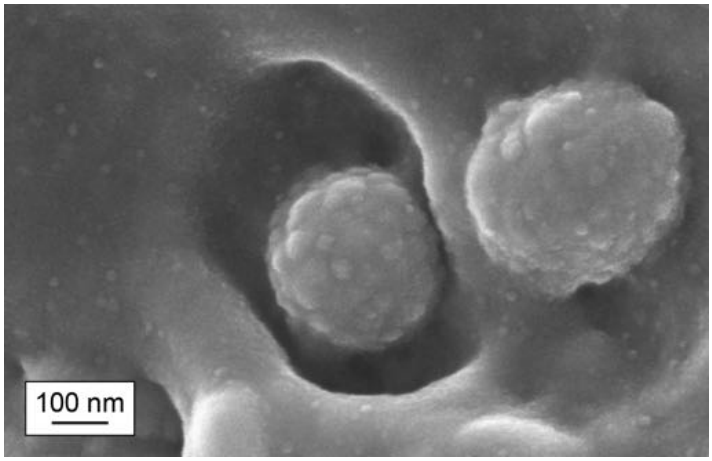
At 10 wt% of M52N MAM, the co-continuous structure is clearly visible for both the LD and AD epoxy systems, as shown in Figures 7.7.3(a) and 7.7.3(c). The spherical particles dispersed in the epoxy rich phase were also found to have cavitated into voids, however these voids did not grow in size and hence would not be expected to contribute much to the toughness. Generally, the morphology observed from the fracture surfaces agrees well with the micrographs from the AFM.

In the LD epoxy system, as shown in Figure 7.7.3(a), debonding and plastic void growth were observed around the epoxy inclusions, and between the MAM and epoxy. Figure 7.7.3(b) shows a close up of an epoxy inclusion in the MAM rich region, which is covered in MAM. There was no change in the measured mean radii of the epoxy inclusions, indicating that the epoxy inclusions did not cavitate. Instead, the deformation appears to be limited to the MAM-rich regions. For the AD epoxy however, debonding was not observed between the MAM and epoxy matrix, which is a prerequisite to plastic void growth, from the relief in crack tip constraint. The deformation was limited to the MAM phase only.

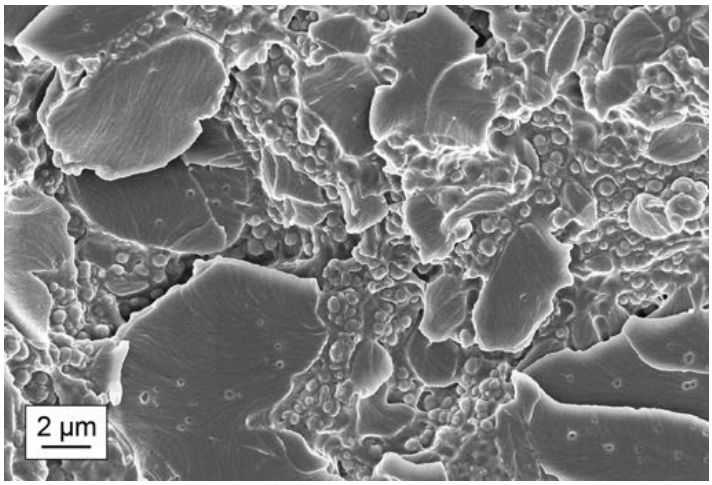
The addition of silica nanoparticles to the 2.5 wt% M52N MAM modified epoxies decreased the cavitated particle radii by 20%, to 0.13 and 0.19 μm for the LD and AD epoxy systems, respectively. The silica nanoparticles increase the stiffness of the matrix, which can suppress the void growth mechanism as observed. Additionally, the silica nanoparticles were well bonded to the epoxy and no voids were observed around the nanoparticles, as shown in Figures 7.7.4(a) and 7.7.5(a). The lack of debonding and plastic void growth for these materials explains the limited increase in toughness.



(a) LD epoxy



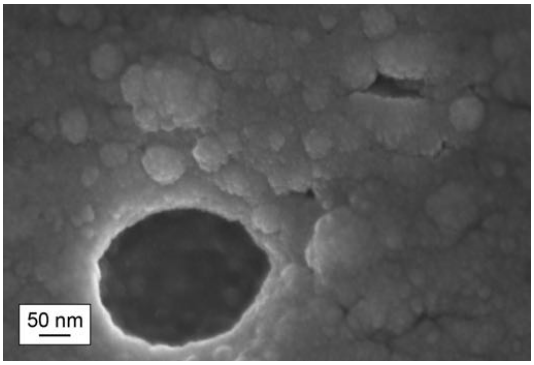
(b) Close up of epoxy inclusion surrounded by MAM, in MAM rich region for 10 wt% M52N modified LD epoxy



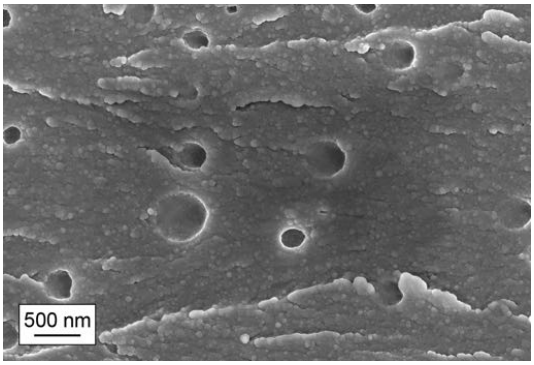
(c) AD epoxy

Figure 7.7.3: FEGSEM micrograph of 10 wt% M52N MAM modified epoxy fracture surfaces.

From Figures 7.7.4(a) and 7.7.5(a), some deformation around the agglomerates of silica nanoparticles suggest that each large agglomerate behaves like a single larger micron-

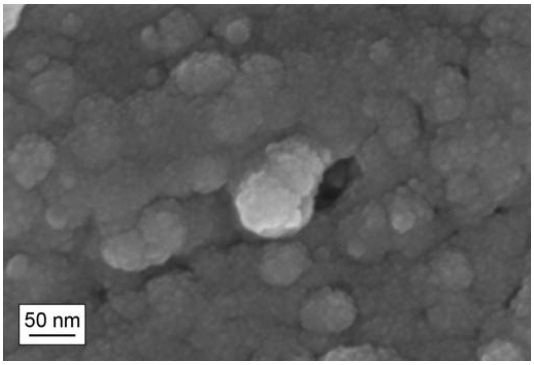


(a) x350k magnification

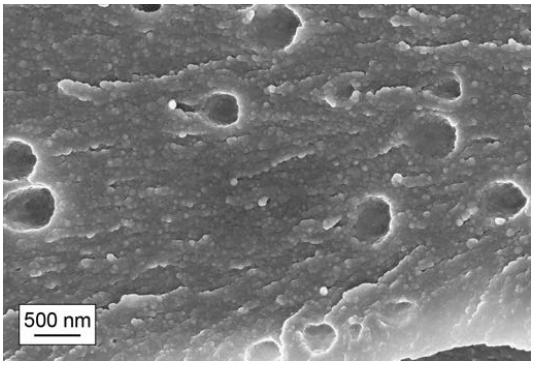


(b) x50k magnification

Figure 7.7.4: FEGSEM micrograph of hybrid 10N2.5M52N modified LD epoxy fracture surfaces.



(a) x500k magnification



(b) x50k magnification

Figure 7.7.5: FEGSEM micrograph of hybrid 10N2.5M52N modified AD epoxy fracture surfaces.

sized particle. Poorly bonded agglomerates of silica nanoparticles can act as stress concentrations that initiate premature failure. This is seen as a decrease in tensile strength and can also be beneficial by initiating void growth around the agglomerates.

The individual silica nanoparticles within the larger clusters in the hybrid 10N10M52N modified epoxies did not show any debonding from the epoxy matrix, as shown in Figures 7.7.6 and 7.7.7. There were also no differences in the MAM rich regions when the silica nanoparticles were added; the mean radii of the epoxy inclusions remained the same as the samples without silica nanoparticles.

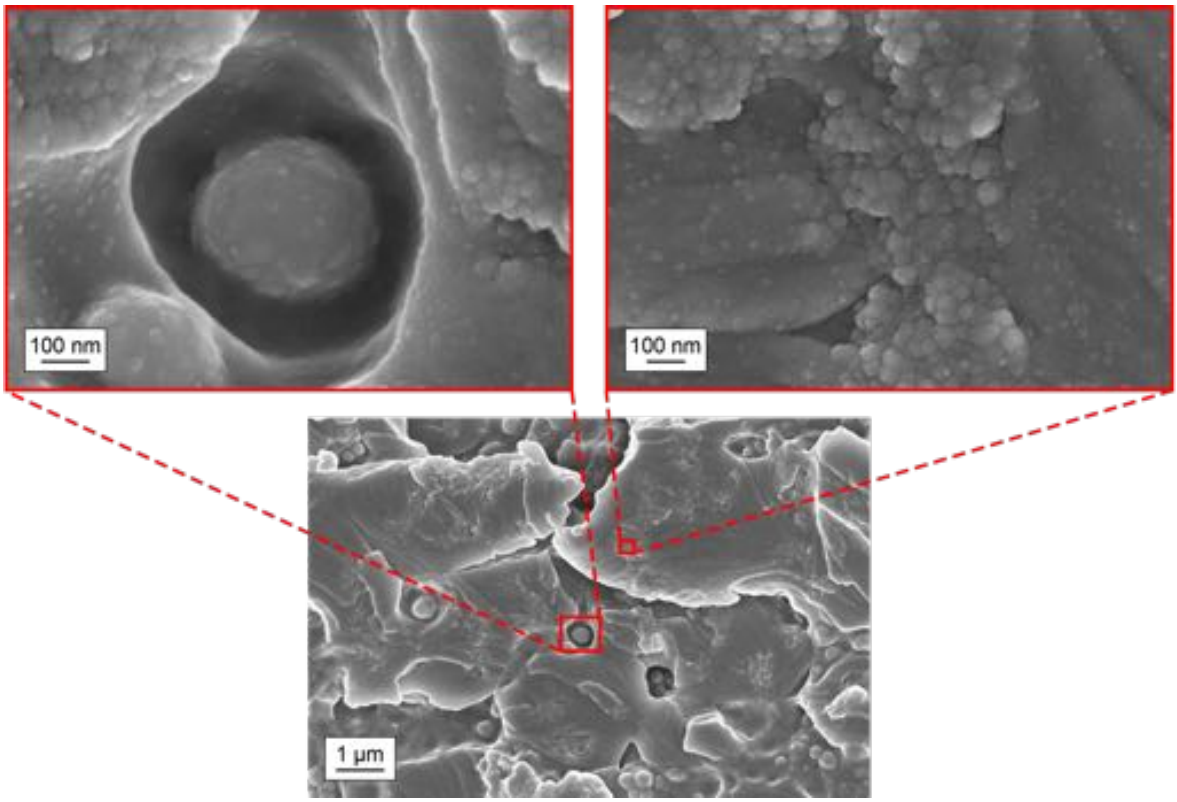


Figure 7.7.6: FEGSEM micrograph of hybrid 10N10M52N modified LD epoxy fracture surfaces.

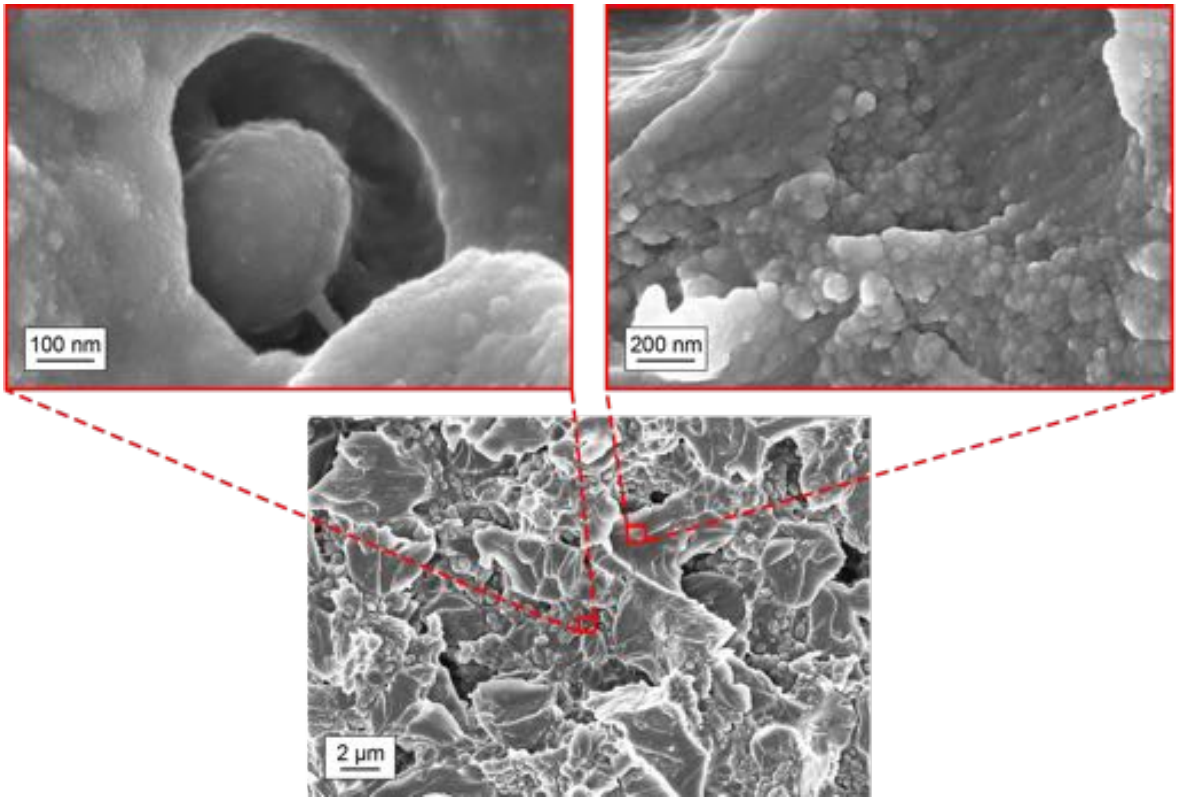
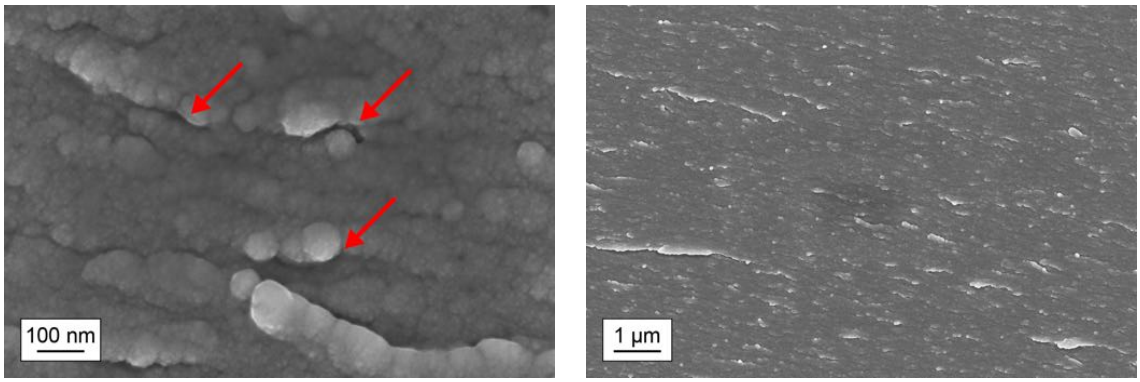


Figure 7.7.7: FEGSEM micrograph of hybrid 10N10M52N modified AD epoxy fracture surfaces.

7.7.2 M22N MAM

The fracture surface of the M22N modified epoxy polymer initially appears to be indicative of a brittle fracture surface at low magnification, see Figures 7.7.8(b) and 7.7.9(b) for example. This is not surprising as the AFM revealed features in the order of 10 nm in size. With higher magnification, the M22N modified epoxy showed a rougher surface and more plastic deformation compared to the unmodified epoxy. The 20 nm diameter worm-like micelles and 9 nm radius core-shell particles were not readily visible on the FEGSEM images, as the relatively small size of these particles are approaching the theoretical limit in resolution of the FEGSEM.

For the LD epoxy system, worm-like micelles were observed from the AFM micrographs. Some of these can be found on the fracture surface, as shown in Figure 7.7.8(a). Some authors [53, 54] have suggested toughening mechanisms of pull-out and bridging for nanoscale worm-like micelles. However, considering the large difference in scale between the worm-like micelles (length = 250 nm) and the crack opening displacement (δ_{tc} = 15 μm), these mechanisms seem unlikely to provide any significant toughening. The crack opening displacement is simply too large for the worm-like micelles to bridge across and pull-out requires them to be strong. From Figure 7.7.8(a), it appears some of the worm-like micelles show nanocavitation and subsequent plastic void growth of the epoxy, observed as black lines, as the dominant toughening mechanism.

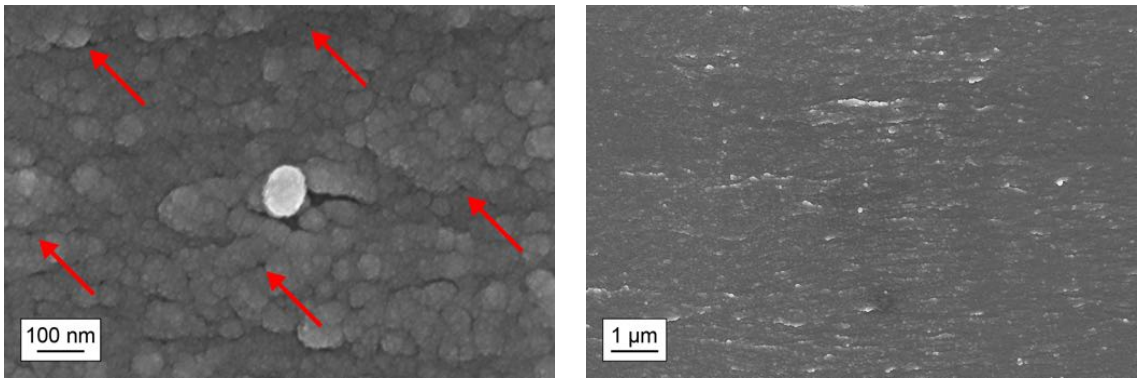


(a) x250k magnification (b) x25k magnification

Figure 7.7.8: FEGSEM micrograph of 10 wt% M22N MAM modified LD epoxy fracture surfaces. Some worm-like micelles are identified with red arrows.

For the AD epoxy system, some holes can be observed suggesting cavitation of the core-shell particles followed by plastic void growth, as identified by the red arrows in Figure 7.7.9(a). Other authors [180, 280] have also reported cavitation for nanometre scale rubbery particles. However, there were not many of these voids, and the lack of

cavitation shows in the low fracture toughness measured. The lack of observable voids could be due to the thickness of the conductive coating obstructing the cavities, as the thickness approaches the size of these features. Thinner coatings did not work well as there was significant charging, even at low accelerating voltages. It should also be expected that at a particle size in the order of 10 nm, the stress required to debond the particle would be above the tensile yield strength of the epoxy polymers [110].



(a) x250k magnification (b) x25k magnification

Figure 7.7.9: FEGSEM micrograph of 10 wt% M22N MAM modified AD epoxy fracture surfaces. Some nanocavities are identified with red arrows.

7.8 Characteristic lengths

The characteristic lengths of the MAM features were calculated using a two point correlation function from binarised AFM and FEGSEM micrographs. The details of the method is described in §4.2.7. The characteristic lengths, expressed as vector lengths, are summarised in Table 7.8.1. The values from the AFM refer to the microstructure that has not been tested, and the values from the FEGSEM refer to the images from the SENB test sample fracture surface.

As expected at MAM concentrations of 2.5 wt% and 5 wt%, the characteristic lengths were comparable to the particle diameters, as shown in Table 7.2.1 previously. The particle diameters should equal the characteristic lengths if a large enough number of vectors were used. However, this also increases the computational cost. For this study, 500,000 vectors per characteristic length was used for each image.

The characteristic lengths increased with MAM content up to a maximum of about 2.5 μm at a loading of 10 wt%, for both LD and AD epoxy systems. This is consistent with the qualitative observations. The standard deviation for some of the formulations were larger due to the coexistence of the nanoscale spherical particles and much larger

co-continuous phase. The addition of 10 wt% of silica nanoparticles to the M52N MAM modified epoxies tended to reduce the characteristic lengths of the MAM phase due to the increased amount of MAM remaining dissolved in the epoxy, as shown in Table 7.2.3.

Table 7.8.1: Characteristic lengths of M52N MAM phase in modified LD and AD epoxies.

M52N (wt%)	LD (μm)		AD (μm)	
	AFM	FEGSEM	AFM	FEGSEM
2.5	0.40 ± 0.03	0.52 ± 0.14	0.52 ± 0.05	0.76 ± 0.05
5	0.51 ± 0.05	–	0.76 ± 0.09	–
7.5	1.94 ± 0.16	–	1.25 ± 0.46	–
10	2.47 ± 0.22	2.52 ± 0.15	2.51 ± 0.10	2.57 ± 0.25
20	2.05 ± 0.32	–	–	–
10N2.5M52N	0.35 ± 0.02	0.41 ± 0.04	0.42 ± 0.15	0.56 ± 0.09
10N7.5M52N	1.78 ± 0.04	–	–	–
10N10M52N	1.95 ± 0.30	2.62 ± 0.16	1.50 ± 0.30	2.69 ± 0.10

For the 2.5 wt% M52N modified epoxies, the characteristic lengths measured from the FEGSEM images were approximately 40% higher than those from the AFM, similar to the increase in radius measured. This indicates significant plastic void growth of the epoxy around the MAM phase. At a loading of 10 wt% M52N, there is little void growth as the characteristic lengths show little change between the AFM and FEGSEM, which was observed as a limited increase in fracture toughness. For both 10N10M52N modified epoxies however, there is a significant increase in characteristic length from the AFM to the FEGSEM. This was perceived experimentally as synergistic effects to the fracture energy.

7.9 Conclusions

Two symmetric acrylic triblock copolymers of poly(methyl methacrylate)-b-poly(butyl acrylate)-b-poly(methyl methacrylate) (MAM) were used to modify two different epoxy systems, a polyether-amine cured DGEBA and a polyether-amine cured DGEBA/F. The two MAM modifiers have different block ratios of PBuA and molecular weight; M22N MAM has a lower PBuA content and higher molecular weight than M52N MAM. The tensile, compression and fracture properties of the two MAM modified epoxy polymers were measured and compared. Silica nanoparticles were added to the M52N modified epoxies to create hybrid modified epoxies, and the effect of this on the mechanical properties was evaluated.

At 5 wt% and below of M52N MAM, the MAM phase separated into spheres of up to 250 nm in radius in both LD and AD epoxies. Above 5 wt%, the morphology transitions into a co-continuous microstructure. When 10 wt% of silica nanoparticles were added to the 2.5 wt% M52N MAM modified epoxies, the silica nanoparticles were well dispersed in the matrix and the MAM particle radius remained the same. However, the silica nanoparticles were agglomerated when used with 7.5 wt% and 10 wt% of M52N MAM. The M22N MAM phase separated into worm-like micelles for the LD epoxy and 9 nm radius spherical particles for the AD epoxy at a concentration of 10 wt%.

The glass transition temperatures of the MAM modified LD epoxies were unaffected by the addition of MAM, however the AD epoxies show an increase in T_g with MAM content of up to 6°C due to some MAM remaining dissolved in the epoxy. This is because the T_g of the PMMA block is higher than the bulk unmodified AD epoxy. The Young's modulus and strength was reduced when the MAM was incorporated into the epoxy as the MAM has a much lower modulus and strength. These properties were recovered by the addition of 10 wt% of silica nanoparticles. The M22N MAM modified epoxies showed a smaller reduction in tensile properties, due to the complex nanostructures formed and lower PBuA block ratio. The compression tests showed similar trends to the tensile tests, and significant diffuse shear banding was observed in the compression samples.

For the M52N modified LD epoxy, the fracture energy increased with MAM content from 0.2 kJ/m^2 to 2.2 kJ/m^2 at 5 wt%. A decrease in G_{IC} was observed as the microstructure was in transition to a co-continuous morphology at 7.5 wt%. When a fully co-continuous microstructure was obtained at 20 wt%, the G_{IC} increased further to 3.0 kJ/m^2. The addition of 10 wt% of silica nanoparticles to the M52N MAM modified epoxies did not always increase the G_{IC} values. The silica nanoparticles greatly increased the G_{IC} values of the 7.5 wt% and 10 wt% M52N modified LD epoxies, contributing up to 15% of the total G_{IC}. However, the 10N2.5M52N modified epoxy showed no improvement over the 2.5 wt% M52N modified epoxy. This is due to more extensive shear yielding associated with the higher M52N content.

The M52N MAM was less effective in toughening the AD epoxy. A linear increase in G_{IC} from 0.2 kJ/m^2 to 1.5 kJ/m^2 at 10 wt% was measured, despite having the same morphology as the LD epoxy. From the fracture surfaces, it was deduced that interfacial adhesion between the MAM and AD epoxy was greater. As such, there is limited debonding at the interface, which meant that the crack tip triaxiality is not relieved and plastic deformation in the region ahead of the crack tip is limited.

Synergistic effects from the addition of 10 wt% of silica nanoparticles were observed for the materials with up to 10 wt% M52N MAM. Observations of the fracture surfaces show cavitation and void growth of the spherical particles below 5 wt%. For the 10 wt% M52N MAM modified epoxies, the co-continuous MAM phase debonded from the matrix and resulted in matrix plastic deformation. The silica nanoparticles were well bonded to the epoxy and did not show any debonding around the nanoparticles.

The lower PBuA content of the M22N MAM resulted in lower values of G_{IC}, compared to the M52N MAM. The M22N modified LD epoxies show a plateau in G_{IC} of about 0.9 kJ/m^2 from 2.5 wt%, whereas the AD epoxies show a linear increase up to 1.2 kJ/m^2 at 10 wt%. There was little evidence of cavitation and void growth on the fracture surfaces of the M22N MAM modified epoxies, hence the limited improvement in fracture performance. The contribution from localised shear yielding also appears to be limited; the true stress-true strain curves show little difference in softening/hardening behaviour compared to the unmodified epoxy and this resulted in shear bands that appear less diffuse in nature, exhibiting only macroscopic inhomogeneous shear bands.

Chapter 8

Graphene nanoplatelet modified epoxy polymers

8.1 Introduction

This chapter investigates the use of graphene nanoplatelets (GNPs) on the mechanical and fracture performance of an anhydride cured DGEBA epoxy system (LY556/HE600). The GNPs used were from XG Sciences, USA, Graphene Supermarket, USA, and Haydale, UK, and are described in §3.3.5. The GNPs used cover a wide range of platelet geometry, aspect ratio and functionality in order to understand the properties that control the mechanical properties. The epoxy was also modified with graphite flakes (GF) as a comparison for the GNP modified epoxies. The formulations of the GNP modified epoxies studied in this Chapter are summarised in Table 8.1.1.

Table 8.1.1: Summary of GNP formulations used in this chapter.

Modifier	Solvent			
	THF wt%	Abbreviation	NMP wt%	Abbreviation
XG-H	0.1	0.1XG-H-THF	0.1	0.1XG-H-NMP
	0.5	0.5XG-H-THF	0.5	0.5XG-H-NMP
	1.0	1.0XG-H-THF	1.0	1.0XG-H-NMP
	2.0	2.0XG-H-THF	2.0	2.0XG-H-NMP
XG-M	0.1	0.1XG-M-THF	0.1	0.1XG-M-NMP
	0.5	0.5XG-M-THF	0.5	0.5XG-M-NMP
	1.0	1.0XG-M-THF	1.0	1.0XG-M-NMP
	2.0	2.0XG-M-THF	–	–
XG-C	0.1	0.1XG-C-THF	0.1	0.1XG-C-NMP
	0.5	0.5XG-C-THF	0.5	0.5XG-C-NMP
	1.0	1.0XG-C-THF	1.0	1.0XG-C-NMP
	2.0	2.0XG-C-THF	2.0	2.0XG-C-NMP
GS	0.1	0.1GS-THF	0.1	0.1GS-NMP
	0.5	0.5GS-THF	0.5	0.5GS-NMP
	1.0	1.0GS-THF	1.0	1.0GS-NMP
	2.0	2.0GS-THF	–	–

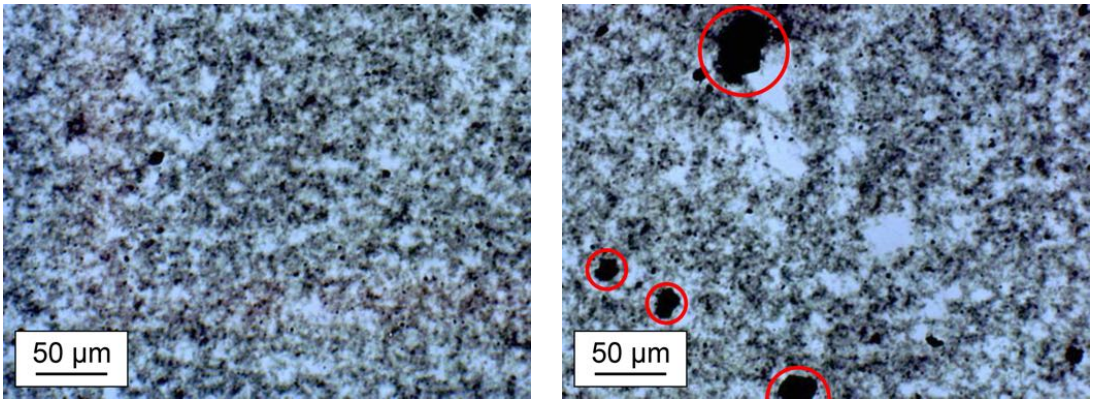
Modifier	No solvent	
	wt%	Abbreviation
GNP-COOH	0.1	0.1GNP-COOH
	0.5	0.5GNP-COOH
	1.0	1.0GNP-COOH
GNP-O_2	0.1	0.1GNP-O2
	0.5	0.5GNP-O2
	1.0	1.0GNP-O2
CNT-COOH	0.1	0.1CNT-COOH
	0.2	0.2CNT-COOH
	0.5	0.5CNT-COOH
GF	0.1	0.1GF
	0.5	0.5GF
	1.0	1.0GF
	1.5	1.5GF
	2.0	2.0GF

8.2 GNP Dispersion

The graphene nanoplatelets were received in powder form and require mechanical agitation to prevent agglomerations being formed. The GNPs have very high aspect ratios, with very large lateral sizes on the micrometre length scale and nanometre-scale thickness. These give rise to the tendency to agglomerate due to the strong van der Waals forces and $\pi - \pi$ interactions between the platelets. Obtaining a good dispersion of GNPs is important in order to fully exploit the mechanical properties of these

nano-reinforcements.

There have been extensive studies that focused on achieving well dispersed GNPs and CNTs, as discussed in §2.2.2.9. This section describes the method to determine the optimum dispersion method through the use of an ultrasonic probe. An ultrasonic probe was chosen over other mechanical force or turbulent methods for cost, time saving and the reduction of possible contamination due to the difficulty of cleaning the equipment. The ultrasonic probe used costs £4,600 [281], compared to a three roll mill (> £30,000), and has a much higher energy density than an ultrasonic bath (ultrasonic probes can have up to 100 times greater intensity than ultrasonic baths [282]). Figure 8.2.1(b) shows how agglomerates (identified in red circles) are still present after 40 hours of sonication in an ultrasonic bath. This is compared to 30 min of using an ultrasonic probe, as shown in Figure 8.2.1(a), where there were no agglomerations of that order of magnitude.

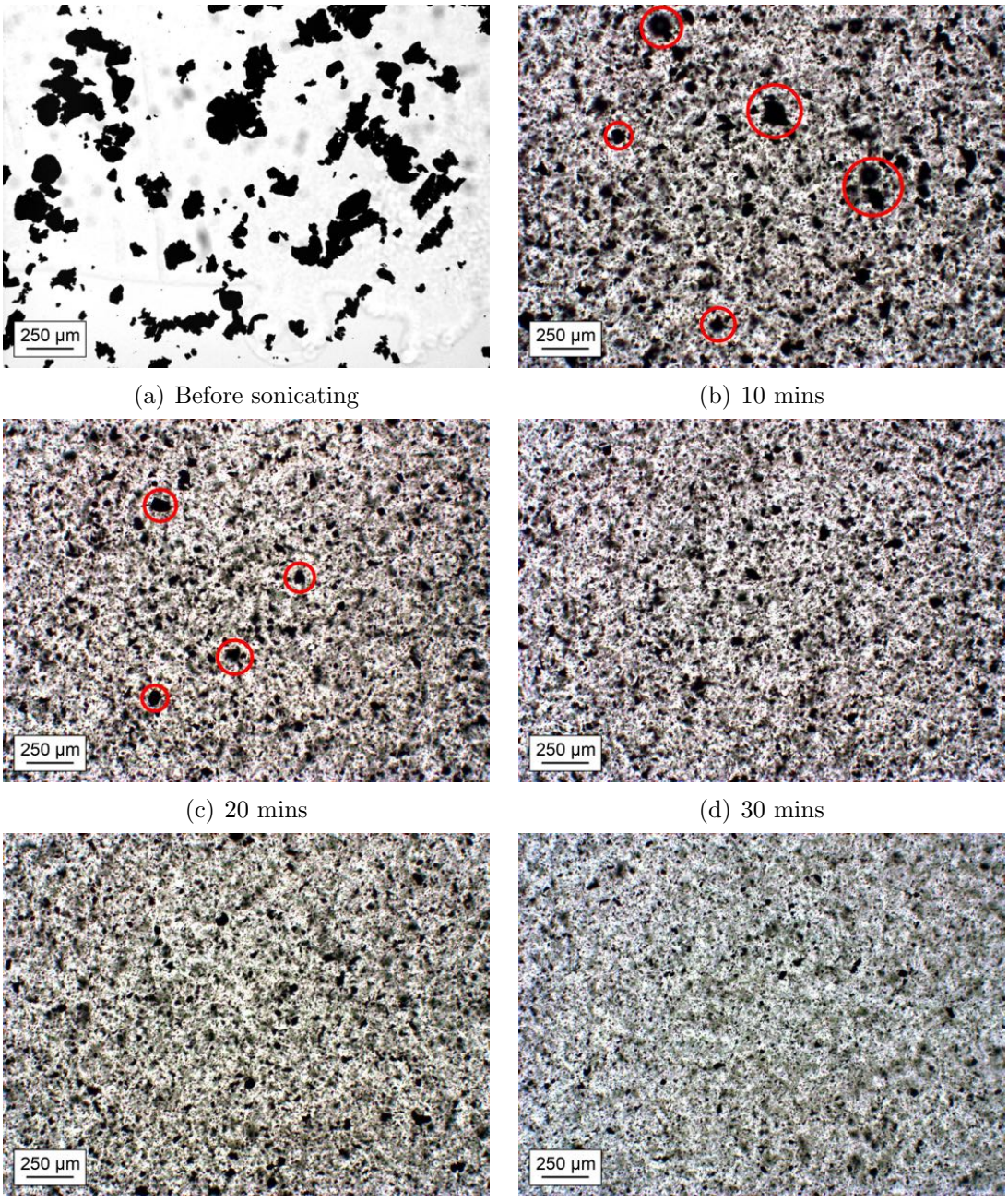


(a) Ultrasonic probe after 30 min (b) Ultrasonic bath after 40 hours

Figure 8.2.1: Comparison between dispersing using different ultrasonic methods. Agglomerates are identified with red circles. Reproduced from [142].

To determine the optimum ultrasonication time, resin samples with GNP were placed under the optical microscope to measure the agglomerate size. For these studies, a loading of 0.05 wt% GNP in epoxy resin was used. Higher GNP contents resulted in an opaque mixture when placed under the optical microscope, thus it was not possible to use transmitted light microscopy. The sonication process generates a significant amount of heat, which increased the temperature of the resin. A thermocouple was used to monitor the temperature during the sonication process, which was stopped when the temperature reached 80 °C. The mixture was then cooled to approximately 30 °C in an ice bath before restarting the sonicator. It should also be noted that glass beakers were used as plastic beakers were susceptible to melting as the local temperature near the probe tip can be very high.

After sonicating for a predetermined time, a droplet of the GNP-epoxy resin mixture was removed from the beaker and placed between two glass slides, separated with a 0.3 mm thick metal spacer. The use of a constant thickness is important so that the same amount of material is under consideration each time. The glass slides were then imaged using an optical microscope in transmission light mode, as shown in Figure 8.2.2.



(a) Before sonicating (b) 10 mins

(c) 20 mins (d) 30 mins

(e) 45 mins (f) 120 mins

Figure 8.2.2: Transmission optical microscope images of uncured 0.05 wt% XG-H GNP modified epoxies showing dispersion quality after the specified sonication time. Agglomerates are identified with red circles.

Figure 8.2.2(a) shows the large agglomerates of GNP when the mixture was mixed by hand before sonicating. After only 10 min of sonication, the quality of the GNP dispersion has improved dramatically as the size of the agglomerates are smaller, as shown in Figure 8.2.2(b). This is reflected in the characteristic length measurements using the two point correlation method, as summarised in Figure 8.2.3. However, large clumps of GNP were still clearly visible, as identified by the red circles in Figures 8.2.2(b) and 8.2.2(c). The characteristic length continues to decrease until a total sonication time of 30 min. There were no further improvements in the quality of GNP dispersion after 30 mins. However, at 120 mins, the characteristic length begins to decrease, indicating possible damage of the platelets. This was also evident in Figure 8.2.2(f) as the GNPs appear to be much smaller than in Figure 8.2.2(e).

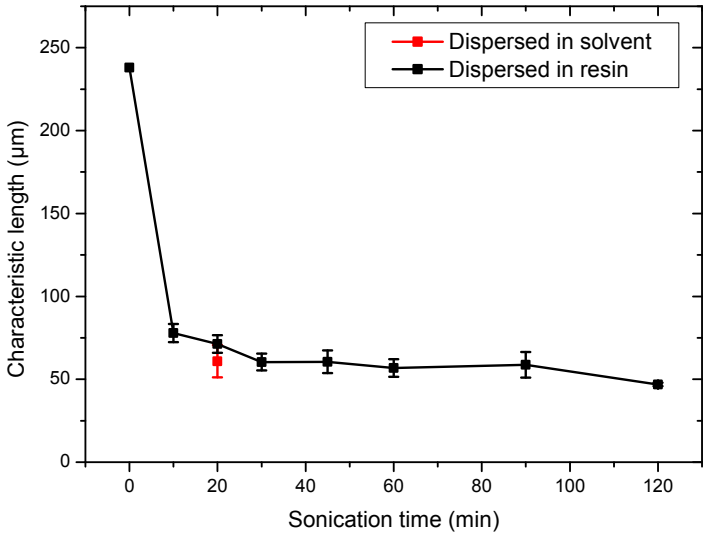
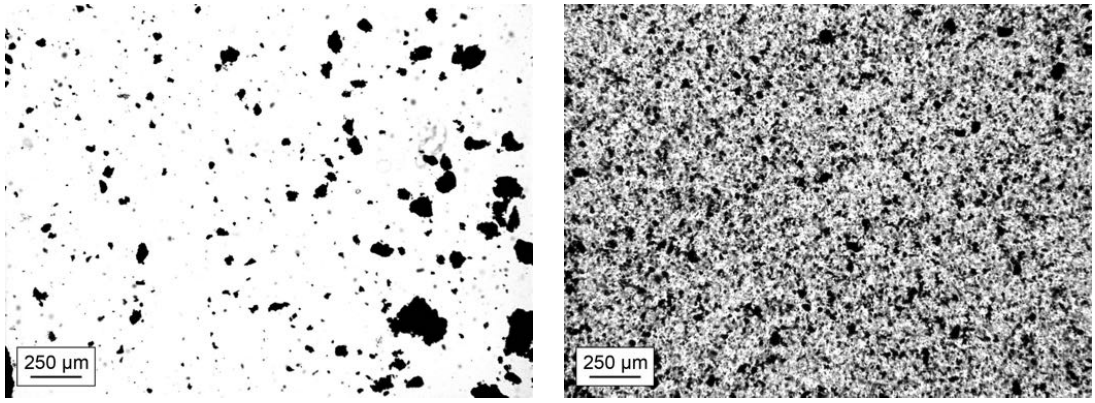


Figure 8.2.3: Characteristic lengths of XG-H GNP in epoxy resin after ultrasonication.

The same method was applied to investigate the use of solvents to disperse the GNPs. Approximately 50 g of solvent was used with 60 mg of GNP, or enough to completely cover the GNP powder. It was found that sonicating the GNPs in THF or NMP first for 10 mins, then adding the epoxy resin, followed by a second ultrasonication process for a further 10 min achieved similar results to 30 min of sonication in resin only, as shown in Figures 8.2.3 and 8.2.4. There was also an additional advantage to using solvents, as they evaporate during the sonication process which helps to reduce the temperature of the mixture during sonication. This meant that the sonication process did not need to be interrupted. The solvent was then evaporated from the mixture by a combination of stirring and heating above the flash point of the solvent.

Previous studies by Brooker [283] and Hsieh [142] found that carbon nanotubes (CNTs) tend to reagglomerate during the curing process as the viscosity of the epoxy decreases with the increasing temperature. Thus it is important to investigate the dispersion of

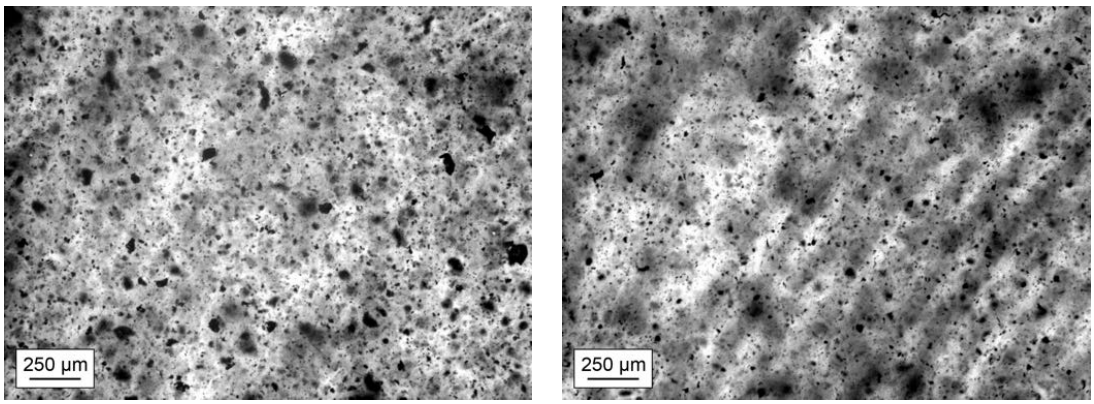


(a) Before sonication (b) After sonication

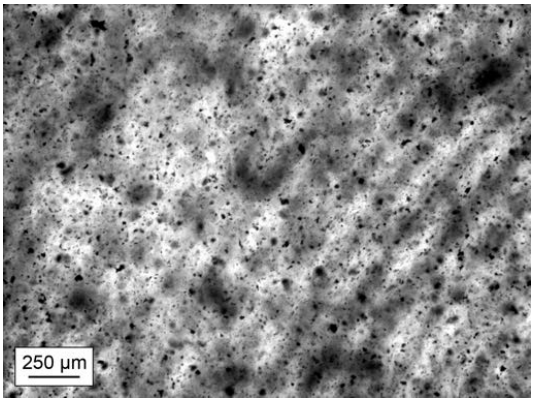
Figure 8.2.4: Transmission optical microscope images of 0.05 wt% GS GNP modified epoxies showing dispersion quality before and after sonicating.

the GNPs as the epoxy is curing. A drop of the prepared GNP modified resin was placed on a hot stage, which was mounted on an optical microscope. A 0.3 mm thick steel spacer was used to control the thickness of the resin between two glass cover slips. The cure cycle used in the hot stage investigation is identical to the cure cycle used to manufacture the bulk samples. A loading of 0.05 wt% XG-H GNP in epoxy was used for this study.

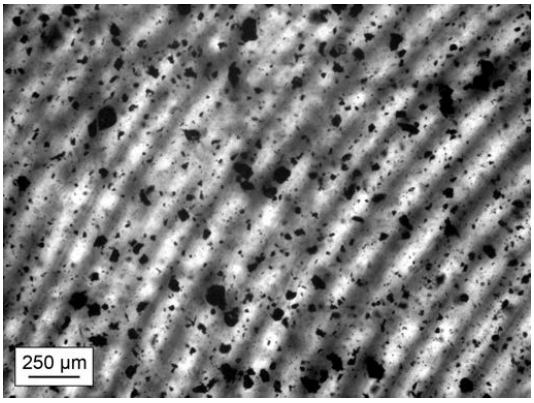
Selected images taken during the curing process are shown in Figure 8.2.5. The dispersion before the cure cycle was started shows a combination of small and large platelets, see Figure 8.2.5(a). As the temperature was increased to 90 °C, there was no reagglomeration of the GNPs. However, the larger GNPs were observed to sediment as can be seen in Figure 8.2.5(c) where there are less large particles at the top of the cured epoxy than at the bottom (Figure 8.2.5(d)). It was possible to observe this due to the small depth of field of the microscope lenses. Comparing Figures 8.2.5(b) and 8.2.5(c), there was no change in dispersion once gelation started at 90 °C.



(a) Before curing (b) 90 °C



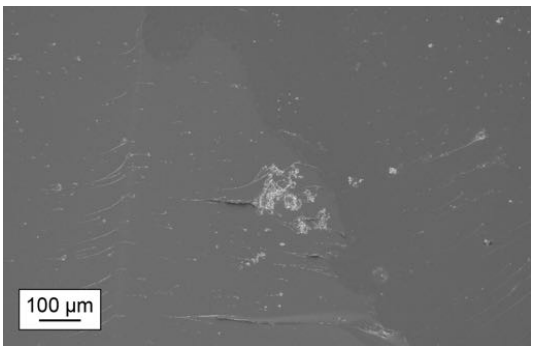
(c) End of cure cycle - Top



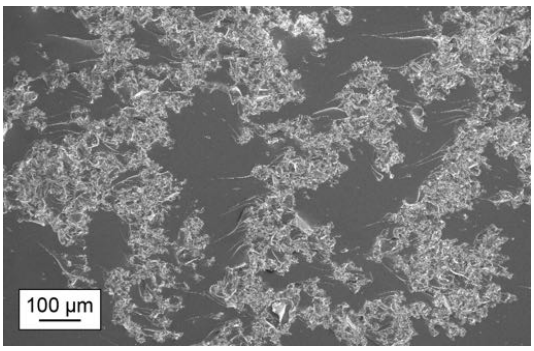
(d) End of cure cycle - Bottom

Figure 8.2.5: Hot stage investigation of 0.05 wt% GS GNP modified epoxies showing dispersion quality before and after curing. The concentric circles in the background are artifacts from the machined surface of the hot stage.

The effect of the sedimentation was evident when comparing the fracture surfaces of test samples taken from the top and bottom of the plate. The amount of GNP present at the top of the plate was significantly less than that at the bottom, as shown in Figure 8.2.6. The bulk plates were cured in vertical moulds so the GNPs at the top fall to the bottom during curing.



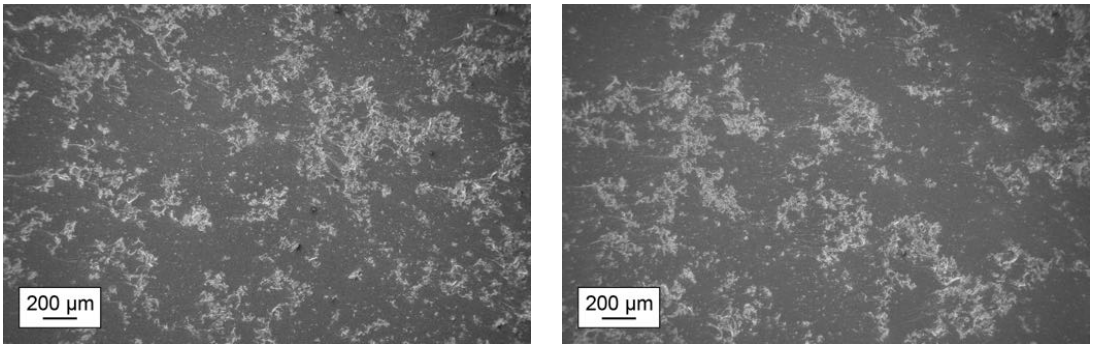
(a) Top of plate



(b) Bottom of plate

Figure 8.2.6: Fracture surface of 1.0 wt% XG-H GNP modified epoxies showing dispersion quality at different locations of the plate.

To address the sedimentation issue, the use of solvents and higher rates of cure were investigated. GNPs were dispersed in THF and a temperature ramp rate of 10°C/min, compared to the 2°C/min used previously, was investigated and found to suppress the sedimentation of the platelets, as shown in Figure 8.2.7. This is because the GNPs dispersed in THF were pulverised more evenly, reducing the size of the clumps, and the higher ramp rate reduces the time available for the platelets to settle.



(a) Top of plate (b) Bottom of plate

Figure 8.2.7: Fracture surface of 1.0 wt% XG-H-THF GNP modified epoxies showing dispersion quality at different locations of the plate.

8.3 Particle size analysis

Laser light spectroscopy (LLS) was used to measure the size of the GNPs prior to incorporation into the epoxy. This technique assumes that the particles are spherical and monodisperse, however the platelets are obviously not spherical and are polydisperse. The diameters measured from LLS are thus taken as the lateral dimensions of the platelets. The particle size distribution follows a log-normal distribution as shown in Figure 8.3.1. The effective particle diameters were measured to be 0.20 μm for the XG-C, 1.04 μm for the XG-H, 16.05 μm for the XG-M and 1.27 μm for the GS GNPs. The XG-H and GS GNPs had similar values of effective diameter, the XG-C GNPs were smaller and XG-M GNPs were larger. This is consistent with the manufacturer data sheets.

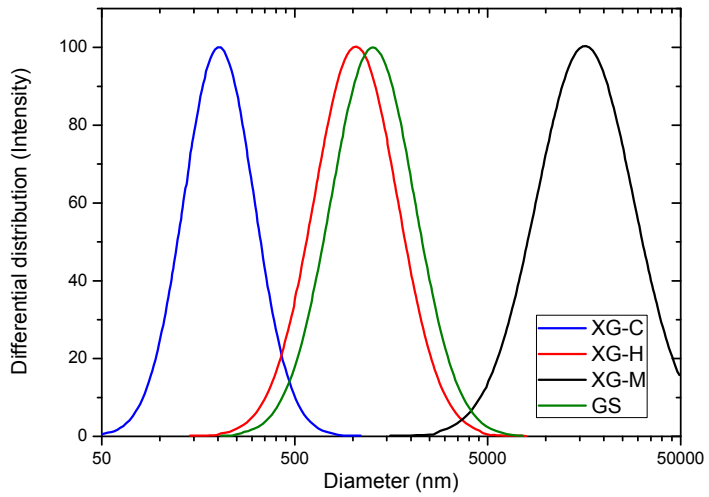


Figure 8.3.1: Particle diameter differential distribution on linear-log scale.

The effective particle diameters are defined as the modal values, which may not be

the most appropriate values to use because of the various orientations that the GNPs can be suspended in, as illustrated in Figure 8.3.2. Clearly, the modal value will correspond to a platelet that is at an angle to the incident laser. While the diffusion coefficents used to determine the effective diameter can be related to the dimensions of non-spherical particles for dynamic light scattering techniques, the analysis is complex and significant errors can be introduced [284]. In order to correctly characterise the lateral dimensions of the GNPs, the 95th percentile value should be used instead. The 95th percentile values of the lateral dimensions are 0.41 μm for the XG-C, 2.36 μm for the XG-H, 41.62 μm for the XG-M and 2.90 μm for the GS GNPs respectively.

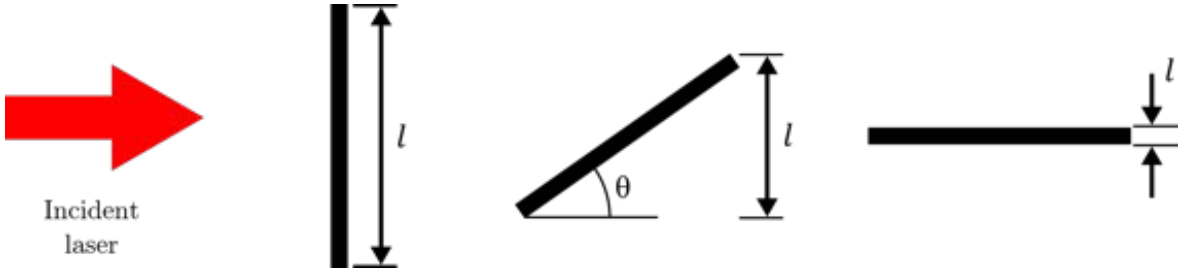


Figure 8.3.2: Illustration demonstrating errors from LLS method to measure the platelet sizes. l is the size measured using the LLS method.

X-ray diffraction (XRD) was used to measure the thickness of the bulk GNPs before they were added into the epoxy resin. The positions of the *00l* peaks was used to calculate the d-spacing of the GNPs in bulk. The GNPs are multi-layer graphitic materials rather than single layer graphene, hence only the peaks from *002* and above are observed.

The XRD patterns are shown in Figure 8.3.3 for the XG-H, XG-M, XG-C, GS, GNP-COOH and GNP-O_2 GNPs. The position of the *002* peaks for all of the GNPs correspond well to those of bulk graphite, typically at $2\theta = 26.7°$ [285]. The *004* peaks were also detected at $2\theta = 54.8°$. The differences in height between each sample is irrelevant because it is dependent on sample preparation. The sharpness of the peaks also clearly indicate that the GNPs have a crystalline structure. The full width at half maximum (FWHM) for all the GNPs, except for the XG-C GNP, were below 0.7°. The XG-C GNPs have a higher FWHM value of 1.67°, which indicates stacking defects and disorder in the crystal structure.

The d-spacing and crystal sizes calculated from the XRD analysis is shown in Table 8.3.1. The d-spacing was measured to be 0.334 nm, similar to graphite which indicates that the processing methods have removed the acid intercalant in the XG-H, XG-M, XG-C and GS GNPs. The calculated values of crystal size for the XG-C, GS, GNP-COOH and GNP-O_2 show good agreement with the values of thickness from the

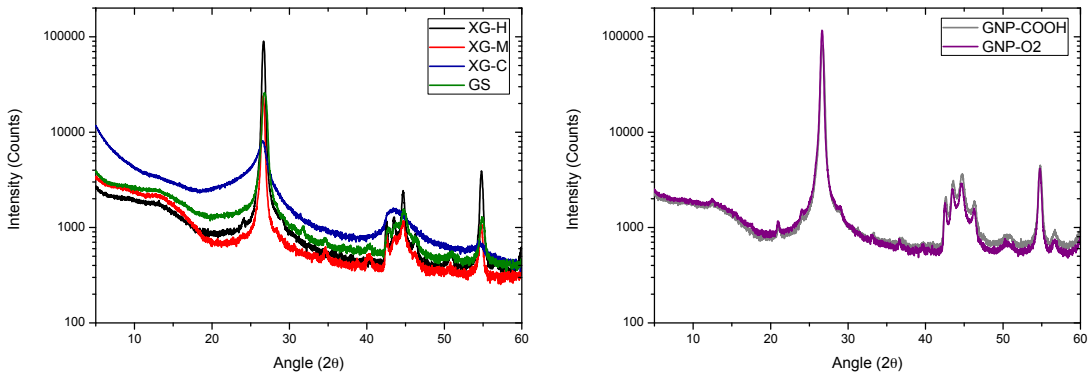


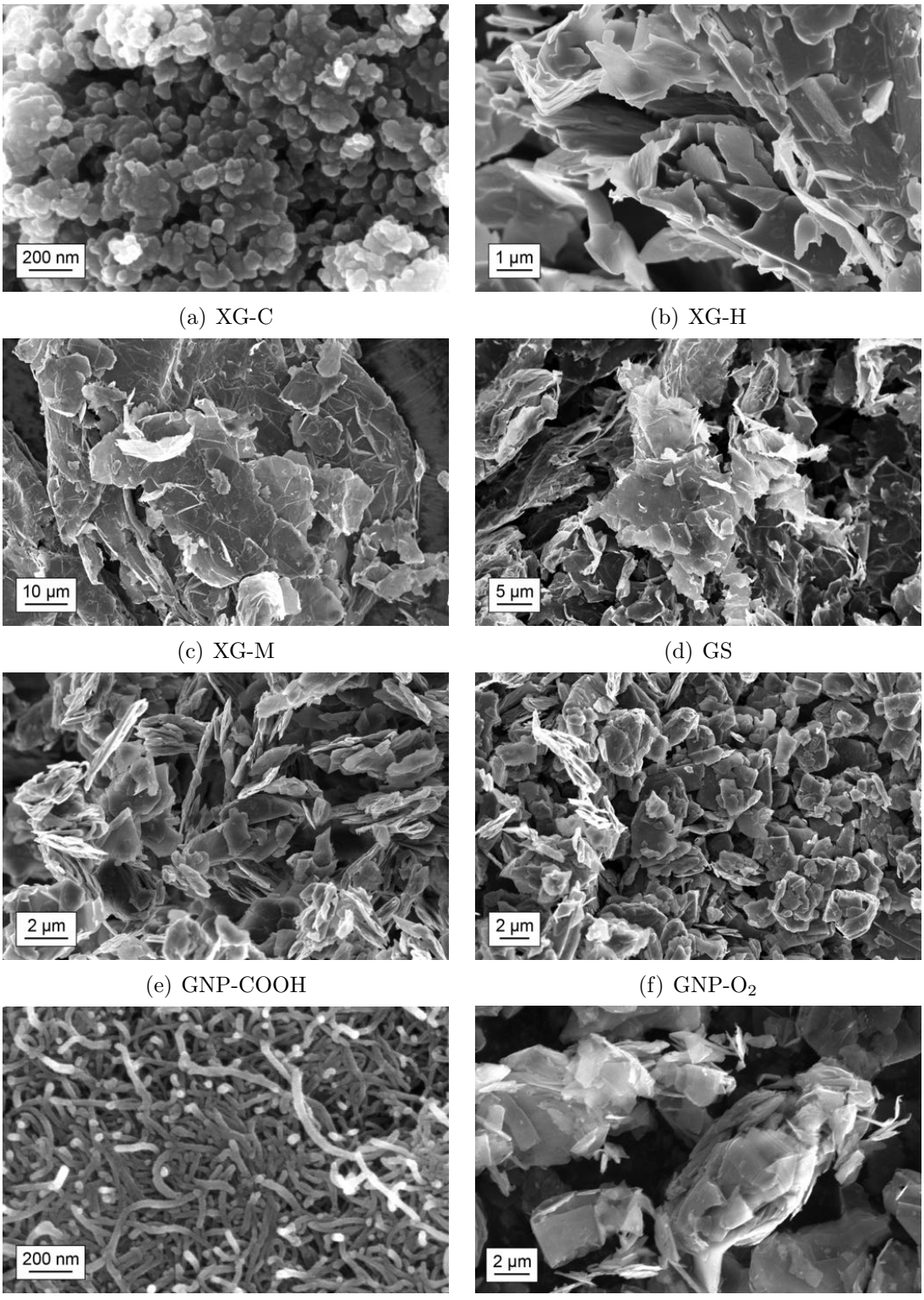
Figure 8.3.3: XRD patterns obtained for bulk GNPs.

manufacturer (see Table 3.3.1). However, the thickness of the XG-H and XG-C GNPs were larger than expected, at 31.1 and 28.8 nm respectively. The average number of layers is also shown in Table 8.3.1 and is directly proportional to the crystal size because the d-spacing is the same for all the GNPs.

Table 8.3.1: d-spacing, FWHM and crystal size measurements from XRD analysis.

Modifier	d-spacing (nm)	FWHM (°)	Crystal size (nm)	Number of layers
XG-H	0.3343	0.38	31.1	93
XG-M	0.3339	0.40	28.8	86
XG-C	0.3354	1.67	5.2	16
GS	0.3342	0.65	15.2	45
GNP-O_2	0.3335	0.36	33.6	101
GNP-COOH	0.3339	0.47	23.1	69

The lateral dimensions and thickness of the GNPs were also measured using the FEGSEM. The samples were prepared by sonicating the GNPs in THF for 10 min, and then drying in air. The carbon based modifiers did not require any coating as they are already conductive. The samples were placed directly onto a SEM stub using conductive tape. Loose particles were then removed using compressed air to prevent contamination of the sample chamber. Selected images are shown in Figure 8.3.4. The XG-C GNPs, which have the smallest effective diameters as measured using LLS, resemble a particulate rather than a platelet structure, as shown in Figure 8.3.4(a).



(a) XG-C (b) XG-H

(c) XG-M (d) GS

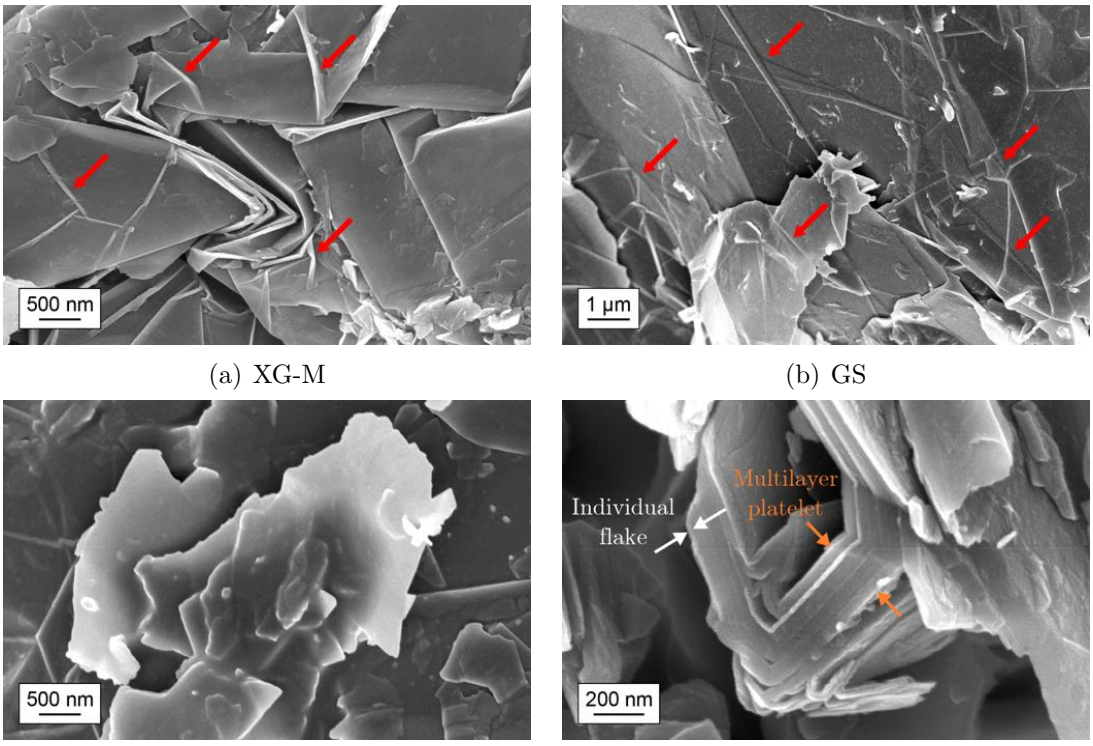
(e) GNP-COOH (f) GNP-O_2

(g) CNT-COOH (h) Graphite flakes

Figure 8.3.4: FEGSEM micrographs of GNPs and CNTs after 20 min of ultrasonication in THF solvent and drying in air.

There were several features that were identifiable from the FEGSEM micrographs. Firstly, wrinkles were observed in the GNPs from XG Sciences and Graphene Supermarket, as shown in Figures 8.3.5(a) and 8.3.5(b). These GNPs were manufactured using an acid exfoliation method, which leaves trace amounts of hydroxyl and carbonyl functional groups. The local strains and electrostatic repulsion caused by the presence of these functional groups are thought to be the cause of the excessive wrinkling. In contrast, the less aggressive "Split-Plasma" process to manufacture the HDPlas GNPs appears to cause less wrinkling, as shown in Figures 8.3.4(e) and 8.3.4(f), even though similar functional groups are present. The bulk functionalised CNTs (CNT-COOH) were highly agglomerated and randomly oriented, as shown in Figure 8.3.4(g). The graphite flakes agglomerates, as shown in Figure 8.3.4(h), were approximately 15 μm in lateral size and 10 μm in thickness. The sheets of graphene were folded over each other, with very few individual platelets.

The edges of the GNPs were also observed to be damaged rather than having perfectly straight interfaces, as shown in Figure 8.3.5(c). Many of the platelets are folded and remain as multilayer platelets after ultrasonication, as shown in Figure 8.3.5(d).



(a) XG-M (b) GS

(c) XG-H (d) GNP-O_2

Figure 8.3.5: FEGSEM micrographs of GNPs showing defects. Wrinkles on the GNPs are identified by the red arrows.

The lateral dimensions and thickness of the GNP flakes measured from the FEGSEM

micrographs are summarised in Table 8.3.2.

Table 8.3.2: Modifier size measurements from FEGSEM micrographs.

Modifier	Mean lateral size (μm)	Mean thickness (nm)	Aspect ratio
XG-H	3.2 ± 1.7	31 ± 7	103
XG-M	21.7 ± 9.4	19 ± 9	1142
XG-C	0.3 ± 0.1	16 ± 4^a	19
GS	3.9 ± 1.6	19 ± 6	205
GNP-COOH	2.3 ± 1.0	27 ± 9	85
GNP-O_2	2.4 ± 0.8	29 ± 9	83
CNT-COOH	1.0 ± 0.2^b	28 ± 5^c	36
GF	–	25 ± 12	–

[a] Particulate diameter.

[b] Carbon nanotube length.

[c] Carbon nanotube diameter.

The values of thickness that are quoted refer to the individual observable flakes, although most of the GNPs were present as multilayer platelets. It was not be expected that the platelets would be exfoliated because they will reagglomerate during the drying process. The individual graphene sheets are not distinguishable from the stack due to the limitation of the FEGSEM, where the resolution limit is 1.5 nm, whereas the individual graphene sheets are approximately 0.335 nm. The average thicknesses measured were approximately 20 to 30 nm, which corresponds to 90 monolayers and agrees well with the XRD results. The stacking of the GNPs also appear to be highly ordered, corroborating with the FWHM values from the XRD analysis. The actual thickness of the GNPs is better determined from the fracture surfaces of the GNP modified epoxies. For comparison, the graphite flakes have a similar range of flake thicknesses, but the mean thickness of each graphite multilayer platelet was measured to be 1.3 ± 0.1 μm. This is expected as the GNPs were manufactured from graphite intercalation compounds.

The mean lateral size measured from the FEGSEM micrographs show good agreement with the 95th percentile laser light spectroscopy results. The results from both techniques are not expected to be equal as the laser light spectroscopy technique gives an intensity-weighted differential size distribution, whereas the microscopy technique gives a number-weighted distribution. The XG-C GNPs did not have a platelet-like structure, as discussed previously, and thus the mean lateral size was approximated to be the size of each particulate agglomerate. This was also the cause of the increase in FWHM from the XRD results. The length of the CNT-COOH modifiers measured from the FEGSEM micrographs agree with the manufacturer's data sheet (0.98 ± 0.22

μm compared to 1 μm), however the measured diameters were much higher (28 $\pm$5 nm compared to 5 nm). The diameters measured here agree well with the literature [117, 118], which have quoted values of nanotube diameters between 15 to 20 nm.

8.4 XPS Spectra

Figure 8.4.1 shows the XPS survey spectra of the bulk GNP powders. For all of the GNPs, the C1s (~284 eV) and O1s (~531 eV) signals are clearly defined. Additionally, weak signals that are characteristic of N1s (~399 eV), Si2p (~103 eV) and S2p (~168 eV) were detected. The high resolution, core level C1s spectra, as shown in Figure 8.4.2, reveal that there was only one peak at 284.2 eV, corresponding to the C-C bond [286]. This was unsurprising given that the GNPs were composed primarily of carbon with atomic concentrations above 90%, as shown in Table 8.4.1.

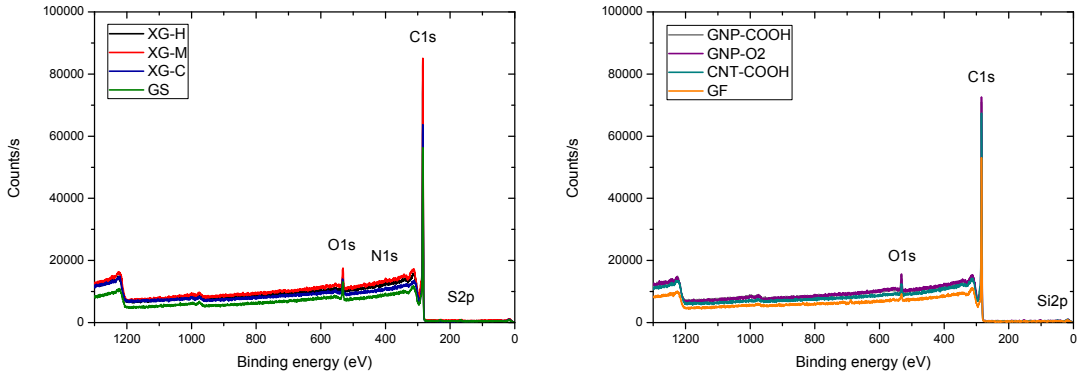
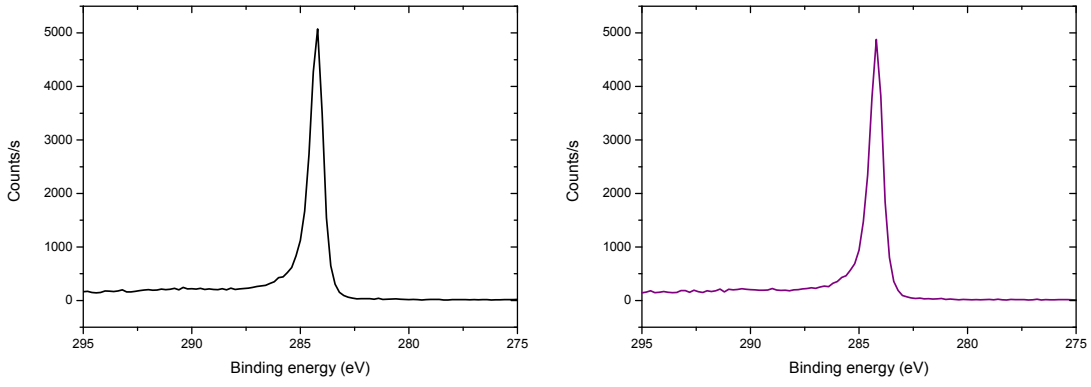


Figure 8.4.1: XPS survey spectra of bulk GNPs.



(a) XG-H (b) GNP-O_2

Figure 8.4.2: Typical high resolution XPS C1s spectra of bulk GNPs.

The atomic concentrations of each element present on the surface of the GNPs are summarised in Table 8.4.1. The carbon content of the GNPs from XG Sciences (XG-

H, XG-M and XG-C) and Graphene Supermarket (GS) were measured to be lower than the manufacturer's quoted values. Trace elements of nitrogen, fluorine, silicon and sulphur were detected and were typically less than 1 at.%. The GS GNP had the lowest carbon content and highest oxygen content, which is indicative of the relatively poor quality of the GNPs, as shown in Figure 8.3.4(d), as the other elements were present as functional groups at defect sites and edges. Indeed, a higher FWHM value was measured from the XRD for the GS GNP, indicating higher disorder in the crystal structure. The XG-M GNPs also have comparatively low carbon content, which could be due to the larger platelet sizes being more prone to defects. The XG-H GNPs have the highest carbon content (96.1 at.%), which is of similar magnitude to the graphite flakes (GF).

The functionalised GNPs from HDPlas (GNP-COOH and GNP-O_2) contain approximately 6 at.% of oxygen, which agrees well with the manufacturer's data sheet. It is of note that this value of oxygen content is not significantly higher than the GNPs that were not functionalised (XG and GS GNPs). This is because the functional groups were only attached to the edges, dislocation sites and defects, similar to the other GNPs. However, there is insufficient information regarding what functionalities these oxygen elements are present as.

Table 8.4.1: Atomic percentage of GNP surface element composition.

Modifier	Element (at.%)					
	Carbon	Oxygen	Nitrogen	Fluorine	Silicon	Sulphur
XG-H	96.08	3.92	–	–	–	–
XG-M	92.43	5.87	0.99	–	–	0.70
XG-C	94.10	5.18	0.71	–	–	–
GS	91.58	7.53	–	–	–	0.89
GF	95.89	3.21	–	0.90	–	–
GNP-COOH	94.07	5.61	–	–	0.31	–
GNP-O_2	93.17	6.51	–	–	0.33	–
CNT-COOH	96.73	3.27	–	–	–	–

8.5 Morphology

The morphology and dispersion of the graphene nanoplatelet modified epoxy polymers were inherently difficult to study using AFM because of the high aspect ratios and low weight percentages used. Figure 8.5.1 illustrates how it can be difficult to obtain a proper representation of the dispersion. At the GNP concentrations used, there is

a low probability of cutting through a significant number of platelets. Additionally, the GNPs themselves were typically larger than the maximum scan size of the AFM, so it can be difficult to measure dispersion quality. However, sufficient images were obtained to determine the quality of these GNPs after they have been incorporated in epoxy.

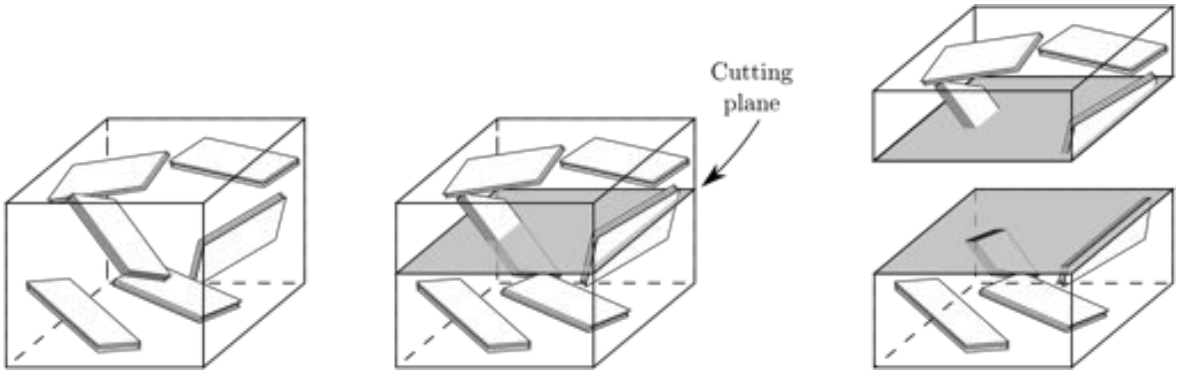
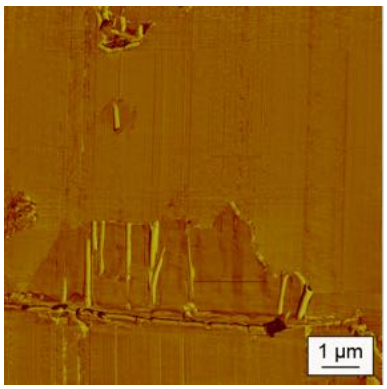
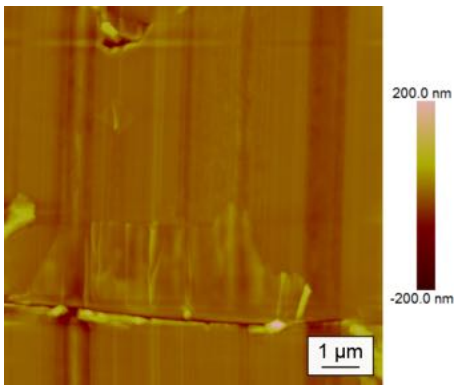


Figure 8.5.1: Preparation of AFM samples of GNP modified epoxies by microtome.

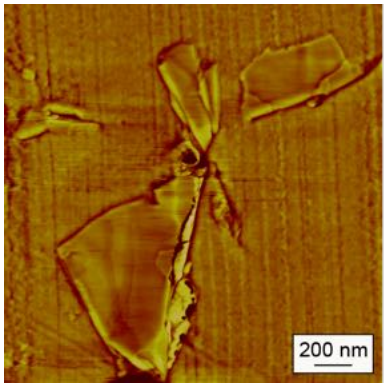
Platelets as large as 8 μm were observed to have pulled out during the microtoming process, as shown in Figure 8.5.2(a). The thickness of the platelet measured from height image, as shown in Figure 8.5.2(b), was measured to be about 20 nm. However, this is not a good method to measure the thickness of the platelets, as it is not clear as to how many of the platelets actually pulled out in each bundle. There were also many platelets measured to be under 1 μm in length, indicating some damage from the sonication process as shown in Figure 8.5.2(c).



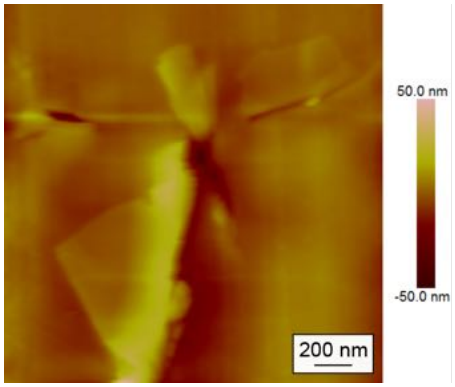
(a) Phase image for 0.5 wt% GS-THF



(b) Height image for 0.5 wt% GS-THF



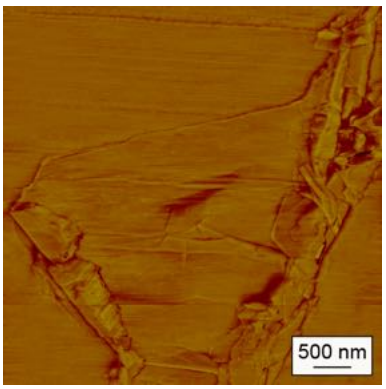
(c) Phase image for 1.0 wt% GS-THF



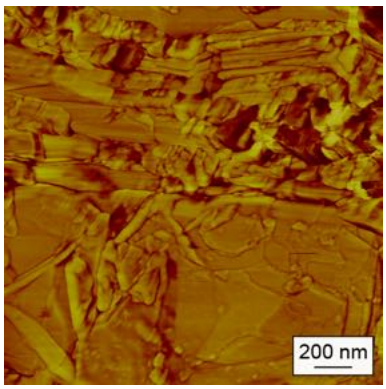
(d) Height image for 1.0 wt% GS-THF

Figure 8.5.2: AFM micrographs of GS GNP in epoxy.

The XG-H GNPs were found to be thicker (see Figure 8.5.3(a)) and more agglomerated (see Figure 8.5.3(b)) than the GS GNPs. There were no significant differences in the hardness of the GNPs (measured as phase difference on the AFM) compared to the epoxy because of the anisotropic nature and the relatively small thickness of these platelets.



(a) Phase image for 0.5 wt% XG-H-THF



(b) Phase image for 1.0 wt% XG-H-THF

Figure 8.5.3: AFM micrographs of XG-H GNP in epoxy.

The graphite flakes were very agglomerated in the epoxy as shown in Figures 8.5.4(a). There are also some defects on the surface of the graphite flakes, shown in Figure 8.5.4(b), which were not prominent in the GNPs. It is clear that the GF is much thicker than the GNPs and of a lower quality. The edges of the platelets appear to be soft from the phase images due to the slippage of the AFM probe.

The dispersion of the graphene nanoplatelets was examined from the FEGSEM images of the fracture surfaces of the GNP modified epoxy polymers. This does not give the true dispersion of the GNPs because of the many step changes as the crack propagates,

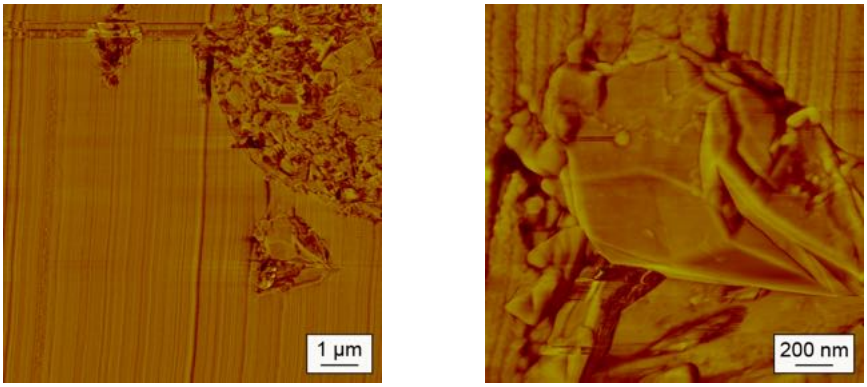
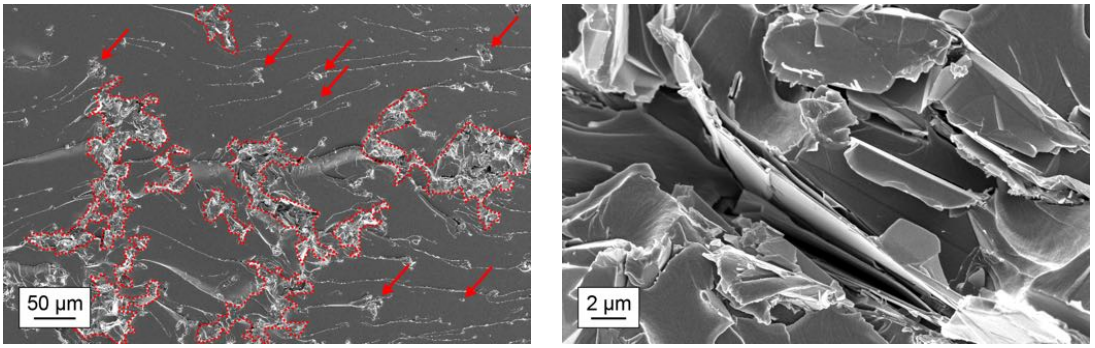


Figure 8.5.4: AFM micrographs of graphite flakes in epoxy.

visible as river lines, and the pullout of the GNPs, which can appear as voids, but can give an indication of the quality of dispersion.

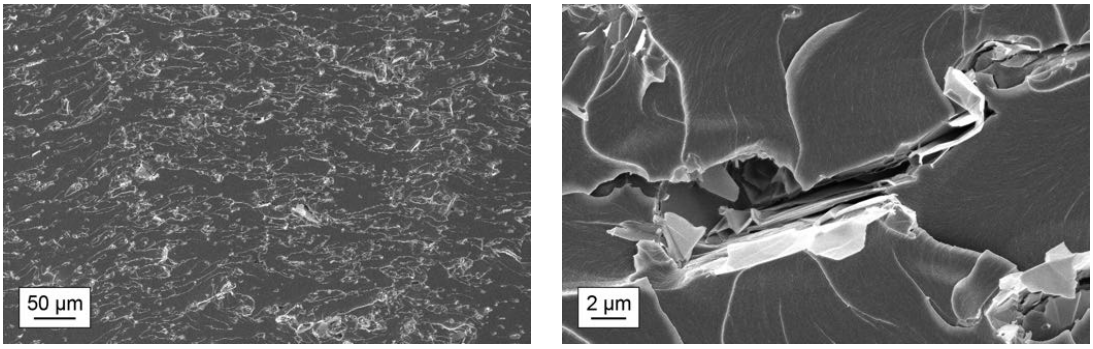
The fracture surface of the 1.0 wt% XG-H-THF modified epoxy is shown in Figure 8.5.5. The large agglomerates are highlighted in red and there were also some smaller platelets dispersed, indicated by the red arrows. The extent of agglomeration can be observed at higher resolution, as shown in Figure 8.5.5(b), where significant clustering of the platelets can be seen.



(a) x500 magnification (b) x10k magnification

Figure 8.5.5: FEGSEM micrograph of 1.0 wt% XG-H-THF modified epoxy. Regions enclosed in red are large agglomerates and the smaller agglomerates of GNP indicated by red arrows.

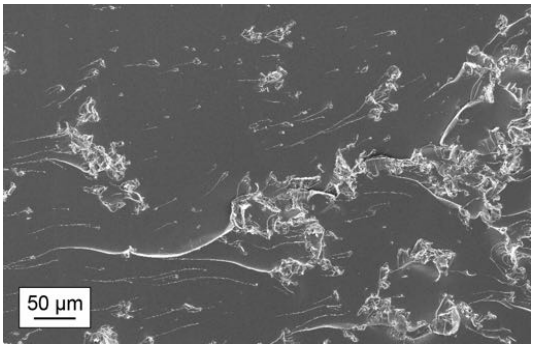
The fracture surface of the 1.0 wt% XG-H-NMP modified epoxy is shown in Figure 8.5.6. Clearly, the graphene nanoplatelets sonicated in NMP were more evenly dispersed, while agglomerates of 50–100 μm were observed for the GNPs sonicated in THF, as shown in Figure 8.5.5. For both solvents, the GNPs were dispersed as stacked platelets, rather than as individual platelets. For both dispersions in THF and NMP, no polymer was found between the layers, hence the dispersion is described as particulate, according to Figure 2.2.25.



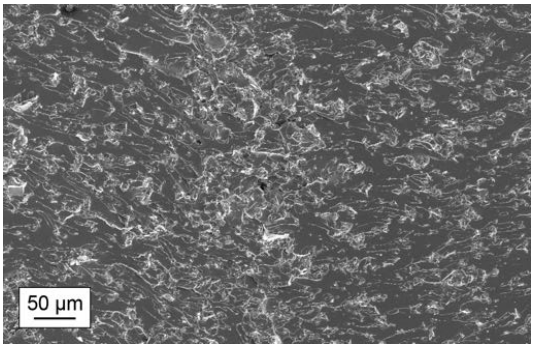
(a) x500 magnification (b) x10k magnification

Figure 8.5.6: FEGSEM micrograph of 1.0 wt% XG-H-NMP modified epoxy.

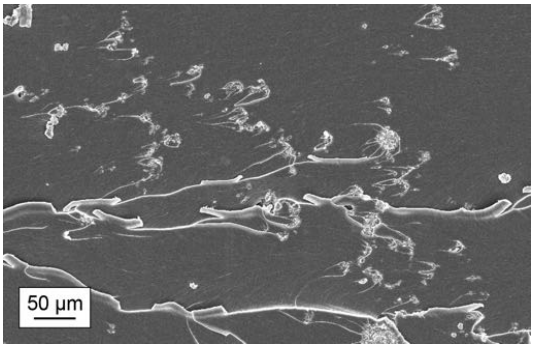
The XG-M, XG-C and GS nanoplatelets also show similar trends in dispersion when comparing the two solvents, as shown in Figure 8.5.7. The XG-M GNPs are have a much larger lateral size and this can result in a more agglomerated structure than the other GNPs. The size of the agglomerates were measured for each of the GNP modified epoxies from the fracture surfaces, and the agglomerates of XG-M GNPs were up to 300 μm and 30 μm in length when dispersed in THF and NMP, respectively. This is compared to 150 μm and 100 μm for the XG-H and GS GNPs dispersed in THF, respectively. Both XG-H and GS GNPs dispersed in NMP have agglomerates of approximately 20 μm in size. The consequence of agglomeration is a lower effective aspect ratio and this can have a negative effect on the mechanical and fracture properties. The agglomerates of XG-C-THF GNPs were up to 4 μm in length. Particulates as small as 100 nm were observed for the XG-C-NMP GNP modified epoxy polymers, however they no longer possess a platelet-like structure but are agglomerated particles.



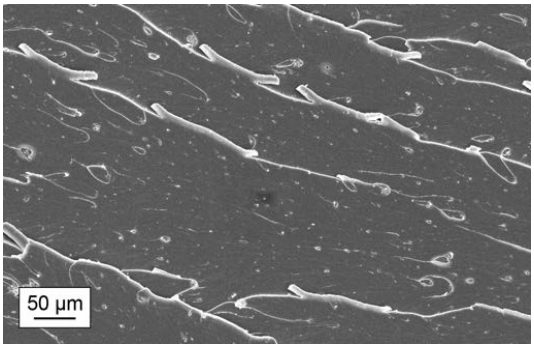
(a) 1.0 wt% XG-M-THF



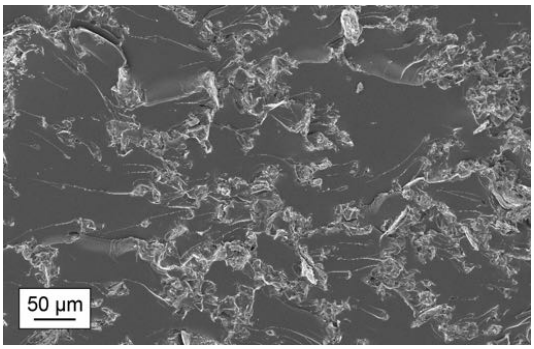
(b) 1.0 wt% XG-M-NMP



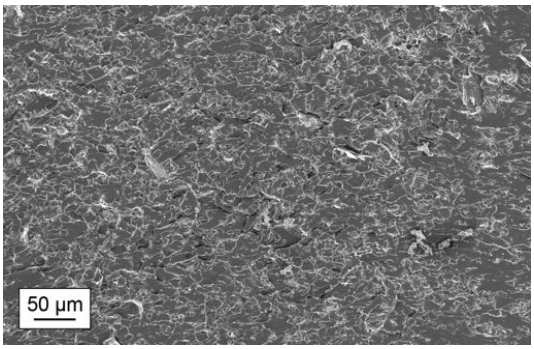
(c) 1.0 wt% XG-C-THF



(d) 1.0 wt% XG-C-NMP



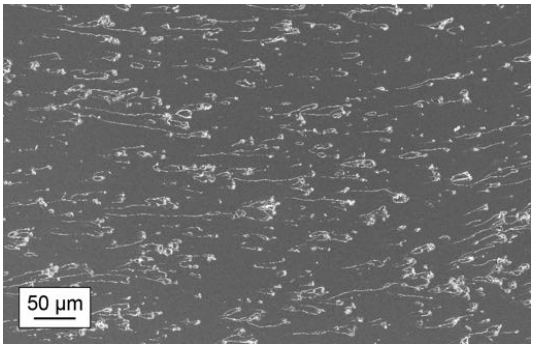
(e) 1.0 wt% GS-THF



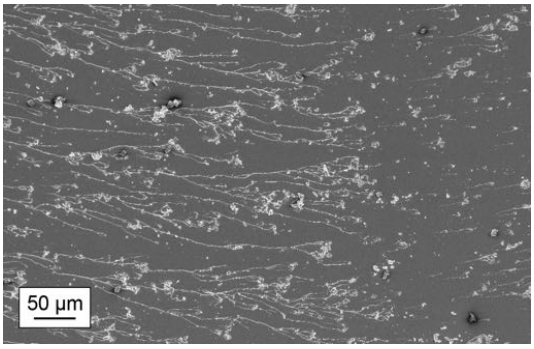
(f) 1.0 wt% GS-NMP

Figure 8.5.7: FEGSEM micrograph of GNP modified epoxy.

At a concentration of 0.5 wt%, the COOH and O_2 functionalised graphene nanoplatelets were found to be well dispersed as stacks of platelets approximately 10 μm in size, as shown in Figure 8.5.8, without the use of solvents, i.e. dispersed directly into the epoxy resin. Increasing the GNP content to 1.0 wt% results in larger agglomerates of approximately 60 μm, as shown in Figure 8.5.9. These are smaller than the agglomerates found for the GNPs that have not been functionalised and which are dispersed in THF. The individual stacks of platelets had smooth surfaces but appear to be damaged at the edges.

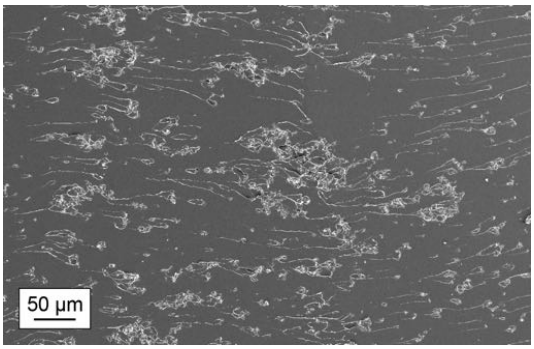


(a) GNP-COOH

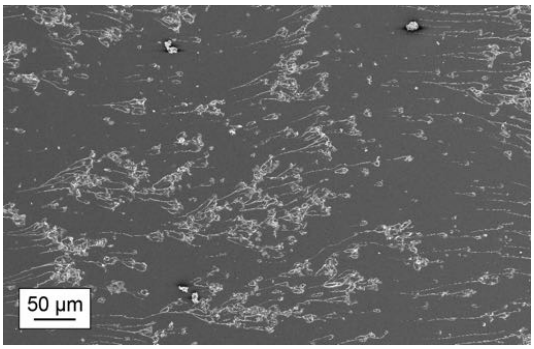


(b) GNP-O_2

Figure 8.5.8: FEGSEM micrograph of epoxy modified with 0.5 wt% functionalised GNPs.



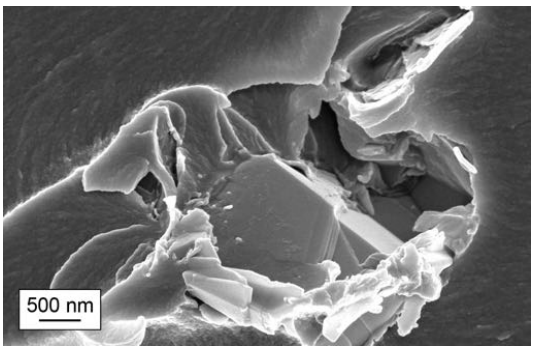
(a) GNP-COOH



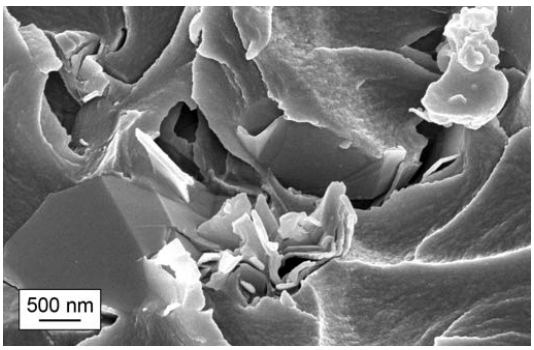
(b) GNP-O_2

Figure 8.5.9: FEGSEM micrograph of epoxy modified with 1.0 wt% functionalised GNPs.

On closer examination of the GNP-COOH and GNP-O_2 GNPs at higher magnifications, such as those in Figure 8.5.10, the stacks of GNPs within the agglomerates appear to be broken into sub-micron sized platelets, presumably caused by the sonication process. Zaldivar *et al.* [287] found that the O_2 plasma treatment can also damage the GNPs, seen as voids throughout the platelet surface and edges.



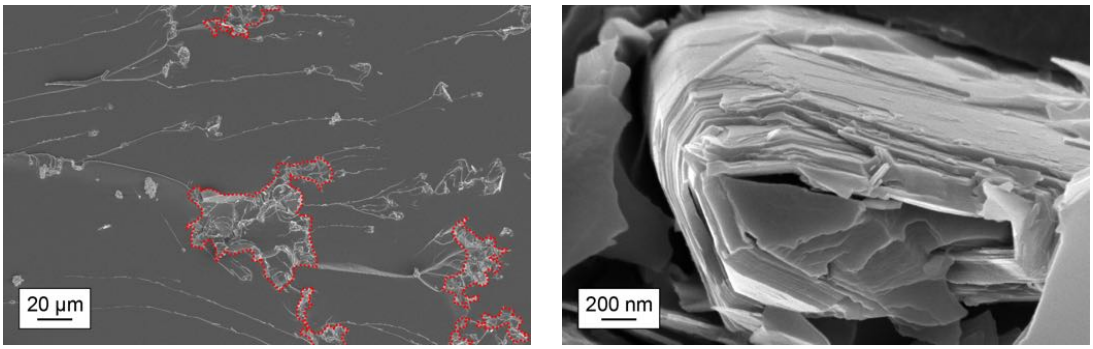
(a) GNP-COOH



(b) GNP-O_2

Figure 8.5.10: FEGSEM micrograph of epoxy modified with 1.0 wt% functionalised GNPs at higher magnification.

The graphite flakes were heavily agglomerated as shown in Figure 8.5.11, where the large agglomerates were highlighted in red. Each graphite flake was observed to have up to 50 stacked plates, which were poorly adhered to the epoxy matrix as indicated by the smooth surfaces in the debonded platelets in Figure 8.5.11(b).



(a) x1000 magnification (b) x100k magnification

Figure 8.5.11: FEGSEM micrograph of graphite flake modified epoxy. Regions enclosed in red are large agglomerates.

The COOH functionalised MWCNT agglomerated into clusters of different sizes in the epoxy, as shown in Figure 8.5.12. Most of the CNTs were clustered into spheres, with diameters ranging from 200 nm to 40 μm, with very few individual nanotubes dispersed in the epoxy. The nanotubes also form "necklace"-like chains of agglomerates, similar to the agglomerated silica nanoparticles in the hybrid CTBN-NS modified epoxy (see §5.2 and [76]).

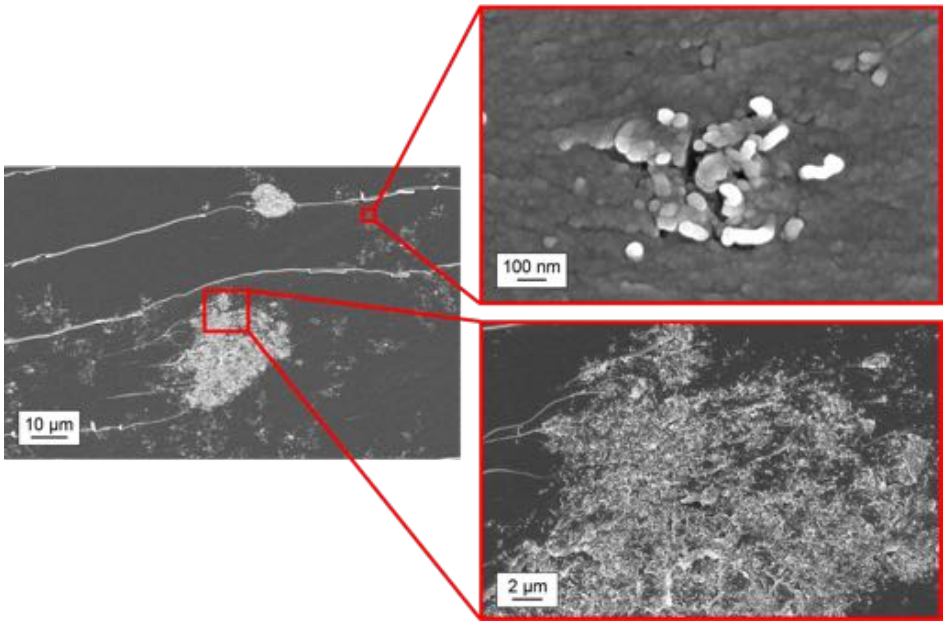


Figure 8.5.12: FEGSEM micrograph of COOH functionalised MWCNT modified epoxy.

8.6 Glass transition temperature

The glass transition temperatures, T_g, of the epoxy were measured for the unmodified epoxy, epoxy with solvents and GNP modified epoxy. Figure 8.6.1 shows that the tetrahydrofuran (THF) had little effect on the T_g when it was evaporated, but that the n-methyl-pyrrolidone (NMP) reduced the T_g by 10 °C. This indicates that NMP may have pre-reacted with the epoxy resin during the solvent removal process. Both solvents reduced the T_g significantly if they were not removed, as indicated by the unevaporated data in Figure 8.6.1.

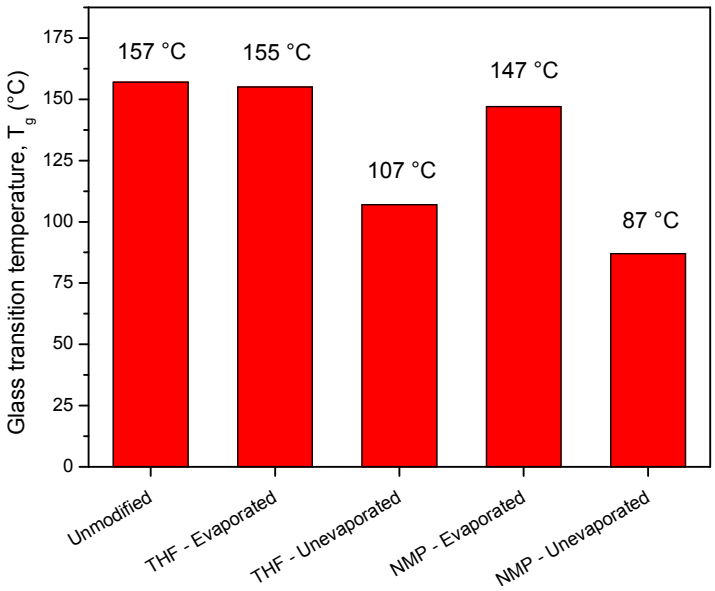


Figure 8.6.1: Effect of solvents on the glass transition temperature of the epoxy polymer.

The glass transition temperatures of the GNP modified epoxy polymers are shown in Figure 8.6.2. The T_g of the unmodified epoxy was measured to be 157 °C. The addition of the GNPs from XG Sciences reduced the T_g of the epoxy with increasing GNP content, irrespective of the size of the nanoplatelets. In general, the GNPs dispersed in NMP exhibited lower glass transition temperatures than the GNPs dispersed in THF, similar to the trend observed for the unmodified epoxies. The GS modified epoxies, dispersed with solvent, show significant reductions in the T_g with GNP content compared to the unmodified epoxy, as shown in Figure 8.6.2(b). This is caused by the entrapment of solvent, rather than an interaction between the GNPs and the epoxy, as the GNPs that were dispersed without solvent into the same epoxy and did not affect the T_g significantly.

The decrease in T_g associated with the higher loadings of GNP is caused by the increase

in solvent required to disperse the GNPs. The GNP powder has a very low density, and thus requires a relatively large volume of solvent to disperse satisfactorily. This increase in the amount of solvent results in a longer time required to remove the solvent, which at elevated temperatures can cause a reaction between the solvent and the epoxy resin. The GNP-COOH, GNP-O_2 and CNT-COOH modified epoxies show a small decrease in T_g with modifier content as the carboxyl and carbonyl functional groups can react with the epoxy resin [288]. The graphite flakes, GF, have a high purity level and did not affect the T_g.

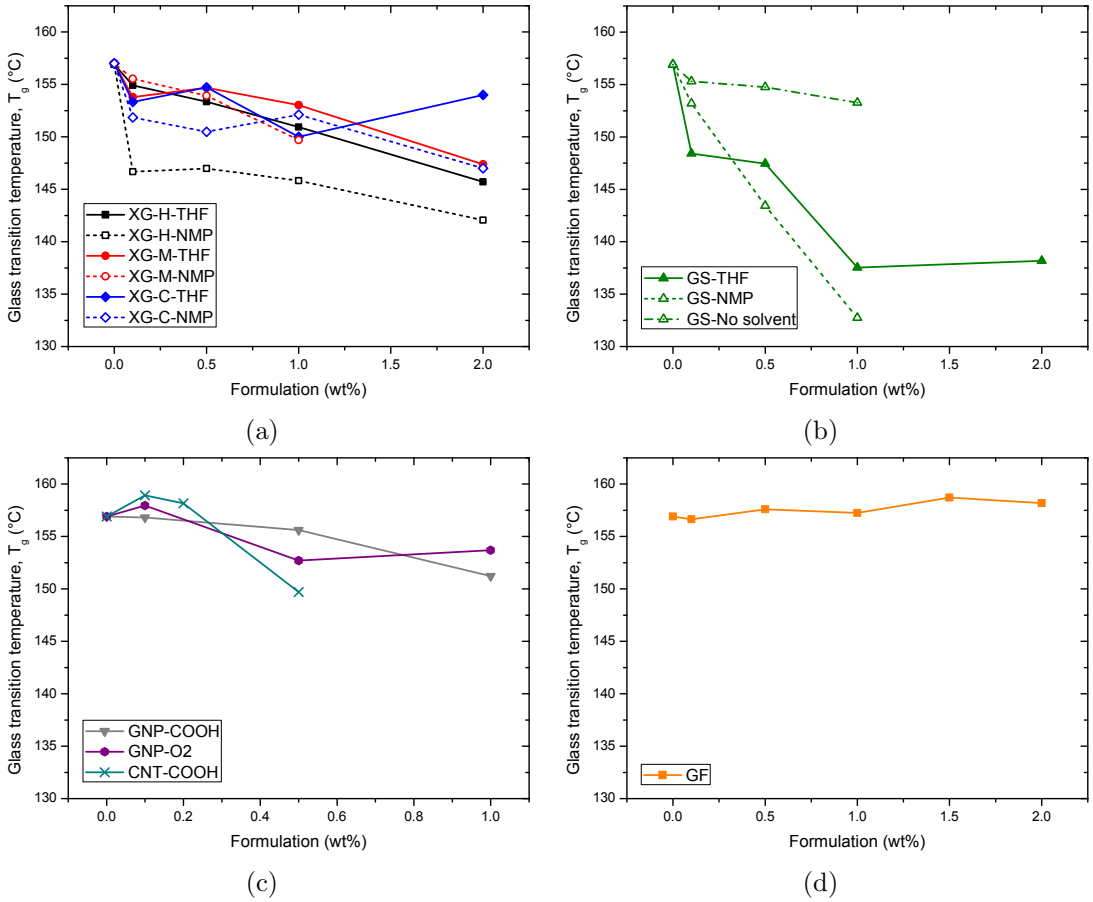
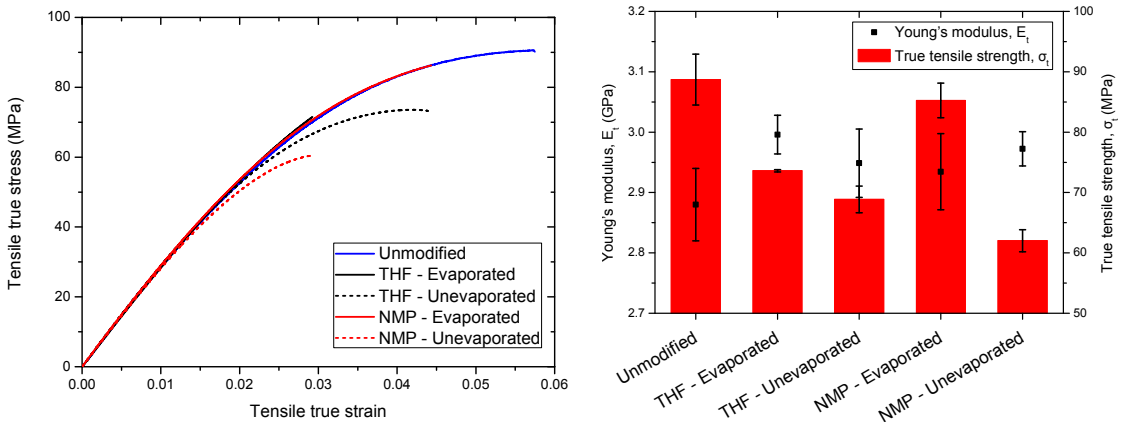


Figure 8.6.2: Glass transition temperatures for the various GNP modified epoxy polymers.

8.7 Tensile properties

The Young's modulus, E_t, of the unmodified epoxy was measured to be 2.9 GPa. Typical true stress-strain curves for the unmodified epoxy and the epoxy with 10 wt% of solvents, both dissolved and evaporated, are shown in Figure 8.7.1(a). The use of solvents did not affect the E_t of the epoxy, however did reduce the tensile strength, σ_t, and tensile strain at break, ε_B, even when the solvents were removed prior to

curing as summarised in Figure 8.7.1(b). The yield strength of the epoxy was reduced significantly when the solvent was not removed, as shown in Figure 8.7.1(a), as the solvent plasticises the epoxy; note that the stress-strain curves for the case when the solvents were evaporated follow the unmodified epoxy exactly.



(a) Typical tensile true stress-strain curve (b) Tensile properties

Figure 8.7.1: Tensile properties of unmodified and 10 wt% solvent modified epoxies.

Typical true stress-strain curves for the unmodified and 2.0 wt% XG-H GNP modified epoxy, with the GNPs dispersed in THF and NMP, are shown in Figure 8.7.2. For both solvents, the addition of 2.0 wt% XG-H GNP to the epoxy reduced the ε_B significantly from 5.7% to 2.3%. The E_t of the composites were also increased by the addition of the GNPs.

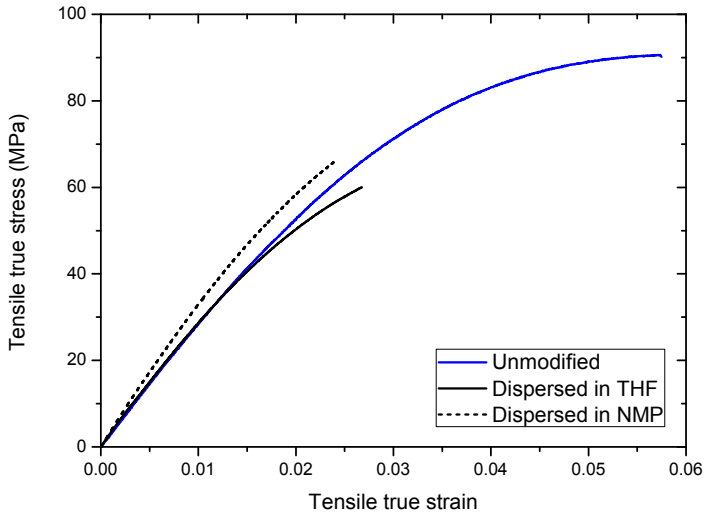
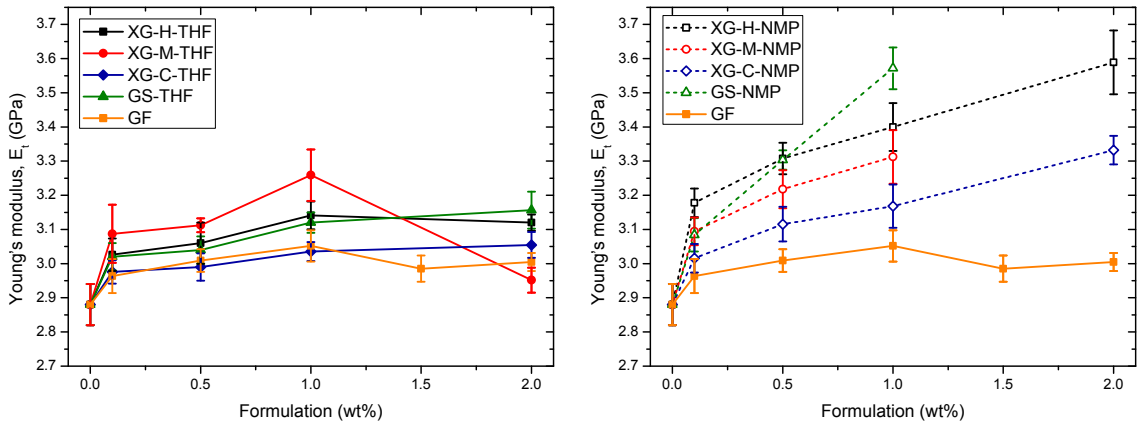


Figure 8.7.2: Typical tensile true stress-strain curves for unmodified and 2 wt% XG-H GNP modified epoxies.

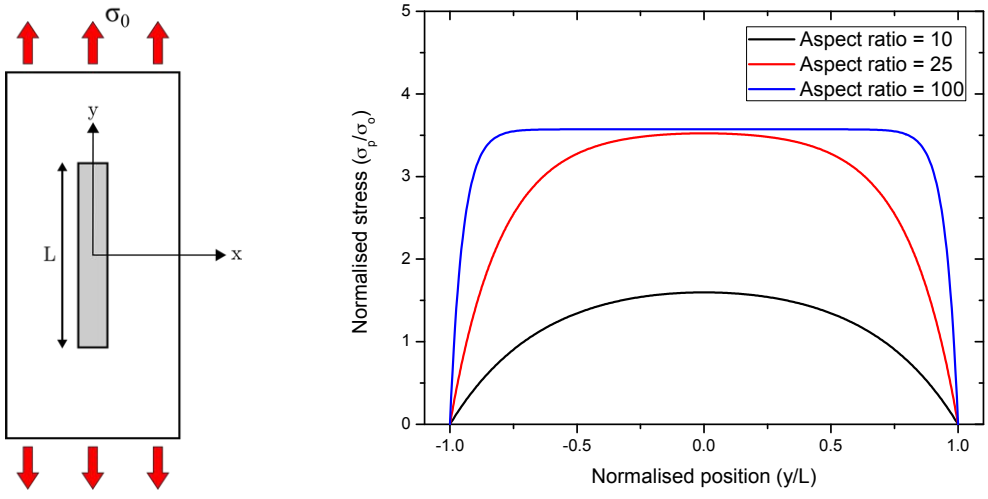
The E_t of the epoxy increases with GNP content as summarised in Figure 8.7.3. This was expected given the high modulus of the GNPs [115]. The epoxies modified with

GNPs dispersed in THF had a lower E_t than the GNPs dispersed in NMP. The E_t of the 2.0 wt% XG-H modified epoxy when dispersed using THF was measured to be 3.1 GPa, whereas the GNPs dispersed using NMP was measured to be 3.6 GPa. This is because of the agglomeration of the platelets when dispersed in THF, as discussed in §8.5. The effect of agglomeration is to reduce the effective aspect ratio of the GNPs, which in turn reduces the stress transfer into the GNPs, as shown in Figure 8.7.4. The stress in the platelet, σ_p, due to an applied stress, σ_0, increases with aspect ratio based on the shear-lag model. In particular, the 2.0 wt% XG-M-THF modified epoxy shows a decrease in E_t.



(a) Dispersed in THF (b) Dispersed in NMP

Figure 8.7.3: Young's modulus for the various GNP modified epoxy polymers.



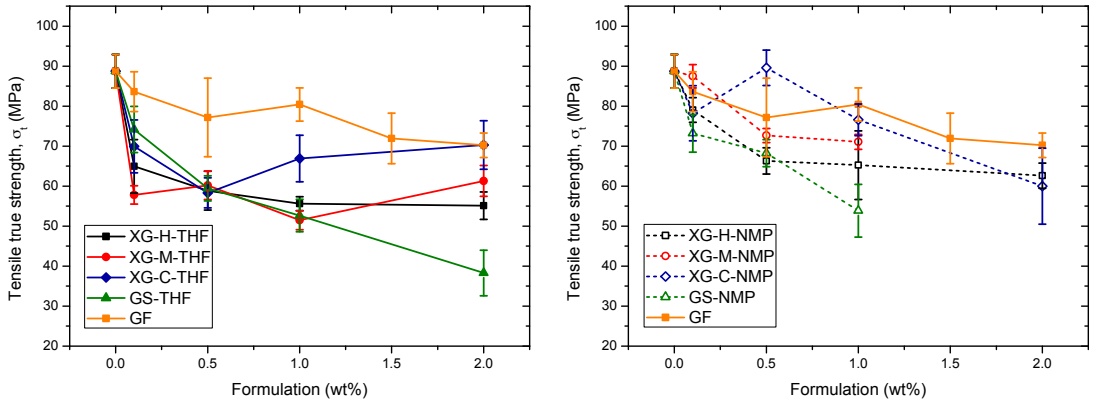
(a) Schematic (b) Stress in platelet

Figure 8.7.4: Normalised stress in platelet for various platelet aspect ratios. Reproduced from [289].

The maximum value of E_t was measured for the GS-NMP and XG-H-NMP modified epoxies, which have an intermediate aspect ratio. Although the highest value of E_t should theoretically be measured for the highest aspect ratio GNP, i.e. the XG-M-

NMP modified epoxy, it is thought that the large lateral size and high aspect ratio of each XG-M platelet causes the GNP to be more agglomerated. Thus this reduces effective aspect ratio of the GNP to a greater degree. The graphite flake modified epoxies have the lowest E_t across the whole range of formulations, due to their low aspect ratios and presumably poor platelet/matrix adhesion.

The σ_t and ε_B decreased with GNP content, as shown in Figure 8.7.5. This is because the GNPs act as stress concentrations to weaken the composite, which initiates failure at a lower strain. There appears to be a dependence of σ_t on the agglomeration size, where a larger agglomerates and lower tensile strengths were found for the GNPs dispersed in THF. The GNPs tend to reduce the σ_t of the epoxy more than other conventional modifiers, such as rubber particles, because of the high aspect ratios and low thickness. The stress concentrations are much higher as the cracks are effectively sharper.



(a) Dispersed in THF (b) Dispersed in NMP

Figure 8.7.5: Tensile true strength for the various GNP modified epoxy polymers.

The tensile strength of the GNP modified epoxies can be predicted from analytical models. The simplest approach for poorly bonded modifiers considers a random distribution of holes, which do not take into account the shape of the modifiers. This model determines the strength of the composite from the remaining effective cross-sectional area of the matrix [290]:

$$\sigma_{tc} = \sigma_{tu}\,(1 - v_f) \tag{8.1}$$

where σ_{tc} and σ_{tu} are the composite and unmodified tensile strengths, respectively, and v_f is the volume fraction. This model can be seen as an upper bound for the strength of poorly bonded particulates as the strength of a composite is typically also affected by additional effects such as sharp cracks. Several authors [291] have modified this approach to include power laws and constants to account for modifier shapes

and arrangements, however these values are empirical and can change significantly for different composite systems. The lower bound of a composite with poorly bonded disc shaped particulates was derived, with an approach similar to Nicolais and Narkis [292]. Consider a unit cell with n^3 cubic distributed disc shaped particulates, as shown in Figure 8.7.6.

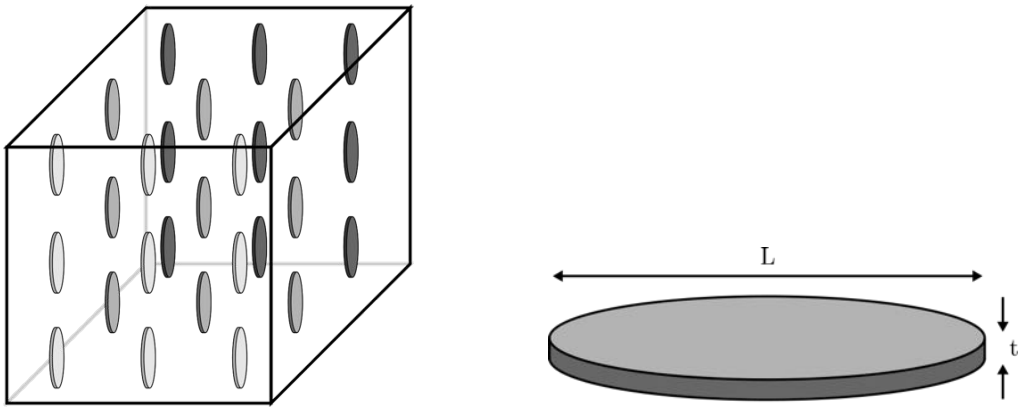


Figure 8.7.6: Illustration showing distribution of particulates in unit cell.

Failure is assumed to occur at the cross-section where the stress is at a maximum, i.e. at the minimum cross-section area perpendicular to the load. The minimum cross-sectional area, A_p, is calculated as:

$$A_p = 1 - \frac{1}{4}\pi \left(nL\right)^2 \tag{8.2}$$

where L is the lateral size of the platelets. The volume fraction, v_f, of the disc shaped particulates in the unit cell is:

$$v_f = \frac{1}{4}\pi L^2 n^3 t \tag{8.3}$$

where t is the thickness of the platelets. By substituting Equation 8.3 into Equation 8.2, the composite strength, σ_{tc}, can be shown to be:

$$\sigma_{tc} = \sigma_{tu}\left[1 - \left(\frac{\pi}{4}AR^2\right)^{1/3} v_f^{2/3}\right] \tag{8.4}$$

where AR is the aspect ratio of the platelets. The same approach can also be taken to derive the equation for rectangular shaped platelets:

$$\sigma_{tc} = \sigma_{tu}\left[1 - \left(AR^2\right)^{1/3} v_f^{2/3}\right] \tag{8.5}$$

The assumption of zero particle/matrix adhesion may not be strictly correct, given that the Young's modulus was observed to increase with GNP content. To take into

account the effect of particle/matrix adhesion, Piggott and Leidner [293] proposed that the composite strength should be of the form:

$$\sigma_{tc} = a\sigma_{tu} - \alpha v_f \tag{8.6}$$

where a is a constant and α is the coefficient of particle/matrix adhesion. For strongly bonded fillers, stress transfer from the matrix to the filler occurs by shear and is normally at the ends. Leidner and Woodhams [294] derived a theoretical relationship for the tensile strength of a composite by summing the maximum load sustained by both the matrix and filler (shown here with consideration of the particle/matrix adhesion as above):

$$\sigma_{tc} = 0.83pfv_f + k\sigma_{tu}\left(1 - v_f\right) + \sigma_a H\left(1 - v_f\right) \tag{8.7}$$

where p is the pressure exerted by the matrix on the filler, f is the friction coefficient, k is the relative change in matrix strength due to the presence of fillers, σ_a is the particle/matrix adhesion strength and H is a stress concentration factor. The first term on the right hand side relates to the contribution from the filler, the second term for the remaining matrix, and the third term for the additional load supported by the matrix due to particle/matrix adhesion. The term pf can be determined by equating $v_f = 1$ and similarly for k, σ_a and H at $v_f = 0$. The first term in Equation 8.7 can be derived for platelet type fillers by averaging the stress in the platelet, σ_p, predicted from shear lag theory [289]:

$$\sigma_p = \frac{bE_p\sigma_{tu}}{\frac{t}{2}E_p + (b - \frac{t}{2})E_m}\left[1 - \frac{e^{\alpha y} + e^{-\alpha y}}{e^{\frac{\alpha L}{2}} + e^{-\frac{\alpha L}{2}}}\right] \tag{8.8}$$

where,

$$\alpha = \frac{1}{b - \frac{t}{2}}\sqrt{\frac{3\left[\frac{t}{2}E_p + (b - \frac{t}{2})E_m\right]}{2\frac{t}{2}(1 + \nu_m)E_p}}, \tag{8.9}$$

b is the width of the unit cell, t is the platelet thickness, E_p is the platelet stiffness, E_m is the matrix modulus and ν_m is the matrix Poisson's ratio. Integrating σ_p across the platelet length gives:

$$\sigma_{tc} = \frac{bE_p\sigma_{tu}}{\frac{t}{2}E_p + (b - \frac{t}{2})E_m}\left[\frac{L}{2} - \frac{tanh\left(\frac{bL}{2}\right)}{b}\right]v_f + k\sigma_{tu}\left(1 - v_f\right) + \sigma_a H\left(1 - v_f\right) \tag{8.10}$$

Alternatively, Pukanszky *et al.* [295] derived an empirical relationship, using a hyper-

bolic function to describe the change in cross-section area with filler content:

$$\sigma_{tc} = \sigma_{tu} \frac{1 - v_f}{1 + A v_f} e^{B v_f} \qquad A = \frac{\psi^* \phi^*}{(1 - \psi^*)\, \phi^*} \tag{8.11}$$

where B is an empirical constant for particle/matrix adhesion, ψ^* is the maximum filled area in plane section and ϕ^* is the maximum packing fraction. Both ψ^* and ϕ^* depend on particle shape and size distribution. Thus a value of $A = 2.5$ was approximated as the upper bound. A value of $B = 0$ corresponds to no interfacial bonding, and values up to 6.5 were obtained by curve fitting [295].

Figure 8.7.7 shows the predicted tensile strengths compared with the XG-H GNP modified epoxies. Clearly, the Nicolais model for discs and platelets shows the best agreement with the experimental results. The model however can be adjusted to fit the results better by increasing the aspect ratio at higher volume fractions. The models derived for spherical fillers did not work well at the low volume fractions involved. The Leidner model, which includes particle/matrix adhesion, predicts an increase in strength because of the high value of tensile strength of the GNPs used.

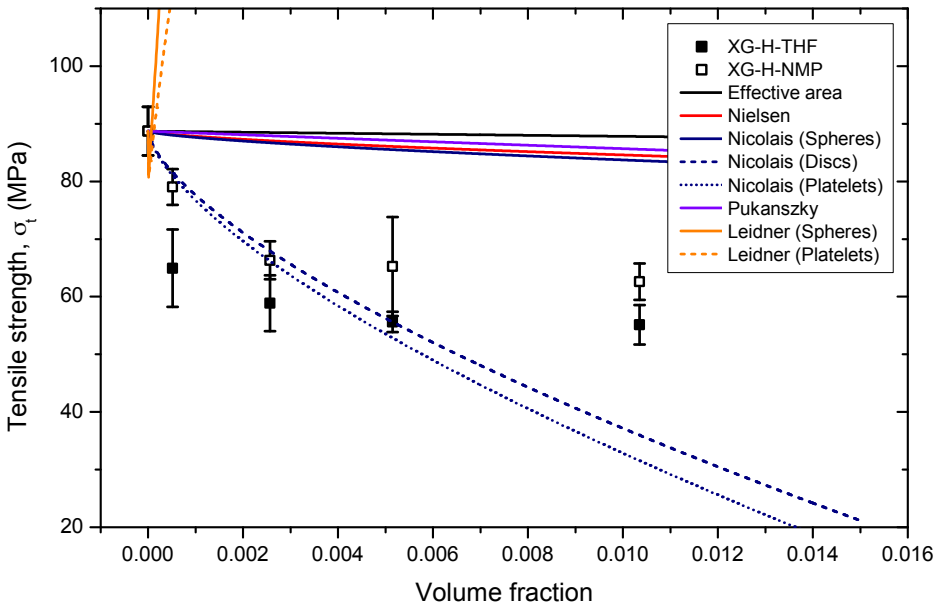
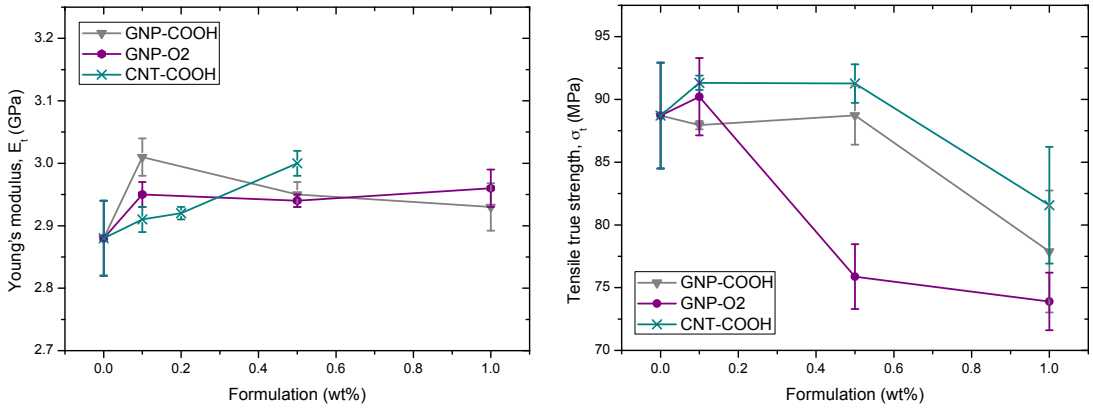


Figure 8.7.7: Predicted tensile strengths compared with XG-H GNP modified epoxies.

The HDPlas GNP modified epoxies show little to no improvement in the Young's modulus, as shown in Figure 8.7.8(a). This is surprising given that these functionalised GNPs were relatively well dispersed and have good adhesion to the epoxy matrix (see §8.10). The cause of the poor tensile properties of the GNPs was damage caused by the sonication process, which resulted in smaller platelet sizes and hence reduces the aspect ratio of the GNPs. The GNP-O2 modified epoxies show the lowest values of σ_t.



(a) Young's modulus (b) Tensile true strength

Figure 8.7.8: Tensile properties for functionalised GNP and CNT modified epoxy polymers.

The functionalised CNT-COOH modified epoxies also show no improvement in the Young's modulus. This is compared to the epoxies modified with CVD produced MWCNT from previous work [117] which show a linear increase to 3.3 GPa at 0.5 wt%, as shown in Figure 8.7.9. This is because the CVD produced MWCNTs were much longer (140 μm compared to 1 μm) and hence have a larger aspect ratio. The CNT-COOH MWCNTs used in this study have a much lower aspect ratio which makes them less effective in increasing modulus.

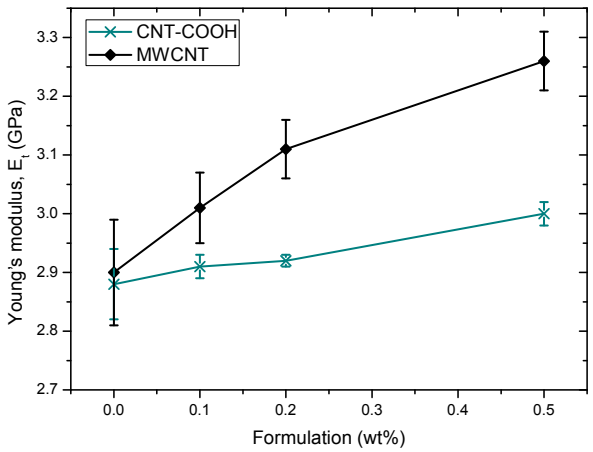
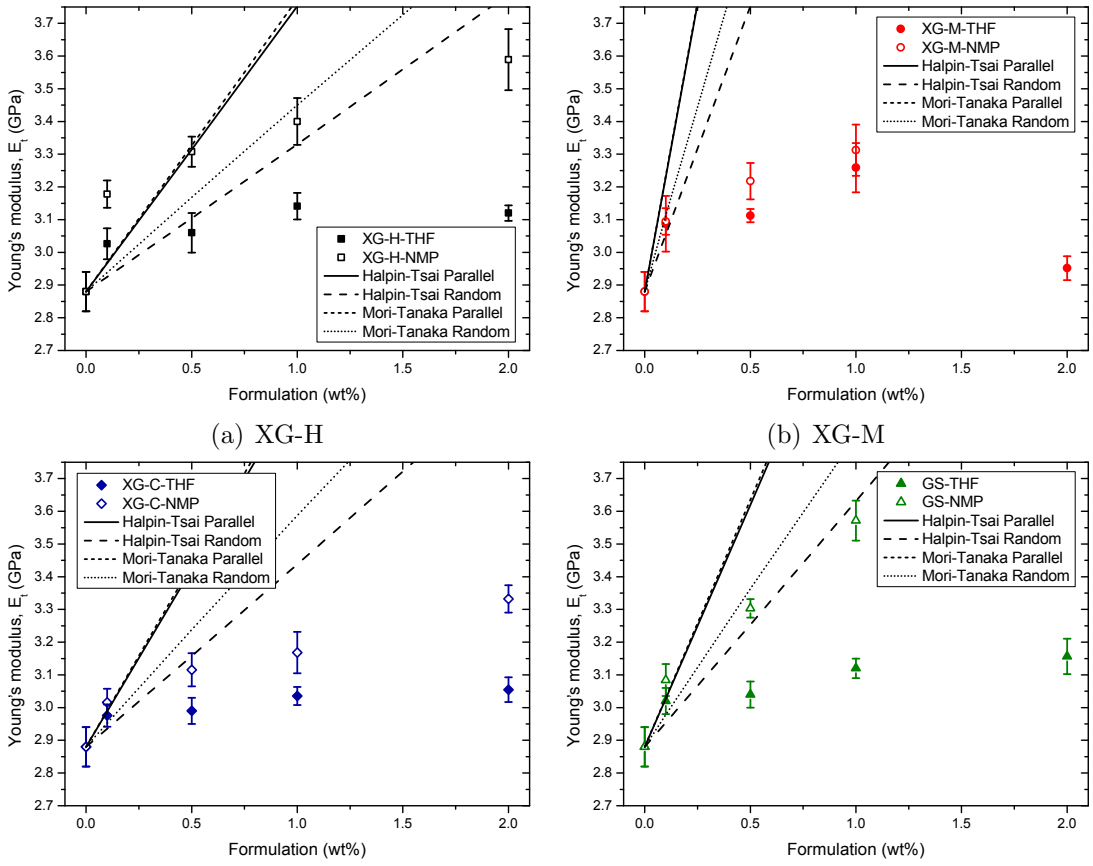


Figure 8.7.9: Young's modulus of unmodified and functionalised MWCNT modified epoxy polymers. Data for MWCNT reproduced from [117].

The measured values of the composite Young's moduli of the GNP modified epoxies were compared to the analytical models. These are the Halpin-Tsai (see Equations 2.11 and 2.19) and Mori-Tanaka (see Equations 2.20 and 2.21) models. A particle modulus, E_p, of 1000 GPa and a Poisson's ratio, ν_p, of 0.3 were used. The matrix modulus, E_m, and Poisson's ratio, ν_m, were measured experimentally. The volume fractions were calculated using the weight percentages and the density of 2.2 g/cm^3.

The platelet thickness and lateral sizes measured from the FEGSEM micrographs were used to calculate the aspect ratios. The composite modulus when the platelets are aligned with the long axis parallel to the loading direction is referred to as "Parallel", i.e. E_{11}, and the composite modulus with randomly oriented platelets is referred to as "Random".



(a) XG-H (b) XG-M

(c) XG-C (d) GS

Figure 8.7.10: Analytical models for Young's moduli of GNP modified epoxy polymers.

From the predictions of composite moduli, as shown in Figure 8.7.10, the Halpin-Tsai Random predictions show good agreement with the XG-H-NMP and GS-NMP modified epoxies. For the other GNP modified epoxies shown, the models can predict the composite moduli at low loadings such as at 0.1 wt%, however they begin to deviate from the experimental results as agglomeration reduces the effective aspect ratios of the modifiers with increasing GNP content. As a consequence, the models overpredict the Young's modulus at higher loadings.

The GNP properties used to model the Young's modulus were obtained from the current experimental results and existing literature. There will invariably be errors introduced from choice of values used. This is because they assume that every platelet in the composite has the same property, which is not the case. As shown in the previous

sections, damage to the GNPs can occur during the manufacturing process and this affects the aspect ratio and platelet mechanical properties, such as modulus, density and Poisson's ratio. The following section investigates the effect this has on the predicted values of moduli. This will also help to identify the properties that are important in order to achieve the optimum tensile properties.

Figure 8.7.11 shows how the predicted moduli for platelets that are aligned parallel and perpendicular to the loading axis change with the aspect ratio of the platelets, at various loadings. The modulus increases with aspect ratio because of the increase in stress transfer at higher aspect ratios, i.e. the stiffer modifiers can take more load. This has implications for intercalated microstructures, as the polymer chains that flow between the platelet increases the thickness of these materials, hence reducing the aspect ratio. The relative moduli reach an asymptote at very high aspect ratios, the magnitude of which varies for different loadings. It was also found that the increase in relative modulus is lower in the transverse direction than in the loading direction, however this does not take into account the properties of the GNPs in the transverse direction.

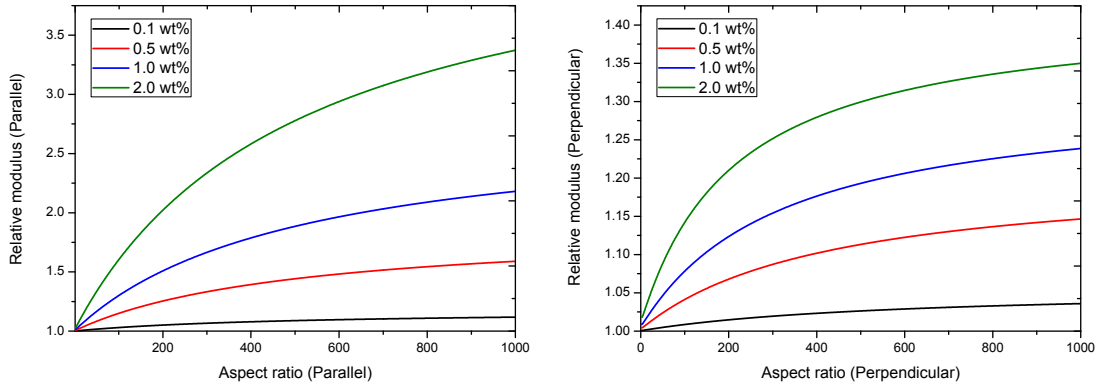


Figure 8.7.11: Variation of predicted moduli with aspect ratio.

To model the Young's modulus of the GNP modified epoxies, the modulus of the GNPs was taken as 1000 GPa, which is the Young's modulus of monolayer graphene [115]. There are also errors in using this value of E_p as monolayer graphene is a 2D material, thus the tensile properties are properly described by a 2D stress, i.e. normalised by the area rather than the volume. Lee *et al.* [115] noted that for comparison purposes, the interlayer spacing of graphite, taken as 0.335 nm, was used to obtain a relevant 3D parameter. Indeed, several authors (see [296]) have taken different approaches to determine the thickness and Young's modulus of CNTs and graphene. The values of Young's modulus from these studies range from 1 TPa to 5 TPa. The modifiers used in the present study comprise of multiple layers of these graphene sheets, and thus the Young's modulus will be lower. Figure 8.7.12 shows how the modelled composite

modulus changes with the particle modulus, E_p. There is a sharp increase in composite modulus as E_p increases up to approximately 500 GPa. Above 500 GPa, the increase in relative modulus is more gradual and reaches an asymptotic value.

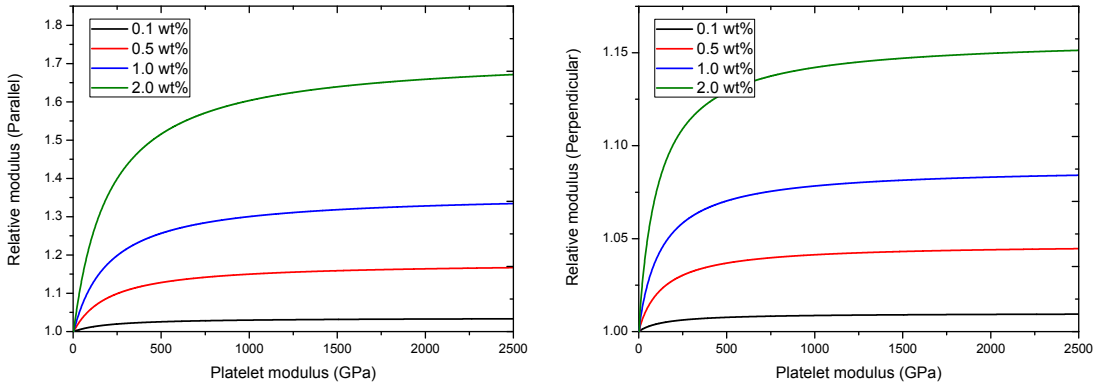


Figure 8.7.12: Variation of predicted moduli with modifier modulus.

The density of the GNPs was used to determine the volume fractions of the GNP modified epoxies. The bulk density of the GNPs can be as low as 0.03 kg/m^3, however this includes the empty voids which will be filled in by the encasing polymer matrix. The density of GNPs is typically assumed to be equal to the density of graphite, although lower values have been quoted by several manufacturers. Figure 8.7.13 shows how the volume fraction and composite modulus changes with GNP density. Similar trends were observed for both properties because of the dependency between the volume fraction and predicted moduli. In the region of interest, between 1.5 kg/m^3 and 2.2 kg/m^3, the predicted moduli do not change significantly at lower weight percentages. At 2.0 wt%, the predicted relative modulus ranges from 1.88 to 1.60 for a density of 1.5 kg/m^3 and 2.2 kg/m^3, respectively.

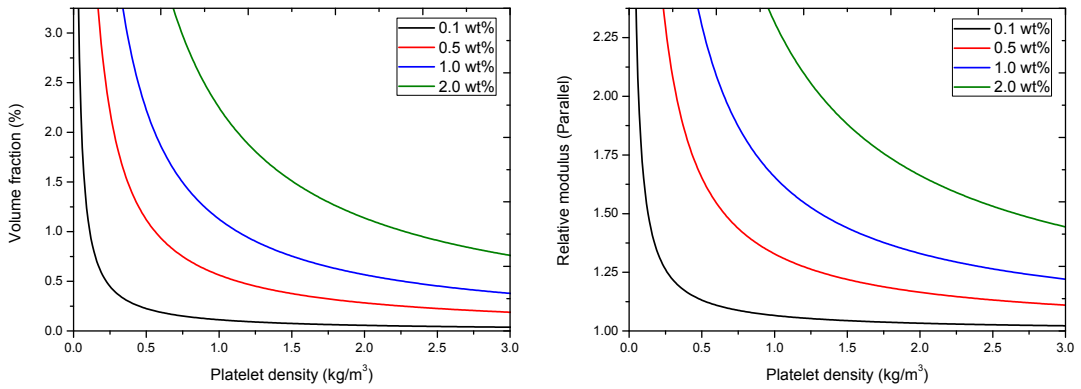


Figure 8.7.13: Variation of volume fraction and predicted moduli with modifier density.

The Poisson's ratio of graphite is approximately 0.2, although some authors [296, 297] have reported values for graphene and CNTs ranging from 0.1 to 0.4 based on ex-

perimental results and analytical models. Furthermore, the Poisson's ratio of epoxy increases as the load increases [270]. Figure 8.7.14 shows the change in predicted moduli with GNP content and epoxy Poisson's ratio. There was virtually no change in modulus with GNP content and epoxy Poisson's ratio. Interestingly, a decrease in the predicted modulus was found for a matrix Poisson's ratio value of approximately 0.3.

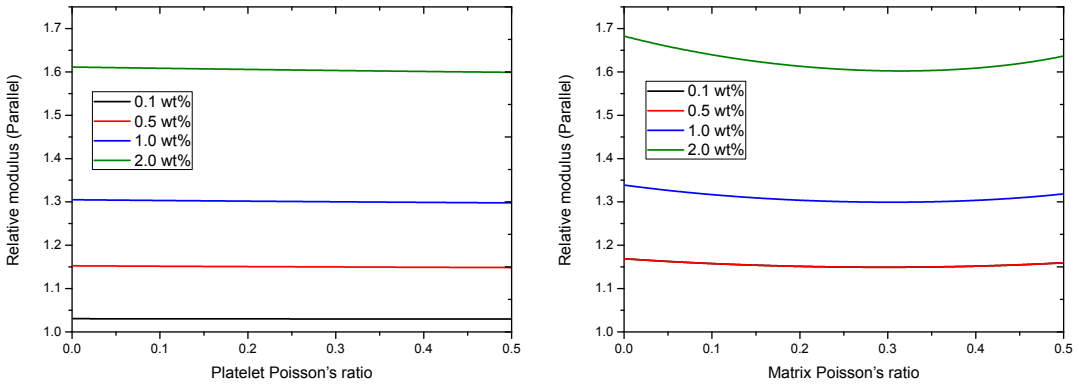


Figure 8.7.14: Variation of predicted moduli with modifier and matrix Poisson's ratio.

One of the important properties that was not taken into account in the modelling is the level of particle-matrix adhesion. While there exist empirical formulae, such as the Lewis-Nielsen model [203], little is known about the specific particle-matrix adhesion between the GNPs and the epoxy matrix used in this study. There are also complex interactions between the particle and matrix for partially bonded particles loaded in uniaxial tension. Hence the effect of particle bonding was not explored.

The critical material properties to maximise the tensile performance were identified from the analytical models, assuming the GNPs are perfectly dispersed. Obviously, higher platelet aspect ratios provide the highest composite moduli. There is potential scope to improve the relative modulus of the nanocomposite, as it was shown to continues increasing sharply up to an aspect ratio of approximately 2000. It is also important to maintain the Young's modulus of the fillers. This can be achieved by minimising the presence of functional groups and defects on the GNPs. However, there is a compromise with achieving good particle/matrix adhesion.

8.8 Compressive properties

The compressive true stress-true strain curves for the unmodified and 10 wt% solvent modified epoxies, both dissolved and evaporated, are shown in Figure 8.8.1. The

trends observed in the plane strain compression tests were similar to the tensile tests. The compressive properties were unaffected when the solvents were removed prior to curing, whereas the yield strength was reduced by up to 26% when the solvents remain in solution in the epoxy due to plasticisation. The compressive true yield stress, σ_{yc}, of the epoxies with unevaporated solvents was lower for the NMP modified epoxy than the THF modified epoxy due to the different molecular mass of the two solvents.

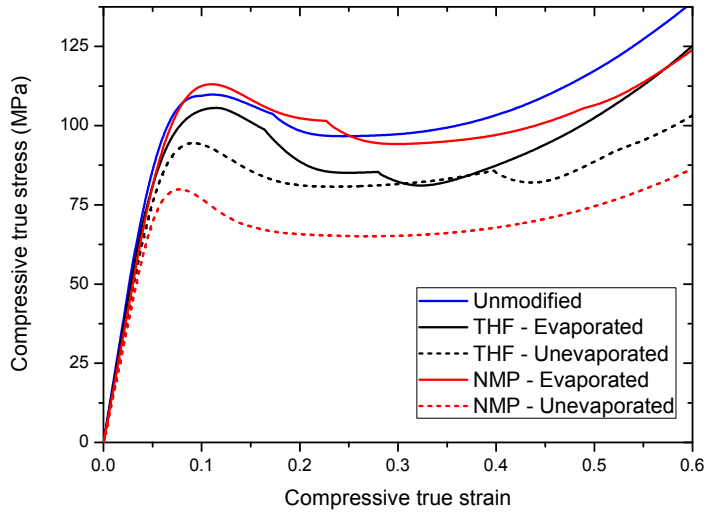


Figure 8.8.1: Compressive true stress-true strain curves for unmodified and 10 wt% solvent modified epoxy polymers.

The compressive true stress-true strain curves are shown for the unmodified and 1.0 wt% GNP modified epoxies in Figure 8.8.2. Unlike the trend observed from the tensile tests, the compressive modulus, E_c, and compressive true yield strength, σ_{yc}, did not show any significant changes with GNP content. It is possible that the higher stresses due to the additional constraint in a plane strain compression test cause the GNPs to debond at low strains, thus limiting the compressive modulus and strength. Secondly, the compression samples were able to yield before cracking due to the compression tests being more stable than tensile tests as the cross-sectional area increases rather than decrease as in a tensile test. Although graphene as a bulk material has a much higher strength than epoxy (130 GPa compared to 86 MPa) [115], at such low concentrations, it would have little to no effect on the composite strength. The compressive true yield strain, ε_{yc}, was also not affected by the addition of the graphene nanoplatelets.

Some of the samples cracked before reaching the strain softening limit, which limits the information available to determine the post-yield behaviour. This is evident from a sudden drop in stress as the sample is loaded. However, from the compressive true stress-true strain curves, there was enough evidence to show that there were no significant changes in the strain softening and strain hardening regions due to the addition

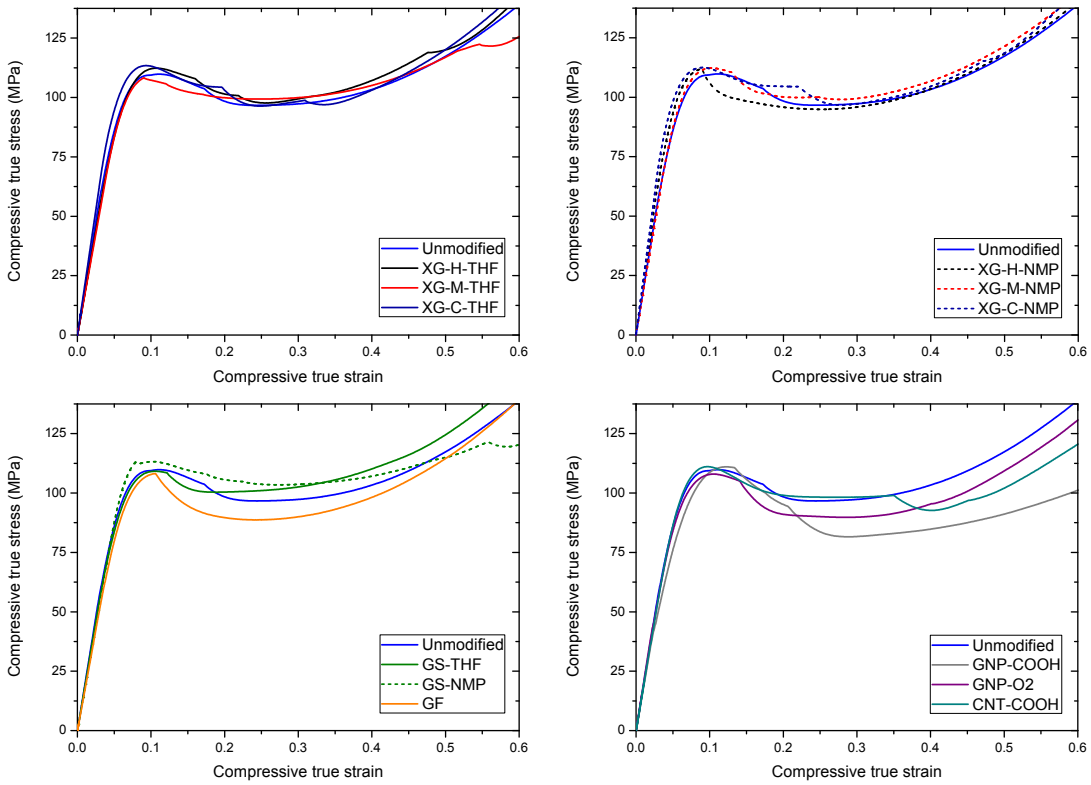


Figure 8.8.2: Compressive true stress-true strain curves for unmodified and 1.0 wt% GNP modified epoxy polymers.

of the GNPs. The compressive true failure stress and strain remain constant at 225 ±26 MPa and 0.91 ±0.05, respectively.

Indeed, this can be observed from the cross-polarised images of the sectioned compressed regions shown in Figure 8.8.3. Inhomogeneous macroscopic yielding and strain localisation [271] were observed in the compressed region of the GNP modified epoxies, which appears to remain largely unchanged in appearance compared to the unmodified epoxy. The absence of a diffuse shear zone in the cross-sections suggests that localised shear bands are not forming between graphene nanoplatelets.

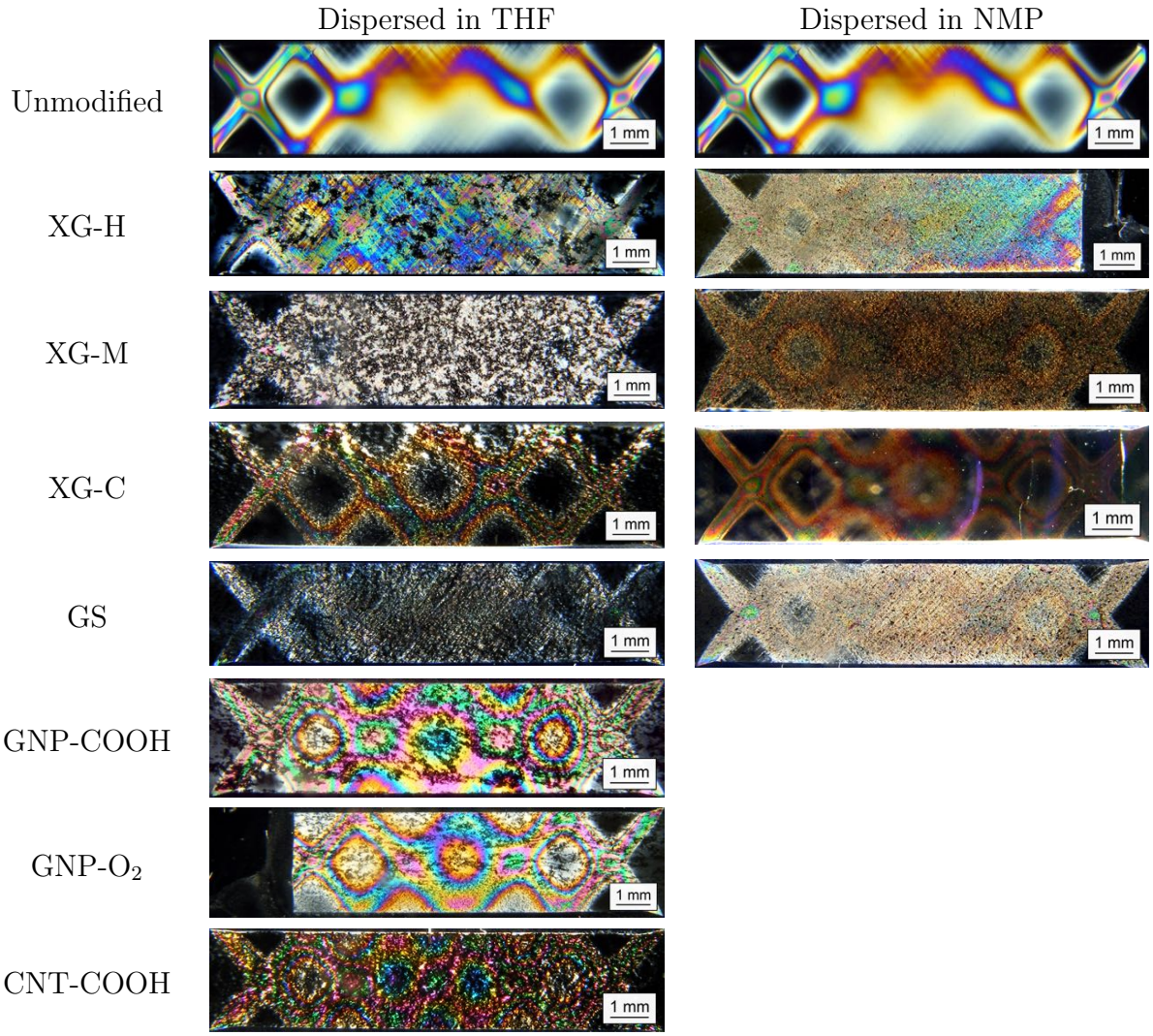


Figure 8.8.3: Transmission optical micrographs, using cross polarised light, of polished specimens loaded to the strain softening region.

8.9 Fracture properties

The fracture toughness, K_{IC}, and fracture energy, G_{IC}, of the epoxies were measured using SENB tests. The results are shown in Figures 8.9.1 to 8.9.4. The values of K_{IC} and G_{IC} for the unmodified epoxy were measured to be 0.6 MPa $m^{1/2}$ and 0.10 kJ/m^2, respectively. The fracture performance was unaffected when the solvents were added to the epoxy resin and subsequently evaporated. However, the fracture energy decreased to 0.07 kJ/m^2 when the solvents were not removed, as shown in Figure 8.9.1.

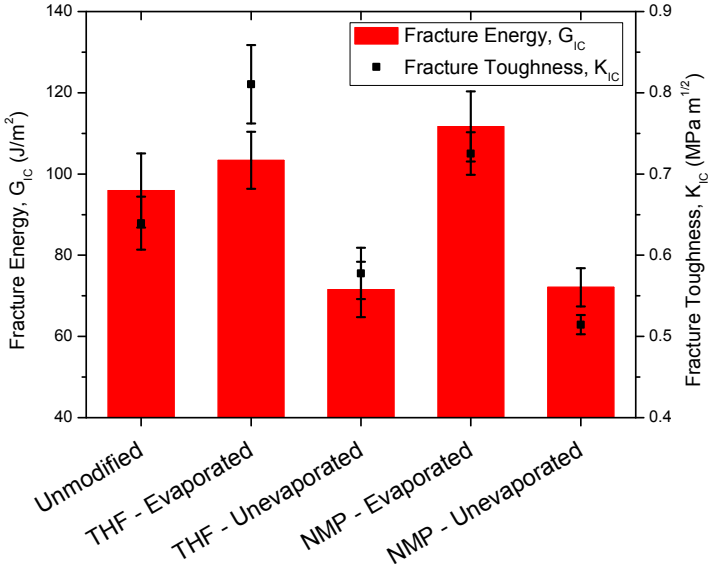
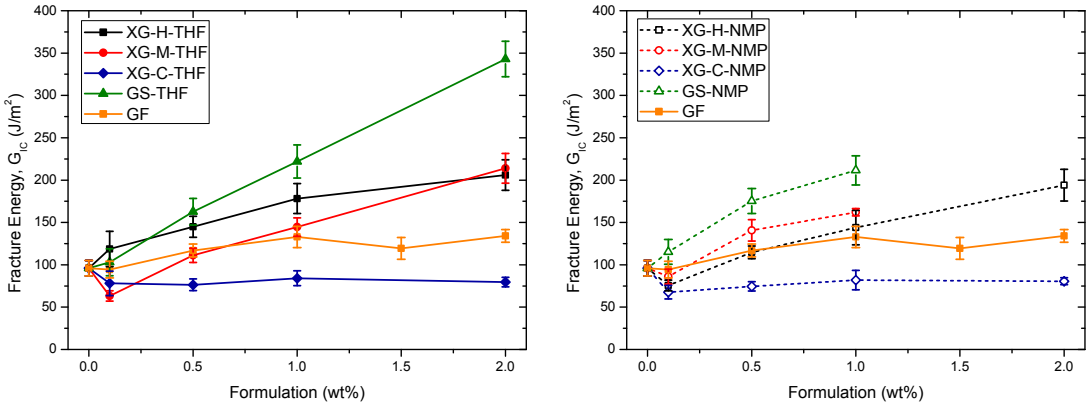


Figure 8.9.1: Effect of solvents on the fracture properties of the epoxy polymer.

The addition of the GNPs at low loadings, such as that at 0.1 wt%, did not affect the fracture properties of the epoxy polymer. At higher concentrations, the addition of the XG-H, XG-M and GS GNPs, dispersed in both THF and NMP, led to an increase in the G_{IC} of the epoxy polymer. A maximum G_{IC} of 0.34 kJ/m^2 was measured for the 2.0 wt% GS-THF modified epoxy, corresponding to an increase of 240%. The toughening mechanisms behind this increase will be discussed in the following section. The XG-H GNPs were more agglomerated than the GS GNPs, as discussed previously, thus the actual aspect ratios would be less than if they were exfoliated, and this lower aspect ratio reduces the maximum toughening effect. Indeed, the XG-M GNPs, which have the largest lateral dimension and aspect ratio, was heavily agglomerated (see §8.5) and thus poor fracture performance. The XG-C GNPs, both dispersed in THF and NMP, and GF modified epoxies did have any affect on the G_{IC} of the epoxy polymer. The G_{IC} of the XG-C GNP and GF modified epoxies remained constant at about 0.08 kJ/m^2 and 0.13 kJ/m^2, respectively, up to 2.0 wt%.

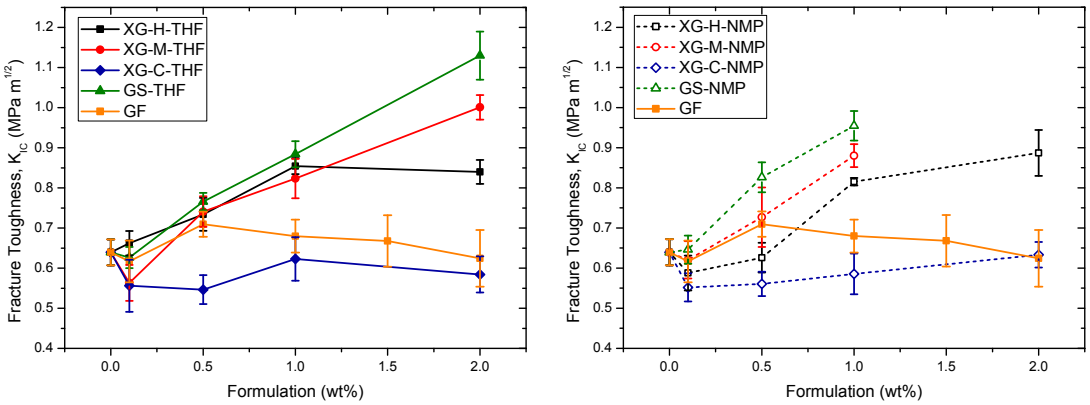
Interestingly, the G_{IC} and K_{IC} values of the epoxy modified with GNPs dispersed in THF and with GNPs dispersed in NMP were roughly equivalent within experimental error, as shown in Figures 8.9.2 and 8.9.3. This suggests that the agglomeration of the GNPs do not affect the fracture performance of the GNP nanocomposites. This will be explored further through an analysis of the fracture surfaces.

The epoxy polymers modified with functionalised GNPs and CNTs did not show any significant increase in the fracture performance, see Figure 8.9.4; up to a loading of 1.0 wt%. The K_{IC} and G_{IC} decreases initially at a content of 0.1 wt% before recovering



(a) Dispersed in THF (b) Dispersed in NMP

Figure 8.9.2: Fracture energy, G_{IC}, for the various GNP modified epoxy polymers.



(a) Dispersed in THF (b) Dispersed in NMP

Figure 8.9.3: Fracture toughness, K_{IC}, for the various GNP modified epoxy polymers.

at higher loadings. The maximum G_{IC} was measured for the 1.0 wt% GNP-COOH modified epoxy, at a value of 0.13 kJ/m^2, corresponding to an increase of 30%. However, this is still lower than the epoxy polymers modified with GNPs that have not been functionalised, namely the XG and GS GNPs.

Previous work [117] involving the same epoxy modified using CVD produced MWCNTs show an increase in G_{IC} from 0.13 to 0.22 kJ/m^2 using 1 wt% of CNTs. However, the carboxyl functionalised MWCNTs used in this study show a decrease of 30% in G_{IC} when incorporated into the epoxy. The K_{IC} and G_{IC} of the two MWCNTs are compared in Figure 8.9.5.

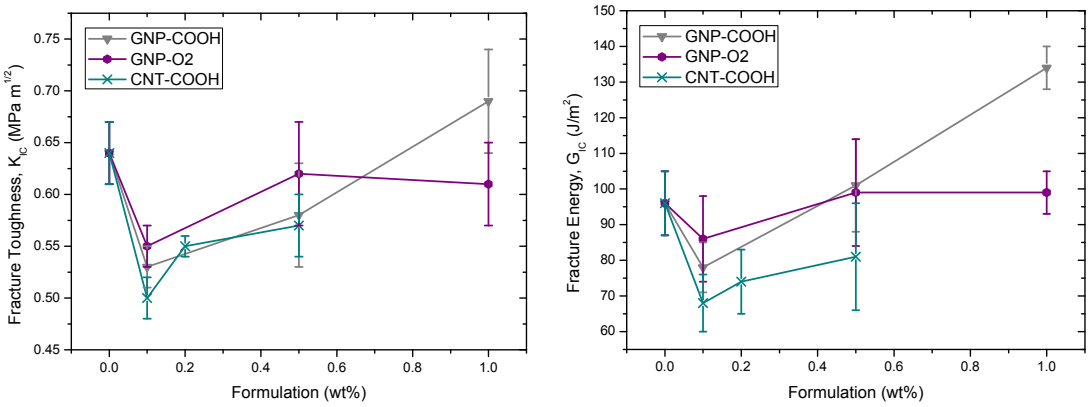


Figure 8.9.4: Fracture toughness and fracture energy of functionalised GNP and CNT modified epoxy polymers.

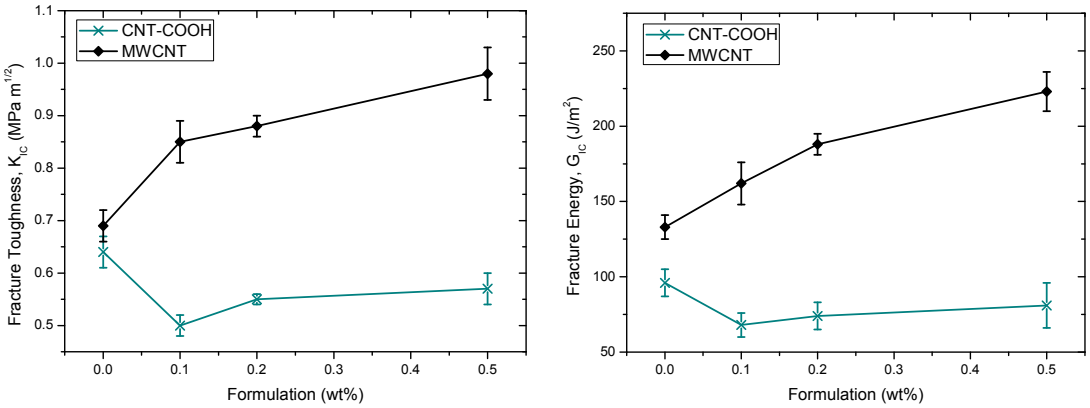


Figure 8.9.5: Fracture toughness and fracture energy of functionalised CNT and as-produced MWCNT modified epoxy polymers. Includes data from [117].

8.10 Fractography

Field emission gun scanning electron microscopy (FEGSEM) of the fracture surfaces was conducted to observe the toughening mechanisms. The crack propagation direction of the selected images shown is from right to left. Selected images are shown in Figures 8.10.1 to 8.10.9. The fracture surfaces of the unmodified epoxy (see Figure 8.10.1) appear smooth, and feature only line marks that represent step changes in height as the crack propagates. Crack forking and the multi-planar nature of the surface observed here are the main mechanisms to absorb excess energy in such brittle materials [272].

With the addition of the GNPs, a much rougher appearance at the process zone indicates significant plastic deformation of the epoxy matrix was observed around the clusters of GNP. For the XG-H, XG-M and GS GNPs dispersed in THF, as shown in Figure 8.10.2, evidence of crack pinning and crack deflection was observed. Crack deflection is seen as the crack paths being redirected around clusters of GNPs. Figure

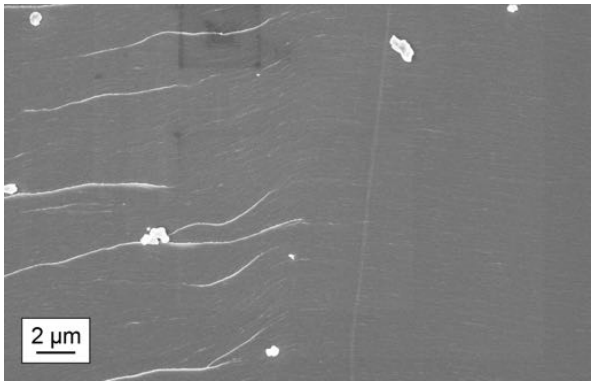
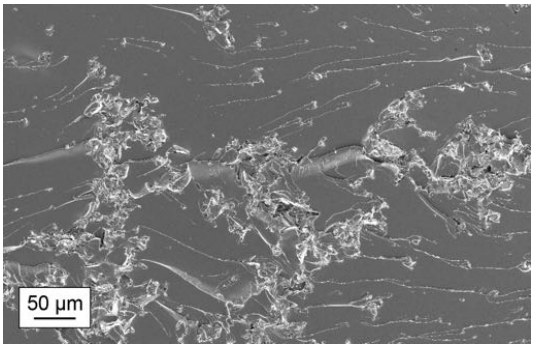
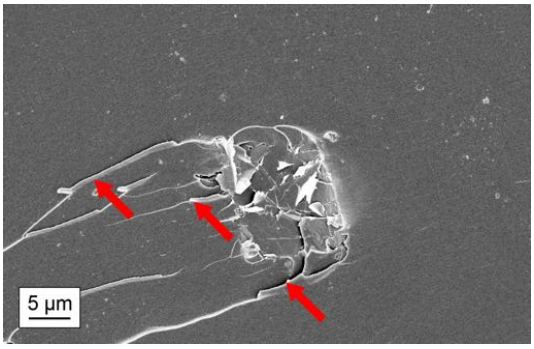


Figure 8.10.1: FEGSEM micrograph of unmodified epoxy fracture surface. Crack propagation from right to left.

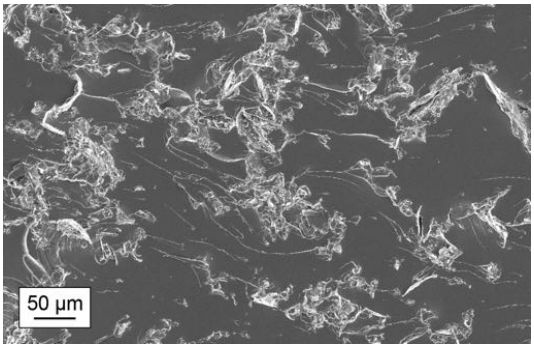
8.10.2(b) shows the tails behind the GNPs which indicate crack pinning. The degree of toughening has a strong proportionality to the aspect ratio of disc-shaped particles [157], i.e. platelets, and this was reflected in the G_{IC} values. Some of the GNPs were also found to have debonded from the epoxy, however voids were not observed around every debonded GNP. This indicates a lack of plastic void growth and has the effect of limiting the maximum fracture toughness, as the debonding process itself does not dissipate much energy for low aspect ratio fillers [298].



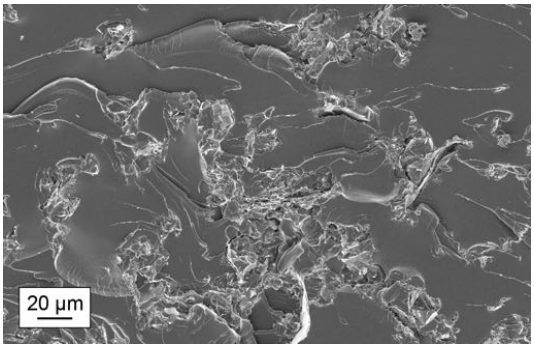
(a) XG-H



(b) Close up of XG-H GNP



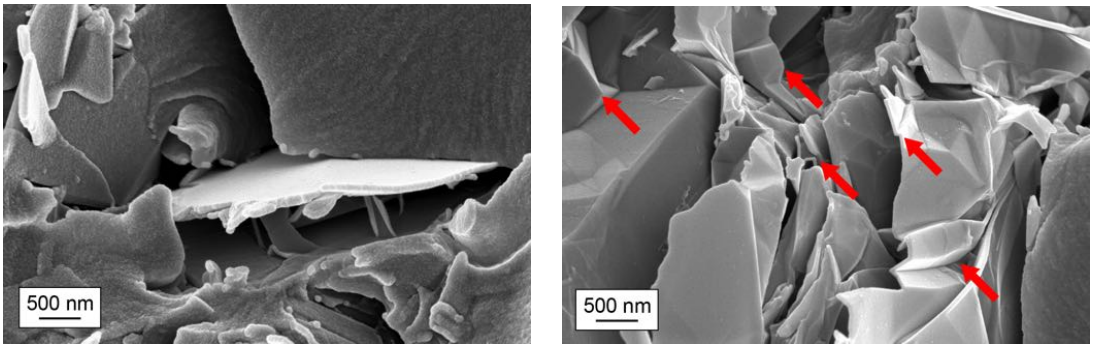
(c) XG-M



(d) GS

Figure 8.10.2: FEGSEM micrograph of 1.0 wt% GNP, dispersed in THF, modified epoxy fracture surfaces. Evidence of crack pinning are identified by red arrows.

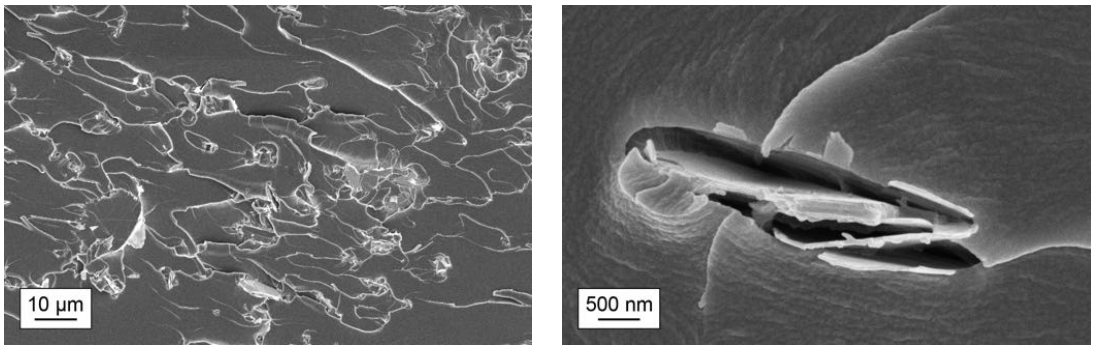
The larger XG-M GNPs dispersed in THF were found to be agglomerated into much larger clusters as discussed in §8.5 and shown in Figure 8.10.2(c). Figure 8.10.3 shows higher resolution FEGSEM micrographs of the XG-H-THF and XG-M-THF GNP modified epoxies. The XG-H GNPs remain flat with very few defects, while the XG-M GNPs are highly wrinkled and folded, as identified by the red arrows in Figure 8.10.3(b). This reduces the effective aspect ratio and hence has a negative effect on the mechanical properties.



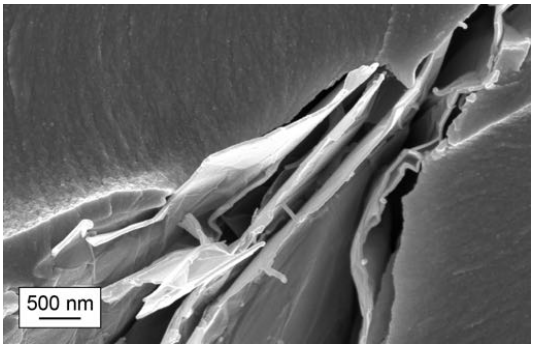
(a) XG-H (b) XG-M

Figure 8.10.3: FEGSEM micrograph of 1.0 wt% GNP, dispersed in THF, modified epoxy fracture surfaces. Defects on the XG-M GNPs are identified by the red arrows.

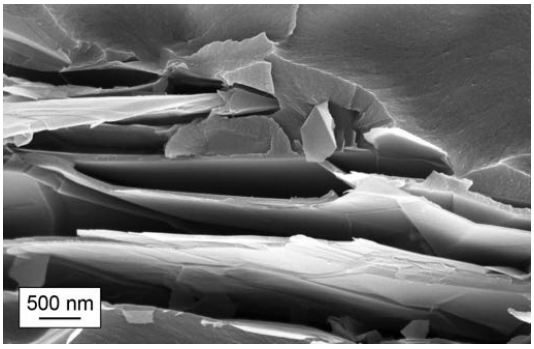
For the XG-H, XG-M and GS GNPs dispersed in NMP, crack pinning and deflection were also observed although to a lesser extent than when dispersed in THF. This can be seen by comparing Figures 8.10.2(a) and 8.10.4(a). The main toughening mechanisms observed for the well dispersed GNPs were found to be debonding of the GNPs, followed by plastic void growth of the epoxy matrix. The large voids between the platelets could be caused by a void growth mechanism or by platelets which have been pulled out. While it would not be possible to identify the same GNPs on the other side of the fracture surface, the remaining platelets appear to have been pulled out. This effect was not seen away from the process zone near the crack tip.



(a) XG-H (x2.5k magnification) (b) XG-H (x50k magnification)



(c) XG-M

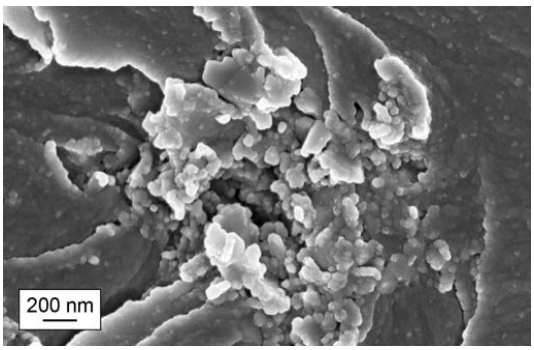


(d) GS

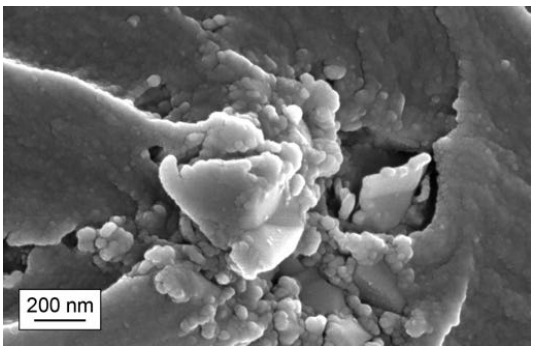
Figure 8.10.4: FEGSEM micrograph of 1.0 wt% GNP, dispersed in NMP, modified epoxy fracture surfaces.

Note that the surfaces of the GNPs appear relatively clean and without any residual epoxy remaining, as shown in Figures 8.10.4(b)–(d), indicative of a poor adhesion between the GNPs and the epoxy. This was to be expected given that graphene sheets have a very low surface energy and trace functional groups from the manufacturing process can only be attached to reactive sites, such as the edges and defects.

The XG-C GNPs were ineffective in toughening the epoxy at loadings up to 2.0 wt%. The fracture surfaces of the XG-C GNPs dispersed in THF and NMP, as shown in Figure 8.10.5, show very little debonding and the degree of crack pinning or deflection is low due to the small size of the particulates. The better apparent adhesion of the GNPs to the epoxy is due to the small size, which results in more edges and hence functional groups at the edges. However, this does not result in an improvement in tensile properties due to the structure and quality of the GNPs, where the surfaces of the platelets appear rough and damaged.



(a) Dispersed in THF

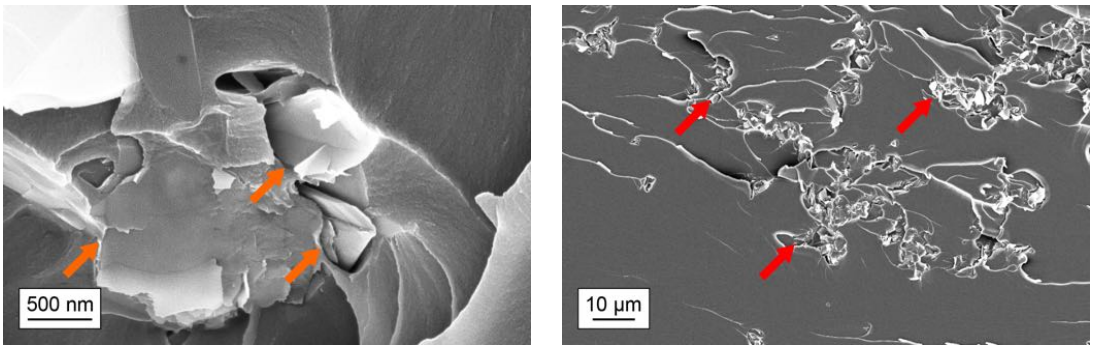


(b) Dispersed in NMP

Figure 8.10.5: FEGSEM micrograph of 1.0 wt% XG-C GNP modified epoxy fracture surfaces.

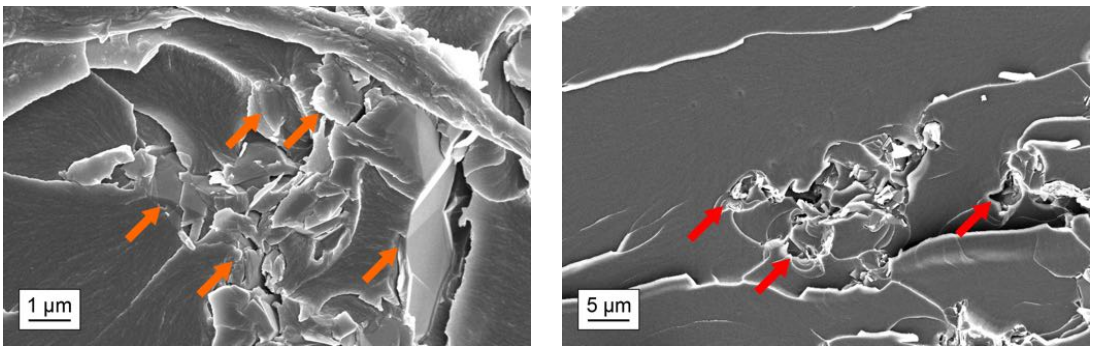
The GNP-COOH and GNP-O_2 functionalised GNPs were well bonded to the epoxy, as shown in Figures 8.10.6(a) and 8.10.7(a), owing to the presence of the functional groups.

This results in limited debonding, and hence little subsequent void growth (see orange arrows in Figures 8.10.6(a) and 8.10.7(a)). On-plane crack front interactions were also restricted by the relatively small size of the agglomerates of GNPs, as identified by the red arrows in Figures 8.10.6(b) and 8.10.7(b).



(a) x75k magnification (b) x2.5k magnification

Figure 8.10.6: FEGSEM micrograph of 1.0 wt% GNP-COOH modified epoxy fracture surfaces. Orange arrows indicate limited debonding and void growth. Red arrows indicate limited crack deflection.

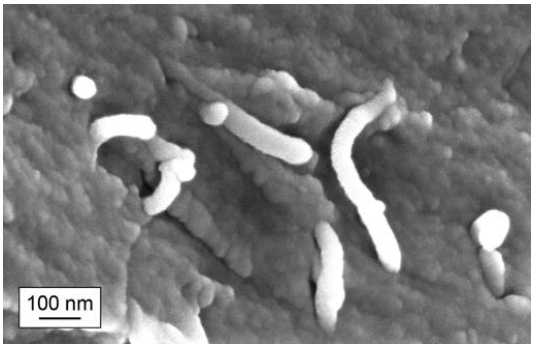


(a) x25k magnification (b) x5k magnification

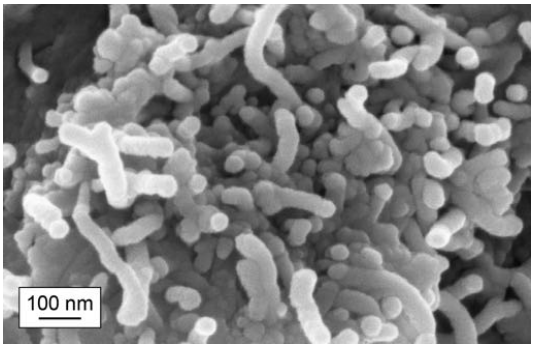
Figure 8.10.7: FEGSEM micrograph of 1.0 wt% GNP-O_2 modified epoxy fracture surfaces. Orange arrows indicate limited debonding and void growth. Red arrows indicate limited crack deflection.

The CNT-COOH modified epoxies do not show any increase in fracture performance and indeed, the FEGSEM micrographs of the fracture surfaces show little evidence of any toughening mechanisms. The small clusters of individual CNTs show some evidence of debonding and pull-out, as shown in Figure 8.10.8(a), however the relative quantity of these were very low compared to the bulk nanocomposite. This lack of CNT debonding means that the triaxial stress state at the crack tip is not relieved and results in very limited plastic deformation of the epoxy. This can be observed macroscopically as the fracture appears smooth and rather featureless. The individual CNTs within the large agglomerates appear to be poorly wetted, as shown in Figure 8.10.8(b), where there was no sign of any epoxy in the large agglomerate. Hence, there were no interactions between the agglomerates and the crack front, such as crack

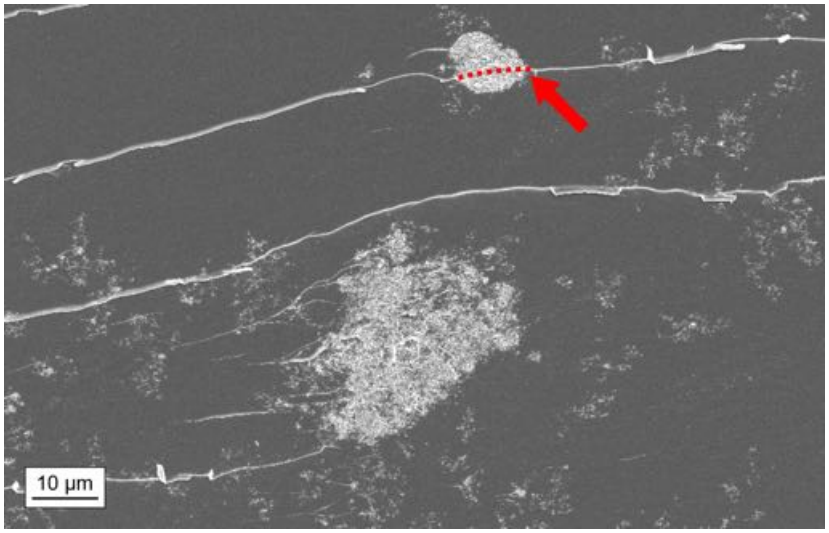
pinning or deflection, as the poor wetting results in slipping between the CNTs. The river lines appear to pass right through the large clusters of CNTs, as identified by the red arrow in Figure 8.10.8(c).



(a) x250k magnification at small clusters



(b) x250k magnification at agglomerate

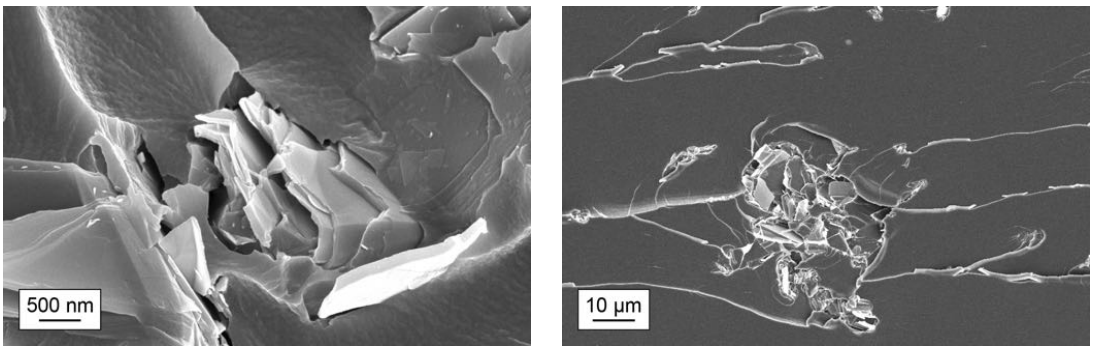


(c) x2.5k magnification

Figure 8.10.8: FEGSEM micrograph of 1.0 wt% functionalised MWCNT modified epoxy fracture surfaces. Red line and arrow points to where the river lines pass straight through the CNT agglomerates.

The fracture surfaces of the graphite flake modified epoxy show limited plastic deformation of the epoxy matrix, see Figure 8.10.9(a), and crack tip interactions, see Figure 8.10.9(b). As a result, the measured values of G_{IC} and K_{IC} did not show any improvement over the unmodified epoxy. All of the graphite flakes were observed to have debonded, suggesting very poor adhesion between the flakes and the epoxy. The lack of plastic deformation of the epoxy could be a result of the lack of strain energy build up due to such an early debonding, thus slowing the growth of shear bands and voids [80, 165]. Slipping between the graphene sheets means that the cracks will propagate through the graphite flakes. This is seen in Figure 8.10.9(a) where voids appear between the layers, but the outer layers are still bonded to the epoxy. Some evidence of

crack deflection or pinning was also observed, as shown in Figure 8.10.9(b), but these were rare.



(a) x50k magnification (b) x2.5k magnification

Figure 8.10.9: FEGSEM micrograph of 1.0 wt% GF modified epoxy fracture surfaces.

8.11 Modelling fracture energy

The major toughening mechanisms for the GNP modified epoxies were different for the GNPs dispersed in THF and those in NMP. For the GNPs dispersed in THF, crack deflection was identified as the major toughening mechanism. For the GNPs dispersed in NMP, debonding followed by platelet pull-out and plastic void growth were observed as the major toughening mechanisms. The energy contributions for each of the toughening mechanisms can be calculated and thus be used to predict the fracture toughness of GNP modified epoxies. The contributions to fracture energy, ψ, of the GNP modified epoxies can be given by:

$$\psi = \Delta G_{cd} + \Delta G_{db} + \Delta G_{po} \tag{8.12}$$

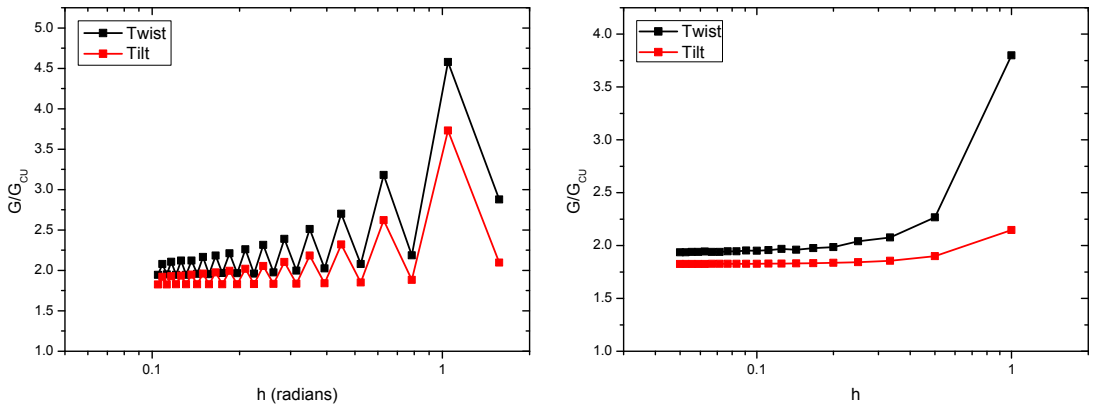
where ΔG_{cd} is the energy contribution from crack deflection, ΔG_{db} is the energy contribution from interfacial debonding and ΔG_{po} is the energy contribution from platelet pull-out. Note that the optical microscopy of the PSC specimens showed that no additional shear banding occurred from the addition of the GNPs, and so there is no contribution from this toughening mechanism.

The energy contribution from crack deflection, ΔG_{cd}, was derived by Faber and Evans [157] using a fracture mechanics approach. The model is summarised in Appendix E. The integrals in Equations 11.4 and 11.5 to calculate the contribution from crack twisting and tilting, respectively, were solved numerically using MATLAB. The total toughening contribution from crack deflection, ΔG_{cd}, for a random distribution of

platelets is then given by [157]:

$$\frac{G_{CU}}{G_{CU} + \Delta G_{cd}} = \frac{2}{\frac{\langle G \rangle^{Twist}}{G_{CU}} + \frac{\langle G \rangle^{Tilt}}{G_{CU}}} \tag{8.13}$$

where $\langle G \rangle^{Twist}$ is the energy contribution from crack twisting and $\langle G \rangle^{Tilt}$ is the energy contribution from crack tilting. The optimum spacing used for the numerical integration was determined systematically to reduce computation time, as shown in Figure 8.11.1. The optimum grid spacing for the θ_1, θ_2, μ_1 and μ_2 integrals is $\frac{\pi}{20}$ radians and for the α and β integrals is 0.1.



(a) Angular spacing (θ_1, θ_2, μ_1, μ_2) (b) Relative location spacing (α, β)

Figure 8.11.1: Optimum spacing for numerical integration.

Figure 8.11.2 shows the change in relative toughening with the Poisson's ratio of the epoxy using the crack deflection model. There were no significant changes in toughening across the whole range of possible Poisson's ratios for both crack twisting and tilting.

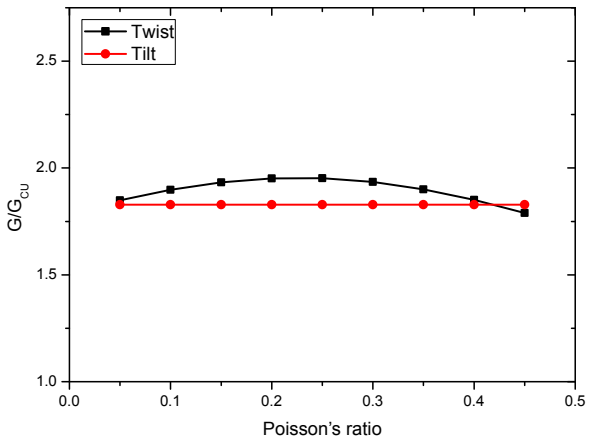


Figure 8.11.2: Change in relative toughening from crack deflection with Poisson's ratio of the epoxy.

For spherical reinforcements, the debonding and pull-out mechanisms typically dissipate an insignificant amount of energy, e.g. [2, 298]. High aspect ratio fillers, such as carbon fibres, carbon nanotubes and platelets have very high specific surface areas, in the order of 1000 m^2/g [236]. Energy dissipation by debonding and friction from the pull-out is proportional to the interfacial area, and hence they are considered major toughening mechanisms.

The process of debonding and pull-out of platelets is similar to that for fibres. Thus, the energy contributions of these mechanisms can be derived in a similar manner as shown by Hull & Clyne [189]. Figure 8.11.3 illustrates the debonding and pull-out process.

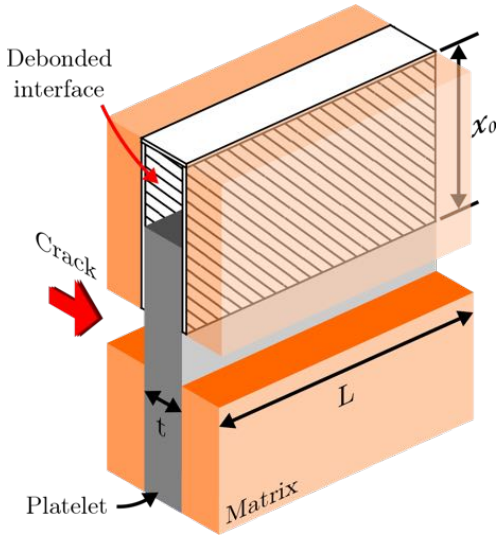


Figure 8.11.3: Schematic of crack passing through platelet, showing debonding at the interface and subsequent pull-out.

The energy to debond a single platelet, ΔU_{db}, is given by:

$$\Delta U_{db} = 2Lx_oG_i \tag{8.14}$$

where L is the width of the platelet, x_o is the embedded length and G_i is the interfacial fracture energy. The total energy dissipated by platelet debonding, ΔG_{db}, is then calculated by simply summing over all platelets intersected by the crack:

$$\Delta G_{db} = \int_0^{L_d} 2Lx_oG_i\frac{Ndx_o}{L} \tag{8.15}$$

where L_d is the debonded length, N is the number of platelets per m^2, $N = \frac{v_f}{L_dt}$.

Integration gives:

$$\Delta G_{db} = \frac{v_f L_d G_i}{t} \tag{8.16}$$

It is interesting to note that the energy contribution from debonding is directly proportional to the ratio of debonded length to thickness. Barber *et al.* [299] measured the interfacial fracture energy between MWCNTs and a polymer matrix and found a strong dependence between G_i and CNT radius. The measured values of G_i ranged from 4 to 70 J/m^2, comparable to other fibre reinforced polymers. For the current study, a value of $G_i = 25$ J/m^2 was used [117].

A similar process was undertaken to calculate the contribution from platelet pull-out. The energy to pull-out a single platelet, ΔU_{po}, is given by [189]:

$$\Delta U_{po} = \int_0^{x_o} 2Lx\tau_i dx \tag{8.17}$$

where τ_i is the interfacial shear strength. The total energy dissipated by platelet debonding, ΔG_{db}, is then calculated by simply summing over all platelets intersected by the crack:

$$\Delta G_{po} = \int_0^{L_d} Lx_o^2 \tau_i \frac{N dx_o}{L} \tag{8.18}$$

This gives the following relationship:

$$\Delta G_{po} = \frac{v_f L_d^3 \tau_i}{3Lt} \tag{8.19}$$

The interfacial shear strength, τ_i, between the GNPs and the epoxy matrix is complicated to calculate experimentally or to estimate analytically. There is an inherent difficulty in isolating and manipulating individual platelets at the nanoscale. Errors may also be introduced in analytical or numerical models to determine this value. This is due to the assumptions made of the structure of these platelets, to which there is a size distribution and not monodisperse. Barber *et al.* [299] found a size dependency between τ_i and the MWCNT radius, however this could be due to sliding between each layer of the MWCNT. They determined experimentally that the maximum value of τ_i for the interface between MWCNT and a polymer matrix was approximately 100 MPa.

To calculate the contribution from the void growth of the matrix around a debonded platelet, some assumptions were made about the shape and size of the final void. It was assumed that the platelets were square and that the void grows to a final lateral size of $(1+\gamma_f)L$ and thickness of $(1+\gamma_f)t$, where γ_f is the failure strain of the unmodified

epoxy measured from the plane strain compression tests. The energy contribution due to void growth can then be calculated from Equation 2.33. Figure 8.11.4 illustrates the shape of the platelet and void.

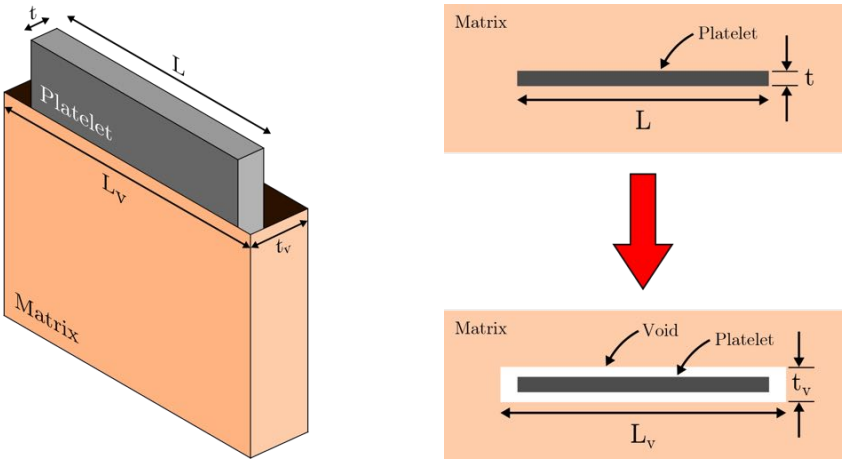


Figure 8.11.4: Illustration of platelet void growth mechanism.

The parameters in the modelling of the GNP modified epoxies are tabulated in Table 8.11.1.

Table 8.11.1: Parameters used in modelling fracture energy of GNP modified epoxies.

Name	Variable	Units	Value
Platelet length	L	nm	Table 8.3.2
Platelet thickness	t	nm	Table 8.3.2
Aspect ratio	AR	–	Table 8.3.2
Void length	L_v	μm	$(1+\gamma_f)L$
Void thickness	t_v	nm	$(1+\gamma_f)t$
Plane strain compressive yield true stress	σ_{yc}	MPa	107
Uniaxial tensile yield true stress	σ_{yt}	MPa	89
Plane strain compressive fracture true strain	γ_f	–	0.91
Pressure-dependent yield stress parameter [3]	μ_m	–	0.2
Unmodified epoxy fracture energy	G_{CU}	kJ/m^2	0.1
Interfacial fracture energy [117]	G_i	J/m^2	25
Interfacial shear strength [299]	τ_i	MPa	47

The predicted and measured values of fracture energy using the crack deflection model for the GNPs dispersed in THF are summarised in Figure 8.11.5. The debonding and void growth mechanisms were not observed from the fracture surfaces, thus was not considered in the model for the epoxies modified with GNPs dispersed in THF. The aspect ratios used were determined from Table 8.3.2. These were 25 for the XG-C, 100 for the XG-H, 1000 for the XG-M and 200 for the GS GNPs. The model assumes that all of the platelets cause crack deflection.

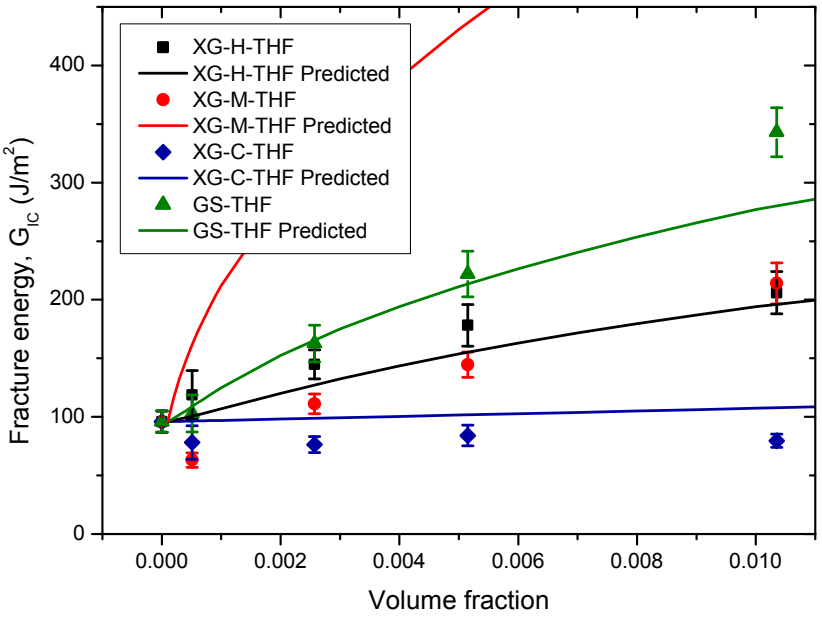


Figure 8.11.5: Predicted and measured values of fracture energy for epoxy polymers modified with GNPs dispersed in THF.

The fracture energy predictions using the crack deflection model agree well with the experimental results for the XG-H-THF and GS-THF modified epoxies. The XG-M-THF modified epoxies show poor agreement with the model with an aspect ratio of 1000, instead it agrees well with the prediction for an aspect ratio of 100. This is due to agglomeration in the cured composite material, which reduces the effective aspect ratio. For the XG-C-THF modified epoxy, the modifiers were more particulate-like, i.e. not platelet-like, and were not as effective at such low volume fractions.

The GNPs dispersed in NMP show debonding, pull-out and plastic void growth on the fracture surfaces, and the analytical models for these mechanisms were used to predict the fracture energy, as shown in Figure 8.11.6. The XG-H-NMP (see Figure 8.11.6(a)) and GS-NMP (see Figure 8.11.6(d)) modified epoxies show good agreement with the models when all three contributions were accounted for. It was found that the contributions from the debonding and pull-out toughening mechanisms were significantly higher than the void growth component for the larger platelets.

The XG-M-NMP and XG-C-NMP modified epoxies show less good agreement with the model presented. For the XG-M GNPs (Figure 8.11.6(b)), the measured values of G_{IC} show good agreement with only the void growth component of the model. This could either be the result of void growth (as observed from the fracture surfaces as shown in Figure 8.10.4(c)) being the only significant process, in which case it suggests very poorly bonded platelets. However, it is more likely that this is the result of agglomeration

resulting in a lower effective aspect ratio. The void growth and debonding mechanisms are directly proportional to the aspect ratio, thus the pull-out mechanism is most likely to be overpredicted as the fracture energy contribution for pull-out is proportional to the debonded length squared, which itself is dependent on the aspect ratio. For the XG-C GNPs (Figure 8.11.6(c)), it would appear that the pull-out and void growth mechanisms have insignificant energy contributions, compared to debonding due to the small lateral lengths of the XG-C GNPs. However, as debonding was not observed from the fracture surfaces, the fracture performance was not improved by the addition of the XG-C GNPs.

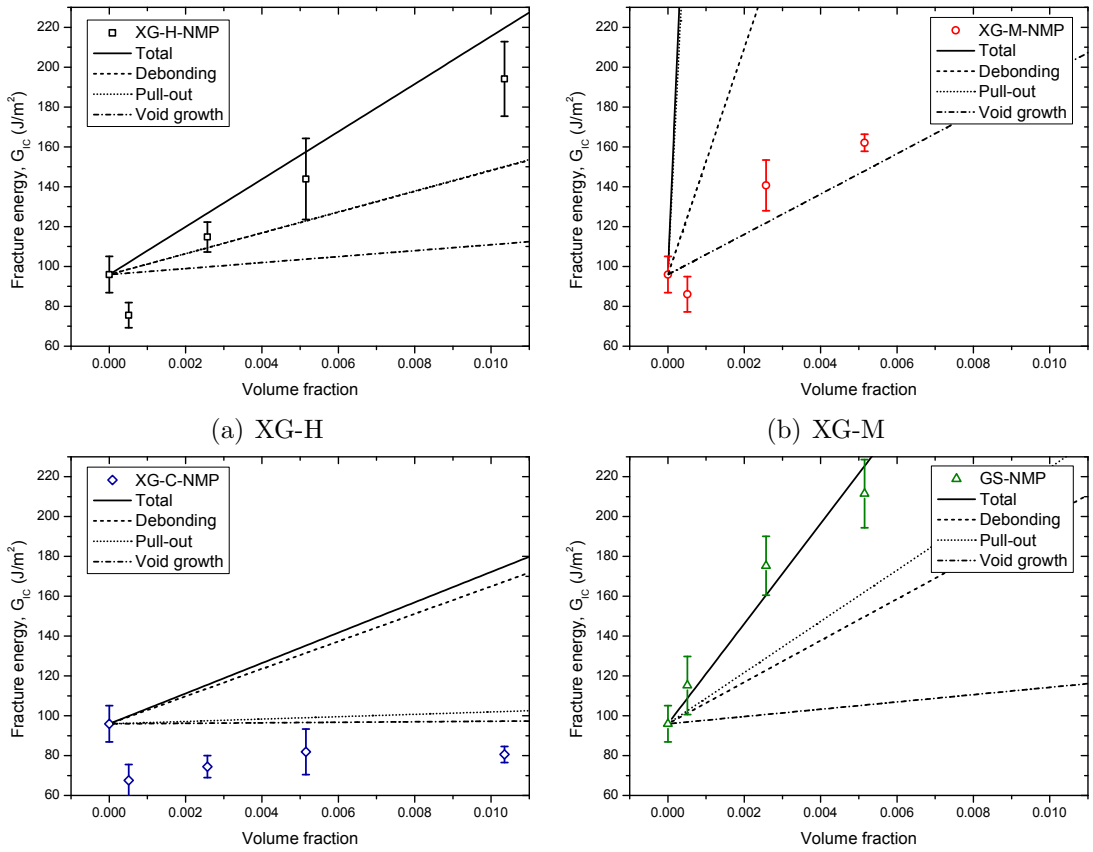


Figure 8.11.6: Predicted and measured values of fracture energy for epoxy polymers modified with GNPs dispersed in NMP.

8.12 Conclusions

Graphene nanoplatelets (GNPs) with a wide range of lateral sizes, thicknesses and aspect ratios were used to modify an anhydride cured DGEBA. GNPs and MWCNTs,

functionalised with carboxyl and oxide groups using a plasma process, were also investigated. XRD analysis and visual inspection using FEGSEM of the bulk GNPs as received showed that they were present as stacked graphene sheets of up to 90 layers. This means that the dispersion GNPs need to be investigated first optimise the mechanical properties.

XPS analysis of the bulk GNP powder shows that the GNPs were composed of at least 90 at.% carbon. The XG-H GNP had the highest carbon content at 96.1 at.% and the GS GNP had the lowest carbon content at 91.6 at.%. The remaining composition of the GNPs was mainly oxygen with trace quantities of nitrogen, fluorine, silicon and sulphur. The GNP-COOH and GNP-O_2 GNPs did not have very high contents of oxygen because the functional groups were only attached to the edges, defect and dislocation sites.

The solvents that were used to assist in dispersion were tetrahydrofuran (THF) and n-methyl-pyrrolidone (NMP). These solvents were removed by heating and mechanical mixing before curing the epoxy. After the resin was cured, the GNPs which were dispersed in THF were found to be heavily agglomerated, whereas the GNPs dispersed in NMP were well dispersed. The functionalised GNPs were also well dispersed, without the need to use a solvent. However, the COOH functionalised MWCNTs were found to be heavily agglomerated into clusters of up to 40 μm in diameter. The GNPs were found to be dispersed as stacked platelets, rather than as individual, exfoliated platelets.

The glass transition temperatures decreased due to residual solvent that remains trapped in the epoxy resin. The GNP modified epoxies show only a small decrease in T_g, compared with the epoxies with solvents that were not evaporated, indicating that the amount of residual solvent remaining is minimal. After evaporation of the solvent, the mechanical and fracture properties of the epoxies were unaffected. However, the properties of those with solvent remaining dissolved reduced dramatically, i.e. the yield strength and fracture toughness decreased.

The tensile Young's modulus values measured for the epoxy with GNPs dispersed in NMP were typically higher than those dispersed in THF. This is due to agglomeration of the platelets dispersed in THF, which reduces the effective aspect ratio. A maximum Young's modulus of 3.6 GPa was measured for the 2.0 wt% XG-H-NMP modified epoxy. Analytical models were able to predict the Young's modulus at lower GNP contents, however they break down at higher contents due to the formation of more agglomerates. The tensile strengths and strain at break decreased with the addition of GNPs. The

GNPs act as stress concentrations, which weaken the composite by initiating failure at a lower strain, much more so than spherical particles because of the shape and size. It was found that larger agglomerates had a stronger effect on the tensile strength.

The addition of GNPs can increase the fracture energy, although this was only observed for the larger platelets. The maximum G_{IC} was measured to be 0.34 kJ/m^2 for the 2.0 wt% GS-THF modified epoxy. For the XG-H, XG-M and GS GNPs, the G_{IC} measured for the GNPs dispersed in both THF and NMP were found to be of the same order. For the GNPs dispersed in THF, crack deflection around the large agglomerates was observed on the fracture surfaces. For the GNPs dispersed in NMP, platelet debonding, pull-out and void growth were observed instead. In contrast, the XG-C GNPs did not increase the G_{IC} because these GNPs appear to be particulate rather than platelet-like. The smaller size of these GNPs results in more edges, and hence more functional groups at the edges. This increases the particle/matrix adhesion and reduces the volume of debonding, and hence the pull-out and void growth. The functionalised GNPs were also found to be well bonded to the epoxy matrix and the lack of debonding similarly limits the fracture performance of these GNPs. The carboxyl functionalised CNTs (CNT-COOH) have a relatively low aspect ratio and this, combined with the significant agglomeration and poorly wetted CNTs, is a limiting factor in the mechanical and fracture performance of the resulting nanocomposites.

Under plane strain compression, the post-yield behaviour was observed to remain unchanged with the addition of GNPs. Cross-polarised images of the sectioned compressed regions show no change in appearance of the shear bands. This suggests that shear bands do not initiate from the GNPs, and hence there is no toughening effect due to this mechanism.

Analytical models for these toughening mechanisms agree well with the experimental results. For the GNPs dispersed in THF, the fracture energies for the XG-H and GS modified epoxies were accurately predicted by the crack deflection model, whereas the other GNPs show significant agglomeration and did not agree well with the model due to the reduction in aspect ratio in the composite. The GNPs dispersed in NMP, which summed the contributions of the three observed predictions for the toughening mechanisms show good agreement with the experimental results.

Chapter 9

System comparisons and Discussion

9.1 Introduction

This thesis has investigated the modification of various epoxy polymers using rubber particles, two types of block copolymers and graphene nanoplatelets. Four epoxy polymers were investigated and the effect of each modifier has been found to vary with each type of epoxy. This chapter provides a review and discussion of the results of these modified epoxies. Namely, the morphology, mechanical properties and fracture performance will be compared. Some of the results will be cited from previous work [84, 142, 180, 184] and selected micrographs and experimental results will be reproduced for ease of reference.

The epoxy systems compared are:

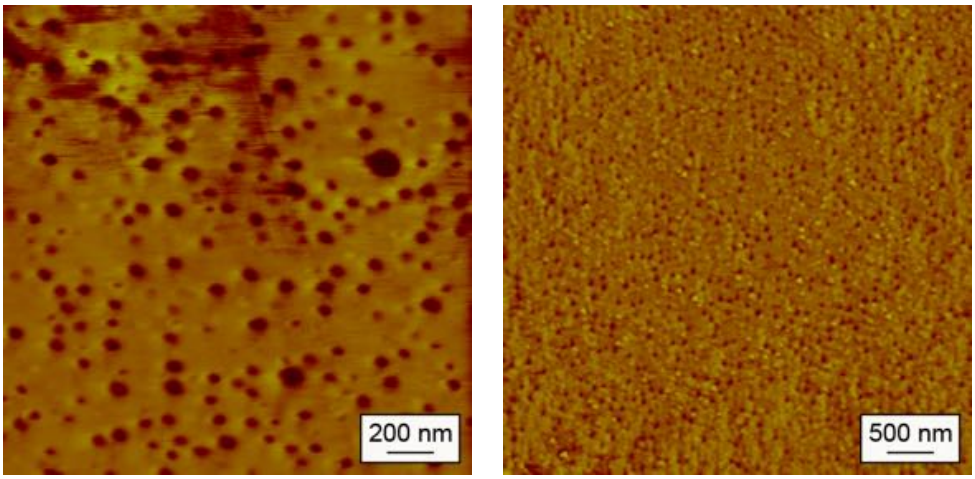
- Polyether-amine cured DGEBA, LY556/D230, denoted as LD
- Polyether-amine cured DGEBA/F, AY105/D230, denoted as AD
- Anhydride cured DGEBA, LY556/HE600, denoted as LH
- Low viscosity epoxy, denoted as LV
- Cycloaliphatic amine cured DGEBA, LY556/286, denoted as L2 [184]
- Aromatic amine cured TGMDA, Epikote 496/MDEA, denoted as EM [84]
- Aromatic amine cured DGEBA, LY556/MCDEA, denoted as LM [180]
- Heterocyclic amine cured DGEBA, DER 331/Piperidine [167]

9.2 Rubber modified epoxies

The morphology and mechanical properties of the CSR and CTBN modified epoxies are reviewed in this section. The core shell rubber particles used were pre-dispersed in epoxy resin as a masterbatch, and the CTBN is a reactive liquid rubber that phase separates during cure to form rubber particles.

9.2.1 Morphology

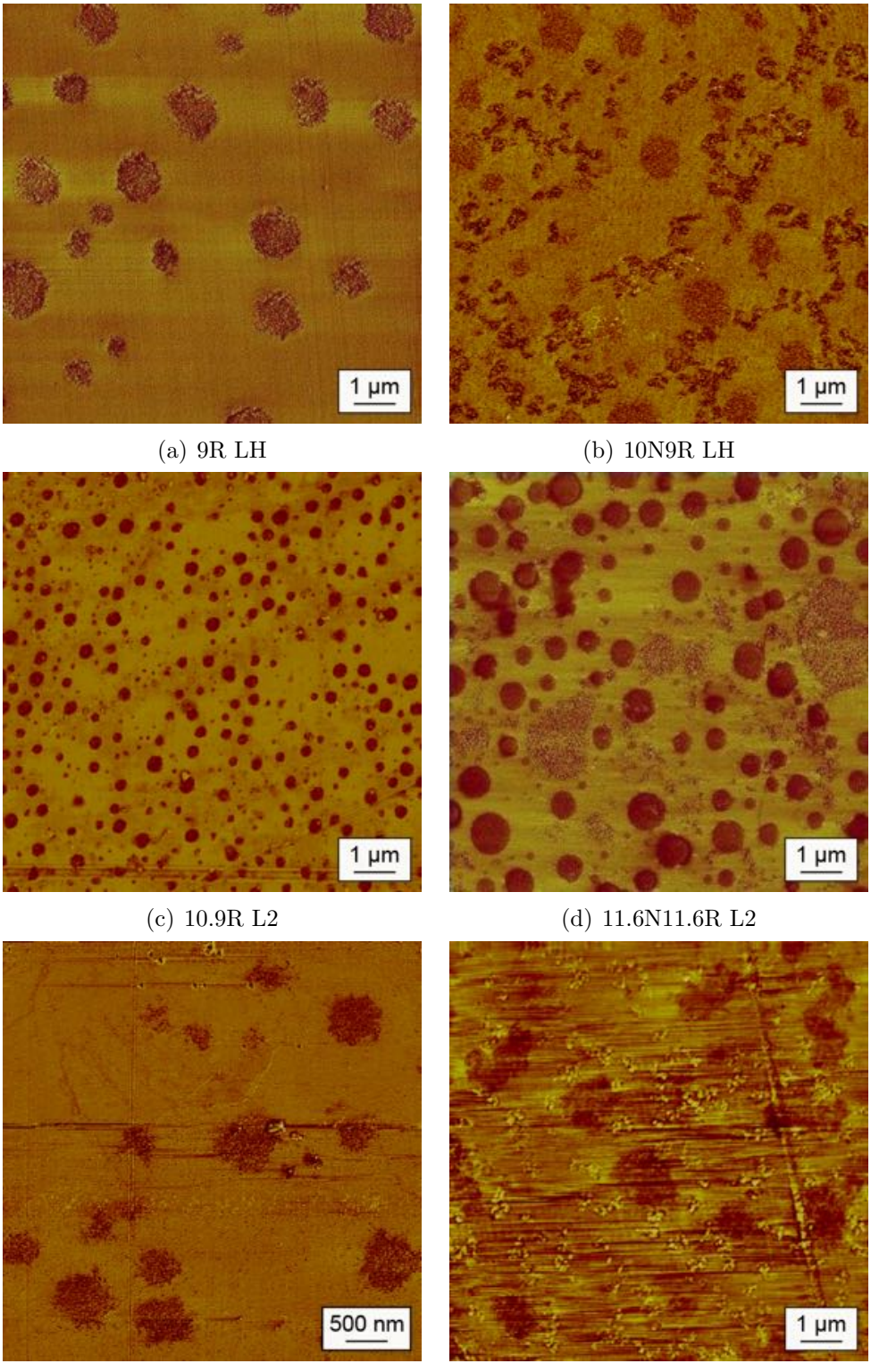
The morphology of the rubber modified LD, AD and LV epoxies were shown in §5.2. They were similar to that of the CSR and CSR-NS hybrid modified LH epoxies [20], as shown in Figure 9.2.1. The dispersion of the CSR particles, in both the rubber and hybrid modified epoxies, were found to be "random-like". The silica nanoparticles were also well dispersed in the epoxy matrix for the hybrid modified epoxies, as shown in Figure 5.2.6(b).



(a) 9C LH (b) 9N9C LH

Figure 9.2.1: AFM phase micrographs of MX156 CSR and hybrid MX156-NS modified LH epoxy polymer. Reproduced from [20].

The morphology of the 9 wt% CTBN and CTBN-NS hybrid (10N9R) modified LH, L2 and EM epoxy polymers are shown in Figure 9.2.2 [84, 184]. The CTBN rubber phase separated into well dispersed micron sized particles for all of the epoxy systems investigated, except for the LV epoxy. However, the silica nanoparticles were agglomerated for all of the 10N9R hybrid modified epoxies. From §5.2, it is known that this is due to the high rubber content, as the silica nanoparticles in the 10N5R hybrid modified LD epoxy were well dispersed.



(a) 9R LH (b) 10N9R LH

(c) 10.9R L2 (d) 11.6N11.6R L2

(e) 9R EM (f) 10N9R EM

Figure 9.2.2: AFM phase micrographs of CTBN modified epoxy polymers. Reproduced from [84, 184].

The rubber particle sizes are summarised in Table 9.2.1. With the exception of the LV and L2 epoxies, the mean radii of the CTBN rubber particles were approximately 400 nm, which agrees well with other model systems reported [23, 81].

Table 9.2.1: Mean particle radius of CTBN rubber particles.

Modifier	Particle radius (μm)	
	9R	10N9R
LD	0.42 ± 0.01	0.46 ± 0.05
AD	0.51 ± 0.03	0.53 ± 0.05
LH	0.35 ± 0.13	0.36 ± 0.05
LV	–	–
L2 [184]	0.09 ± 0.01	0.21
EM [84]	0.44 ± 0.05	0.42

Previous studies typically focuses on a limited range of concentrations, e.g. 10 wt% [23, 165], however there are more conclusions to be made by expanding this range. As shown in Table 5.2.2, increasing the concentration of CTBN decreases the particle radius. This is due to the lower viscosity of the 5 wt% CTBN/epoxy resin; the diffusion rate is higher and hence the growth rate of the rubber particle is higher. The viscosities of the CTBN rubber and CTBN-NS hybrid modified LD epoxy as a function of temperature are shown in Figure 9.2.3. The results show an increase in viscosity as the rubber content was increased.

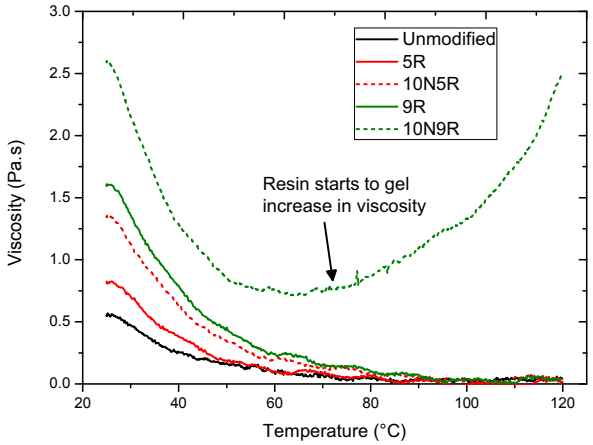


Figure 9.2.3: Viscosity as a function of temperature for CTBN rubber and CTBN-NS hybrid modified LD epoxy polymers.

With the addition of silica nanoparticles, the 5 wt% and 7 wt% CTBN modified epoxies show a decrease in particle radius. This is also due to the viscosity effect, where the viscosity is increased by the presence of the silica nanoparticles (see Figure 9.2.3). However, there was no change in particle size when comparing the the 9R and 10N9R

modified epoxies. This was also shown for other epoxy systems (see Table 9.2.1). In fact, the L2 epoxy system even shows an increase in particle radius when silica nanoparticles were added. This would suggest some effect on the phase separation process, either by a change in reactivity or kinetics.

From Figure 9.2.3, the 10N9R modified LD epoxy shows increased reactivity, noted as an early onset of resin curing. However, this implies that the particle radius should decrease due to less time available for phase separation. A more reasonable explanation is that the clustered silica nanoparticles in these high wt% CTBN resins allow the rubber to flow more easily, hence able to increase the particle size, i.e. there is less obstruction to the resin flow.

In summary, the results suggest that the morphology of rubber modified epoxies is rather complex. The use of core-shell rubber particles is the most consistent and predictable. The CSR particles and silica nanoparticles were well dispersed for the CSR and CSR-NS hybrid modified epoxy systems observed. For the CTBN modified epoxies, the phase separation process can be strongly dependent on the type of epoxy resin, hardener and cure cycle used. For example, the rubber particles were much smaller for the L2 epoxy system than the LD epoxy system despite being composed of the same base epoxy resin. The LD and AD epoxy systems are composed of the same hardener and have the same cure cycle, and differs in that the AD epoxy resin comprises partially of DGEBF resin. This is enough to cause a change in the rubber particle radius.

The addition of silica nanoparticles increases the complexity of the phase separation process. The silica nanoparticles reduces the heat of reaction and curing kinetics of the epoxies due to the lower epoxy content and increases the viscosity. This results in a change in rubber particle radius and distribution of the silica nanoparticles. In addition, the dispersion of the silica nanoparticles is dependent on both the rubber content, as shown in Figure 5.2.6, and silica content [184].

The next section reviews how the morphological changes affect the mechanical properties of these rubber modified epoxies.

9.2.2 Tensile properties

The normalised Young's moduli of the CSR and CTBN modified epoxies decreases linearly with increasing rubber content because rubber has a much lower modulus of approximately 2 MPa, compared to the bulk unmodified epoxy, which has a modulus

of approximately 3 GPa.

For the CSR modified epoxies, the trend in relative Young's modulus was almost identical for all of the epoxy systems investigated, as shown in Figure 9.2.4. There was no correlation between the modulus and glass transition temperature or fracture performance. This indicates that the modulus is primarily controlled by the relative difference in moduli of the matrix and modifier. This can be visualised by application of the Mori-Tanaka model, as shown in Figure 9.2.5(a). For the low volume fractions used in the present work (up to 10 vol%), the model also predicts a linear decrease in modulus. It is also interesting to note that above a ratio of matrix to particle modulus of 500, the decrease in modulus does not change even when the particle modulus decreases further.

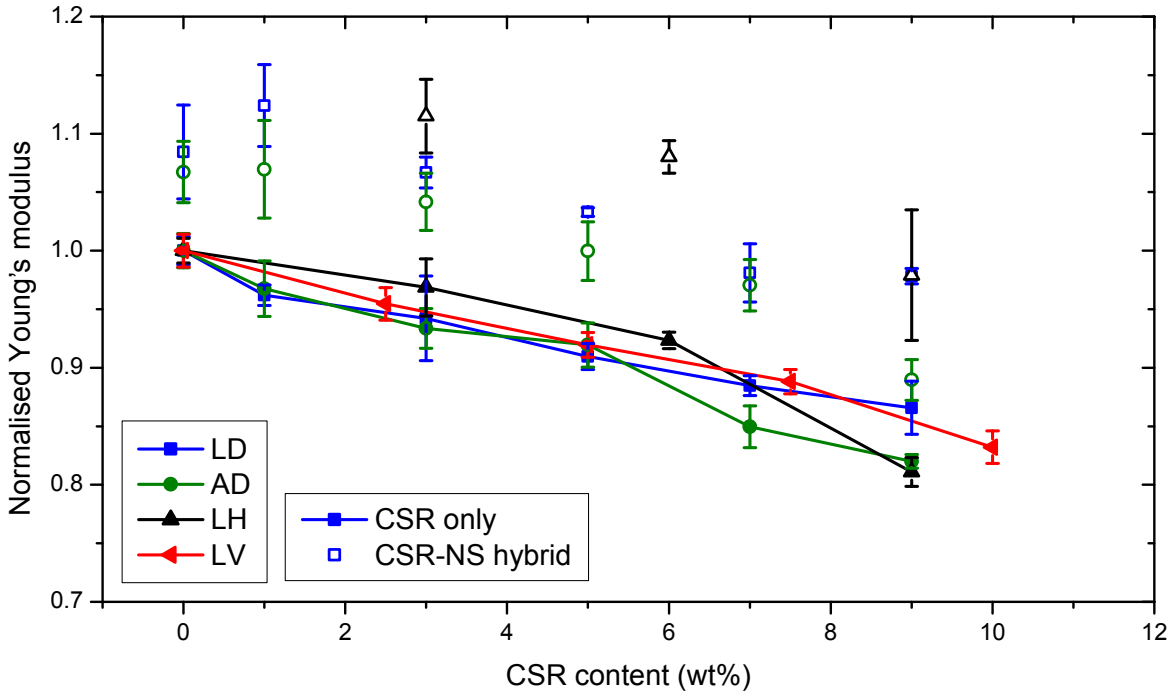
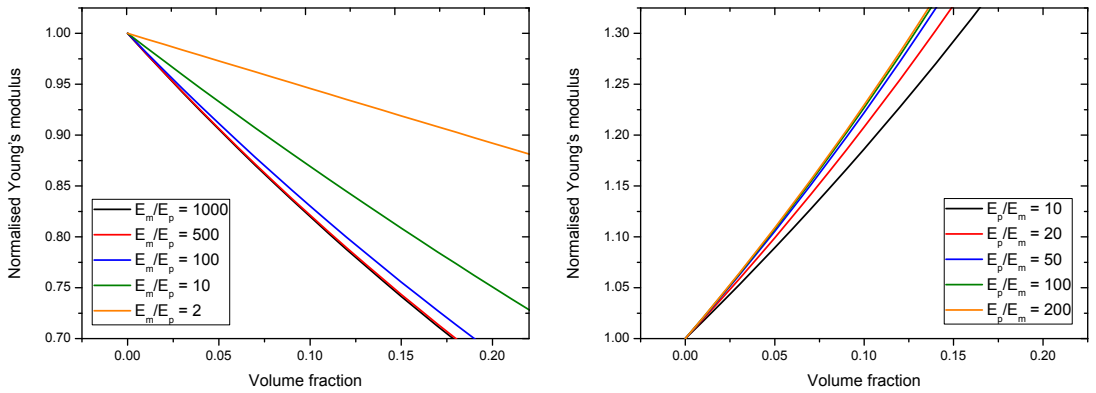


Figure 9.2.4: Normalised Young's moduli of different epoxy systems for CSR modified epoxies. Includes data from [20, 84]. Solid points (■) are CSR only and open points (□) are CSR-NS hybrid formulations.

The silica nanoparticles in the hybrid CSR-NS epoxies were well dispersed and increased the modulus of the rubber modified epoxies. The increase in modulus was approximately 10% for all formulations which had approximately 6 vol% of silica, as shown in Figure 9.2.4. The Mori-Tanaka model predicts an increase of 10% for a volume fraction of 6 vol.%, as shown in Figure 9.2.5(b). This would suggest that the effect of modulus on the composite from the CSR particles and silica nanoparticles are independent of each other.



(a) Soft particles (b) Rigid particles

Figure 9.2.5: Normalised Young's modulus predicted using Mori-Tanaka model for different ratios of matrix to particle modulus.

For the CTBN modified epoxies, a linearly decreasing modulus with rubber content was also observed for all the epoxy systems, as shown in Figure 9.2.6.

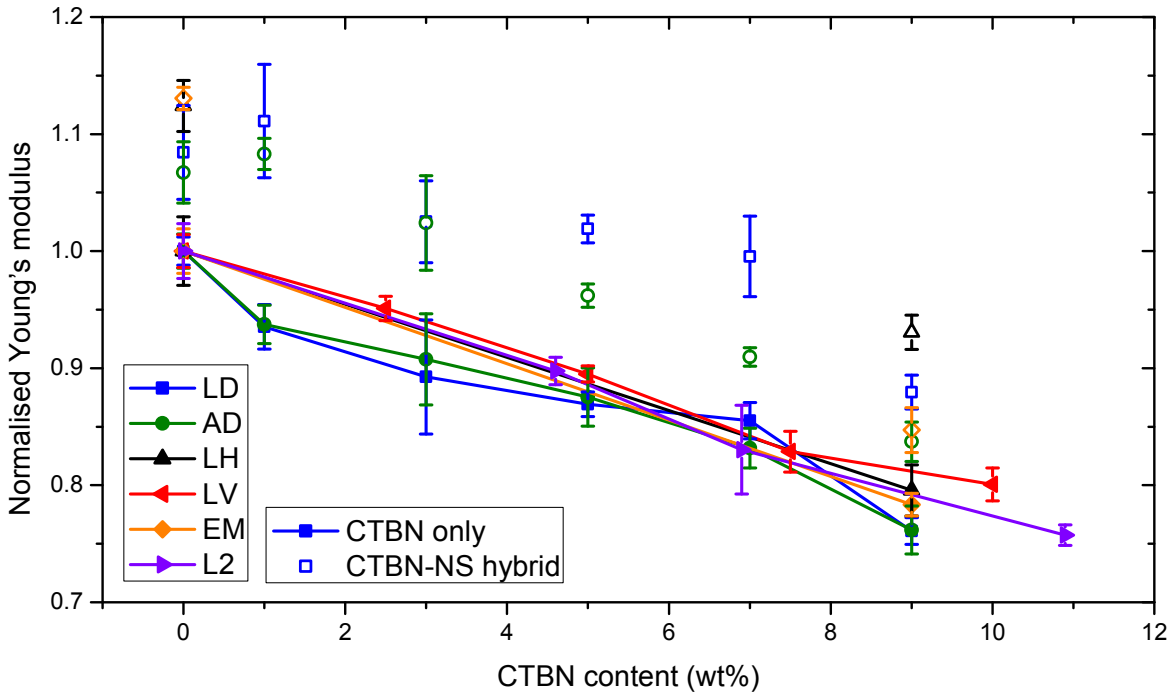


Figure 9.2.6: Normalised Young's moduli of different epoxy systems for CTBN modified epoxies. Includes data from [84, 184]. Solid points (■) are CTBN only and open points (□) are CTBN-NS hybrid formulations.

The CTBN modified L2 epoxy polymers, which have rubber particles with a smaller mean radius also fit with this trend. The Young's moduli of the CSR modified epoxies also fit well with this trend when only the total rubber content was considered i.e. by reducing the volume fraction to exclude the PMMA shell. This confirms that there

is no size effect on the Young's modulus for rubber modified epoxies, as was shown for rigid particles [93]. There is also no change with the amount of dissolved rubber, as shown by the CTBN modified LV epoxy, indicating that the modulus is dominated purely by the volume fraction of rubber added. This is consistent with the analytical models that show that the modulus is dependent only on volume fraction.

With the addition of approximately 6 vol% of silica nanoparticles, a 10% increase in modulus was also observed for the CTBN modified epoxies. The percentage increase in modulus was the same for all the formulations investigated. Hence the quality of particle dispersion does not affect the modulus, and the modulus is dependent only on the vol% of the particles and their relative moduli.

9.2.3 Fracture properties

The normalised fracture energies of the rubber modified epoxies for the different epoxy systems are shown in Figures 9.2.7 and 9.2.8, for the CSR and CTBN modified epoxies respectively. The fracture energy, G_{IC}, of all the rubber modified epoxies increased with rubber content, at different rates for each epoxy system. The typical trend for the G_{IC} of the CSR and CTBN modified epoxies is a linear increase with weight percentage, with the exception of the LD and AD epoxy systems.

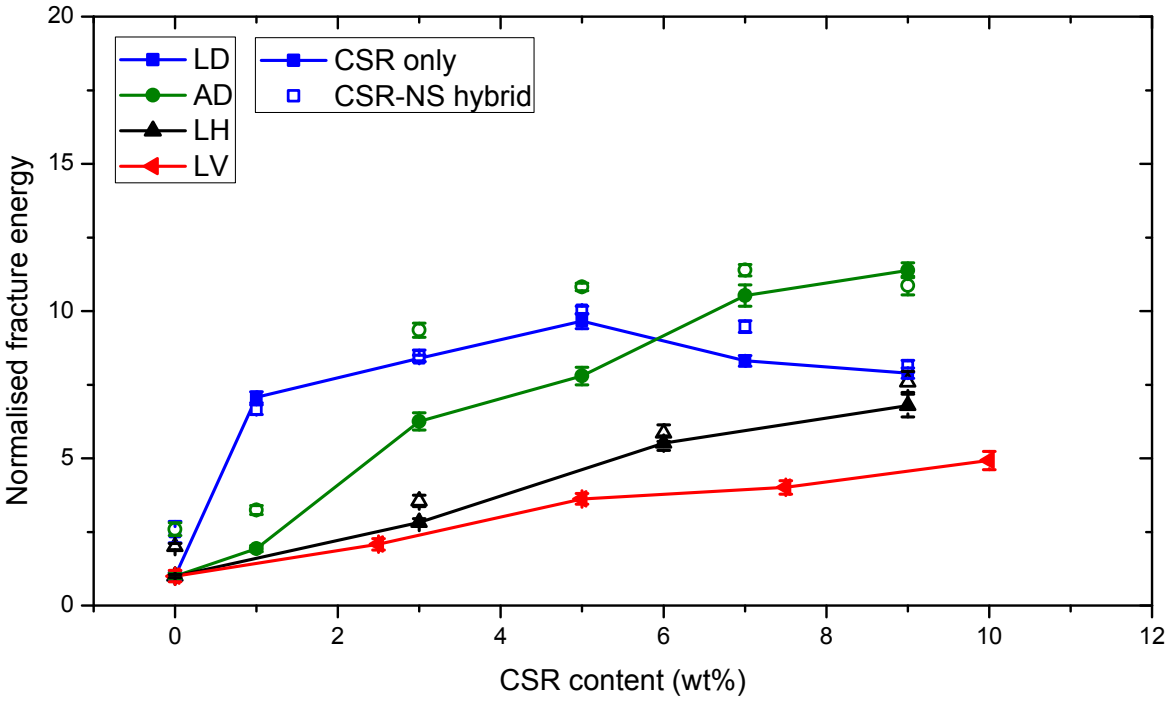


Figure 9.2.7: Normalised fracture energy of different epoxy systems for CSR modified epoxies. Includes data from [20]. Solid points (■) are CSR only and open points (□) are CSR-NS hybrid formulations.

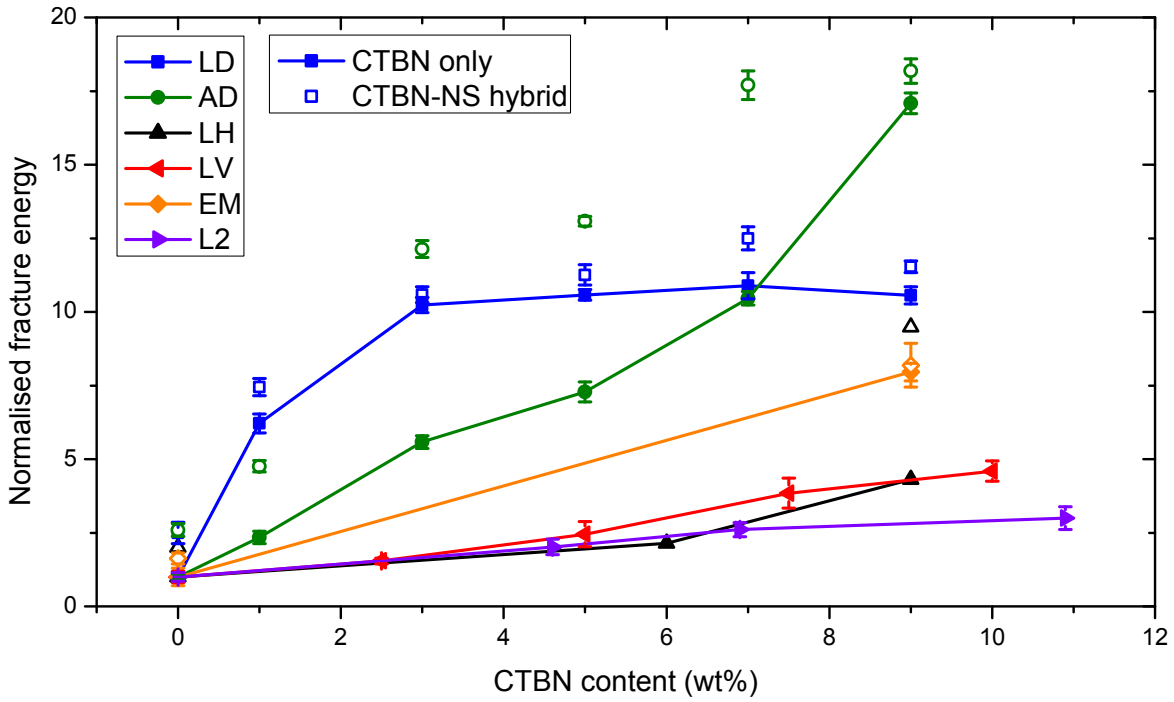


Figure 9.2.8: Normalised fracture energy of different epoxy systems for CTBN modified epoxies. Includes data from [84, 184]. Solid points (■) are CTBN only and open points (□) are CTBN-NS hybrid formulations.

The rubber modified LD and AD epoxies show significant increases in G_{IC} at low concentrations, followed by a plateau in G_{IC} at higher loadings. The balance between the rubber cavitation stress and shear yield stress of the epoxy is what gives this particular combination the high toughness at low concentrations of rubber. The other epoxies are more highly crosslinked, thus have higher shear yield stress. This results in little shear yielding following the cavitation process and the increase in G_{IC} is more gradual, i.e. linear. The plateau in G_{IC} observed is due to the extent of plasticity between the rubber particles. As the rubber content is increased, the distance between the rubber particles decreases, and the degree of plasticity at a specified load increases. As the interparticle distance continues to decrease, the extent of plasticity at that specified load reaches a peak, and hence a plateau in G_{IC}, and the fracture energy will eventually decrease with rubber content.

The toughening mechanisms observed for all the rubber modified epoxies were particle cavitation, followed by plastic void growth of the epoxy matrix, and localised shear band yielding initiated by the rubber particles. The addition of silica nanoparticles has little effect on the fracture energy of the CSR modified epoxies, as shown by the open points (□) in Figure 9.2.7. For the CTBN modified epoxies, as shown in Figure 9.2.8, the effect of adding silica nanoparticles is more complicated. Some of the epoxy

systems, such as the AD and LH epoxies exhibit a large increase in fracture energy, whereas the LD and EM epoxy systems do not show any improvement. One of the possible reasons is that the LD and EM epoxies already show significant shear yielding, as observed from the plane strain compression tests [84]. This limits the effectiveness of any modifiers which enhance shear yielding. The degree of void growth typically remains constant or decreases with the addition of silica nanoparticles, which suggests shear yielding is the only significant mechanism for these hybrid modified epoxies.

Regarding the order of toughening mechanisms which allow for these synergistic effects, it is possible that the cavitation of the rubber particles reduces the constraint at the crack tip, hence allowing more intense localised shear band yielding between the silica nanoparticles. It is more logical to assume in this case that cavitation of the rubber particles would occur first, based on size effects of debonding and cavitation. This is because the silica nanoparticles are much smaller than the rubber particles, and would require a much higher stress or energy to debond, compared to the energy required to cavitate a much larger rubber particle [218]. However, the synergy was not observed for the LD epoxy polymers. The plateau in fracture energies for spherical particles was measured at G_{IC} values of 2.0 kJ/m^2 and 2.5 kJ/m^2 for the CSR and CTBN modified epoxies. These values are different which suggests that this is a particle size effect. The addition of silica nanoparticles appears to only be synergistic below this limit.

The lack of synergy and lower G_{IC} values for the CSR modified epoxies could be due to the size effect. The smaller diameter CSR particles require a higher energy or stress to cavitate and hence cavitation occurs at a later stage and dissipates less energy through plastic void growth. Debonding of the CSR particles is unlikely as the functionalised shell would be well bonded to the epoxy.

It is perhaps more useful to visualise the fracture performance as a function of the glass transition temperature. Firstly, the yield behaviour of the modified epoxies varies with the T_g as shown in Figure 9.2.9. Decreasing the T_g results in a decrease in compressive yield strength, σ_{yc}. This indicates that the lower T_g epoxies are more likely to deform plastically. This is because the lower T_g epoxies have a higher molecular weight between cross-links, hence less highly crosslinked and are able to deform more easily.

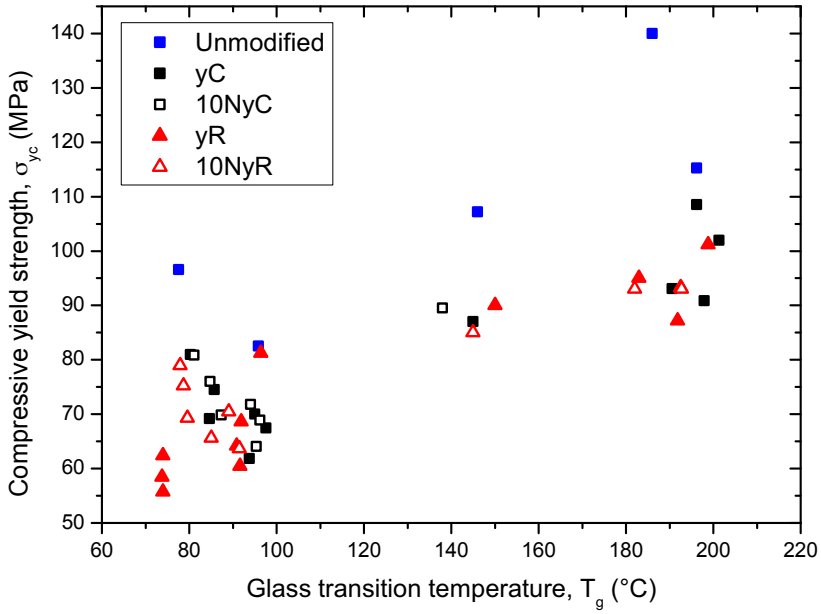
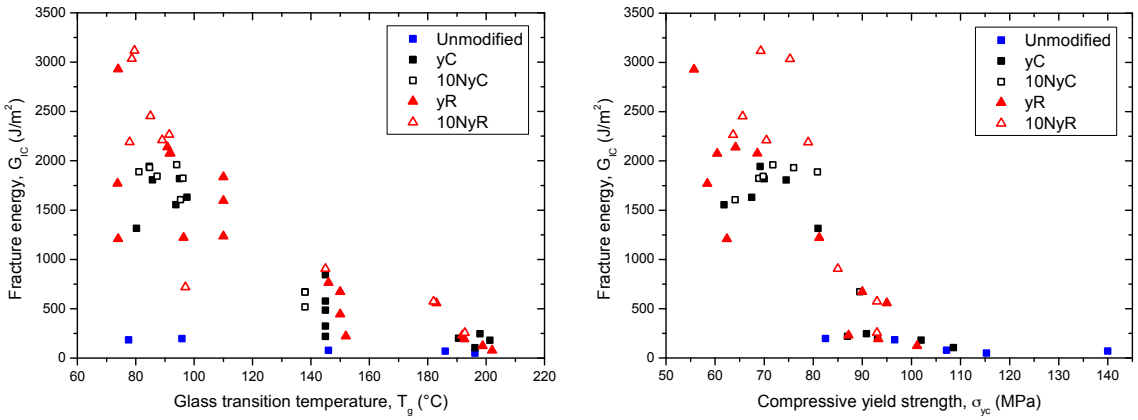


Figure 9.2.9: Compressive yield strength as a function of glass transition temperature for the rubber modified epoxy polymers. Includes data from [20, 84, 184].

The G_{IC} is plotted against T_g for the rubber modified epoxies in Figure 9.2.10(a). The trend is as expected, with an increase in toughenability with a decrease in T_g. Higher values of G_{IC} were measured for materials with lower T_g. This would indicate that the increases in fracture toughness are dominated by the yield characteristics of the epoxy matrix, as shown in Figure 9.2.10(b). As the T_g and σ_{yc} decreases, the G_{IC} values increase dramatically.



(a) (b)

Figure 9.2.10: Fracture energy as a function of (a) glass transition temperature and (b) compressive yield strength for the rubber modified epoxy polymers. Includes data from [20, 84, 184].

9.3 Block copolymer modified epoxies

Two main types of block copolymers were investigated as part of this thesis. The first was an asymmetric triblock copolymer of polystyrene-b-polybutadiene-b-poly(methyl methacrylate), i.e. SBM, and the second was a symmetric triblock copolymer of poly(methyl methacrylate)-b-poly(butylacrylate)-b-poly(methyl methacrylate), i.e. MAM. The structure/property relationships of these SBM and MAM modified epoxies are reviewed in this section.

The available literature typically comes from manufacturer laboratories or those sponsored by them [56, 58, 280]. As such, these studies only feature specific modifiers and are not compared with other conventional modifiers or epoxy matrices. This section will address this issue by directly comparing the different modifiers in different epoxy matrices.

9.3.1 Morphology

The BCPs were initially dissolved in the epoxy resin and phase separate into complex morphologies at different loadings. A comparison of different epoxy systems modified with BCPs will help explain some of the properties that control the final morphology.

The morphology of the E21 SBM modified epoxies shown in §6.2 all show some form of evolution in size with SBM content. At higher weight percentages, co-continuous microstructures were observed. However, other authors have found for other epoxy systems that this may not always be the case. An example given here in Figure 9.3.1 shows the morphology of a piperidine cured DGEBA, modified with E21 SBM up to a content of 15 phr [167].

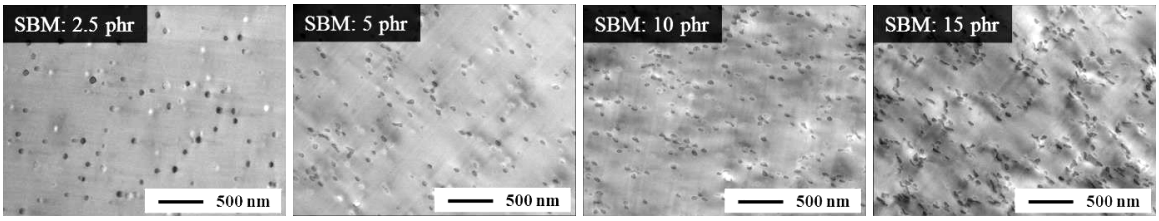


Figure 9.3.1: STEM-IN-SEM micrographs of E21 SBM modified piperidine cured DGEBA epoxy. Reproduced from [167].

Spherical micelles with a mean radius of 25 nm were observed for the E21 modified epoxies up to 15 phr, which did not increase in size with BCP content. They also

found that increasing the loading causes the SBM particles to agglomerate, as shown in Figure 9.3.2.

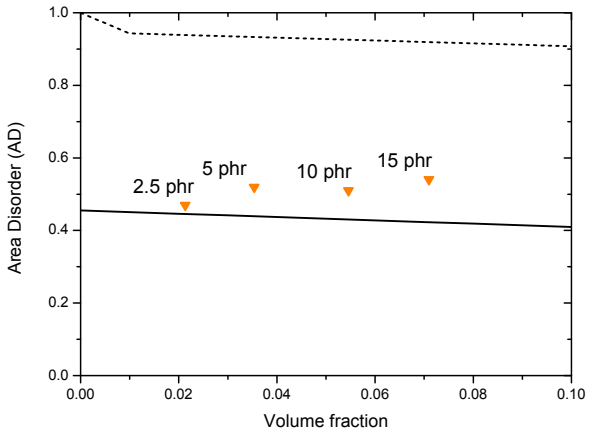
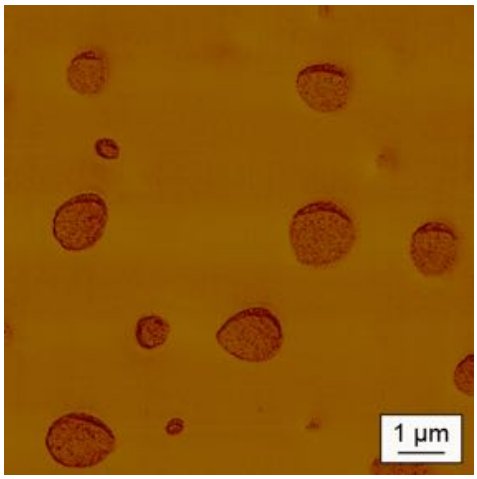
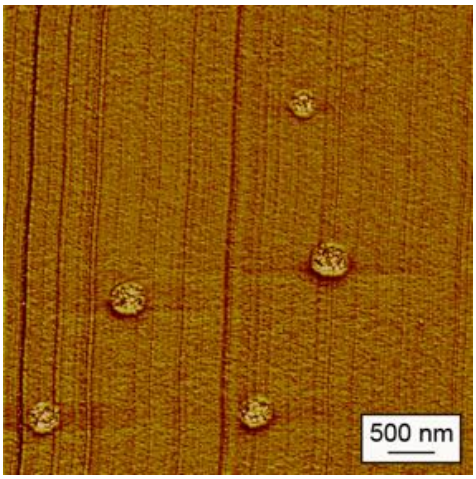


Figure 9.3.2: Area disorder of E21 SBM modified piperidine cured DGEBA epoxy.

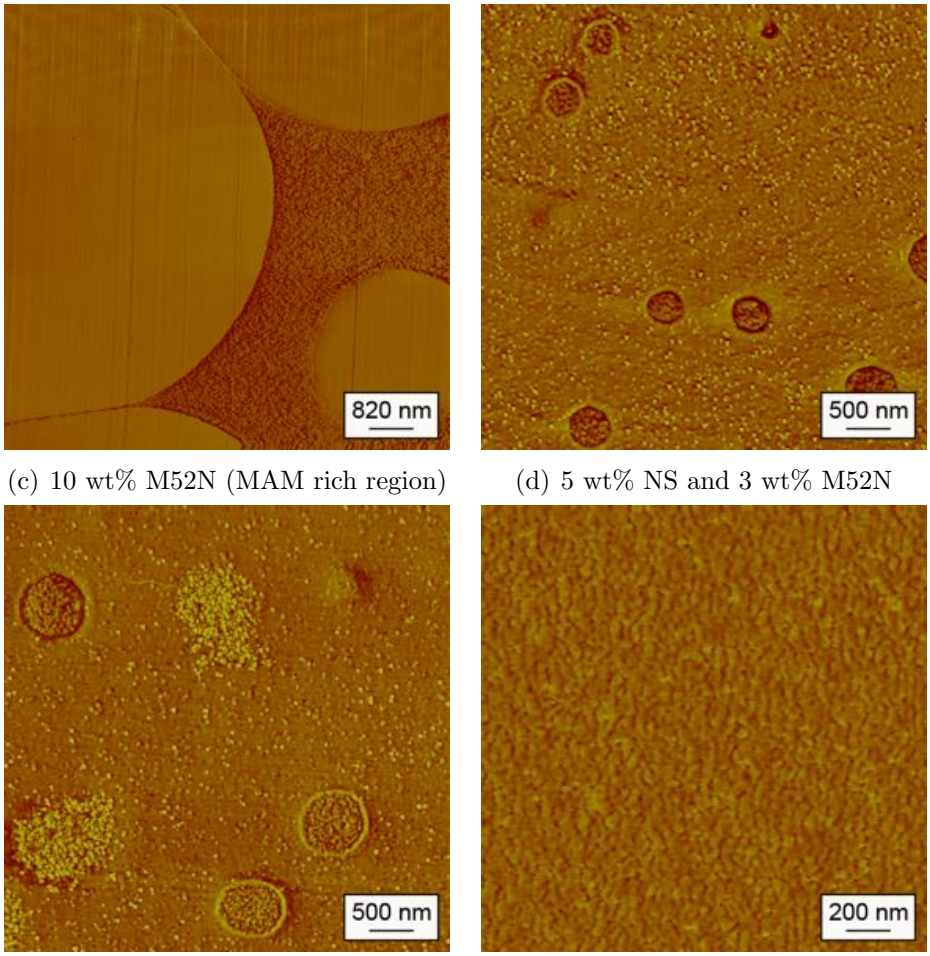
The morphology of the MAM modified LD and AD epoxies were shown in §7.2.1. Figures 9.3.3 and 9.3.4 shows the AFM phase micrographs of the M52N MAM, hybrid M52N-NS and M22N MAM modified LH and LM epoxies, respectively. At lower MAM concentrations of up to 5 wt%, the LD and AD epoxies phase separate into spherical particles. Similarly for the LH epoxy, spherical particles were observed with the addition of 7 wt% M52N MAM, as shown in Figure 9.3.3(a). For the LM epoxy system, both spherical particles and worm-like micelles were observed. Further increasing the MAM content results in an increase in particle size before a change in morphology to a co-continuous microstructure for the LD and AD systems occurs, and there is partial phase inversion for the LH system (see Figure 9.3.3(c)).



(a) 7 wt% M52N



(b) 10 wt% M52N (Epoxy rich region)



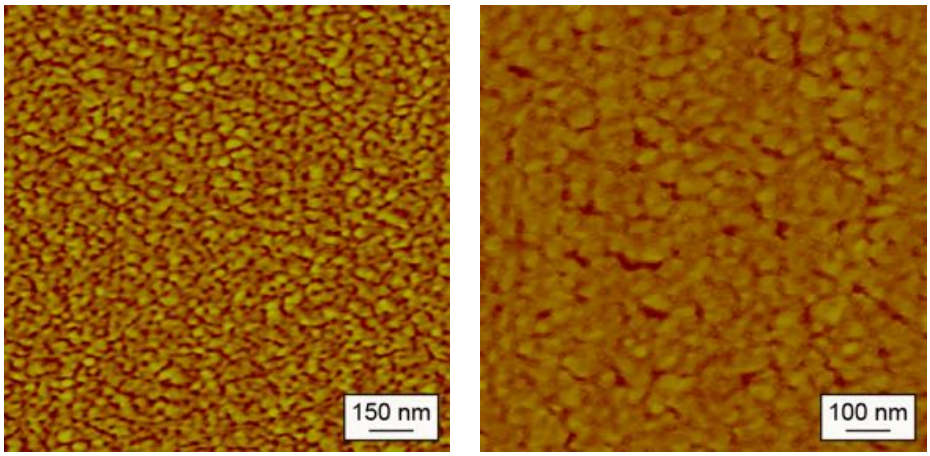
(c) 10 wt% M52N (MAM rich region)

(d) 5 wt% NS and 3 wt% M52N

(e) 5 wt% NS and 7 wt% M52N

(f) 12 wt% M22N

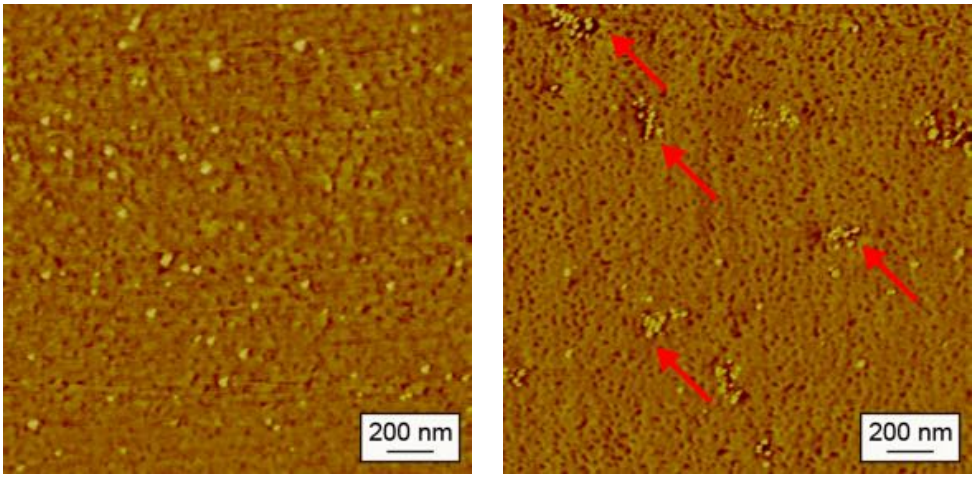
Figure 9.3.3: AFM phase micrographs of MAM modified LH epoxy polymer. Reproduced from [180].



(a) 10 wt% M52N

(b) 5 wt% M22N

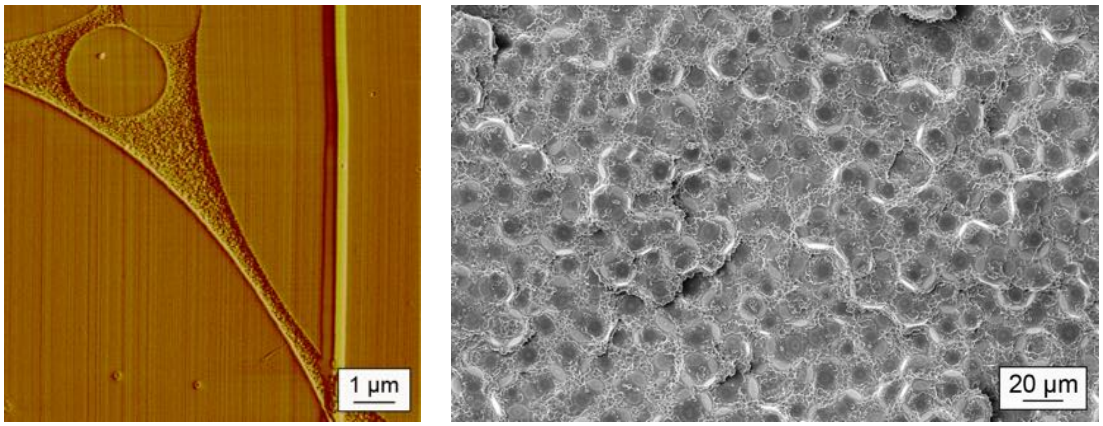
Further increasing the MAM content can result in a completely phase inverted microstructure, as shown in Figure 9.3.5. The cross-section of the material, as shown by the AFM phase micrograph in Figure 9.3.5(a), shows that the spherical particles are



(c) 3 wt% NS and 7 wt% M52N (d) 3 wt% NS and 15 wt% M52N

Figure 9.3.4: AFM phase micrographs of MAM modified LM epoxy polymer. Agglomerates of silica nanoparticles identified with red arrows. Reproduced from [180].

of epoxy surrounded by a matrix of M52N MAM. The low magnification FEGSEM micrograph of the fracture surface shows a better overall image of the microstructure. It is also interesting to note from the fracture surface that there were no regions of exposed epoxy, i.e. brittle fracture of the epoxy particles. This means that the crack is preferentially propagating through the weaker MAM phase although it is more ductile due to strong MAM/epoxy interfacial adhesion.



(a) (b)

Figure 9.3.5: AFM phase micrographs of 12 wt% M52N MAM modified LH epoxy polymer. Reproduced from [180].

A similar trend was also observed for the SBM modified epoxies, i.e. a dispersion of spherical particles at low BCP content, which changes to a co-continuous or phase inverted structure at higher loadings, as discussed in §6.2. Some qualitative comments can be made about the miscibility of PMMA in the epoxy systems investigated. For

the same epoxy resin, cured with different hardeners, different morphologies and characteristic lengths were observed with increasing BCP content. Similarly, the LD and AD epoxies have the same hardener and slightly different epoxy resins, which resulted in different particle sizes and characteristic lengths. The E21 SBM modified LV epoxy exhibits phase inversion at 5 wt%, whereas the E21 SBM modified LH epoxy phase separates as a co-continuous structure at 10 wt%. These differences are due to the miscibility of the PMMA block in the different epoxy systems. Both the epoxy resin and curing agent affect the miscibility of the BCP.

At contents of up to 10 wt%, the M22N MAM phase separates into worm-like micelles. The M22N MAM has a higher PMMA content than the M52N MAM, which is the epoxy miscible block. This means that the M22N has a higher energy barrier to phase separation, i.e. it will phase separate at a higher conversion. Thus, macrophase separation such as co-continuous structures and phase inversion was not observed for the M22N MAM, even at high contents. This also results in very small spherical or worm-like micelle, as there is less time for the particles to grow before the epoxy is fully cured.

The dispersion of the silica nanoparticles in the hybrid BCP-NS modified epoxies varied for the SBM and MAM BCPs. When added to the SBM BCP modified epoxies, 10 wt% of silica nanoparticles tended to be well dispersed in the epoxy matrix for all of the formulations examined. The silica nanoparticles were also well dispersed when added to an epoxy modified with a low concentration of MAM. Increasing the MAM content (such as at 10 wt%) causes the silica nanoparticles to be agglomerated. This was found even at low weight percentages of silica nanoparticles, as shown in Figure 9.3.4(d). None of the silica nanoparticles were found to be present in the SBM or MAM phases.

Given that the silica nanoparticles are initially well dispersed in the epoxy, the agglomeration must have occured during phase separation of the MAM. It is unlikely that this is due to the kinetics of cure alone [300], as the 10 wt% E21 and 10 wt% M52N modified epoxies have similar values of viscosities with temperature, as shown in Figure 9.3.6. Instead, it is more likely to be due to the miscibility of the modifiers. It is hypothesised that the SBM has the lowest miscibility, as it has the lowest percentage of the epoxy-miscible block (i.e. PMMA block). The M52N MAM is composed of approximately 50% PMMA block, and the CTBN used was an adduct, both of which would be expected to have higher miscibility [64]. There is some evidence for this from the higher volume fraction of SBM phase measured from the AFM for the SBM modified epoxies. This means that the SBM undergoes phase separation at an earlier

stage. At this stage, the silica nanoparticles have more time, and the resin is also at a lower viscosity before gelation occurs, to reorganise in a more favourable position, i.e. random-like dispersion.

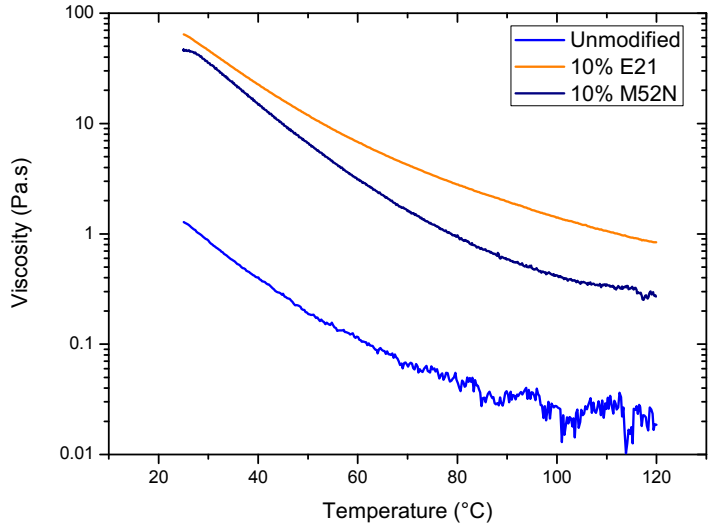


Figure 9.3.6: Viscosity as a function of temperature for 10 wt% E21 and M52N modified LH epoxy resins.

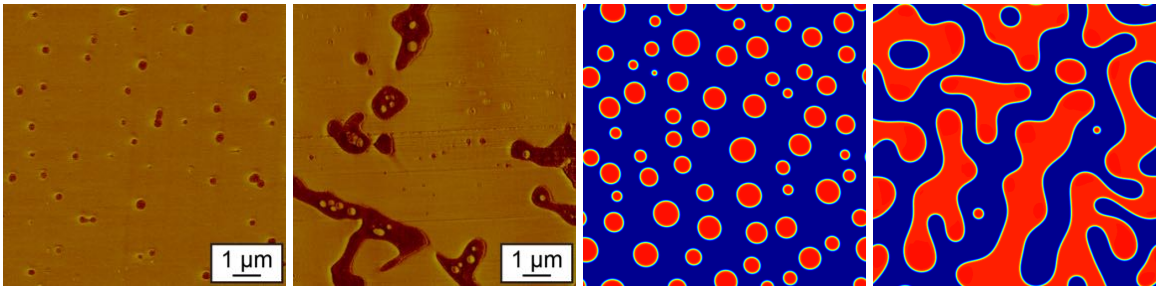
The addition of the silica nanoparticles was found to affect the morphologies of the BCP modified LH epoxies more significantly. The addition of silica nanoparticles caused an earlier onset of the change in morphology, i.e. reducing the weight percentage at which the transition from spherical particles to a co-continuous microstructure, and to a phase inverted microstructure occurs. In contrast, the morphology of the hybrid BCP-NS modified LD, AD and LM epoxies remained the same in type and size when silica nanoparticles were added. This suggests that the silica nanoparticles can affect the miscibility and kinetics of cure.

9.3.2 Comparison with phase field model

This section compares the morphologies observed experimentally with those generated from the phase field model presented in §2.2.2.5. This helps provide a visual representation of the results when changing the volume fraction, viscosity (mobility) and miscibility (thermodynamic barrier). The experimental and numerical results cannot be compared directly due to the assumptions made for simplicity, mainly concerning the mobility and free energy functional. However, the qualitative trends observed between the two were similar.

Figure 9.3.7 shows the AFM phase micrographs for the M52N MAM modified LD epoxy

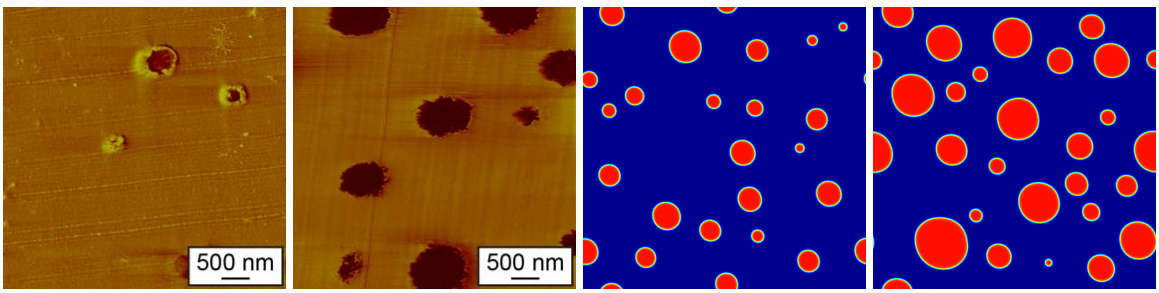
polymers. The other BCP modified epoxies investigated in this study also exhibited similar trends. There is a clear transition from a droplet-type to a co-continuous microstructure with increasing volume fraction of BCP, as noted from the numerical models in Figures 9.3.7(c) to 9.3.7(d). The maximum characteristic length measured is limited by the conversion rate of the epoxy, and the final evolved microstructure is fixed by the gelation process. The concentration at which this transition occurs in the model is different from that for the experimental due to the assumptions made.



(a) 2.5 wt% M52N LD (b) 10 wt% M52N LD (c) Model (c = 0.32) (d) Model (c = 0.5)

Figure 9.3.7: Comparison between AFM phase micrographs of M52N MAM modified LD epoxy polymers and Cahn-Hilliard models at t = 10,000. c represents initial concentration of second phase material.

The effect of initial concentration from the phase field models can also be compared with the CTBN modified epoxies. From §5.2, it was observed that increasing the rubber content increases the size and number of rubber particles. Figure 9.3.8 illustrates this with the AFM phase micrographs of the 1 wt% and 9 wt% CTBN modified epoxy. The phase field model results corroborate well with the experimental results in this case, comparing the phase fields at $v_f = 0.32$ and $v_f = 0.4$ at t = 30000 in Figures 9.3.8(c) to 9.3.8(d).

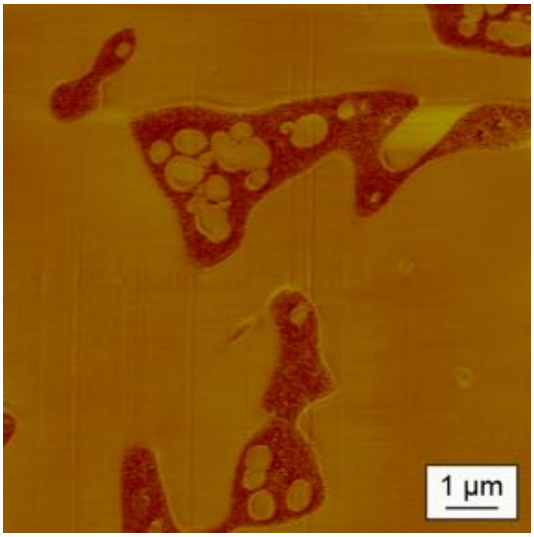


(a) 1 wt% CTBN LD (b) 9 wt% CTBN LD (c) Model (c = 0.32) (d) Model (c = 0.4)

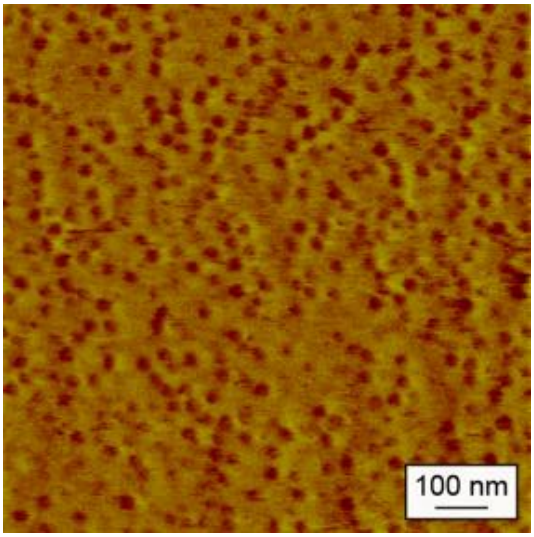
Figure 9.3.8: Comparison between AFM phase micrographs of CTBN modified LD epoxy polymers and Cahn-Hilliard models at t = 30,000. c represents initial concentration of second phase material.

From §7.2.1, the morphologies of the M52N and M22N MAM modified epoxies were found to be different, reproduced here in Figure 9.3.9. Macroscale phase separation was found for the M52N modified epoxies, whereas nanoscale features were observed for the

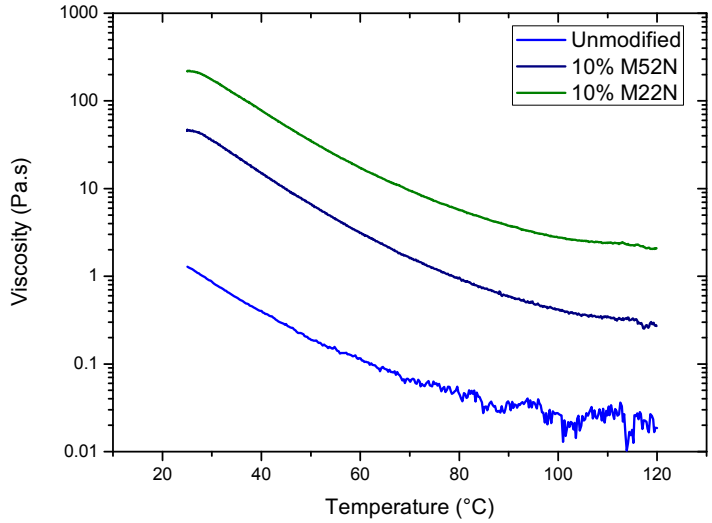
M22N modified epoxies. The viscosities of the modified epoxy resins were measured and are shown in Figure 9.3.9(c). The M22N modified epoxies have higher viscosity and miscibility, implied by the higher PMMA content. From the phase field models, lower mobility and high thermodynamic barriers result in smaller, less developed features as the coarsening rate is lower.



(a) 10 wt% M52N AD



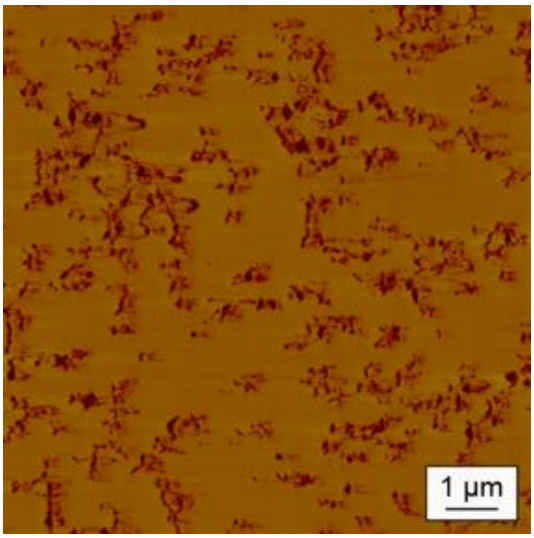
(b) 10 wt% M22N AD



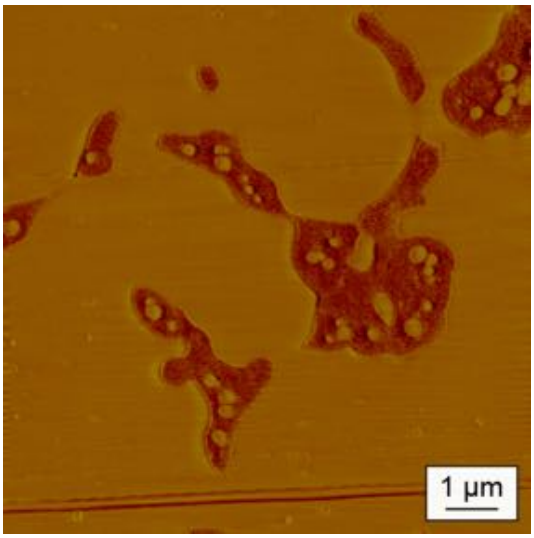
(c) Viscosity profile with temperature

Figure 9.3.9: AFM phase micrographs and change in viscosity with temperature of MAM modified AD epoxy polymers.

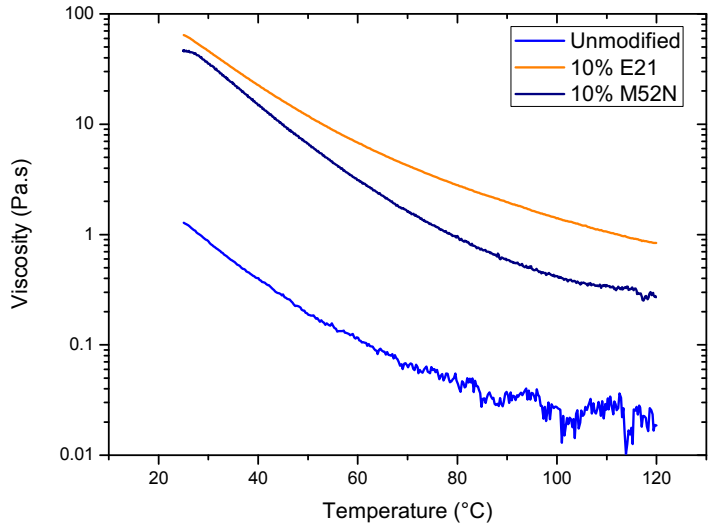
A similar argument can be made when comparing the morphologies of the E21 SBM and M52N MAM modified epoxies, as shown in Figure 9.3.10. At the same BCP content of 10 wt%, the M52N MAM phases are clearly larger; with characteristic lengths of 0.8 μm and 2.5 μm for the E21 and M52N modified LD epoxies, respectively. The difference in viscosity is more pronounced at higher temperature, which helps the M52N reach the steady state at a faster rate. However, the exact details of the difference in miscibility are not known.



(a) 10 wt% E21 LD



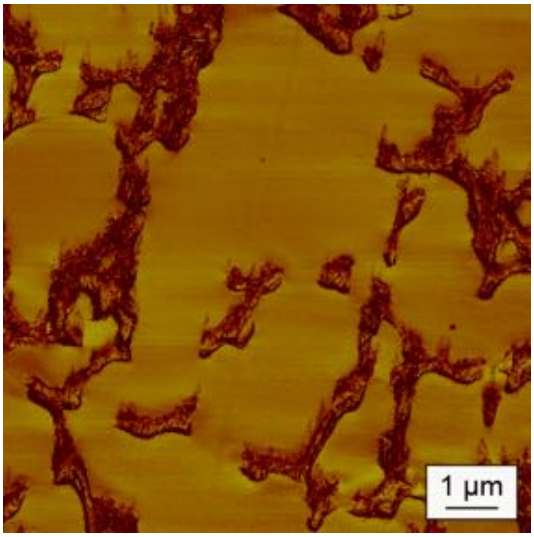
(b) 10 wt% M52N LD



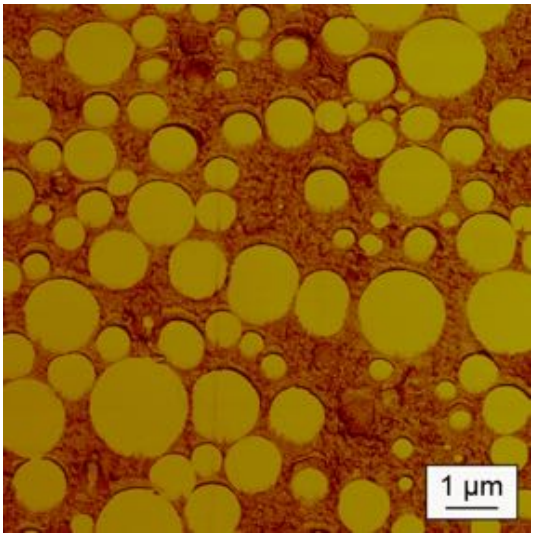
(c) Viscosity profile with temperature

Figure 9.3.10: AFM phase micrographs and change in viscosity with temperature of BCP modified LD epoxy polymers.

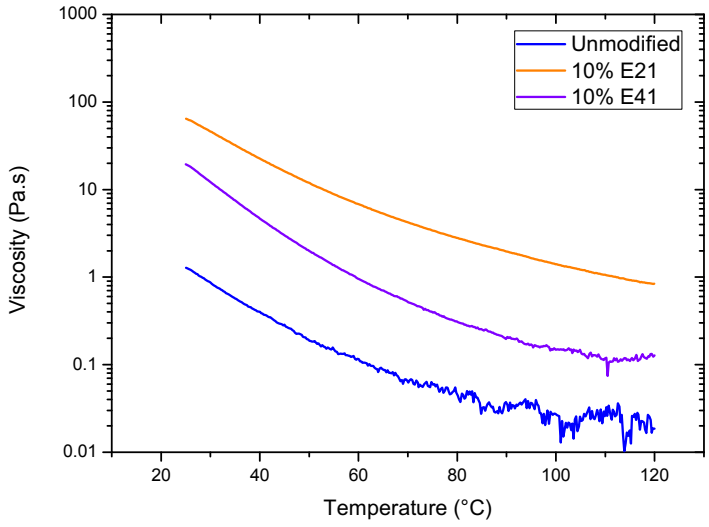
Figure 9.3.11 compares the morphology of the E21 and E41 SBM modified epoxies. The E41 SBM can be thought of as being more miscible in the epoxy; a higher PMMA content can be inferred from the lower PB content. The lower thermodynamic barrier and the lower viscosity, see Figure 9.3.11(c), allow the coarsening process to proceed at a faster rate for the M52N. Hence the E41 features tend to be larger in size. The phase field model in its present form cannot predict phase inversion, as observed for the 10 wt% E41 modified LH epoxy (see Figure 9.3.11(b)), because it is a stability and hydrodynamics problem. The fluid properties such as the viscosity was considered, however the density and interfacial tension also need to be considered.



(a) 10 wt% E21 LH



(b) 10 wt% E41 LH

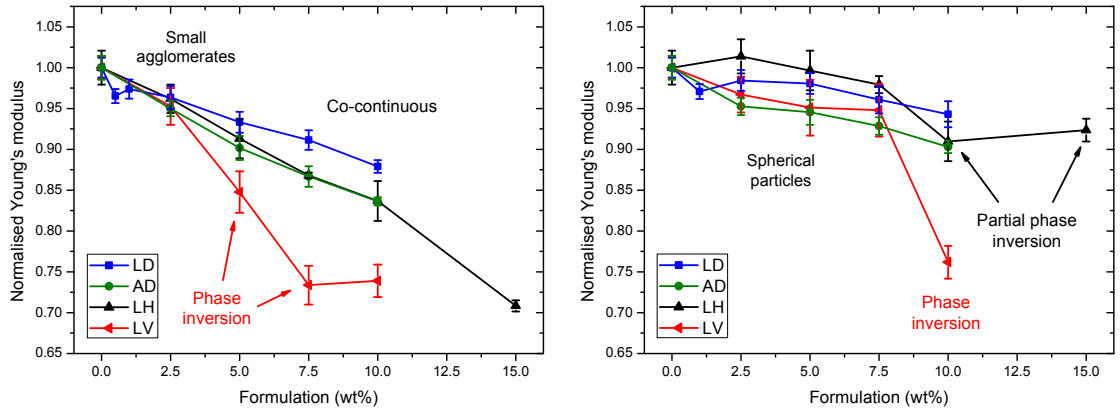


(c) Viscosity profile with temperature

Figure 9.3.11: AFM phase micrographs and change in viscosity with temperature of SBM modified LH epoxy polymers.

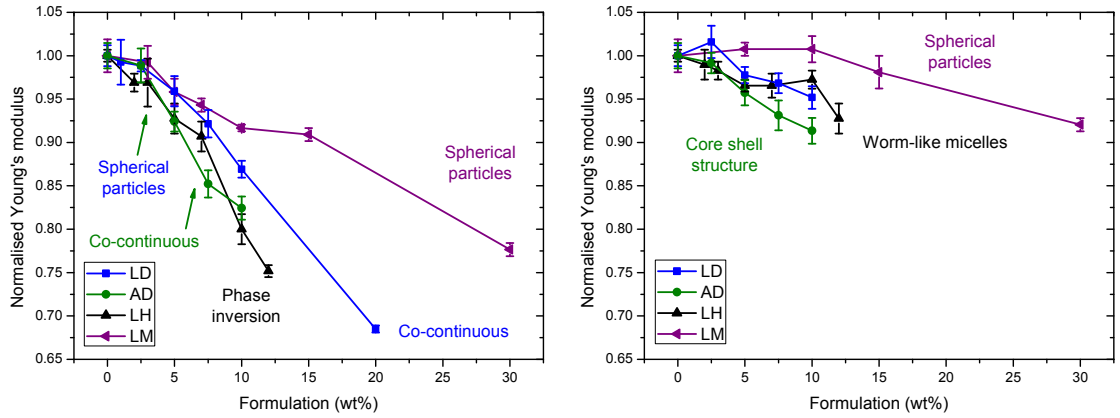
9.3.3 Tensile properties

The normalised tensile Young's moduli of the BCP modified epoxies for the different epoxy systems are shown in Figures 9.3.12 and 9.3.13, for the SBM and MAM modified epoxies respectively. The tensile moduli of the E21 SBM, M52N MAM and M22N MAM BCPs were measured as 0.30, 0.48 and 0.49 GPa, respectively, from tensile tests. For comparison, the tensile modulus of CTBN rubber is approximately 2 MPa [217].



(a) E21 SBM (b) E41 SBM

Figure 9.3.12: Normalised Young's moduli of different epoxy systems for SBM modified epoxies.



(a) M52N MAM (b) M22N MAM

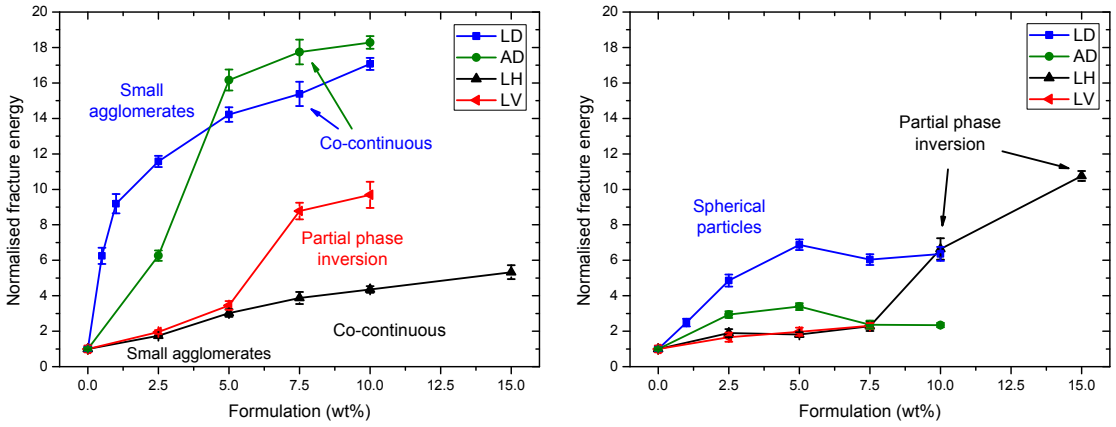
Figure 9.3.13: Normalised Young's moduli for different epoxy systems for MAM modified epoxies. Includes data from [180].

For both the SBM and MAM modified epoxies, the Young's moduli decrease with BCP content. There were no significant changes in the trend when the morphology changed from spherical particles to a co-continuous microstructure, i.e. the moduli were mainly dependent on the volume fraction. This was also the case for partially phase inverted structures, e.g. the 10 wt% and 15 wt% E41 SBM modified LH epoxy as shown in Figure 9.3.12(b). This illustrates how the load is still able to be carried by the stiffer

phase (epoxy phase) in co-continuous and partially phase inverted microstructures. However, when complete phase inversion occurs (e.g. SBM modified LV epoxy), a sharp decrease in modulus was observed. The much softer, weaker second phase in phase inverted structures carries the load, and thus results in poor tensile properties.

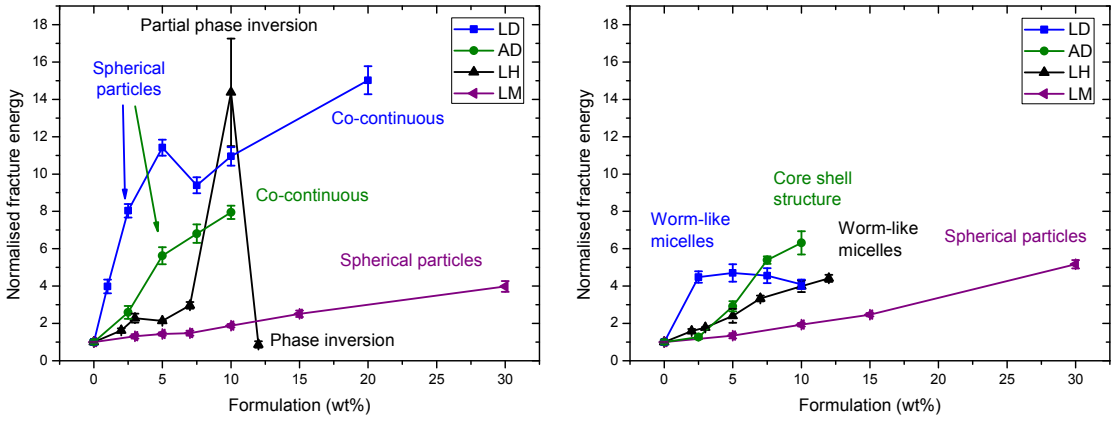
9.3.4 Fracture properties

The normalised fracture energies of the BCP modified epoxies for the different epoxy systems are shown in Figures 9.3.14 and 9.3.15, for the SBM and MAM modified epoxies respectively. The fracture energies increased with BCP content, but at different rates for different BCPs and epoxy systems. The trend of G_{IC} vs wt% is often assumed to be the same for all epoxy systems, provided the same morphology is observed, however this is not the case as will be discussed.



(a) E21 SBM (b) E41 SBM

Figure 9.3.14: Normalised fracture energy of different epoxy systems for SBM modified epoxies.



(a) M52N MAM (b) M22N MAM

Figure 9.3.15: Normalised fracture energy of different epoxy systems for MAM modified epoxies. Includes data from [180].

The fracture energies of the BCP modified epoxies are strongly dependent on the morphology. The change to a partially phase inverted structure results in the largest increase in fracture performance, as seen for the E21 modified LV epoxy, E41 modified LH epoxy and M52N modified LH epoxy. This is because the interconnected nature of the BCP and epoxy phases in such partial phase inverted structures gives a good balance between deformability and strength. The low strength and high ductility of the BCP phase is stabilised by the stronger, more brittle epoxy phase. This is contrasted by complete phase inversion, where the fracture performance decreases dramatically with increasing BCP content, such as that observed for the 12 wt% M52N modified LH epoxy, as shown in Figure 9.3.15(a) [54]. Here, the low strength of the BCP phase dominates the failure process and leads to failure at a much lower stress and hence, low toughness.

When the morphology changes from spherical particles to a co-continuous microstructure, no abrupt changes in the value of G_{IC} was observed. Instead, the change in fracture energy was found to be more linear and gradual with BCP content, consistent with some findings for thermoplastic modified epoxies [35]. However, there is not sufficient evidence to suggest that the increase in fracture energy was solely the result of the change in morphology. The higher toughness could simply be the result of increasing the BCP content. In some cases, such as the 7.5 wt% M52N MAM modified LD epoxy, a decrease in fracture energy was measured. This could be due to the lower surface area of a co-continuous structure compared to spherical particles.

It was also found that the fracture toughness was much less when the second phase remains in the nanoscale and does not macrophase separate, as shown with the E41 SBM (see Figure 9.3.14(b)) and M22N MAM (see Figure 9.3.15(b)) modified epoxies. This could also be the result of a lower "soft" block ratio of the BCPs. Hence, the yield stress is higher and allows less plastic deformation to occur overall.

9.4 Discussion

The modifiers that were investigated in each Chapter were chosen for systematic purposes. The CSR, CTBN and SBM modifiers have polybutadiene "soft" blocks. The MAM BCP gives similar microstructures to the SBM modified epoxies, and has a different "soft" block of poly(butylacrylate). This allows for a better system comparison with controlled variables.

9.4.1 Effect of morphology on properties

The previous section has shown that the tensile modulus of the composite is dominated by the modulus of the modifier. The particle size, morphology of the second phase and epoxy system does not affect the modulus significantly. The only exception would be fully phase inverted structures, which are undesirable as they have poor mechanical properties.

Figure 9.4.1 shows the normalised Young's moduli of the rubber and BCP modified LD epoxies. The tensile modulus of the E21, E41, M52N and M22N BCPs are all higher than that of the CSR and CTBN rubber. Hence the Young's moduli of the BCP modified epoxies were typically higher than those of the rubber modified epoxies. The Young's modulus, E_t, of the modified epoxies were typically in the order: M22N > E41 > M52N > E21 > CSR > CTBN.

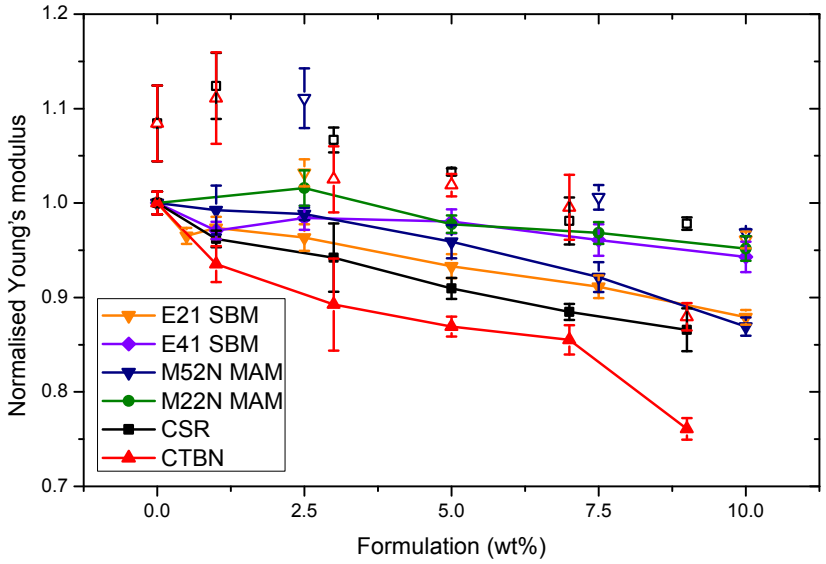


Figure 9.4.1: Normalised Young's moduli of rubber and BCP modified LD epoxies.

The issue of particle/matrix adhesion was not discussed in this section because the phase separating rubbers and BCPs can be assumed to be very well bonded to the epoxy matrix. The CTBN reactive liquid rubber is covalently bonded to the epoxy resin from the pre-reaction to form the adduct [301], and the BCPs form strong hydrogen bonds between the carbonyl groups from the PMMA block and hydroxyl groups in the epoxy resin. The CSR nanoparticles used in this study have PMMA shells which are also chemically compatible with the epoxy resins. Indeed, the fracture surfaces do not show any evidence of complete debonding of the rubber particles or BCP phases.

One of the key advantages of the co-continuous microstructure is better shown in Figure 9.4.2. The change in fracture energy, G_{IC}, with modifier content is shown for each of the modifiers for the LD epoxy system. Where a plateau in fracture energy was observed for the conventional CTBN rubber modified LD epoxy, the change to a co-continuous microstructure in the E21 SBM modified LD epoxy at 7.5 wt% allows the G_{IC} to keep increasing (note that the orange curve has consistently higher values of G_{IC}, while the red curve remains horizontal). The CTBN, CSR and E21 SBM have similar "soft" blocks, namely the polybutadiene rubber. This continuous increase is mainly due to the more gradual onset of plasticity and ability to deform at multiple locations, more than for a conventional distributed spherical particle based structure [302].

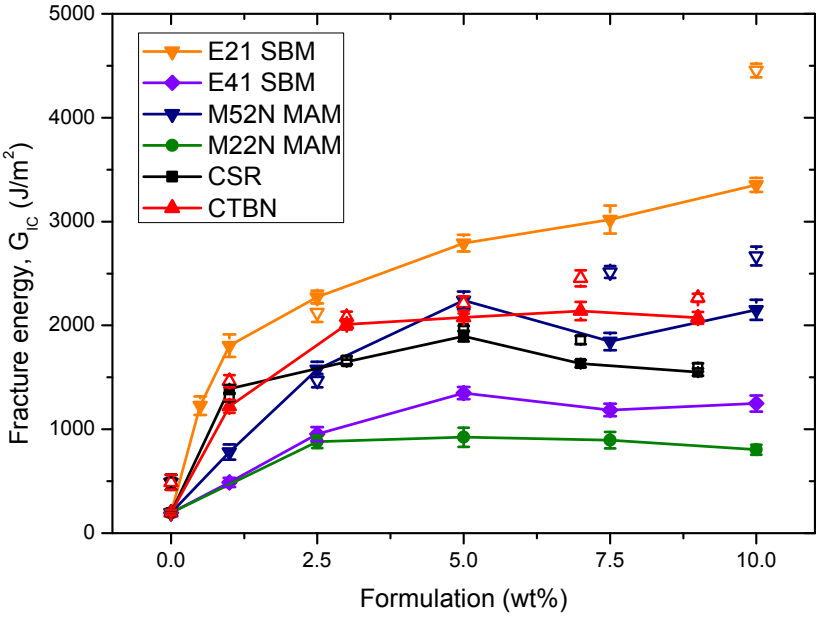


Figure 9.4.2: Comparison of fracture energies of rubber and BCP modified LD epoxies. Solid points (■) are rubber or BCP only and open points (□) are the hybrid formulations.

The M52N MAM modified LD epoxy also has a co-continuous microstructure, but does not exhibit the same level of increase in G_{IC}. One of the reasons could be the different "soft" block material, being poly(butylacrylate), which has a slightly higher modulus than polybutadiene. The M52N MAM phase is also significantly larger than the E21 SBM phase, with characteristic lengths of 2.5 μm and 0.8 μm being measured respectively. This limits the number of locations that initiate plastic deformation, hence reducing the fracture performance. Indeed, it was observed from the fracture surfaces that the deformation was limited to the MAM phase rather than the epoxy. The low strength of the MAM phase means that it would fail before much energy was absorbed by the void growth process. For the LD epoxy system, the fracture energy

of the modified epoxies is in the order: E21 > M52N = CTBN > CSR > E41 > M22N.

From Figure 9.4.3, the AD epoxy system also shows similar trends when comparing the E21 SBM to the CTBN and CSR modified epoxies. At the higher weight percentages, the values of G_{IC} of the E21 and CTBN modified epoxies begin to converge. This can be explained by the very high compressive strain to failure of the AD epoxy system, which was measured to be 1.16. This value is the von Mises equivalent strain, so it can be greater than 1 [263]. This high strain to failure allows more material around the second phase to deform before failure occurs. Hence the G_{IC} of the AD epoxy can continually increase with CTBN rubber content, up to a higher plateau than for the LD epoxy. Indeed, a much higher mean void radius was measured for the CTBN modified AD epoxy than the LD epoxy, where the strain to failure is 0.84.

This plateau in G_{IC} can be seen as the maximum fracture energy possible for the AD epoxy as the addition of silica nanoparticles or E21 SBM does not increase the G_{IC} beyond the plateau. However, it should also be noted that the addition of 10 wt% of silica nanoparticles to the lower concentrations of E21 SBM or CTBN enables the plateau to be reached at lower rubber or BCP contents, e.g. 10N2.5E21 or 10N7R.

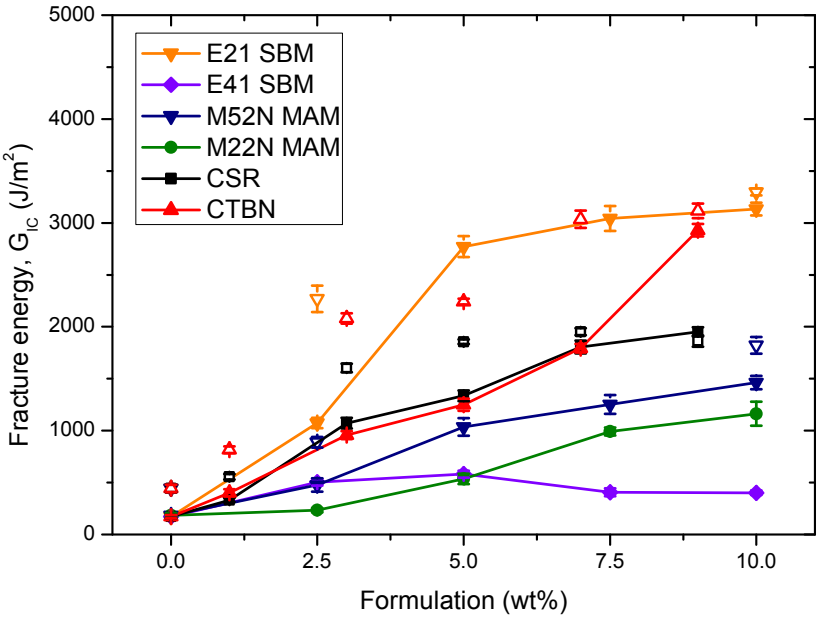


Figure 9.4.3: Comparison of fracture energies of rubber and BCP modified AD epoxies. Solid points (■) are rubber or BCP only and open points (□) are the hybrid formulations.

With the LH epoxy system, as shown in Figure 9.4.4, the E21 SBM was not as effective a toughening agent as the CTBN rubber or CSR particles. Although significant void growth was observed around the co-continuous E21 SBM phases, the relatively large characteristic lengths of the SBM phase may have limited the total surface area available for debonding per unit volume. The mean radius of the CTBN rubber particles was 0.35 μm, whereas the characteristic lengths of the E21 phase were approximately 1.9 μm at 10 wt%. The deformability of higher T_g epoxies such as this is also lower, as the measured values of σ_{yc} were higher. This means that the co-continuous microstructures cannot fully exploit the difference in onset of plasticity as with the lower T_g epoxies (LD and AD epoxies). The partially phase inverted microstructures show much more significant increases in G_{IC} by stabilising the deformations with large sections of the softer second phase, effectively blunting the crack tip.

Furthermore, for the case of the 10N10E21 modified LH epoxy (see orange open triangle in Figure 9.4.4), the silica nanoparticles are dispersed only in the epoxy phase, hence it does not strengthen the SBM phase. The load in the phase inverted structure is carried by the weaker SBM phase as it is the continuous phase, thus the material has low strength, modulus and toughness.

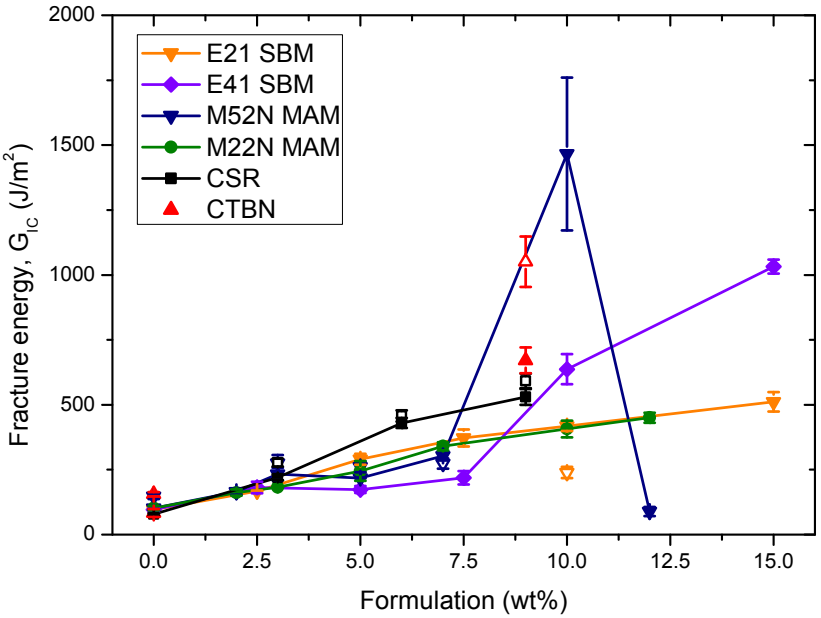


Figure 9.4.4: Comparison of fracture energies of rubber and BCP modified LH epoxies. Solid points (■) are rubber or BCP only and open points (□) are the hybrid formulations.

For the LV epoxy system, as shown in Figure 9.4.5, the E21 SBM modified epoxies have similar values of G_{IC} to the CSR and CTBN modified epoxies, up to 5 wt%. At 7.5 wt% and above of E21, the partially phase inverted structure results in the large increase in fracture energy as described previously. Despite having similar chemistry to the E21 SBM, the E41 SBM was ineffective in toughening the LV epoxy. The low "soft" block content, tensile and compressive strength, and complete phase inversion contribute to the low fracture toughness of the E41 SBM modified LV epoxies.

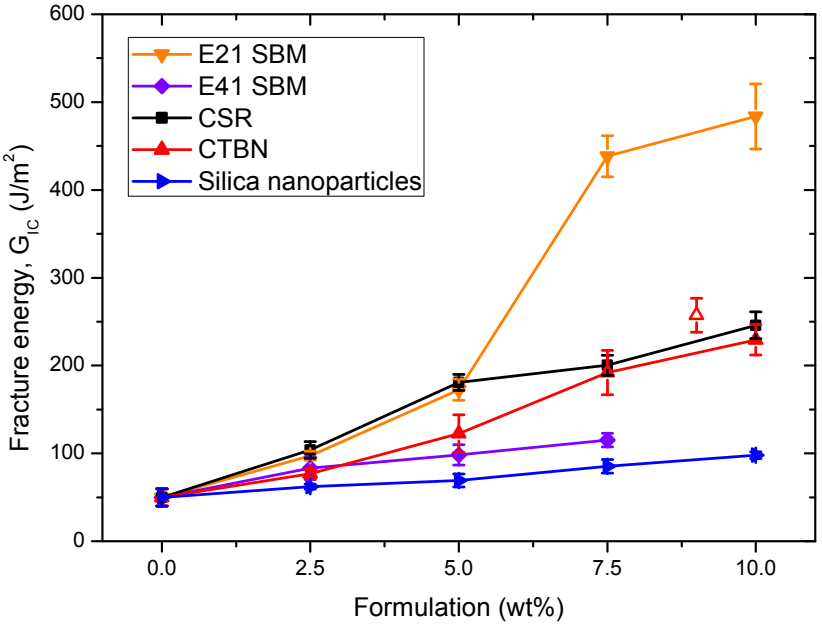


Figure 9.4.5: Comparison of fracture energies of modified LV epoxies. Solid points (■) are rubber only and open points (□) are the hybrid formulations.

The results from the rubber modified epoxies suggest that the fracture performance is strongly correlated with σ_{yc}. However, the results for the BCP modified epoxies clearly show values of σ_{yc} that are higher than the rubber modified epoxies, as shown in Figure 9.4.6, yet the fracture performance is comparable or higher for the E21 and M52N modified epoxies. This stresses the importance of morphology for low T_g, highly toughenable epoxy systems.

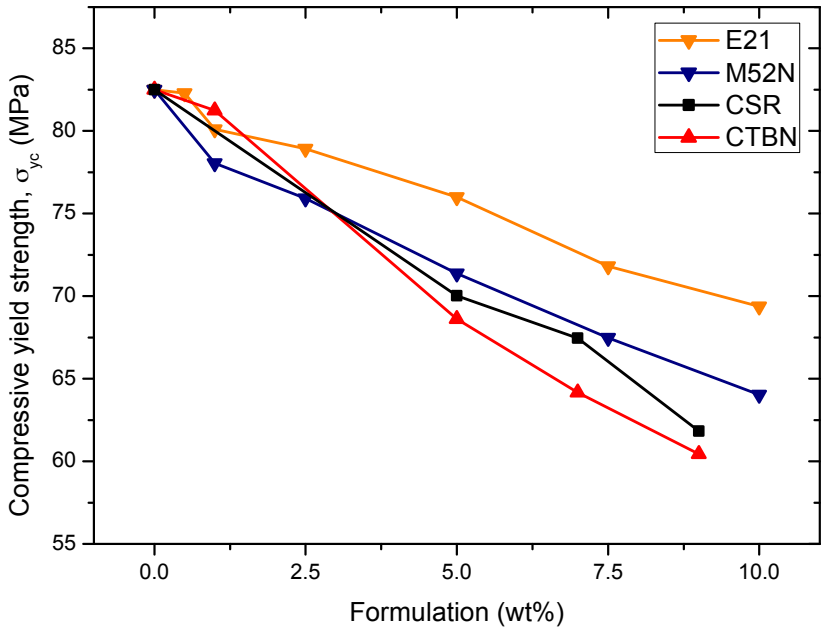


Figure 9.4.6: Change in compressive yield strength with modifier content for LD epoxy system.

9.4.2 Modifier composition

From the results presented, some general comments can be made about the BCP composition. Changing the "soft" block material from PB to PBuA also has a negative impact on the maximum fracture performance (see E21 SBM vs M52N MAM). From these results, it is observed that higher concentration and lower modulus of the "soft" block tends to give higher fracture performance. This could be used in future to fine-tune the block ratios and block materials to improve fracture performance.

With regards to the block copolymer modified epoxies, these materials provide a platform for high fracture toughness epoxy polymers, with minimal negative impact on the other properties, through the creation of a complex 3D nanostructure. The higher G_{IC} values in low T_g epoxies are understood to have come from more extensive plastic deformation from debonding, plastic void growth and shear banding. Put simply, it is an evolutionary step at higher fracture toughness materials, compared to conventional spherical particle modification, which further translates into the use in lightweight applications. Table 9.4.1 shows the glass transition temperature, Young's modulus and fracture energies for the rubber and BCP modified LD epoxies. The E21 SBM modified epoxy shows increased values of G_{IC} with little impact on the T_g and E_t. Adding 10 wt% of silica nanoparticles increases the G_{IC} to an even higher value of 4.5 kJ/m^2.

Table 9.4.1: Summary of glass transition temperature, Young's modulus and fracture energy for LD epoxy. Hybrid materials refer to the further addition of 10 wt% silica nanoparticles.

Modifier	**Soft block**		**wt%**	$\mathbf{T_g}$ **(°C)**	$\boldsymbol{E_t}$ **(GPa)**	$\boldsymbol{G_{IC}}$ **(kJ/m²)**
	Material	**Content**				
Unmodified	–	–	0	96	3.0	0.2
CSR	PB	High	9	94	2.6	1.6
CSR-NS hybrid	PB	High	9	95	2.9	1.6
CTBN	PB	High	9	92	2.3	2.1
CTBN-NS hybrid	PB	High	9	92	2.6	2.3
E21 SBM	PB	High	10	96	2.6	3.4
E21 SBM-NS hybrid	PB	High	10	89	2.9	4.5
E41 SBM	PB	Low	10	96	2.8	1.2
M52N MAM	PBuA	High	10	95	2.6	2.2
M52N MAM-NS hybrid	PBuA	High	10	95	2.9	2.7
M22N MAM	PBuA	Low	10	96	2.8	0.8

9.4.3 Addition of silica nanoparticles

The addition of silica nanoparticles to the rubber and BCP modified epoxies was to recover the loss in Young's modulus, and also to examine if there were synergistic effects in these hybrid modified materials. This inherently adds complexity to the composite material, thus only the addition of 10 wt% of silica nanoparticles were investigated. There are other various factors to consider for these hybrid modified materials, such as interaction between the different modifiers, phase separation behaviour, weight percentage and the curing process.

There is clear evidence that the silica nanoparticles accelerate the curing process of the resin, as measured from the rheology experiments (see Figure 5.2.8). It also causes the M22N MAM mixture to gel without adding the curing agent. There is a reduction in volume fraction measured from the AFM micrographs for the E21-NS and M52N-NS hybrid modified epoxies, which suggests that more BCP remains dissolved in the epoxy. This could be a result of a decrease in gel time and/or effect from increased viscosity. Regardless, the silica nanoparticles are affecting the morphology of the composite.

For the CSR and CTBN rubber modified epoxies, the value of G_{IC} was found to either increase or remain constant from the addition of the NS particles. The plane strain compression tests show an increase or no change in σ_{yc} when the nanoparticles were added, which suggests strong particle/matrix adhesion. The strong adhesion also results in higher strain hardening modulus, which can increase plastic zone size, and hence the fracture toughness, by stabilising the strain localisation. However, there were

cases for the BCP modified epoxies where the value of G_{IC} would decrease due to a significant change in morphology (see change from 10E21 to 10N10E21 modified LH epoxy). This is important as it implies that the further addition of silica nanoparticles or other such modifiers should not be simply accounted for as additive towards the fracture energy. The addition of a small amount of silica nanoparticles can have enough of an effect on the resin such that phase inversion can occur.

There is a reduction in ε_{yc} when silica nanoparticles are added to 10 wt% E21 and M52N modified LD epoxies. This indicates an earlier onset of plastic deformation brought on by the presence of the silica nanoparticles, through localised shear yielding, initiated by partial debonding of the co-continuous phase. The fracture surfaces do not show any debonding of the nanoparticles. This translates into an increase in G_{IC} for those materials, i.e. synergy. The AD epoxy has a higher yield stress, thus shows less plastic deformation and the ε_{yc} does not change. Consequently, the 10N10E21 and 10N10M52N modified AD epoxies do not show any synergy between the BCP and silica nanoparticles.

The results suggest that co-continuous microstructures are more effective in increasing G_{IC} than spherical particles in hybrid modified epoxies, when silica nanoparticles are added. Such co-continuous microstructures have lower specific surface area than spheres, thus can have more potential in improving by adding more particles within the phases. The tensile tests show a decrease in σ_t when silica nanoparticles were added to E21 modified epoxies, indicating that the nanoparticles were enhancing cavitation or damage mechanisms of the E21 structures. In contrast, the CSR, CTBN and M52N MAM modified epoxies show little or no increase in σ_t. These were also the modifiers which show little synergy with the silica nanoparticles.

9.5 Graphene nanoplatelets

Within the area of graphene filled composites, there are several methods to produce these materials, each with its own advantage and disadvantages. As such, there is a large variation in results in the literature regarding the mechanical performance of graphene modified polymers. In this work, the factors that contribute to this discrepancy in mechanical and fracture properties were examined, namely platelet size, aspect ratio, quality, dispersion and surface functionalities.

Each of these factors were found to be important in contributing to the mechanical and fracture performanc. In general, the larger platelet size, and hence aspect ratio, GNPs

give higher values of modulus and G_{IC}. For example, at 2.0 wt%, the XG-C-NMP (lateral size = 0.3 μm) increased the E_t from 2.9 GPa to 3.3 GPa, whereas the XG-H-NMP (lateral size = 3.2 μm) increased the E_t to 3.6 GPa. However, the largest GNPs (XG-M) did not disperse wel and large agglomerates were observed. Large, higher aspect ratio would also tend to wrinkle more. As such, an optimum GNP lateral size of 3 – 4 μm was determined (XG-H and GS). Furthermore, a minimum platelet size was observed to be required for toughening. Similarly, Kinloch and Taylor [99] found that silicates with larger diameters and aspect ratios were most efficient for toughening epoxy polymers.

Interestingly, the fracture energy was of similar values for the GNPs which were well dispersed as stacks of platelets, and for the GNPs that were heavily agglomerated. This was determined to be coincidence that the different toughening mechanisms produce similar toughening contributions.

The results for these GNP modified epoxies will undoubtedly be compared to CNTs and silicate modifiers, as they similar in composition and morphology. The glass transition temperature, Young's modulus and fracture energy of an anhydride cured DGEBA epoxy (LH epoxy) reinforced with various modifiers is shown in Table 9.5.1.

Compared to other rigid modifiers, the 2.0 wt% GS-THF modified epoxy has the highest value of G_{IC} at 0.34 kJ/m^2. However, this is still low compared to the rubber modified epoxies which can have G_{IC} values above 1 kJ/m^2. Clearly, the GNP modified epoxies are still relatively brittle, even at high concentrations. A combination of poor platelet/matrix adhesion and sharp edges of the GNPs (observed as fracture before yielding in the plane strain compression tests) act as high stress concentrations, effectively acting as a sharp crack. The GNPs do not provide any additional contribution by localised shear yielding as a result of this. Strong platelet/matrix from the functionalised GNPs do not appear to alleviate the deficit in G_{IC}, as toughening mechanisms such as debonding and pull-out are inhibited.

A relatively high Young's modulus can also be achieved, as shown by the 2.0 wt% XG-H-NMP modified epoxy (3.6 GPa compared to 2.9 GPa for the unmodified epoxy). This is at much lower concentrations than achievable using silica nanoparticles (3.9 GPa at 20 wt%), showing the advantage of having high aspect ratios. Current research on graphene materials focuses on creating large (millimetre scale), pristine monolayers at high rates [303]. These materials can bring substantial improvements, provided that they can be well dispersed as high aspect ratio platelets, of which studies are also being conducted [146].

Table 9.5.1: Comparison of glass transition temperatures, Young's modulus and fracture energy of various modifiers in the LH epoxy. The epoxy used in [124] is a diethyltoluenediamine cured DGEBA epoxy. L represents lateral size, length or characteristic length as appropriate. Some noteworthy values have been highlighted in bold.

Modifier	**wt%**	**Morphology**	**Size**	$\mathbf{T_g}$ **(°C)**	$\boldsymbol{E_t}$ **(GPa)**	$\boldsymbol{G_{IC}}$ **(kJ/m²)**	**Processing**	**Other**
Unmodified	0	–	–	157	2.9	0.10	–	–
XG-H-NMP	2	Stacked platelets	$L = 3$ μm $t = 30$ nm	142	**3.6**	0.19	Ultrasonication in solvent, followed by removal of solvent	Solvent entrapment reduces mechanical properties
GS-THF	2	Agglomerated platelets	$L = 100$ μm	138	3.2	0.34		
Functionalised GNP	1	Stacked platelets	$L = 2$ μm $t = 27$ nm	151	3.0	0.13	Ultrasonication in epoxy resin	High viscosity, highly dependent on modifier properties, high cost
MWCNT [117]	0.5	Agglomerated nanotubes	$L = 140$ μm $\varnothing = 120$ nm	144[a]	3.3	0.22		
Functionalised MWCNT	0.5		$L = 1$ μm $\varnothing = 28$ nm	150	3.0	0.08		
Nanoclay [124]	2.5	Uniformly dispersed platelets	$L < 3$ μm	210[b]	2.2[c]	0.31	Mechanical mixing of dry powder into liquid resin	High viscosity, solvent required
Silica nanoparticles	20	Well dispersed spherical particles	$\varnothing = 20$ nm	150	**3.9**	0.21	Simplest to process. Available as masterbatch or adduct, which is diluted by adding epoxy resin via mechanical mixing	High viscosity at useful concentrations, Difficult to control particle size and agglomeration
CSR	9		$\varnothing = 100$ nm	146[a]	2.3	0.60		
CTBN	9		$\varnothing = 1$ μm	137[a]	2.4	0.67		
CTBN-NS hybrid	9	Agglomerated	$\varnothing = 0.8$ μm	145	2.8	**0.91**		
E21 SBM	10	Co-continuous	$L = 2$ μm	**157**	2.4	0.42		
E41 SBM	10	Partial phase inversion	–	158	2.6	0.64		
M52N MAM [180]	10		–	**159**	2.2	**1.47**		
M22N MAM [180]	10	Worm-like micelles	$\varnothing = 10$ nm	154	2.7	0.41		

[a] Unmodified $T_g = 145$ °C.
[b] Unmodified $T_g = 211$ °C.
[c] Unmodified $E_t = 1.9$ GPa.

9.6 Conclusions

The morphology, mechanical and fracture performance of rubber, BCP and GNP modified epoxies were reviewed and discussed, including data reproduced from the literature for the relevant materials.

It was found that while the CTBN rubber phase separates into well dispersed spherical particles for all the epoxy systems, the particle size and trend in fracture performance are different for different epoxy systems. The BCP modified epoxies show well dispersed spherical particles, co-continuous microstructures, partial and complete phase inverted structures within the epoxy. The onset of the change in morphology also differs between the epoxy systems. The phase field models show that this is due to the differences in miscibility, viscosity and curing time. The addition of silica nanoparticles were also found to affect the morphology, through changing the interactions between particles, phase separation behaviour and reactivity.

The result of the change in microstructures is a higher plateau in fracture energy for the lower T_g epoxies and high G_{IC} values due to a partially phase inverted structure for the higher T_g epoxy systems. The addition of silica nanoparticles can also provide synergistic increases in the fracture performance to give even higher values of G_{IC}, and also recovers the loss in modulus.

Chapter 10

Conclusions

The work presented in this thesis was primarily to investigate the structure/property relationships and toughening mechanisms of epoxy polymers modified with various novel tougheners. This chapter summarises the main findings and results from this PhD project.

The mechanical and fracture performance of four epoxy polymers modified using core-shell rubber (CSR) particles and two types of block copolymers (BCP) were measured and compared with conventional CTBN rubber modified epoxies. Silica nanoparticles were also added at a concentration of 10 wt% to create hybrid modified epoxies.

- The CTBN rubber, E41 SBM and M52N MAM (at lower concentrations) phase separated into well dispersed spherical particles. The E21 SBM phase separates into a network of small agglomerates. The morphology of the BCP modified epoxies change at higher concentrations:
    - Co-continuous microstructure; E21 SBM in LD, AD and LH epoxy and M52N MAM in LD and AD epoxy
    - Partially phase inverted; E41 SBM in LH epoxy
    - Multi-scale of micron sized spherical particles and network of small agglomerates; E41 SBM in LD and AD epoxy
    - Complete phase inversion; E21 and E41 SBM in LV epoxy
    - Nanoscale core-shell and worm-like micelles; M22N MAM in LD and AD epoxy
- The silica nanoparticles were well around the rubber and BCP phases in the CSR-NS and E21 SBM-NS hybrid modified epoxies, and lower concentrations of

CTBN and MAM.

- At higher weight percentages of CTBN and MAM, the silica nanoparticles were agglomerated in the CTBN-NS and M52N MAM-NS hybrid modified epoxies.
- The CSR and BCP modified epoxies better maintains the thermomechanical properties of the epoxy polymers than the CTBN rubber, due to the higher amount of CTBN rubber that remains dissolved in the epoxy.
- The Young's modulus decreases with rubber and BCP content. Adding silica nanoparticles recovered some of this loss in E_t.
    - The spherical rubber particles reduced the Young's modulus of the epoxies relative to the total amount of rubber in the particles; e.g. the E_t reduced from 3.0 GPa to 2.6 GPa and 2.3 GPa for the 9C and 9R modified LD epoxies. Adding 10 wt% of silica nanoparticles increased the E_t to 2.9 GPa and 2.6 GPa for the 10N9C and 10N9R modified LD epoxies. This is an increase in E_t of 10%, which corresponds well to the Mori-Tanaka model.
    - There were no significant changes in the trend in E_t when the morphology changed from spherical particles to a co-continuous or partially phase inverted microstructure.
    - A sharp decrease in modulus was observed when complete phase inversion occurs. The E_t decreased from 2.9 GPa for the unmodified epoxy to 2.1 GPa for the 10 wt% E21 SBM modified LV epoxy.
    - The E_t of the BCP modified epoxies were typically higher than the CSR and CTBN modified epoxies, as the BCPs have higher modulus than the rubber modifiers.
- The fracture energy, G_{IC}, of the modified epoxy polymers is more highly dependent on the morphology and composition of the modifier.
    - For the lower T_g epoxies (LD and AD epoxies), the E21 SBM modified epoxies show the highest values of G_{IC} at 3.4 kJ/m^2. The spherical particle modified epoxies show a plateau in G_{IC} as the extent of plastic deformation reaches a maximum, whereas the co-continuous microstructure can achieve higher values of G_{IC} by more gradual and extensive plastic deformation.
    - Further addition of 10 wt% of silica nanoparticles to the 10 wt% E21 SBM modified LD epoxy (10N10E21LD) increases the G_{IC} to 4.5 kJ/m^2.

    - The M52N MAM modified epoxies, which also have a co-continuous microstructure, is less effective due to the higher "soft" block modulus, lower "soft" block content and higher characteristic length.
    - The higher T_g epoxies (LH and LV epoxies) have higher yield stress, and hence is unable to fully exploit the co-continuous microstructure.
    - The partially phase inverted microstructures show significant increases in G_{IC} by stabilising the deformations with large sections of the softer second phase, effectively blunting the crack tip.
    - This is contrasted with completely phase inverted microstructures, which have very low values of G_{IC}. This is because the load is carried by the weaker and softer BCP phase, failure occurs due to the instability of the second phase.
- The main toughening mechanisms observed were localised shear band yielding and plastic void growth, initiated by cavitation or debonding of the rubber and BCP phases, of the epoxy matrix.

An anhydride cured DGEBA epoxy was modified using graphene nanoplatelets (GNP) of varying sizes, aspect ratio, quality, dispersion and surface functionalities. The mechanical and fracture properties were measured and compared to those of CNTs and graphite flakes.

- The properties of the bulk GNPs were characterised using XRD, XPS, laser light spectroscopy and high resolution SEM. The GNP platelet size ranges from 0.3 μm (XG-C) to 21.7 μm (XG-M).
- The use of different solvents results in different GNP dispersion using ultrasonication.
    - Dispersing the GNPs in tetrahydrofuran (THF) first results in large agglomerates of 50 – 100 μm in size.
    - The GNPs dispersed in n-methyl-pyrrolidone (NMP) by ultrasonication were more evenly dispersed as stacked platelets.
    - The solvents do not significantly affect the mechanical properties, provided they are removed fully from the resin. The solvents can significantly reduce the T_g of the epoxies.
- The Young's moduli of the GNP modified epoxies is strongly dependent on the quality of dispersion and platelet sizes.

  - An optimum platelet size and good dispersion was observed to provide the highest increase in E_t; the 1.0 wt% GS-NMP increased the E_t from 2.9 GPa to 3.6 GPa.
  - The largest GNP (XG-M) is more difficult to disperse and has a higher tendency to wrinkle.
  - The functionalised GNPs (GNP-COOH and GNP-O2) were well dispersed and bonded to the epoxy, however, damage caused by the ultrasonication process limited the tensile and fracture properties of the epoxies modified with these GNPs.

- The values of G_{IC} for the GNPs dispersed in THF and NMP were of similar magnitude. A maximum G_{IC} value was measured to be 0.34 kJ/m^2 for the 2.0 wt% GS-THF modified epoxy.
  - For the GNPs dispersed in THF, crack deflection around the large agglomerates was observed as the main toughening mechanism.
  - The GNPs dispersed in NMP were better dispersed and show debonding, pull-out and plastic void growth.

Chapter 11

Future Work

The research that has been presented in this PhD thesis has aimed to be novel and complete in the field of toughening epoxy polymers. However, there are still areas that could be studied further, as well as other areas of research that have emerged during the course of this PhD. This chapter outlines some recommendations for future work that would be interesting, based on the findings from the current work.

11.1 Rubber particles

The dispersion of the silica nanoparticles were found to be dependent on both the rubber and silica content. It would be interesting to model the flow behaviour of these modifiers by extension of the phase field model presented in §2.2.2.5. This would require knowledge of how the particles behave in each phase at a local level. It would perhaps be beneficial to start with larger rigid particles, as these are easier to observe experimentally than these silica nanoparticles. Glass microparticles are readily available and would be inert with regards to curing reactions and inter-phase behaviour.

In the current work, the core-shell rubber particle sizes were obtained from the manufacturer's data. While it agrees well with the particle sizes measured from AFM phase micrographs, this only provides a mean value for the particle radius. It would be useful for further analysis or future work to obtain the size distribution using an X-ray scattering or laser diffraction method.

11.2 Block copolymer

Two types of triblock copolymers, with two different block ratios and molecular weights, were used in the current study of block copolymer modified epoxies. As explained in §2.2.2.3, there exists a large number of combinations of different homopolymers that can be synthesised into well behaved block copolymers. Having a larger range of precise block ratios and copolymer species would give the ability to control the resultant morphology, as predicted using the Cahn-Hilliard model or self-consistent field theories. Diblock copolymers can also play a role in generating alternative morphologies to triblock copolymer modified epoxies.

Following on from the morphology predictions using the Cahn-Hilliard model, it would be advantageous to validate the models with an experimentally obtained 3D model. One of the ways to achieve this is by X-ray microtomography, similar to a CT scan. The highest resolution attainable from conventional, laboratory based systems reach a limit of 50 nm. This means that the co-continuous features would likely span just 1 voxel at its thinnest. However, this method requires sufficient contrast between the phases, which may be significant and staining methods may not penetrate deep enough. An alternative to X-ray microtomography is to use a dual beam FIB-SEM. The focused ion beam (FIB) can mill sections of material at nanometre resolution. This way, sections can be milled with the FIB and subsequently imaged with the SEM within the same machine. The images can then be built up to form a 3D reconstruction.

An increasing trend in fracture energy with BCP content was observed up to the maximum weight percentage used in the current study, for example the 20 wt% M52N MAM modified LD epoxy. This maximum wt% is limited by the large increases in viscosities. Higher BCP contents lead to a gel-like material which proves to be impossible to mechanically mix with the curing agent and degas to produce bulk material of sufficient quality. This can be circumvented by using alternative methods of mixing, such as with a centrifugal mixer which does not entrap air bubbles in the mixture. This would allow the use of higher BCP contents, and to further establish whether the fracture energy continues to increase due to the observed co-continuous structure.

The glass transition temperature of the SBM BCP modifier was measured to be approximately -90°C. This has advantages in low temperature performance, as the soft block remains rubbery at lower temperatures than conventional CTBN rubber modified epoxies. The demand for strong low temperature performance is increasing with applications in aerospace and liquified gas processing. Thus, it would be of interest to investigate the fracture performance of the BCP modified epoxies under cryogenic

temperatures.

In the present study, only quasi-static conditions were considered. The high rate fracture performance of modified epoxies with co-continuous morphologies are yet to be investigated and could prove to be interesting.

11.3 Graphene nanoplatelets

It was noted in §8.2 that an ultrasonic probe was used to disperse the GNPs. However, a three roll mill may be preferred if larger quantities of material were being produced. Therefore it may be compelling for future work to investigate the dispersion of the GNPs in an epoxy resin, and compare it to that from an ultrasonic probe.

It was found in the current study that the adhesion between the GNPs and anhydride cured DGEBA epoxy was poor. This reduced the tensile strength and modulus of the GNP modified epoxies. Given that the GNPs have trace amounts of acidic groups, it may be more beneficial to use amine based curing agents which can react with these functional groups. Alternatively, the platelet/matrix adhesion can be improved by chemical modification using coupling agents, such as silanes.

Plastic void growth was identified as one of the major toughening mechanisms of the modified epoxies. Thus, it would be interesting to investigate if the void growth mechanism can be enhanced by reducing the platelet/matrix adhesion. This would work by providing more sites to debond and hence initiate void growth. This effect can be achieved by applying release agents on the bulk GNPs before they are incorporated into the epoxy resin.

The use of graphene based materials has shown that electrical percolation can be achieved at very low loadings due to the high aspect ratio [304]. From the BCP modified epoxies, co-continuous microstructures can be achieved at relatively low loadings. When silica nanoparticles were added to the BCP modified epoxies, they were found to be dispersed entirely in the epoxy-rich phase. Hence one would expect if GNPs were added to the BCP modified epoxies, the GNPs would only be dispersed in the epoxy-rich phase as well. This could potentially have applications in further reducing the electrical percolation threshold.

References

[1] J. Glazer. Monolayer studies of some ethoxylin resin adhesives and related compounds. *Journal of Polymer Science*, 13(70):355–369, 1954.

[2] A. J. Kinloch. *Adhesion and Adhesives: Science and Technology*. Chapman & Hall, London, 1987.

[3] J. N. Sultan and F. J. McGarry. Effect of rubber particle size on deformation mechanisms in glassy epoxy. *Polymer Engineering & Science*, 13(1):29–34, 1973.

[4] A. J. Kinloch. Toughening epoxy adhesives to meet today's challenges. *MRS Bulletin*, 28(6):445–448, 2003.

[5] T. H. Hsieh, A. J. Kinloch, K. Masania, A. C. Taylor, and S. Sprenger. The mechanisms and mechanics of the toughening of epoxy polymers modified with silica nanoparticles. *Polymer*, 51(26):6284–6294, 2010.

[6] J. M. Dean, N. Verghese, H. Q. Pham, and F. S. Bates. Nanostructure toughened epoxy resins. *Macromolecules*, 36(25):9267–9270, 2003.

[7] A. J. Kinloch and R. J. Young. *Fracture behaviour of polymers*. London: Applied Science Publishers, 1983.

[8] Y. Chen and R. A. Pearson. Epoxies toughened with self-assembling block copolymers. *36th Annual Meeting of the Adhesion Society, 3-6 March 2013, Daytona Beach, USA*, 2013.

[9] M. Murali, D. Ratna, A. B. Samui, and B. C. Chakraborty. Synthesis, characterization, and evaluation of carboxyl-terminated poly(ethylene glycol) adipate-modified epoxy networks: Effect of molecular weight. *Journal of Applied Polymer Science*, 103(3):1723–1730, 2007.

[10] J. V. Aleman, A. V. Chadwick, J. He, M. Hess, K. Horie, R. G. Jones, P. Kratochvil, I. Meisel, I. Mita, G. Moad, S. Penczek, and R. F. T. Stepto. Definitions of terms relating to the structure and processing of sols, gels, networks, and inorganic-organic hybrid materials (IUPAC Recommendations 2007). 79(10): 1801–1829, 2007.

[11] M.-S. Lin, C.-C. Liu, and C.-T. Lee. Toughened interpenetrating polymer network materials based on unsaturated polyester and epoxy. *Journal of Applied Polymer Science*, 72(4):585–592, 1999.

[12] K. Dinakaran and M. Alagar. Preparation and characterization of epoxy-cyanate ester interpenetrating network matrices/organoclay nanocomposites. *Polymers for Advanced Technologies*, 14(8):574–585, 2003.

[13] Z. G. Shaker, R. M. Browne, H. A. Stretz, P. E. Cassidy, and M. T. Blanda. Epoxy-toughened, unsaturated polyester interpenetrating networks. *Journal of Applied Polymer Science*, 84(12):2283–2286, 2002.

[14] A. B. Cherian, L. A. Varghese, and E. T. Thachil. Epoxy-modified, unsaturated polyester hybrid networks. *European Polymer Journal*, 43(4):1460–1469, 2007.

[15] L. H. Sperling. *Interpenetrating Polymer Networks: An Overview*, volume 239 of *Advances in Chemistry*, chapter 1, pages 3–38. American Chemical Society, 1994.

[16] R. Bagheri, B. T. Marouf, and R. A. Pearson. Rubber-toughened epoxies: A critical review. *Polymer Reviews*, 49(3):201–225, 2009.

[17] D. Ratna and A. K. Banthia. Rubber toughened epoxy. *Macromolecular Research*, 12(1):11–21, 2004.

[18] J. W. Aylsworth. *Plastic composition.* US1111284 (Patent), 1914.

[19] A. J. Kinloch, R. D. Mohammed, A. C. Taylor, C. Eger, S. Sprenger, and D. Egan. The effect of silica nano particles and rubber particles on the toughness of multiphase thermosetting epoxy polymers. *Journal of Materials Science*, 40(18): 5083–5086, 2005.

[20] G. Giannakopoulos, K. Masania, and A. C. Taylor. Toughening of epoxy using coreshell particles. *Journal of Materials Science*, 46(2):327–338, 2011.

[21] R. Bagheri and R. A. Pearson. Role of particle cavitation in rubber-toughened epoxies: 1. microvoid toughening. *Polymer*, 37(20):4529–4538, 1996.

[22] R. A. Pearson and A. F. Yee. Toughening mechanisms in elastomer-modified epoxies. *Journal of Materials Science*, 24(7):2571–2580, 1989.

[23] A. J. Kinloch, S. J. Shaw, D. A. Tod, and D. L. Hunston. Deformation and fracture behaviour of a rubber-toughened epoxy: 1. Microstructure and fracture studies. *Polymer*, 24(10):1341–1354, 1983.

[24] S. C. Kunz and P. W. R. Beaumont. Low-temperature behaviour of epoxy-rubber particulate composites. *Journal of Materials Science*, 16(11):3141–3152, 1981.

[25] R. Mülhaupt and U. Buchholz. Compatibilized, segmented liquid rubbers as epoxy-toughening agents. In *Toughened Plastics II*, volume 252 of *Advances in Chemistry*, chapter 6, pages 75–94. American Chemical Society, 1996.

[26] A. F. Yee and R. A. Pearson. Toughening mechanisms in elastomer-modified epoxies. *Journal of Materials Science*, 21(7):2462–2474, 1986.

[27] A. J. Kinloch, S. J. Shaw, and D. L. Hunston. Deformation and fracture behaviour of a rubber-toughened epoxy: 2. Failure criteria. *Polymer*, 24(10):1355–1363, 1983.

[28] J. Chen, A. J. Kinloch, S. Sprenger, and A. C. Taylor. The mechanical properties and toughening mechanisms of an epoxy polymer modified with polysiloxane-based core-shell particles. *Polymer*, 54(16):4276–4289, 2013.

[29] G. Levita, S. De Petris, A. Marchetti, and A. Lazzeri. Crosslink density and fracture toughness of epoxy resins. *Journal of Materials Science*, 26(9):2348–2352, 1991.

[30] C. B. Bucknall and I. K. Partridge. Phase separation in epoxy resins containing polyethersulphone. *Polymer*, 24(5):639–644, 1983.

[31] B. B. Johnsen, A. J. Kinloch, and A. C. Taylor. Toughness of syndiotactic polystyrene/epoxy polymer blends: microstructure and toughening mechanisms. *Polymer*, 46(18):7352–7369, 2005.

[32] B. J. Cardwell and A. F. Yee. Toughening of epoxies through thermoplastic crack bridging. *Journal of Materials Science*, 33(22):5473–5484, 1998.

[33] B. Francis, S. Thomas, S. P. Thomas, R. Ramaswamy, and V. R. Lakshmana. Diglycidyl ether of bisphenol-A epoxy resin-polyether sulfone/polyether sulfone ether ketone blends: phase morphology, fracture toughness and thermomechanical properties. *Colloid and Polymer Science*, 285(1):83–93, 2006.

[34] B. Francis, S. Thomas, J. Jose, R. Ramaswamy, and V. R. Lakshmana. Hydroxyl terminated poly(ether ether ketone) with pendent methyl group toughened epoxy resin: miscibility, morphology and mechanical properties. *Polymer*, 46(26):12372–12385, 2005.

[35] A. J. Kinloch, M. L. Yuen, and S. D. Jenkins. Thermoplastic-toughened epoxy polymers. *Journal of Materials Science*, 29(14):3781–3790, 1994.

[36] K. Mimura, H. Ito, and H. Fujioka. Improvement of thermal and mechanical properties by control of morphologies in pes-modified epoxy resins. *Polymer*, 41 (12):4451–4459, 2000.

[37] R. S. Raghava. Development and characterization of thermosetting-thermoplastic polymer blends for applications in damage-tolerant composites. *Journal of Polymer Science Part B: Polymer Physics*, 26(1):65–81, 1988.

[38] R. A. Pearson. Toughening epoxies using rigid thermoplastic particles. In *Toughened Plastics I*, volume 233 of *Advances in Chemistry*, chapter 17, pages 405–425. American Chemical Society, 1993.

[39] J. H. Hodgkin, G. P. Simon, and R. J. Varley. Thermoplastic toughening of epoxy resins: a critical review. *Polymers for Advanced Technologies*, 9(1):3–10, 1998.

[40] A. D. Jenkins, P. Kratochvil, R. F. T. Stepto, and U. W. Suter. Glossary of basic terms in polymer science (IUPAC Recommendations 1996). *Pure and Applied Chemistry*, 68(12):2287–2311, 1996.

[41] R. Nagarajan. Molecular packing parameter and surfactant self-assembly: The neglected role of the surfactant tail. *Langmuir*, 18(1):31–38, 2002.

[42] J. N. Israelachvili, D. J. Mitchell, and B. W. Ninham. Theory of self-assembly of hydrocarbon amphiphiles into micelles and bilayers. *Journal of the Chemical Society, Faraday Transactions 2: Molecular and Chemical Physics*, 72:1525–1568, 1976.

[43] M. R. Villarreal. Phospholipids aqueous solution structures. [Online]. *Available from: http://commons.wikimedia.org/wiki/File:Phospholipids_aqueous_solution_structures.svg*, 2007. [Accessed 6th March 2014].

[44] M. A. Hillmyer, P. M. Lipic, D. A. Hajduk, K. Almdal, and F. S. Bates. Self-assembly and polymerization of epoxy resin-amphiphilic block copolymer nanocomposites. *Journal of American Chemical Society*, 119:2749–2750, 1997.

[45] R. B. Grubbs, J. M. Dean, M. E. Broz, and F. S. Bates. Reactive block copolymers for modification of thermosetting epoxy. *Macromolecules*, 33(26):9522–9534, 2000.

[46] S. Ritzenthaler, F. Court, E. Girard-Reydet, L. Leibler, and J.-P. Pascault. Abc triblock copolymers-epoxy-diamine blends. 2. parameters controlling the morphologies and properties. *Macromolecules*, 36(1):118–126, 2003.

[47] J. Liu, Z. J. Thompson, H.-J. Sue, F. S. Bates, M. A. Hillmyer, M. Dettloff, G. Jacob, N. Verghese, and H. Pham. Toughening of epoxies with block copolymer micelles of wormlike morphology. *Macromolecules*, 43(17):7238–7243, 2010.

[48] S. M. George, D. Puglia, J. M. Kenny, J. Parameswaranpillai, and S. Thomas. Reaction-induced phase separation and thermomechanical properties in epoxidized styrene-block-butadiene-block-styrene triblock copolymer modified epoxy/ddm system. *Industrial & Engineering Chemistry Research*, 53(17):6941–6950, 2014.

[49] P. Helene, B. Martin, C. Franois, and L. Ludwik. Design and properties of co-continuous nanostructured polymers by reactive blending. *Nature Materials*, 1 (1):54–58, 2002.

[50] T. J. Hermel-Davidock, H. S. Tang, D. J. Murray, and S. F. Hahn. Control of the block copolymer morphology in templated epoxy thermosets. *Journal of Polymer Science Part B: Polymer Physics*, 45(24):3338–3348, 2007.

[51] Y. S. Thio, J. Wu, and F. S. Bates. Epoxy toughening using low molecular weight poly(hexylene oxide)-poly(ethylene oxide) diblock copolymers. *Macromolecules*, 39(21):7187–7189, 2006.

[52] Z. J. Thompson, M. A. Hillmyer, J. Liu, H.-J. Sue, M. Dettloff, and F. S. Bates. Block copolymer toughened epoxy: Role of cross-link density. *Macromolecules*, 42(7):2333–2335, 2009.

[53] J. Wu, Y. S. Thio, and F. S. Bates. Structure and properties of pbopeo diblock copolymer modified epoxy. *Journal of Polymer Science Part B: Polymer Physics*, 43(15):1950–1965, 2005.

[54] J. Chen and A.C. Taylor. Epoxy modified with triblock copolymers: morphology, mechanical properties and fracture mechanisms. *Journal of Materials Science*, 47(11):4546–4560, 2012.

[55] H. Kishi, Y. Kunimitsu, J. Imade, S. Oshita, Y. Morishita, and M. Asada. Nanophase structures and mechanical properties of epoxy/acryl triblock copolymer alloys. *Polymer*, 52(3):760–768, 2011.

[56] P. Gerard, N. P. Boupat, T. Fine, L. Gervat, and J.-P. Pascault. Toughness properties of lightly crosslinked epoxies using block copolymers. *Macromolecular Symposia*, 256(1):55–64, 2007.

[57] W. Fan and S. Zheng. Reaction-induced microphase separation in thermosetting blends of epoxy resin with poly(methyl methacrylate)-block-polystyrene block copolymers: Effect of topologies of block copolymers on morphological structures. *Polymer*, 49(13-14):3157–3167, 2008.

[58] V. Rebizant, A.-S. Venet, F. Tournilhac, E. Girard-Reydet, C. Navarro, J.-P. Pascault, and L. Leibler. Chemistry and mechanical properties of epoxy-based thermosets reinforced by reactive and nonreactive sbmx block copolymers. *Macromolecules*, 37(21):8017–8027, 2004.

[59] J.-P. Pascault and R. J. J. Williams. *Epoxy Polymers- New Materials and Innovations*. Wiley-VCH Verlag GmbH & Co. KGaA, Weinheim, 2010.

[60] S. Maiez-Tribut, J. P. Pascault, E. R. Soul, J. Borrajo, and R. J. J. Williams. Nanostructured epoxies based on the self-assembly of block copolymers: A new miscible block that can be tailored to different epoxy formulations. *Macromolecules*, 40(4):1268–1273, 2007.

[61] J. M. Dean, R. B. Grubbs, W. Saad, R. F. Cook, and F. S. Bates. Mechanical properties of block copolymer vesicle and micelle modified epoxies. *Journal of Polymer Science Part B: Polymer Physics*, 41(20):2444–2456, 2003.

[62] R. M. Hydro and R. A. Pearson. Epoxies toughened with triblock copolymers. *Journal of Polymer Science Part B: Polymer Physics*, 45(12):1470–1481, 2007.

[63] C. Declet-Perez, E. M. Redline, L. F. Francis, and F. S. Bates. Role of localized network damage in block copolymer toughened epoxies. *ACS Macro Letters*, 1 (2):338–342, 2012.

[64] D. Verchere, H. Sautereau, J. P. Pascault, S. M. Moschiar, C. C. Riccardi, and R. J. J. Williams. Miscibility of epoxy monomers with carboxyl-terminated butadiene-acrylonitrile random copolymers. *Polymer*, 30(1):107–115, 1989.

[65] D. Ratna. Phase separation in liquid rubber modified epoxy mixture. relationship between curing conditions, morphology and ultimate behavior. *Polymer*, 42(9): 4209–4218, 2001.

[66] D. Verchere, J. P. Pascault, H. Sautereau, S. M. Moschiar, C. C. Riccardi, and R. J. J. Williams. Rubber-modified epoxies. II. Influence of the cure schedule and rubber concentration on the generated morphology. *Journal of Applied Polymer Science*, 42(3):701–716, 1991.

[67] F. S. Bates. Polymer-polymer phase behavior. *Science*, 251(4996):898–905, 1991.

[68] J. W. Cahn and J. E. Hilliard. Free energy of a nonuniform system. I. Interfacial free energy. *The Journal of Chemical Physics*, 28(2):258–267, 1958.

[69] L. Q. Chen. Phase-field models for microstructure evolution. *Annual Review of Materials Research*, 32(1):113–140, 2002.

[70] V. Cristini, X. Li, J. S. Lowengrub, and S. M. Wise. Nonlinear simulations of solid tumor growth using a mixture model: invasion and branching. *Journal of Mathematical Biology*, 58(4-5):723–63, 2009.

[71] A. L. Bertozzi, S. Esedoglu, and A. Gillette. Inpainting of binary images using the cahn-hilliard equation. *IEEE Transactions on Image Processing*, 16(1):285–291, 2007.

[72] M. Burger, L. He, and C. B. Schonlieb. Cahn-Hilliard inpainting and a generalization for grayvalue images. *SIAM Journal on Imaging Sciences*, 2(4):1129–1167, 2009.

[73] I. M. Lifshitz and V. V. Slyozov. The kinetics of precipitation from supersaturated solid solutions. *Journal of Physics and Chemistry of Solids*, 19(1):35–50, 1961.

[74] C. Wagner. Theorie der alterung von niederschlägen durch umlösen (Ostwald-reifung). *Zeitschrift für Elektrochemie*, 65(7-8):581–591, 1961.

[75] Y. Huang and A. J. Kinloch. Modelling of the toughening mechanisms in rubber-modified epoxy polymers part ii a quantitative description of the microstructure-fracture property relationships. *Journal of Materials Science*, 27:2763–2769, 1992.

[76] T. H. Hsieh, A. J. Kinloch, K. Masania, J. Sohn Lee, A. C. Taylor, and S. Sprenger. The toughness of epoxy polymers and fibre composites modified with rubber microparticles and silica nanoparticles. *Journal of Materials Science*, 45(5):1193–1210, 2010.

[77] S. Kunz-Douglass, P. W. R. Beaumont, and M. F. Ashby. A model for the toughness of epoxy-rubber particulate composites. *Journal of Materials Science*, 15:1109–1123, 1980.

[78] C. B. Bucknall, I. K. Partridge, and M. V. Ward. Rubber toughening of plastics. *Journal of Materials Science*, 19(6):2064–2072, 1984.

[79] Y. Huang and A. J. Kinloch. Modelling of the toughening mechanisms in rubber-modified epoxy polymers part i finite element analysis studies. *Journal of Materials Science*, 27:2753–2762, 1992.

[80] F. J. Guild, A. J. Kinloch, and A. C. Taylor. Particle cavitation in rubber toughened epoxies: the role of particle size. *Journal of Materials Science*, 45 (14):3882–3894, 2010.

[81] R. A. Pearson and A. F. Yee. Toughening mechanisms in elastomer-modified epoxies. *Journal of Materials Science*, 21(7):2475–2488, 1986.

[82] M. L. Arias, P. M. Frontini, and R. J. J. Williams. Analysis of the damage zone around the crack tip for two rubber-modified epoxy matrices exhibiting different toughenability. *Polymer*, 44(5):1537–1546, 2003.

[83] P. B. Bowden and S. Raha. The formation of micro shear bands in polystyrene and polymethylmethacrylate. *Philosophical Magazine*, 22(177):463–482, 1970.

[84] K. Masania. Toughening mechanisms of silica nanoparticle-modified epoxy polymers. *PhD Thesis, Department of Mechanical Engineering, Imperial College London*, 2010.

[85] L. E. Govaert, H. G. H. van Melick, and H. E. H. Meijer. Temporary toughening of polystyrene through mechanical pre-conditioning. *Polymer*, 42(3):1271–1274, 2001.

[86] K. Chen and K. S. Schweizer. Theory of yielding, strain softening, and steady plastic flow in polymer glasses under constant strain rate deformation. *Macromolecules*, 44(10):3988–4000, 2011.

[87] H. E. H. Meijer and L. E. Govaert. Mechanical performance of polymer systems: The relation between structure and properties. *Progress in Polymer Science*, 30 (89):915–938, 2005.

[88] L. E. Govaert, T. A. P. Engels, M. Wendlandt, T. A. Tervoort, and U. W. Suter. Does the strain hardening modulus of glassy polymers scale with the flow stress? *Journal of Polymer Science Part B: Polymer Physics*, 46(22):2475–2481, 2008.

[89] J. G. Williams. Particle toughening of polymers by plastic void growth. *Composites Science and Technology*, 70(6):885–891, 2010.

[90] A. F. Yee, D. Li, and X. Li. The importance of constraint relief caused by rubber cavitation in the toughening of epoxy. *Journal of Materials Science*, 28(23): 6392–6398, 1993.

[91] Y. Huang and A.J. Kinloch. The sequence of initiation of the toughening micromechanisms in rubber-modified epoxy polymers. *Polymer*, 33(24):5338–5340, 1992.

[92] H. R. Azimi, R. A. Pearson, and R. W. Hertzberg. Role of crack tip shielding mechanisms in fatigue of hybrid epoxy composites containing rubber and solid glass spheres. *Journal of Applied Polymer Science*, 58(2):449–463, 1995.

[93] J. Spanoudakis and R.J. Young. Crack propagation in a glass particle-filled epoxy resin Part 1 Effect of particle volume fraction and size. *Journal of Materials Science*, 19:473–486, 1984.

[94] J. Spanoudakis and R.J. Young. Crack propagation in a glass particle-filled epoxy resin Part 2 Effect of particle-matrix adhesion. *Journal of Materials Science*, 19: 487–496, 1984.

[95] J. Lee and A. F. Yee. Fracture of glass bead/epoxy composites: on micromechanical deformations. *Polymer*, 41(23):8363–8373, 2000.

[96] B. Bittmann, F. Haupert, and A. K. Schlarb. Preparation of TiO_2 epoxy nanocomposites by ultrasonic dispersion and resulting properties. *Journal of Applied Polymer Science*, 124(3):1906–1911, 2012.

[97] L. M. McGrath, R. S. Parnas, S. H. King, J. L. Schroeder, D. A. Fischer, and J. L. Lenhart. Investigation of the thermal, mechanical, and fracture properties of aluminaepoxy composites. *Polymer*, 49(4):999–1014, 2008.

[98] S. H. Lim, K. Y. Zeng, and C. B. He. Morphology, tensile and fracture characteristics of epoxy-alumina nanocomposites. *Materials Science and Engineering: A*, 527(2122):5670–5676, 2010.

[99] A. J. Kinloch and A. C. Taylor. The mechanical properties and fracture behaviour of epoxy-inorganic micro- and nano-composites. *Journal of Materials Science*, 41 (11):3271–3297, 2006.

[100] Y. Nakamura, M. Yamaguchi, M. Okubo, and T. Matsumoto. Effect of particle size on the fracture toughness of epoxy resin filled with spherical silica. *Polymer*, 33(16):3415–3426, 1992.

[101] A. C. Moloney, H. H. Kausch, T. Kaiser, and H. R. Beer. Parameters determining the strength and toughness of particulate filled epoxide resins. *Journal of Materials Science*, 22(2):381–393, 1987.

[102] S.-C. Kwon, T. Adachi, and W. Araki. Temperature dependence of fracture toughness of silica/epoxy composites: Related to microstructure of nano- and micro-particles packing. *Composites Part B: Engineering*, 39(5):773–781, 2008.

[103] P. Dittanet and R. A. Pearson. Effect of silica nanoparticle size on toughening mechanisms of filled epoxy. *Polymer*, 53(9):1890–1905, 2012.

[104] B. B. Johnsen, A. J. Kinloch, R. D. Mohammed, A. C. Taylor, and S. Sprenger. Toughening mechanisms of nanoparticle-modified epoxy polymers. *Polymer*, 48 (2):530–541, 2007.

[105] E. Vassileva and K. Friedrich. Epoxy/alumina nanoparticle composites. II. Influence of silane coupling agent treatment on mechanical performance and wear resistance. *Journal of Applied Polymer Science*, 101(6):4410–4417, 2006.

[106] S. Sprenger. Epoxy resin composites with surface-modified silicon dioxide nanoparticles: A review. *Journal of Applied Polymer Science*, 130(3):1421–1428, 2013.

[107] A. J. Kinloch, J. H. Lee, A. C. Taylor, S. Sprenger, C. Eger, and D. Egan. Toughening structural adhesives via nano- and micro-phase inclusions. *The Journal of Adhesion*, 79(8-9):867–873, 2003.

[108] B. R. K. Blackman, A. J. Kinloch, J. Sohn Lee, A. C. Taylor, R. Agarwal, G. Schueneman, and S. Sprenger. The fracture and fatigue behaviour of nano-modified epoxy polymers. *Journal of Materials Science*, 42(16):7049–7051, 2007.

[109] Y. L. Liang and R. A. Pearson. Toughening mechanisms in epoxy-silica nanocomposites (ESNs). *Polymer*, 50(20):4895–4905, 2009.

[110] J.-K. Chen, Z.-P. Huang, and J. Zhu. Size effect of particles on the damage dissipation in nanocomposites. *Composites Science and Technology*, 67(14):2990–2996, 2007.

[111] S. Iijima. Helical microtubules of graphitic carbon. *Nature*, 354(6348):56–58, 1991.

[112] K. S. Novoselov, A. K. Geim, Morozov. S. V., D. Jiang, Y. Zhang, S. V. Dubonos, I. V. Grigorieva, and A. A. Firsov. Electric field effect in atomically thin carbon films. *Science*, 306(5696):666–669, 2004.

[113] H. W. Kroto, J. R. Heath, S. C. O'Brien, R. F. Curl, and R. E. Smalley. C60: Buckminsterfullerene. *Nature*, 318:162–163, 1985.

[114] M. A. Rafiee, F. Yavari, J. Rafiee, and N. Koratkar. Fullereneepoxy nanocomposites-enhanced mechanical properties at low nanofiller loading. *Journal of Nanoparticle Research*, 13(2):733–737, 2011.

[115] C. Lee, X. Wei, J. W. Kysar, and J. Hone. Measurement of the elastic properties and intrinsic strength of monolayer graphene. *Science*, 321(5887):385–8, 2008.

[116] F. H. Gojny, J. Nastalczyk, Z. Roslaniec, and K. Schulte. Surface modified multi-walled carbon nanotubes in cnt/epoxy-composites. *Chemical Physics Letters*, 370 (5-6):820–824, 2003.

[117] T. H. Hsieh, A. J. Kinloch, A. C. Taylor, and I. A. Kinloch. The effect of carbon nanotubes on the fracture toughness and fatigue performance of a thermosetting epoxy polymer. *Journal of Materials Science*, 46(23):7525–7535, 2011.

[118] E. T. Thostenson and T.-W. Chou. Processing-structure-multi-functional property relationship in carbon nanotube/epoxy composites. *Carbon*, 44(14):3022–3029, 2006.

[119] F. H. Gojny, M. H. G. Wichmann, U. Kpke, B. Fiedler, and K. Schulte. Carbon nanotube-reinforced epoxy-composites: enhanced stiffness and fracture toughness at low nanotube content. *Composites Science and Technology*, 64(15):2363–2371, 2004.

[120] A. Okada and A. Usuki. Twenty years of polymer-clay nanocomposites. *Macromolecular Materials and Engineering*, 291(12):1449–1476, 2006.

[121] S. G. Miller and M. A. Meador. Polymer-layered silicate nanocomposites for cryotank applications. *48th AIAA/ASME/ASCE/AHS/ASC Structures, Structural Dynamics, and Materials Conference, Honolulu, Hawaii*, 2007.

[122] S. D. Burnside and E. P. Giannelis. Synthesis and properties of new poly(dimethylsiloxane) nanocomposites. *Chemistry of Materials*, 7(9):1597–1600, 1995.

[123] D. D. L. Chung. Exfoliation of graphite. *Journal of Materials Science*, 22(12): 4190–4198, 1987.

[124] K. Wang, L. Chen, J. Wu, M. L. Toh, C. He, and A. F. Yee. Epoxy nanocomposites with highly exfoliated clay: Mechanical properties and fracture mechanisms. *Macromolecules*, 38(3):788–800, 2005.

[125] H. Miyagawa and L. T. Drzal. The effect of chemical modification on the fracture toughness of montmorillonite clay/epoxy nanocomposites. *Journal of Adhesion Science and Technology*, 18(13):1571–1588, 2004.

[126] W. Liu, S. V. Hoa, and M. Pugh. Organoclay-modified high performance epoxy nanocomposites. *Composites Science and Technology*, 65(2):307–316, 2005.

[127] R. J. Young, I. A. Kinloch, L. Gong, and K. S. Novoselov. The mechanics of graphene nanocomposites: A review. *Composites Science and Technology*, 72 (12):1459–1476, 2012.

[128] J. R. Potts, D. R. Dreyer, C. W. Bielawski, and R. S. Ruoff. Graphene-based polymer nanocomposites. *Polymer*, 52(1):5–25, 2011.

[129] D. R. Bortz, E. G. Heras, and I. Martin-Gullon. Impressive fatigue life and fracture toughness improvements in graphene oxide/epoxy composites. *Macromolecules*, 45(1):238–245, 2011.

[130] C. Bao, Y. Guo, L. Song, Y. Kan, X. Qian, and Y. Hu. In situ preparation of functionalized graphene oxide/epoxy nanocomposites with effective reinforcements. *Journal of Materials Chemistry*, 21(35):13290, 2011.

[131] Q. Liu, X. Zhou, X. Fan, C. Zhu, X. Yao, and Z. Liu. Mechanical and thermal properties of epoxy resin nanocomposites reinforced with graphene oxide. *Polymer-Plastics Technology and Engineering*, 51(3):251–256, 2012.

[132] L. Ramos-Galicia, L. N. Mendez, A. L. Martnez-Hernndez, A. Espindola-Gonzalez, I. R. Galindo-Esquivel, R. Fuentes-Ramirez, and C. Velasco-Santos. Improved performance of an epoxy matrix as a result of combining graphene oxide and reduced graphene. *International Journal of Polymer Science*, 2013:1–7, 2013.

[133] H. Kim, A. A. Abdala, and C. W. Macosko. Graphene/polymer nanocomposites. *Macromolecules*, 43(16):6515–6530, 2010.

[134] S. Chatterjee, F. Nafezarefi, N. H. Tai, L. Schlagenhauf, F. A. Nesch, and B. T. T. Chu. Size and synergy effects of nanofiller hybrids including graphene nanoplatelets and carbon nanotubes in mechanical properties of epoxy composites. *Carbon*, 50(15):5380–5386, 2012.

[135] M. A. Rafiee, J. Rafiee, Z. Wang, H. Song, Z. Z. Yu, and N. Koratkar. Enhanced mechanical properties of nanocomposites at low graphene content. *ACS Nano*, 3 (12):3884–3890, 2009.

[136] I. Zaman, T. T. Phan, H.-C. Kuan, Q. Meng, L. T. B. La, L. Luong, O. Youssf, and J. Ma. Epoxy/graphene platelets nanocomposites with two levels of interface strength. *Polymer*, 52(7):1603–1611, 2011.

[137] I. Zaman, H. C. Kuan, J. Dai, N. Kawashima, A. Michelmore, A. Sovi, S. Dong, L. Luong, and J. Ma. From carbon nanotubes and silicate layers to graphene platelets for polymer nanocomposites. *Nanoscale*, 4(15):4578–86, 2012.

[138] C. M. White, R. Banks, B. Norton, I. Hamerton, and J. F. Watts. Development of an anti-static coating incorporating multi-walled carbon nanotubes as an alternative to graphite. *36th Annual Meeting of the Adhesion Society, 3-6 March 2013, Daytona Beach, USA*, 2013.

[139] Graphene Supermarket. Graphene Nanopowder: 12 nm Flakes-25 g. [Online]. *Available from: https:// graphene-supermarket.com/ Graphene-Nanopowder-12-nm-Flakes-5-g-SKU-NP-FLAO3-5G11.html*. [Accessed 23rd June 2014].

[140] H. Yoon, M. Yamashita, S. Ata, D. N. Futaba, T. Yamada, and K. Hata. Controlling exfoliation in order to minimize damage during dispersion of long swcnts for advanced composites. *Scientific Reports*, 4:3907–3914, 2014.

[141] P.-C. Ma, N. A. Siddiqui, G. Marom, and J.-K. Kim. Dispersion and functionalization of carbon nanotubes for polymer-based nanocomposites: A review. *Composites Part A: Applied Science and Manufacturing*, 41(10):1345–1367, 2010.

[142] T. H. Hsieh. Properties and toughening of silica nanoparticle- and carbon nanotube- modified epoxy polymers. *PhD Thesis, Department of Mechanical Engineering, Imperial College London*, 2011.

[143] M. M. Shokrieh, M. Esmkhani, H. R. Shahverdi, and F. Vahedi. Effect of graphene nanosheets (GNS) and graphite nanoplatelets (GNP) on the mechanical properties of epoxy nanocomposites. *Science of Advanced Materials*, 5(3): 260–266, 2013.

[144] J. L. Capelo-Martnez. *Ultrasound in Chemistry: Analytical Applications*. Wiley-VCH Verlag GmbH & Co. KGaA, Weinheim, 2008.

[145] S. G. Prolongo, A. Jimenez-Suarez, R. Moriche, and A. Urena. In situ processing of epoxy composites reinforced with graphene nanoplatelets. *Composites Science and Technology*, 86(0):185–191, 2013.

[146] T. Herceg, M. S. Z. Abidin, C. Delfour, Greenhalgh E., A. Bismarck, and M. Shaffer. Scalable production of epoxy based nanocomposites and hierarchical composites with high cnt loadings. *19th International Conference on Composite Materials, 28 July-2 August 2013, Montreal, Canada*, 2013.

[147] M. S. Z. Abidin, T. Herceg, A. Bismarck, Greenhalgh E., and M. Shaffer. Scalable production of epoxy based nanocomposites and hierarchical composites with high cnt loadings. *6th International Conference on Carbon NanoParticle Based Composites, 22-25 September 2013, Dresden, Germany*, 2013.

[148] H. Kim and C. W. Macosko. Processing-property relationships of polycarbonate/graphene composites. *Polymer*, 50(15):3797–3809, 2009.

[149] P. Steurer, R. Wissert, R. Thomann, and R. Mulhaupt. Functionalized graphenes and thermoplastic nanocomposites based upon expanded graphite oxide. *Macromolecular Rapid Communications*, 30(4-5):316–327, 2009.

[150] Y. Fan, L. Wang, J. Li, J. Li, S. Sun, F. Chen, L. Chen, and W. Jiang. Preparation and electrical properties of graphene nanosheet/al2o3 composites. *Carbon*, 48(6): 1743–1749, 2010.

[151] W. Zhao, F. Wu, H. Wu, and G. Chen. Preparation of colloidal dispersions of graphene sheets in organic solvents by using ball milling. *Journal of Nanomaterials*, 2010:1–5, 2010.

[152] V. V. Ivanovskaya, P. Wagner, A. Zobelli, I. Suarez-Martinez, A. Yaya, and C. P. Ewels. *Graphene Edge Structures: Folding, Scrolling, Tubing, Rippling and Twisting*, chapter 10, pages 75–85. Carbon Nanostructures. Springer Berlin Heidelberg, 2012.

[153] W. Gao and R. Huang. Thermomechanics of monolayer graphene: Rippling, thermal expansion and elasticity. *Journal of the Mechanics and Physics of Solids*, 66(0):42–58, 2014.

[154] C. Wang, Y. Liu, L. Lan, and H. Tan. Graphene wrinkling: formation, evolution and collapse. *Nanoscale*, 5(10):4454–4461, 2013.

[155] F. F. Lange. The interaction of a crack front with a second-phase dispersion. *Philosophical Magazine*, 22(179):0983–0992, 1970.

[156] F. J. Guild and R. J. Young. A predictive model for particulate-filled composite materials. *Journal of Materials Science*, 24(1):298–306, 1989.

[157] K. T. Faber and A. G. Evans. Crack deflection processesI. Theory. *Acta Metallurgica*, 31(4):565–576, 1983.

[158] D. Quan, D. McAuliffe, N. Murphy, and A. Ivankovic. An investigation of toughness mechanisms and synergistic effects in nano-toughened epoxy adhesives. *37th Annual Meeting of the Adhesion Society, 23-26 February 2014, San Diego, USA*, 2014.

[159] T. Kawaguchi and R. A. Pearson. The effect of particle–matrix adhesion on the mechanical behavior of glass filled epoxies. Part 2. A study on fracture toughness. *Polymer*, 44(15):4239–4247, 2003.

[160] M. H. G. Wichmann, K. Schulte, and H. D. Wagner. On nanocomposite toughness. *Composites Science and Technology*, 68(1):329–331, 2008.

[161] E. T. Thostenson, C. Li, and T.-W. Chou. Nanocomposites in context. *Composites Science and Technology*, 65(34):491–516, 2005.

[162] A. J. Kinloch, C. A. Finch, and S. Hashemi. Effect of segmental molecular mass between crosslinks of the matrix phase on the toughness of rubber-modified epoxies. *Polymer Communications*, 28:322–325, 1987.

[163] F. Lu, H. H. Kausch, W. J. Cantwell, and M. Fischer. The effect of crosslink density on the fracture toughness of core-shell modified epoxy resins. *Journal of Materials Science Letters*, 15(12):1018–1021, 1996.

[164] M. C. M. van der Sanden and H. E. H. Meijer. Deformation and toughness of polymeric systems: 3. influence of crosslink density. *Polymer*, 34(24):5063–5072, 1993.

[165] R. A. Pearson and A. F. Yee. Influence of particle size and particle size distribution on toughening mechanisms in rubber-modified epoxies. *Journal of Materials Science*, 26(14):3828–3844, 1991.

[166] D. S. Kim, K. Cho, J. K. Kim, and C. E. Park. Effects of particle size and rubber content on fracture toughness in rubber-modified epoxies. *Polymer Engineering & Science*, 36(6):755–768, 1996.

[167] L. N. Bacigalupo and R. A. Pearson. Predicting the fracture toughness of rubber modified epoxy. *36th Annual Meeting of the Adhesion Society, 3-6 March 2013, Daytona Beach, USA*, 2013.

[168] R. J. Day, P. A. Lovell, and D. Pierre. Toughening of epoxy resins using particles prepared by emulsion polymerization: effects of particle surface functionality, size and morphology on impact fracture properties. *Polymer International*, 44 (3):288–299, 1997.

[169] E. Girard-Reydet, J.-P. Pascault, A. Bonnet, F. Court, and L. Leibler. A new class of epoxy thermosets. *Macromolecular Symposia*, 198(1):309–322, 2003.

[170] Y. Huang, D. L. Hunston, A. J. Kinloch, and C. K. Riew. *Mechanisms of Toughening Thermoset Resins*, volume 233 of *Advances in Chemistry*, chapter 1, pages 1–35. American Chemical Society, Washington, 1993.

[171] B. Lauke. On the effect of particle size on fracture toughness of polymer composites. *Composites Science and Technology*, 68(15-16):3365–3372, 2008.

[172] Y. Huang, A. J. Kinloch, R. J. Bertsch, and A. R. Siebert. Particle-matrix interfacial bonding. In *Toughened Plastics I*, volume 233 of *Advances in Chemistry*, chapter 8, pages 189–210. American Chemical Society, 1993.

[173] A. J. Kinloch, D. L. Maxwell, and R. J. Young. Micromechanisms of crack propagation in hybrid-particulate composites. *Journal of Materials Science Letters*, 4(10):1276–1279, 1985.

[174] A. J. Kinloch, D. L. Maxwell, and R. J. Young. The fracture of hybrid-particulate composites. *Journal of Materials Science*, 20(11):4169–4184, 1985.

[175] R. J. Young, D. L. Maxwell, and A. J. Kinloch. The deformation of hybrid-particulate composites. *Journal of Materials Science*, 21(2):380–388, 1986.

[176] C. I. Vallo, L. Hu, P. M. Frontini, and R. J. J. Williams. Toughened-hybrid epoxies: influence of the rubber-phase morphology on mechanical properties. *Journal of Materials Science*, 29(9):2481–2486, 1994.

[177] B. Geisler and F. N. Kelley. Rubbery and rigid particle toughening of epoxy resins. *Journal of Applied Polymer Science*, 54(2):177–189, 1994.

[178] I. M. Low, S. Bandyopadhyay, and Y. W. Mai. On hybrid toughened dgeba epoxy resins. *Polymer International*, 27(2):131–137, 1992.

[179] Y. L. Liang and R. A. Pearson. The toughening mechanism in hybrid epoxy-silica-rubber nanocomposites (HESRNs). *Polymer*, 51(21):4880–4890, 2010.

[180] J. Chen. Toughening epoxy polymers and carbon fibre composites with core-shell particles, block copolymers and silica nanoparticles. *PhD Thesis, Department of Mechanical Engineering, Imperial College London*, 2013.

[181] B. T. Marouf, R. A. Pearson, and R. Bagheri. Anomalous fracture behavior in an epoxy-based hybrid composite. *Materials Science and Engineering: A*, 515 (1-2):49–58, 2009.

[182] M. d. M. Salinas-Ruiz, A. A. Skordos, and I. K. Partridge. Rubber-toughened epoxy loaded with carbon nanotubes: structureproperty relationships. *Journal of Materials Science*, 45(10):2633–2639, 2010.

[183] W. P. Liu, S. V. Hoa, and M. Pugh. Morphology and performance of epoxy nanocomposites modified with organoclay and rubber. *Polymer Engineering & Science*, 44(6):1178–1186, 2004.

[184] R. D. Mohammed. Material properties and fracture mechanisms of epoxy nanocomposites. *PhD Thesis, Department of Mechanical Engineering, Imperial College London*, 2007.

[185] M. J. Boynton and A. Lee. Fracture of an epoxy polymer containing recycled elastomeric particles. *Journal of Applied Polymer Science*, 66(2):271–277, 1997.

[186] M. F. DiBerardino and R. A. Pearson. The effect of particle size on synergistic toughening of boron nitride-rubber hybrid epoxy composites. In R. A. Pearson, H. J. Sue, and A. F. Yee, editors, *Toughening of Plastics*, volume 759 of *ACS Symposium Series*, chapter 13, pages 213–229. American Chemical Society, 2000.

[187] J. L. Tsai, B. H. Huang, and Y. L. Cheng. Enhancing fracture toughness of glass/epoxy composites by using rubber particles together with silica nanoparticles. *Journal of Composite Materials*, 43(25):3107–3123, 2009.

[188] S. Sprenger. Epoxy resins modified with elastomers and surface-modified silica nanoparticles. *Polymer*, 54(18):4790–4797, 2013.

[189] D. Hull and T.W. Clyne. *An Introduction to Composite Materials*. Cambridge University Press, Cambridge, 1981.

[190] NASA. Final report of the X-33 liquid hydrogen tank test investigation team. *George C. Marshall Space Flight Center, Huntsville, NASA Report*, 2000.

[191] D. L. Hunston, R. J. Moulton, N. J. Johnston, and W. D. Bascom. Matrix resin effects in composite delamination: Mode I fracture aspects. *Toughened Composites: Symposium on Toughened Composites*, ASTM STP 937:74–94, 1987.

[192] W.L. Bradley. Understanding the translation of neat resin toughness into delamination toughness in composites. *Key Engineering Materials*, 37:161–198, 1989.

[193] W.L. Bradley. Relationship of matrix toughness to interlaminar fracture toughness. In F. Klaus, editor, *Application of fracture mechanics to composite materials*, pages 159–187. Elsevier, 1989.

[194] P. Compston, P. Y. B. Jar, P. J. Burchill, and K. Takahashi. The transfer of matrix toughness to composite Mode I interlaminar fracture toughness in glass-fibre/vinyl ester composites. *Applied Composite Materials*, 9(5):291–314, 2002.

[195] J. M. Scott and D. C. Phillips. Carbon fibre composites with rubber toughened matrices. *Journal of Materials Science*, 10(4):551–562, 1975.

[196] O. A. Stapountzi, M. N. Charalambides, and J. G. Williams. Micromechanical models for stiffness prediction of alumina trihydrate (ATH) reinforced poly (methyl methacrylate) (PMMA): Effect of filler volume fraction and temperature. *Composites Science and Technology*, 69(1112):2015–2023, 2009.

[197] J. C. Halpin and J. L. Kardos. The Halpin-Tsai equations: A review. *Polymer Engineering & Science*, 16(5):344–352, 1976.

[198] L. E. Nielsen and R. F. Landel. *Mechanical properties of polymers and composites*. Marcel Dekker, New York, 1994.

[199] W. Voigt. Ueber die beziehung zwischen den beiden elasticitätsconstanten isotroper Körper. *Annalen der Physik*, 274(12):573–587, 1889.

[200] A. Reuss. Berechnung der Flieβgrenze von Mischkristallen auf Grund der Plastizitätsbedingung für Einkristalle. *ZAMM - Journal of Applied Mathematics and Mechanics / Zeitschrift fur Angewandte Mathematik und Mechanik*, 9(1): 49–58, 1929.

[201] Z. Hashin and S. Shtrikman. A variational approach to the theory of the elastic behaviour of multiphase materials. *Journal of the Mechanics and Physics of Solids*, 11(2):127–140, 1963.

[202] J. C. Halpin and N. J. Pagano. The laminate approximation for randomly oriented fibrous composites. *Journal of Composite Materials*, 3(4):720–724, 1969.

[203] T. B. Lewis and L. E. Nielsen. Dynamic mechanical properties of particulate filled composites. *Journal of Applied Polymer Science*, 14(6):1449–1471, 1970.

[204] S. McGee and R. L. McCullough. Combining rules for predicting the thermoelastic properties of particulate filled polymers, polymers, polyblends, and foams. *Polymer Composites*, 2(4):149–161, 1981.

[205] L. E. Nielsen. The relation between viscosity and moduli of filled systems. *Journal of Composite Materials*, 2(1):120–123, 1968.

[206] T. Mori and K. Tanaka. Average stress in matrix and average elastic energy of materials with misfitting inclusions. *Acta Metallurgica*, 21(5):571–574, 1973.

[207] Y. Benveniste. A new approach to the application of Mori-Tanaka's theory in composite materials. *Mechanics of Materials*, 6(2):147–157, 1987.

[208] M. A. Van Es. Polymer-clay nanocomposites: the importance of particle dimensions. *PhD Thesis, Faculty of Applied Sciences, Delft University of Technology*, 2001.

[209] G. P. Tandon and G. J. Weng. The effect of aspect ratio of inclusions on the elastic properties of unidireectionally aligned composites. *Polymer Composites*, 5(4):327–333, 1984.

[210] H. Veenstra, P. C. J. Verkooijen, B. J. J. van Lent, J. van Dam, A. P. de Boer, and A. P. H. J. Nijhof. On the mechanical properties of co-continuous polymer blends: experimental and modelling. *Polymer*, 41(5):1817–1826, 2000.

[211] J. F. Wang, J. K. Carson, M. F. North, and D. J. Cleland. A knotted and interconnected skeleton structural model for predicting young's modulus of binary phase polymer blends. *Polymer Engineering & Science*, 50(4):643–651, 2010.

[212] X.-Q. Feng, Y.-W. Mai, and Q.-H. Qin. A micromechanical model for interpenetrating multiphase composites. *Computational Materials Science*, 28(34): 486–493, 2003.

[213] J. Kolařík. Three-dimensional models for predicting the modulus and yield strength of polymer blends, foams, and particulate composites. *Polymer Composites*, 18(4):433–441, 1997.

[214] W. E. A. Davies. The theory of elastic composite materials. *Journal of Physics D: Applied Physics*, 4(9):1325–1339, 1971.

[215] W. E. A. Davies. The elastic constants of a two-phase composite material. *Journal of Physics D: Applied Physics*, 4(8):1176–1181, 1971.

[216] M. E. J. Dekkers and D. Heikens. Shear band formation in polycarbonate-glass bead composites. *Journal of Materials Science*, 19(10):3271–3275, 1984.

[217] F. J. Guild and R. J. Young. A predictive model for particulate filled composite materials. *Journal of Materials Science*, 24(7):2454–2460, 1989.

[218] F. J. Guild, D. Alvarez, A. J. Kinloch, and A. C. Taylor. Modelling the toughness of rubber-toughened epoxies: A critical distance criterion. *36th Annual Meeting of the Adhesion Society, 3-6 March 2013, Daytona Beach, USA*, 2013.

[219] F. J. Guild and A. J. Kinloch. Modelling the properties of rubber-modified epoxy polymers. *Journal of Materials Science*, 30(7):1689–1697, 1995.

[220] Y. M. Poon, W. L. Luk, and F. G. Shin. Statistical spherical cell model for the elastic properties of particulate-filled composite materials. *Journal of Materials Science*, 37(23):5095–5099, 2002.

[221] P. J. Davy and F. J. Guild. The distribution of interparticle distance and its application in finite- element modelling of composite materials. *Proceedings of the Royal Society A: Mathematical, Physical and Engineering Sciences*, 418(1854): 95–112, 1988.

[222] X.-H. Chen and Y.-W. Mai. Micromechanics of rubber-toughened polymers. *Journal of Materials Science*, 33(14):3529–3539, 1998.

[223] J. Bishopp. Reports for nanotube-modified adhesive and ceramic foam projects. Technical report, Star Adhesion Limited, Cambridge, 2002.

[224] B. Burton, D. Alexander, H. Klein, A. Garibay-Vasquez, A. Pekarik, and C. Henkee. *Epoxy Formulations using Jeffamine Polyetheramines*. TX, Huntsman, 2005.

[225] J.-M. Boutillier. Nanostrength. *Innov'days, 22nd November 2012, Dijon, France*, 2012.

[226] C. Navarro, X. Marcarian, and B. Vuillemin. Ligated anionic polymerization: An innovative elf-atochem technology for the polymerization of (meth)acrylates. *Macromolecular Symposia*, 132(1):263–272, 1998.

[227] Arkema. Technical Data Sheet - Nanostrength for Epoxies. Arkema, France. 2011.

[228] S. Ritzenthaler, F. Court, L. David, E. Girard-Reydet, L. Leibler, and J.-P. Pascault. Abc triblock copolymers-epoxy-diamine blends. 1. keys to achieve nanostructured thermosets. *Macromolecules*, 35(16):6245–6254, 2002.

[229] Emerald Performance Materials LLC. Hypro Reactive Liquid Polymers 1300X8 CTBN & 1300X8F CTBN Technical data sheet. Emerald Performance Materials, LLC, Ohio. 2012.

[230] Kaneka. KANE ACE MX Technical data sheet. Kaneka, Houston.

[231] K. Yamaguchi, M. Ueno, and M. Miyamoto. *Process for producing modified epoxy resin*. US8680180B2 (Patent), 2007.

[232] J.-W. Ha, I. J. Park, S.-B. Lee, and D.-K. Kim. Preparation and characterization of core-shell particles containing perfluoroalkyl acrylate in the shell. *Macromolecules*, 35(18):6811–6818, 2002.

[233] D.J. Sober. Kaneka core-shell toughening systems for thermosetting resins. Kaneka, Houston. 2007.

[234] J. Adam. *Silicon dioxide dispersion*. US2004/01470229 A1 (Patent), 2004.

[235] XG Sciences. xGnP Grade H product characteristics. XG Sciences, Lansing. 2013.

[236] XG Sciences. xGnP Grade C product characteristics. XG Sciences, Lansing. 2013.

[237] Haydale Ltd. HDPlas^{TM} GNP-COOH Technical data sheet. Haydale Ltd, Carmarthenshire. .

[238] Haydale Ltd. HDPlas^{TM} GNP-O_2 Technical data sheet. Haydale Ltd, Carmarthenshire. .

[239] Haydale Ltd. HDPlas^{TM} MWCNT-COOH Technical data sheet. Haydale Ltd, Carmarthenshire. .

[240] XG Sciences. xGnP Grade M product characteristics. XG Sciences, Lansing. 2013.

[241] L. T. Drzal. Graphite nanoreinforcements for aerospace nanocomposites. *Final Report, NAG1-01004*, 2005.

[242] XG Sciences. Characterization of xGnP Grade C materials. XG Sciences, Lansing. 2012.

[243] R. J. Zaldivar, P. M. Adams, H. I. Kim, J. P. Nokes, and D. N. Patel. Strength improvements in toughened epoxy composites using surface treated gnps. *Journal of Applied Polymer Science*, 131(18):40802, 2014.

[244] Haydale Ltd. HDPlas^{TM} GNP Technical data sheet. Haydale Ltd, Carmarthenshire. 2013.

[245] ASTM-D5418. *Standard Test Method for Plastics: Dynamic Mechanical Properties: In Flexure (Dual Cantilever Beam)*. American Society for Testing and Materials, West Conshoshocken, 2007.

[246] N. Hawkins. *Novel holder for investigating powders by dynamic mechanical analysis*. TA Instruments, Crawley, UK.

[247] T. G. Fox. Influence of diluent and of copolymer composition on the glass temperature of a polymer system. *Bulletin of American Physical Society*, 1(3):123, 1956.

[248] A. E. O. J. Delesse. Pour déterminer la composition des roches. *Annales des Mines*, 13(4):379–388, 1848.

[249] J. C. Russ. *Practical Stereology*. Springer, New York, 1986.

[250] S. H. Lee. The fatigue and fracture properties of nano-modified epoxy polymers. *PhD Thesis, Department of Mechanical Engineering, Imperial College London*, 2013.

[251] A. Tewari, A. M. Gokhale, J. E. Spowart, and D. B. Miracle. Quantitative characterization of spatial clustering in three-dimensional microstructures using two-point correlation functions. *Acta Materialia*, 52(2):307–319, 2004.

[252] S. Torquato. *Random heterogeneous materials: Microstructure and macroscopic properties*. Springer-Verlag, New York, 2002.

[253] P. B. Corson. Correlation functions for predicting properties of heterogeneous materials. III. Effective elastic moduli of two–phase solids. *Journal of Applied Physics*, 45(7):3171–3179, 1974.

[254] H. L. Frisch and F. H. Stillinger. Contribution to the statistical geometric basis of radiation scattering. *The Journal of Chemical Physics*, 38(9):2200–2207, 1963.

[255] D. J. Bray, S. G. Gilmour, F. J. Guild, T. H. Hsieh, K. Masania, and A. C. Taylor. Quantifying nanoparticle dispersion: application of the Delaunay network for objective analysis of sample micrographs. *Journal of Materials Science*, 46(19): 6437–6452, 2011.

[256] A. Al-Ostaz, A. Diwakar, and K. I. Alzebdeh. Statistical model for characterizing random microstructure of inclusionmatrix composites. *Journal of Materials Science*, 42(16):7016–7030, 2007.

[257] J. F. Watts and J. Wolstenholme. *An Introduction to Surface Analysis by XPS and AES*. John Wiley & Sons, New York, 2003.

[258] P. Scherrer. Bestimmung der grösse und der inneren struktur von kolloidteilchen mittels röntgenstrahlen. *Nachrichten von der Gesellschaft der Wissenschaften zu Göttingen, Mathematisch-Physikalische Klasse*, 2:98–100, 1918.

[259] ISO 527-2. *Plastics - Determination of tensile properties - Part 2: Test conditions for moulding and extrusion plastics*. International Standards Organisation: Geneva, 1996.

[260] ISO 527-1. *Plastics - Determination of tensile properties - Part 1: General Principles*. International Standards Organisation: Geneva, 1996.

[261] ISO 13586. *Plastics - Determination of fracture toughness (G_{IC} and K_{IC}) - Linear elastic fracture mechanics (LEFM) approach*. International Standards Organisation: Geneva, 2000.

[262] A. Salazar, Y. Patel, and J. G. Williams. Influence of crack sharpness on the fracture toughness of epoxy resins. *13th International Conference on Fracture, 16-21 June 2013, Beijing, China*, 2013.

[263] J. G. Williams and H. Ford. Stress-strain relationships for some unreinforced plastics. *Journal of Mechanical Engineering Science*, 6(4):405–417, 1964.

[264] ISO 14125. *Fibre-reinforced plastic composites - Determination of flexural properties*. International Standards Organisation: Geneva, 1998.

[265] BS-ISO-14130. *Fibre-reinforced plastic composites - Determination of apparent interlaminar shear strength by short-beam method*. International Standards Organisation: Geneva, 1998.

[266] ISO 15024. *Fibre-reinforced plastic composites - Determination of mode-I interlaminar fracture toughness, G_{IC}, for unidirectionally reinforced materials*. International Standards Organisation: Geneva, 2001.

[267] Huntsman Advanced Materials. Araldite 2014-1 Technical data sheet. Huntsman Advanced Materials, Salt Lake City. 2007.

[268] BS-7991. *Determination of the mode I adhesive fracture energy G_{IC} of structure adhesives using the double cantilever beam (DCB) and tapered double cantilever beam (TDCB) specimens*. British Standards Institution: London, 2001.

[269] K. J. Pascoe. *An Introduction to the Properties of Engineering Materials*. Van Nostrand Reinhold, Berkshire, England, 1978.

[270] B. Duncan and G. Dean. Measurements and models for design with modern adhesives. *International Journal of Adhesion and Adhesives*, 23(2):141–149, 2003.

[271] R. N. Haward and R. J. Young. *The physics of glassy polymers*. Applied Science Publishers Ltd., London, 1997.

[272] E. H. Andrews. *Fracture in Polymers*. Oliver & Boyd, Edinburgh, 1968.

[273] F. J. Guild, A. J. Kinloch, and A. C. Taylor. The debonding of nanoparticles in toughening adhesives. *37th Annual Meeting of the Adhesion Society, 23-26 February 2014, San Diego, USA*, 2014.

[274] G. Kraus, C. W. Childers, and J. T. Gruver. Properties of random and block copolymers of butadiene and styrene. i. dynamic properties and glassy transition temperatures. *Journal of Applied Polymer Science*, 11(8):1581–1591, 1967.

[275] R. Marissen and H. R. Brouwer. The significance of fibre microbuckling for the flexural strength of a composite. *Composites Science and Technology*, 59:327–330, 1999.

[276] G. R. Irwin. Structural aspects of brittle fracture. *Applied Material Research*, 3 (2):65–81, 1964.

[277] M. Quaresimin and R. J. Varley. Understanding the effect of nano-modifier addition upon the properties of fibre reinforced laminates. *Composites Science and Technology*, 68(3-4):718–726, 2008.

[278] R. J. Barsotti, T. Fine, R. Inoubli, P. Gerard, S. Schmidt, N. Macy, S. Magnet, and C. Navarro. Nanostrength block copolymers for epoxy toughening. *Thermoset Resin Formulators Association, 15-16 September 2008, Chicago, USA*, 2008.

[279] M. C. Boyce, D. M. Parks, and A. S. Argon. Large inelastic deformation of glassy polymers. Part I: Rate dependent constitutive model. *Mechanics of Materials*, 7 (1):15–33, 1988.

[280] J. Liu, H.-J. Sue, Z. J. Thompson, F. S. Bates, M. Dettloff, G. Jacob, N. Verghese, and H. Pham. Nanocavitation in self-assembled amphiphilic block copolymer-modified epoxy. *Macromolecules*, 41(20):7616–7624, 2008.

[281] Cole-Parmer Instrument Co. Ltd. Cole Parmer 500 and 750 Watt Ultrasonic Processors with Temperature Controller. [Online]. *Available from: http://www.coleparmer.com/Category/Cole_Parmer_500_and_750_Watt_Ultrasonic_Processors_with_Temperature_Controller/16400*. [Accessed 22nd October 2014].

[282] J. L. Capelo, C. Maduro, and C. Vilhena. Discussion of parameters associated with the ultrasonic solidliquid extraction for elemental analysis (total content) by electrothermal atomic absorption spectrometry. an overview. *Ultrasonics Sonochemistry*, 12(3):225–232, 2005.

[283] R. D. Brooker. The morphology and toughness of thermoplastic-modified epoxy polymer with carbon nanotubes or silica nanoparticles. *PhD Thesis, Department of Mechanical Engineering, Imperial College London*, 2008.

[284] S. Badaire, P. Poulin, M. Maugey, and C. Zakri. In situ measurements of nanotube dimensions in suspensions by depolarized dynamic light scattering. *Langmuir*, 20(24):10367–10370, 2004.

[285] J. S. Lukesh and L. Pauling. The problem of the graphite structure. *American Mineralogist*, 35:125, 1950.

[286] G. Beamson and D. Briggs. *High Resolution XPS of Organic Polymers: The Scienta ESCA300 Database*. John Wiley & Sons, New York, 1992.

[287] R. J. Zaldivar, J. P. Nokes, P. M. Adams, K. Hammoud, and H. I. Kim. Surface functionalization without lattice degradation of highly crystalline nanoscaled carbon materials using a carbon monoxide atmospheric plasma treatment. *Carbon*, 50(8):2966–2975, 2012.

[288] G. Tillet, B. Boutevin, and B. Ameduri. Chemical reactions of polymer crosslinking and post-crosslinking at room and medium temperature. *Progress in Polymer Science*, 36(2):191–217, 2011.

[289] C.-H. Hsueh. A two-dimensional stress transfer model for platelet reinforcement. *Composites Engineering*, 4(10):1033–1043, 1994.

[290] F. Danusso and G. Tieghi. Strength versus composition of rigid matrix particulate composites. *Polymer*, 27(9):1385–1390, 1986.

[291] S.-Y. Fu, X.-Q. Feng, B. Lauke, and Y.-W. Mai. Effects of particle size, particle/matrix interface adhesion and particle loading on mechanical properties of particulatepolymer composites. *Composites Part B: Engineering*, 39(6):933–961, 2008.

[292] L. Nicolais and M. Narkis. Stress-strain behavior of styrene-acrylonitrile/glass bead composites in the glassy region. *Polymer Engineering & Science*, 11(3): 194–199, 1971.

[293] M. R. Piggott and J. Leidner. Misconceptions about filled polymers. *Journal of Applied Polymer Science*, 18(6):1619–1623, 1974.

[294] J. Leidner and R. T. Woodhams. The strength of polymeric composites containing spherical fillers. *Journal of Applied Polymer Science*, 18(6):1639–1654, 1974.

[295] B. Turcsanyi, B. Pukanszky, and F. Tudos. Composition dependence of tensile yield stress in filled polymers. *Journal of Materials Science Letters*, 7(2):160–162, 1988.

[296] Y. Huang, J. Wu, and K. C. Hwang. Thickness of graphene and single-wall carbon nanotubes. *Physical Review B*, 74(24):245413, 2006.

[297] D. Sanchez-Portal, E. Artacho, J. M. Soler, A. Rubio, and P. Ordejon. *Ab initio* structural, elastic, and vibrational properties of carbon nanotubes. *Physical Review B*, 59(19):12678–12688, 1999.

[298] A. N. Gent. Detachment of an elastic matrix from a rigid spherical inclusion. *Journal of Materials Science*, 15(11):2884–2888, 1980.

[299] A. H. Barber, S. R. Cohen, S. Kenig, and H. D. Wagner. Interfacial fracture energy measurements for multi-walled carbon nanotubes pulled from a polymer matrix. *Composites Science and Technology*, 64(15):2283–2289, 2004.

[300] C. B. Bucknall and I. K. Partridge. Phase separation in crosslinked resins containing polymeric modifiers. *Polymer Engineering & Science*, 26(1):54–62, 1986.

[301] A. R. Siebert and C. K. Riew. Chemistry of rubber toughened epoxy resins. *Abstracts of Papers of the American Chemical Society*, page 57, 1971.

[302] D. Carolan, H. M. Chong, A. Ivankovic, A. J. Kinloch, and A. C. Taylor. Co-continuous polymer systems: A numerical investigation. *Computational Materials Science*, 98(0):24–33, 2015.

[303] Y. Lee, S. Bae, H. Jang, S. Jang, S.-E. Zhu, S. H. Sim, Y. I. Song, B. H. Hong, and J.-H. Ahn. Wafer-scale synthesis and transfer of graphene films. *Nano Letters*, 10(2):490–493, 2010.

[304] R. Verdejo, M. M. Bernal, L. J. Romasanta, and M. A. Lopez-Manchado. Graphene filled polymer nanocomposites. *Journal of Materials Chemistry*, 21 (10):3301–3310, 2011.

List of Figures

2.2.1 Toughening of epoxy polymers by chemical modification. 5
2.2.2 Variation of Young's modulus and yield strength with CTBN rubber content for: (○) 828-8, (◊) 828-15, (▲) 828-BPA(24)-8. Reproduced from [26]. 7
2.2.3 Fracture toughness of neat and CTBN rubber modified epoxies [29]. . . 7
2.2.4 Change in microstructure for PES modified epoxy polymer. (a) Particulate, (b) Transition between particulate and co-continuous, (c) Co-continuous and (d) Phase-inverted microstructures. Reproduced from [35]. 8
2.2.5 Different types of copolymers [40]. 10
2.2.6 Possible self-assembly micellar structures. Reproduced from [43]. . . . 10
2.2.7 TEM micrographs showing BCP morphologies in epoxy. Reproduced from [6]. 11
2.2.8 Variation of morphology of SBM BCP with content. [1] Higher PB block ratio. Reproduced from [46]. 12
2.2.9 Time evolution of structure by two phase separation methods. Reproduced from [67]. 14
2.2.10 Nucleation and growth process. 15
2.2.11 Three main stages of spinodal decomposition process. 16
2.2.12 Colour scale bar for the order parameter, ϕ, for the phase fields diagrams. 16
2.2.13 Evolution of characteristic length with time for $v_f = 0.32$ and $v_f = 0.5$. 18
2.2.14 3D phase fields as predicted using the Cahn-Hilliard equation at t = 10,000. 23
2.2.15 Normalised free energy of Cahn-Hilliard phase field models with time. . 25
2.2.16 Schematic representation of toughening mechanisms for soft modifiers. Reproduced from [75, 77]. 26
2.2.17 Observation of plastic zone with optical microscopy. Reproduced from [81]. 27
2.2.18 Polished cross-sections of unmodified epoxy polymers tested under plane strain compression, loaded to the strain softening region (typically at true compressive strain values of 0.15 to 0.20) observed by cross-polarised light [84]. 27
2.2.19 Uniaxial compression stress-strain curve for polystyrene and polycarbonate. Reproduced from [87]. 28

2.2.20 Rubber particle cavitation observed by electron microscopy. (a) Rubber particle cavitation observed on fracture surface, (b) Size of rubber particles and voids before and after loading. TEM images obtained before loading represent undeformed particles and SEM images are of the cavities. Reproduced from [81]. 29
2.2.21 Fracture toughness for particles with a range of cavitation resistance. Reproduced from [21]. 29
2.2.22 Relative modulus (E_c/E_m) of some rigid particle modified epoxy polymers [93, 103–105]. 30
2.2.23 Fracture properties of silica nanoparticle modified epoxies; Experimental (■), Model (−). Reproduced from [5]. 31
2.2.24 Incorporation of carbon nanotubes in epoxy polymer. 32
2.2.25 Microstructures of silicate modified epoxy polymers. Reproduced from [99]. 32
2.2.26 TEM micrographs of nanoclay modified epoxy polymers. Reproduced from [124]. 33
2.2.27 Typical CNTs and GNPs as-received from suppliers. Reproduced from [138, 139]. 34
2.2.28 Illustration showing difference in shear loading between mechanical force and turbulent flow methods. Reproduced from [140]. 36
2.2.29 SEM micrograph showing dispersion of CNTs obtained using a twin screw extruder. Reproduced from [146]. 36
2.2.30 Illustrations showing possible distortion shapes of graphene sheets. Reproduced from [152]. 37
2.2.31 Crack pinning mechanism. Some of the tails are identified with arrows. Reproduced from [92]. 38
2.2.32 Crack deflection mechanism. Reproduced from [157]. 38
2.2.33 Crack deflection for micro and nanocomposites. Reproduced from [104]. 39
2.2.34 Debonding of glass microparticles and silica nanoparticles from the epoxy matrix. Reproduced from [5, 159]. 39
2.2.35 Toughening mechanisms for CNT and GNP modified epoxy polymers: (a) Pull-out, (b) Fracture, (c) Fracture and pull-out, (d) Debonding, (e) Bridging. 40
2.2.36 Effect of crosslink density on the toughness of CTBN rubber modified epoxy polymers. 41
2.2.37 Effect of crosslink density on the fracture energy of various modified epoxy polymers. 42
2.2.38 Particle size effect from cavitation criterion under uniaxial and triaxial loading. Reproduced from [80]. 43
2.2.39 Critical stress to debond for different particle sizes [110, 171]. 44
2.2.40 Young's modulus and fracture strength of glass filled epoxies with varying interfacial adhesion. Reproduced from [94]. 45
2.2.41 Fracture properties as a function of particle/matrix adhesion. Reproduced from [94, 170]. 45
2.2.42 Hybrid modified epoxy polymers. 46

2.2.43 TEM micrographs of hybrid CTBN-silica nanoparticle (NS) modified epoxy polymers. Reproduced from [179, 184]. 47
2.2.44 Fracture energy for hybrid CTBN-silica nanoparticle modified epoxy polymers. Reproduced from [109, 179]. 48
2.2.45 Fracture energy for hybrid modified epoxy polymers. Reproduced from [84, 180]. 49
2.3.1 Composite interlaminar fracture energy as a function of resin fracture energy. Reproduced from [191]. 51
2.3.2 Transfer of G_{IC} from bulk to interlaminar fracture energy $G_{IC}(composite)$. Reproduced from [76]. 51
2.3.3 Fracture surfaces of DCB test samples of glass fibre reinforced composites tested in mode I. Reproduced from [84]. 52
2.4.1 Example of upper and lower bounds of predicted modulus. 54
2.4.2 Framework of co-continuous model. m and f represent the matrix and filler, respectively. Reproduced from [210]. 57
2.4.3 Experimental and predicted values of Young's modulus for PS/poly(ether-ester) polymer blend. Reproduced from [210] 58
2.5.1 Comparison of the energy contributions from shear banding, void growth and rubber bridging from the Huang-Kinloch model. 61
2.6.1 Axisymmetric finite element model. Reproduced from Guild and Young [217]. 62
2.6.2 Von Mises stress concentration factors as a function of volume fraction. Reproduced from [79, 156, 217]. 63
2.6.3 Single spherical cell model. Reproduced from Guild and Kinloch [219]. 63

3.2.1 Molecular structures of epoxy resins. 67
3.3.1 Molecular structure of block copolymer modifiers used [227]. 68
3.3.2 Comparison of conventional and core shell rubber used in this study [233]. 70
3.3.3 Properties of the silica nanoparticles used in this study [184]. 71
3.3.4 Illustration of graphene nanoplatelet manufacturing process by microwave exfoliation of intercalated graphite. 72
3.3.5 Raman spectra for xGnP GNPs [235, 242]. 73
3.3.6 Particle size distribution of the HDPlas graphene nanoplatelets measured using dynamic light scattering [237–239]. 74
3.4.1 Cross-section showing RIFT set-up. 77
3.4.2 (a) Cure cycle used for RIFT panels and (b) Typical C-scan image. . . 78

4.2.1 Illustration of AFM sample preparation. 81
4.2.2 Illustration of SEM sample preparation. 82
4.2.3 Calibration of AFM and FEGSEM. 83
4.2.4 AFM micrograph image processing sequence. 83
4.2.5 Illustration showing difference in observed diameters from sectioning. . 84
4.2.6 Illustration of sputter coated specimens. Reproduced from [250]. 84
4.2.7 Two point characteristic functions. 86
4.2.8 Randomly located vectors on a thresholded image. 86
4.2.9 Process of obtaining the area disorder [255]. 87

4.2.10 Correspondence diagram of dispersion for combinations of area disorder and area fraction. Insets shown are for samples of a lattice-like, random or clustered system [255]. 87
4.2.11 High resolution XPS spectra with Shirley baseline background subtraction. 89
4.3.1 Tensile test. 90
4.3.2 Tensile test sample. 91
4.3.3 Single edge notched bending (SENB) test. 92
4.3.4 Plane strain compression (PSC) test. 94
4.3.5 Illustration of steps to observe shear bands from PSC test samples. . . 95
4.4.1 Short beam shear failure modes [265]. 96
4.4.2 Dimensions for DCB test sample. 97
4.4.3 Typical DCB load-displacement curve. 97

5.2.1 AFM phase micrographs of unmodified (a) LV, (b) LD and (c) AD epoxy polymer. 100
5.2.2 AFM phase micrographs of MX551 CSR modified LV epoxy polymer. . 101
5.2.3 AFM phase micrographs of CSR and CSR-NS hybrid modified LD epoxy polymer. 101
5.2.4 AFM phase micrographs of MX156 and MX156-NS hybrid modified AD epoxy polymer. 102
5.2.5 AFM phase micrographs of NS, CTBN and CTBN-NS hybrid modified LV epoxy polymer. 103
5.2.6 AFM phase micrographs of CTBN and CTBN-NS hybrid modified LD epoxy polymer. 104
5.2.7 AFM phase micrographs of CTBN and CTBN-NS hybrid modified AD epoxy polymer. 105
5.2.8 Viscosity as a function of temperature for the unmodified LD and AD epoxy polymers. 105
5.2.9 Area disorder of rubber modified LD epoxy. 106
5.2.10 Area disorder of rubber modified AD epoxy. 106
5.2.11 Area disorder of rubber modified LV epoxy. 107
5.3.1 Glass transition temperatures of rubber modified epoxy polymers. Error bars represent standard error of $\pm 1^{\circ}$C. 108
5.4.1 Typical tensile true stress-strain curves for unmodified and rubber modified LD epoxies tested at room temperature. 109
5.4.2 Young's moduli of rubber modified LD epoxy. 109
5.4.3 Young's moduli of rubber modified AD epoxy. 109
5.4.4 Young's moduli of rubber modified LV epoxy. 110
5.4.5 Tensile true strength, σ_t, of rubber modified epoxy polymers. 111
5.4.6 Tensile engineering stress versus engineering strain for unmodified and 9R modified LD epoxy. 112
5.4.7 Poisson's ratio of unmodified and 9R modified LD epoxy under uniaxial tensile loading. 112
5.5.1 Compressive true stress-true strain curves for unmodified and rubber modified epoxy polymers. 113

5.5.2 Transmission optical micrographs, using cross polarised light, of polished specimens loaded to the strain softening region for the LD and AD epoxy polymers. . . . 115
5.5.3 Transmission optical micrographs, using cross polarised light, of polished specimens loaded to the strain softening region for the LV epoxy polymers. . . . 116
5.6.1 Fracture toughness and fracture energy of rubber modified LV epoxy. . 117
5.6.2 Fracture toughness and fracture energy of rubber modified LD epoxy. . 117
5.6.3 Fracture toughness and fracture energy of rubber modified AD epoxy. . 118
5.7.1 FEGSEM micrograph of unmodified AD epoxy. . . . 118
5.7.2 FEGSEM micrograph of CSR modified epoxy fracture surfaces. . . . 120
5.7.3 FEGSEM micrograph of CSR-NS hybrid modified epoxy fracture surfaces. Some silica nanoparticles are identified with arrows. . . . 121
5.7.4 FEGSEM micrograph of CTBN modified epoxy fracture surfaces. . . . 121
5.7.5 FEGSEM micrograph of CTBN-NS hybrid 10N9R modified LD epoxy fracture surfaces. . . . 122
5.7.6 FEGSEM micrograph of CTBN-NS hybrid 10N9R modified AD epoxy fracture surfaces. . . . 122
5.7.7 FEGSEM micrograph of CTBN modified LV epoxy fracture surfaces. . 123
5.8.1 Predicted and measured values of fracture energy for CSR modified epoxy polymers. Insets show contributions from shear yielding, ΔG_s, and void growth ΔG_v. . . . 125
5.8.2 Predicted and measured values of fracture energy for CTBN modified epoxy polymers. Insets show contributions from shear yielding, ΔG_s, and void growth ΔG_v. . . . 127

6.2.1 AFM phase micrographs of E21 SBM modified LD epoxy polymer. . . 132
6.2.2 AFM phase micrographs of E21 SBM modified AD epoxy polymer. . . 132
6.2.3 AFM phase micrographs of E21 SBM modified LH epoxy polymer. . . 133
6.2.4 AFM phase micrographs of E21 SBM modified LV epoxy polymer. . . 135
6.2.5 AFM phase micrographs of E21 SBM-NS hybrid modified LD epoxy polymer. . . . 136
6.2.6 AFM phase micrographs of E21 SBM-NS hybrid modified AD epoxy polymer. . . . 137
6.2.7 AFM phase micrographs of 10N10E21 hybrid modified LH epoxy polymer. 137
6.2.8 AFM phase micrographs of E41 SBM modified LD epoxy polymer. . . 138
6.2.9 AFM phase micrographs of E41 SBM modified AD epoxy polymer. . . 138
6.2.10 AFM phase micrographs of E41 SBM modified LH epoxy polymer. . . 139
6.2.11 AFM phase micrographs of E41 SBM modified LV epoxy polymer. . . 140
6.2.12 Area disorder of SBM block copolymer modified epoxy polymers. . . . 142
6.3.1 Variation of tan δ with temperature of E21 and E41 SBM block copolymer. 143
6.3.2 Glass transition temperatures of SBM modified epoxy polymers. Error bars represent standard error of $\pm 1^{\circ}$C. . . . 144
6.3.3 Variation of tan δ with temperature of E21 and E41 SBM modified LV epoxy polymer. . . . 145

6.4.1 Tensile true stress-true strain curves for E21 and E41 SBM block copolymers. . . . 145
6.4.2 Typical tensile true stress-strain curves for unmodified and SBM modified LD epoxies. . . . 146
6.4.3 Young's moduli of SBM modified LD epoxy. . . . 147
6.4.4 Young's moduli of SBM modified AD epoxy. . . . 147
6.4.5 Young's moduli of SBM modified LH epoxy. Epoxies with phase inverted structures are labelled PI. . . . 147
6.4.6 Young's moduli of SBM modified LV epoxy. Epoxies with phase inverted structures are labelled PI. . . . 148
6.4.7 Tensile true strength, σ_t, of SBM modified epoxy polymers. . . . 149
6.4.8 Extensive stress whitening along gauge length of 10 wt% E21 modified LH epoxy polymer. . . . 150
6.5.1 Compressive true stress-true strain curves for unmodified and 10 wt% SBM modified epoxy polymers. . . . 151
6.5.2 Transmission optical micrographs, using cross polarised light, of polished PSC specimens loaded to the strain softening region for the LD and AD epoxies. . . . 152
6.5.3 Transmission optical micrographs, using cross polarised light, of polished PSC specimens loaded to the strain softening region for the LH and LV epoxies. . . . 152
6.6.1 Fracture toughness and fracture energy of SBM modified LD epoxy. . . . 153
6.6.2 Fracture toughness and fracture energy of SBM modified AD epoxy. . . . 153
6.6.3 Fracture toughness and fracture energy of SBM modified LH epoxy. Epoxies with phase inverted structures are labelled PI. . . . 155
6.6.4 Fracture toughness and fracture energy of SBM modified LV epoxy. Epoxies with phase inverted structures are labelled PI. . . . 156
6.7.1 FEGSEM micrograph of 2.5 wt% E21 SBM modified LD epoxy fracture surface. . . . 157
6.7.2 FEGSEM micrograph of 5 wt% E21 SBM modified LH epoxy fracture surface. . . . 157
6.7.3 FEGSEM micrograph of 2.5 wt% E21 SBM modified LV epoxy fracture surface. . . . 157
6.7.4 FEGSEM micrograph of E21 SBM modified AD epoxy fracture surface. 158
6.7.5 FEGSEM micrograph of 10 wt% E21 SBM modified LD epoxy fracture surface. . . . 158
6.7.6 FEGSEM micrograph of 10 wt% E21 SBM modified AD epoxy fracture surface. . . . 158
6.7.7 FEGSEM micrograph of 10 wt% E21 SBM modified LH epoxy fracture surface. . . . 159
6.7.8 FEGSEM micrograph of 10 wt% E21 SBM modified LV epoxy fracture surface. . . . 160
6.7.9 FEGSEM micrograph of hybrid 10N2.5E21 modified LD epoxy fracture surface. . . . 160
6.7.10 FEGSEM micrograph of hybrid 10N2.5E21 modified AD epoxy fracture surface. . . . 161

6.7.11 FEGSEM micrograph of hybrid 10N10E21 modified LD epoxy fracture surface. . . . 161
6.7.12 FEGSEM micrograph of hybrid 10N10E21 modified AD epoxy fracture surface. . . . 162
6.7.13 FEGSEM micrograph of hybrid 10N10E21 modified LH epoxy fracture surface. . . . 162
6.7.14 FEGSEM micrograph of 5 wt% E41 SBM modified LD epoxy fracture surface. . . . 163
6.7.15 FEGSEM micrograph of 10 wt% E41 SBM modified AD epoxy fracture surface. . . . 163
6.7.16 FEGSEM micrograph of 5 wt% E41 SBM modified LH epoxy fracture surface. . . . 164
6.7.17 FEGSEM micrograph of 10 wt% E41 SBM modified LH epoxy fracture surface. . . . 165
6.7.18 FEGSEM micrograph of 5 wt% E41 SBM modified LV epoxy fracture surface. . . . 165
6.10.1 Change in viscosity as a function of temperature for SBM modified LH epoxy resins. . . . 170
6.10.2 Backscattered electron micrograph showing cross-section for unmodified and E21 SBM modified LH CFRP. . . . 171
6.10.3 R-curve showing mode I fracture energy, $G_{IC(composite)}$, versus crack length, a, for unmodified and E21 SBM modified LH CFRP. . . . 173
6.10.4 Propagation G_{IC} and initiation G_{IC} for E21 SBM modified LH CFRP, showing plastic zone radius (r_{pz}) calculated using the Irwin model for the bulk materials. . . . 173
6.10.5 FEGSEM micrograph of unmodified and E21 SBM modified CFRP fracture surface. . . . 175

7.2.1 AFM phase micrographs of M52N MAM modified LD epoxy polymer. . 181
7.2.2 AFM phase micrographs of M52N MAM modified AD epoxy polymer. 181
7.2.3 AFM phase micrographs of M52N MAM modified LD epoxy polymer. . 182
7.2.4 AFM phase micrographs of M52N MAM modified AD epoxy polymer. 183
7.2.5 AFM phase micrographs of M52N MAM-NS hybrid modified LD epoxy polymer. . . . 184
7.2.6 AFM phase micrographs of M52N MAM-NS hybrid modified AD epoxy polymer. . . . 184
7.2.7 AFM phase micrographs of 10 wt% M22N MAM modified epoxy polymers. 186
7.2.8 TEM images of self-assembled nanostructures in epoxy: (a) Worm-like micelles (b) Core-shell particle. Reproduced from [278]. . . . 186
7.2.9 Area disorder of MAM block copolymer modified epoxy polymers. . . . 187
7.3.1 Variation of tan δ with temperature of M52N and M22N MAM block copolymers. . . . 188
7.3.2 Glass transition temperatures of MAM modified epoxy polymers. Error bars represent standard error of $\pm 1^{\circ}$C. . . . 188
7.3.3 Variation of tan δ with temperature of M52N MAM modified epoxy polymers. . . . 189

7.4.1 Tensile true stress-true strain curves for M52N and M22N MAM block copolymers. . . . 190
7.4.2 Typical tensile true stress-strain curves for unmodified and MAM modified LD epoxies. . . . 191
7.4.3 Young's moduli of MAM modified LD epoxy. . . . 191
7.4.4 Young's moduli of MAM modified AD epoxy. . . . 192
7.4.5 Tensile true strength, σ_t, of MAM modified epoxy polymers. . . . 192
7.5.1 Compressive true stress-true strain curves for unmodified and 2.5 wt% MAM modified epoxy polymers. . . . 193
7.5.2 Compressive true stress-true strain curves for unmodified and 10 wt% MAM modified epoxy polymers. . . . 194
7.5.3 Transmission optical micrographs, using cross polarised light, of polished specimens loaded to the strain softening region. . . . 195
7.6.1 Fracture toughness and fracture energy of MAM modified LD epoxy. . 196
7.6.2 Fracture toughness and fracture energy of MAM modified AD epoxy. . 196
7.7.1 FEGSEM micrograph of unmodified LD epoxy. . . . 198
7.7.2 FEGSEM micrograph of 2.5 wt% M52N MAM modified epoxy fracture surfaces. . . . 199
7.7.3 FEGSEM micrograph of 10 wt% M52N MAM modified epoxy fracture surfaces. . . . 200
7.7.4 FEGSEM micrograph of hybrid 10N2.5M52N modified LD epoxy fracture surfaces. . . . 201
7.7.5 FEGSEM micrograph of hybrid 10N2.5M52N modified AD epoxy fracture surfaces. . . . 201
7.7.6 FEGSEM micrograph of hybrid 10N10M52N modified LD epoxy fracture surfaces. . . . 202
7.7.7 FEGSEM micrograph of hybrid 10N10M52N modified AD epoxy fracture surfaces. . . . 202
7.7.8 FEGSEM micrograph of 10 wt% M22N MAM modified LD epoxy fracture surfaces. Some worm-like micelles are identified with red arrows. . 203
7.7.9 FEGSEM micrograph of 10 wt% M22N MAM modified AD epoxy fracture surfaces. Some nanocavities are identified with red arrows. . . . 204

8.2.1 Comparison between dispersing using different ultrasonic methods. Agglomerates are identified with red circles. Reproduced from [142]. . . . 210
8.2.2 Transmission optical microscope images of uncured 0.05 wt% XG-H GNP modified epoxies showing dispersion quality after the specified sonication time. Agglomerates are identified with red circles. . . . 211
8.2.3 Characteristic lengths of XG-H GNP in epoxy resin after ultrasonication. 212
8.2.4 Transmission optical microscope images of 0.05 wt% GS GNP modified epoxies showing dispersion quality before and after sonicating. . . . 213
8.2.5 Hot stage investigation of 0.05 wt% GS GNP modified epoxies showing dispersion quality before and after curing. The concentric circles in the background are artifacts from the machined surface of the hot stage. . 214
8.2.6 Fracture surface of 1.0 wt% XG-H GNP modified epoxies showing dispersion quality at different locations of the plate. . . . 214

8.2.7 Fracture surface of 1.0 wt% XG-H-THF GNP modified epoxies showing dispersion quality at different locations of the plate. 215
8.3.1 Particle diameter differential distribution on linear-log scale. 215
8.3.2 Illustration demonstrating errors from LLS method to measure the platelet sizes. l is the size measured using the LLS method. 216
8.3.3 XRD patterns obtained for bulk GNPs. 217
8.3.4 FEGSEM micrographs of GNPs and CNTs after 20 min of ultrasonication in THF solvent and drying in air. 218
8.3.5 FEGSEM micrographs of GNPs showing defects. Wrinkles on the GNPs are identified by the red arrows. 219
8.4.1 XPS survey spectra of bulk GNPs. 221
8.4.2 Typical high resolution XPS C1s spectra of bulk GNPs. 221
8.5.1 Preparation of AFM samples of GNP modified epoxies by microtome. . 223
8.5.2 AFM micrographs of GS GNP in epoxy. 224
8.5.3 AFM micrographs of XG-H GNP in epoxy. 224
8.5.4 AFM micrographs of graphite flakes in epoxy. 225
8.5.5 FEGSEM micrograph of 1.0 wt% XG-H-THF modified epoxy. Regions enclosed in red are large agglomerates and the smaller agglomerates of GNP indicated by red arrows. 225
8.5.6 FEGSEM micrograph of 1.0 wt% XG-H-NMP modified epoxy. 226
8.5.7 FEGSEM micrograph of GNP modified epoxy. 227
8.5.8 FEGSEM micrograph of epoxy modified with 0.5 wt% functionalised GNPs. 228
8.5.9 FEGSEM micrograph of epoxy modified with 1.0 wt% functionalised GNPs. 228
8.5.10 FEGSEM micrograph of epoxy modified with 1.0 wt% functionalised GNPs at higher magnification. 228
8.5.11 FEGSEM micrograph of graphite flake modified epoxy. Regions enclosed in red are large agglomerates. 229
8.5.12 FEGSEM micrograph of COOH functionalised MWCNT modified epoxy. 229
8.6.1 Effect of solvents on the glass transition temperature of the epoxy polymer. 230
8.6.2 Glass transition temperatures for the various GNP modified epoxy polymers. 231
8.7.1 Tensile properties of unmodified and 10 wt% solvent modified epoxies. 232
8.7.2 Typical tensile true stress-strain curves for unmodified and 2 wt% XG-H GNP modified epoxies. 232
8.7.3 Young's modulus for the various GNP modified epoxy polymers. 233
8.7.4 Normalised stress in platelet for various platelet aspect ratios. Reproduced from [289]. 233
8.7.5 Tensile true strength for the various GNP modified epoxy polymers. . . 234
8.7.6 Illustration showing distribution of particulates in unit cell. 235
8.7.7 Predicted tensile strengths compared with XG-H GNP modified epoxies. 237
8.7.8 Tensile properties for functionalised GNP and CNT modified epoxy polymers. 238
8.7.9 Young's modulus of unmodified and functionalised MWCNT modified epoxy polymers. Data for MWCNT reproduced from [117]. 238

8.7.10 Analytical models for Young's moduli of GNP modified epoxy polymers. 239
8.7.11 Variation of predicted moduli with aspect ratio. 240
8.7.12 Variation of predicted moduli with modifier modulus. 241
8.7.13 Variation of volume fraction and predicted moduli with modifier density. 241
8.7.14 Variation of predicted moduli with modifier and matrix Poisson's ratio. 242
8.8.1 Compressive true stress-true strain curves for unmodified and 10 wt% solvent modified epoxy polymers. 243
8.8.2 Compressive true stress-true strain curves for unmodified and 1.0 wt% GNP modified epoxy polymers. 244
8.8.3 Transmission optical micrographs, using cross polarised light, of polished specimens loaded to the strain softening region. 245
8.9.1 Effect of solvents on the fracture properties of the epoxy polymer. . . . 246
8.9.2 Fracture energy, G_{IC}, for the various GNP modified epoxy polymers. . 247
8.9.3 Fracture toughness, K_{IC}, for the various GNP modified epoxy polymers. 247
8.9.4 Fracture toughness and fracture energy of functionalised GNP and CNT modified epoxy polymers. 248
8.9.5 Fracture toughness and fracture energy of functionalised CNT and as-produced MWCNT modified epoxy polymers. Includes data from [117]. 248
8.10.1 FEGSEM micrograph of unmodified epoxy fracture surface. Crack propagation from right to left. 249
8.10.2 FEGSEM micrograph of 1.0 wt% GNP, dispersed in THF, modified epoxy fracture surfaces. Evidence of crack pinning are identified by red arrows. 249
8.10.3 FEGSEM micrograph of 1.0 wt% GNP, dispersed in THF, modified epoxy fracture surfaces. Defects on the XG-M GNPs are identified by the red arrows. 250
8.10.4 FEGSEM micrograph of 1.0 wt% GNP, dispersed in NMP, modified epoxy fracture surfaces. 251
8.10.5 FEGSEM micrograph of 1.0 wt% XG-C GNP modified epoxy fracture surfaces. 251
8.10.6 FEGSEM micrograph of 1.0 wt% GNP-COOH modified epoxy fracture surfaces. Orange arrows indicate limited debonding and void growth. Red arrows indicate limited crack deflection. 252
8.10.7 FEGSEM micrograph of 1.0 wt% GNP-O_2 modified epoxy fracture surfaces. Orange arrows indicate limited debonding and void growth. Red arrows indicate limited crack deflection. 252
8.10.8 FEGSEM micrograph of 1.0 wt% functionalised MWCNT modified epoxy fracture surfaces. Red line and arrow points to where the river lines pass straight through the CNT agglomerates. 253
8.10.9 FEGSEM micrograph of 1.0 wt% GF modified epoxy fracture surfaces. 254
8.11.1 Optimum spacing for numerical integration. 255
8.11.2 Change in relative toughening from crack deflection with Poisson's ratio of the epoxy. 255
8.11.3 Schematic of crack passing through platelet, showing debonding at the interface and subsequent pull-out. 256
8.11.4 Illustration of platelet void growth mechanism. 258

8.11.5 Predicted and measured values of fracture energy for epoxy polymers modified with GNPs dispersed in THF. 259
8.11.6 Predicted and measured values of fracture energy for epoxy polymers modified with GNPs dispersed in NMP. 260

9.2.1 AFM phase micrographs of MX156 CSR and hybrid MX156-NS modified LH epoxy polymer. Reproduced from [20]. 264
9.2.2 AFM phase micrographs of CTBN modified epoxy polymers. Reproduced from [84, 184]. 265
9.2.3 Viscosity as a function of temperature for CTBN rubber and CTBN-NS hybrid modified LD epoxy polymers. 266
9.2.4 Normalised Young's moduli of different epoxy systems for CSR modified epoxies. Includes data from [20, 84]. Solid points (■) are CSR only and open points (□) are CSR-NS hybrid formulations. 268
9.2.5 Normalised Young's modulus predicted using Mori-Tanaka model for different ratios of matrix to particle modulus. 269
9.2.6 Normalised Young's moduli of different epoxy systems for CTBN modified epoxies. Includes data from [84, 184]. Solid points (■) are CTBN only and open points (□) are CTBN-NS hybrid formulations. 269
9.2.7 Normalised fracture energy of different epoxy systems for CSR modified epoxies. Includes data from [20]. Solid points (■) are CSR only and open points (□) are CSR-NS hybrid formulations. 270
9.2.8 Normalised fracture energy of different epoxy systems for CTBN modified epoxies. Includes data from [84, 184]. Solid points (■) are CTBN only and open points (□) are CTBN-NS hybrid formulations. 271
9.2.9 Compressive yield strength as a function of glass transition temperature for the rubber modified epoxy polymers. Includes data from [20, 84, 184].273
9.2.10 Fracture energy as a function of (a) glass transition temperature and (b) compressive yield strength for the rubber modified epoxy polymers. Includes data from [20, 84, 184]. 273
9.3.1 STEM-IN-SEM micrographs of E21 SBM modified piperidine cured DGEBA epoxy. Reproduced from [167]. 274
9.3.2 Area disorder of E21 SBM modified piperidine cured DGEBA epoxy. . 275
9.3.3 AFM phase micrographs of MAM modified LH epoxy polymer. Reproduced from [180]. 276
9.3.4 AFM phase micrographs of MAM modified LM epoxy polymer. Agglomerates of silica nanoparticles identified with red arrows. Reproduced from [180]. 277
9.3.5 AFM phase micrographs of 12 wt% M52N MAM modified LH epoxy polymer. Reproduced from [180]. 277
9.3.6 Viscosity as a function of temperature for 10 wt% E21 and M52N modified LH epoxy resins. 279
9.3.7 Comparison between AFM phase micrographs of M52N MAM modified LD epoxy polymers and Cahn-Hilliard models at t = 10,000. c represents initial concentration of second phase material. 280

9.3.8 Comparison between AFM phase micrographs of CTBN modified LD epoxy polymers and Cahn-Hilliard models at t = 30,000. c represents initial concentration of second phase material. 280
9.3.9 AFM phase micrographs and change in viscosity with temperature of MAM modified AD epoxy polymers. 281
9.3.10 AFM phase micrographs and change in viscosity with temperature of BCP modified LD epoxy polymers. 282
9.3.11 AFM phase micrographs and change in viscosity with temperature of SBM modified LH epoxy polymers. 283
9.3.12 Normalised Young's moduli of different epoxy systems for SBM modified epoxies. 284
9.3.13 Normalised Young's moduli for different epoxy systems for MAM modified epoxies. Includes data from [180]. 284
9.3.14 Normalised fracture energy of different epoxy systems for SBM modified epoxies. 285
9.3.15 Normalised fracture energy of different epoxy systems for MAM modified epoxies. Includes data from [180]. 285
9.4.1 Normalised Young's moduli of rubber and BCP modified LD epoxies. . 287
9.4.2 Comparison of fracture energies of rubber and BCP modified LD epoxies. Solid points (■) are rubber or BCP only and open points (□) are the hybrid formulations. 288
9.4.3 Comparison of fracture energies of rubber and BCP modified AD epoxies. Solid points (■) are rubber or BCP only and open points (□) are the hybrid formulations. 289
9.4.4 Comparison of fracture energies of rubber and BCP modified LH epoxies. Solid points (■) are rubber or BCP only and open points (□) are the hybrid formulations. 290
9.4.5 Comparison of fracture energies of modified LV epoxies. Solid points (■) are rubber only and open points (□) are the hybrid formulations. . 291
9.4.6 Change in compressive yield strength with modifier content for LD epoxy system. 292

List of Tables

2.2.1 Properties of the thermoplastics used to modify a piperidine cured DGEBA epoxy polymer [38]. 9
2.2.2 Evolution of morphology with time at different volume fractions, v_f. . 17
2.2.3 Evolution of morphology with time at different values of mobility, M, for an initial concentration of $v_f = 0.5$. 20
2.2.4 Evolution of morphology with time at different values of energy barrier, A, for an initial concentration of $v_f = 0.5$. 22
2.2.5 Evolution of morphology with time at different values of initial concentration, v_f. 24

3.2.1 Formulation of low viscosity epoxy polymer. 66
3.2.2 Summary of epoxy systems used in this study. 67
3.3.1 Various carbon-based modifiers used in this study. Values quoted are from manufacturer data sheets [139, 235–240]. 72
3.3.2 Functionalities of HDPlas modifiers. 73
3.3.3 Summary of modifiers used in this study. 75

5.1.1 Summary of CSR and CTBN formulations used in this chapter. 100
5.2.1 Comparison of theoretical and measured values of volume fraction for CSR and NS modified epoxies. 102
5.2.2 Mean particle radius of CTBN rubber particles for LD and AD epoxy systems. 104
5.5.1 Compressive true yield stress, σ_{yc}, Tensile true yield stress, σ_{yt}, and σ_{yt} calculated using Equation 4.25 for the unmodified epoxy polymers. . . 114
5.6.1 Fracture toughness, K_{IC}, and fracture energy, G_{IC} of unmodified and 10 wt% silica nanoparticle modified epoxy polymers [84]. 116
5.8.1 Parameters used in modelling fracture energy. 123
5.8.2 Predicted and measured values of fracture energy for CSR modified epoxy polymers. 124
5.8.3 Predicted and measured values of fracture energy for CTBN modified epoxy polymers. 126

6.1.1 Summary of SBM formulations used in this chapter. 131
6.2.1 Mean particle radius and characteristic lengths of E21 SBM phases in epoxy. 134
6.2.2 Formulations of SBM block copolymer modified epoxies. 136
6.2.3 Measured values of volume fraction from AFM phase images. 136

6.2.4 Mean particle radius and characteristic lengths of E41 SBM phases in epoxy. . . . 141
6.4.1 Young's modulus, E_t, yield stress, σ_y, yield strain, ε_y, fracture strength, σ_f, and fracture strain, ε_f for E21 and E41 SBM block copolymers. . . 146
6.6.1 Fracture energy, G_{IC}, change in fracture energy, ΔG_{IC}, and synergy, $G_{synergy}$, for hybrid E21 SBM-NS modified epoxies. . . . 154
6.8.1 Characteristic lengths of E21 SBM phase in modified LD and AD epoxies. 166
6.8.2 Characteristic lengths of E21 SBM phase in modified LH and LV epoxies. 166
6.8.3 Characteristic lengths of E41 SBM phase in modified LD and AD epoxies. 167
6.8.4 Characteristic lengths of E41 SBM phase in modified LH and LV epoxies. 167
6.9.1 Parameters used in modelling fracture energy. . . . 167
6.9.2 Predicted and measured values of fracture energy for E21 modified epoxy polymers. . . . 168
6.9.3 Predicted and measured values of fracture energy for E41 modified epoxy polymers. . . . 169
6.10.1 Interlaminar shear strength, τ_{SBS}, flexural modulus, E_f, and propagation fracture energy, $G_{IC(composite)}$, for E21 SBM modified LH CFRP. . 172

7.1.1 Summary of MAM formulations used in this chapter. . . . 180
7.2.1 Mean particle radius and characteristic lengths of M52N MAM phases in epoxy. . . . 182
7.2.2 Mean radius of epoxy inclusions in M52N MAM modified LD and AD epoxy polymers. . . . 183
7.2.3 Comparison of theoretical and measured values of volume fraction. . . 185
7.4.1 Young's modulus, E_t, yield stress, σ_y, yield strain, ε_y, fracture strength, σ_f, and fracture strain, ε_f for M52N and M22N MAM block copolymers. 190
7.6.1 Fracture energy, G_{IC}, change in fracture energy, ΔG_{IC}, and synergy, $G_{synergy}$, for hybrid M52N-NS modified epoxies. . . . 197
7.8.1 Characteristic lengths of M52N MAM phase in modified LD and AD epoxies. . . . 205

8.1.1 Summary of GNP formulations used in this chapter. . . . 209
8.3.1 d-spacing, FWHM and crystal size measurements from XRD analysis. . 217
8.3.2 Modifier size measurements from FEGSEM micrographs. . . . 220
8.4.1 Atomic percentage of GNP surface element composition. . . . 222
8.11.1 Parameters used in modelling fracture energy of GNP modified epoxies. 258

9.2.1 Mean particle radius of CTBN rubber particles. . . . 266
9.4.1 Summary of glass transition temperature, Young's modulus and fracture energy for LD epoxy. Hybrid materials refer to the further addition of 10 wt% silica nanoparticles. . . . 293
9.5.1 Comparison of glass transition temperatures, Young's modulus and fracture energy of various modifiers in the LH epoxy. The epoxy used in [124] is a diethyltoluenediamine cured DGEBA epoxy. L represents lateral size, length or characteristic length as appropriate. Some noteworthy values have been highlighted in bold. . . . 296

11.3.1 Glass transition temperature, Young's modulus, tensile yield stress, fracture toughness and fracture energy for MX551 CSR modified low viscosity epoxy . . . 347
11.3.2 Glass transition temperature, Young's modulus, tensile yield stress, fracture toughness and fracture energy for CTBN modified low viscosity epoxy . . . 347
11.3.3 Glass transition temperature, Young's modulus, tensile yield stress, fracture toughness and fracture energy for NS modified low viscosity epoxy . . . 348
11.3.4 Glass transition temperature, Young's modulus, tensile yield stress, fracture toughness and fracture energy for MX156 CSR modified polyether-amine cured DGEBA . . . 348
11.3.5 Glass transition temperature, Young's modulus, tensile yield stress, fracture toughness and fracture energy for CTBN modified polyether-amine cured DGEBA . . . 348
11.3.6 Glass transition temperature, Young's modulus, tensile yield stress, fracture toughness and fracture energy for MX156 CSR modified polyether-amine cured DGEBA/F . . . 349
11.3.7 Glass transition temperature, Young's modulus, tensile yield stress, fracture toughness and fracture energy for CTBN modified polyether-amine cured DGEBA/F . . . 349
11.3.8 Glass transition temperature, Young's modulus, tensile yield stress, fracture toughness and fracture energy for E21 modified polyether-amine cured DGEBA . . . 350
11.3.9 Glass transition temperature, Young's modulus, tensile yield stress, fracture toughness and fracture energy for E41 modified polyether-amine cured DGEBA . . . 350
11.3.10 Glass transition temperature, Young's modulus, tensile yield stress, fracture toughness and fracture energy for E21 modified polyether-amine cured DGEBA/F . . . 350
11.3.11 Glass transition temperature, Young's modulus, tensile yield stress, fracture toughness and fracture energy for E41 modified polyether-amine cured DGEBA/F . . . 351
11.3.12 Glass transition temperature, Young's modulus, tensile yield stress, fracture toughness and fracture energy for E21 modified anhydride cured DGEBA . . . 351
11.3.13 Glass transition temperature, Young's modulus, tensile yield stress, fracture toughness and fracture energy for E41 modified anhydride cured DGEBA . . . 351
11.3.14 Glass transition temperature, Young's modulus, tensile yield stress, fracture toughness and fracture energy for E21 modified low viscosity epoxy . . . 352
11.3.15 Glass transition temperature, Young's modulus, tensile yield stress, fracture toughness and fracture energy for E41 modified low viscosity epoxy . . . 352

11.3.16 Glass transition temperature, Young's modulus, tensile yield stress, fracture toughness and fracture energy for M52N modified polyetheramine cured DGEBA . . . 352
11.3.17 Glass transition temperature, Young's modulus, tensile yield stress, fracture toughness and fracture energy for M22N modified polyetheramine cured DGEBA . . . 352
11.3.18 Glass transition temperature, Young's modulus, tensile yield stress, fracture toughness and fracture energy for M52N modified polyetheramine cured DGEBA/F . . . 353
11.3.19 Glass transition temperature, Young's modulus, tensile yield stress, fracture toughness and fracture energy for M22N modified polyetheramine cured DGEBA/F . . . 353
11.3.20 Glass transition temperature, Young's modulus, tensile yield stress, fracture toughness and fracture energy for anhydride cured DGEBA with solvents . . . 353
11.3.21 Glass transition temperature, Young's modulus, tensile yield stress, fracture toughness and fracture energy for GS-THF anhydride cured DGEBA . . . 353
11.3.22 Glass transition temperature, Young's modulus, tensile yield stress, fracture toughness and fracture energy for GS-NMP anhydride cured DGEBA . . . 354
11.3.23 Glass transition temperature, Young's modulus, tensile yield stress, fracture toughness and fracture energy for XG-H-THF anhydride cured DGEBA . . . 354
11.3.24 Glass transition temperature, Young's modulus, tensile yield stress, fracture toughness and fracture energy for XG-M-THF anhydride cured DGEBA . . . 354
11.3.25 Glass transition temperature, Young's modulus, tensile yield stress, fracture toughness and fracture energy for XG-C-THF anhydride cured DGEBA . . . 354
11.3.26 Glass transition temperature, Young's modulus, tensile yield stress, fracture toughness and fracture energy for XG-H-NMP anhydride cured DGEBA . . . 355
11.3.27 Glass transition temperature, Young's modulus, tensile yield stress, fracture toughness and fracture energy for XG-M-NMP anhydride cured DGEBA . . . 355
11.3.28 Glass transition temperature, Young's modulus, tensile yield stress, fracture toughness and fracture energy for XG-C-NMP anhydride cured DGEBA . . . 355
11.3.29 Glass transition temperature, Young's modulus, tensile yield stress, fracture toughness and fracture energy for GF anhydride cured DGEBA 356
11.3.30 Glass transition temperature, Young's modulus, tensile yield stress, fracture toughness and fracture energy for CNT-COOH anhydride cured DGEBA . . . 356

11.3.31 Glass transition temperature, Young's modulus, tensile yield stress, fracture toughness and fracture energy for GNP-COOH anhydride cured DGEBA . . . 356
11.3.32 Glass transition temperature, Young's modulus, tensile yield stress, fracture toughness and fracture energy for GNP-O2 anhydride cured DGEBA . . . 356
11.3.33 Compressive modulus, compressive true yield stress, compressive true yield strain, failure stress and failure strain for MX551 CSR modified low viscosity epoxy . . . 357
11.3.34 Compressive modulus, compressive true yield stress, compressive true yield strain, failure stress and failure strain for CTBN modified low viscosity epoxy . . . 357
11.3.35 Compressive modulus, compressive true yield stress, compressive true yield strain, failure stress and failure strain for MX156 CSR modified polyether-amine cured DGEBA epoxy . . . 358
11.3.36 Compressive modulus, compressive true yield stress, compressive true yield strain, failure stress and failure strain for CTBN modified polyether-amine cured DGEBA epoxy . . . 358
11.3.37 Compressive modulus, compressive true yield stress, compressive true yield strain, failure stress and failure strain for MX156 CSR modified polyether-amine cured DGEBA/F epoxy . . . 358
11.3.38 Compressive modulus, compressive true yield stress, compressive true yield strain, failure stress and failure strain for CTBN modified polyether-amine cured DGEBA/F epoxy . . . 359
11.3.39 Compressive modulus, compressive true yield stress, compressive true yield strain, failure stress and failure strain for E21 SBM modified polyether-amine cured DGEBA epoxy . . . 359
11.3.40 Compressive modulus, compressive true yield stress, compressive true yield strain, failure stress and failure strain for E41 SBM modified polyether-amine cured DGEBA epoxy . . . 359
11.3.41 Compressive modulus, compressive true yield stress, compressive true yield strain, failure stress and failure strain for E21 SBM modified polyether-amine cured DGEBA/F epoxy . . . 360
11.3.42 Compressive modulus, compressive true yield stress, compressive true yield strain, failure stress and failure strain for E41 SBM modified polyether-amine cured DGEBA/F epoxy . . . 360
11.3.43 Compressive modulus, compressive true yield stress, compressive true yield strain, failure stress and failure strain for E21 SBM modified anhydride cured DGEBA epoxy . . . 360
11.3.44 Compressive modulus, compressive true yield stress, compressive true yield strain, failure stress and failure strain for E41 SBM modified anhydride cured DGEBA epoxy . . . 360
11.3.45 Compressive modulus, compressive true yield stress, compressive true yield strain, failure stress and failure strain for E21 SBM modified low viscosity epoxy . . . 361

11.3.46 Compressive modulus, compressive true yield stress, compressive true yield strain, failure stress and failure strain for E41 SBM modified low viscosity epoxy . . . 361
11.3.47 Compressive modulus, compressive true yield stress, compressive true yield strain, failure stress and failure strain for M52N MAM modified polyether-amine cured DGEBA epoxy . . . 361
11.3.48 Compressive modulus, compressive true yield stress, compressive true yield strain, failure stress and failure strain for M22N MAM modified polyether-amine cured DGEBA epoxy . . . 361
11.3.49 Compressive modulus, compressive true yield stress, compressive true yield strain, failure stress and failure strain for M52N MAM modified polyether-amine cured DGEBA/F epoxy . . . 362
11.3.50 Compressive modulus, compressive true yield stress, compressive true yield strain, failure stress and failure strain for M22N MAM modified polyether-amine cured DGEBA/F epoxy . . . 362
11.3.51 Compressive modulus, compressive true yield stress, compressive true yield strain, failure stress and failure strain for anhydride cured DGEBA epoxy with solvents . . . 362
11.3.52 Compressive modulus, compressive true yield stress, compressive true yield strain, failure stress and failure strain for GS-THF modified anhydride cured DGEBA epoxy . . . 362
11.3.53 Compressive modulus, compressive true yield stress, compressive true yield strain, failure stress and failure strain for GS-NMP modified anhydride cured DGEBA epoxy . . . 363
11.3.54 Compressive modulus, compressive true yield stress, compressive true yield strain, failure stress and failure strain for XG-H-THF modified anhydride cured DGEBA epoxy . . . 363
11.3.55 Compressive modulus, compressive true yield stress, compressive true yield strain, failure stress and failure strain for XG-H-NMP modified anhydride cured DGEBA epoxy . . . 363
11.3.56 Compressive modulus, compressive true yield stress, compressive true yield strain, failure stress and failure strain for XG-M-THF modified anhydride cured DGEBA epoxy . . . 364
11.3.57 Compressive modulus, compressive true yield stress, compressive true yield strain, failure stress and failure strain for XG-M-NMP modified anhydride cured DGEBA epoxy . . . 364
11.3.58 Compressive modulus, compressive true yield stress, compressive true yield strain, failure stress and failure strain for XG-C-THF modified anhydride cured DGEBA epoxy . . . 364
11.3.59 Compressive modulus, compressive true yield stress, compressive true yield strain, failure stress and failure strain for XG-C-NMP modified anhydride cured DGEBA epoxy . . . 364
11.3.60 Compressive modulus, compressive true yield stress, compressive true yield strain, failure stress and failure strain for GF modified anhydride cured DGEBA epoxy . . . 365

11.3.61 Compressive modulus, compressive true yield stress, compressive true yield strain, failure stress and failure strain for CNT-COOH modified anhydride cured DGEBA epoxy 365
11.3.62 Compressive modulus, compressive true yield stress, compressive true yield strain, failure stress and failure strain for GNP-COOH modified anhydride cured DGEBA epoxy 365
11.3.63 Compressive modulus, compressive true yield stress, compressive true yield strain, failure stress and failure strain for GNP-O2 modified anhydride cured DGEBA epoxy 365

Appendix A

Mechanical and fracture properties of epoxy polymers

The mechanical and fracture properties of the modified epoxy polymers are summarised in this Appendix.

Table 11.3.1: Glass transition temperature, Young's modulus, tensile yield stress, fracture toughness and fracture energy for MX551 CSR modified low viscosity epoxy

MX551	T_g (°C)	E_t (GPa)	σ_y (MPa)	K_{IC} (MPa $m^{1/2}$)	G_{IC} (kJ/m^2)
Unmodified	196	2.9 ± 0.0	32 ± 3	0.5 ± 0.0	0.05 ± 0.01
2.5C	196	2.7 ± 0.0	56 ± 5	0.6 ± 0.0	0.10 ± 0.01
5C	201	2.6 ± 0.0	60 ± 3	0.8 ± 0.1	0.18 ± 0.01
7.5C	197	2.5 ± 0.0	58 ± 3	0.8 ± 0.1	0.20 ± 0.01
10C	198	2.4 ± 0.0	54 ± 6	0.9 ± 0.1	0.25 ± 0.02

Table 11.3.2: Glass transition temperature, Young's modulus, tensile yield stress, fracture toughness and fracture energy for CTBN modified low viscosity epoxy

CTBN	T_g (°C)	E_t (GPa)	σ_y (MPa)	K_{IC} (MPa $m^{1/2}$)	G_{IC} (kJ/m^2)
Unmodified	196	2.9 ± 0.0	32 ± 3	0.5 ± 0.0	0.05 ± 0.01
2.5R	202	2.7 ± 0.0	56 ± 4	0.5 ± 0.0	0.08 ± 0.01
5R	199	2.6 ± 0.0	52 ± 5	0.6 ± 0.0	0.12 ± 0.02
7.5R	193	2.4 ± 0.1	50 ± 3	0.8 ± 0.0	0.19 ± 0.03
10R	192	2.3 ± 0.0	51 ± 4	0.8 ± 0.0	0.23 ± 0.02
3.4N7.5R	197	2.6 ± 0.0	57 ± 2	0.7 ± 0.0	0.19 ± 0.02
10N9R	193	2.6 ± 0.0	54 ± 2	0.9 ± 0.0	0.26 ± 0.02

Table 11.3.3: Glass transition temperature, Young's modulus, tensile yield stress, fracture toughness and fracture energy for NS modified low viscosity epoxy

NS	T_g (°C)	E_t (GPa)	σ_y (MPa)	K_{IC} (MPa $m^{1/2}$)	G_{IC} (kJ/m^2)
Unmodified	196	2.9 ± 0.0	32 ± 3	0.5 ± 0.0	0.05 ± 0.01
2.5%	202	3.0 ± 0.0	34 ± 1	0.6 ± 0.0	0.06 ± 0.00
5.0%	201	3.1 ± 0.1	37 ± 4	0.7 ± 0.0	0.07 ± 0.01
7.5%	202	3.2 ± 0.0	41 ± 3	0.8 ± 0.0	0.09 ± 0.01
10.0%	198	3.2 ± 0.1	43 ± 3	0.8 ± 0.0	0.10 ± 0.00

Table 11.3.4: Glass transition temperature, Young's modulus, tensile yield stress, fracture toughness and fracture energy for MX156 CSR modified polyether-amine cured DGEBA

MX156	T_g (°C)	E_t (GPa)	σ_y (MPa)	K_{IC} (MPa $m^{1/2}$)	G_{IC} (kJ/m^2)
Unmodified	96	3.0 ± 0.0	66 ± 0	0.9 ± 0.1	0.2 ± 0.0
1C	98	2.9 ± 0.0	63 ± 2	2.1 ± 0.1	1.4 ± 0.0
3C	98	2.8 ± 0.1	61 ± 1	2.2 ± 0.0	1.6 ± 0.0
5C	95	2.7 ± 0.0	60 ± 0	2.1 ± 0.1	1.9 ± 0.1
7C	98	2.6 ± 0.0	58 ± 0	2.0 ± 0.0	1.6 ± 0.0
9C	94	2.6 ± 0.1	54 ± 0	1.9 ± 0.0	1.6 ± 0.0
10N1C	97	3.4 ± 0.1	64 ± 1	2.1 ± 0.0	1.3 ± 0.0
10N3C	96	3.2 ± 0.0	62 ± 1	2.3 ± 0.1	1.7 ± 0.0
10N5C	94	3.1 ± 0.0	60 ± 0	2.3 ± 0.0	2.0 ± 0.0
10N7C	96	2.9 ± 0.1	58 ± 0	2.2 ± 0.0	1.9 ± 0.0
10N9C	95	2.9 ± 0.0	55 ± 0	2.0 ± 0.0	1.6 ± 0.0

Table 11.3.5: Glass transition temperature, Young's modulus, tensile yield stress, fracture toughness and fracture energy for CTBN modified polyether-amine cured DGEBA

CTBN	T_g (°C)	E_t (GPa)	σ_y (MPa)	K_{IC} (MPa $m^{1/2}$)	G_{IC} (kJ/m^2)
Unmodified	96	3.0 ± 0.0	66 ± 0	0.9 ± 0.1	0.2 ± 0.0
1R	96	2.8 ± 0.1	59 ± 1	2.0 ± 0.0	1.2 ± 0.1
3R	95	2.7 ± 0.2	59 ± 0	2.4 ± 0.0	2.0 ± 0.1
5R	92	2.6 ± 0.0	57 ± 0	2.2 ± 0.1	2.1 ± 0.0
7R	91	2.6 ± 0.1	54 ± 0	2.2 ± 0.1	2.1 ± 0.1
9R	92	2.3 ± 0.0	48 ± 1	2.1 ± 0.1	2.1 ± 0.1
10N1R	96	3.3 ± 0.1	64 ± 0	2.3 ± 0.1	1.5 ± 0.1
10N3R	92	3.1 ± 0.1	61 ± 1	2.6 ± 0.0	2.1 ± 0.1
10N5R	89	3.0 ± 0.0	58 ± 0	2.6 ± 0.0	2.2 ± 0.1
10N7R	85	3.0 ± 0.1	54 ± 0	2.6 ± 0.1	2.5 ± 0.1
10N9R	92	2.6 ± 0.0	53 ± 0	2.3 ± 0.1	2.3 ± 0.0

Table 11.3.6: Glass transition temperature, Young's modulus, tensile yield stress, fracture toughness and fracture energy for MX156 CSR modified polyether-amine cured DGEBA/F

MX156	T_g (°C)	E_t (GPa)	σ_y (MPa)	K_{IC} (MPa $m^{1/2}$)	G_{IC} (kJ/m^2)
Unmodified	78	3.6 ± 0.1	79 ± 1	0.9 ± 0.0	0.2 ± 0.0
1C	83	3.5 ± 0.1	74 ± 3	1.2 ± 0.1	0.3 ± 0.0
3C	83	3.3 ± 0.1	73 ± 1	2.1 ± 0.1	1.1 ± 0.1
5C	80	3.3 ± 0.1	68 ± 1	2.0 ± 0.0	1.3 ± 0.1
7C	86	3.0 ± 0.1	64 ± 1	2.2 ± 0.0	1.8 ± 0.1
9C	85	2.9 ± 0.0	60 ± 0	2.3 ± 0.0	2.0 ± 0.0
10N1C	84	3.8 ± 0.2	75 ± 0	1.7 ± 0.0	0.6 ± 0.0
10N3C	86	3.7 ± 0.1	70 ± 1	2.5 ± 0.0	1.6 ± 0.0
10N5C	81	3.6 ± 0.1	67 ± 0	2.5 ± 0.0	1.9 ± 0.0
10N7C	85	3.5 ± 0.1	63 ± 0	2.5 ± 0.1	2.0 ± 0.0
10N9C	87	3.2 ± 0.1	60 ± 1	2.3 ± 0.0	1.9 ± 0.1

Table 11.3.7: Glass transition temperature, Young's modulus, tensile yield stress, fracture toughness and fracture energy for CTBN modified polyether-amine cured DGEBA/F

CTBN	T_g (°C)	E_t (GPa)	σ_y (MPa)	K_{IC} (MPa $m^{1/2}$)	G_{IC} (kJ/m^2)
Unmodified	78	3.6 ± 0.1	79 ± 1	0.9 ± 0.0	0.2 ± 0.0
1R	80	3.4 ± 0.1	71 ± 2	1.3 ± 0.1	0.4 ± 0.0
3R	83	3.2 ± 0.1	70 ± 0	2.0 ± 0.1	1.0 ± 0.0
5R	74	3.1 ± 0.1	67 ± 1	2.0 ± 0.0	1.2 ± 0.1
7R	74	3.0 ± 0.1	64 ± 0	2.1 ± 0.1	1.8 ± 0.0
9R	74	2.7 ± 0.1	57 ± 1	2.5 ± 0.1	2.9 ± 0.1
10N1R	86	3.9 ± 0.1	73 ± 0	2.0 ± 0.0	0.8 ± 0.0
10N3R	85	3.7 ± 0.1	68 ± 1	2.8 ± 0.1	2.1 ± 0.0
10N5R	78	3.4 ± 0.0	66 ± 0	2.7 ± 0.1	2.2 ± 0.0
10N7R	79	3.3 ± 0.0	61 ± 1	2.8 ± 0.1	3.0 ± 0.1
10N9R	80	3.0 ± 0.1	58 ± 1	2.8 ± 0.0	3.1 ± 0.1

Table 11.3.8: Glass transition temperature, Young's modulus, tensile yield stress, fracture toughness and fracture energy for E21 modified polyether-amine cured DGEBA

E21	T_g (°C)	E_t (GPa)	σ_y (MPa)	K_{IC} (MPa $m^{1/2}$)	G_{IC} (kJ/m^2)
Unmodified	96	3.0 ± 0.0	66 ± 0	0.9 ± 0.1	0.2 ± 0.0
0.5%	95	2.9 ± 0.0	60 ± 0	2.0 ± 0.1	1.2 ± 0.1
1.0%	95	2.9 ± 0.0	62 ± 1	2.3 ± 0.1	1.8 ± 0.1
2.5%	96	2.9 ± 0.0	64 ± 1	2.5 ± 0.1	2.3 ± 0.1
5.0%	95	2.8 ± 0.0	62 ± 0	2.6 ± 0.0	2.8 ± 0.1
7.5%	96	2.7 ± 0.0	59 ± 0	2.7 ± 0.1	3.0 ± 0.1
10.0%	96	2.6 ± 0.0	56 ± 1	2.7 ± 0.0	3.4 ± 0.1
10N2.5E21	94	3.1 ± 0.0	58 ± 0	2.5 ± 0.1	2.1 ± 0.1
10N10E21	89	2.9 ± 0.0	51 ± 1	3.2 ± 0.1	4.5 ± 0.1

Table 11.3.9: Glass transition temperature, Young's modulus, tensile yield stress, fracture toughness and fracture energy for E41 modified polyether-amine cured DGEBA

E41	T_g (°C)	E_t (GPa)	σ_y (MPa)	K_{IC} (MPa $m^{1/2}$)	G_{IC} (kJ/m^2)
Unmodified	96	3.0 ± 0.0	66 ± 0	0.9 ± 0.1	0.2 ± 0.0
1.0%	94	2.9 ± 0.0	62 ± 0	1.3 ± 0.1	0.5 ± 0.0
2.5%	96	2.9 ± 0.0	65 ± 0	1.9 ± 0.0	1.0 ± 0.1
5.0%	96	2.9 ± 0.0	61 ± 4	2.0 ± 0.1	1.4 ± 0.1
7.5%	96	2.9 ± 0.1	59 ± 4	1.8 ± 0.1	1.2 ± 0.1
10.0%	96	2.8 ± 0.1	55 ± 4	1.9 ± 0.0	1.2 ± 0.1

Table 11.3.10: Glass transition temperature, Young's modulus, tensile yield stress, fracture toughness and fracture energy for E21 modified polyether-amine cured DGEBA/F

E21	T_g (°C)	E_t (GPa)	σ_y (MPa)	K_{IC} (MPa $m^{1/2}$)	G_{IC} (kJ/m^2)
Unmodified	78	3.6 ± 0.1	79 ± 1	0.9 ± 0.0	0.2 ± 0.0
2.5%	79	3.4 ± 0.0	71 ± 1	2.1 ± 0.1	1.1 ± 0.1
5.0%	78	3.2 ± 0.1	67 ± 0	2.7 ± 0.1	2.8 ± 0.1
7.5%	78	3.1 ± 0.0	63 ± 1	2.8 ± 0.1	3.0 ± 0.1
10.0%	76	3.0 ± 0.0	58 ± 2	2.9 ± 0.1	3.1 ± 0.1
10N2.5E21	89	3.4 ± 0.0	64 ± 0	2.8 ± 0.1	2.3 ± 0.1
10N10E21	81	3.2 ± 0.1	50 ± 3	3.1 ± 0.1	3.3 ± 0.0

Table 11.3.11: Glass transition temperature, Young's modulus, tensile yield stress, fracture toughness and fracture energy for E41 modified polyether-amine cured DGEBA/F

E41	T_g (°C)	E_t (GPa)	σ_y (MPa)	K_{IC} (MPa $m^{1/2}$)	G_{IC} (kJ/m^2)
Unmodified	78	3.6 ± 0.1	79 ± 1	0.9 ± 0.0	0.2 ± 0.0
2.5%	79	3.4 ± 0.0	71 ± 2	1.5 ± 0.1	0.5 ± 0.0
5.0%	78	3.4 ± 0.1	66 ± 1	1.5 ± 0.1	0.6 ± 0.0
7.5%	76	3.3 ± 0.0	49 ± 11	1.3 ± 0.1	0.4 ± 0.0
10.0%	80	3.2 ± 0.0	59 ± 2	1.3 ± 0.1	0.4 ± 0.0

Table 11.3.12: Glass transition temperature, Young's modulus, tensile yield stress, fracture toughness and fracture energy for E21 modified anhydride cured DGEBA

E21	T_g (°C)	E_t (GPa)	σ_y (MPa)	K_{IC} (MPa $m^{1/2}$)	G_{IC} (kJ/m^2)
Unmodified	157	2.9 ± 0.1	86 ± 0	0.6 ± 0.0	0.1 ± 0.0
2.5%	157	2.8 ± 0.1	69 ± 9	0.8 ± 0.0	0.2 ± 0.0
5.0%	158	2.6 ± 0.1	62 ± 5	1.0 ± 0.0	0.3 ± 0.0
7.5%	158	2.5 ± 0.0	58 ± 2	1.1 ± 0.1	0.4 ± 0.0
10.0%	157	2.4 ± 0.1	45 ± 3	1.2 ± 0.0	0.4 ± 0.0
15.0%	160	2.0 ± 0.0	32 ± 3	1.2 ± 0.0	0.5 ± 0.0
10N10E21	154	2.5 ± 0.0	26 ± 7	0.9 ± 0.0	0.2 ± 0.0

Table 11.3.13: Glass transition temperature, Young's modulus, tensile yield stress, fracture toughness and fracture energy for E41 modified anhydride cured DGEBA

E41	T_g (°C)	E_t (GPa)	σ_y (MPa)	K_{IC} (MPa $m^{1/2}$)	G_{IC} (kJ/m^2)
Unmodified	157	2.9 ± 0.1	86 ± 0	0.6 ± 0.0	0.1 ± 0.0
2.5%	156	2.9 ± 0.1	79 ± 4	0.9 ± 0.1	0.2 ± 0.0
5.0%	157	2.9 ± 0.1	58 ± 5	0.8 ± 0.1	0.2 ± 0.0
7.5%	159	2.8 ± 0.0	68 ± 6	0.9 ± 0.0	0.2 ± 0.0
10.0%	158	2.6 ± 0.1	31 ± 3	1.7 ± 0.0	0.6 ± 0.1
15.0%	157	2.7 ± 0.0	22 ± 2	1.7 ± 0.1	1.0 ± 0.0

Table 11.3.14: Glass transition temperature, Young's modulus, tensile yield stress, fracture toughness and fracture energy for E21 modified low viscosity epoxy

E21	T_g (°C)	E_t (GPa)	σ_y (MPa)	K_{IC} (MPa $m^{1/2}$)	G_{IC} (kJ/m^2)
Unmodified	196	2.9 ± 0.0	32 ± 3	0.5 ± 0.0	0.1 ± 0.0
2.5%	188	2.7 ± 0.1	50 ± 10	0.6 ± 0.0	0.1 ± 0.0
5.0%	204	2.4 ± 0.1	33 ± 2	0.8 ± 0.0	0.2 ± 0.0
7.5%	207	2.1 ± 0.1	24 ± 1	1.2 ± 0.1	0.4 ± 0.0
10.0%	206	2.1 ± 0.1	18 ± 1	1.2 ± 0.1	0.5 ± 0.0

Table 11.3.15: Glass transition temperature, Young's modulus, tensile yield stress, fracture toughness and fracture energy for E41 modified low viscosity epoxy

E41	T_g (°C)	E_t (GPa)	σ_y (MPa)	K_{IC} (MPa $m^{1/2}$)	G_{IC} (kJ/m^2)
Unmodified	196	2.9 ± 0.0	32 ± 3	0.5 ± 0.0	0.1 ± 0.0
2.5%	207	2.8 ± 0.1	47 ± 4	0.6 ± 0.0	0.1 ± 0.0
5.0%	204	2.7 ± 0.1	53 ± 4	0.6 ± 0.0	0.1 ± 0.0
7.5%	204	2.7 ± 0.1	54 ± 9	0.6 ± 0.0	0.1 ± 0.0
10.0%	211	2.2 ± 0.1	11 ± 1	-	-

Table 11.3.16: Glass transition temperature, Young's modulus, tensile yield stress, fracture toughness and fracture energy for M52N modified polyether-amine cured DGEBA

M52N	T_g (°C)	E_t (GPa)	σ_y (MPa)	K_{IC} (MPa $m^{1/2}$)	G_{IC} (kJ/m^2)
Unmodified	96	3.0 ± 0.0	66 ± 0	0.9 ± 0.1	0.2 ± 0.0
1.0%	96	3.0 ± 0.1	64 ± 0	1.6 ± 0.1	0.8 ± 0.1
2.5%	97	3.0 ± 0.0	65 ± 1	2.1 ± 0.0	1.6 ± 0.1
5.0%	93	2.9 ± 0.1	62 ± 0	2.3 ± 0.0	2.2 ± 0.1
7.5%	95	2.8 ± 0.1	56 ± 0	2.2 ± 0.4	1.8 ± 0.1
10.0%	95	2.6 ± 0.0	51 ± 1	2.3 ± 0.0	2.2 ± 0.1
20.0%	98	2.1 ± 0.0	37 ± 1	2.2 ± 0.0	3.0 ± 0.1
10N2.5M52N	96	3.3 ± 0.1	66 ± 1	2.2 ± 0.0	1.5 ± 0.1
10N7.5M52N	95	3.0 ± 0.0	53 ± 0	2.6 ± 0.0	2.5 ± 0.1
10N10M52N	95	2.9 ± 0.0	52 ± 0	2.6 ± 0.0	2.7 ± 0.1

Table 11.3.17: Glass transition temperature, Young's modulus, tensile yield stress, fracture toughness and fracture energy for M22N modified polyether-amine cured DGEBA

M22N	T_g (°C)	E_t (GPa)	σ_y (MPa)	K_{IC} (MPa $m^{1/2}$)	G_{IC} (kJ/m^2)
Unmodified	96	3.0 ± 0.0	66 ± 0	0.9 ± 0.1	0.2 ± 0.0
2.5%	93	3.0 ± 0.1	65 ± 0	1.7 ± 0.0	0.9 ± 0.1
5.0%	96	2.9 ± 0.0	65 ± 0	1.7 ± 0.1	0.9 ± 0.1
7.5%	96	2.9 ± 0.0	63 ± 1	1.7 ± 0.0	0.9 ± 0.1
10.0%	96	2.8 ± 0.0	63 ± 0	1.6 ± 0.0	0.8 ± 0.1

Table 11.3.18: Glass transition temperature, Young's modulus, tensile yield stress, fracture toughness and fracture energy for M52N modified polyether-amine cured DGEBA/F

M52N	T_g (°C)	E_t (GPa)	σ_y (MPa)	K_{IC} (MPa $m^{1/2}$)	G_{IC} (kJ/m^2)
Unmodified	78	3.6 ± 0.1	79 ± 1	0.8 ± 0.1	0.2 ± 0.0
2.5%	78	3.5 ± 0.1	75 ± 1	1.4 ± 0.1	0.5 ± 0.1
5.0%	81	3.3 ± 0.0	70 ± 1	2.0 ± 0.1	1.0 ± 0.1
7.5%	83	3.0 ± 0.1	59 ± 1	2.0 ± 0.1	1.3 ± 0.1
10.0%	82	2.9 ± 0.1	53 ± 0	2.0 ± 0.0	1.5 ± 0.1
10N2.5M52N	83	3.8 ± 0.0	76 ± 1	2.0 ± 0.1	0.9 ± 0.1
10N10M52N	81	3.3 ± 0.0	53 ± 1	2.3 ± 0.0	1.8 ± 0.1

Table 11.3.19: Glass transition temperature, Young's modulus, tensile yield stress, fracture toughness and fracture energy for M22N modified polyether-amine cured DGEBA/F

M22N	T_g (°C)	E_t (GPa)	σ_y (MPa)	K_{IC} (MPa $m^{1/2}$)	G_{IC} (kJ/m^2)
Unmodified	78	3.6 ± 0.1	79 ± 1	0.8 ± 0.1	0.2 ± 0.0
2.5%	80	3.5 ± 0.0	75 ± 0	1.1 ± 0.1	0.2 ± 0.0
5.0%	81	3.4 ± 0.1	76 ± 1	1.5 ± 0.1	0.5 ± 0.1
7.5%	81	3.3 ± 0.1	69 ± 1	2.1 ± 0.1	1.0 ± 0.0
10.0%	82	3.3 ± 0.1	70 ± 3	2.1 ± 0.1	1.2 ± 0.1

Table 11.3.20: Glass transition temperature, Young's modulus, tensile yield stress, fracture toughness and fracture energy for anhydride cured DGEBA with solvents

Solvent	T_g (°C)	E_t (GPa)	σ_y (MPa)	K_{IC} (MPa $m^{1/2}$)	G_{IC} (kJ/m^2)
Unmodified	157	2.9 ± 0.1	86 ± 0	0.6 ± 0.0	0.10 ± 0.01
10% THFe	155	3.0 ± 0.1	67 ± 2	0.6 ± 0.0	0.07 ± 0.01
10% THF	107	3.0 ± 0.0	71 ± 0	0.8 ± 0.1	0.10 ± 0.01
10% NMPe	147	3.0 ± 0.0	80 ± 3	0.5 ± 0.0	0.07 ± 0.01
10% NMP	87	2.9 ± 0.1	60 ± 2	0.7 ± 0.0	0.11 ± 0.01

Table 11.3.21: Glass transition temperature, Young's modulus, tensile yield stress, fracture toughness and fracture energy for GS-THF anhydride cured DGEBA

GS-THF	T_g (°C)	E_t (GPa)	σ_y (MPa)	K_{IC} (MPa $m^{1/2}$)	G_{IC} (kJ/m^2)
Unmodified	157	2.9 ± 0.1	86 ± 0	0.6 ± 0.0	0.09 ± 0.01
0.1%	148	3.0 ± 0.0	72 ± 5	0.6 ± 0.0	0.10 ± 0.02
0.5%	148	3.0 ± 0.0	58 ± 3	0.8 ± 0.0	0.16 ± 0.02
1.0%	138	3.1 ± 0.0	52 ± 4	0.9 ± 0.0	0.22 ± 0.02
2.0%	138	3.2 ± 0.1	38 ± 5	1.1 ± 0.1	0.34 ± 0.02

Table 11.3.22: Glass transition temperature, Young's modulus, tensile yield stress, fracture toughness and fracture energy for GS-NMP anhydride cured DGEBA

GS-NMP	T_g (°C)	E_t (GPa)	σ_y (MPa)	K_{IC} (MPa $m^{1/2}$)	G_{IC} (kJ/m^2)
Unmodified	157	2.9 ± 0.1	76 ± 12	0.5 ± 0.0	0.10 ± 0.01
0.1%	153	3.1 ± 0.1	71 ± 4	0.7 ± 0.0	0.12 ± 0.02
0.5%	143	3.3 ± 0.0	62 ± 10	0.8 ± 0.0	0.18 ± 0.02
1.0%	133	3.6 ± 0.1	50 ± 8	1.0 ± 0.0	0.21 ± 0.02

Table 11.3.23: Glass transition temperature, Young's modulus, tensile yield stress, fracture toughness and fracture energy for XG-H-THF anhydride cured DGEBA

XG-H-THF	T_g (°C)	E_t (GPa)	σ_y (MPa)	K_{IC} (MPa $m^{1/2}$)	G_{IC} (kJ/m^2)
Unmodified	157	2.9 ± 0.1	86 ± 0	0.6 ± 0.0	0.10 ± 0.01
0.1%	155	3.0 ± 0.1	63 ± 6	0.7 ± 0.0	0.12 ± 0.02
0.5%	153	3.1 ± 0.1	56 ± 5	0.7 ± 0.0	0.15 ± 0.01
1.0%	151	3.1 ± 0.0	54 ± 2	0.9 ± 0.0	0.19 ± 0.01
2.0%	146	3.1 ± 0.0	54 ± 3	0.8 ± 0.0	0.21 ± 0.02

Table 11.3.24: Glass transition temperature, Young's modulus, tensile yield stress, fracture toughness and fracture energy for XG-M-THF anhydride cured DGEBA

XG-M-THF	T_g (°C)	E_t (GPa)	σ_y (MPa)	K_{IC} (MPa $m^{1/2}$)	G_{IC} (kJ/m^2)
Unmodified	157	2.9 ± 0.1	86 ± 0	0.6 ± 0.0	0.10 ± 0.01
0.1%	154	3.1 ± 0.1	56 ± 2	0.6 ± 0.0	0.06 ± 0.01
0.5%	155	3.1 ± 0.0	57 ± 5	0.7 ± 0.0	0.11 ± 0.01
1.0%	153	3.3 ± 0.1	50 ± 2	0.8 ± 0.1	0.15 ± 0.01
2.0%	147	3.0 ± 0.0	58 ± 5	1.0 ± 0.0	0.21 ± 0.02

Table 11.3.25: Glass transition temperature, Young's modulus, tensile yield stress, fracture toughness and fracture energy for XG-C-THF anhydride cured DGEBA

XG-C-THF	T_g (°C)	E_t (GPa)	σ_y (MPa)	K_{IC} (MPa $m^{1/2}$)	G_{IC} (kJ/m^2)
Unmodified	157	2.9 ± 0.1	86 ± 0	0.6 ± 0.0	0.10 ± 0.01
0.1%	153	3.0 ± 0.0	66 ± 7	0.6 ± 0.1	0.08 ± 0.01
0.5%	155	3.0 ± 0.0	57 ± 7	0.6 ± 0.0	0.08 ± 0.01
1.0%	150	3.0 ± 0.0	67 ± 6	0.6 ± 0.1	0.08 ± 0.01
2.0%	154	3.1 ± 0.0	64 ± 11	0.6 ± 0.1	0.08 ± 0.01

Table 11.3.26: Glass transition temperature, Young's modulus, tensile yield stress, fracture toughness and fracture energy for XG-H-NMP anhydride cured DGEBA

XG-H-NMP	T_g (°C)	E_t (GPa)	σ_y (MPa)	K_{IC} (MPa $m^{1/2}$)	G_{IC} (kJ/m^2)
Unmodified	157	2.9 ± 0.1	86 ± 0	0.6 ± 0.0	0.10 ± 0.01
0.1%	147	3.2 ± 0.0	69 ± 11	0.6 ± 0.0	0.08 ± 0.01
0.5%	137	3.3 ± 0.1	62 ± 6	0.6 ± 0.0	0.12 ± 0.01
1.0%	146	3.4 ± 0.1	64 ± 8	0.8 ± 0.0	0.14 ± 0.02
2.0%	142	3.6 ± 0.1	52 ± 12	0.9 ± 0.1	0.19 ± 0.02

Table 11.3.27: Glass transition temperature, Young's modulus, tensile yield stress, fracture toughness and fracture energy for XG-M-NMP anhydride cured DGEBA

XG-M-NMP	T_g (°C)	E_t (GPa)	σ_y (MPa)	K_{IC} (MPa $m^{1/2}$)	G_{IC} (kJ/m^2)
Unmodified	157	2.9 ± 0.1	86 ± 0	0.6 ± 0.0	0.10 ± 0.01
0.1%	156	3.1 ± 0.0	78 ± 9	0.6 ± 0.1	0.09 ± 0.01
0.5%	154	3.2 ± 0.1	69 ± 4	0.7 ± 0.1	0.14 ± 0.01
1.0%	150	3.3 ± 0.1	69 ± 2	0.9 ± 0.0	0.16 ± 0.00

Table 11.3.28: Glass transition temperature, Young's modulus, tensile yield stress, fracture toughness and fracture energy for XG-C-NMP anhydride cured DGEBA

XG-C-NMP	T_g (°C)	E_t (GPa)	σ_y (MPa)	K_{IC} (MPa $m^{1/2}$)	G_{IC} (kJ/m^2)
Unmodified	157	2.9 ± 0.1	86 ± 0	0.6 ± 0.0	0.10 ± 0.01
0.1%	152	3.0 ± 0.0	70 ± 9	0.6 ± 0.0	0.07 ± 0.01
0.5%	151	3.1 ± 0.1	71 ± 20	0.6 ± 0.0	0.07 ± 0.01
1.0%	152	3.2 ± 0.1	73 ± 5	0.6 ± 0.1	0.08 ± 0.01
2.0%	147	3.3 ± 0.0	57 ± 15	0.6 ± 0.0	0.08 ± 0.00

Table 11.3.29: Glass transition temperature, Young's modulus, tensile yield stress, fracture toughness and fracture energy for GF anhydride cured DGEBA

GF	T_g (°C)	E_t (GPa)	σ_y (MPa)	K_{IC} (MPa $m^{1/2}$)	G_{IC} (kJ/m^2)
Unmodified	157	2.9 ± 0.1	86 ± 0	0.6 ± 0.0	0.10 ± 0.01
0.1%	157	3.0 ± 0.1	80 ± 4	0.6 ± 0.1	0.09 ± 0.01
0.5%	158	3.0 ± 0.0	78 ± 5	0.7 ± 0.0	0.12 ± 0.01
1.0%	157	3.1 ± 0.1	78 ± 4	0.7 ± 0.0	0.13 ± 0.01
1.5%	159	3.0 ± 0.0	72 ± 4	0.7 ± 0.1	0.12 ± 0.01
2.0%	158	3.0 ± 0.0	68 ± 3	0.6 ± 0.1	0.13 ± 0.01

Table 11.3.30: Glass transition temperature, Young's modulus, tensile yield stress, fracture toughness and fracture energy for CNT-COOH anhydride cured DGEBA

CNT-COOH	T_g (°C)	E_t (GPa)	σ_y (MPa)	K_{IC} (MPa $m^{1/2}$)	G_{IC} (kJ/m^2)
Unmodified	157	2.9 ± 0.1	86 ± 0	0.6 ± 0.0	0.10 ± 0.01
0.1%	159	2.9 ± 0.0	87 ± 0	0.5 ± 0.0	0.07 ± 0.01
0.2%	158	2.9 ± 0.0	87 ± 1	0.6 ± 0.0	0.07 ± 0.01
0.5%	150	3.0 ± 0.0	84 ± 5	0.6 ± 0.0	0.08 ± 0.02

Table 11.3.31: Glass transition temperature, Young's modulus, tensile yield stress, fracture toughness and fracture energy for GNP-COOH anhydride cured DGEBA

GNP-COOH	T_g (°C)	E_t (GPa)	σ_y (MPa)	K_{IC} (MPa $m^{1/2}$)	G_{IC} (kJ/m^2)
Unmodified	157	2.9 ± 0.1	86 ± 0	0.6 ± 0.0	0.10 ± 0.01
0.1%	147	3.0 ± 0.0	84 ± 0	0.5 ± 0.0	0.08 ± 0.01
0.5%	156	3.0 ± 0.0	83 ± 4	0.6 ± 0.1	0.10 ± 0.01
1.0%	151	3.0 ± 0.2	72 ± 8	0.7 ± 0.1	0.13 ± 0.01

Table 11.3.32: Glass transition temperature, Young's modulus, tensile yield stress, fracture toughness and fracture energy for GNP-O2 anhydride cured DGEBA

GNP-O2	T_g (°C)	E_t (GPa)	σ_y (MPa)	K_{IC} (MPa $m^{1/2}$)	G_{IC} (kJ/m^2)
Unmodified	157	2.9 ± 0.1	86 ± 0	0.6 ± 0.0	0.10 ± 0.01
0.1%	158	3.0 ± 0.0	86 ± 2	0.6 ± 0.0	0.09 ± 0.01
0.5%	153	2.9 ± 0.0	76 ± 5	0.6 ± 0.1	0.10 ± 0.02
1.0%	155	3.0 ± 0.0	65 ± 9	0.6 ± 0.0	0.10 ± 0.01

Appendix B

Compressive properties of epoxy polymers

The compressive properties of the modified epoxy polymers are summarised in this Appendix.

Table 11.3.33: Compressive modulus, compressive true yield stress, compressive true yield strain, failure stress and failure strain for MX551 CSR modified low viscosity epoxy

MX551	E_c (GPa)	σ_{yc} (MPa)	ε_{yc}	σ_f (MPa)	ε_f
Unmodified	1.7 ± 0.2	115 ± 2	0.10 ± 0.00	272	0.98
2.5C	1.4 ± 0.1	109 ± 0	0.12 ± 0.00	246	0.95
5C	1.4 ± 0.1	102 ± 1	0.12 ± 0.00	229	0.88
7.5C	1.4 ± 0.0	93 ± 3	0.11 ± 0.01	187	0.88
10C	1.4 ± 0.0	91 ± 0	0.11 ± 0.00	174	0.89

Table 11.3.34: Compressive modulus, compressive true yield stress, compressive true yield strain, failure stress and failure strain for CTBN modified low viscosity epoxy

CTBN	E_c (GPa)	σ_{yc} (MPa)	ε_{yc}	σ_f (MPa)	ε_f
Unmodified	1.7 ± 0.2	115 ± 2	0.10 ± 0.00	272	0.98
5R	1.6 ± 0.1	101 ± 0	0.13 ± 0.01	196	0.83
7.5R	1.5 ± 0.0	93 ± 0	0.12 ± 0.00	205	0.82
10R	1.6 ± 0.1	87 ± 0	0.12 ± 0.00	209	0.86
3.4N7.5R	1.5 ± 0.0	93 ± 0	0.12 ± 0.00	205	0.82
10N9R	1.6 ± 0.0	93 ± 0	0.12 ± 0.00	301	0.96

Table 11.3.35: Compressive modulus, compressive true yield stress, compressive true yield strain, failure stress and failure strain for MX156 CSR modified polyether-amine cured DGEBA epoxy

MX156	E_c (GPa)	σ_{yc} (MPa)	ε_{yc}	σ_f (MPa)	ε_f
Unmodified	2.2 ± 0.1	83 ± 0	0.08 ± 0.00	182	0.84
5C	2.2 ± 0.1	70 ± 0	0.08 ± 0.00	187	0.91
7C	2.0 ± 0.0	67 ± 0	0.08 ± 0.00	176	0.89
9C	1.9 ± 0.1	62 ± 0	0.08 ± 0.00	141	0.97
10N5C	2.4 ± 0.1	72 ± 0	0.07 ± 0.00	266	0.93
10N7C	2.3 ± 0.1	69 ± 0	0.07 ± 0.00	269	0.92
10N9C	2.2 ± 0.0	64 ± 0	0.07 ± 0.00	237	0.94

Table 11.3.36: Compressive modulus, compressive true yield stress, compressive true yield strain, failure stress and failure strain for CTBN modified polyether-amine cured DGEBA epoxy

CTBN	E_c (GPa)	σ_{yc} (MPa)	ε_{yc}	σ_f (MPa)	ε_f
Unmodified	2.2 ± 0.1	83 ± 0	0.08 ± 0.00	182	0.84
1R	2.0 ± 0.0	81 ± 0	0.08 ± 0.00	170	0.91
5R	2.0 ± 0.0	69 ± 0	0.08 ± 0.00	164	0.96
7R	1.8 ± 0.0	64 ± 0	0.07 ± 0.00	150	0.93
9R	1.8 ± 0.2	60 ± 1	0.07 ± 0.00	140	0.94
10N5R	2.3 ± 0.1	70 ± 0	0.07 ± 0.00	216	0.91
10N7R	2.2 ± 0.1	66 ± 1	0.07 ± 0.01	198	1.04
10N9R	2.1 ± 0.2	64 ± 0	0.07 ± 0.01	181	0.94

Table 11.3.37: Compressive modulus, compressive true yield stress, compressive true yield strain, failure stress and failure strain for MX156 CSR modified polyether-amine cured DGEBA/F epoxy

MX156	E_c (GPa)	σ_{yc} (MPa)	ε_{yc}	σ_f (MPa)	ε_f
Unmodified	2.4 ± 0.0	97 ± 1	0.07 ± 0.00	180	1.16
5C	2.2 ± 0.1	81 ± 0	0.06 ± 0.00	218	1.07
7C	2.1 ± 0.1	75 ± 0	0.06 ± 0.00	191	1.01
9C	2.0 ± 0.0	69 ± 1	0.06 ± 0.00	201	1.02
10N5C	2.4 ± 0.0	81 ± 0	0.06 ± 0.00	280	1.01
10N7C	2.2 ± 0.1	76 ± 0	0.06 ± 0.00	289	1.00
10N9C	2.0 ± 0.0	70 ± 0	0.06 ± 0.00	264	0.98

Table 11.3.38: Compressive modulus, compressive true yield stress, compressive true yield strain, failure stress and failure strain for CTBN modified polyether-amine cured DGEBA/F epoxy

CTBN	E_c (GPa)	σ_{yc} (MPa)	ε_{yc}	σ_f (MPa)	ε_f
Unmodified	2.4 ± 0.0	97 ± 1	0.07 ± 0.00	180	1.16
5R	2.0 ± 0.1	79 ± 0	0.07 ± 0.00	176	1.22
7R	1.8 ± 0.1	74 ± 1	0.07 ± 0.01	177	1.14
9R	1.7 ± 0.0	70 ± 1	0.07 ± 0.00	162	1.09
10N5R	1.9 ± 0.1	79 ± 0	0.08 ± 0.00	212	1.02
10N7R	1.9 ± 0.0	75 ± 0	0.07 ± 0.00	206	1.02
10N9R	1.8 ± 0.1	69 ± 0	0.07 ± 0.00	195	1.03

Table 11.3.39: Compressive modulus, compressive true yield stress, compressive true yield strain, failure stress and failure strain for E21 SBM modified polyether-amine cured DGEBA epoxy

E21	E_c (GPa)	σ_{yc} (MPa)	ε_{yc}	σ_f (MPa)	ε_f
Unmodified	2.2 ± 0.1	83 ± 0	0.08 ± 0.00	182	0.84
0.5%	2.1 ± 0.0	82 ± 1	0.07 ± 0.00	178	0.89
1.0%	2.1 ± 0.1	80 ± 0	0.07 ± 0.00	163	0.82
2.5%	2.2 ± 0.1	79 ± 0	0.08 ± 0.00	152	0.88
5.0%	2.0 ± 0.1	76 ± 0	0.08 ± 0.00	168	0.82
7.5%	1.8 ± 0.1	72 ± 0	0.08 ± 0.00	184	0.92
10.0%	1.7 ± 0.1	69 ± 0	0.08 ± 0.00	189	0.90
10N25E21	2.3 ± 0.0	81 ± 1	0.07 ± 0.00	246	0.88
10N10E21	1.9 ± 0.1	69 ± 0	0.06 ± 0.00	272	0.96

Table 11.3.40: Compressive modulus, compressive true yield stress, compressive true yield strain, failure stress and failure strain for E41 SBM modified polyether-amine cured DGEBA epoxy

E41	E_c (GPa)	σ_{yc} (MPa)	ε_{yc}	σ_f (MPa)	ε_f
Unmodified	2.2 ± 0.1	83 ± 0	0.08 ± 0.00	182	0.84
1.0%	2.2 ± 0.0	81 ± 0	0.07 ± 0.00	167	0.94
2.5%	2.1 ± 0.2	81 ± 1	0.08 ± 0.00	159	0.79
5.0%	2.3 ± 0.7	81 ± 0	0.08 ± 0.01	163	0.84
7.5%	2.0 ± 0.1	79 ± 1	0.08 ± 0.00	174	0.88
10.0%	1.9 ± 0.2	77 ± 1	0.08 ± 0.01	186	0.86

Table 11.3.41: Compressive modulus, compressive true yield stress, compressive true yield strain, failure stress and failure strain for E21 SBM modified polyether-amine cured DGEBA/F epoxy

E21	E_c (GPa)	σ_{yc} (MPa)	ε_{yc}	σ_f (MPa)	ε_f
Unmodified	2.4 ± 0.0	97 ± 1	0.07 ± 0.00	180	1.16
2.5%	2.0 ± 0.2	88 ± 3	0.07 ± 0.01	194	1.18
5.0%	1.9 ± 0.1	82 ± 0	0.07 ± 0.00	200	1.17
7.5%	1.7 ± 0.0	78 ± 1	0.08 ± 0.01	196	1.18
10.0%	1.6 ± 0.0	76 ± 0	0.07 ± 0.00	219	1.21
10N25E21	2.2 ± 0.0	89 ± 0	0.07 ± 0.00	280	0.98
10N10E21	1.7 ± 0.0	74 ± 1	0.07 ± 0.00	283	1.09

Table 11.3.42: Compressive modulus, compressive true yield stress, compressive true yield strain, failure stress and failure strain for E41 SBM modified polyether-amine cured DGEBA/F epoxy

E41	E_c (GPa)	σ_{yc} (MPa)	ε_{yc}	σ_f (MPa)	ε_f
Unmodified	2.4 ± 0.0	97 ± 1	0.07 ± 0.00	180	1.16
2.5%	2.3 ± 0.0	92 ± 3	0.07 ± 0.01	185	1.08
5.0%	2.3 ± 0.0	90 ± 2	0.07 ± 0.01	214	1.23
7.5%	2.2 ± 0.1	88 ± 1	0.07 ± 0.00	212	1.19
10.0%	2.1 ± 0.1	85 ± 0	0.07 ± 0.00	225	1.11

Table 11.3.43: Compressive modulus, compressive true yield stress, compressive true yield strain, failure stress and failure strain for E21 SBM modified anhydride cured DGEBA epoxy

E21	E_c (GPa)	σ_{yc} (MPa)	ε_{yc}	σ_f (MPa)	ε_f
Unmodified	1.8 ± 0.2	107 ± 3	0.10 ± 0.01	216	0.91
2.5%	1.7 ± 0.0	103 ± 0	0.10 ± 0.00	180	0.78
5.0%	1.6 ± 0.0	97 ± 0	0.09 ± 0.00	216	0.88
7.5%	1.5 ± 0.0	91 ± 0	0.10 ± 0.00	189	0.90
10.0%	1.3 ± 0.1	85 ± 2	0.12 ± 0.00	224	0.98
15.0%	1.1 ± 0.1	77 ± 0	0.14 ± 0.01	183	0.88
10N10E21	1.42 ± 0.03	88 ± 3	0.14 ± 0.01	132	0.62

Table 11.3.44: Compressive modulus, compressive true yield stress, compressive true yield strain, failure stress and failure strain for E41 SBM modified anhydride cured DGEBA epoxy

E41	E_c (GPa)	σ_{yc} (MPa)	ε_{yc}	σ_f (MPa)	ε_f
Unmodified	1.8 ± 0.2	107 ± 3	0.10 ± 0.01	216	0.91
2.5%	1.7 ± 0.3	105 ± 1	0.11 ± 0.02	159	0.87
5.0%	1.8 ± 0.0	103 ± 0	0.10 ± 0.00	225	0.88
7.5%	1.6 ± 0.1	100 ± 0	0.11 ± 0.00	189	0.88
10.0%	1.6 ± 0.1	94 ± 2	0.11 ± 0.00	195	0.91
15.0%	1.8 ± 0.0	93 ± 1	0.11 ± 0.00	174	0.88

Table 11.3.45: Compressive modulus, compressive true yield stress, compressive true yield strain, failure stress and failure strain for E21 SBM modified low viscosity epoxy

E21	E_c (GPa)	σ_{yc} (MPa)	ε_{yc}	σ_f (MPa)	ε_f
Unmodified	1.7 ± 0.2	115 ± 2	0.10 ± 0.00	272	0.98
2.5%	1.4 ± 0.2	106 ± 1	0.11 ± 0.02	244	1.02
5.0%	1.3 ± 0.1	96 ± 3	0.14 ± 0.01	102	0.60
7.5%	1.2 ± 0.1	82 ± 1	0.11 ± 0.02	189	2.06
10.0%	0.8 ± 0.0	63 ± 1	0.10 ± 0.00	134	2.23

Table 11.3.46: Compressive modulus, compressive true yield stress, compressive true yield strain, failure stress and failure strain for E41 SBM modified low viscosity epoxy

E41	E_c (GPa)	σ_{yc} (MPa)	ε_{yc}	σ_f (MPa)	ε_f
Unmodified	1.7 ± 0.2	115 ± 2	0.10 ± 0.00	272	0.98
2.5%	1.2 ± 0.0	110 ± 1	0.13 ± 0.01	250	1.02
5.0%	1.7 ± 0.0	108 ± 2	0.10 ± 0.02	212	0.88
7.5%	1.3 ± 0.2	97 ± 1	0.13 ± 0.06	228	0.88
10.0%	1.2 ± 0.1	81 ± 2	0.13 ± 0.00	163	1.77

Table 11.3.47: Compressive modulus, compressive true yield stress, compressive true yield strain, failure stress and failure strain for M52N MAM modified polyether-amine cured DGEBA epoxy

M52N	E_c (GPa)	σ_{yc} (MPa)	ε_{yc}	σ_f (MPa)	ε_f
Unmodified	2.2 ± 0.1	83 ± 0	0.08 ± 0.00	182	0.84
1.0%	2.1 ± 0.1	78 ± 0	0.08 ± 0.00	201	0.90
2.5%	2.0 ± 0.3	76 ± 0	0.08 ± 0.00	164	0.99
5.0%	2.0 ± 0.1	71 ± 0	0.08 ± 0.00	204	0.99
7.5%	1.9 ± 0.0	67 ± 0	0.08 ± 0.00	222	0.97
10.0%	1.7 ± 0.1	64 ± 0	0.10 ± 0.01	220	0.99
20.0%	1.1 ± 0.1	55 ± 2	0.15 ± 0.01	192	1.05
10N2.5M52N	2.4 ± 0.0	78 ± 0	0.07 ± 0.00	265	0.88
10N7.5M52N	2.2 ± 0.1	69 ± 0	0.09 ± 0.01	311	0.98
10N10M52N	2.0 ± 0.0	67 ± 0	0.1 ± 0.00	267	0.97

Table 11.3.48: Compressive modulus, compressive true yield stress, compressive true yield strain, failure stress and failure strain for M22N MAM modified polyether-amine cured DGEBA epoxy

M22N	E_c (GPa)	σ_{yc} (MPa)	ε_{yc}	σ_f (MPa)	ε_f
Unmodified	2.2 ± 0.1	83 ± 0	0.08 ± 0.00	182	0.84
2.5%	2.2 ± 0.0	76 ± 0	0.08 ± 0.00	209	0.97
5.0%	1.9 ± 0.0	76 ± 0	0.08 ± 0.00	221	0.97
7.5%	2.0 ± 0.0	74 ± 0	0.08 ± 0.00	185	0.96
10.0%	2.0 ± 0.0	72 ± 0	0.08 ± 0.00	212	0.96

Table 11.3.49: Compressive modulus, compressive true yield stress, compressive true yield strain, failure stress and failure strain for M52N MAM modified polyether-amine cured DGEBA/F epoxy

M52N	E_c (GPa)	σ_{yc} (MPa)	ε_{yc}	σ_f (MPa)	ε_f
Unmodified	2.4 ± 0.0	97 ± 1	0.07 ± 0.00	180	1.16
2.5%	2.7 ± 0.0	87 ± 0	0.06 ± 0.00	194	1.11
5.0%	2.6 ± 0.0	83 ± 0	0.06 ± 0.00	257	1.09
7.5%	2.3 ± 0.0	76 ± 0	0.06 ± 0.00	247	1.05
10.0%	2.1 ± 0.0	70 ± 0	0.07 ± 0.00	272	1.14
10N2.5M52N	3.2 ± 0.0	88 ± 1	0.05 ± 0.00	266	0.95
10N10M52N	2.7 ± 0.0	71 ± 0	0.06 ± 0.01	310	1.15

Table 11.3.50: Compressive modulus, compressive true yield stress, compressive true yield strain, failure stress and failure strain for M22N MAM modified polyether-amine cured DGEBA/F epoxy

M22N	E_c (GPa)	σ_{yc} (MPa)	ε_{yc}	σ_f (MPa)	ε_f
Unmodified	2.4 ± 0.0	97 ± 1	0.07 ± 0.00	180	1.16
2.5%	3.0 ± 0.1	89 ± 1	0.06 ± 0.00	211	1.17
5.0%	2.9 ± 0.1	87 ± 0	0.06 ± 0.00	234	1.07
7.5%	2.9 ± 0.1	83 ± 0	0.06 ± 0.00	223	1.10
10.0%	2.9 ± 0.1	83 ± 0	0.06 ± 0.00	255	1.09

Table 11.3.51: Compressive modulus, compressive true yield stress, compressive true yield strain, failure stress and failure strain for anhydride cured DGEBA epoxy with solvents

Solvent	E_c (GPa)	σ_{yc} (MPa)	ε_{yc}	σ_f (MPa)	ε_f
Unmodified	1.8 ± 0.2	107 ± 3	0.10 ± 0.01	216	0.91
10% THFe	2.3 ± 0.7	108 ± 3	0.10 ± 0.02	227	0.84
10% THF	1.7 ± 0.1	95 ± 0	0.09 ± 0.00	162	0.98
10% NMPe	1.6 ± 0.1	113 ± 0	0.11 ± 0.00	185	0.86
10% NMP	1.4 ± 0.1	79 ± 2	0.08 ± 0.01	139	0.89

Table 11.3.52: Compressive modulus, compressive true yield stress, compressive true yield strain, failure stress and failure strain for GS-THF modified anhydride cured DGEBA epoxy

GS-THF	E_c (GPa)	σ_{yc} (MPa)	ε_{yc}	σ_f (MPa)	ε_f
Unmodified	1.8 ± 0.2	107 ± 3	0.10 ± 0.01	216	0.91
0.1%	2.0 ± 0.0	112 ± 1	0.10 ± 0.00	210	0.78
0.5%	2.0 ± 0.0	109 ± 1	0.10 ± 0.00	233	0.87
1.0%	1.8 ± 0.0	107 ± 3	0.11 ± 0.00	262	0.92
2.0%	1.7 ± 0.0	102 ± 6	0.11 ± 0.02	217	0.91

Table 11.3.53: Compressive modulus, compressive true yield stress, compressive true yield strain, failure stress and failure strain for GS-NMP modified anhydride cured DGEBA epoxy

GS-NMP	E_c (GPa)	σ_{yc} (MPa)	ε_{yc}	σ_f (MPa)	ε_f
Unmodified	1.8 ± 0.2	107 ± 3	0.10 ± 0.01	216	0.91
0.1%	1.7 ± 0.0	111 ± 0	0.10 ± 0.00	223	0.92
0.5%	1.8 ± 0.1	112 ± 4	0.09 ± 0.00	253	0.94
1.0%	1.8 ± 0.0	113 ± 0	0.11 ± 0.01	271	1.04

Table 11.3.54: Compressive modulus, compressive true yield stress, compressive true yield strain, failure stress and failure strain for XG-H-THF modified anhydride cured DGEBA epoxy

XG-H-THF	E_c (GPa)	σ_{yc} (MPa)	ε_{yc}	σ_f (MPa)	ε_f
Unmodified	1.8 ± 0.2	107 ± 3	0.10 ± 0.01	216	0.91
0.1%	1.7 ± 0.1	112 ± 1	0.11 ± 0.00	186	0.88
0.5%	1.8 ± 0.0	111 ± 1	0.10 ± 0.01	259	0.89
1.0%	1.8 ± 0.0	112 ± 1	0.11 ± 0.00	254	0.88
2.0%	1.6 ± 0.0	103 ± 5	0.11 ± 0.02	228	0.92

Table 11.3.55: Compressive modulus, compressive true yield stress, compressive true yield strain, failure stress and failure strain for XG-H-NMP modified anhydride cured DGEBA epoxy

XG-H-NMP	E_c (GPa)	σ_{yc} (MPa)	ε_{yc}	σ_f (MPa)	ε_f
Unmodified	1.8 ± 0.2	107 ± 3	0.10 ± 0.01	216	0.91
0.1%	2.0 ± 0.1	114 ± 1	0.09 ± 0.02	208	0.92
0.5%	2.0 ± 0.0	117 ± 0	0.10 ± 0.00	270	0.93
1.0%	2.1 ± 0.1	109 ± 5	0.09 ± 0.01	246	0.93
2.0%	2.0 ± 0.1	113 ± 1	0.08 ± 0.01	252	1.00

Table 11.3.56: Compressive modulus, compressive true yield stress, compressive true yield strain, failure stress and failure strain for XG-M-THF modified anhydride cured DGEBA epoxy

XG-M-THF	E_c (GPa)	σ_{yc} (MPa)	ε_{yc}	σ_f (MPa)	ε_f
Unmodified	1.8 ± 0.2	107 ± 3	0.10 ± 0.01	216	0.91
0.1%	1.4 ± 0.0	109 ± 0	0.12 ± 0.00	201	0.94
0.5%	1.4 ± 0.3	107 ± 3	0.10 ± 0.01	243	0.97
1.0%	1.7 ± 0.0	108 ± 0	0.10 ± 0.01	229	0.90
2.0%	1.7 ± 0.0	105 ± 1	0.11 ± 0.00	190	0.84

Table 11.3.57: Compressive modulus, compressive true yield stress, compressive true yield strain, failure stress and failure strain for XG-M-NMP modified anhydride cured DGEBA epoxy

XG-M-NMP	E_c (GPa)	σ_{yc} (MPa)	ε_{yc}	σ_f (MPa)	ε_f
Unmodified	1.8 ± 0.2	107 ± 3	0.10 ± 0.01	216	0.91
0.1%	1.6 ± 0.1	109 ± 1	0.11 ± 0.00	201	0.94
0.5%	1.8 ± 0.1	109 ± 1	0.10 ± 0.01	231	0.92
1.0%	1.8 ± 0.0	112 ± 0	0.10 ± 0.01	251	0.91

Table 11.3.58: Compressive modulus, compressive true yield stress, compressive true yield strain, failure stress and failure strain for XG-C-THF modified anhydride cured DGEBA epoxy

XG-C-THF	E_c (GPa)	σ_{yc} (MPa)	ε_{yc}	σ_f (MPa)	ε_f
Unmodified	1.8 ± 0.2	107 ± 3	0.10 ± 0.01	216	0.91
0.1%	1.9 ± 0.1	111 ± 1	0.10 ± 0.00	179	0.88
0.5%	2.0 ± 0.0	110 ± 0	0.10 ± 0.00	198	0.90
1.0%	2.1 ± 0.1	113 ± 0	0.09 ± 0.00	227	0.88
2.0%	2.2 ± 0.0	110 ± 4	0.09 ± 0.01	193	0.78

Table 11.3.59: Compressive modulus, compressive true yield stress, compressive true yield strain, failure stress and failure strain for XG-C-NMP modified anhydride cured DGEBA epoxy

XG-C-NMP	E_c (GPa)	σ_{yc} (MPa)	ε_{yc}	σ_f (MPa)	ε_f
Unmodified	1.8 ± 0.2	107 ± 3	0.10 ± 0.01	216	0.91
0.1%	1.9 ± 0.4	113 ± 1	0.11 ± 0.02	203	0.96
0.5%	2.1 ± 0.4	113 ± 1	0.10 ± 0.02	204	0.89
1.0%	2.3 ± 0.1	112 ± 1	0.10 ± 0.01	204	0.86
2.0%	2.3 ± 0.7	115 ± 3	0.10 ± 0.02	229	0.87

Table 11.3.60: Compressive modulus, compressive true yield stress, compressive true yield strain, failure stress and failure strain for GF modified anhydride cured DGEBA epoxy

GF	E_c (GPa)	σ_{yc} (MPa)	ε_{yc}	σ_f (MPa)	ε_f
Unmodified	1.8 ± 0.2	107 ± 3	0.10 ± 0.01	216	0.91
0.1%	1.8 ± 0.3	108 ± 1	0.11 ± 0.01	246	0.94
0.5%	2.0 ± 0.2	110 ± 1	0.10 ± 0.01	263	0.89
1.0%	1.8 ± 0.1	109 ± 1	0.10 ± 0.00	264	0.89
1.5%	2.0 ± 0.2	109 ± 1	0.10 ± 0.01	260	0.87
2.0%	2.1 ± 0.0	109 ± 2	0.09 ± 0.01	272	0.89

Table 11.3.61: Compressive modulus, compressive true yield stress, compressive true yield strain, failure stress and failure strain for CNT-COOH modified anhydride cured DGEBA epoxy

CNT-COOH	E_c (GPa)	σ_{yc} (MPa)	ε_{yc}	σ_f (MPa)	ε_f
Unmodified	1.8 ± 0.2	107 ± 3	0.10 ± 0.01	216	0.91
0.1%	1.7 ± 0.0	109 ± 0	0.10 ± 0.00	184	0.85
0.2%	1.8 ± 0.0	110 ± 0	0.10 ± 0.00	182	0.85
0.5%	1.9 ± 0.0	111 ± 0	0.10 ± 0.00	190	0.97

Table 11.3.62: Compressive modulus, compressive true yield stress, compressive true yield strain, failure stress and failure strain for GNP-COOH modified anhydride cured DGEBA epoxy

GNP-COOH	E_c (GPa)	σ_{yc} (MPa)	ε_{yc}	σ_f (MPa)	ε_f
Unmodified	1.8 ± 0.2	107 ± 3	0.10 ± 0.01	216	0.91
0.1%	1.8 ± 0.1	112 ± 0	0.11 ± 0.00	192	0.96
0.5%	1.9 ± 0.1	112 ± 0	0.11 ± 0.00	222	0.92
1.0%	1.9 ± 0.1	112 ± 1	0.12 ± 0.00	248	1.23

Table 11.3.63: Compressive modulus, compressive true yield stress, compressive true yield strain, failure stress and failure strain for GNP-O2 modified anhydride cured DGEBA epoxy

GNP-O2	E_c (GPa)	σ_{yc} (MPa)	ε_{yc}	σ_f (MPa)	ε_f
Unmodified	1.8 ± 0.2	107 ± 3	0.10 ± 0.01	216	0.91
0.1%	1.8 ± 0.0	111 ± 0	0.10 ± 0.00	227	0.94
0.5%	2.0 ± 0.1	112 ± 0	0.11 ± 0.00	197	0.91
1.0%	2.0 ± 0.0	109 ± 1	0.11 ± 0.00	192	0.87

Appendix C

Components for Mori-Tanaka model

The components of A, A_2, A_3, A_4 and A_5 for the Mori-Tanaka model for fibre-like spheroidal inclusions, first described by Tandon and Weng [209], are given as:

$$
\begin{aligned}
A &= 2B_2B_3 - B_1\left(B_4 + B_5\right) \\
A_1 &= D_1\left(B_4 + B_5\right) - 2B_2 \\
A_2 &= \left(1 + D_1\right)B_2 - \left(B_4 + B_5\right) \\
A_3 &= B_1 - D_1B_3 \\
A_4 &= \left(1 + D_1\right)B_1 - 2B_3 \\
A_5 &= \frac{1 - D_1}{B_4 - B_5}
\end{aligned}
$$

where,

$$
\begin{aligned}
B_1 &= v_fD_1 + D_2 + \left(1 - v_f\right)\left(D_1S_{1111} + 2S_{2211}\right) \\
B_2 &= v_f + D_3 + \left(1 - v_f\right)\left(D_1S_{1122} + S_{2222} + S_{2233}\right) \\
B_3 &= v_f + D_3 + \left(1 - v_f\right)\left(S_{1111} + \left(1 + D_1\right)S_{2211}\right) \\
B_4 &= v_fD_1 + D_2 + \left(1 - v_f\right)\left(S_{1122} + D_1S_{2222} + S_{2233}\right) \\
B_5 &= v_f + D_3 + \left(1 - v_f\right)\left(S_{1122} + S_{2222} + D_1S_{2233}\right)
\end{aligned}
$$

and

$$
\begin{aligned}
D_1 &= 1 + \frac{2\left(\mu_1 - \mu_0\right)}{\left(\lambda_1 - \lambda_0\right)} \\
D_2 &= \frac{\lambda_0 + 2\mu_0}{\lambda_1 - \lambda_0} \\
D_3 &= \frac{\lambda_0}{\lambda_1 - \lambda_0}
\end{aligned}
$$

where μ and λ are the Lam*é* constants, and the subscripts 0 and 1 represent the matrix and filler, respectively.

$$\mu = \frac{E}{2\left(1+\nu\right)} \tag{11.1}$$

$$\lambda = \frac{E\nu}{\left(1+\nu\right)\left(1-2\nu\right)} \tag{11.2}$$

The components of Eshelby's tensor, S_{ijkl}, for fibre-like spheroidal inclusions are given by:

$$S_{1111} = \frac{1}{2\left(1-\nu_0\right)}\left\{1-2\nu_0+\frac{3\alpha^2-1}{\alpha^2-1}-\left[1-2\nu_0+\frac{3\alpha^2}{\alpha^2-1}\right]g\right\}$$

$$S_{2222} = S_{3333} = \frac{3}{8\left(1-\nu_0\right)}\frac{\alpha^2}{\alpha^2-1}+\frac{1}{4\left(1-\nu_0\right)}\left[1-2\nu_0-\frac{9}{4\left(\alpha^2-1\right)}\right]g$$

$$S_{2233} = S_{3322} = \frac{1}{4\left(1-\nu_0\right)}\left\{\frac{\alpha^2}{2\left(\alpha^2-1\right)}-\left[1-2\nu_0+\frac{3}{4\left(\alpha^2-1\right)}\right]\right\}$$

$$S_{2211} = S_{3311} = -\frac{1}{2\left(1-\nu_0\right)}\frac{\alpha^2}{\alpha^2-1}+\frac{1}{4\left(1-\nu_0\right)}\left\{\frac{3\alpha^2}{\alpha^2-1}-\left(1-2\nu_0\right)\right\}g$$

$$S_{1122} = S_{1133} = -\frac{1}{2\left(1-\nu_0\right)}\left[1-2\nu_0+\frac{1}{\alpha^2-1}\right]+\frac{1}{2\left(1-\nu_0\right)}\left[1-2\nu_0+\frac{3}{2\left(\alpha^2-1\right)}\right]g$$

$$S_{2323} = S_{3232} = \frac{1}{4\left(1-\nu_0\right)}\left\{\frac{\alpha^2}{2\left(\alpha^2-1\right)}+\left[1-2\nu_0-\frac{3}{4\left(\alpha^2-1\right)}\right]g\right\}$$

$$S_{1212} = S_{1313} = \frac{1}{4\left(1-\nu_0\right)}\left\{1-2\nu_0-\frac{\alpha^2+1}{\alpha^2-1}1\frac{1}{2}\left[1-2\nu_0-\frac{3\left(\alpha^2+1\right)}{\alpha^2-1}\right]g\right\}$$

where ν_0 is the Poisson's ratio of the matrix, α is the aspect ratio of the filler and g is given by:

$$g = \frac{\alpha}{\left(\alpha^2-1\right)^{3/2}}\left[\alpha\left(\alpha^2-1\right)^{1/2}-cosh^{-1}\alpha\right] \tag{11.3}$$

Appendix D

Crack deflection model by Faber and Evans

The following is the crack deflection model as first described by Faber and Evans [157], reproduced here for clarity:

The average toughening contribution from crack twisting per unit length of crack front is:

$$\frac{\langle G\rangle^{Twist}}{G_{CU}} = \frac{4}{\pi^4}\int_{-\frac{\pi}{2}}^{\frac{\pi}{2}}\int_{-\frac{\pi}{2}}^{\frac{\pi}{2}}\int_{0}^{1}\int_{0}^{1}\int_{-\frac{\pi}{2}}^{0}\int_{0}^{\frac{\pi}{2}} \eta\Bigg[\cos^4\left(\frac{\langle\theta\rangle}{2}\right)\Bigg\{2v\sin^2\psi_T + \cos^2\psi_T\cos^2\left(\frac{\langle\theta\rangle}{2}\right) \times\left[1+2\sin^2\left(\frac{\langle\theta\rangle}{2}\right)\right]\Bigg\}^2 + \Bigg\{\sin\psi_T\cos\psi_T\left[\cos^2\left(\frac{\langle\theta\rangle}{2}\right)-2v\right] + \sin^2\left(\frac{\langle\theta\rangle}{2}\right)\left[3\cos^2\left(\frac{\langle\theta\rangle}{2}\right)-2v\right]\Bigg\}^2\Bigg] d\theta_1\, d\theta_2\, d\alpha\, d\beta\, d\mu_1\, d\mu_2 \tag{11.4}$$

and for crack tilting:

$$\frac{\langle G\rangle^{Tilt}}{G_{CU}} = \frac{4}{\pi^4}\int_{-\frac{\pi}{2}}^{\frac{\pi}{2}}\int_{-\frac{\pi}{2}}^{\frac{\pi}{2}}\int_{0}^{1}\int_{0}^{1}\int_{0}^{\frac{\pi}{2}}\int_{0}^{\frac{\pi}{2}} \zeta\cos^4\left(\frac{\bar{\theta}}{2}\right) d\theta_1\, d\theta_2\, d\alpha\, d\beta\, d\mu_1\, d\mu_2 \tag{11.5}$$

where,

$$\eta = \frac{\frac{\Delta}{H} - \alpha\cos\theta_1\sin\mu_1 + (1-\beta)\cos\theta_2\sin\mu_2}{\sqrt{\Delta^{*2} + \left[\alpha\sin\theta_1 + (1-\beta)\sin\theta_2\right]^2}} \tag{11.6}$$

$$\zeta = \frac{\frac{\Delta}{H} - \alpha\cos\theta_1\sin\mu_1 + (1-\beta)\cos\theta_2\sin\mu_2}{\sqrt{\Delta^{*2} + \left[\alpha\sin\theta_1 - (1-\beta)\sin\theta_2\right]^2}} \tag{11.7}$$

$$\frac{\Delta_{cyl}}{r_{cyl}} \approx \frac{e^{4v_f}}{\sqrt{v_f}} \int_{4v_f}^{\infty} \sqrt{x} e^{-x}\, dx \tag{11.8}$$

$$\frac{\langle\Delta\rangle_{disc}}{\bar{t}} = AR^{\frac{1}{3}} \frac{\Delta_{cyl}}{r_{cyl}} \tag{11.9}$$

$$AR = \frac{\bar{H}}{\bar{t}} \tag{11.10}$$

$$\langle\theta\rangle = \frac{\frac{\alpha}{2}\theta_1\sin\theta_1 + \frac{1-\beta}{2}\theta_2\sin\theta_2}{\alpha\sin\theta_1 + (1-\beta)\sin\theta_2} \tag{11.11}$$

$$\bar{\theta} = \frac{\theta_1 + \theta_2}{2} \tag{11.12}$$

$$\psi_T = \tan^{-1}\frac{\alpha\sin\theta_1 + (1-\beta)\sin\theta_2}{\Delta^*} \tag{11.13}$$

$$\Delta^* = \left\{ \left[\frac{\Delta}{H} - \alpha\cos\theta_1\sin\mu_1 + (1-\beta)\cos\theta_2\sin\mu_2 \right]^2 + \left[\alpha\cos\theta_1\cos\mu_1 - (1-\beta)\cos\theta_2\cos\mu_2\right]^2 \right\} \tag{11.14}$$

θ_1, θ_2, μ_1 and μ_2 refer to the angles at which the discs are presumed to be oriented, ψ_T is the twist angle, α and β are the relative locations where the crack front meets the discs, and Δ is the distance between a disc and the nearest disc. η and ζ are the ratios of undeflected to deflected crack lengths for the twisting and tilting, respectively. v is the Poisson's ratio and is assumed to be 0.35.

List of Publications

Journal Papers

D. Carolan, H. M. Chong, A. Ivankovic, A. J. Kinloch, and A. C. Taylor. Co-continuous polymer systems: A numerical investigation. *Computational Materials Science*, 98(0):24-33, 2015.

H. M. Chong and A. C. Taylor. The microstructure and fracture performance of styrene-butadiene-methylmethacrylate block copolymer-modified epoxy polymers. *Journal of Materials Science*. 48(19):6762-77, 2013.

Conference Papers

A. C. Taylor and H. M. Chong. Mechanical properties and toughening mechanisms of epoxy modified with block copolymers. *38th Annual Meeting of the Adhesion Society, 20-25 February 2015, Savannah, USA*, 2015.

D. Carolan, H. M. Chong, A. C. Taylor, A. Ivankovic, and A. J. Kinloch. Energy dissipation mechanisms in co-continuous polymer structures. *7th International Conference on Fracture of Polymers, Composites and Adhesives, 14-18 September 2014, Les Diablerets, Switzerland*, 2014.

H. M. Chong and A. C. Taylor. The fracture performance of hybrid silica nanoparticle/block copolymer-modified epoxy polymers. *5th World Congress on Adhesion and Related Phenomena, 7-11 September 2014, Nara, Japan*, 2014.

H. M. Chong and A. C. Taylor. The effect of graphene nanoplatelets on the fracture toughness of epoxy polymers. *5th World Congress on Adhesion and Related Phenomena, 7-11 September 2014, Nara, Japan*, 2014.

H. M. Chong and A. C. Taylor. The fracture performance of hybrid silica nanoparticle/block copolymer-modified epoxy polymers. *10th European Adhesion Conference*

(EURADH) 2014, 22-25 April 2014, Alicante, Spain, 2014.

H. M. Chong and A. C. Taylor. The microstructure and fracture performance of hybrid silica nanoparticle/block copolymer-modified epoxy polymers. *37th Annual Meeting of the Adhesion Society, 20-25 February 2014, San Diego, USA*, 2014.

H. M. Chong and A. C. Taylor. The effect of graphene nanoplatelets on the fracture toughness of epoxy polymers. *37th Annual Meeting of the Adhesion Society, 20-25 February 2014, San Diego, USA*, 2014.

H. M. Chong and A. C. Taylor. The effect of graphene nanoplatelets on the fracture toughness of epoxy polymers. *Adhesion '13, 4-6 September 2013, York, UK*, 2014.

H. M. Chong and A. C. Taylor. The microstructure and fracture performance of block copolymer-modified epoxy polymers. *36th Annual Meeting of the Adhesion Society, 3-6 March 2013, Daytona Beach, USA*, 2013.